Silk Based Three Dimensional Bioprinting for Meniscus Tissue Engineering

A Thesis

Submitted in Partial Fulfilment of the

Requirements for the Degree of

DOCTOR OF PHILOSOPHY

by

ASHUTOSH BANDYOPADHYAY

Department of Biosciences and Bioengineering

Indian Institute of Technology Guwahati

Guwahati – 781039, Assam, India

June 2024

Dedicated to my Family and Friends

"ज्ञानं कर्म च कर्तव्यं अविरिष्टं च सर्वथा||"

"ज्ञान और कर्म सभी परिस्थितियों में संतुलित होना चाहिए||"

"Knowledge and action should be balanced in all circumstances."

INDIAN INSTITUTE OF TECHNOLOGY GUWAHATI

DEPARTMENT OF BIOSCIENCES AND BIOENGINEERING

STATEMENT

I do hereby declare that the research findings of this thesis are the result of research work carried out by me in the Department of Biosciences and Bioengineering, Indian Institute of Technology Guwahati, Guwahati, India, under the supervision of Prof. Biman B. Mandal.

As per the general norms of reporting research findings, due acknowledgments have been made, wherever the research findings of other researchers have been cited in this thesis.

Date: 25/01/2024

Ashutosh Bandyopadhyay

INDIAN INSTITUTE OF TECHNOLOGY GUWAHATI

DEPARTMENT OF BIOSCIENCES AND BIOENGINEERING

CERTIFICATE

It is certified that the work described in this thesis entitled "***Silk based three dimensional bioprinting for meniscus tissue engineering***" by **Mr. Ashutosh Bandyopadhyay** for the award of degree of **Doctor of Philosophy (Ph.D.)** is an authentic record of the results obtained from the research work carried out under my supervision in the Department of Biosciences and Bioengineering, Indian Institute of Technology Guwahati, India, and this work has not been submitted elsewhere for the award of any other degree.

Ashutosh Bandyopadhyay
(Candidate)
Roll No: 176106019

CERTIFIED

Biman B. Mandal, Ph.D.
(Thesis Supervisor)

ACKNOWLEDGEMENTS

Ph.D. has been a life changing and transformative journey for me. To imagine and realise myself in this juncture of life is to be appreciative of the support and guidance that I received from the numerous people from all paths of life.

First and foremost, I would like to express my sincere gratitude to my thesis advisor and mentor Prof. Biman B. Mandal, for his constant help, support, opportunities, and guidance. His continuous motivations, reality checks, anchoring and steering has been a key towards my journey of becoming an independent researcher. His insights and inputs in the scientific domain were instrumental in shaping my thesis over the years. Being in the Biomaterials and Tissue Engineering laboratory has been a superlative and enriching experience personally, academically, and professionally.

I would express my sincere gratitude towards my Doctoral committee members: Prof. Bithiah G. Jaganathan and Prof. Manish Kumar from Department of Biosciences and Bioengineering, IIT Guwahati and Prof. Lal Mohan Kundu from the Department of Chemistry, IIT Guwahati. Their invaluable suggestions and scientific inputs and discussions helped improve my thesis work.

I would also thank the present and former Heads of Department of Biosciences and Bioengineering, IIT Guwahati; Prof. Rakhi Chaturvedi, Prof. Latha Rangan and Prof. Kannan Pakshirajan for extending their support through various academic and research activities and departmental instrumentation facilities. I acknowledge the support received from the Department of Biosciences and Bioengineering, IIT Guwahati, administrative and technical staff in providing and maintenance of research infrastructure. I am also grateful to all staff of the Institute R&D section, Student Affairs, and Academic section for all their help throughout my Ph.D. tenure. I would also acknowledge the Central Instrumentation Facility (CIF) IIT Guwahati for providing the high-end instrumentation facilities.

I gratefully acknowledge the funding received from the funding agencies that provided me the financial support to conduct my research. I am grateful to the funding support from several research grants received by Prof. Mandal from Department of Biotechnology (DBT), Science and Engineering Research Board (SERB) and Department of Science and Technology (DST) Government of India. I am sincerely grateful to Ministry of Education (MoE) and IIT Guwahati for providing me with fellowship during my Ph.D. tenure.

I would like to express my sincere gratitude to all my collaborators Prof. Samit K. Nandi (West Bengal University of Animal and Fishery Sciences, Kolkata, India) for helping with the animal experiments and Dr. Manoj Agarwala (GNRC Institute of Medical Sciences, Guwahati, India) for extending his help towards the collection of samples from the hospital. I acknowledge Prof. Niranjan Karak (Department of Chemical Sciences, Tezpur University) and Prof. V. Manivannan. (Department of Chemistry, IIT Guwahati) for scientific collaborations.

I would like to extend my special thanks to Dr. Nandana Bhardwaj (Department of Science and Mathematics, IIIT Guwahati) for collaborative works and giving her invaluable suggestions and scientific advice whenever needed. Her friendly guidance, unconditional support and technical suggestions were instrumental in my thesis work.

It is indeed my pleasure and delight to thank all of my lab mates for providing a positive, cooperative and scientific environment. They have been critical part of my professional, academic and personal journey and helped me

through the thick and thin. I want to thank my beloved seniors Dr. Manishekhar, Dr. Praveen, Dr. Dimple, Dr. Bibhas, Dr. Ankit, Dr. Shreya, Dr. Yogendra, Mr. Omkar, Dr. Joseph, Dr. Janani and Ms. Sohenii for their immense support and guidance in all of my personal, academic and professional fronts. My Ph.D. journey wouldn't have been so delightful without your presence. I would also especially thank my current lab-mates Bibrita, Chitra, Souradeep, Sayanti, Kodieswaran, Rajat, Sanu, Maheswari, Puja, Victoria, Richa, Ravi, Saki, Komal, Arnab and Aman, and my former lab mates Dr. Deepika, Dr. Rajiv, Dr. Chandramouli, Dr. Bhaskar, Dr. Priyanka, Dr. Avipsa, Dr. Vimal, Dr. Aparajita, Tarishi, Soumashree, Jennie, Dr. Namit, Suvro, Prerna, Monisha, Smriti, Nikhil, Sakshi, Princy, Sangeeta, Anupam, Nakhul, Priyanka, Azole, Vaishali, Swapnil, Gaurang, Prerna, Triya, Himanjal, Rupam, Saptarshi, Amritha, Vartik, Shubham, Anushka, Shruti, Varnit, Pragya, Sayantanee, Eshani, Baishali, Animesh and Ananya for the great company, scientific feedback, formal discussion and making countless memories that I am going to cherish forever. I would also like to extend my special gratitude to Dr. Araghni (IIT Guwahati), Samiran (Tezpur University), Dr. Samsamul (WBUAFS) and Dr. Debajyoti (WBUAFS) for their collaborations, scientific inputs, and help.

Thanks to my fellow marathon runners Dr. Joseph, Dr. Yogendra, Dr. Praveen and Dr. Prerak who taught me the art of running, helped me gain perseverance and kept me healthy, happy, and stress-free. I thank my friends at IIT Guwahati Dr. Chandi, Santanu, and Priyam for their company and their camaraderie during my journey.

I am grateful to have furry friends near my lab, whom I took care of, for teaching me patience and making me a better empathetic human.

Finally, I would be indebted to my parents, sister (Aditi), wife (Nabagata), mama, mami, pishi, pisha and other family members for their unconditional love and support in shaping everything in my life. You walked miles barefoot to make sure that I could run towards my dreams. Your immense patience, countless sacrifices and exceptional faith motivated me to persist in this journey and undertake any difficulties and challenges head-on.

Thank you, Universe and its maker, for showering your grace and blessings upon me.

Ashutosh Bandyopadhyay

THESIS ABSTRACT

Meniscus is a fibrocartilaginous avascular tissue present in the knee joint between the femoral condyles and tibial plateau. The heterogenous cellular composition of fibrogenic, chondrogenic and fibrochondrogenic phenotypes and extracellular composition of collagen, glycosaminoglycans and adhesion glycoproteins dictates the physiological function of this load-bearing tissue. Meniscus is prone to tears and injuries due to various trauma, accidents, and physiological conditions. These tears are conventionally treated with resection, suturing and implants. Most of them have their respective drawbacks related to patient-specificity for size and shape, material properties, cellular make-up and mechanical resilience being the major factors. This thesis identifies the requisite design considerations for treatment of full and partial thickness meniscus tears of both larger and smaller dimensions. 3D printing, injectable hydrogel and ultrasound-based strategies have been explored to potentially treat meniscus defects. Silk fibroin from mulberry (*B. mori*) and non-mulberry (*A. assama*) sources have been blended with various other bioactive polymers to formulate shear-thinning and thermo-reversible hydrogel inks for 3D printing and injection.

In the first objective, a silk fibroin/gelatin based bioink was formulated to 3D print physiologically relevant meniscus constructs to recapitulate the tri-layered macro-architecture of the native meniscus. The seeded fibrochondrocytes were found to be proliferating and maintaining their phenotype on these constructs. In the second objective, we formulated a photo-polymerizing silk-fibroin methacrylate(silkMA)/gelatin methacrylate (gelMA)/A. assama ink for encapsulation of growth factor loaded microspheres. These microspheres were loaded with fibrogenic and chondrogenic differentiation factors and used for fabricating constructs that aided in mimicking the zonal biochemical and cellular makeup of the red, red-white and white zones of the meniscus. In the third objective, we further enhanced the biomaterial-ink composition with polyethylene glycol di-methacrylate (PEGDMA) and autologous growth factor rich plasma (GFRP) to formulate silkMA/gelMA/PEGDMA/GFRP ink. The constructs 3D printed using this ink composition enabled sustained release of growth factors, slowed degradability and significantly enhanced mechanical resilience. The printed constructs also aided in fibrochondrogenic differentiation of neonatal human stem cells *in vitro*. This photo-polymerizing ink was further improved with polyethylene glycol di-acrylate (PEGDA) to formulate silkMA/gelMA/PEGDA/GFRP hydrogel in the fourth objective for minimally invasive injectable treatment approach for smaller meniscus tears. This hydrogel composition aided in neonatal stem cell proliferation, migration and fibrochondrogenic differentiation *in vitro*. *In vivo* evaluation yielded healing of full-thickness tears of the meniscus using this hydrogel composition. In the fifth objective, the injectable hydrogel composition was further used for 3D printing of constructs that were seeded with neonatal human stem cells and stimulated with low intensity pulsed ultrasound (LIPUS). This augmented the differentiation towards fibrochondrogenic phenotype and extracellular matrix deposition.

Thus, the biomaterial inks, injectable hydrogel composition and the LIPUS stimulation approach evaluated and demonstrated in this thesis could be envisaged for the development of holistic patient-specific clinically applicable meniscus tear remediation strategies in the future.

TABLE OF CONTENTS

ABBREVIATIONS

µL	:	Microliter
µm	:	Micrometer
µM	:	Micromolar
2D	:	2-dimentional
3D	:	3-dimentional
AA	:	Antheraea assama/ Antheraea assamensis
ACAN	:	Aggrecan
ADAMTSs	:	A Disintegrins and metalloproteinases with thrombospondin motifs
ADMSCs	:	Adipose derived mesenchymal stem cells
BMMSCs	:	Bone marrow derived mesenchymal stem cells
BMMA/ silkMA	:	Bombyx mori methacrylate
CAD	:	Computer aided design
CBFA1	:	core-binding factor subunit alpha-1
CCN2	:	Cellular Communications Network Factor 2
CD68	:	Cluster of differentiation 68
CEACAM	:	Carcinoembryonic antigen-related cell adhesion molecules
COX	:	Cyclooxygenase
CT	:	Computed tomography
CTGF	:	Connective Tissue Growth Factor
Cy5	:	Cyanine5
DAB	:	3,3'-diaminobenzidine
DAPI	:	4′,6-diamidino-2-phenylindole
DICOM	:	Digital Imaging and Communications in Medicine
DLP	:	Digital light processing
DMEM	:	Dulbecco's modified eagle medium
DMMB	:	1,9-dimethylmethylene blue
DNA	:	Deoxyribonucleic acid
ECM	:	Extracellular matrix
EDC	:	1-ethyl-3(3-dimethyl aminopropyl) carbodiimide
EDTA	:	Ethylenediaminetetraacetic acid
ELISA	:	Enzyme linked Immunosorbent Assay
FBS	:	Fetal bovine serum
FESEM	:	Field emission scanning electron microscope
FDA	:	Food and drug administration
FDM	:	Fused deposition modelling
FGF	:	Fibroblast growth factor
FITC	:	Fluorescein isothiocyanate
FTIR	:	Fourier transform infrared spectroscopy
G′	:	Storage modulus
G″	:	Loss modulus
GAPDH	:	Glyceraldehyde-3-phosphate-dehydrogenase
GelMA	:	Gelatin methacryloyl
GFs	:	Growth factors
GFRP	:	Growth Factor Rich Plasma
GPa	:	Gigapascal

h/hr/hrs	:	Hour/hours
H&E	:	Hematoxylin and eosin
HA	:	Hyaluronic acid
HCl	:	Hydrochloric acid
HYP	:	Hydroxyproline
hwJMSCs/ wJMSCs	:	Human Wharton's Jelly Mesenchymal Stem Cells
IHC	:	Immunohistochemistry
IL	:	Interleukin
IPN	:	Interpenetrating network
iPSCs	:	Induced pluripotent stem cells
ITS+	:	Insulin-transferrin-sodium selenite
kDa	:	Kilo dalton
kPa	:	Kilopascal
kV	:	Kilo volt
LED	:	Light Emitting Diode
LiBr	:	Lithium bromide
LIPUS	:	Low Intensity Pulsed Ultrasound
LPS	:	Lipopolysaccharide
LVER	:	Linear viscoelastic region
M	:	Molar
mg	:	Milligram
min	:	Minutes
mL	:	Milliliter
mM	:	Millimolar
mm	:	Millimeter
MMPs	:	Matrix metalloproteinases
MPa	:	Megapascal
MRI	:	Magnetic resonance imaging
MSCs	:	Mesenchymal stem cells
MTT	:	3-(4,5-dimethylthiazol-2-yl)-2,5-diphenyltetrazolium bromide
MW	:	Molecular weight
MWCO	:	Molecular weight cut-off
NBF	:	Neutral buffered saline
NF-κB	:	Nuclear factor kappa B
ng	:	Nanogram
NHS	:	N-hydroxysuccinimide
nM	:	Nanomole
nm	:	Nanometer
OA	:	Osteoarthritis
pADSCs/ pADMSCs	:	Porcine Adipose derived Mesenchymal Stem cells
PBS	:	Phosphate buffered solution
PCL	:	Poly(ε-caprolactone)
PDLLA	:	Poly(D,L-lactide)
PDMS	:	Polydimethylsiloxane
PEGDA	:	Poly(ethylene glycol) diacrylate
PEGDMA	:	Poly(ethylene glycol) dimethacrylate
pg	:	Picogram
PGA	:	Polyglycolic acid

PGE2	:	Prostaglandin E2
PLGA	:	Poly(lactic-co-glycolic)
PLLA	:	Poly(L-lactic acid)
PNIPPAm	:	Poly(N-isopropyl acrylamide)
PRP	:	Platelet rich plasma
PTGS2	:	Prostaglandin-endoperoxide synthase 2
PVA	:	Polyvinyl alcohol
PVP	:	Poly(vinyl pyrrolidone)
RGD	:	Arginine-glycine-aspartic acid
RHOA	:	Ras homolog family member A
ROCK1	:	rho-associated, coiled-coil-containing protein kinase 1
RNA	:	Ribonucleic acid
RT	:	Room temperature
RT-PCR	:	Real time polymerase chain reaction
RUNX-2	:	Runt-related transcription factor 2
SD	:	Standard deviation
SDS	:	Sodium dodecyl sulfate
SEM	:	Scanning electron microscopy
SF	:	Silk fibroin
SS	:	Silk sericin
STL	:	Stereolithography
sGAGs	:	Sulfated glycosaminoglycans
tan δ	:	Loss Factor = Loss modulus/storage modulus
TCP	:	Tissue culture plate
TEAD	:	Transcriptional enhancer factor TEF-1 also known as TEA domain family member 1
TGF-β	:	Transforming growth factor-β
TIMPs	:	Tissue inhibitors of MMPs
TNF-α	:	Tumor necrosis factors-α
UTM	:	Universal testing machine
v/v	:	Volume/volume
w/v	:	Weight/volume
YAP	:	yes-associated protein
µg	:	Microgram
ω	:	Angular frequency

LIST OF TABLES

LIST OF FIGURES

List of Figures

CHAPTER 3

CHAPTER 1

Introduction and review of literature

This chapter provides a comprehensive overview of the current status of meniscus tissue engineering and the application of various treatment modalities applied for the same. The review of literature encompasses the different characteristics of meniscus tissue and the mechanical forces borne by the menisci, the various meniscal tears, their types, their healing pathways and conventional treatment modalities. Though conventional treatments include meniscus implants, they suffer several drawbacks which prompts focus on the design considerations, materials used, cell sources and fabrication techniques. This chapter also enlists various advantages of silk fibroin and its blends towards fabrication of mechanically resilient tissues. This chapter provides an overview of the various 3D printing techniques, the current state of injectable hydrogels and the mechanical stimulation approaches for meniscus tissue engineering.

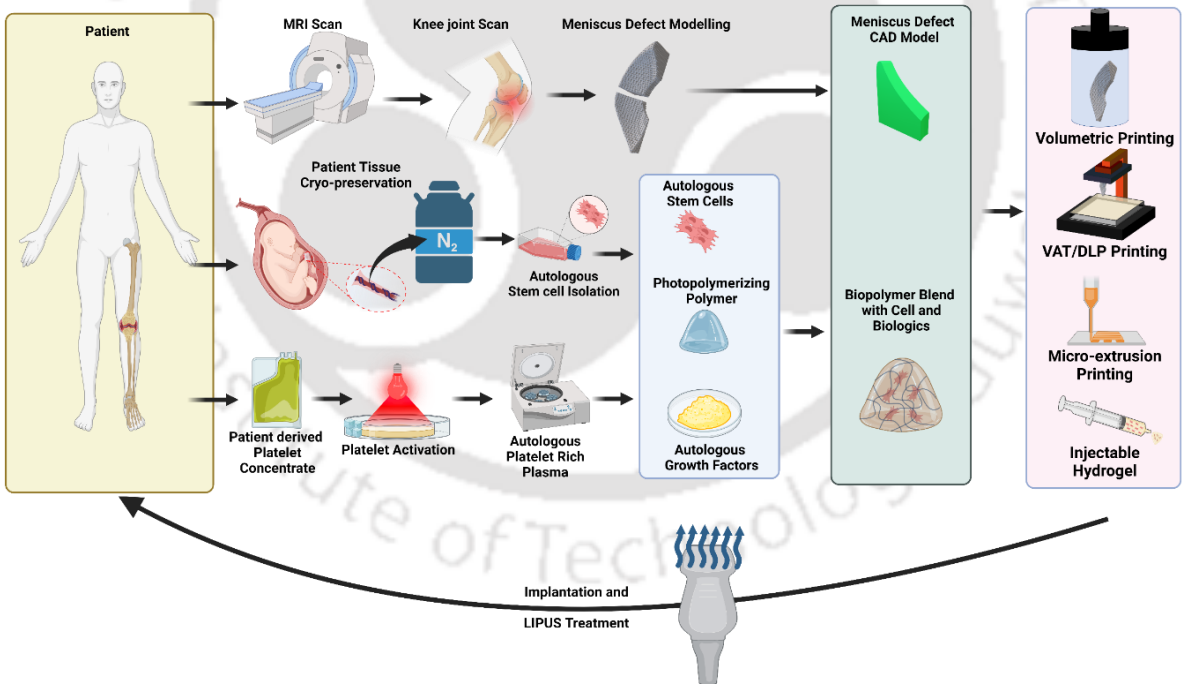

Parts of this chapter have been published as:

- Ashutosh Bandyopadhyay, Suvro Kanti Chowdhury, Souradeep Dey, Joseph Christakiran Moses, and Biman B. Mandal. '*Silk: A promising biomaterial opening new vistas towards affordable healthcare solutions*', ***Journal of the Indian Institute of Science*** 2019, 99(3), 445-487. **DOI:** 10.1007/s41745-019-00114-y.

- Ashutosh Bandyopadhyay**,** Baishali Ghibhela, Biman B. Mandal. '*Current advances in engineering meniscal tissues: Insights into 3D printing, injectable hydrogels and physical stimulation based strategies*', ***Biofabrication*** 2024, 16(2), 022006. **DOI:** 10.1088/1758-5090/ad22f0

1.1 Introduction

Meniscus is a glossy-white fibro-cartilaginous tissue present in duplicate between femoral condyles and tibial plateau in the knee joint to prevent degeneration of the articular cartilage. Meniscus tissue is majorly composed of cells and specialized ECM components such as collagen, elastin, sulphated glycosaminoglycans and other adhesion glycoproteins [1, 2]. Its semi-lunar wedge-shaped structure confers compressive stress to the inner region and tensile hoop stress to the outer edges. A fully functional meniscus is vital for the homeostasis of the knee joint, load bearing, load transmission, shock absorption, joint stability and joint lubrication [2].

1.1.1 Complexity of meniscal tissue: cellularity, biochemical composition and mechanical properties of meniscus

The meniscus is considered a mechanically biphasic viscoelastic tissue comprising of a porous and permeable phase of collagen and proteoglycan accommodating the other phase of water and salts [3-5]. Superficial meniscus layers house oval and fusiform fibroblasts-like cells, while the deeper meniscus zones contain rounded chondrocyte-like cells [6-9] **(Figure 1.1 A)**. This heterogenous population of cells, reported as meniscal fibrochondrocytes [6-12], exhibit both fibroblastic and chondrocytic morphology and gene expression patterns. The major cellular phenotypes of the knee menisci have been determined to be chondrocytic, fibroblastic, fibrochondrocytic and endothelial. Endothelial cells maintain the microvasculature towards the outer meniscus [11, 13-16], inner chondrocytic cells exhibit articular cartilage like properties [17-22] and outer cells maintain fibroblastic characteristics [7, 17, 19, 21] and aid in cell migration and tissue remodelling post-injury.

Fibrillar collagen protein in meniscus is aligned randomly in the superficial and lamellar layers, circumferentially in the deep layer and as radial tie fibers throughout the meniscus conferring mechanical integrity and endurance to hoop stresses [23]. Collagen fibers are oriented amorphously in superior superficial and lameller layers, radially in the inferior superficial layer, circumferentially in deep layer and as short radial fibers in posterior and anterior horns and the deep layer [24-27]. Meniscus matrix contains a miniscule amount of elastin (<1% of dry weight), hypothesized to confer resilience and high strain recovery cycles [28]. Proteoglycans, protein cores decorated with glycosaminoglycans (GAGs), attract water and assist in maintaining hydration, lubrication and compressive stiffness during load bearing. Inner two-thirds of the menisci show vast synthesis and deposition of GAGs which progressively reduces towards the outer regions [29-32]. Minute amounts of adhesion

glycoproteins (collagen type VI, fibronectin and thrombospondin) facilitate cell binding via Arginine-Glycine-Aspartic acid (RGD) motifs [26].

Wedge shaped menisci grant surface congruency and stability to the femoral head during articulation with the tibial plateau **(Figure 1.1 A)** and act as spacers between the articulating cartilages, reducing their contact to 10% [33]. Their microscopic architectural features impart tensile stiffness, resistance to mediolateral splitting [27, 34] and tensile hoop stresses [35], and compressive integrity [36]. They are fixed into place by several attachment points, in their anterior and posterior horns as well as medial and lateral sides, connecting them to the ligaments and stabilizing the knee joint **(Figure 1.1 B)**. Inner meniscus experiences highest compressive stress and outer edges undertake tensile hoop stress. Spatially organized proteoglycans bear the compressive loading while collagen fibrils withstand tensile stresses [37]. Posterior and anterior attachments of menisci on the tibial plate prevent radial displacement, enabling radial deformation via hoop stress under femoral load, thus sparing the tibial cartilage. Despite varying joint flexion and tissue health, menisci bear 45-75% [33, 36, 38] of the elevated joint load during daily activities [39] such as walking or ascending stairs. Menisci demonstrate anisotropic load bearing at full extension, with the medial meniscus bearing only 50% of the medial load. The anisotropic collagen fibers within the menisci absorb shocks of varying load frequencies [24]. In the absence of the menisci, the femoral condyles are destabilized, concentrating the joint load and 2-3 times the normal stress on the hyaline cartilages [38].

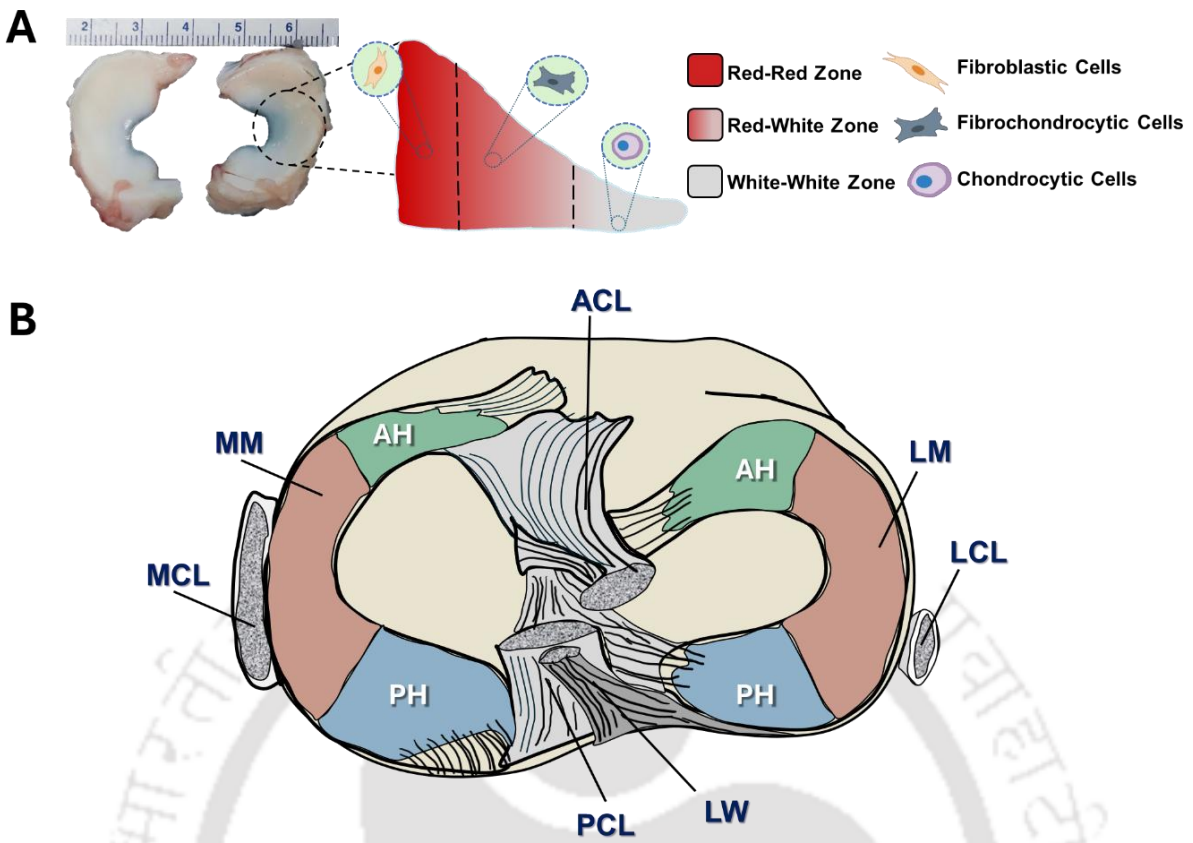

Figure 1.1: *(A) Representative image of porcine menisci isolated from adult pig and schematic representation of the various regions of the meniscus according to the presence of vasculature and the respective cellular phenotype majorly present in these regions. (B) Schematic showing the anatomy of native meniscus. ACL: Anterior Cruciate Ligament, PCL: Posterior Cruciate Ligament, LM: Lateral Meniscus, MM: Medial Meniscus, AH: Anterior Horn, PH: Posterior Horn, LCL: Lateral Collateral Ligament, MCL: Medial Collateral Ligament, LW: Ligament of Wrisberg.*

1.1.2 Meniscus Tears

An estimated 1 million cases of meniscus tear occur in India each year and the United States counts for the highest incidence of intra-articular knee damage with a major chunk preferring meniscectomy [40-42]. Meniscus injury/tear is known to be responsible for causing abnormal stress distribution, instability in the knee joint, reduced lubrication, and articular cartilage degeneration. Chronic effects of meniscal injuries are substantial and about 50% of all patients develop osteoarthritis (OA)[43, 44]. Commonly occurring meniscus tears and injuries due to trauma, sports and age-related degeneration are: radial, vertical, longitudinal, oblique and horizontal tears[45, 46]. The risk of these injuries increases in the case of frequently occurring development abnormalities of lateral menisci, such as a discoid meniscus which consists of an extended inner portion forming a disc like shape [23]. Though healing of menisci is possible in the outer vascular regions, injuries at inner regions of meniscus affect normal functioning. Poor vascularization of inner meniscus hinders the healing process [2, 47]

accompanied by formation of fibrous tissue with impaired mechanical properties [23, 48]. Particularly, the larger and complex tears have limited repairing capacity, especially if there is any knee instability due to additional ligamentous trauma [49]. Additionally, loss of meniscus tissue causes higher peak stresses on the articular cartilage as well as swelling and locking of the knee joint, resulting in cartilage degeneration and osteoarthrosis [43, 50-52]. Therefore, providing an effective treatment modality is of utmost important to prevent the current scenario.

1.1.3 Meniscus Pathology

Though normal meniscus is composed of lateral and medial wedge-shaped semi-circular structures (**Figure 1.2 A i**), many deviations can exist due to abnormalities caused by developmental disorders, disease, degenerative conditions or traumatic injuries. The most commonly occurring abnormal development in lateral menisci is a discoid meniscus, having an extended inner portion forming a disc-like shape (**Figure 1.2 A ii**). This condition occurs in a very small population of 0.4–5% [53]. Though majorly left undetected they might can cause occasional locking of the knee and pain and are more susceptible to tears.

Meniscus may also be inflicted with metabolic diseases such as calcium pyrophosphate crystal deposition, hemochromatosis, and ochronosis, resulting in calcification, gross discoloration, and interference with the overall consistency of the tissue[4]. Though causes of meniscal degeneration are mostly undiscovered, but degeneration of the meniscus makes it prone to injuries [4, 54]. Osteoarthritic condition causes degenerative changes in meniscus and hyaline cartilage of the knee leading to meniscal injuries. Studies have found that meniscal injury is prevalent in around 75% of patients with osteoarthritis [55-57]. Osteoarthritis affects the geometry of the menisci and causes thickening of the meniscus horns, in turn compromising the biomechanics of the meniscus [58]. Changes in the biochemical content of the meniscus can be caused due to osteoarthiritis [59]. Severe osteoarthiritis may cause the medial joint space to become narrow and result in loss of meniscus functionality as well as its degeneration [60] can be an important contributor to meniscal injuries.

Early approaches to (prior to the mid-1960s) meniscal damage were limited to total resection of meniscus known as meniscectomy [61]. Later, the surgical interventions were modified to partial resection, surgical repair and transplantation of the meniscus due to further studies revealing the importance of the meniscus tissue [52, 62-65].

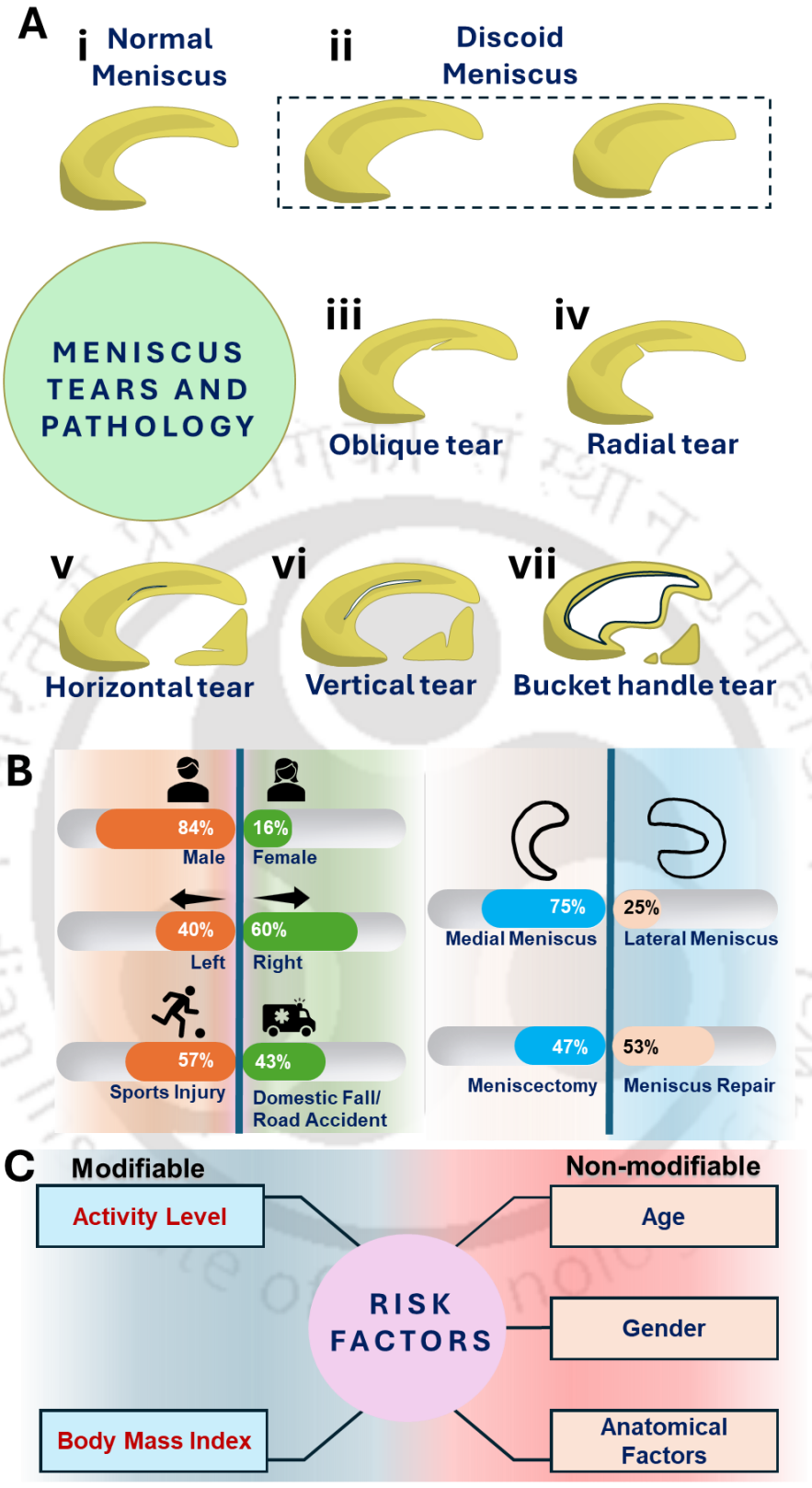

Figure 1.2: *(A) (i) Normal meniscus and (ii) Discoid meniscus morphology. Types of meniscus tears. (iii) Oblique tears, (iv) radial tears, (v) Horizontal tears, (vi) vertical longitudinal tear and (vii) bucket-handle tear (B) Statistics of meniscus tears as described by [66, 67]. (C) Risk factors to meniscus injury as described by [66].*

1.1.4 Types of meniscus tears and their consequences

The normal meniscus is smooth, wedge-shaped, and semicircular. Complex (degenerative) tears result in a jagged edge and combine many different types of tears. The major types of meniscal tears that can occur due to degeneration and/or trauma are : vertical longitudinal, oblique, radial, and horizontal tears [68]. The various kinds of meniscal tears have been shown in **Figure 1.2 A iii-vii**. Oblique tears and radial tears typically propagate from the inner portion of the meniscus to its periphery. Horizontal tears split the tissue into superior and inferior parts and also typically propagate outward. Vertical longitudinal tears, split the meniscus along the direction of collagen orientation. When a vertical longitudinal tear passes through the tissue's thickness it is called a bucket-handle tear.

Due to its inhomogeneity, meniscus self-repair is a difficult process. Though lesions or tears on the outer periphery can regenerate by the virtue of the higher extent of vascularization, but any damage to the inner avascular region is unable to heal on its own [2, 4, 48].

Injury of the vascular sites leads to proinflammatory healing pathway to form a fibrous scar tissue which further matures into a tissue with inferior mechanical properties after a few months[2, 16]. For injuries in the avascular region, only matrix reorganization may occur but it is not followed by a healing response [2, 69]. Moreover, torn menisci are most often calcified and followed by osteoarthiritis [56].

Even if the damaged regions undergo some repair, the regenerated tissue mostly lacks in quantity or has insufficient strength due to the avascular inhibitory environment. This necessitates the development of tissue engineering based technologies for meniscus healing and regeneration without calcification and apoptosis.

1.1.5 Epidemiology of meniscus tears and associated risk factors

Meniscal tears are known to compromise the structural integrity of the joint and lead to symptoms such as locking and catching of the knee, asensation and joint pain [48, 69]. According to a previously published survey, meniscus tears are more prevalent in the right knee (56.5%) [70]. They have been known to affect more men (70-80%) than women [69]. Moreover, men in the age group of 21–30 years and women in the age group of 11-20 suffer the most number of meniscal tears [69]. Traumatic tears are more common in younger patients while degenerative tears occur more often in old patients. In a recent study conducted in the Indian scenario, Chaudhary et al. [67] (**Figure 1.2 B)** reported in their meniscus repair study that among the total incidences of meniscus tears 84% occured in men while 16% in women.

Additionally, they observed the frequency of injury was higher for the right leg (60%) as compared to left leg (40%) and sports related injuries accounted for 57% while domestic fall/road accident accounted for 43% of the meniscus tears. As recently reported in the review of Gee et al. [66], ratio of medial:lateral meniscus tears is 3:1, with the exceptions of ACL tears which lead to a 1:1 ratio and occupations requiring kneeling which lead to a 20:1 ratio (**Figure 1.2 B)**. Jackson et al. [71], reported that higher fraction of surgeries of their 16 years single center study consisted of meniscus repair (53%) as compared to meniscectomy (47%) (**Figure 1.2 B)**. The various risk factors associated with the occurrence of meniscus tears (**Figure 1.2 C)** include several modifiable factors such as activity level and body mass index of the individual and non-modifiable factors such as the age, gender and anatomical characteristics of the knee joint (posterior tibial slope, medial meniscus slope, biconcave medial tibial plateau and meniscal-extrusion-causing knee malalignment) of the individual [66].

1.1.6 Current Treatment approaches

To address the meniscus tears, the strategy currently being employed as a gold standard treatment includes removal of total or partial meniscal tissue i.e., total/partial meniscectomy and sutures [43, 63, 72]. Though the above strategy delays the immediate onset of degeneration of articular cartilage; however, they increase the risk of osteoarthritis in the long run [50-52, 64, 68, 73].

Cadaveric meniscus allograft transplantation (MAT) is the primal graft in clinical practice till recent times for partial or total meniscectomy [74, 75]. They are sutured into meniscal root arthroscopically, which upon rehabilitation [76] aids in restoring knee mechanics for irreparable pathologies [77]. In certain cases of severe degeneration, meniscal allograft transplantations (MAT) have been used to replace the entire meniscus tissue [74, 77-80]. MATs are limited by lack of healthy cadaveric donors, processing and storage difficulties [65], implant method variations [78], loss of fixture [81], graft failure [82], extrusion [83], infection, arthrofibrosis, septic synovitis, hematoma, joint effusion, lack of proper sizing [76]. Current 3D implants, both natural and synthetic, are more compatible and tuneable but require additional procedures such as anterior cruciate ligament reconstruction (ACLR) or high tibial osteotomy (HTO) for better clinical outcomes [84]. CMI (Collagen Meniscus Implant) is the most frequently used FDA approved 3D fabricated natural material implant that has many reported long term clinical studies [85-88] with satisfactory performance and limited serious complications. Actifit [89-91] and NUsurface are the synthetic acellular implants with similar clinical outcomes to CMI [84, 92]. Actifit implants, composed of polyurethane and

polycaprolactone [93], are hypothesized to degrade over 5 years [94]. Despite their mechanical durability, both CMI and Actifit have significantly lower stiffness and lack viscoelasticity compared to the native menisci [95]. NUsurface, a non-anatomically shaped discoid implant designed with ultra high molecular weight polyethylene (UHMWPE) fibers reinforced with polycarbonate-urethane (PCU) [96, 97], is still under long term surgical evaluation. Moreover, Actifit and NUsurface do not replicate the microarchitecture of native menisci including the special orientation of the circumferential and radial collagen fibres. Despite the high failure rates due to shrinkage of implants and insufficient degradation along with uncertain long-term effects, current meniscal scaffolds endow chondroprotection and prevent secondary osteoarthritis as compared to non-surgical treatment strategies [65, 92, 98-100].

1.1.7 Tissue Engineering Approaches

Recently, the emergence of tissue-engineering approaches has become suitable alternative to the above-mentioned clinical strategies and mainstream choices in meniscus regenerative field [101-104]. Fabricating an ideal tissue-engineered meniscus requires specific biological and mechanical considerations such as cell types, biomaterial-based scaffolds, growth factors, bioreactor design, and environmental conditions to be addressed **(Figure 1.3)** in order to mimic the mechanical anisotropy of native tissues which can functionally replace the meniscus within short span of time while promoting the regeneration and repair of damaged tissues [102-105]. To date, a wide range of tissue-engineering techniques have been used for biomimetic applications including silk-collagen scaffold prepared by freeze-drying method[106, 107], BMSCs-laden extracellular matrix based injectable hydrogel [108], PLA (polylactic acid) based electrospun scaffolds with human meniscus cells encapsulated in ECM hydrogels [109, 110] and so on. Previous studies have highly explored on the mesenchymal stem cells (MSCs) augmented scaffolds owing to their tissue regeneration potential, multi-directional differentiation, mechanical strength, self-renewal, chondroprotection and immunomodulatory properties [111-113].

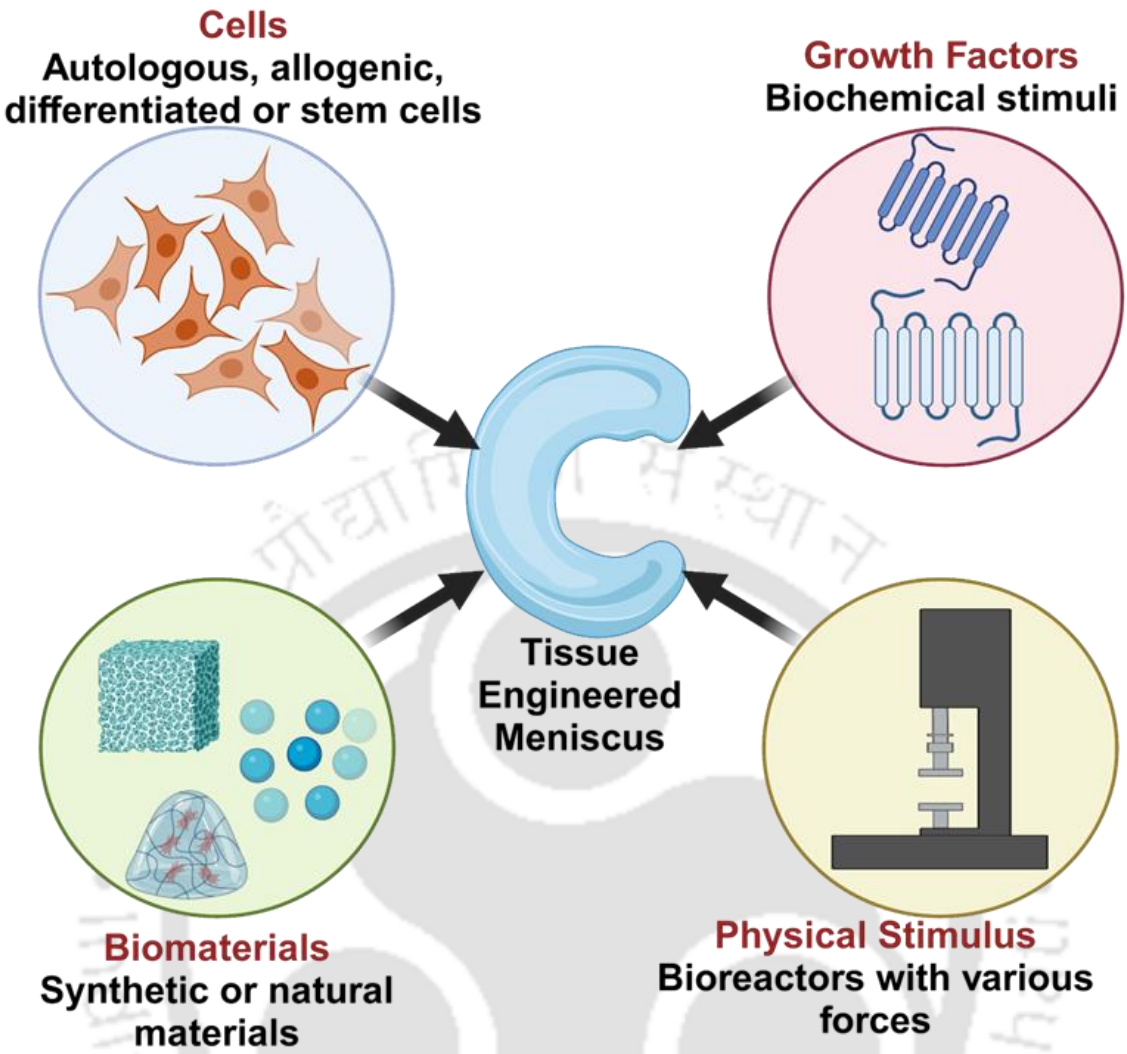

Figure 1.3: *Schematic showing the components of tissue engineering required for meniscus tissue engineering. (Made using www.biorender.com)*

Among several additive processing technologies in the field of tissue engineering, three-dimensional (3D) printing is one of the most promising ways to fabricate meniscal scaffold with controlled size, pores and microstructures [114] with optimal mechanical properties. In general, 3D printing manufactures the scaffolds in a layer-by-layer fashion based on 3D model data resulting in zone-specific cell differentiation to rejuvenate tissues mimicking the native menisci with patient's specificity [115]. 3D printer delivers the biomaterial-based hydrogel (e.g., biomaterial ink) with cells/without cells and other molecules to engineer the meniscal tissue [116]. Previously, many attempts have already been done to fabricate 3D printed meniscal scaffold using synthetic polymers such as poly(ε-caprolactone) (PCL), poly (lactic-co-glycolic acid) (PLGA), polylactic acid (PLA), Natural polymers such as collagen, gelatin, silk, and dECM bioink, as well as the blend of natural and synthetic polymers.

1.2 Review of Literature

1.2.1 Delineating the Design Considerations for 3D Printing of Meniscus

Meniscal tears and resection both can be partial thickness and full thickness which leads to the varying types of treatment strategies that need to be adapted for the irregularly shaped defects in an already structurally complex load bearing tissue. Early meniscus repair approaches were restricted to either total or partial resection/meniscectomy which yielded better short-term results than the non-surgical and conservative management [117-119] but these are reported to have severe degenerative changes in the long run [50-52, 62-64]. Later, following the realization of the importance of meniscus in the knee joint, surgical interventions such as repair and transplantation followed by rehabilitation were stressed upon [120, 121].

Due to the complex non-coherence of the meniscus ECM, cellular phenotypes and the specialized mechanical properties shown by the menisci, their self-repair as well as interventional repair is a truly difficult task. Outer region lesions and tears could be regenerated by the vascularization prevalent in the region but inner regions are scanty in terms of their healing capacity[48, 122-124] sometimes leading to calcification[125] and mostly leading to a mechanically compromised regenerative tissue. This necessitates the development of tissue engineering based approaches for meniscus healing and regeneration without calcification and apoptosis while maintaining the mechanical load-bearing capacity of the knee joint.

To our understanding and pre-knowledge, the foremost design consideration of any meniscal tissue engineering modality is the fabrication of constructs that mimic the internal layered collagenous fibrillar microarchitecture and the macroscopic semi-lunar wedge shape **(Figure 1.4)**. These in-turn should also give providence to the mechanical resilience of the tissue (tensile, compressive and shear strength) under static as well as dynamic loading conditions. The higher tensile loading capacity of menisci along the circumferential direction as compared to the radial direction and the higher compressive load bearing properties of the inner portions of the menisci as compared to the outer portions is a remarkable feat which is yet to be achieved by artificially fabricated meniscal implants. The mechanical stability of the meniscal implants also entails its ability to bear surgical implantations such as suturing and screwing procedures for affixation and withstanding the stresses generated by the attachment points along the tibial horns. Further, implants and treatment modalities need to be synthetic or natural or blended biocompatible and non-immunogenic implantable materials that possess cell attachment domains, support the proliferation of the diverse meniscal/progenitor cells, mimic

the biochemical make-up of the menisci, promote and support vascularization and be sustainably degradable with non-cytotoxic degradation products. The knee joint is a very susceptible region towards the development of inflammatory osteoarthritis pertaining to caused by abrasion[126] and biochemical changes[127]. Hence, non-inflammatory and immuno-compatible materials are of prime importance for meniscal treatment.

According to the literature, Rongen et al. [128] have defined the basic metrics for success a meniscal substitute, that aids in the prevention of articular cartilage damage and osteoarthritis. (1) Implants should match initial mechanical properties to native meniscus (compressive modulus range: 75–150 kPa, tensile modulus range: 75-150 MPa) as high-stiffness materials would prevent tissue ingrowth and damage the cartilage while soft and pliable materials would be insufficient for transfer of load and accumulate peak stress. (2) Fabricated implants should match the initial tribological properties (COF≤0.05) for smooth articulation. (3) The implants need to mimic the shape and size of the patient's meniscus with only an allowed variation of ±10% and a preference towards the slightly larger implants. (4) Implant materials need to be non-cytotoxic/non-carcinogenic along with its degradation products. (5) Cellular adhesion, migration, vascularization, and matrix deposition should be supported by the implant. (6) Tissue in-growth via highly interconnected and anisotropic macroporous (±200–300 μm) and microporous (±10–50 μm) architectures and optimal porosity (±70% or higher) is desired for the implant. (7) Optimal degradation profile for allowing tissue ingrowth, organization, maturation, and integration is essential for the implant. (8) Optimized of surgical fixation to enable the constructs bear the hoop stress, resist movements, and conform to the knee dynamics during flexion. (9) Inclusion of relevant bioactive moieties such as cell seeding, growth factor encapsulation and mechanical stimulation for accelerating the tissue organization and reducing the healing timeline.

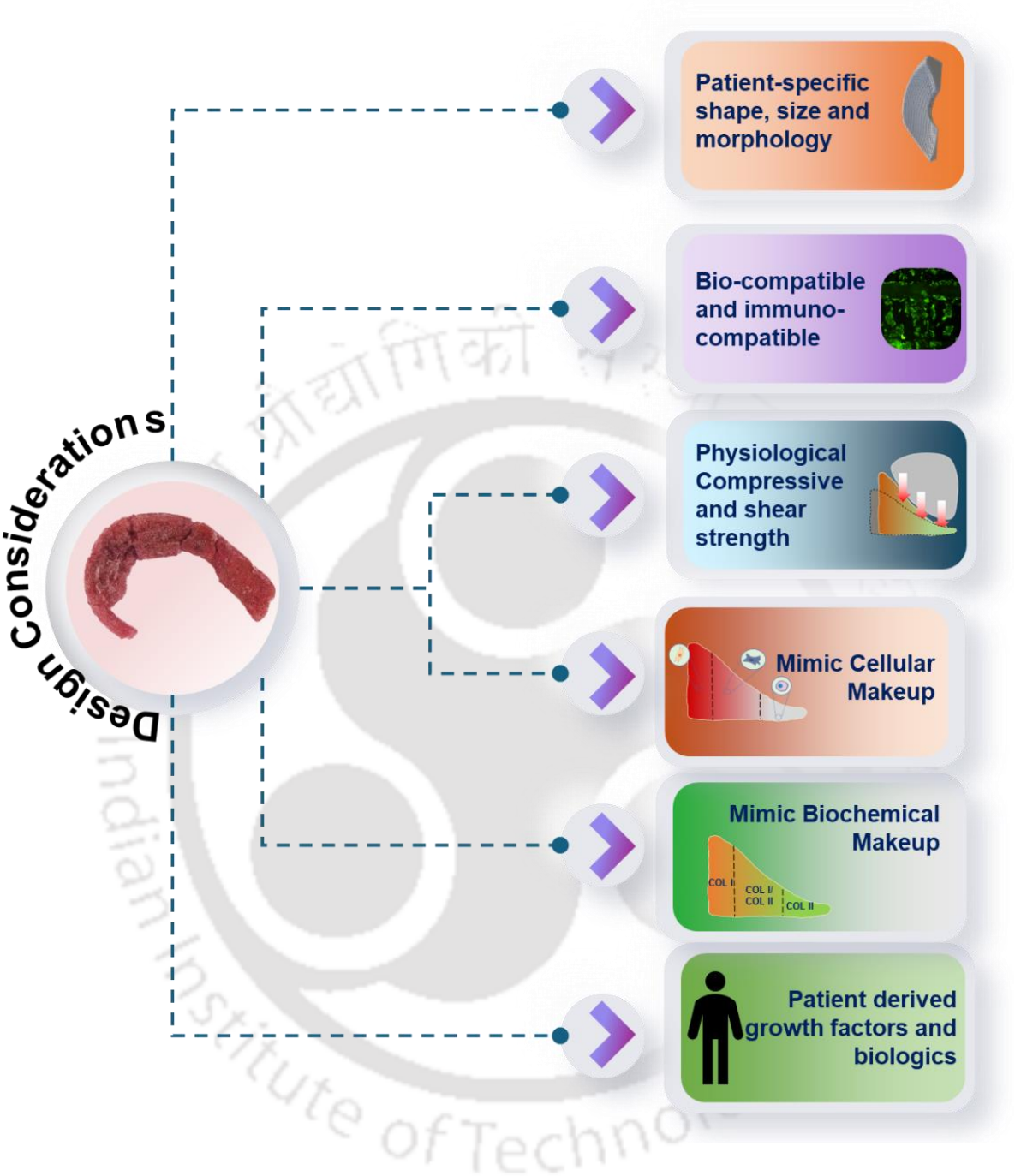

Figure 1.4: *Schematic showing the essential design considerations for meniscus construct fabrication.*

1.2.1.1 3D designing and computer aided modelling of knee menisci

There are various modes of computer aided designing a 3D printable tissue construct documented in the present literature which take into account the orientation of collagen fibrils within the menisci, their wedge-shaped macro-structure as well as their mechanical resilience. Reconstructing the meniscus using laser scanning and visual scanning methods **(Figure 1.5)** has been a common practice [129, 130]. Concomitantly, there have been customized designs

produced using CAD designing softwares for the fabrication of whole menisci as well [72, 131-133]. The most precise meniscus models from the patient could be achieved with the aid of MRI/ CT scan images and reconstructing the same using segmentation [72, 113, 114, 134-144]. In our study we adopted a hybrid approach where a reconstructed MRI model was used in conjunction with a 3D CAD designed model for fabrication of meniscus constructs [46]. The mechanical properties of menisci are dictated by the macro as well as micro architecture of the constructs. 3D printed models demonstrate design and material specific differences in their mechanical properties w.r.t. the changes in the infill pattern and densities. These can be refined based on the native meniscal strength characteristics and applied for fabrication. The discretion of selection of meniscal design should however rest with the opinion of medical professionals take the native micro-architecture of the menisci into consideration to optimize the load bearing, long term stability and the minimization of size and shape mismatch in the clinical setting.

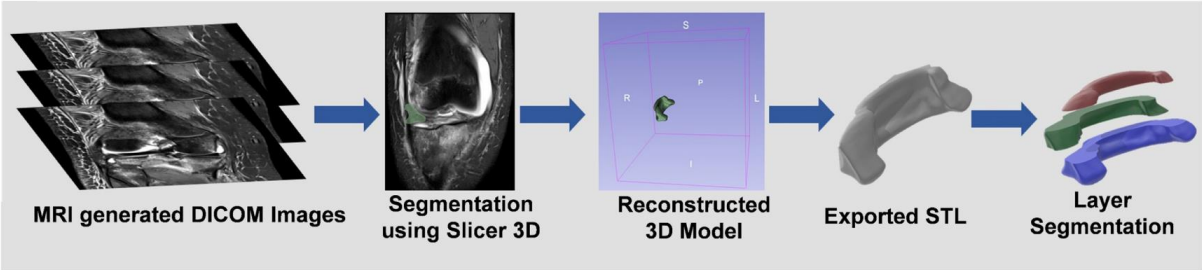

Figure 1.5: *Schematic showing the conversion of human meniscus MRI into 3D model where the MRI DICOM images are segmented manually and reconstructed using Slicer3D and exported as STL file post smoothing to generate patient specific model.*

1.2.1.2 Cell sources

The choice of cell source depends upon various underlying factors such as the regenerative potential of the cells, the ECM production potential, ease of availability, facile *in vitro* growing conditions and many more. The native meniscal fibrochondrocytes have been well characterized and employed extensively in the past for tissue engineering applications including their origin, biochemical secretion, response to growth factors and utilization in various meniscal tissue constructs [9, 11, 12, 30, 145-148]. While these cells could be chosen as optimal for meniscus tissue constructs but their relative scarcity and slower rate of proliferation inhibits their large-scale tissue engineering application. Henceforth, other progenitor and somatic cell types such as chondrocytes, mesenchymal stem cells, synovial cells

and embryonic stem cells have been used for various studies over the past decades [149-162]. However, in the present scenario the plethora of cell sources for meniscal regeneration using 3D scaffolds are listed in the **Table 1.1**.

Table 1.1: *Major cell sources used for meniscus tissue engineering and regeneration*

Cell classification	**Cell**	**Tissue source**	**Ref.**
Mature cells	Fibrochondrocytes	Meniscus	[46, 134, 149, 163-171]
	Chondrocytes	Cartilage	[107, 172-176]
Stem/ progenitor/ multipotent cells	Bone marrow-derived mesenchymal stem cells (BM-MSCs)	Marrow	[177-182]
	Synovium-derived mesenchymal stem cells (SMSCs)	Synovium	[183-188]
	Adipose-derived stem cells (ASCs)	Fat	[189-192]
	Meniscus-derived mesenchymal stem cells (MMSCs)	Meniscus	[193-195]

An ideal progenitor cell source for meniscus tissue engineering and regeneration applications should be resistant to cellular hypertrophy and terminal differentiation while also maintaining multi-potency. BM-MSCs, despite being relatively easy to collect and demonstrating strong chondrogenic differentiation potential, are a scarce population amongst other bone marrow cells [196] and are known to show propensity towards hypertrophic differentiation [197]. ADSCs can be derived as multi-potent cells from fat tissues [198] in large quantities but they are inferior to BM-MSCs in their chondrogenic potential [199]. SMSCs are a small population of colony forming progenitor cells that can be derived from the synovium by arthroscopic surgery [200] and are known to increase in number during meniscus injuries [183]. Though SMSCs possess a higher chondrogenic potential [201] as compared to BM-MSCs, but their high osteogenic potential [202] might prove detrimental in the long run. MMSCs are a very sparse population of multi-lineage differentiating cells on the menisci [203] that are very difficult to isolate. Hence their use has been limited for meniscal tissue engineering applications.

1.2.1.3 Material sources

As we have discussed in the previous section, materials used for the meniscus tissue engineering inclusive of the grafts, scaffolds, hydrogels and others could have significant effects on the homing, survivability, proliferation and synthetic profile of cells and profoundly influence the knee micro-environment. As the tissue is debrided and implants are sutured in place, materials dictate their integration with the host tissue. Meniscus ameliorative materials could be synthetic, natural and composites which uphold the ability of cell encapsulation, growth factor reservoir and sustained release, excellent compressive strain bearing, regulated degradation, generating non-cytotoxic degradation products and causing no inflammatory response. Micro-extrusion printing necessitates selection of a shear thinning polymer that can maintain its stability post extrusion to enable layer-by-layer fabrication of the implants, while low viscosity materials can be used for inkjet and nozzle-free 3D printing modalities [204]. Conventionally, synthetic materials such as PLLA [205-208], PGA and PGA/PLA composites [209-213], polyurethane and its composites [99, 214-218], polycarbonate based composites [219] and PCL and its composites [72, 134, 135, 138, 220-224] have been used for the micro-extrusion-based fabrication of meniscus scaffolds. Additionally, synthetic photocrosslinking polymers [225-227] undergo facile crosslinking and high-resolution printing using nozzle-free photocuring printers. They are known for their excellent mechanical strength and porosity. But they are limited by their inability to encapsulate cells and biologics (high temperature fabrication or use of organic solvents), poor cellular attachment without chemical modifications or coating with natural polymers, non-degradability and shrinkage and tensile and compressive non-congruence with the native meniscus. The lack of bioactivity has prompted the application of natural polymers for 3D printing of meniscus both in a standalone fashion and in conjunction with synthetic polymers for nozzle-based and nozzle-free printing. Natural material derived scaffolds have the advantage of enabling cellular and growth factor encapsulation, enhanced cell proliferation and biochemical synthesis. The major natural scaffolding materials that have been used for meniscal tissue engineering are collagen and its composites [85, 228-236], hyaluronic acid [237-243], agarose [224, 241, 244, 245], decellularized ECM from various tissues [109, 113, 138, 246-256], gelatin and its derivatives [220, 224, 257-262] and silk fibroin [46, 72, 106, 107, 208, 220, 223, 263-265]. The natural materials mimic the ECM as they are laced with enhanced cytocompatibility, cellular attachment domains in most cases, regulated degradability and non-cytotoxic degradation products, and immuno-compatibility. But these natural materials also suffer from mechanical instability, higher degradation to regeneration rate and the hazard of residual immunogenic

components. Natural polymers/polymer blends (as shown in **Table 4**) need to be biologically tuned to mimic the natural ECM and optimized for viscosity and crosslinking to realise intricate 3D models into standalone structures that mimic native meniscus physico-chemically and mechanically as well via nozzle-based and nozzle-free 3D printing. Recently the facile and versatile photo-polymerizing natural and synthetic polymers are on the rise in the field of tissue engineering due to their ease of applicability for fabrication of 3D architecture and inherent mechanical stability while being biologically active and compatible [266]. Jeencham et al. demonstrated the use of an injectable hydrogel composed of cellulose nanofibers, gelatin methacrylate (gelMA) and PEO-PPO-PEO-DA for meniscus tissue engineering applications [267]. Hao et al. integrated synovial aptamers within gelMA for the recruitment of endogenous cells for the repair of avascular meniscus lesions [268]. Prendergast et al. encapsulated meniscal fibrochondrocytes and norborene modified hyaluronic acid within gelMA hydrogels for fabrication of constructs that could be used for alignment of cells and ECM [269]. Bahcecioglu et al. fabricated zone-specific PCL scaffolds loaded with wither gelMA or agarose for mimicking meniscus specific biochemical composition [224]. Andress et al. used compositions of polyethylene glycol diacrylate (PEGDA) and gelMA for the fabrication of meniscal constructs embedded with cells for potential reversal of dedifferentiation of long-term meniscal cell culture [258]. Zihna et al. encapsulated meniscus decellularized ECM within various compositions involving gelMA, polyethylene glycol dimethacrylate (PEGDMA) and hyaluronic acid methacrylate (HAMA) for meniscal tissue engineering applications [270]. Bernal et al. demonstrated gelMA based volumetric printing of cell laden meniscal tissue constructs with very short times [271]. The use of ECM-based and natural polymer-based (gelatin, hyaluronic acid, collagen and silk fibroin) inks have been reported to trigger the intrinsic regenerative tendency of the residual tissue following vascularization, resorption and integration of fabricated 3D constructs leading to better healing possibilities. Furthermore, photo-polymerizable forms of natural materials enable room temperature printing, visible light polymerization and high throughput fabrication [266]. This would tremendously enhance the ease of fabrication, speed of treatment modalities and provide functional bioactive tissue constructs with preserved cells and biologics. Hence, a combinatorial approach for designing a biomaterial blend would usher better meniscus regeneration.

1.2.1.4 Silk : Biomaterial for Meniscus Tissue Engineering

Silk is a structural protein that represents a distinct class of biocompatible and green polymers. It has been valued in biomedical research for its biodegradability, low immunogenicity and facile processability [272]. Its use dates back to 131-211 A.D. when it was used as medical sutures by Greek physician Aelius Galenus [273]. The US pharmacopeia (USP) classifies conventional wax coated *Bombyx mori* silk fibroin (SF) sutures as non-degradable, non-adsorbent and resistant to proteolytic digestion *in vivo* [274]. Biocompatibility, biodegradability and green processing (from cocoons and glands) of SF earned it the status of bioresorbable material, as it is physiologically acceptable by the body and can be broken down to get assimilated or safely eliminated from the body without eliciting any adverse reaction.

Commercial silk production has exploited Lepidopterans larvae belonging to *Bombycidae* (mulberry silk) and *Saturniidae* (non-mulberry silk), classified based on their feeding habitat. The diversity of silk and silkworms, their lifecycle, feeding habitat have been exhaustively reviewed elsewhere [275, 276]. Silkworm silk protein biopolymer comprises two components. A central core silk fibroin (SF) that provides toughness and load bearing attributes [276], and surrounding water soluble glue silk sericin (SS) protein accounting for 25-30% (w/w) [272]. The functional diversity observed of silk spun by silkworms is influenced by feeding habitat, nutritional indices and environmental factors like temperature and humidity [277], affecting the amino-acid composition of SF and the presence of flavonoids or carotenoid in SS.

Mulberry silk cocoons can undergo aqueous processing, a significant advantage over biopolymers like collagen and chitosan that require acidic conditions which is a major concern when dealing with delivery of bioactive molecules or cells for therapeutic applications. Regeneration of silk fibroin from mulberry silk cocoons involves degumming for removal of silk sericin from raw silk using sodium carbonate and dissolution of obtained silk fibroin fibres in lithium bromide (chaotropic agent) to obtain regenerated silk fibroin solution after thorough dialysis in water to remove LiBr [272]. The obtained aqueous regenerated silk fibroin solution can be concentrated, and stored in liquid form in cold storage (1 month or lesser) or as lyophilized powder at 25 °C for longer durations.

Non-mulberry silk fibroins possess unique physico-chemical properties such as poly(A) stretches which confer superior mechanical resilience [278, 279] and RGD tripeptide which confer cell adhesion features [280], making them suitable for tissue engineering applications. Silk fibroin from the silk glands of 5th instar silk worms (*A. mylitta* [281-283], *A. assama* [278,

279, 284-286], *P. ricini* [287-289]) is directly dissolved in anionic surfactant, sodium dodecyl sulphate (SDS) (1% w/v) to disrupt the hydrogen bonding in the native silk fibroin, and dialysed to remove SDS and finally obtain the aqueous regenerated silk fibroin solution. This process preserves the biomechanical properties of SF (unlike with chaotropic agents which shear the protein during isolation) and enables high yields (1 – 1.5 g protein per silk gland), making it amenable for scaling up in biomedical research [281].

Silk structure is well explored for chemical modifications for more precise applications [290]. SF has been used for coupling reaction (cyanuric chloride activated or carbodiimide) based addition of polyethylene glycol or oligosaccharides or specific peptide chains (RGD tripeptide) [291, 292]. SF has been grafted with chemical moieties such as poly-methacrylate for photo-crosslinking based 3D printing applications [293]. Silk matrices are also endowed with thermal stability, which allows them to be autoclaved for sterilization post fabrication (β-sheet induced matrices) [294]. Unlike other polymers such as PCL and PLGA, silk matrices can withstand sterilization using ethylene oxide treatment, 70 % ethanol disinfection, γ-irradiation or UV-irradiation without drastic alteration of mechanical properties [295].

The antigenicity and cytocompatibility of SF based scaffolds (in different forms such as 3D porous matrices, 2D electrospun mats and films, gels, micro/nano particles) have been extensively studied over the years [296, 297], affirming their compatibility for use *in vitro* and *in vivo* within animal models. The non-mulberry SF additionally benefits from the intrinsic arginine-glycine-aspartate, i.e., RGD tri-peptide in the N and C termini of G_C motifs of H-chain [280]. RGD enhance the cell adhesion and proliferation via integrin mediated pathway [278] and hence non-mulberry SF finds immense potential in designing smart biomaterials for tissue engineering.

Silk being a protein polymer is prone to undergo proteolytic digestion owing to the presence of proteolytic cleavage sites [298]. The intrinsic physico-chemical attributes possessed by SF such as ß-crystal polymorphism, strong intermolecular and hydrophobic interactions govern the rate of degradation of silk [297]. The self-assembled regenerated SF based matrices also exhibit similar biodegradation kinetics. Unlike other FDA approved synthetic polymers such as PLGA and PLA which undergo rapid dissolution *in vivo* and whose degraded products increases local pH, the degraded products of silk include soluble amino-acids and shorter peptide fragments which are resorbed by the system. High content of ß-sheet results in slow degradation and vice versa [299]. This degree of crystallinity of regenerated SF based matrices can be used to fine-tune the requisite degradation rate. Hence, SF can endow

the necessary mechanical strength, durability, degradability, biocompatibility and immuno-compatibility for applications in meniscus tissue engineering.

1.2.1.5 Growth Factors

In the past, delivery of growth factors in various forms such as those loaded in macro-/micro-/nano-carries, application of extracellular vesicles and platelet enriched plasma for meniscal tissue regeneration has been a common endeavour. Already deficient in healing potential, the avascular regions of meniscus are further reprimanded by the various inflammatory factors released during meniscal lesions [300]. Delivery of relevant growth factors is hence known to accentuate the healing process by aiding in the production of collagen and glycoproteins. Most of the reported growth factors reported in literature (**Table 1.2**) for meniscus healing contribute to the anabolic pathways of the resident fibrochondrocytes and nearby synovial progenitors [301, 302] to induce cellular proliferation, deposition of meniscus ECM and the migration of cells onto the delivery vehicles that have been employed to release them. Platelet rich plasma is a complex pool of growth factors and provides an apt source of meniscal tissue regenerative factors for meniscus healing. Similarly precise delivery of specific growth factors via vesicles and other delivery vehicles has been known to influence the regeneration of meniscus. Some of the significant studies have been listed in **Table 1.2** below. The encapsulation of growth factors is majorly dictated by the encapsulation and release profile of the materials. Various micro-carriers, hydrogels and scaffolds have been used for the encapsulation of growth factors for an efficient delivery at the site of meniscus healing (**Table 1.2**). These materials, of both synthetic and natural origin, need to be optimized for their release characteristics to match the slow regenerative and remodelling nature of the meniscus [69] that spans from weeks to years *in vivo* as observed for current clinical implants.

The set of materials, cell source and growth factors best suited for meniscus regeneration is a topic of extensive evaluations *in vivo* and can be optimized with a preference towards autologous sources for either. Since patient-derived treatment approaches with natural biomaterial scaffolds and grafts are on the rise, due to their better integration, host-tissue compatibility and least chances of immune rejection, it would be highly imperative to develop natural biomaterial constructs loaded with autologous growth factors and autologous cell sources for repair and regeneration of menisci.

Table 1.2: *Various growth factor delivery mechanisms for meniscus regeneration*

Growth Factors/ Source	Delivery and conditions	Effect	Ref.
Platelet rich plasma (PRP)	Ultrasound guided injection in the knee of patients with intramural meniscal lesions post trauma	Improvement of daily activities, pain, sports and recreational activities and knee related quality of life 4 months after treatment in patients.	[303]
PDGF-BB, TGF-β1 and CTGF conjugated to heparin	Collagen nanofibrous scaffolds functionalized with the growth factors	Enhanced human meniscal and synovial cell viability, proliferation and infiltration of cells ex vivo, upregulated key meniscus ECM synthetic genes.	[230]
Leucocyte enriched platelet rich plasma (L-PRP)	Intrarticular injection with low molecular weight hyaluronic acid for traumatic meniscus injuries in human patients	Follow-up from 3 months to 3 years yielded a significant reduction of joint pain, improvement of joint function after 3 years as compared to NSAID treatment group	[304]
Wnt5a/PRP	Wnt5a/PRP *in vitro* and Wnt5a/PRP gel *in vivo* in rabbit major meniscus excision model	Reduced IL-1β induced inflammation and improve chondrogenic differentiation of meniscus cells and promoted meniscus regeneration	[305]
IGF-1, PDGF, VEGF, TGF-β1, FGF, PL, VEGF binding peptide and PRP	IGF-1, PDGF, VEGF, TGF-β1, FGF and PL supplied via media to mesenchymal stromal cells and meniscus cells; Collagen Meniscus Implant (CMI) functionalized with VEGF binding peptide and PRP as proof-of-concept	*In vitro* observation of mesenchymal stromal and meniscus cells cellular proliferation and migration with the growth factors in culture medium and enhanced cellular infiltration within the CMI	[306]
Clotted autologous PRP or Bone Marrow Aspirate Concentrate (BMAC)	Direct healing using autologous clotted PRP or BMAC with suture in rabbit meniscus incision	BMAC rendered better healing than PRP healing groups	[180]
CTGF and TGF-β3	PLGA microspheres loaded with growth factors in explant-based meniscus tear models	High CTGF and slow TGF-β3 release showed the most effective healing of inner avascular meniscus with better collagen fibre alignment, ECM secretion and mechanical properties	[302]
CTGF and TGF-β3	PLGA microspheres loaded with growth factors on PCL printed constructs	Regeneration of total meniscus in sheep with zonal	[115]

	in sheep total meniscectomy implants	biochemical and cellular characteristics	
FGF, IGF-1, VEGF and TGF-β	Growth factors directly added to cells from various vascular and avascular regions of the meniscus	Synovial area showed sensitivity to bFGF, TGF-β or IGF and resulted in fibroblastic functions. VEGF stimulates Col 2A and MMP-2 in from synovial area cells, Col 2A in vascular area cells and Col 1 in avascular area cells.	[307]
FGF	PLGA microsphere containing growth factors embedded in electrospun PCL fibers	Growth factor release promoted cell proliferation *in vitro* and *in vivo* subcutaneous pockets.	[308]
TGF-β1 and C-ABC (chondroitinase-ABC)	Cocultures of self-assembled fibrocartilages formed by seeding meniscal fibrochondrocytes and articular chondrocytes in agarose wells with growth factors in culture medium	Increased collagen synthesis, Young's modulus and ultimate tensile strength of the developed fibrocartilage.	[309]
TGF-β1 transduction using retroviral vector	Retroviral vector transduced human synovial MSCs turned into aggregates and compared with non-transduced cell aggregates in presence of chondrogenic medium without exogenous TGF-β	Higher cellular proliferation and chondrogenesis potential	[310]
TGF-β3	*In vitro*: Meniscal explants punches treated with collagenase, applied with tissue glue, placed in explant cavity and supplied with TGF-β3	Healing potential is improved and the cells migrated towards the gap.	[311]
BMP-7	*In vitro*: Applied directly to cells *in vitro* *In vivo*: Blended in cellulose glue carrier for delivery into meniscus defects in sheep	Increased collagen and inhibited MMP expression *in vitro* and fibrous tissue formation within 12 weeks *in vivo*	[312]
BMP-7	BMP-7 injected in situ into achilles tendon of rats and transplanted into meniscal defects thereafter.	Induced ectopic cartilage formation in rat tendons and its transplantation resulted in meniscal regeneration and prevented cartilage degradation	[313]
bFGF and TGF-β3	Juvenile and adult meniscus explants were cultured with growth	Short term bFGF and sustained TGF-β3 delivery enhanced the integration	[314]

	factors while the defects were either filled with the excised tissue or nanofibrous PCL mats	strength of both kinds of meniscus	
IGF-1	Growth factor in culture medium of alginate constructs seeded with meniscus fibrochondrocytes	Significantly improved mechanical properties and biochemical deposition of collagen and sGAG	[315]
CTGF	CTGF/fibrin glue used to treat rabbit meniscus defects	Enhanced *in vivo* meniscus tear regeneration	[316]

1.2.1.6 Fixation and Lubrication strategies

Mechanical and tribological properties of the knee joint are crucial for determining joint health and they are dependent upon the anatomical fixation of the meniscus implant and the lubrication present between the implant and articular cartilage. Meniscus allograft transplants need to be debrided appropriately by the surgeons to prevent undersizing [76] and typically placed into position relative to femoral condyles by few cycles of flexion and extension and then sutured into place by inside-out [74, 76] or all inside [75, 76] suturing of the body and outside-in [74, 75] suturing of the meniscus horns. The attachment points of MATs are traditionally tailored for attachment in different ways: (1) direct attachment of horns to ligamentous soft tissue points, (2) via bone plugs at horns and accompanied by body sutures and (3) via a complete bone bridge/trough at the horns of the meniscus [77, 317]. The meniscus allograft failures have been shown to occur frequently with suture-only fixation as compared to bone block fixation [82]. On the other hand, the implantation of Actifit polyurethane scaffolds has been traditionally done by debriding the residual meniscus portions to the vascular region to obtain a bleeding edge followed by measurement and cutting of the implant to exact size and suturing it in place using specialized ultra fast-fix sutures and outside-in sutures [84, 92]. Similarly, CMI implantation is carried out by obtain a bleeding edge by either reaching the red zone via debridement of damaged tissue or by microfracture awl along the peripheral rim, followed by trimming implant to the requisite size (Teflon measuring device is used for size measurement) and thereafter suturing the implant to the remnant meniscus using standard inside-out technique [84, 92].

In various studies, 3D printed meniscus implants have been sutured to residual debrided meniscus using outside-in suturing [115], affixed to synovial capsule and ligamentous structures after total meniscectomy [135, 226, 318], affixed vertically to joint capsule and

circumferentially to residual meniscus after partial posterior meniscectomy [319], sutured by the implant body to the capsule of the original meniscus rim and by the anterior and posterior horns to tibial bony tunnel [72] or to the residual rim [134] after total medial meniscectomy. In another study, suturing tabs for soft tissue suturing have been placed in implant design during modelling [46, 129]. Loosening of implants can pose a major threat to the efficacy of meniscus repair and regeneration process by detaching the implant from the surface of the synovial capsule and the tibial surface, consequently resulting in extrusion of the implants, debridement of the implant, actuation of the femoral condyles upon the articular cartilages and the significant increase in the coefficient of friction within the joint. These might lead to further pain, patient discomfort, repetitive surgeries and onset of inflammation and osteoarthritis.

Hence, the inclusion of suturing points along the anterior and posterior horns and the body of the 3D implants while designing them would significantly aid in the fixation of the implants without compromising the mechanical stability created by these suturing points. Also, these suturing points can be designed and strengthened for the different suturing techniques that would be recommended for the specific patient.

Coefficient of friction (COF) in the native cartilage-meniscus interface has been found to be significantly lower than PU and PCL implants than the cartilage-implant interface [320]. This is a result of the deficiency posed by synthetic implants in adsorbing the major components of synovial fluid, i.e., water, hyaluronic acid (HA), albumin, proteoglycan 4 (PRG-4 also known as lubricin) and surface-active phospholipids (SAPL) [321]. The unique native ultra-low COF of knee joint is provided by the meniscus, cartilage and the synovial fluid via various lubrication mechanisms such as IFPW, hydrodynamic, boundary, elasto-hydrodynamic, boosted, squeeze-film and biphasic lubrication [322]. The issue of reduced COF and lubrication have been approached by designing surface properties that are tribologically compatible, possess the ability to adsorb the components of the synovial fluid [323] and can behave in a hydrophilic [324] or hydrophobic [320] or zwitterionic manner [325]. Non-porous PCU materials have been tested for their efficacy as low friction meniscus implants and it was found that during the swing-phase the COF rises drastically suggesting the importance of porosity and surface modification required for meniscus implants [320]. In accordance to this, several material modifications have been proposed for reduced COF. Hu et al. [325] developed PU with sulfobetaine content (PU-SBs) that are zwitterionic in nature, aid in the adsorption of HA and were shown to perform at par with the native menisci under *in vitro* conditions. Morgese at al. [326] developed brush-forming polyoxazoline grafted

polyglutamic acid (PGA) co-polymers that can be injected onto joint surfaces and possess tissue-reactive reparative effects while enhancing lubrication. Tan et al. [327] fabricated mechanised silica nanoparticles functionalized with betaine for the reduction of joint friction by forming tenacious hydration layers to enhance lubrication. Liu et al. [328] formulated a gelatin based nano-liposomal friction responsive hydrogel formulation loaded with anti-inflammatory molecules that demonstrates self-lubrication by the nano-liposomes forming hydration layers to improve joint performance *in vivo*. Fan et al. [329] formulated a HA/curcumin nanomicelle formulation that demonstrated enhanced knee joint lubrication and prevented arthritis induced damages. Following its synthesis and low COF demonstration by Moro et al. [330], 2-methacryloyloxyethyl phosphorylcholine (MPC) has been reported widely for potential joint lubrication applications. This stems from the observed similarity of MPC polyzwitterioinic brushes to that of the native molecular brushes present in articulating joints [331, 332]. MPC has been used as a surface initiated polymer brush on mica[332], polystyrene microspheres and silicon wafer [333], poly(ether-ether-ketone) (PEEK) [334] and HA (forming HAMPC) [335]. These form tenacious water hydration shells, effectively reducing friction and resist being squeezed out during loading. In another approach, Das et al. [336] demonstrated that chemical adsorption of HA reduced friction in the presence of lubricin as compared to physically adsorbed HA.

Hence, a high-throughput approach for endowing meniscal implants with native-like lubrication could be to design highly porous implants which encompass a friction-responsive nano-liposomal formulation or a surface functionalized with poly-zwitterionic moieties. Such implants would be able to mimic multi-factorial native-like lubrication mechanisms.

1.2.2 Physical stimulation strategies for meniscal tissue maturation

Menisci are mechanically loaded tissues that act a cushion for the femoral head by providing a compatible interface with the tibial plateau. The menisci are known to undergo cell and matrix specialization based upon the mechanical stress being borne by the menisci [337]. Meniscal cells can be influenced by various mechanical cues both static as well as dynamic. Mechanical stimuli influence the synthesis of protein and alter cellular processes in the menisci both in the vascular as well as avascular region [338]. Mechano-stimulation that mimics the natural weight bearing phenomena acts as an impetus for the cells to assess the need to synthesize or degrade the surrounding matrix [339]. So it is pertinent to note that tissue engineered meniscal replacements need to be mechanically stimulated to produce favourable

results in terms of matrix production [224, 340] as well as minimizing the inflammatory cytokine production [341]. In this regard, many different bioreactors have been developed and modified for their application in meniscus tissue engineering. The major bioreactors or stimulation devices developed fall into five categories: direct compression, hydrostatic pressure, shear-based reactors, ultrasound-based and composite reactors. Various studies based on the application of bioreactors and stimulation for meniscus tissue engineering have been listed in **Table 1.3** below. Upon careful observation it can be implied that the compression, tensile and hydrological stimuli could be used for *in vitro* maturation of the cell laden constructs and *in vivo* implantation of these matured constructs would aid in the regeneration. While the ultrasound-based modality could be used both *in vitro* as well as *in vivo* in conjunction with other biomaterial-based treatment modalities. Additionally, ultrasound can be used under non-motile conditions following the surgery in a minimally invasive manner, enforcing its suitability for meniscal regeneration.

Table 1.3: *Effects of Mechanical Loading on Meniscus cells, explants and tissue engineering constructs*

Stimulus	Platform/ Device	Stimulation Details	Cells/ Tissue/ Constructs	Effect	Ref.
Dynamic compression	Biopress Flexcell	0-0.1 MPa, 0.5Hz square wave, 24h	Porcine meniscal explants	Increased NO levels, significantly increased protein and proteoglycan synthesis, downregulation of decorin, collagen type I, II, upregulation of MMP-1	[342-344]
Static compression	Custom designed polycarbonate static compression chambers	0%, 25%, or 50% strain, 4 days	Bovine Meniscal Explants	Static compression inhibited the effect of growth factors	[345]
Hydro-static	Custom designed hydrostatic pressure chambers	4MPa pressure, 4h, Static or cyclic (1Hz)	Human Meniscal cells in alginate beads	Static: Downregulated MMP 1 and 13 Dynamic: Upregulated Collagen I, TIMP 1 and 2	[346]

	Custom designed hydrostatic pressure system	4 h/day loading, 1 Hz, 0.55-5.03 MPa	Human fibro-chondro-cytes in aggregates form	Enhanced chondrogenesis, higher and early potential for chondrogenesis in outer zone cells	[347]
	Computer controlled pressure chamber, OTS	Static 150kPa hydrostatic compress, 12h	Rat fibro-chondro-cytes on culture dishes	Apoptosis and consequent degeneration is caused	[348]
Hydro-dynamic	Rotatoy Cell Culture System (RCCS)	Rotation, 4 weeks	Bovine articular chondro-cytes seeded on Hyaluronan scaffolds	Outer region: Deposition of collagen I Inner region: Deposition of collagen I, collagen II and GAG	[349]
Uniaxial compression	Customized direct compression stimulator	2% cyclic strain, 1Hz, 4h	Bovine meniscus explants (medial and lateral)	Upregulation of aggrecan, no effect on collagen type II expression	[350]
	Customized compression reactor	0%, 5%, 10%, 15% or 20% strain, 0.05MPa/0.1 MPa stress, 2h, 1Hz	Porcine meniscal explants	20% compression : Increased iNOS and IL-1 gene expression and NO release	[341]
	Custom built compression reactor	0%, 10% or 20% strain, 2h, 1Hz	Porcine meniscal explants	20% strain: upregulated MMP-1, MMP-3, MMP-13 and ADAMTS4 10% strain: upregulated Aggrecan, COX-2, and ADAMTS5 TIMP-1, and TGFβ unaffected by strain%	[53]
	Custom designed compression reactor	7% and 15% strain, 1 h loading/1 h unloading, 3 days/week, 6 weeks	Bovine meniscal fibro-chondro-cytes seeded on alginate	Loading for 2 Weeks: higher ECM production Loading for 6 Weeks: decreased GAG and increased collagen deposition	[351]
	Custom designed compression reactor	10% strain, 1Hz, 1h/day, 30cyles of 1min compression	Bovine meniscal fibro-chondro-cytes in	Anatomic meniscus constructs, contains collagen and GAG content mimicking native tissue	[352]

		and 1min uncompressed rest	agarose constructs		
	Custom designed compression reactor	1h loading, 3 days/week, 1/2/4 weeks	Bovine meniscal fibro-chondro-cytes seeded on alginate	No change in continuous 2/4 week stimulation 2 week dynamic followed by 4 week static culture yields best collagen and GAG deposition	[353]
	Custom designed bioreactor	Cyclic 1Hz, 1h/day, 5 days/week, 4 weeks	Bone marrow derived MSCs from rabbits seeded on PCL scaffolds	Upregulation of collagen I and collagen II, aggrecan and sox9, fibronectin and TNC	[340]
	Customized polysulfone loading platten	Static 4 weeks, Dynamic 4 weeks,1Hz, 1h/day, 5 days/week, 10% strain superimposed over 5% static strain	Porcine fibro-chondro-cytes within Agarose/GelMA, seeded on PCL	Enhanced production of GAG and collagen II in the inner region and collagen I in the outer region.	[224, 354]
	Biodynamic 5210, Texas Instruments	Static 30% Static 30%+Cyclic 10% 1Hz, 5min	Human meniscal fibro-chondro-cytes seeded in Collagen type I scaffolds	Supported hyaline cartilage like matrix when coupled with hypoxia	[355]
	Biodynamic 5210, Texas Instruments	Cyclic, 10% strain, 1Hz, 1h per day, 2-6 weeks	Human meniscal cells seeded on Collagen I scaffolds	No inner cartilage-like matrix formation without TGFβ3	[339]
	Customized compression reactor	1h of 5% strain, ± 25°shear at 1Hz followed by 1h rest, alternate days	Rabbit chondro-cytes seeded into de-cellularized rabbit meniscus scaffolds	Upregulation of collagen I, collagen II, aggrecan and MMP3, enhanced GAG deposition	[356]

Biaxial Cellular Strain	Bioflex II plates, Flexcell	Cyclic, 5%, 0.5Hz, 24h	Porcine meniscal cells from different regions	Increased protein synthesis (larger for outer cells than for inner cells), increased NO levels	[357]
Tensile	PDMS stretch chambers, STREX	Cyclic 5%/10%, 2-4h	Human meniscal root/horn cells seeded on Collagen type I gel	Cellular morphologies were evaluated and sox-9, collagen II expression enhanced after tensile strain	[358]
	Biaxial strain system, Flexcell	Cyclic 5%/10%, 0.5Hz, 4h	Porcine fibro-chondro-cytes seeded on collagen type I coated flexible silicone membrane	Regulation of TRPV4, NOS2 and Collagen I genes	[359]
	Customized clamps	Static clamping	Bovine fibro-chondro-cytes in high density collagen gel	Better tensile properties, aligned collagen fibers induced by fibrillogenesis, significantly higher GAG production	[360]
Ultrasound	Low-intensity pulsed ultrasound stimulations (LIPUS)	100-300 mW/cm^2, 20 min/day	Chondro-cytes seeded on Poly-urethance scaffolds dip coated with gellan gum, hyaluronic acid and glucosamine	Upregulation of aggrecan and collagen II	[361]
	Low-intensity pulsed ultrasound stimulations (LIPUS)	*In vitro*: 60 mW/cm^2, 20 min/day, 3 MHz *In vivo*: 60 mW/cm^2, 20 min/day, 1.5 MHz	*In vitro* cells were stimulated and *in vivo* injured menisci were stimulated	*In vitro* cell proliferation, migration, CCN2 and sox9 expression were enhanced and led to meniscal healing in 5 weeks via migration and VEGF secretion *in vivo* in rat model.	[362]

1.2.3 3D Printing and bioprinting of meniscus tissue constructs for implantation and regeneration

1.2.3.1 Nozzle-based printing method

The technique involves dispensing the biomaterial ink/bioink through its printer nozzle onto a printing surface for developing biologically functional constructs mimicking the native tissues/organs. Ink can be ejected through nozzle orifice via various mechanism, based on which the given printing methods is classified into (a) inkjet printing, and (b) micro-extrusion printing.

1.2.3.1.1 Inkjet printing/bioprinting

Inkjet printing have been moulded from a slightly modified commercial inkjet printers; however, a moving platform is present instead of a paper. It has a cartridge that can hold biomaterial ink/bioink which can be ejected from the nozzle onto printing surface via a piezoelectric actuator that creates enough pressure to expel the ink, and the second method being the thermal approach, has a heating element to increase the temperature of ink at nozzle surface to raise more than 300ºC for a microseconds, resulting in air bubbles formation that ultimately collapse to eject out in the form of biomaterial ink/bioink from the nozzle head onto print bed[363]. The ink viscosity, comprising of cell density and material concentration, that is required for inkjet printing is usually very low and there are chances of nozzle-clogging at higher ink viscosities. Filardo et al.[364] fabricated a custom-made human cell-laden collagen type I meniscus using an inkjet dispensing technique (RegenHU) in order to mimic the native menisci morphology. Cell friendly technology used the lifeink-200 bioink consisting of highly purified concentrated collagen type I with embedded human derived MSCs into a cartridge in order to mimic the natural one. The instrument had multiple printheads to eject out different types of polymers (thermoplastic based) and cell-encapsulated hydrogels. Additionally, it had a tri-axis motion system to fabricate custom-made tissues into various shapes and sizes, a pressure controller to manage precise ejection of hydrogels, and separate temperature control unit regulating the collector and cartridge temperature to be set.

1.2.3.1.2 Micro-extrusion printing/bioprinting

Extrusion based printing technique has been the most commonly used and feasible technique for fabrication of tissue/organ constructs, especially in the domain of meniscus tissue fabrication **(Table 1.4)**. It works based on the principle involving layer-by-layer deposition of

biomaterial ink/bioink in a continuous manner through a dispensing nozzle/printing head via a screw/piston/ pneumatic dispensing system. Discrete volumes of ink in the range of microlitres can be deposited on print bed through the nozzle orifice which relies on pneumatic actuator and stepper motors for the motion along tri-axis (X, Y, and Z axis). Deposition of the biomaterial ink/bioink via nozzle is followed by their immediate polymerization leading to a self-standing assembly in each layer. Various biopolymers such as natural polymers, synthetic polymers and combination of both along with cells or without cells can be used to via extrusion-based technique for fabrication of meniscus constructs.

Both inkjet and micro-extrusion-based printing modalities are endowed with the flexibility of using cell laden biomaterial composites and acellular biomaterials. Though, superior in material deposition fidelity, inkjet printing suffers from the drawbacks of nozzle clogging, requisites of low material viscosity and cellular density and volumetric printing rate [204]. Micro-extrusion printing qualifies on all of these fronts and could be a versatile and facile method for the fabrication of larger meniscal implants with high-viscosity high strength materials with or without cells. Crosslinkers pose a major threat to cellular viability and the inclusion of crosslinker-free approaches and the development of non-cytotoxic crosslinker based approaches needs to be adapted for fabrication of implants for *in vivo* applications [365].

Table 1.4: *Microextrusion based 3D printing approaches for meniscus implantation and tissue engineering*

Bio-polymers	**Cells used/Printing parameters and technique/ Additives**	**Scaffold dimension and properties**	***In vivo***	**Ref.**
3D printed synthetic polymer-based meniscus scaffolds and implants				
Liquid silicone rubbers (silicone elastomers)	**Cells:** NA 3D extrusion printer, double-barrel-syringe; **Printing area:** 25 cm × 25 cm; **extrusion rate:** 0.5mL/min; **Nozzle size:** 21G; **Nozzle-Platform distance:** 15mm; **Print speed:** 4800mm/min **Additives:** NA	Meniscus like, 4cm × 2cm × 1cm; **Swelling/Aqueous Weight Gain:** Nil **Compressive Modulus:** 0.16-0.241 MPa	NA	[366]
Poly-carbonate-urethane (PCU) and ultra-high-molecular weight poly-	**Cells:** NA 3D Fused deposition model-based extrusion printing (Lulzbot TAZ 6 with FlexuDually V2 print head); **Nozzle size:** 0.25mm;	Square shape; CF0 (PCU: UHMWPE wt. %) - 100:0; CF10 (PCU:UHMWPE wt. %) - 90:10, 32mm × 32mm × 3mm; **porosity %:** 13.61%	NA	[367]

ethylene (UHMWPE)	**Nozzle & print bed temp:** 225-235^{o}C & 50^{o}C respectively; **Layer height:** 0.125mm; **Print speed:** 15mm/s **Additives:** NA	**Swelling/Aqueous Weight Gain:** ~1.25% **Compressive Modulus:** NA		
PCL (~65,000 g/mol)	**Cells:** *In vitro* evaluation with human synovium MSCs 3D extrusion printing, layer-by-layer deposition; **Melting temp:** 120^{o}C **Nozzle size:** 100 µm forming 100-200 µm channels **Additives:** PLGA µsphere carrying rhCTGF and rhTGFβ3 growth factors	For human meniscus shape material scaffold: interlaid stands and interconnecting microchannels had diameter of 100 µm, 15mm (40% human size); For sheep meniscus scaffold: 300 µm microstands & 100 µm microchannels **Swelling/Aqueous Weight Gain:** NA Dynamic **Compressive Modulus:** >2 MPa	In sheep meniscus model	[115]
PCL (43-50kDa)	**Cells:** NA 3D Bioplotter (EnvisionTec)printing; **Layers spacing:** 200 µm, 90^{o} grid pattern; **Material temp:** 110^{o}C; **Platform temp:** 20^{o}C; **Extrusion pressure:** 6 bar; **Extrusion speed:** 1.4mm/s; **Needle gauge:** 24G; **Needle cannula length:** 3mm **Additives:** NA	Meniscus-like, 40 × 40 × 3mm^{3}; **Swelling/Aqueous Weight Gain:** NA **Compressive Modulus:** 5-40 MPa	NA	[129]
Poly-urethane (PU)	**Cells:** hMSCs 3D extrusion cryo-printing method **Additives:** Surface modification with fibronectin and collagen I	Meniscus-like (~5 mm × 5mm × 2mm); Porosity percentage and diameter: 20-60% & 0.25mm-0.7mm respectively **Swelling/Aqueous Weight Gain:** NA **Compressive Modulus:** ~0.26MPa	In rat sub-cutaneous model	[368]
PLA filament (1.75mm)	**Cells:** hMSCs 3D extrusion printing; **Extrusion temperature:** 200^{o}C; **Nozzle speed:** 20mm/s; **Fibre diameter and spacing:** 200 µm & 400 µm	Square sheet like (10 × 10 × 3 mm); scaffold dimension was made up of 0.2mm diameter fibre with 0.4mm pore size	In rat sub-cutaneous model	[369]

	respectively; **Layer thickness:** 0.3mm **Additives:** Post fabrication the scaffolds were collagen crosslinked & immersed in hydrogel comprising collagen I, alginate & alginate dialdehyde	**Swelling/Aqueous Weight Gain:** ~40 at 28 days **Compressive Modulus:** >100MPa		
PCU filament (3mm)	**Cells:** NIH 3T3 fibroblasts 3D extrusion printing, rectilinear infill pattern; **Nozzle size:** 0.4mm; **Print bed temperature and speed:** 40^{o}C & 360mm/min respectively; **Layer height:** 333 µm **Additives:** NA	Structure with crosshatch pattern (0-800 µm pore size); **Swelling/Aqueous Weight Gain:** ~40 at 28 days Ultimate Tensile Strength: ~2-12MPa	NA	[370]
PCU pellets	**Cells:** NA 3D Fused deposition model-based extrusion printing; **Material melting temperature:** 200^{o}C; **Nozzle diameter:** 400 µm; **Extrusion pressure and speed:** 300kPa & 6mm/s respectively **Additives:** NA	Meniscus -like; Porosity percentage and size: 34-63% & 400-800 µm respectively	NA	[371]
PCL (74,600 g/mol)	**Cells:** BMSCs 3D Fused deposition model-based extrusion printing **Additives:** NA	Meniscus-like (3 distinct specification was fabricated); **Pore size:** 215, 320 and 515 µm; **Porosity %:** 61-64% **Swelling/Aqueous Weight Gain:** NA Tensile Modulus: ~10-40MPa **Compressive Modulus:** ~5-20MPa	In rabbit meniscus model	[318]
PCL (80,000 g/mol)	**Cells:** MSCs and Meniscal fibrocartilage cells (MFCs) 3D Fused deposition model-based extrusion printing; **Additives:** NaOH modification of scaffold post fabrication	Rounded scaffold (6mm diameter & 2.5mm height); **Swelling/Aqueous Weight Gain:** NA Tensile Modulus: ~50-150MPa **Compressive Modulus:** ~50-100MPa	NA	[372]
3D printed natural polymer-based meniscus scaffolds and implants				
Cellulose nanocrystal (CNC), hard phenyl	**Cells:** NA 3D extrusion printing (Allevi 1); **Needle size:** 24G; **Printing**	Meniscus-like; **Swelling/Aqueous Weight Gain:** NA	NA	[114]

acrylate (PA), and soft acrylamide (AAm)	**speed and pressure:** 2mm/s & 5-10 psi respectively **Additives:** DMSO	**Tensile Strength:** ~2.5-20MPa **Compressive Strength:** ~2.5-40MPa		
Gellan gum/ fibrinogen (GG/FB) composite with silk fibroin meth-acrylate (Sil-MA)	**Cells:** Porcine primary meniscus cells (pMCs) 3D integrated tissue-organ printing based extrusion technique; **Nozzle diameter:** 240µm; **Printing speed and pressure:** 250mm/min & 45-65 kPa respectively **Additives:** Crosslinking using thrombin solution	Meniscus-like; **Swelling/Aqueous Weight Gain:** NA **Compressive Modulus:** >300kPa after 14 days	In mice sub-cutaneous model	[373]
Collagen	**Cells:** Primary meniscal fibrochondrocytes 3D extrusion printing with infrared heat lamp attached to the printer; **Base plate temp:** 37^{o}C **Additives:** NA	Meniscus-like; **Swelling/Aqueous Weight Gain:** NA **Equilibrium Compressive Modulus:** ~10-25kPa	NA	[374]
3D printed natural-synthetic hybrid polymer-based meniscus scaffold and implants				
PCL (80,00 g/mol) with silk fibroin	**Cells:** Synovium-derived mesenchymal stem cell (SMSC) 3D Bioplotter (EnvisionTEC) based extrusion printing; **Melting temperature:** 130^{o}C; **Nozzle diameter, pressure and speed:** 300 µm, 0.8 MPa and 7mm/s respectively **Additives:** Ethanol crosslinking	Meniscus-like; **Swelling/Aqueous Weight Gain:** NA **Compressive Modulus:** ~7MPa **Tensile Modulus:** ~15MPa	In rabbit meniscus model	[72]
p(DTD DD) infused with Collagen with hyaluronan	**Cells:** NA 3D Bioplotter; **Printing speed:** 1.2mm/s; **Printing temperature:** 160^{o}C **Additives:** NA	Meniscus-like; **Swelling/Aqueous Weight Gain:** NA **Instantaneous Compressive Modulus:** >1-2MPa	In sheep meniscus model	[233, 319]
Poly- ε-capro-lactone (PCL)	**Cells:** MSC (encapsulated in hydrogel) 3D extrusion bioprinting (OPUS bioprinter); **Needle size:** 200µm; **Layer thickness:** 200µm; **Print speed:** 180mm/min; **Fibre spacing:** 300µm **Additives:** Poly Lactic-co-Glycolic Acid (PLGA) µsphere carrying TGFβ3 or CTGF	Meniscus like; 3D CAD model used to design 3D bioprinted rabbit meniscus; **Swelling/Aqueous Weight Gain:** NA *After retrieval from animals:* **Bulk Tensile Modulus:** ~150MPa **Radial Tensile Modulus:** ~60MPa	In rabbit meniscus model and mice sub-cutaneous model	[137]

	growth factors & magnesium ions			
PCL with agarose (Ag) and gelatin meth-acrylate (GelMA)	**Cells:** Primary porcine fibrochondrocytes 3D Bioscaffolder system-based extrusion printing; **Stand distance and orientation:** 1mm & 0/90^{o} respectively **Additives:** NA	Meniscus-like; **(outer diameter:** 30 mm, **height at periphery:** 5 mm, **inner diameter:** 10 mm; **Swelling/Aqueous Weight Gain:** NA **Tensile Elastic Modulus:** ~30MPa **Compressive Elastic Modulus:** ~10MPa	NA	[224]
PCL (45,000 g/mol) with meniscal extracellular matrix (MECM)	**Cells:** Primary rabbit fibrochondrocytes 3D extrusion printing **Additives:** NA	Meniscus-like; **Swelling/Aqueous Weight Gain:** NA Tensile Modulus: ~20-60MPa **Compressive Modulus:** ~20-60MPa	In rabbit meniscus model	[135]
PCL filament (diameter 1.75 mm) with chitosan and MECM hydrogel	**Cells:** Adipose derived stem cells (ADSCs) 3D fused deposition model, extrusion printing, layer-by-layer deposition, 10 layers of 0.2mm strand thickness; **Material temp:** 130^{o}C; **Nozzle size and speed:** 200 µm & 10mm/s respectively **Additives:** NA	Cylindrical geometry (2mm height & 15mm diameter); **Strand space:** 0.2mm **Swelling/Aqueous Weight Gain:** NA **Compressive Modulus:** ~5-6MPa	NA	[138]
PU-PCL polymer (60/40 weight ratio) with MECM	**Cells:** Human bone-marrow-derived mesenchymal stem cells (hBMMSCs) 3D integrated tissue/organ building system-based extrusion bioprinting **Additives:** NA	Meniscus-like (5 mm × 5 mm × 1 mm); **Pore size:** 600 µm **Swelling/Aqueous Weight Gain:** NA **Compressive Modulus:** ~5-10MPa **Compressive Strength:** ~1-4MPa	In sub-cutaneous mice and orthotopic rabbit models	[113]
PCL with GelMA and MECM	**Cells:** Meniscal fibrocartilage chondrocytes (MFCs) 3D Bioprinter (Biomaker), dual nozzle multitemperature printing system; **Nozzle 1:** for PCL, 400 µm diameter, 5mm/s speed, 85^{o}C melting temperature; **Nozzle 2:** for hydrogel, 500 µm diameter, 5mm/s speed; 20^{o}C temperature; **Printing temperature:** 20^{o}C; **Strand spacing:** 1.5mm	Meniscus-like; **Swelling/Aqueous Weight Gain:** NA **Compressive Young's Modulus:** ~10-12MPa **Tensile Young's Modulus:** ~25MPa	In sheep meniscus model	[144]

	Additives: NA			
PCL (45,000 g/mol) with MECM	**Cells:** Synovium derived mesenchymal stem cells 3D Fused deposition model-based extrusion printing; **Nozzle diameter:** 0.25mm; **Printing speed:** 220mm/min **Additives:** PLGA microsphere loaded with kartogenin followed by EDC-NHS crosslinking	Meniscus-like; **Swelling/Aqueous Weight Gain:** NA **Compressive Modulus:** ~4-4.5MPa	In rabbit meniscus model	[221]
PLA nanofibers with sodium alginate	**Cells:** Human adipose-derived stem cells (hASC) 3D Bioplotter based extrusion printing (EnvisionTEC); **Nozzle diameter:** 0.81mm; **Extrusion pressure:** 0.02N/mm^2; **Stage temperature:** 37^{o}C **Additives:** $CaCl_2$ crosslinking	Meniscus-like; **Swelling/Aqueous Weight Gain:** NA **Compressive Modulus:** **Ramp** ~50MPa **Equilibrium** ~28MPa **Dynamic** ~190MPa	NA	[375]
PCL (45,000 g/mol) with MECM and Ca-alginate hydrogel	**Cells:** MFCs 3D Fused deposition model based- extrusion printing **Additives:** NA	3D wedge shaped model (10mm × 4mm × 1mm); **Swelling/Aqueous Weight Gain:** NA **Compressive Modulus:** ~6-8MPa **Tensile Modulus:** ~30-35MPa	In rabbit meniscus model	[134]

1.2.3.2 Nozzle-less 3D printing of Menisci

Nozzle free approaches abolish the problem of clogging of the printing nozzle caused by using high viscosity polymers. Various nozzle free techniques are applied in the field of tissue engineering. However, the commonly used technique in the area of meniscus tissue engineering is stereolithography (STL). It has evolved from the classical laser-based printing with the advent use of photocurable polymers and biomaterials such as methacrylates, diacrylates and epoxies [204]. It has digital microarray mirrors regulating the pattern of light that falls on platform consisting of photosensitive biomaterial ink/bioink which ultimately gets solidified in a layer-by-layer fashion, resulting in the formation of tissue/organ constructs. Bochove et al. [225] reported a meniscus implant fabricated using poly(trimethylene carbonate) (PTMC)-methacrylate anhydride in presence of triethylamie (tMA) and propylene carbonate resins by nozzle-free stereolithography (STL) 3D printing technique. In this digital light processing STL technique, thin layers of liquid resin (prepared using 40-70 wt% solutions of PTMC-tMA in

propylene carbonate) are subsequently photo-crosslinked to develop a 3D cylindrical structure with a gyroid pore architecture (3mm diameter, 6mm height, 60-80% porosity and 300-1000 μm pore size) that can eventually be used as meniscus implants. The pixel resolution of DLP SLA instrument was mentioned to be 35 × 35 μm^2, and the thickness of illuminated layer was found out to be 50 μm. This enables high resolution fabrication that is better and consistent as compared to nozzle-based printing approaches which are often limited by the nozzle diameter, ink viscosity and range of linear movement actuators. Grogan et al. [376] fabricated a gelatin methacrylate (GelMA) based scaffold incorporated with $CaCO_3$ particles using a modified version of digital micromirror device projection stereolithography (DMD-PSL) technique to mimic the circumferentially oriented cells in native meniscus tissue. This system consist of a 200W UV light source, glass coverslip window that is replaceable, a UV grade projection lens, and an array of micro-mirrors with 1920 × 1080 pixel resolution. UV light is focused onto the photosensitive GelMA solution placed in between glass coverslip and the servo-controlled stage via UV projection lens to develop GelMA scaffolds mimicking meniscus tissue. Ding et al. [226] fabricated polyurethane acrylate (PU) based elastomeric meniscus scaffolds loaded with kartogenin (KGN) using DLP printing and further modified them with polydopamine (PDA). These constructs demonstrated superior biocompatibility with stem cells, mitigation of osteoarthritis and excellent *in vivo* performance in rabbit model. Surface modification of PDA on the PU improved the biocompatibility and stem cell adherence of the constructs as compared to the commercial polyurethane constructs. While the encapsulated KGN was released, it produced a therapeutic effect for attracting meniscus cells. The optimized fabrication of meniscus model reduced shape non-conformity and prevented osteoarthritis. Ge et al. [227] developed a novel acrylamide-PEGDA hydrogel covalently bonded with diverse UV-curable polymers such as rigid polymers and elastomers for differential mechanical properties. They also demonstrated potential application in load-bearing meniscus via multi-material fabrication. Yang et al. [377] showed fabrication of anisotropic reinforced meniscus constructs by the virtue of electrically assisted Vat printing. This printing modality could be used for controlling the carbon nanotube fiber orientation within a biomimetic construct printed using a commercial polymer and hence aid in replicating the internal micro-architecture and render high mechanical strength and stability. Further, Bernal et al. [271] demonstrated a rapid volumetric fabrication method for cell laden meniscus tissues using gelRESIN within 30 s that showed adequate cellular proliferation and matrix deposition within the printed constructs after 28 days. Volumetric printing, hence, proves to be arguably the quickest printing modality which would be an ideal fabrication approach for patient-specific meniscal implants.

1.2.4 Injectable strategies for meniscus regeneration

Conventional repair of larger meniscus ensues partial or total meniscectomy followed by the either meniscal grafts of natural or synthetic polymers or suturing as discussed in the previous sections. Smaller tears on the other hand, face resection or suturing [2, 378]. Most of the meniscal implants are not patient-specific in mechanical behaviour which are trimmed to required shape and size by the surgeons on the operating table. These limitations make them unsuitable for smaller tears which do not require resection. Also, clinically available grafts suffer from non-integration, breakage [98] or shrinking [84, 379]. Integration can be achieved by various implant types, but smaller irregular meniscal tears need to be addressed as their resection and/or debridement could destabilize the knee joint and their suture might fail upon constant compression and relaxation cycles. Also, for translational needs, there might be regulatory hurdles with stem cells and decellularized matrix or shape and size conformity issues with scaffolds and 3D printed constructs for small meniscus tear healing. Injectable hydrogels are minimally invasive treatment modality with an inherent shape conformal property and sustained delivery of growth factors, drugs and biologics. These properties make it imperative for healing of meniscus defects which are irregular and small in size. Though extensively evaluated for healing of articular cartilage, bone and osteochondral defects [380, 381], injectable hydrogels have been sparingly optimized for meniscus tissue engineering applications. Wua et al. [382] used the decellularized ECM (dECM) derived from porcine meniscus and prepared an injectable hydrogel for meniscus healing. Through sub-cutaneous implantation and *in vitro* evaluation, the penetration of cells throughout the thickness of the hydrogel was shown. This is achieved by the meniscus dECM which undergoes degradation by the endogenous enzymes and enables cellular migration. Cellular migration is an essential criterion for designing injectable hydrogels for meniscus healing applications. Puetzer et al. [383] explored the feasibility of the fabrication of a high density collagen hydrogel laden with meniscal fibrochondrocytes for the treatment of major meniscectomy. *In vitro* evaluations yielded that the cell laden collagen menisci, though highly supportive of cell proliferation and ECM deposition, could only reach ~50kPa compressive strength after 4 weeks of culture. The initial deficiency in mechanical strength could lead to further expansion of the tear and risk of dislodging of the delivered hydrogel. Overcoming this hurdle is a crucial step towards wide-spread applications of injectable hydrogel formulations in meniscus treatment approaches. Further, Yuan et al. [112] formulated a human MSC (hMSC) laden bovine meniscus dECM hydrogel which was successfully evaluated for the treatment of partial meniscectomy in nude

mice. The inclusion of MSC along with the dECM enhanced mechanical integration significantly *in vitro*. An excised portion anterior horn of medial meniscus, when treated with intra-articular injection of this hydrogel, demonstrated healing due to hMSC retention, infiltration and fibrocartilage-like differentiation. Recently, Zhong et al. [108] established that dECM hydrogel could heal major meniscal defects better than collagen. Bone marrow stem cells (BMSCs) were encapsulated in either porcine meniscus dECM or commercial type I collagen for the treatment of a through-hole defect in medial meniscus and revealed that dECM was a better candidate. Also, injection did not affect the cellular viability even at 10^7 cells/mL density using a 25 gauge needle. Resmi et al. developed a gelatin-alginate self-gelling hydrogel [384] with limited evaluation of cellular growth on the hydrogel and a proof-of-concept ex vivo tissue integration in meniscus explant defects. Chen et al. [385] introduced a schiff's base reaction between glycol chitosan and PEG-CHO via a dual syringe approach to form a hydrogel in-situ at physiological temperature and pH. *In vivo* evaluation was performed with BMSCs and TGF-β1 loaded hydrogels and used for treating a punch-hole defect in the lateral meniscus. Hydrogels containing cells and growth factor performed significantly better than just cell encapsulated hydrogels. Kim et al. [386] developed their hydrogel blend on a similar concept where the dual syringe system comprised of fibrinogen phase and a PEO/thrombin phase that formed the gel instantly. These hydrogels were evaluated for a 60% medial meniscectomy model and fibrin/PEO group formed significantly better biomechanically stable meniscus that closely mimicked the native meniscus. Some of the other approaches are listed in **Table 5** below. The use of dual-syringe method is an interesting approach that could be used for instantaneous crosslinking in-situ. Current meniscus curing injectable hydrogels possess efficient integration, cellular infiltration and degradability, but lack in the mechanical stability on several occasions with natural polymers similar to natural polymer-based biomaterial-inks and bioinks. Though, this has been overcome with synthetic polymers for 3D printed constructs, injectable hydrogels comprising of synthetic polymers have not been reported extensively as mentioned in **Table 1.5**. It is generally observed in the reported literature on injectable hydrogels for meniscus healing (**Table 1.5**) that the inclusion of growth factors and stem cells within the hydrogel aided in accelerated healing of the meniscus. Though popular for 3D printing/bioprinting, growth factor laden hydrogel blends have been relatively unexplored as injectable hydrogels. Moreover, photo-polymerizing natural [373] and synthetic [226] hydrogels have shown excellent mechanical and biological properties for 3D printed meniscus constructs. Hence, they could be lucrative option as injectable hydrogels for arthroplasty-based treatment of small/major and regular/irregular meniscus defect. Future

studies could be focussed on the development of injectable hydrogels which could serve as both bioinks/biomaterial-inks and injectable hydrogels.

Table 1.5: *Injectable hydrogels for meniscus healing and tissue engineering applications*

Hydrogels	***In vitro/In vivo* evaluation**	**Injection Para-meters**	**Properties**	**Ref.**
Chitosan-graft-PNIPAM	***In vitro:*** Encapsulating Rabbit articular chondrocytes and Meniscal Cells ***In vivo:*** NA	~$7x10^4$ cells/mL	Thermoresponsive phase transition between 25°C and 37°C, improved mechanical strength over bare NIPAM	[387]
Meniscus dECM	***In vitro:*** Bovine chondrocytes and NIH3T3 on coated surface, inside hydrogel and cellular infiltration ***In vivo:*** Subcutaneous in Balb-C mice	21 gauge needle; $5x10^5$ cells/mL	Native ECM hydrogel alone so biocompatible and non-immunogenic; mechanical properties tunable with ECM concentration (0.5-1.5kPa)	[382]
Oxidized alginate (alginate Dialdehyde) and gelatin	***In vitro:*** i) Fibrochondrocytes seeded inside and on hydrogel; ii) Pig meniscus explant culture ***In vivo:*** NA	NA	Gelation at 37°C in 4 minutes, Mechanically strong (>200 kPa)	[384]
Glycol Chitosan/4-Arm PEG-CHO/ TGF-β1	***In vitro:*** BMSCs on hydrogel surface ***In vivo:*** 1.5mm meniscal defect filled with BMSC laden and BMSC+ TGF-β1 laden hydrogels	$2x10^7$ cells/mL	Thermoresponsive sol-gel transition at body temperature, induces fibrochondrocytic differentiation	[385]
hIGF-1 overexpressing BMSC encapsulated Calcium alginate gel	***In vitro:*** NA ***In vivo:*** Meniscal defect in goat model	$3x10^7$ cells/mL	Full thickness defects without blood supply were reconstructed	[388]
Collagen I and Alginate groups	***In vitro:*** Meniscal fibrochondrocytes encapsulated injection molded constructs ***In vivo:*** NA	$5x10^7$ cells/mL	Mechanically stable (>50 kPa after 4 week maturation); bioactive	[383]
Meniscus dECM compared with Collagen	***In vitro:*** BMSC encapsulated hydrogel ***In vivo:*** Subcutaneous and Orthotopic meniscus injury model	25 gauge needle; $\geq 1.5x10^7$ cells/mL	Superior than collagen I scaffold in reduction of osteophyte formation and prevention of joint	[108]

			space narrowing and osteoarthritis development	
Gelatin/PRP hydrogel	***In vitro:*** PRP supplementation in the media of fibrochondrocytes ***In vivo:*** 1.5mm punch hole defect filled with hydrogel	NA	Healing of menisci with ECM equivalent to inner regions	[389]
Fibrin/PEO	***In vitro:*** NA ***In vivo:*** Rabbit defect injection	NA	Regenerates 60% of the medial meniscus	[386]
Bovine meniscus dECM	***In vitro:*** hMSCs in hydrogel ***In vivo:*** Subcutaneous implantation in mice and orthotopic model	$1.5x10^7$ cells/mL	High integration strength achieved *in vitro*	[112]

The future treatment line-up could feature a multi-step patient-centric approach **(Figure 1.6)**. In the first stage, physicians would recommend the patient to undergo a MRI/CT scan which could be then fed into a MRI segmentation and 3D reconstruction software to obtain the 3D model of the intact and injured menisci of the patient. This will be ensued with the collection of autologous PRP and culture of autologous cryopreserved stem cells. In the second stage, the generated 3D model would be utilized for determining the appropriate treatment modality. Larger defects would be prescribed a volumetric printed construct and smaller defects would be prescribed an injectable hydrogel. The third stage would ensue blending of autologous PRP and stem cells with the physician-preferred biomaterial and fabrication of a 3D construct or formulation of the hydrogel for injection. In the fourth stage, the 3D printed construct would be implanted in the patient defect site or the injectable hydrogel would be delivered via surgical intervention of the patient-knee. After a post-surgical initial settling period, a final stage of LIPUS therapy would be provided to the patient's knee and a subsequent rehabilitation regimen would be followed for the patient. This approach would aid in the accelerated recovery of the patient with minimal loss of function. Moreover, a reduction might be observed in the treatment period, leading to early patient discharge and in essence a reduced burden on the medical infrastructure could be observed. The use of tuned patient-specific acellular implants or injectable hydrogels with suitable autologous growth factors could also be an economic alternative to this approach. The removal of cellularity would allow low-cost solution for mass treatments due to the preservation of resources required for cellular expansion while providing patient-centric solutions.

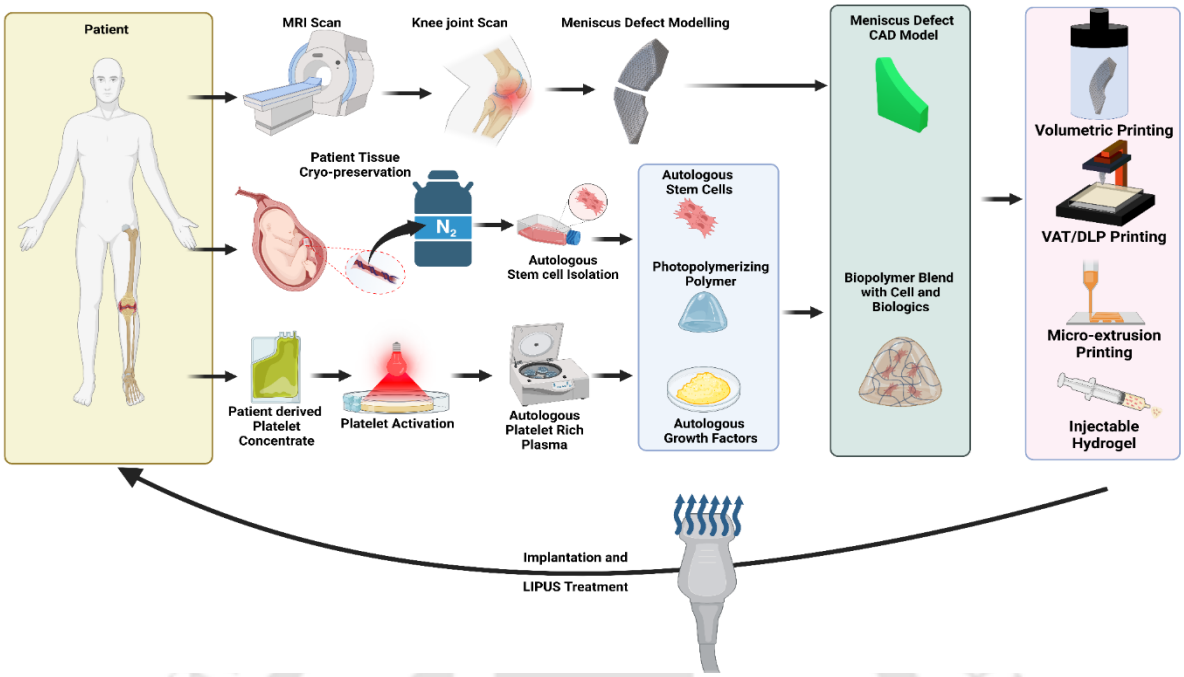

Figure 1.6: *Schematic showing the future of personalized meniscus treatment modality where patients suffering from meniscus tears will get MRI scan of knee to determine the meniscus defect morphology followed by its modelling. This is in concurrence with the development of autologous stem cells (isolated from cryopreserved patient tissue) and growth factor (derived from patient blood) laden photopolymerizing hydrogel composite which will be utilized for either 3D printing a meniscal implant and surgically placing it in patient's knee or injecting the hydrogel and crosslinking it in situ. This would be followed by the maturation of the meniscus using low intensity pulsed ultrasound regimen for accelerated healing. (Made using www.biorender.com)*

MOTIVATION AND OBJECTIVES OF THE PRESENT THESIS

MOTIVATION AND OBJECTIVES OF THE PRESENT THESIS

Tears of the knee meniscus are caused by a variety of traumas and old age amongst the whole spectrum of populace worldwide. When left untreated, meniscal tears destabilize the knee joint and eventually lead to osteoarthritis, pain and locking of knee joint. Menisci are largely avascular and hence do not have the inherent ability to heal. This leads to surgical intervention of the knee joint to suture or resect out the damaged meniscus tissues. Both of these treatment modalities suffer from extensive manipulation of the knee joint with prospects of suture breakage and the onset of knee osteoarthritis in case of partial or total resection. The current FDA approved meniscal implants are either made of natural collagen-based materials or synthetic polyurethane-based materials. Both kinds of implants have their respective drawbacks such as non-conformity of shape and size due to the one-size-fits-all design, mechanical non-compliance, breakage, shrinkage and unusually slow or quick and unregulated degradation and minimal or no regeneration. Thus, the development of regenerative strategies hinged on the concept of tissue engineering are of prime importance in the healing of meniscal tissue. Various scaffolds have been developed in the past with a wide range of materials, growth factors, cells and fabrication modalities that support meniscus regeneration. Amongst these the natural polymers-based approaches (such as silk, chitosan, gelatin, agarose and collagen) and the synthetic polymers approaches (such as polyurethane, polycaprolactone, polylactic acid, polyglycolic acid and others) have been prevalent. Natural polymers provide inherent regeneration supportive niche, while synthetic polymers provided apt mechanical and durability characteristics. But these approaches are limited by the same drawbacks as listed for the conventional meniscal implants.

With the advent of additive manufacturing technologies in the field of tissue engineering, three-dimensional (3D) printing is one of the most promising ways to fabricate meniscal scaffold with controlled size and micro-/macro-architectures, and optimal mechanical properties. In general, 3D printing manufactures the scaffolds in a layer-by-layer fashion on the basis of 3D model data which could aid in the zone-specific cell differentiation to rejuvenate tissues mimicking the native menisci with patient's specificity. Furthermore, the choice of material, cells and growth factors for 3D printing is of prime concern due to the fact that menisci are mechanically active and load-bearing tissue, have several cellular phenotypes and have zone-specific biochemical composition. We chose silk fibroin as our base polymer along with other additives. Silk fibroin (SF), a natural polymer, is gaining immense attention in the field of tissue

engineering due to its biocompatibility, tuneable biodegradability to amino acids, robust mechanical properties, ease of processing, and ability to undergo aqueous processing into different formats such as gels, films, powder, and sponges. Silk has been extensively explored for biomedical applications and is Food and Drug Administration (FDA) approved for use as biomedical sutures, surgical mesh and hydrogels. SF from silkworms such as *Bombyx mori* (mulberry silk) silkworms is the most commonly explored silk type. While SF from non-mulberry wild species such as *Antheraea assamensis*, *Antheraea mylitta,* and *Philosamia ricini* silkworms have gained attention due to their notable mechanical properties and presence of intrinsic cell-binding arginine–glycine–aspartic acid (RGD) tripeptide domains. The abovementioned characteristics of silk render it suitable for the development of bioinks for meniscal tissue 3D printing. Hence, silk based bioinks with additives have been used in the current thesis.

Objective 1 aimed at formulation of a biomaterial ink comprising of silk fibroin from *B. mori* cocoons (BMSF) and *A. assama* glands (AASF) blended with gelatin that could be used to 3D print the tri-layered structure of the meniscus with the desired microarchitecture. This objective, further, aimed at the fabricated 3D constructs mimicking the native mechanical strength of meniscus, while supporting the growth and proliferation of meniscal fibrochondrocytes and possessing apt *in vivo* immuno-compatibility. Further, the zone-specific cellularity and biochemical composition is necessary for achieving smooth integration with the resected/debrided meniscus. Hence, objective 2 aimed to encapsulate fibrogenic and chondrogenic growth factors in a photo-polymerizing bioink comprising of BMSF methacrylate (silkMA), AASF and gelatin methacrylate (gelMA) and 3D print the inner, middle and outer regions of the meniscus. Also, this objective focussed on one-step facile fabrication of scaffolds as compared to the carbodiimide crosslinking presented in objective 2. Inclusion of an autologous source of growth factor, such as platelet rich plasma, has been a common regenerative strategy for various osteochondral tissues. Hence, objective 3 was focussed on the formulation of a more robust photocrosslinking ink comprising of silkMA/gelMA/poly-ethylene-glycol di-methacrylate (PEGDMA) incorporated with human derived growth factor rich plasma (GFRP). This ink was poised for sustained release of GFRP growth factors and add higher patient-specificity to the constructs. Bioinks can be tweaked to formulate excellent injectable hydrogels and they have been shown to be ideal for treatment of small meniscus injuries and tears that are perilous to treat using suturing or 3D printing. Hence, in objective 4, the GFRP loaded ink was tweaked with poly-ethylene-glycol di-acrylate (PEGDA) to formulate an injectable hydrogel that

could be photo-crosslinked in situ into small meniscus tears. The hydrogel was evaluated for its ability to support cell migration, proliferation, GFRP release and fibrochondrogenic differentiation. Further, the in vivo healing of full thickness meniscus defects was evaluated in rabbit model. Meniscus, being a mechanically active tissue, has been shown to respond to mechanical stimulus which promotes accelerated healing. In this regard, the objective 5 was aimed at 3D biofabrication of constructs using the injectable hydrogel composition, seeding the same with stem cells and stimulating with therapeutic ultrasound (LIPUS). Objective 5 henceforth aimed evaluating the anabolic and catabolic pathways and their respective effects produced by the various intensities of ultrasound stimulation *in vitro*. These strategies have been covered in the following defined objectives:

Objectives:

1. Development of physiologically relevant silk-based tri-layered bio-mimetic hierarchical meniscus constructs and its evaluation *in vitro*.
2. Development of photo-polymerised silk-based 3D printed constructs embedded with growth factor loaded micro-spheres for potential biomimetic recapitulation of meniscus.
3. Development of photo-crosslinked silk-based autologous growth factor loaded 3D constructs for patient-specific treatment of partial and full thickness meniscal defects.
4. Formulation of an injectable silk-based autologous growth factor incorporated photo-polymerizing hydrogel for patient-specific repair of meniscal defects and its functional analysis in rabbit meniscus defect model.
5. Evaluation of low intensity pulsed ultrasound actuation augmented maturation of human neonatal stromal cell-seeded autologous growth factor loaded silk-based 3D printed meniscus constructs.

CHAPTER 2

Development of physiologically relevant silk-based tri-layered bio-mimetic hierarchical meniscus constructs and its evaluation *in vitro*

This chapter presents the formulation of a B. mori silk fibroin/A. assama silk fibroin/gelatin based bioink formulation; patient-derived MRI based reconstruction for modelling a meniscus; followed by the rapid prototyping of tri-layered biomimetic meniscus tissue scaffolds. These scaffolds were evaluated physico-chemically, mechanically and biologically. Tri-layered meniscus constructs with the composite concentric, lamellar and grid infill layers were fabricated to mimic the native architecture of the menisci. The 3D printed scaffolds were evaluated in vitro with porcine meniscus fibrochondrocytes for their phenotype maintenance and ECM deposition. In vitro macrophage assessment and in vivo subcutaneous implantation in rats was carried out to assess the immuno-compatibility of the 3D printed constructs.

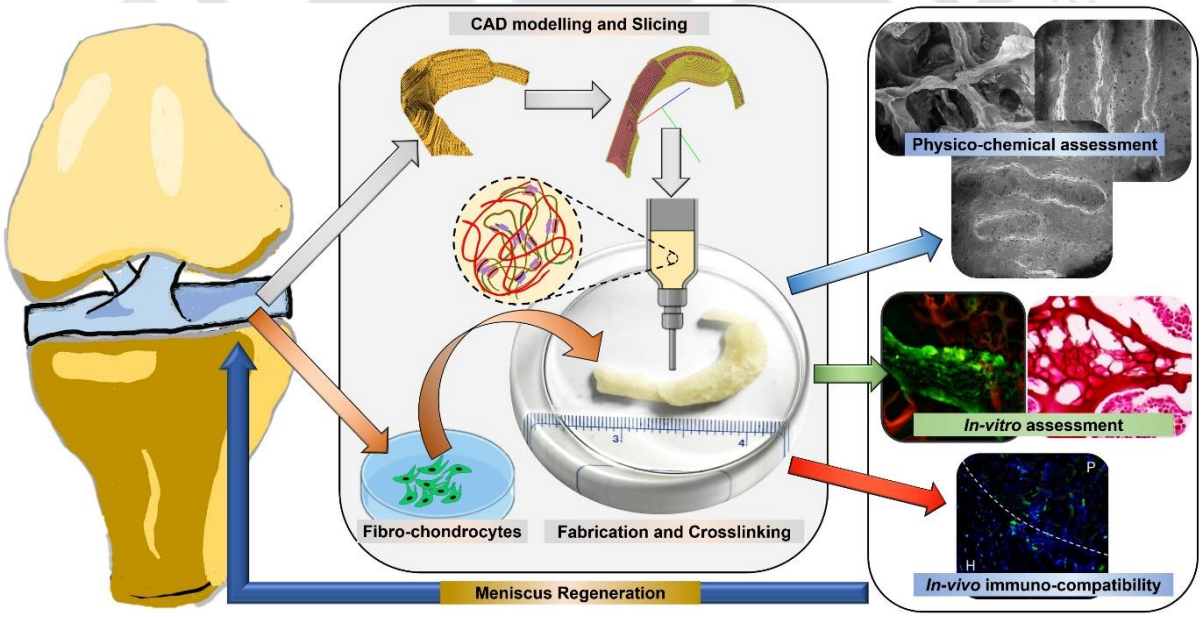

Outcomes of this chapter have been published as:

Ashutosh Bandyopadhyay and Biman B. Mandal. A three-dimensional printed silk-based biomimetic tri-layered meniscus for potential patient-specific implantation. ***Biofabrication***. 2019, 12(1), 015003. DOI: 10.1088/1758-5090/ab40fa.

ABSTRACT

Employing tissue engineering principles aided by 3D printing strategies to fabricate meniscus tissue constructs could help meniscus injury patients regain mobility, improve pain management as well as reduce the risk of development of knee osteoarthritis. Here we report a 3D printed meniscus scaffold to biomimic the internal and bulk architecture of the menisci. A shear-thinning novel silk fibroin-gelatin based bioink with high print fidelity was optimized for fabrication of scaffolds to serve as potential meniscus implants. Physicochemical characterization of the fabricated scaffolds shows optimum swelling, degradation, and mechanical properties. Further, the scaffolds were seeded with meniscus fibrochondrocytes to validate their bioactivity. Fibrochondrocytes seeded on the scaffolds maintained their phenotype and proliferation, as well as enhanced glycosaminoglycan (sGAG) and total collagen synthesis, was observed. Gene expression profile, biochemical quantification, and histological studies confirmed the efficacy of the scaffolds to form meniscus-like tissue constructs. The scaffolds were found to possess amenable immuno-compatibility *in-vitro* as well as *in-vivo.* Attributing to the excellent biological and physicochemical characteristics, these 3D printed scaffolds may be fine-tuned into viable alternatives to the present clinical treatment approaches of meniscus repair.

2.1 Introduction

The semi-lunar wedge-shaped fibrocartilaginous tissue present between the femoral condyles and tibial plateau are knee menisci. They act as load-bearing structures that protect the osteochondral tissue on the femoral and tibial surfaces. The major extracellular matrix (ECM) components of the meniscus tissue include collagen (~75%), sulphated glycosaminoglycans (sGAG,~15%), elastin (<1%) and other adhesion glycoproteins [26, 390, 391]. The extracellular matrix components are arranged in a unique tri-layered architecture which renders them with functional mechano-elastic properties. The superficial layer of meniscal tissue is a mesh of collagen fibres. Thereafter an intermediate radially lamellar layer which is further followed by the innermost circumferentially oriented collagen fibres. Radial tie fibres emanating from the superficial layers reinforce the circumferential collagen fibres throughout the tissue [26, 392]. This intricate arrangement of collagen fibres along with the presence of sGAG facilitate the axial, hoop, and compressive load transmission in the menisci for stabilization of the knee joint [4]. The menisci comprise of three cellular phenotypes based upon the vascularity of the region of meniscal tissue. The vascular region is mostly comprised of fibroblast-like/fibroblastic cells; the avascular region houses the chondrocyte-like/chondrocytic cells while the sparsely vascularized region has fibro-chondrocytes [7, 8].

Menisci are prone to tears and injuries due to sports, trauma and age-related complications. Though healing of meniscal tissue is successful in the vascularized regions, the avascular regions undergo impaired healing accompanied by the formation of a fibrous tissue with inferior mechanical properties [16, 23, 48, 393]. The occurrence of osteoarthritic degeneration is prevalent in patients with torn menisci that may get enhanced by the resection and failed corrective surgeries [44, 73]. Owing to these drawbacks, tissue engineering strategies made their way through traditional surgical approaches. Previously reported approaches for repair and regeneration of the meniscal tissue include the delivery of precursor cells at the defect site [176, 394, 395] as well as total or partial replacement with synthetic [147, 169, 396, 397] and natural biomaterial [107, 265, 349, 398] based scaffolds. Though, tested for stabilization and chondroprotection of the knee joint, the traditional scaffold fabrication technologies lack the ability to recapitulate patient-specific geometries as well as the internal architecture and bulk mechanical properties of the menisci. The advanced three-dimensional (3D) fabrication technologies possess a plethora of potential for application in this regard. 3D bioprinting entails efficient, rapid and repeatable fabrication of patient-specific scaffolds and cell-laden tissue constructs using biomaterial blends known as “bioinks”. The spatial control

of deposition and high fidelity of suitable bioink ensures the fabrication of micron-level architectures.

Previously reported efforts in 3D fabrication of soft and hard tissues have used integrated thermoplastic polymer framework and cell-laden hydrogels such as Poly(ε-caprolactone) (PCL)/Chitosan [399], silk fibroin/bioactive glass [400], silk fibroin/cellulose nanofiber scaffolds [401] and photo-crosslinked gelatin methacryloyl cell-laden hydrogels [402]. Concurrently, meniscus scaffolds have been majorly focussed on the mimicry of the bulk architecture, and in some cases, the mimicking of circumferential-radial collagen fibre orientation using thermoplastic polymers such as PCL [129, 132] and PCL functionalized with growth factors microparticles [115] or ECM [403]. Though the scaffolds possess ample mechanical stability and support the knee joint post-implantation but need compensation for their lack in bioactivity, supporting tissue regeneration and possess slow degradability. Therefore, natural biomaterials with necessary mechanical, degradation and bioactive properties need to be incorporated in the bioinks for the fabrication of meniscus tissue constructs. Silk fibroin has been used in the past for meniscus tissue engineering applications due to its excellent biocompatibility, resorbability, tuneability and minimal immunogenicity [275, 404]. Moreover, the presence of non-mulberry silk fibroin enhances the cell-attachment efficacy due to the presence of arg-gly-asp (RGD) domains [280, 405].

In this study, we aimed to fabricate biomimetic; physiologically relevant; patient-specific 3D printed meniscus scaffolds. Based on our previous reports, the intrinsic RGD present in *Antheraea assama* silk fibroin improved the cellular fate and downstream extracellular matrix secretion. In this context, a blend of silk fibroin from mulberry (*Bombyx mori*) and non-mulberry (*A. assama*) has been used in combination with gelatin as a bioink to mimic the extracellular microenvironment of menisci that contains cell-binding domains and collagen fibrils. Concurrently, scaffolds with different infill patterns to mimic each layer of the meniscal microarchitecture were fabricated along with a trilayered full-scale meniscus construct to assess the feasibility of its fabrication. Additionally, mechanical robustness of the scaffolds was achieved by crosslinking the same using EDC (1-ethyl-3-(3-dimethylaminopropyl) carbodiimide hydrochloride) and NHS (N-hydroxysuccinimide) chemistry. The scaffolds were, thereafter, characterized for their biocompatibility using primary porcine meniscus fibrochondrocytes. The proliferation, gene expression, and extracellular matrix deposition of seeded fibrochondrocytes was evaluated over 3 weeks of incubation and maturation. Moreover, immuno-compatibility evaluation of the constructs was carried out *in-vitro* as well as *in-vivo.* We hypothesize that these printed 3D scaffolds, with the meniscus specific micro- and macro-

architecture, can be seeded with cells and utilized for implantation in cell-laden as well as acellular forms with ease.

2.2 Materials and Methods

2.2.1 Materials

B. mori silk cocoons and mature 5th instar larvae of *A. assama* silkworms were procured from Assam (India) based local silk farms. Reagents such as protease XIV from Streptomyces griseus, sodium azide, Lithium bromide (LiBr), collagenase (type II), 1,9 dimethylmethylene blue (DMMB), alcian blue dye, fast red dye, Hoechst 33342 dye solution, calcein-AM solution, ethidium homo-dimer II (EthD II) solution, lipopolysaccharide (LPS) powder and 12 kDa dialysis membrane were procured from Sigma-Aldrich (USA). Reagents such as trypsin–EDTA, fetal bovine serum (FBS), Dulbecco's modified Eagle's medium (DMEM), antibiotic and antimycotic solution and amphotericin B for cell culture were procured from Gibco BRL (Rockville, USA). Pico-Green dye, SYBR Green master mix, Alamar blue dye, and interleukin 1ß (IL-1ß) kit were purchased from Invitrogen (USA). Other reagents used were of analytical grade.

2.2.2 Silk fibroin Isolation

Silk fibroin (SF) solution was extracted from *B. mori* silkworm cocoons and *A. assama* silk glands according to published protocols [406]. Concisely, *B. mori* cocoons were chopped into small pieces and boiled in 0.02 M Na_2CO_3 solution for 30 min. Thereafter the degummed fibres were dissolved in 9.3 M LiBr maintained at 60 °C. The dissolution was followed by dialysis against Milli-Q water using a 12kDa dialysis membrane for 48 h. *A. assama* SF was gently extracted by squeezing the silk glands of mature 5^{th} instar larvae of silkworm [406]. The squeezed out fibroin protein was dissolved in 1% (w/v) sodium dodecyl sulphate (SDS) and dialyzed against Milli-Q water. Extracted SF concentrations were determined gravimetrically.

2.2.3 Bioink Optimization and Printability

2.2.3.1 Gelation and Printability

Gelation of the bioink was determined spectrophotometrically by recording the absorbance of the components of the bioink and the bioink at specific intervals at 595nm using a spectrophotometer (Tecan Infinite Pro, Switzerland). Absorbance of the individual

components was plotted with the bioink to obtain the time-dependent gelation profile of the bioink. Moreover, the printability of the bioink was determined by assessing the gelation, stability, shear-thinning, and self-standing nature of bioink compositions. The concentration of *B. mori, A. assama* and gelatin were varied, and the printability was checked for the same.

2.2.3.2 Rheological Characterization

Rheological characterization of the optimized bioink composition chosen for printing was carried using MCR 302 (Anton Paar, Austria) rheometer. The bioink composition was subjected to Amplitude sweep, Frequency sweep, Temperature sweep and Three Interval Thixotropy (3ITT) to affirm the optimal conditions for it printability and determine the gel strength. The temperature sweep was carried out between 4°C - 45°C, before and after gelation of silk, to ascertain the temperature range of printability for the bioink composition. Amplitude sweep was performed from 0.01% to 10% shear strain, post gelation of silk at 37°C for 5 min, at 25°C. The respective storage and loss moduli were recorded to determine the linear viscoelastic range (LVER) and affirm the shear-thinning nature of the bioink. Thereafter, the frequency sweep of the bioink was carried out, after gelation of silk at 37°C for 5 min, within the viscoelastic range by varying the angular frequency of shear from 0.1 to 100 rad/s at 25°C to determine the stability of the bioink at various frequencies of shear. This was followed by the three interval thixotropy at 25°C wherein, the first interval consists of a very low shear strain as well as angular frequency followed by a brief interval of very high shear strain and high angular frequency and then reverting to the previous state of low strain and low angular frequency. This test aids in determining the self-standing nature of the bioink after being exposed to severe shear-thinning while undergoing extrusion from a thin nozzle.

2.2.3.3 Fourier Transform Infrared (FTIR) Spectroscopy

The infrared spectra of individual components and the optimized bioink were acquired using an FTIR-ATR (Shimadzu, IR Affinity-1S WL). Samples of each component and the bioink were freeze-dried and placed over the ATR crystal. Thereafter, spectra were acquired over the range of 400 and 4000 cm^{-1} and averaged over 32 scans. The characteristic peaks of SF and gelatin were observed for changes due to the gelation and crosslinking phenomena.

2.2.4 Scaffold Layer Design and Bio-fabrication

Digital Imaging and Communications in Medicine (DICOM) images of Magnetic Resonance Imaging (MRI) scan of the human knee were obtained from open source repository

[407]. These images were then opened in 3D Slicer [408] and segmented manually to obtain a 3D model of the lateral meniscus. The model was trimmed and smoothened before conversion to Stereolithography (STL) format (shown in **Scheme 2.1**). Another standard knee model was obtained from GRABCAD repository [409, 410], and the lateral meniscus was isolated from the same for comparison with the MRI reconstructed model and slicing. The scaffold layers were split, designed and sliced from the GRABCAD model to obtain the design of tri-layered meniscus constructs with the different alignment of fibres arranged in each layer. The bottom circumferential layer (L1) was set to be the thickest layer followed by a radially lamellar (tie-fibre) layer (L2) and a thin mesh layer (L3) on the top. The ratios of height were kept to be 2:2:1 (L1:L2:L3) so as to mimic their physiological proportions. The scaffolds for further studies were fabricated by keeping in mind the infill pattern of each layer namely Circumferential (L1), Lamellar (L2) and Grid (L3). Blocks and scaffolds of each infill pattern were fabricated using customized g-codes for each on a Cellink BioX (Cellink, Sweden) bioprinter by virtue of the optimized bioink composition. Briefly, the bioink was prepared in 3-5 ml volumes by blending the silk fibroin and gelatin in the optimized composition, loading into a syringe and incubating at 37°C for 20-25 minutes (to achieve gelation of the silk fibroin) followed by 3D printing at 25°C. The print-bed temperature was maintained within the range of 4°C-5°C, and the print speed and pressure were kept at 6-8 mm/s and 185-200 kPa for optimal printing. The printed scaffolds were freeze-dried, followed by crosslinking using EDC/NHS chemistry [411]. Briefly, the freeze-dried scaffolds were immersed in a solution of 40 mmol EDC (1-ethyl-3-(3-dimethylaminopropyl)carbodiimide hydrochloride), and 10 mmol NHS (N-hydroxysuccinimide) prepared in 80% (v/v) of ethanol for overnight. Thereafter the crosslinked constructs were thoroughly rinsed with milli-Q water for 30 minutes, 3 times to wash off the excess reaction mixture and by-products formed. The crosslinked constructs were used in the further experiments.

2.2.5 Physicochemical Characterization

2.2.5.1 Swelling Study

Swelling ratio of the constructs was obtained using previously established protocol [412]. Concisely, the fabricated grid-infill constructs (n=3) were weighed dry (W_d) and immersed in phosphate buffered saline (PBS; pH 7.4). The weight of the swollen constructs (W_s) was measured at regular intervals by gently dabbing off the excess PBS using filter paper. Swelling ratio was calculated using the following equation : $Swelling\ ratio = \left(\frac{W_s - W_d}{W_d}\right) x100$

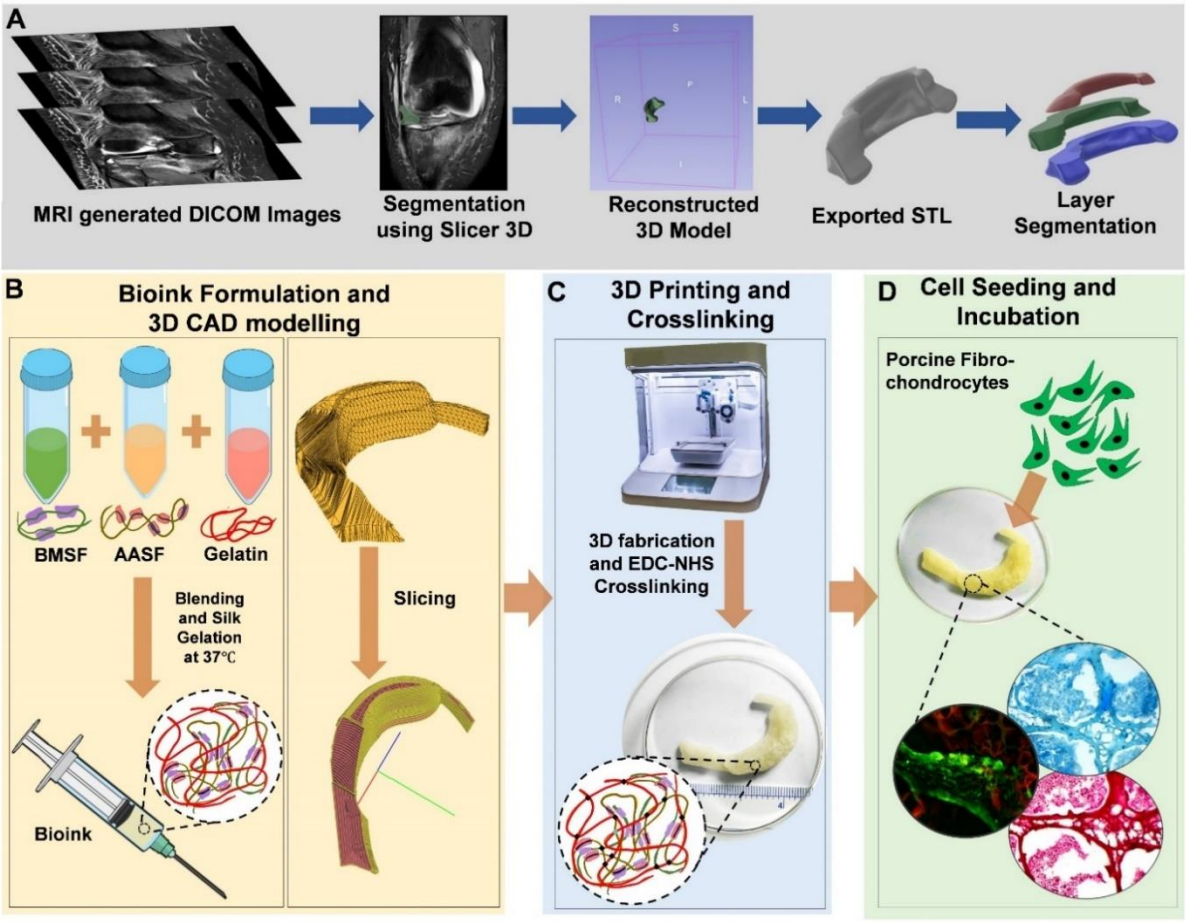

Scheme 2.1: *(A) Representative methodology to retrieve patient-specific meniscus design based on MRI scan data using segmentation and remodelling software. Representation of the process of (B) bioink formulation and layer slicing to obtain a gcode, (C) 3D printing using the bioink to fabricate biomimetic scaffolds and (D) seeding of isolated fibrochondrocytes for biological evaluation of the scaffolds.*

2.2.5.2 Enzyme-assisted degradability

Enzyme-assisted degradation study was performed on the constructs *in-vitro* in the presence of protease XIV (Sigma-Aldrich, ≥3.5 U/mg) according to previous reports [413]. In brief, grid infill constructs (n=3) were weighed dry (W_i) and thereafter immersed in 0.5 U/ml protease XIV containing PBS (pH 7.4) solution at 37 °C. The constructs were retrieved at regular intervals and washed with PBS (pH 7.4) and freeze-dried. The remaining mass (W_r)of the constructs was measured at these time points, and the consequent percentage of mass remaining was calculated as follows : $\%Weight\ Remaining = \left(\frac{W_r}{W_i}\right) x100$

2.2.5.3 Surface Morphology

The surface morphology of the fabricated scaffolds with varying infill patterns was visualized using Field Emission Scanning Electron Microscopy (Zeiss, Germany). The fabricated constructs with different infill patterns were crosslinked and freeze-dried before observing their fibre alignment and resolution of the fabricated scaffolds.

2.2.5.4 Mechanical Strength

Compressive mechanical strength of the constructs with different infill was measured using universal tensile testing machine (Model 5944, Instron, USA). Cuboid constructs of 7x7x7mm^3 were fabricated and crosslinked. The constructs were subjected to compressive strain of 60% at 5mm/min while immersed in PBS (pH 7.4), and the compressive stress was measured and plotted for each construct. The average compressive strength was calculated for each construct at peak strain. The constructs were also subjected to cyclic strain of 20% over 200 cycles of compression at 5mm/s. The compressive stress of 10 cycles were plotted after an interval of every 50 cycles. Moreover, the hysteresis loop of compressive stress-strain was plotted for the first and last cycle to determine the deviation in the strength and stress profile of the constructs before and after the experiment.

2.2.6 Biological Characterization

2.2.6.1 Cell Isolation and Cell Seeding on Bio-fabricated Scaffolds

Primary porcine meniscal fibrochondrocytes were isolated from porcine knee samples in accordance with previously published protocols [241]. Briefly, porcine knee were collected from the local abattoir, and the menisci were resected from the ligaments they are attached to. The menisci were chopped into fine pieces and treated with antibiotic-antimycotic solution of PBS (pH 7.4) briefly. Thereafter, the chopped menisci were subjected to 1.5 mg/ml of collagenase II. The digested tissue was passed through a 40 µm cell strainer and centrifuged to obtain cell pellet. The cell pellet was rinsed 2-3 times using DMEM containing 10% FBS and 1% antibiotic–antimycotic solution. Thereafter, the cells were plated in monolayer and cultured in the same media for one passage before seeding. Scaffolds of grid and concentric infill were fabricated, crosslinked and washed followed by an autoclave sterilization cycle and a conditioning cycle in cell culture medium for 12 h prior to seeding. The scaffolds were seeded with cells at different densities ranging from 10^3-10^4 cells/mm^2 for assessing their viability and

proliferation. Further, the scaffolds were seeded with optimized seeding density for gene expression, biochemical and histological studies.

2.2.6.2 Cell Viability and Proliferation

Scaffolds of concentric infill seeded with 10^4 cells/mm^2 were used to observe the viability of fibrochondrocytes after 1, 7, 14, and 21 days of incubation. The live and dead cells were visualized for their distribution using calcein-AM and ethidium homodimer solutions using manufacturer's protocol (Sigma-Aldrich). Concisely, the constructs were washed gently with PBS (pH 7.4) and incubated at 37°C and 5% CO_2 with calcein-AM (40 nM) and ethidium homodimer (20 nM) solution in PBS for 20 min. The live-dead solution was removed, and the constructs were washed in PBS prior to imaging under an inverted fluorescence microscope (EVOS FL digital microscope), and representative images of the concentric infill constructs are presented.

Cell proliferation study was performed on the grid infill scaffolds (n=3) seeded with different cell densities of 10^3, $5x10^3$ and 10^4 cells/mm^2 using Alamar blue (Invitrogen) assay by following manufacturer's protocol at 1, 7, 14 and 21 days. In brief, the grid infill scaffolds were seeded with varying cell densities and cultured in DMEM supplemented with 10% FBS and 1% antibiotic-antimycotic at 37°C and 5% CO_2. Thereafter, scaffolds were incubated with 10% (v/v) Alamar blue dye in culture medium for 3 h at the defined observation time points. Post incubation, 100 µL of culture media from each sample type were read at 570/600 nm using microplate reader (Tecan Infinite Pro, Switzerland). The results have been represented as normalized Alamar units at different time points.

2.2.6.3 Biochemical Analysis

2.2.6.3.1 DNA and Sulphated GAG content

Grid infill scaffolds seeded (n=3) with 10^4 cells/mm^2 were used for estimation of DNA and GAG content using manufacturer's and previously established protocols [414]. Briefly, the constructs were collected at various time points and digested for 16 h using papain solution containing 125 µg per mL papain, 5 mM L-cysteine, 100 mM Na_2HPO_4, and 5 mM EDTA (pH 6.2) at 60 °C. Thereafter, the DNA content was quantified using PicoGreen DNA assay kit. Each digested sample (25 µL) was taken, and 1× TE buffer (75 µL) was added to it. Further, 100 µL of Quant-iT PicoGreen reagent (1:200 dilution in 1 x TE buffer) was added. Measurement was carried out fluorometrically with an excitation/emission maxima of 480/528

nm. Total sulphated GAG (sGAG) content was measured using 1,9-dimethylmethylene blue (DMMB) assay. Papain digested sample (50 µL) or the collected secreted media (50 µL) was added to DMMB reagent (200 µL). Absorbance was measured immediately at 525 nm. The sGAG content has been represented per construct as well as after normalization w.r.t., the DNA content of the respective constructs at different time points.

2.2.6.3.2 Total Collagen content

The total collagen content of the seeded scaffolds (n=3) was measured using hydroxyproline as an index after different culture durations. The samples were acid hydrolysed in oil bath, and the hydroxyproline content was quantified by treatment with p-dimethylaminobenzaldehyde (PDAB, Sigma-Aldrich, USA) and chloramine-T (Sigma-Aldrich, USA) according to previously established protocol [415]. The hydroxyproline content in samples was calculated by referring to the standard curve generated using rat tail collagen. The hydroxyproline (HYP) content has been represented per construct as well as after normalization with the DNA content of the respective constructs.

2.2.6.4 Gene Expression Studies

Total RNA was isolated from cell-seeded scaffolds (n=3) at various culture time points using TRIzol reagent (Sigma-Aldrich). Isolated mRNA content was quantified using nanophotometer instrument (Implen, Germany). Thereafter, a high-capacity cDNA reverse transcription kit (Applied Biosystems) was used in conjunction with a PCR thermal cycler (Applied Biosystems) to obtain complimentary cDNA copies of the mRNA. Real-time PCR was carried out with the prepared cDNA using SYBR Green reagent (Invitrogen) in QuantStudio 5 (Applied Biosystems, USA) real-time PCR system for aggrecan, sox-9, collagen Iα and collagen IIα genes. The final reaction volume including SYBR Green master mix, forward and reverse primers and cDNA was kept 20 µL and the standard run conditions of holding stage (50 °C for 2 min, 95 °C for 10 min) and cycling stage (40 cycles of 95 °C for 15 s, and 60 °C for 45 s) was used. Relative expression of aggrecan, sox-9, collagen Iα and collagen IIα genes were quantified by normalizing to glyceraldehyde-3-phosphate-dehydrogenase (GAPDH), the endogenous housekeeping gene. The results were analyzed through C_t method ($2^{-\Delta\Delta Ct}$). The primer sequences used have been listed in **Table 2.1**.

Table 2.1: *Primer sequences used for the gene expression analysis*

Gene	Sequence	Accession No.
Porcine aggrecan (ACAN)	F:5′-CCCAACCAGCCTGACAACTT-3′ R:5′-CCTTCTCGTGCCAGATCATCA-3′	NM_001164652.1
Porcine sox-9 (sox-9)	F:5′-TTCCGCGACGTGGACAT-3′ R:5′-GGCGGCAGGTACTGGTCAAACTC-3′	NM_213843.1
Porcine Collagen I (Col I)	F:5′-AGAAGAAGACATCCCACCAGTCA-3′ R:5′-AGATCACGTCATCGCACAACA-3′	XM_021067153.1
Porcine Collagen II (Col II)	F:5′-CAGGTGAAGGTGGGAAACCA-3′ R:5′-ACCCACGAGGCCAGGA-3′	AF201724.1
Porcine GAPDH (GAPDH)	F:5′-TCGGAGTGAACGGATTTGG-3′ R:5′-CCAGAGTTAAAAGCAGCCCT-3′	NM_001206359.1

2.2.6.5 Histological Analysis

The cell-seeded grid infill scaffolds were fixed in 10% neutral buffered formalin (NBF) for 24 h, followed by fixing in 15% (w/v) sucrose and 30% (w/v) sucrose solution for 6 h and 12 h respectively for cryoprotection. The sucrose fixed scaffolds were embedded in Tissue Freezing Medium (Leica) and snap-frozen before sectioning. The sample blocks were sectioned (12-15 μm thick) using cryomicrotome (Leica). The obtained sections were stained by hematoxylin and eosin (H&E) to observe cell morphology, 1% alcian blue (dissolved in 3% acetic acid solution at pH 2.5) to visualize sulphated proteoglycan deposition and 0.1% (w/v) direct red 80 (in saturated aqueous picric acid solution) to assess the total collagen deposition. Micrographs of the stained sections were obtained by inverted bright-field microscopy (EVOS FL, Life Technologies, USA).

2.2.6.6 Macrophage stimulation and IL-1ß release

Assessment of the immunogenic response *in-vitro* was carried out using RAW 264.7 cells (mouse macrophages, obtained from National Center for Cell Science, NCCS, Pune). The cells were seeded at 5×10^4 cells per well in a 24-well plate and cultured for 24 h. Thereafter the constructs were placed on seeded cells for 24 h. The spent media were collected for quantification of IL-1ß released using manufacturer's protocol for the IL-1ß ELISA kit (Invitrogen, USA). Lipopolysaccharide (LPS, Sigma-Aldrich, USA) at 1000 $ng \cdot mL^{-1}$ served as positive control, and untreated cell-seeded wells on standard tissue culture plate (TCP) were taken as a negative control.

2.2.6.7 *In-vivo* biocompatibility assessment of acellular scaffolds

In-vivo biocompatibility of the scaffolds was assessed by implanting acellular scaffolds in subcutaneous abdominal pockets of Sprague Dawley (SD) rats. The experimental and animal handling protocols were reviewed and sanctioned by the Institutional Animal Ethical Committee (IAEC), National Institute of Pharmaceutical Education and Research (NIPER), Guwahati, India. Six healthy female SD rats, each weighing 170-120 g (45 – 58 days old) procured from National Institute of Nutrition, Hyderabad, India were used. Subcutaneous pockets were surgically created by a small incision in the thoracolumbar region, and one sterile scaffold (autoclaved, 6x6x1mm^3) was inserted per animal (n=6). Thereafter the pockets were closed in place via surgical staples and the animals were closely monitored. The wound areas were cleaned superficially every day with 10 % povidone-iodine and draped. Three animals from were sacrificed, after 7 and 14 days, by cervical dislocation. The implant site tissue surrounding the samples were retrieved along with the scaffold and preserved for histological processing in 10% neutral buffered formalin (NBF) for 24 h, followed by dehydration, clearing using xylene and paraffin wax embedding to form blocks. The blocks were sectioned, and the sections were further processed and stained by hematoxylin and eosin (H&E) to observe cellular infiltration and immuno-stained for CD68 marker using fluorescence-based antibody and Vectastain universal elite kit and DAB substrate (Vector Laboratories) to observe the infiltration of macrophages within the implanted scaffolds. Micrographs of stained sections were obtained using an inverted fluorescence and bright-field microscope (EVOS FL, Life Technologies, USA).

2.2.7 Statistical Analysis

All experimental data have been reported in the form of mean ± standard deviation (n = 3). Statistical analysis was carried out by one-way analysis of variance (ANOVA) using Origin 9.1 (OriginLab, USA), and a Tukey test assessed the variance across groups. Groups were considered to possess statistically significant difference when *$p \leq 0.05$.

2.3 Results

2.3.1 Bioink optimization and printability

2.3.1.1 Gelation and printability

Gelation of the bioink is important for ensuring printability as shear-thinning can be improved by induction of gel formation. Moreover, the self-standing nature of the blend hydrogel is enhanced with the increase in viscosity that is a resultant of the gel formation. Gelation of the components of the bioink and the blend itself was evaluated by measurement of their absorbance at 595nm wavelength at 37°C (**Figure 2.1A**). 7% (w/v) *B. mori* silk fibroin and 20% (w/v) gelatin solutions were unaffected at 37°C and their absorbance were found to be constant. Whereas the absorbance of 3.5% (w/v) *A. assama* silk fibroin was found to rise slowly after 25 minutes due to the temperature-induced gelation of the same at 37°C. Concurrently the rise in the absorbance of the bioink blend formed by blending *B. mori*, *A. assama* and gelatin, to obtain a final concentration of 0.5% (w/v), 0.5% (w/v) and 1% (w/v) respectively, was found to rise substantially after 20 minutes indicating the formation of a gel. The printability of the blend was assessed by mixing the components in various ratios to reach various final concentrations and marking them printable/non-printable according to their extrudability, self-standing nature and gelation time period (**Figure 2.1B**). *B. mori* and *A. assama* concentrations of 1% (w/v) in the final blend were found to be printable with considerably high gelatin concentrations to obtain shear-thinning. Consequently, gelatin concentration of more than 5% (w/v) in the final blend was found to be essential to obtain shear-thinning at 25°C post silk fibroin gelation. Henceforth, the final concentration of 1.5% (w/v) for *B. mori* and *A. assama* silk fibroin and 7% (w/v) for gelatin was chosen (eliminating the boundary concentrations) for further experiments due to its quick SF gelation within 20 minutes and its adequate shear-thinning and self-standing nature post-extrusion. This composition is referred to as the optimized bioink composition, bioink composition or bioink in further experiments.

2.3.1.2 Infrared Spectroscopy

The FTIR spectra of the individual silk fibroin, gelatin, and bioink before and after crosslinking have been depicted in **Figure 2.1C**. The amide I (1710-1590cm^{-1}), amide II (1570-1480cm^{-1}) and amide III (1270-1200 cm^{-1}) region peaks are prevalent in all the samples [279, 405, 411]. The shift of amide I (1631cm^{-1}), amide II (1523cm^{-1}) and amide III (1240cm^{-1}) peaks in the bioink blend gel and their broadening post EDC/NHS crosslinking of the bioink blend

can be attributed to the formation of gel by the two SF and the conformational changes occurring due to EDC/NHS crosslinking of the bioink.

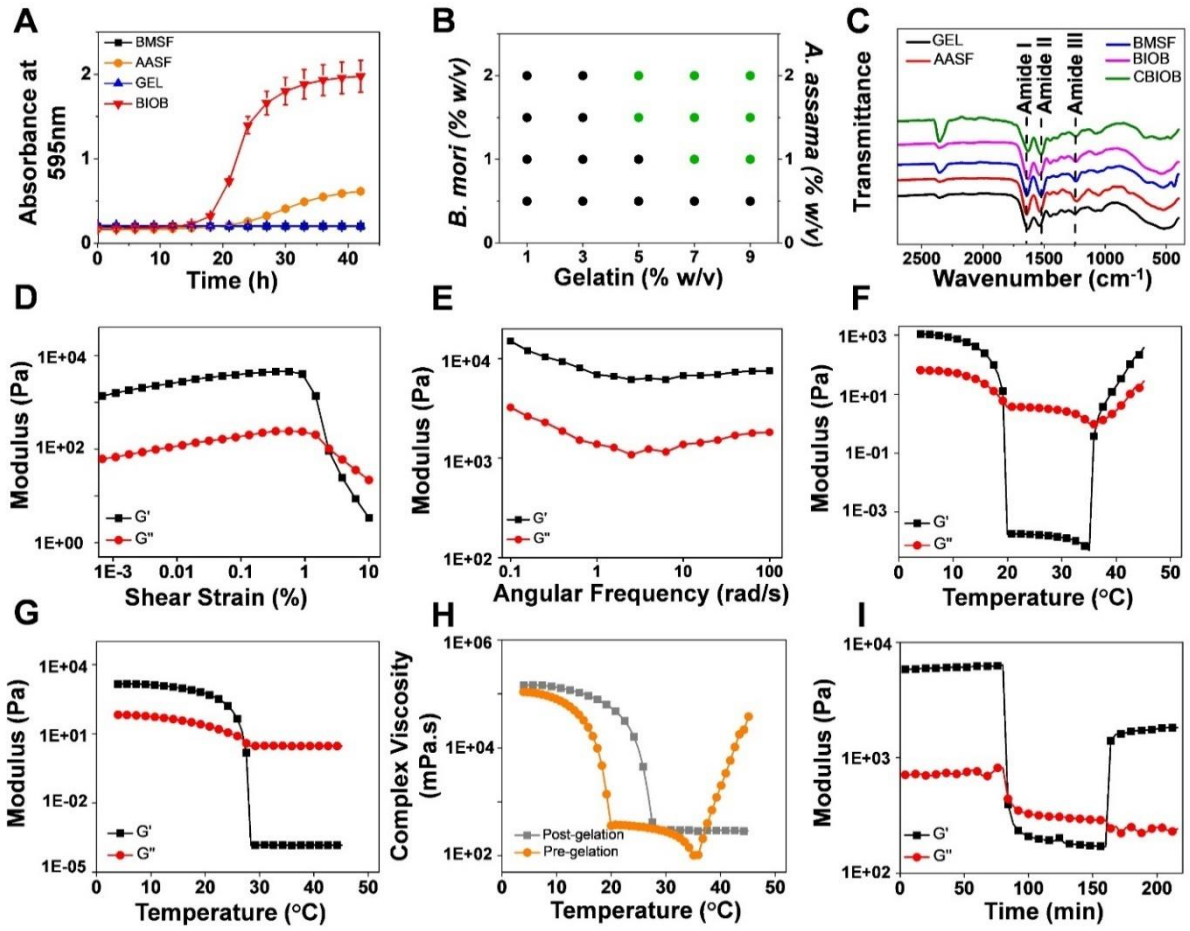

Figure 2.1: *(A) Gelation profile for B. mori silk fibroin (BMSF), A. assama silk fibroin (AASF), gelatin (GEL) and bioink blend (BIOB) obtained by their absorbance at 595 nm. (B) Printability matrix for varying compositions of the bioink blend. The green symbols represent printable compositions, and black symbols represent non-printable compositions. (C) FTIR transmittance spectra for BMSF, AASF, GEL, BIOB and crosslinked BIOB (CBIOB) with the amide I, II and III peaks highlighted for all spectra. Rheological characterization of optimized bioink concentration through (D) amplitude sweep post- SF gelation, (E) frequency sweep post-SF gelation, (F) pre-SF gelation temperature ramp, (G) post-SF gelation temperature ramp, (H) complex viscosity pre-SF gelation; post-SF gelation and (I) 3 Interval thixotropy test (3ITT) post- SF gelation.*

2.3.1.3 Rheological Characteristics

Shear-thinning property of bioink is the most pertinent requirement for micro-extrusion based 3D fabrication. The amplitude sweep of optimized bioink under varying shear strain at 25°C post-SF gelation at 37°C was found to elicit shear-thinning shear above 1.5% shear strain indicated by the cross-over point of the storage (G') and loss (G'') moduli (**Figure 2.1D**).

Consequently, the linear viscoelastic range (LVER) of the bioink can be assigned up to 0.75% shear strain where the bioink is found to be stable and demonstrate its gel-like nature. The frequency sweep within the LVER of bioink showed no deviation in the gel-like nature of the bioink, indicating its stability under varying angular frequency (**Figure 2.1E**). Also, temperature sweep of the bioink (pre- and post-SF gelation) from 4°C to 45°C showed that the bioink forms gel below 20°C and above 37°C due to the presence of gelatin and blend of mulberry and non-mulberry silk fibroin respectively (**Figure 2.1F and 2.1G**). However, as opposed to the pre-SF gelation state, post the gelation of mulberry and non-mulberry silk fibroin, the bioink retain the gel-like nature up to 27°C and a loss of viscosity is observed above 27°C (**Figure 2.1H**). This shows that gel formation by the two SF is beneficial for the extension of range of printing temperature. Moreover, the three-interval thixotropic test of the bioink showed the self-standing and gel-strength recovering nature of the bioink after it was subjected to shear thinning (**Figure 2.1I**).

2.3.1.4 Scaffold bio-fabrication and surface morphology

The scaffolds of circumferential, lamellar, and grid infill, as well as composite total meniscus scaffolds, were fabricated with high precision, as shown in **Figure 2.2A**. The surface morphology of the constructs was observed using field emission scanning electron micrographs, and the alignment of the deposited fibres can be seen to conform with the 3D CAD (Computer Aided Design) models designed for the same (**Figure 2.2B**). Crosslinked scaffolds of grid infill were mostly used for further studies and relevance of the difference between each infill pattern was derived whenever necessary. **Figure 2.2C-D** show the whole meniscus construct printed as a proof-of-concept and the attachment tabs that have been incorporated into the design for facile fixation of the implants.

2.3.2 Physicochemical characterization

2.3.2.1 Swelling Characteristics

The absorption of surrounding body fluids and facilitating the transfer of metabolites and nutrients is very crucial for any scaffolding material. The swelling profile of the constructs is shown in **Figure 2.3A**. The constructs immersed in PBS were found to absorb >7 times their own weight within 3 h and thereafter attaining an equilibrium, as observed up to 48 h.

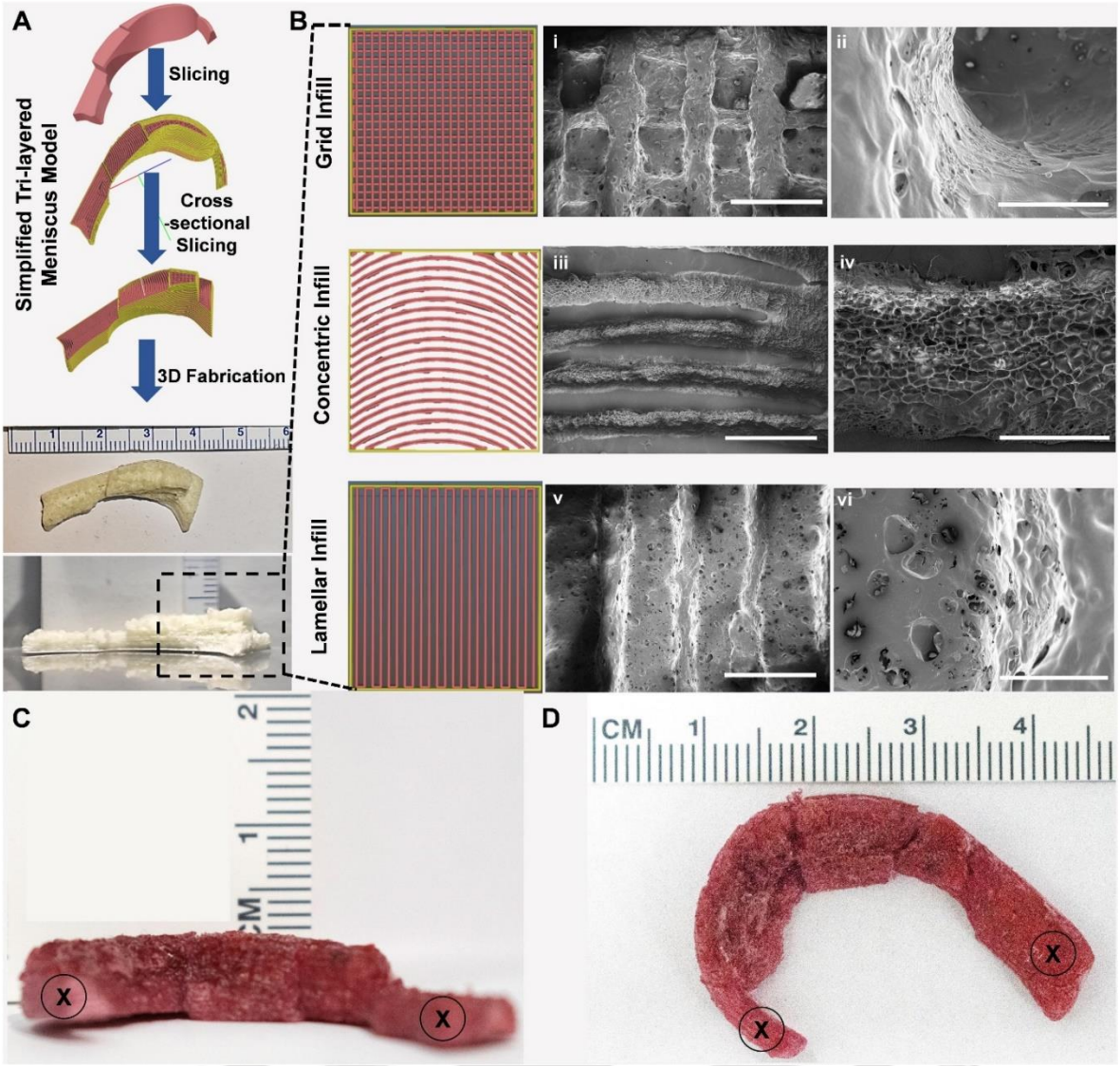

Figure 2.2: *(A) Schematic of simplified meniscus tri-layered model sectioned, and 3D printed to show the 3 different layers. (B) Representative FESEM images for grid (i,ii), concentric (iii,iv) and lamellar (v,vi) infill. Scale bar: 800µm (B.i,iii,v) and 200µm (B.ii,iv,vi). (C) Side and (D) top views of the representative complete trilayered meniscus scaffolds printed with red-dye for clear visualization of the gross morphology. The X marks represent points for suturing the meniscus into place.*

2.3.2.2 Degradation profile

Degradation profile of the scaffolding material plays an important role in the extent of regeneration achieved within a given duration. Under *in-vivo* conditions, the degradation process is actively managed by ECM modulatory enzymes such as matrix metalloproteinases (MMPs) [416]. To achieve similar functional efficacy protease XIV was chosen as a non-specific proteolytic enzyme for *in-vitro* degradation profiling. The constructs showed time-dependent degradation in the positive control, i.e., in PBS as well as under protease treatment, as shown in **Figure 2.3B**. The scaffolds immersed in PBS retained ~50% of their mass, and those treated with protease retained less than 20% of their mass after 21 d.

2.3.2.3 Compressive Mechanical Strength

Compressive strength of the scaffolds with different infill provided an insight into the applicability of the scaffolds in meniscus regeneration. The physiological cyclic compression experienced by the menisci is generally 10-15%. So the scaffolds were subjected to 60% static compressive strain (**Figure 2.3C**) as well as 200 cycles of 20% cyclic compression (**Figure 2.3D**). The moduli of the scaffolds at 60% compressive strain were highest in grid infill (188.5 ± 25.4 kPa) followed by concentric infill (152.4 ± 31.1 kPa) followed by lamellar infill (130 ± 6.5 kPa) (**Figure 2.3E**). The full-thickness tri-layered scaffolds possessed a compressive modulus of 147 ± 4.8 kPa which was higher than lamellar infill scaffolds and lower than the concentric, and grid infill scaffolds with no prominent reduction. A similar trend was observed in the cyclic compression cycles where the grid infill scaffolds peaked in strength. Moreover, all the scaffolds were found to be stable after 200 cycles of compression as shown by the cyclic and hysteresis loop profile of cycles 1 and 200 (**Figure 2.3F, 2.3G, 2.3H, and 2.3I**).

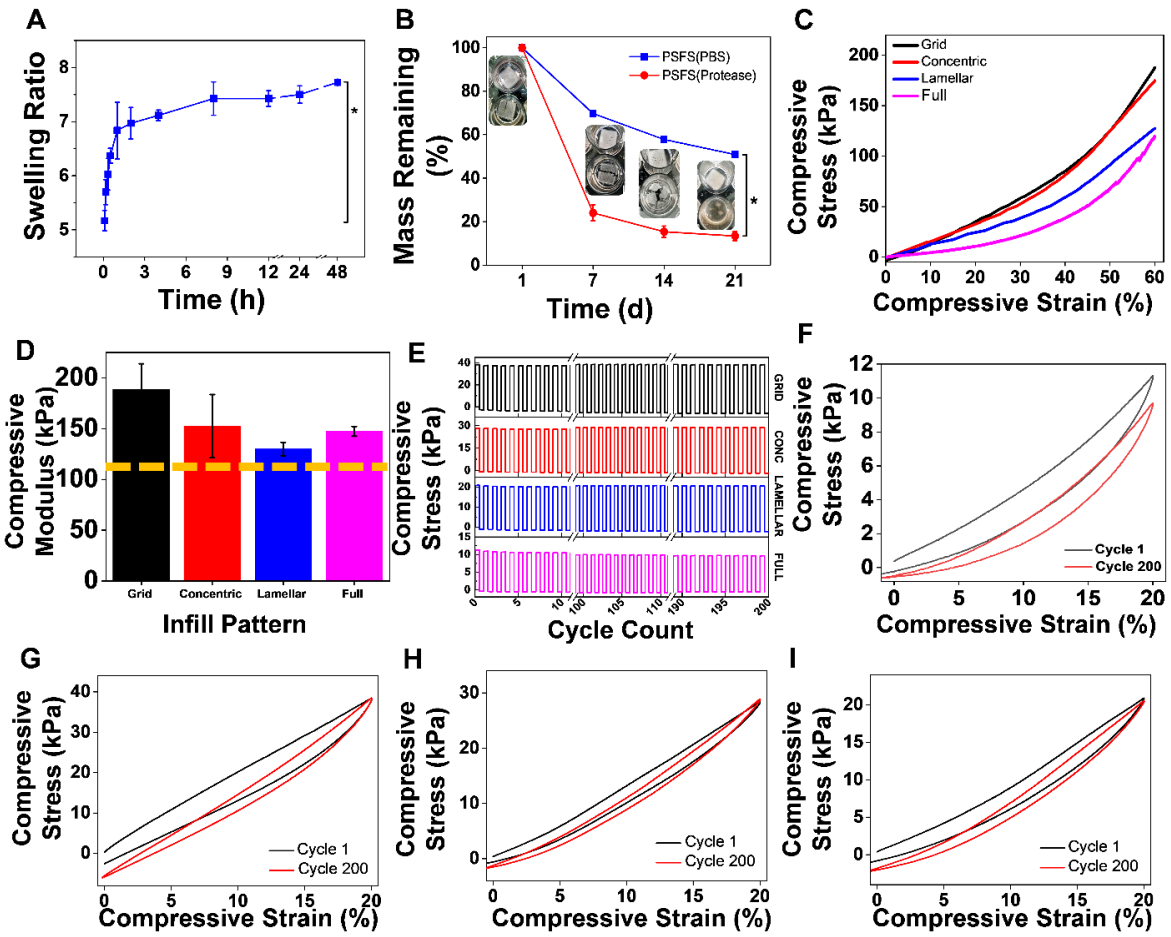

Figure 2.3: *(A) Swelling ratio of printed constructs immersed in PBS for 48h. (B) Degradation profile of printed constructs in PBS and protease enzyme (0.5U/ml) with representative images of constructs in protease (bottom) and PBS (top) at each time point. (C) Representative stress-strain curve of 3D printed constructs having concentric, grid and lamellar infill and tri-layered constructs (Full). (D) Compressive moduli of 3D printed constructs having concentric, grid and lamellar infill and tri-layered (Full) construct. The dotted line represents native meniscus modulus. (E) Representative stress-cycle curve of 3D printed constructs having grid, concentric (CONC.) and lamellar infill and tri-layered (Full) construct subjected to 200 cycles of 20% compressive strain at 5mm/s. Representative stress-strain curves for loading and unloading cycle 1 and 200 for (F) full-thickness constructs, (G) grid, (H) concentric and (I) lamellar infill constructs showing the deviation of mechanical strength. *p ≤ 0.05.*

2.3.3 Biological Characterization

2.3.3.1 Cell viability and proliferation

The constructs seeded with the meniscal fibrochondrocytes showed excellent cellular viability over the culture period of 21 days (**Figure 2.4A**). The green dots represent cells, and the red dots represent dead cells. The silk fibroin scaffolds are prominently visible due to their auto-fluorescence, which in turn helps in determining the distribution of green cells within the

scaffolds. Moreover, there was no discernible cytotoxicity as the cells proliferated by 1.8-2 times at different seeding densities over the grid infill scaffolds up to 21 days (**Figure 2.4B and 2.4C**). The distribution of cells at various depths and planes of the lamellar infill constructs in the micrographs of **Figure 2.4A** show that the cells were evenly spread and attached over the scaffolds.

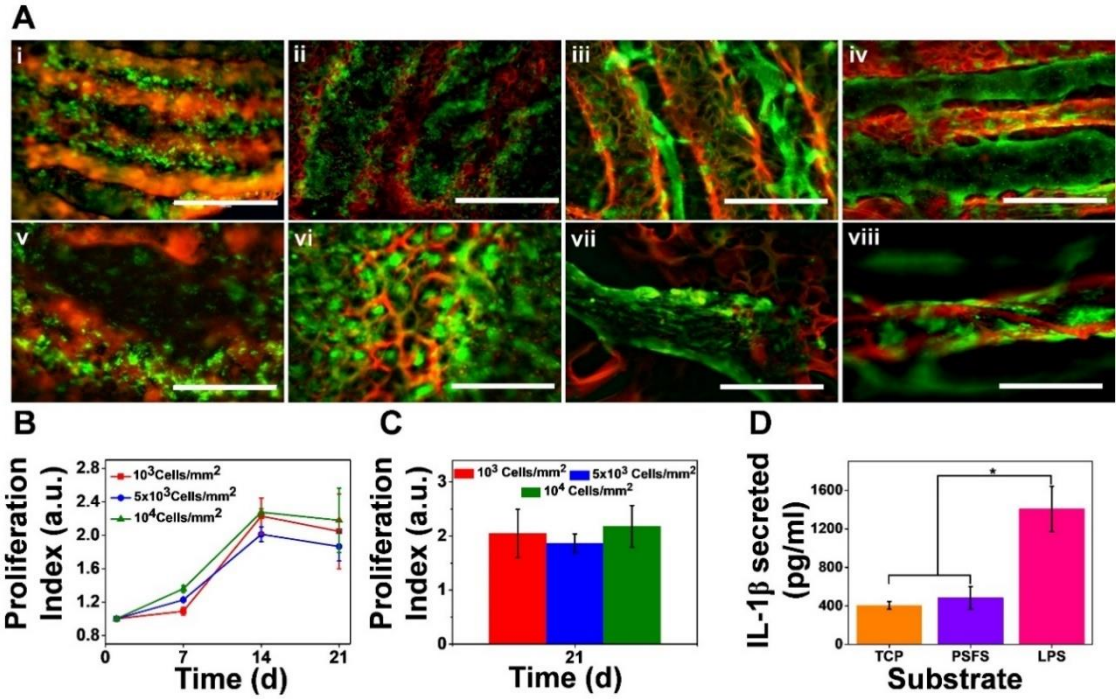

Figure 2.4:*(A) Representative microscopic images for in-vitro cytocompatibility of printed scaffolds by live-dead staining of meniscus derived primary porcine fibrochondrocytes seeded constructs after 1 day (i, v), 7 days (ii, vi), 14 days (iii, vii) and 21 days (iv, viii). (B) Cell proliferation quantified by Alamar blue assay of printed constructs with different cell seeding densities. (C) Cell proliferation index represented as normalized Alamar units in 21 days between printed constructs with different cell densities. (D) In-vitro immuno-compatibility assessment of printed silk fibroin constructs (PSFS) w.r.t. tissue culture plate (TCP) and lipopolysaccharide (LPS) by measuring murine IL-1β release from RAW 264.7 cells through ELISA. Scale bar :1000µm (A.i-iv) and 400µm (A.v-viii). *p≤0.05*

2.3.3.2 *In-vitro* immuno-compatibility

The constructs were compared for their macrophage stimulation ability by measuring the IL-1ß released by murine macrophages in the presence of the scaffolds *in-vitro*. The scaffolds show excellent immuno-compatibility, as depicted in **Figure 2.4D**. The scaffolds had an identical response to the tissue culture plate (positive control) which was significantly (~4 times) lower secretion of IL-1ß than the lipopolysaccharide negative control.

2.3.3.3 Biochemical synthesis and gene expression profile

Gene expression profile of the fibrochondrocytes shown in **Figure 2.5** shows significant upregulation in the expression of sox-9 (~2 fold increase), aggrecan (~10 fold increase) and collagen II (~8 fold increase) genes after 7 days followed by their maintenance along with collagen I expression over the period of 21 days. This indicates the maintenance of fibro-chondrocytic phenotype of the seeded cells with no downregulation of chondrogenic (sox-9, aggrecan and collagen II) and fibroblastic (collagen I) genes.

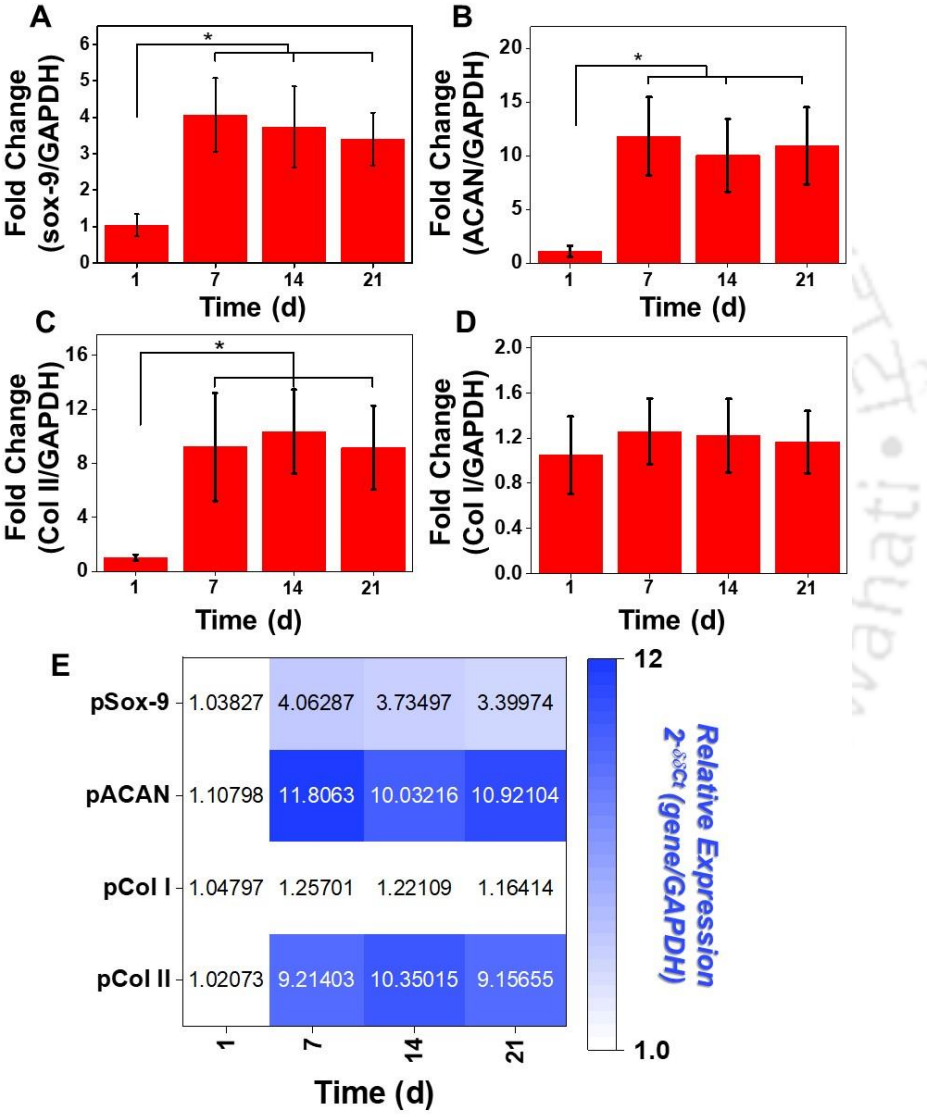

Figure 2.5: *Real-time PCR results showing transcript levels of fibro-chondrocyte-related genes during 21 days of culture on printed constructs: (A) sox-9, (B) aggrecan, (C) collagen type II and (D) collagen type I. The genes have been normalized to GAPDH and expressed as relative values to day 1. (E) Heat-map representation of the relative gene expression for fibrochondrogenic genes. *p ≤ 0.05.*

The enhanced protein level synthesis and deposition of extracellular matrix components, i.e., sulphated glycosaminoglycans (sGAG) and collagens are depicted in **Figure 2.6**. The cellular proliferation derived from the Alamar blue assay is restated by the increase in total DNA content. The amount of sGAG secreted and deposited increased significantly by ~ 2 times after 21 days of culture. Similarly, the deposition of hydroxyproline per construct increased by ~ 5 folds after 21 days. Though the deposited amount of sGAG rises per construct but the cellular proliferation and the resultant increase in DNA contents lead to no significant increase in the sGAG deposited after 7 days when normalized to the DNA content. On the other hand, the hydroxyproline content, measured and normalized to the DNA content, shows a significant rise after 21 days.

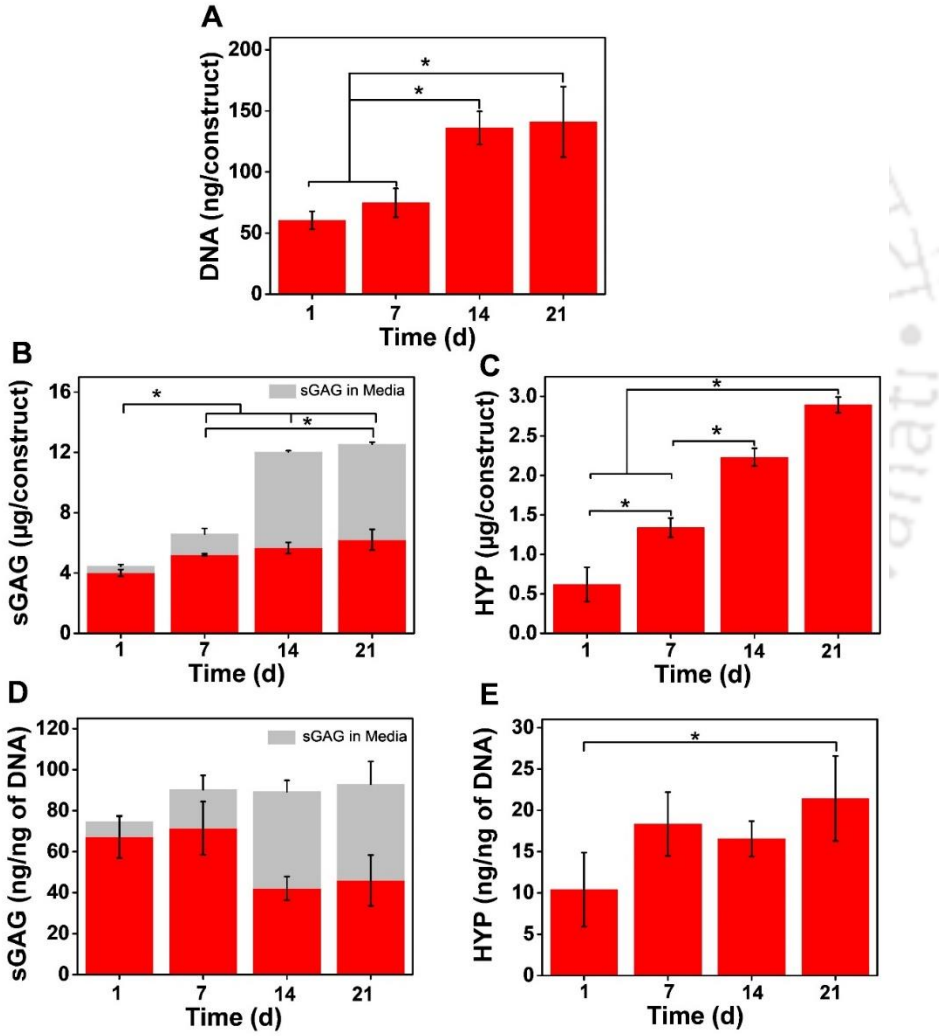

Figure 2.6: *Biochemical assay quantifying (A) DNA content (per construct), (B) sulphated glycosaminoglycans (sGAG) retrieved from constructs and secreted in media per construct, (C) hydroxyproline (HYP) content per construct, (D) total sGAG secreted normalized to DNA content and (E) total HYP deposited normalized to DNA content after 1, 7, 14 and 21 days of culture on printed constructs. *p ≤ 0.05.*

2.3.3.4 Histological Analysis

Histological staining of the scaffolds after 21 days of culture was done using H&E staining. The micrographs of the histological sections showed a uniform distribution of cells within the grids of the scaffolds (**Figure 2.7A**). The histochemical staining of sGAG using alcian blue showed positive results (**Figure 2.7B**) showing the abundant deposition of sGAG evenly distributed over the scaffolds.

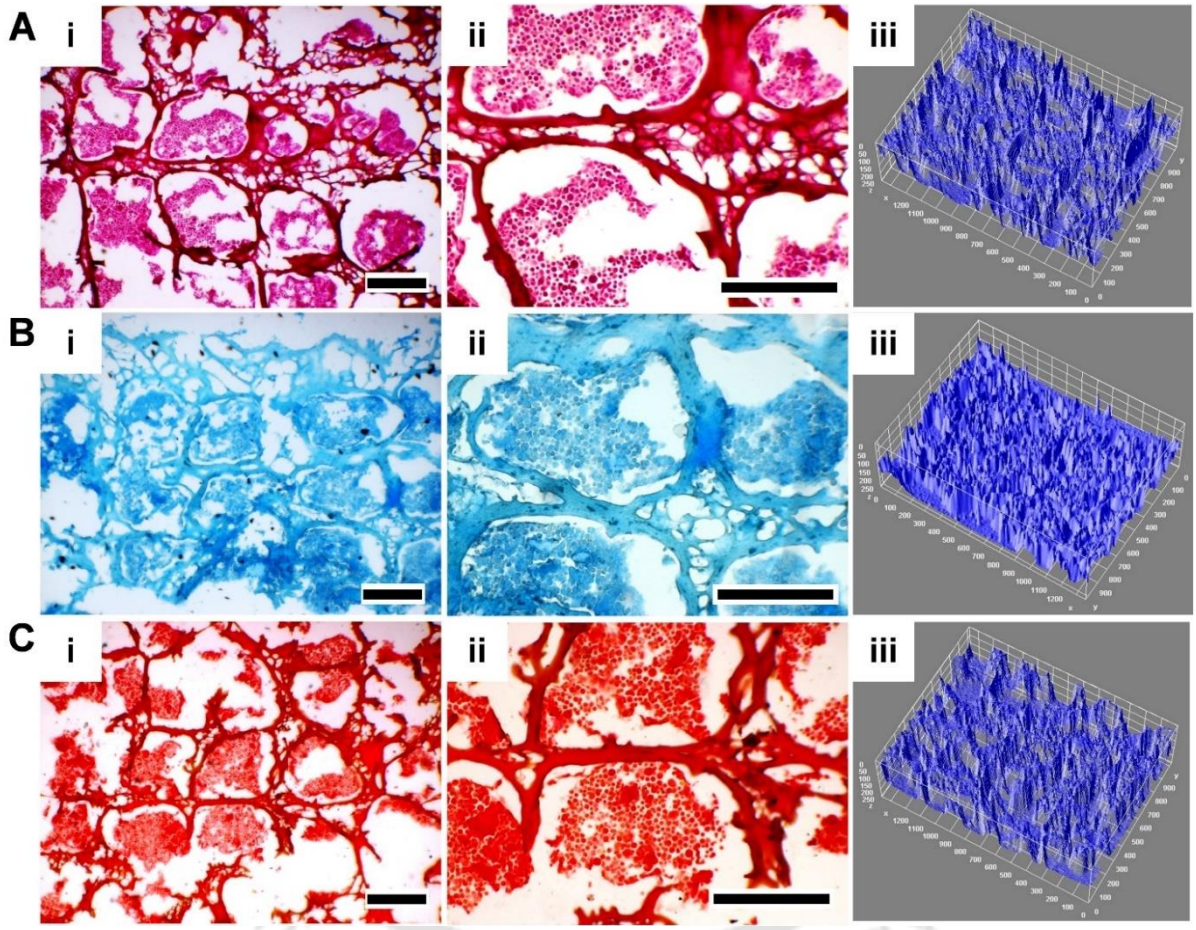

Figure 2.7: *Representative stained images of histological sections of grid infill constructs seeded with fibrochondrocytes and matured for 21 days in-vitro. (A) Hematoxyline and Eosin stained sections, showing the distribution and alignment of cells within the grid. (B) Alcian blue-stained sections, showing the deposition of sGAG by the fibrochondrocytes. (C) Picrosirus red-stained sections, showing the deposition of collagen by fibrochondrocytes. (A)i, B(i) and C(i) are lower magnification micrographs. A(ii), B(ii) and C(ii) are magnified micrographs focussing within the region. A(iii), B(iii) and C(iii) are distribution profile of cells stained by H&E, alcian blue stain and picrosirus red stain using 3D surface plot feature of ImageJ. Scale bar: 200µm*

Moreover, the total collagen secreted has been stained using fast red, showing the deposition of collagen within the grids of the scaffolds (**Figure 2.7C**). Additionally, the distribution of the cells, sGAG, and collagen within the section of the scaffolds were plotted to

obtain surface plots showing the placement of the cells and the peak deposition areas within the scaffolds.

2.3.3.5 *In-vivo* biocompatibility assessment

The infiltration of cells into the scaffolds from the surroundings as well as the degradation of scaffolds retrieved after 7 and 14 days of subcutaneous implantation is shown in the stained micrographs (**Figure 2.8**). The scaffolds show enhanced cellular infiltration and scanty presence of macrophages shown by green fluorescence (**Figure 2.8A**) and brown colour (**Figure 2.9A**) after 7 days of implantation. The enhanced degradation of the constructs and their resorption can be observed in the section retrieved after 14 days of implantation (**Figure 2.8B**). The intensity of green fluorescence (**Figure 2.8B**) and DAB stain (**Figure 2.9B**) can be observed to reduce within the remnants of the scaffolds after 14 days showing excellent immuno-compatibility of the scaffolds *in-vivo*.

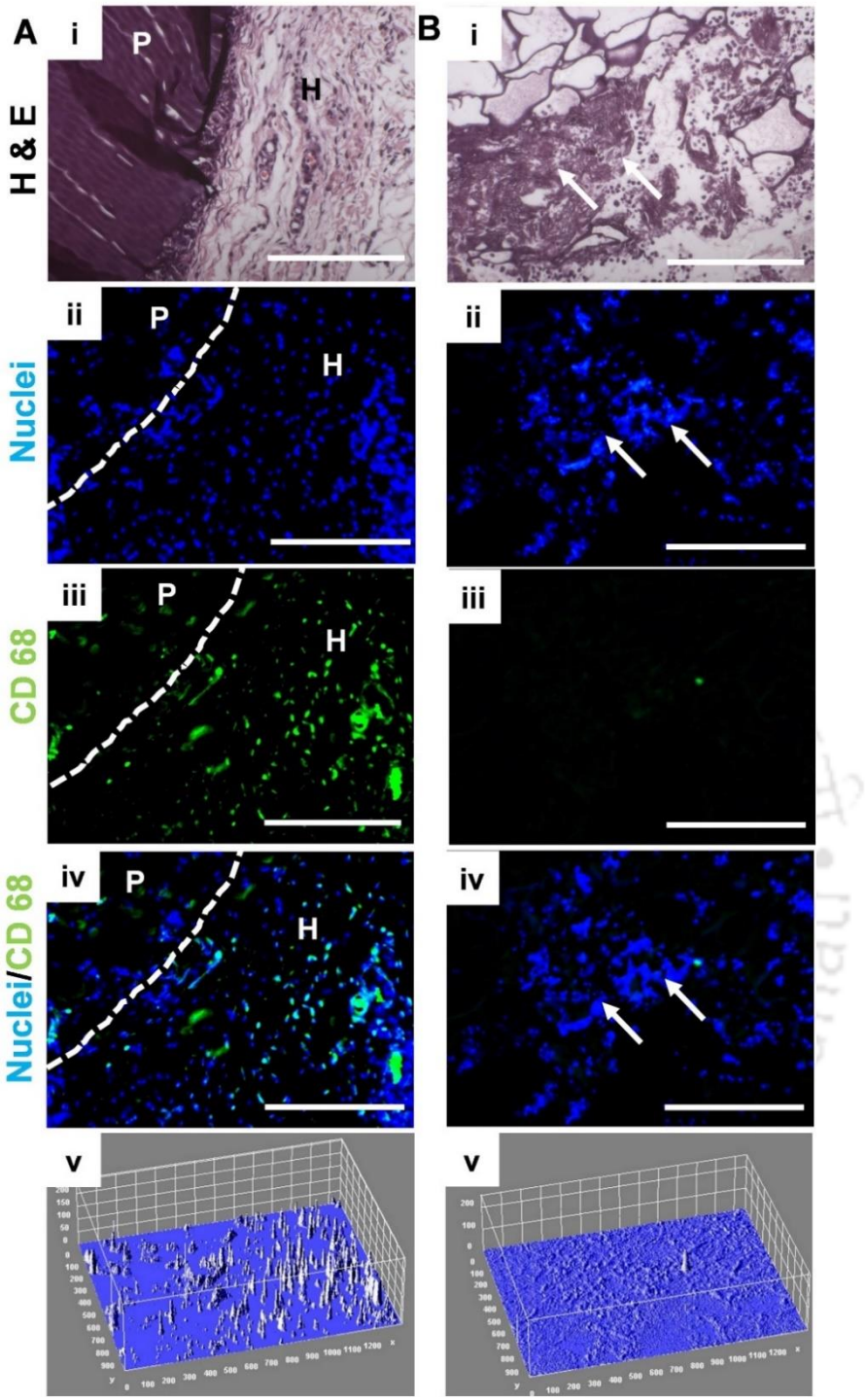

Figure 2.8: *H&E and CD68 antibody stained images showing the in-vivo cell infiltration and immuno-compatibility of subcutaneously implanted cross-linked bioprinted scaffolds in mice retrieved after (A) 7 days and (B) 14 days. (A)i and (B)i are H&E micrographs; (A)ii-iv and (B)ii-iv represent the nuclei, CD68 positive cells, and merged micrographs respectively; (A)v and (B)v represent the surface plot showing the distribution of CD68 positive cells within the scaffolds and the host tissue nearby. Symbols P and H stand for printed construct and host tissue, respectively. Arrows denote the infiltration of host tissue within the printed constructs retrieved after 14 days. Scale bar: 200µm.*

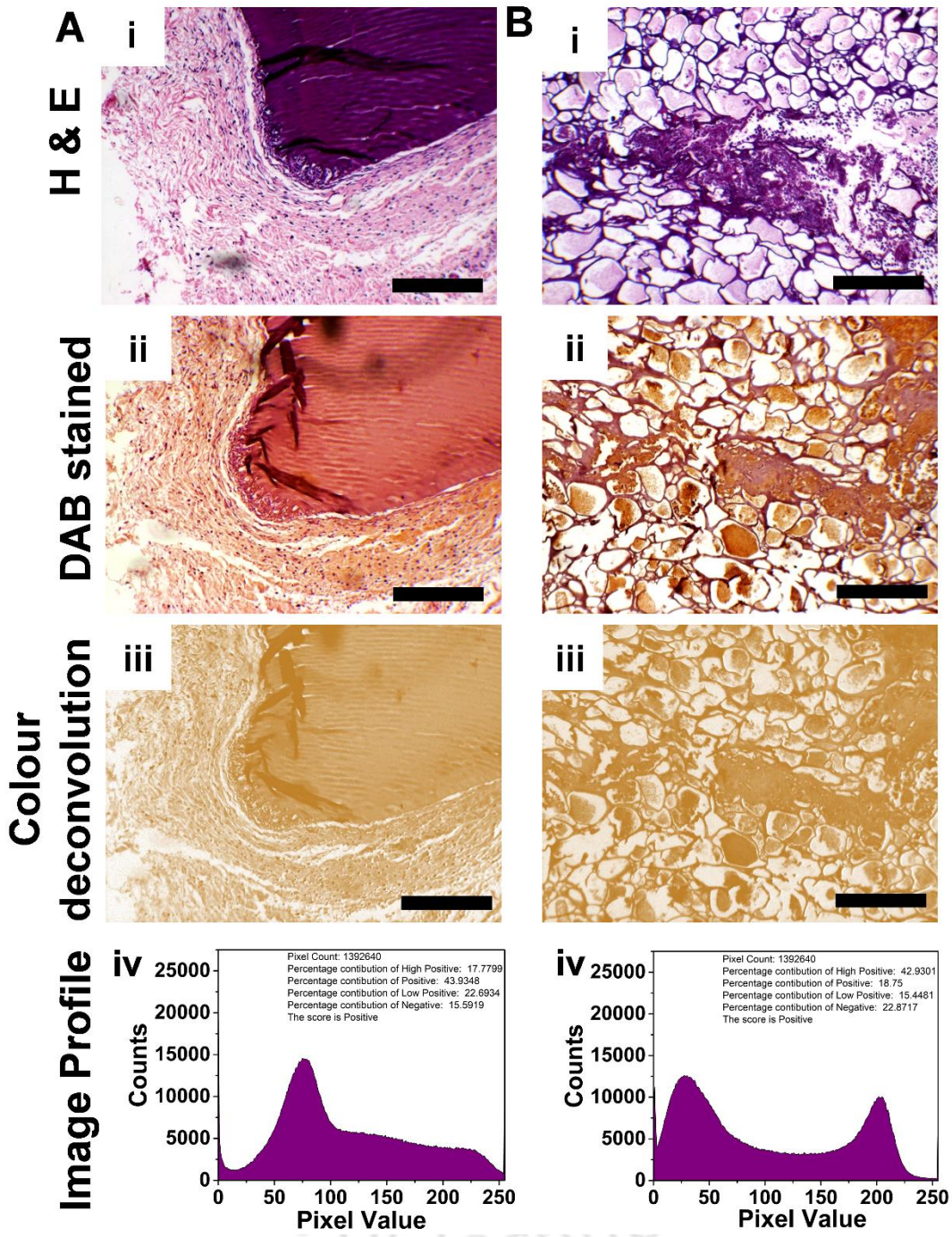

Figure 2.9: *H&E and CD68 antibody stained DAB-chromogen images showing the in-vivo cell infiltration and immuno-compatibility of subcutaneously implanted cross-linked bioprinted scaffolds in mice retrieved after (A) 7 days and (B) 14 days. (A)i and (B)i represent the H&E stained microgrpahs, (A)ii and (B)ii represent the DAB stained micrographs, (A)iii and (B)iii represent the color deconvoluted DAB stained micrographs and (A)iv and (B)iv are the profiles of DAB staining. The colour deconvoluted images, histogram profile and pixel analysis data obtained from DAB image analysis, using ImageJ, represent the scoring of stained zones using IHC profiler plugin. Scale bar: 400µm.*

2.4. Discussion

In this study, we fabricated biomimetic meniscus scaffolds with the intricate internal fibre architecture of the native meniscus containing circumferentially lamellar and radially emanating fibres followed by grid mesh region at the top layer. The initial physical entanglement of the mulberry (*B. mori*) and non-mulberry (*A. assama*) SF renders excellent viscoelastic properties to the SF-gelatin based bioink for high-resolution micro-extrusion printing. This also serves as an initial crosslinking phase followed by the freeze-drying and another cycle of crosslinking using EDC/NHS chemistry. This sequential crosslinking renders the scaffolds with improved mechanical strength and durability similar to native menisci [416]. The compressive modulus of our scaffolds (with 10% (w/v) bioink protein content) is comparable to similar silk constructs with higher (30% (w/v)) bioink protein concentration reported elsewhere [293]. The porosity and pore interconnectivity of a scaffold determine their efficacy in tissue engineering application. Application of 3D printing helped in the fabrication of scaffolds with total interconnectivity and high water absorption ability. Moreover, the fibre orientation and spacing may be modified to produce changes in the mechanical stability of the scaffolds. Porosity may be increased by reducing the inner diameter of the extrusion needle; however, it becomes increasingly difficult to print lower fibre diameters owing to the high pressure and slower speed required for the same.

We used an open-source model for knee joint from GRABCAD community to isolate and slice the meniscus model and fabricate the respective scaffolds. This was practical for the initial validation studies performed but may not be translational for clinical applications. MRI imaging for creation of 3D meniscus models non-invasively reported by many groups [132] can be used as an ideal source to produce patient-specific results. An approach to the same has been shown in **Scheme 1(A)**. Furthermore, due to the presence of highly biocompatible and functional scaffold matrix of mulberry and non-mulberry silk fibroin along with gelatin, a functional meniscus can be easily developed by producing a contralateral model of the healthy knee and seeding the requisite cells derived from the resected or damaged menisci.

Primary porcine fibrochondrocytes were selected as the model cells due to their abundance in the native menisci as well as their essential role in functioning as both partially fibroblastic and partially chondrogenic. Silk fibroin and gelatin were used as a blend to form a shear-thinning bioink which was chemically crosslinked to produce structurally strong and highly compressive scaffolds. The presence of silk fibroin renders unique material durability and bioactivity while the presence of gelatin has two folds of advantages namely, mimicking

the bulk ECM component (collagen) for the menisci and providing temperature-based shear thinning for excellent printing resolution. The innermost layer of the meniscus is circumferential fibres running along the length of the menisci followed by a layer of radially lamellar tie fibres perpendicular to the bottom layer fibres superseded by an external grid mesh layer as reported by Peterson and Tillmann [392]. Thus, the corresponding layers were designed accordingly and fabricated. We carried out the study based on the hypothesis that post-fabrication of the scaffolds using the optimized bioink, the seeded fibrochondrocytes over the scaffolds will proliferate and deposit their native ECM within the pores of the scaffolds and form a tissue construct with further maturation.

The initial studies involved optimization of bioink composition. The blending of mulberry (*B. mori*) and non-mulberry (*A. assama*) silk fibroin formed a gel rapidly at 37°C within 20 minutes due to hydrophobic interactions between the silk fibroin chains [417] while entrapping the gelatin within. Thereafter the bioink was cooled to 25°C to reach enhanced viscoelasticity and shear thinning. The optimized composition was chosen based upon the gel strength and shear-thinning of the bioink. Gel strength of the bioink is necessary for fabrication of self-standing 3D constructs while the shear-thinning behaviour of the bioink improves the resolution of fabrication. The optimized bioink composition of 1.5% (w/v) *B. mori,* 1.5% (w/v) *A. assama* silk fibroin and 7% (w/v) gelatin were found to possess the necessary gel strength and shear-thinning well within the pressure extrusion range of 700kPa of the bioprinter. The bioink was further validated rheologically for its shear-thinning nature, stability under various frequencies of shear strain, gel-strength retention, and temperature-based viscoelastic changes. Building upon these studies, constructs was fabricated with high resolution, and the cross-linking was carried out by EDC/NHS chemistry. Thereafter, the scaffolds were first physicochemically and mechanically characterized to evaluate their suitability in mimicking the physicochemical and mechanical properties of meniscus tissue. Mesh grid constructs were used for the swelling characterization and were found to uptake PBS >7 times their dry weight indicating that the scaffolds were highly porous and could remain hydrated while promoting the exchange of nutrients and metabolites through diffusion. The degradability of the constructs was characterized using mesh grid constructs, and the constructs retained 20% of their weight after 21 days in proteolytic conditions. This rapid degradation can be majorly attributed to the fact that gelatin is abundantly used as a zymography substrate and presents target sequences for enzymes such as MMPs [279].

Mechanically the grid, concentric, lamellar infill, as well as the tri-layered full-thickness constructs, had the compressive moduli comparable to or greater than the equilibrium modulus of native menisci [418]. The menisci bear 5-15% compression under physiologically relevant loading conditions [416]. So, we subjected our scaffolds of various infill and the trilayered constructs to 20% strain, and in-turn found their stability under repeated loading and unloading compression cycles. The scaffolds of all four kinds displayed excellent stability under 200 cycles of compression without any significant loss of strength indicated by the small deviations between cycles 1 and 200 in the stress-time and stress-strain regime. Though, degradation of the scaffolds needs to be evaluated under mechanically loaded conditions, but the mechanical stability and potential of the scaffolds for *in-vivo* implantation is promising with the current observations.

The bioactivity of meniscus scaffolds is highly dependent on the proliferation of fibrochondrocytes and the maintenance of their phenotype to aid in the synthesis of native ECM components. The cells were found to attach to the scaffold matrices very conveniently due to the copious cell-binding domains that are present on non-mulberry *A. assama* silk fibroin [280, 405] as well as the biocompatibility of gelatin [416]. Proliferation index of seeded fibrochondrocytes was observed to rise and saturate at ~2 folds post 14 days until 21 days with no significant difference in the proliferation indices at different seeding densities suggesting the limited proliferative ability of the cells following the initial rise. So to compensate for the same, cells were seeded at the highest density of 10^4 cells/mm^2, and further studies were carried out at this seeding density. The seeded fibrochondrocytes that were attached to the edges of the scaffold pores could find more adhesive surfaces so as to attain dendritic morphology while those in the central portion of the scaffold pores formed aggregates and achieved more rounded morphologies. Consequently, we observed that the chondrogenic (sox-9, aggrecan and collagen II), as well as fibroblastic (collagen I) genes, were upregulated and maintained for the entirety of culture duration. The total sGAG and collagen (hydroxyproline) content secreted was estimated, and it was found to gradually rise by ~2 times and ~5 times, respectively. Moreover, when normalized with the DNA content, the sGAG and collagen content were found to possess no significant difference at 7, 14 and 21 days. This, along with the proliferation index values, shows the maintenance of the fibrochondrocyte ECM synthesis phase while they are proliferating concurrently.

Host tissue acceptance and immune response are majorly a challenge for any tissue engineering scaffold. An adverse immune reaction from the implanted scaffold material would

further result in acute inflammation, tissue destruction and interference in the healing mechanism of the host tissue, which may eventually lead to rejection of the graft [419]. Henceforth, a quantitative *in-vitro* assay and subcutaneous *in-vivo* implantation were carried out for the scaffold post-crosslinking. Murine macrophages cultured *in-vitro* showed negligible response (similar to TCP) to the scaffold after 24 h when compared with the lipopolysaccharide positive control. This was in accordance with the previous reports of silk-based biomaterials being immuno-compatible [412, 419]. Furthermore, acellular scaffolds were subcutaneously implanted in rats which led to the findings that the scaffolds were intact until 7 days while being infiltrated by host cells and eventually degraded after 14 days with heavy infiltration of cells and host tissue within. The stained sections of retrieved scaffolds show infiltration of host cells and some macrophages in 7 days. At 14 days, the scaffold is degraded and shows the skeletal framework that has been infiltrated by the host cells and tissue. Moreover, macrophages are not visible in the vicinity. This shows the immuno-compatibility, degradability, and integration potential of the scaffolds *in-vivo*. Though the meniscus tissue is vastly avascular, the interaction of the implant towards its outer periphery with the native vasculature is essential for cellular survival towards the inner periphery.

Though the 3D scaffolds possess the potential to be utilized in both acellular as well as cell-seeded forms pertaining to their mechanical stability, cytocompatibility and minimal immunogenicity, the degradation of the scaffolds in the subcutaneous pockets compels further characterization of the degradation of scaffolds by implantation at partially or completely resected meniscus animal models. Consequently, necessary additions need to be made in the design of the scaffolds in terms of their size and inclusion of suturing nodes at both ends of the meniscus constructs. Moreover, the degradability of the constructs needs to be scrutinized after compressive loading cycles. Also, we hypothesize that the scaffolds can be seeded with native meniscus fibrochondrocytes or pre-differentiated stem cells and post *in-vitro* maturation under mechanical (compressive stress) and biological (growth factor cocktails) stimuli for 7-14 days can be implanted *in-vivo*. This would eliminate any limitations encountered due to degradation of the scaffolds.

2.5 Salient Outcomes and Findings

1. Through the present study, we demonstrated the rapid prototyping of a biomimetic tri-layered meniscus tissue scaffolds using a novel SF-gelatin based bioink with excellent mechanical, swelling, and degradation properties.
2. The tri-layered nature of the meniscus aids in mimicking the native architecture of the menisci that are poised to make the constructs conducive for bearing high mechanical stress and the concomitant loading-unloading cycles for a longer duration.
3. The scaffolds supported the growth of native meniscus fibrochondrocytes as well as assisted in the maintenance of their phenotype evident by the gene expression profile and ECM components secreted.
4. The scaffolds possess appropriate immuno-compatibility rendering suitability for implantation.
5. Although the present scaffolds encompass the potential for meniscus defect repair, actual implantation into defect sites for evaluation of load-bearing and regeneration in smaller and larger animals needs to be done. Further, optimization is needed for fabricating scaffolds suitable for attracting and homing of the resident mesenchymal progenitor cell population for achieving better regeneration *in-vivo*.

CHAPTER 3

Development of photo-polymerised silk-based 3D printed constructs embedded with growth factor loaded micro-spheres for potential biomimetic recapitulation of meniscus

This chapter describes the development of a growth factor loaded gelMA microsphere incorporated biomaterial ink blend that consists of silkMA/gelMA/A. assama silk fibroin for 3D printing meniscal defect implants to potentially treat full thickness meniscal defects. The gelMA microspheres were fabricated using an oil-emulsion based microfluidic method and incorporated into the optimized photo-curable ink. The developed ink showed optimal printability and sustained release of the fibrogenic (CTGF) and chondrogenic (TGFβ3) growth factors over long duration. The fabricated constructs were then evaluated for their potential to recapitulate the inner (chondrogenic), middle (fibrochondrogenic) and outer (fibrogenic) zone cellular phenotypes and ECM of the native meniscus.

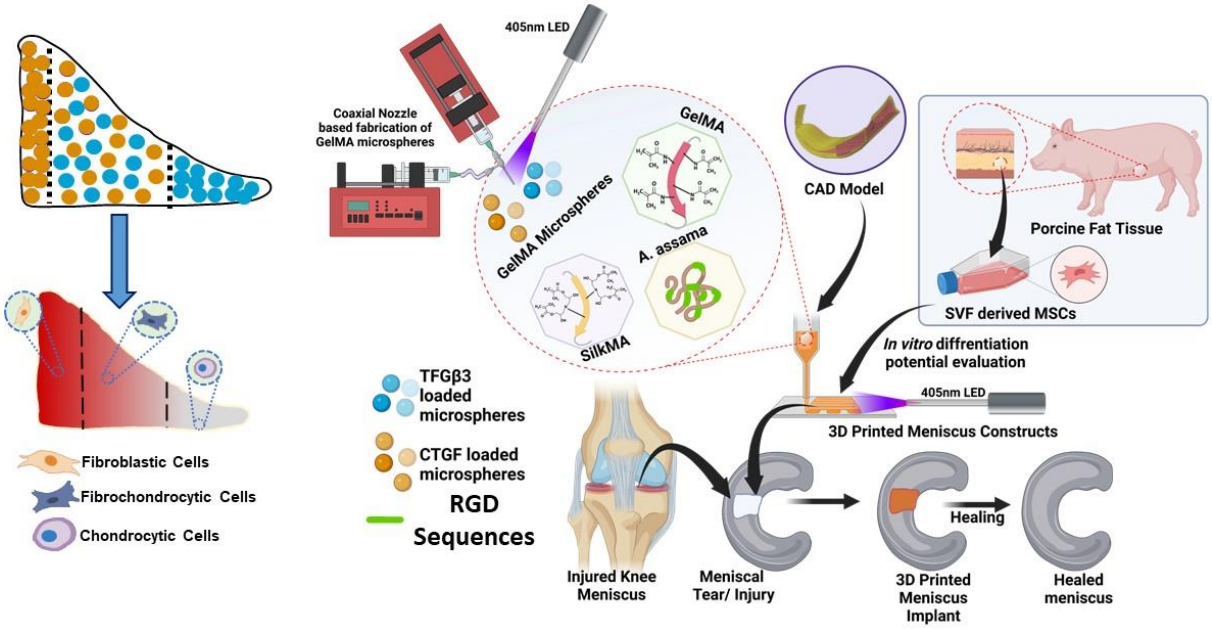

Outcomes of this chapter have been published as:

Ashutosh Bandyopadhyay, Biman B. Mandal. *Photocrosslinkable silk-based bioinks embedded with growth factor loaded microspheres towards cell-free 3D printing approach for biomimetic regeneration of meniscal tissue*, **Applied Materials Today.** 2023, 36, 102049. DOI: 10.1016/j.apmt.2023.102049

ABSTRACT

Fibrocartilaginous meniscal tear regeneration is a major challenge due to the large avascular regions which suffer several injuries among all age-groups. Mostly, meniscus implants are focused on the development of multi-layered meniscus constructs and scaffolds that mimic the macro-architecture, functionality and mechanical strength. The native human menisci consist of vascular and avascular regions that contain different cellular phenotypes and are hence composed of a gradient of extracellular matrix (ECM) components. The biochemical composition of the inner, middle and outer regions of the knee menisci plays a significant role in the mechanical behavior and its overall functionality. We have developed a photo-polymerizing mulberry and non-mulberry silk-based biomaterial ink which is laden with growth factor loaded gelMA microspheres for the zone-specific regeneration of full thickness meniscus tears using three-dimensional (3D) fabrication. We have fabricated growth factor loaded gelMA microspheres and encapsulated them within the biomaterial ink for controlled release of Connective Tissue Growth Factor (CTGF) and Transforming Growth Factor-beta3 (TGFβ3) from the different zones of the meniscus constructs. The growth factor releasing constructs demonstrate the requisite mechanical resilience, degradability and release behaviour for regeneration of meniscal tissue. The developed growth factor loaded constructs demonstrate zone specific phenotypic differentiation of adipose derived stem cells and extracellular matrix deposition by the differentiated stem cells *in vitro*. The microsphere loaded constructs were found to be immuno-compatible as well. Therefore, these bioactive microsphere-laden 3D printed meniscus constructs would potentially promote regeneration and integration of meniscal tissue *in vivo*.

3.1 Introduction

The knee menisci are semi-circular heterogenous fibrocartilages that aid in the absorption and redistribution of forces generated by the upper body through the femoral condyles into the tibial plateau. This mechanism of action is achieved by the robust mechanical properties endowed by the internal collagen microarchitecture of the menisci that is divided into 3 layers i.e., the circumferential, radial and mesh from bottom to top [26, 392]. This precise micro-arrangement of the collagen fibres within the menisci is a result of the zonal distribution of cells within the menisci and their respective synthetic properties. The meniscus is hetero-cellular and is mainly composed of three regions as we move from the outer towards the inner edge of the menisci: the red, the red-white and the white region [4]. Each region is populated by its characteristic cellular phenotype, i.e., the fibroblastic, fibro-chondrocytic and the chondrocytic phenotype in the outer, middle and inner regions of the menisci respectively [7, 8]. The respective regions of the menisci are rich in varying types of collagen, i.e., collagen I in the outer region, collagen II in the inner region and a fairly equalized ratio of both the types within the middle two thirds [5]. Similarly, glycosaminoglycan distribution increases as we move from the outer regions to the inner portions of the menisci. Recapitulation of the cellularity and biochemical makeup of these regions is necessary to ensure complete regeneration of full-thickness meniscus tears and meniscus resections [23, 48].

The current clinical practices involve the total or partial resection of torn menisci [2, 420] and replacing them with patient-suggested natural [88], synthetic [89] or hybrid materials [421] meniscal implants or leaving the cavity as sham. While the resection leads to osteoarthritis in the long run, patients with implants have been known to suffer from shape, size and macroscopic incongruence of the implants due their fabrication process and a potential for mechanical incompatibility due to the synthetic polymers of the implants [79, 422]. Hence, 3D printing based fabrication for meniscal grafts is necessary for ensuring patient specificity of macroscopic architecture, biological functionality and ease of implantation [46].

Fabrication of a zone-specific tissue would require the establishment of a gradient of differentiation agents/growth factors to achieve the cellularity and hence the biochemical synthesis and consequent distribution of the extra-cellular matrix (ECM) components in a zonal fashion. There have been studies that have shown zonal mimicry of meniscal cell phenotypes using 3D printing of thermoplastic polymers in conjunction with the use of growth factors [115, 139, 244, 423]. Though successful in the domain of mechanical resilience, thermoplastic

polymers demonstrate considerably slower degradability, potentially harmful degradation products and potential for failure. These factors encourage the application of nascent or minimally processed natural biopolymer inks that possess better bioactivity, degradability and integration potential, while ensuring the mechanical stability.

Conventionally available biopolymers have found special interest in the formulation of bioinks for 3D printing such as both mulberry and non-mulberry silk [365, 424, 425], gelatin [426, 427], hyaluronic acid [428], carrageenan [429] and so on. Moreover, photo-crosslinking variations of these materials such HAMA [430, 431], ColMA [432], gelMA [424, 433], Car-MA [433, 434] and silkMA [293, 435] have found facile applicability, enhanced mechanical resilience, safe encapsulation of growth factors and cells.

The use of growth factors for recruitment and differentiation of progenitor cells has been widely evaluated in many tissue engineering platforms. The differentiation into chondrogenic phenotype without cartilage hypertrophy and abundant chondrocyte proliferation has been achieved [436, 437] in previously published studies through the treatment of Transforming growth factor-beta (TFG-β) superfamily [438, 439]. Similarly, fibroblastic differentiation of progenitor and stem cells has been achieved by the virtue of CTGF [440, 441]. Studies in the past have also reported the fibrochondrogenic differentiation of stem cells and meniscus healing with a sequential treatment or a cocktail of CTGF and TGF-β3 [115, 442]. The use of microparticles, microcapsules and microspheres within hydrogels, molded scaffolds and printed constructs has been practised avidly by many researchers for the various additive effects such as enhanced mechanical strength, delivery of growth factors and biologics and priming of differentiation of progenitor/stem cells into specific phenotypes. Gelatin and its methacrylate have found copious applications in these scenarios due to their easy fabrication into microparticles and their excellent biocompatibility and degradability [443-445]. Post fabrication, growth factor microsphere laden scaffolds could be seeded onto with mesenchymal progenitor cells for *in vitro* maturation and implantation. Alternatively, such fabricated scaffolds could serve as a directly implantable solution for the *in vivo* recruitment of nearby synovial and infra-patellar fat pad stem cells [446] within the body of the recipient for regeneration of meniscal tissue.

In the present study, we have fabricated 3D growth factor loaded microsphere laden constructs that would aid in mimicking the zonal biochemical make-up of the meniscal tissue. We optimized a biomaterial-ink that consists of a blend of *B. mori* silk fibroin methacrylate

(silkMA), gelMA and non-mulberry *A.assama* silk fibroin (AASF) along with LAP (Lithium phenyl-2,4,6-trimethylbenzoylphosphinate) as a photo-initiator which results in a photo-curable blend that encapsulates the gelMA microspheres. These gelMA microspheres have been fabricated using a customized micro-fluidic method and have been loaded with TFGβ3 or CTGF and blended to form two different bioinks for the fabrication of the gradient microarchitecture of the meniscal constructs. The microsphere laden constructs were characterized for their enhanced swelling, degradability, mechanical durability and release of growth factors. Thereafter their biological assessment was carried out with porcine adipose derived mesenchymal stem cells (pADMSCs). Their ability to support proliferation and differentiation of pADMSCs into the chondrogenic (inner), fibrochondrogenic (middle) and fibroblastic (outer) phenotypes was assessed by both gene expression and region specific matrix deposition. The constructs were also assessed for their *in vitro* immuno-compatibility and a proof-of-concept gradient construct was printed using the dual ink fabrication strategy to evaluate the defect congruence and shape fidelity of our proposed method. The developed one-step silk-based growth factor releasing constructs could be used for patient-specific treatment of partial or full thickness meniscal defects.

3.2 Materials and Methods

3.2.1 Synthesis of *B. mori* Methacrylate (silkMA) and Gelatin Methacrylate (gelMA) and isolation of *A. assama* silk fibroin

B. mori cocoons were degummed and dissolved in LiBr to make a solution that was used to prepare *B. mori* Methacrylate (silkMA) solution using a protocol described previously [293]. Briefly, the silk-fibroin LiBr (SF-LiBr) solution was stirred at 60°C and 300 rpm for 1 h. Glycidyl methacrylate (GMA) was added dropwise to the SF-LiBr solution dropwise at a ratio of 60 µl/ml of SF-LiBr and left to stir for 3 h while maintaining the temperature and thereafter dialysed against deionised water for 5 days in a 14kDa dialysis bag. A. assama silk fibroin (AASF) was isolated as per previously defined protocols [46, 424, 425].

Gelatin methacrylate was synthesized from type-B gelatin (bovine source) using a previously described protocol [447]. Briefly, a carbonate buffer (CB) consisting of sodium carbonate (3.18 g) and sodium bicarbonate (5.86 g) was prepared in 1 L of deionised water. 20 g of type-B Gelatin was added to 200 mL of the CB and mixed thoroughly. The solution was adjusted pH 9 using 5 N NaOH. Thereafter Methacrylate anhydride (MAA, 94%, Sigma-Aldrich, USA) was added to the gelatin solutions at a ratio of 0.1mL of MAA/g of gelatin drop-

wise and kept at 60°C for 1.5 h. The solution was then dialyzed against deionized water for 48 h in a 12-14 kDa dialysis bag.

3.2.2 Microfluidic fabrication of gelMA microspheres for delivery of growth factors

Spherical gelMA microspheres were fabricated using a customized coaxial needle setup **(Figure 3.1)** that consists of a 23G blunt needle (ID:330µm) on the outside housing a 30G blunt needle (ID:160µm) inside [424]. The inner needle is adjusted to protrude out slightly through the outer housing needle for focusing of the flow. The outer needle is attached to a compatible diameter outlet tubing and laid out to the crosslinking area. A customized laser focusing setup was 3D printed for the crosslinking area. A 80 W visible light LED array (405 nm) was used for the crosslinking of the microspheres post exit from the outlet tube in a petri dish. 7.5% (w/v) gelMA blended with 1% Lithium phenyl-2,4,6-trimethylbenzoylphosphinate (LAP, SIGMA Aldrich, USA) was selected for fabrication of microspheres as per previous literature [443] and almond oil (SIGMA Aldrich, USA) was used for the oil phase. The coaxial flow-focusing device was used for the present study due to its superior emulsification, higher polydispersity and size control as compared to sonication and other mechanical agitation methods [443, 448]. The flow rates of aqueous phase and oil phase were varied using syringe pumps (New Era Pump Systems, USA) and found to be optimum at 2000:20 µL/min (oil phase:aqueous phase) for fabrication of microspheres. The formed microspheres were simultaneously crosslinked using 405 nm visible light for 20 seconds before washing them using distilled water 2-3 times followed by collecting them using centrifugation. The obtained microspheres were freeze-dried for longer storage and loading purposes.

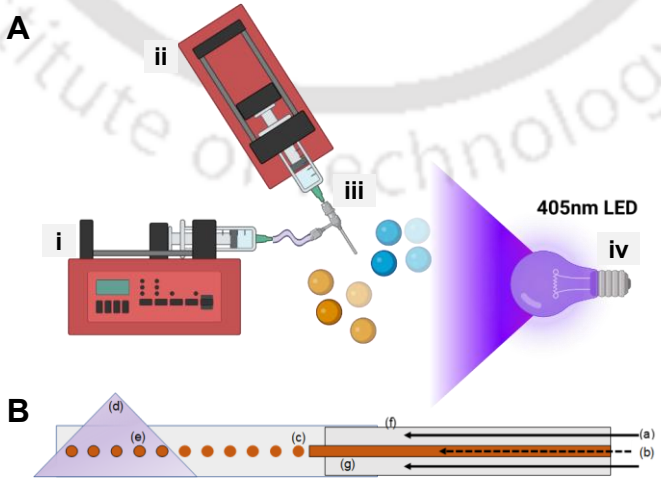

Figure 3.1: *(A) The setup for fabrication of microspheres denoting (i) Oil phase, (ii) aqueous phase, (iii) coaxial nozzle and (iv) 405nm LED. (B) Schematic showing the fabrication*

mechanism of microspheres (a) oil phase, (b) aqueous phase containing 7.5%(w/v) gelMA and 1%(w/v) LAP, (c) uncrosslinked gelMA spheres, (d) 405nm LED based crosslinking, (e) crosslinked gelMA spheres, (f) 23G needle and (g) 30G needle. The flow rate of oil phase was set to 2000 µL/min and the aqueous phase was set to 20 µL/min. The spheres, post fabrication, were washed with 5% (v/v) aqueous ethanol solution and centrifuged for collection.

3.2.3 Characterization of gelMA microspheres

3.2.3.1 Swelling of Microspheres

Post fabrication, the microspheres were allowed to swell for 12h and their initial and final diameters were determined using analysis of their images by ImageJ. 50 samples of the microspheres from 3 different imaged areas were selected for determination of microsphere diameter before and after swelling. Consecutively the swelling ratio of the microspheres was measured by weighing them in freeze-dried condition (W_d) followed by soaking in PBS for different durations and weighing them at specified intervals (W_w) till they reached equilibrium. This helped in determining the time required for their loading. Triplicates of 10mg spheres were used for the measurement and the following equation was used for the calculation of swelling ratio: $Swelling\ ratio = \left(\frac{W_w - W_d}{W_d}\right)$

3.2.3.2 Loading of microspheres

The microspheres were loaded with fluorescently labelled FITC Dextran through adsorption for assessing their loading efficiency. The fabricated microspheres were freeze-dried and weighed. Thereafter, 200 ng/ml and 50 ng/ml solutions of CTGF and TFGβ3 were used for the loading of the microspheres. 4 mg of microspheres were incubated in each of the solutions kept under shaking for 24 h at 4 ºC for loading. The amount of TFGβ3 and CTGF loading per unit weight of microspheres was determined by quantifying the amount of growth factors remaining in the supernatant post loading.

3.2.3.3 Release profile of microspheres

Batches of 4 mg growth factor loaded microspheres of both TFGβ3 and CTGF were encapsulated in 1 ml biomaterial-ink separately and 3D printed. The 3D printed constructs (n=5) were incubated in PBS at 37 ºC for evaluating the release of the growth factors from printed constructs for a period of 15 days. The cumulative release from the incubated supernatant collected at each time point was determined using ELISA based quantification.

3.2.4 Preparation of photo-crosslinking biomaterial-ink blend and its characterization

3.2.4.1 Printability and Gelation

Bioink blends were prepared, and printability of the formulations was assessed on the observed factors including gelation behaviour, structural stability, shear-thinning nature, and self-standing behavior. The concentration of *B. mori* methacrylate (silkMA) and gelatin methacrylate (gelMA) were varied while keeping the concentration of *A. assama* silk fibroin (AASF) constant, and the printability was checked for the same.

3.2.4.2 Fourier Transform Infrared Spectroscopy

Infrared spectroscopy was carried out for the individual biomaterial-ink components (silkMA, gelMA, *A. assama* SF) as well as the optimized biomaterial-ink blend using an FTIR-ATR (Shimadzu, IR Affinity-1S WL). Freeze-dried samples were cut and small part of the same were placed over the ATR crystal individually for acquisition of infrared spectra over wavenumbers between 600 and 2500 cm^{-1} and averaged over 16 scans. The characteristic peaks of biomaterial-ink components and the biomaterial-ink were observed for gelation induced changes and crosslinking related phenomena.

3.2.4.3 Rheological Characterization

Rheological assessment of the optimized biomaterial-ink composition which was chosen for printing was carried using an MCR 302 (Anton Paar, Austria) rheometer. The biomaterial-ink composition with and without microspheres was evaluated through Amplitude, Frequency and Temperature sweep as well as Three Interval Thixotropy (3ITT). These tests were deemed essential to ascertain the optimal conditions for biomaterial-ink printability along with the determination of the hydrogel's gel strength. The biomaterial-ink (with and without microspheres) was subjected to a temperature sweep of 4°C - 45°C, before and after gelation of silkMA and *A. assama* silk. This was done to evaluate the printability temperature range. Thereafter the biomaterial-ink (with and without microspheres) was subjected to an amplitude sweep from shear strain of 0.01% to 1000%, post 20 min gelation of silk fibroin (at 37°C). The temperature of the test was maintained at 20°C which was deemed to be optimal printing temperature. The respective complex viscosity was recorded to determine the linear viscoelastic range (LVER) and to ascertain the shear-thinning of the biomaterial-ink with and without microspheres. Henceforth, the LVER range was used to carry out the frequency sweep test on the biomaterial-ink (with and without microspheres), after gelation of silk at 37°C for 5

min. The angular frequency of shear was varied from 0.3 to 100 rad/s at 20°C testing temperature and the biomaterial-ink was evaluated for its stability at various frequencies of shear. Finally, the gel strength of biomaterial-ink (with and without microspheres) was determined using alternating low shear/low angular frequency and high shear strain/high angular frequency intervals. This test mimics the shear experienced by the biomaterial-ink during extrusion momentarily and thereafter the return to its low/no shear condition where its needs to exhibit self-standing behavior.

3.2.4.4 Gelation, printing resolution, buckling test and multi-layer grid fabrication

The optimized bare biomaterial-ink and microsphere loaded biomaterial-ink were assessed for gelation, printing resolution and buckling test using custom g-code files **(Figure 3.2)**. The assessment of multi-layer grid fabrication was conducted for 15 mm x 15 mm grid constructs using custom g-code files **(Figure 3.2)** of 2, 5 and 10 layers for both bare biomaterial-ink and microsphere loaded biomaterial-ink.

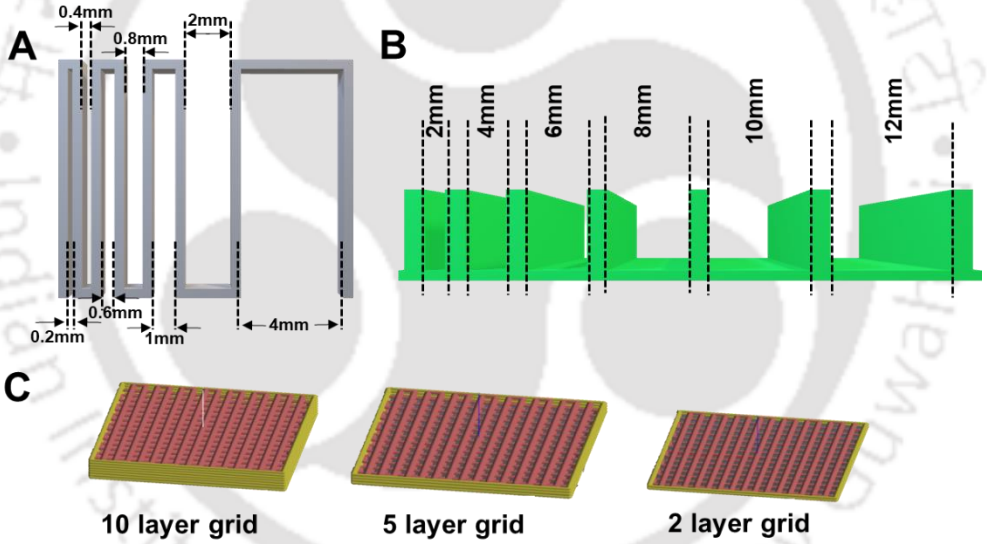

Figure 3.2: *(A) 3D CAD model for evaluation of printability of various inks. (B) 3D CAD model of custom designed PLA construct for evaluation of buckling of ink. (C) 3D CAD model of custom designed 15mm x 15mm grids with 10, 4 and 2 layers.*

3.2.4.5 Porosity and Wettability studies

Apparent porosity of printed constructs with and without microspheres was conducted using hexane displacement method according to previously optimized method [406]. Briefly, hexane was taken in a graduated cylinder and the initial volume was noted (V_1), freeze-dried constructs were immersed in hexane for 20 minutes to reach equilibrium and the volume was noted down (V_2) and finally the constructs were carefully removed without squeezing and the

reduced volume was noted down (V_3). The apparent porosity was calculated based on the formula: $Apparent\ Porosity\ (\%) = \frac{V_1 - V_3}{V_2 - V_3} \times 100$

Biomaterial ink with or without microspheres were poured onto a glass slide to form a layer and photocrosslinked. The photocrosslinked layers were subjected to aqueous contact angle measurement using a Drop Shape Analyzer (KRUSS, DSA25). 5 µL of deionized water was used to form pendant droplets on the coated surfaces followed by contact angle measurement after 30s.

3.2.5 3D Fabrication of Dual Ink Gradient Constructs

Bioinks were fluorescently labelled using 2 different colours (red/pink and green/yellow) and encapsulated within the optimized biomaterial-ink for printing. A gradient grid model with the an outer section of Ink1 (green), an inner section of Ink 2 (red) and an intermediate section of Ink 1 and Ink 2 in alternating layer was used for the mimicking the gradient of growth factor laden spheres required for the zonal differentiation of mesenchymal stem cells. The constructs were freeze-dried and electron microscopic imaging was carried out to reveal the presence of microspheres within the 3D printed constructs.

The CAD model of a human meniscus was used according to our previous study [46] to fabricate a proof-of-concept construct with the dual biomaterial-ink. An intact meniscus was printed and a meniscus with a defined full thickness defect was fabricated. The defect site was modelled, larger part in the middle was assigned fibrochondrogenic with alternating ink 1 and ink 2 layers while the outer part was assigned to ink 1 (yellow) and inner part to ink 2 (pink). Thereafter the defect replacement construct was printed using the dual biomaterial-ink strategy and evaluated for conformity of shape, size and geometry along with the regions of the menisci namely, outer, middle and inner regions.

3.2.6 Swelling study

3D printed constructs were subjected to swelling studies to determine the water uptake ratio using a previously established protocol. In brief, grid-infill constructs (n=3, with and without microspheres) were weighed post fabrication (W_f) to determine their initial weight. Henceforth, these constructs were immersed in phosphate buffered saline (PBS; pH 7.4) and the weight of the constructs was measured post water uptake (W_s) at various time intervals after

gently dabbing off the excess PBS. Weight gain (%) was calculated using the following equation: $\%\ Weight\ Gain = \left(\frac{W_f - W_s}{W_s}\right) \times 100$

3.2.7 Degradability study

Degradability study was carried out for the constructs *in-vitro* (with and without the microspheres) both in the presence of protease XIV (Sigma-Aldrich, ≥3.5 U/mg) [413] as well as saline (PBS, pH 7.4). Initial dry weights (W_i) of the 3D printed constructs (n=3, with and without microspheres) was measured and these were immersed in either 0.5 U/ml protease XIV containing PBS or control saline (PBS, pH 7.4) at 37 °C. The constructs were weighed intermittently for the remaining mass (W_r) after washing in saline (PBS, pH 7.4) and freeze-drying. The % weight remaining was calculated from day 1 to day 35 as follows: $\%Weight\ Remaining = \left(\frac{W_r}{W_i}\right) \times 100$

3.2.8 Confined uniaxial compressive and cyclic compressive mechanical testing

Compressive mechanical strength of the constructs (with and without microspheres) was carried out using a universal tensile testing machine (Model 5944, Instron, USA). 3D printed constructs (with and without microspheres) of dimensions 7x7x7mm^3 were subjected to uniaxial compressive strain of 60% at a crosshead speed of 5 mm/min under hydrated conditions (PBS, pH 7.4). The compressive stress-strain curve was plotted for the various constructs and the average compressive strength modulus was calculated for each construct at peak strain. Uniaxial cyclic compression was carried out at 20% strain over 100 cycles at crosshead speed of 5 mm/s for determining the durability of the constructs. Compressive stress-time graphs were plotted for the first and last 20 cycles along with the compressive stress-strain hysteresis loop of the first and last cycle to visualize any deviation during the test.

3.2.9 Biological Characterization

3.2.9.1 Cell Isolation and seeding on microsphere laden constructs

Primary porcine adipose derived mesenchymal stem cells (pADMSCs) were isolated from porcine belly fat samples in accordance with previously published protocols [425]. Briefly, subcutaneous fat tissue was procured from the local abattoir in cold PBS. The surrounding dermal and muscle tissues are removed, the fat is minced finely and washed gently with PBS containing penicillin (100 units/mL, Gibco, USA), streptomycin (100 µg/mL, Gibco, USA) and amphotericin-B (2.5 µg/mL, Gibco, USA) for sterilization. Minced and sterile fat

tissue was digested using collagenase enzyme solution (type-IA, (≥ 125 CDU/mg, Sigma, USA, 0.1 %wt/v) made in incomplete DMEM under constant agitation (2 h, 37 °C). The digested suspension was neutralised with equal volume serum supplemented medium and centrifuged (300g, 15 min) hence, pelleting down the stromal vascular fraction (SVF). The obtained SVF was washed with complete medium, passed through a cell strainer (40µm) and plated in cell culture dishes. The plated cells were maintained in high glucose DMEM supplemented with 10 % (v/v) FBS, 1X antibiotic/antimycotic solution, 2 mM L-glutamine (Gibco, USA) and 1 ng/mL basic fibroblast growth factor (bFGF) (Sigma, USA). The cells were used within passages 3 to 7 for seeding during the biological evaluation of 3D printed constructs.

Scaffolds of grid infill with 4 mg of blank microspheres/ml of biomaterial-ink were fabricated under sterile conditions with a 22G needle (to avoid nozzle clogging) and photo-crosslinked using a 40W LED light source of 405 nm wavelength for 30 seconds. This was followed by a conditioning cycle in cell culture medium for 12 h prior to seeding. The scaffolds were seeded with cells at previously used cell density of 10^4 cells/mm^2 for assessing their viability and proliferation.

3.2.9.2 Cell Viability and Proliferation

Cellular viability of the pADMSCs seeded onto the blank microsphere laden constructs was evaluated using the live-dead assay where live cells are stained with calcein-AM and dead cells are stained with ethidium homodimer solutions using manufacturer's protocol (Sigma-Aldrich). Cell seeded constructs were gently washed with PBS (pH 7.4) and incubated in a solution of calcein-AM (40 nM) and ethidium homodimer (20 nM) solution. The constructs were gently washed with PBS prior to flourescence imaging using an inverted fluorescence microscope (EVOS FL digital microscope).

Alamar blue based cellular proliferation study was performed on the blank microsphere laden cell seeded constructs (n=3). Constructs were seeded with pADMSCs at 10^4 cells/mm^2 and Alamar blue (Invitrogen) assay was done after 1, 7, 14 and 21 days of incubation by following manufacturer's protocol. Briefly, cell seeded constructs were incubated with 10% (v/v) Alamar blue dye in culture medium for 3 h. 100 µL of conditioned alamar containing culture media was read at 570/600 nm using microplate reader (Tecan Infinite Pro, Switzerland) and the results have been represented as normalized Alamar units for different culture timepoints.

3.2.9.3 DNA and Sulphated GAG content

DNA and sGAG content was evaluated for gradient scaffolds with growth factor loaded and blank microspheres (4mg/ml) using previously optimized protocols [414]. Briefly, pADMSC seeded (n=3) gradient constructs (10^4 cells/mm^2) were collected at various time points and digested for 16 h using papain solution containing 125 µg per mL papain, 5 mM L-cysteine, 100 mM Na_2HPO_4, and 5 mM EDTA (pH 6.2) at 60 °C. Thereafter, PicoGreen based DNA quantification was carried out using the kit following manufacturer's protocol. Digested samples were centrifuged and 25 µL of it was taken, added with 75 µL of 1× TE buffer and 100 µL of Quant-iT PicoGreen reagent (1:200 dilution in 1 x TE buffer). Florescence was measured with an excitation/emission maxima of 480/528 nm using a spectrophotometer (TECAN infinite M200 pro). Further, Papain digested sample was used to measure the total sulphated GAG (sGAG) content using 1,9-dimethylmethylene blue (DMMB) assay. 50 µL of the papain digested sample was added with 200 µL DMMB reagent and absorbance was measured immediately at 525 nm using a spectrophotometer (Multiskan Sky, Thermofisher Scientific, USA). The total sGAG content as well as the DNA normalized sGAG content were plotted.

3.2.9.4 Total Collagen content

Hydroxyproline content was used as a metric to measure the total collagen content of the different sections of the cell seeded scaffolds (n=3). Samples were collected and acid hydrolysed in oil bath. Post hydrolysis, the hydroxyproline was quantified using p-dimethylaminobenzaldehyde (PDAB, Sigma-Aldrich, USA) and chloramine-T (Sigma-Aldrich, USA) [415]. Rat tail collagen was used to make a standard curve and the hydroxyproline (HYP) content was plotted after normalization with DNA content of the respective constructs.

3.2.9.5 Gene Expression Studies

Total RNA was isolated from the different sections of the cell-seeded scaffolds (n=3) at various culture time points using TRIzol reagent (Sigma-Aldrich). Isolated mRNA content was quantified using nanophotometer instrument (Implen, Germany). cDNA was synthesized from the isolated mRNA using a high-capacity cDNA reverse transcription kit (Applied Biosystems) in a PCR thermal cycler (Applied Biosystems). Further the synthesized cDNA was used for real-time PCR using SYBR Green master mix reagent (Invitrogen) in a qPCR (QuantStudio 5, Applied Biosystems, USA) for fibrochondrocytic genes, i.e., aggrecan, sox-9, collagen Iα and

collagen IIα genes. The final reaction volume for qPCR was kept 20 µL and the standard run conditions of holding stage (50 °C for 2 min, 95 °C for 10 min) and cycling stage (40 cycles of 95 °C for 15 s, and 60 °C for 45 s) was used. Relative expression of aggrecan, sox-9, collagen Iα and collagen IIα genes were quantified by normalizing to glyceraldehyde-3-phosphate-dehydrogenase (GAPDH) as the endogenous housekeeping gene. The results were analyzed through Ct method ($2^{-\Delta\Delta Ct}$). The primer sequences used have been listed in **Table 1**.

Table 3.1: *Primer sequences used for gene expression analysis*

Gene	Sequence	Accession No.
Porcine aggrecan (ACAN)	F:5′-CCCAACCAGCCTGACAACTT-3′ R:5′-CCTTCTCGTGCCAGATCATCA-3′	NM_001164652.1
Porcine sox-9 (sox 9)	F:5′-TTCCGCGACGTGGACAT-3′ R:5′-GGCGGCAGGTACTGGTCAAACTC-3′	NM_213843.1
Porcine Collagen I (Col I)	F:5′-AGAAGAAGACATCCCACCAGTCA-3′ R:5′-AGATCACGTCATCGCACAACA-3′	XM_021067153.1
Porcine Collagen II (Col II)	F:5′-CAGGTGAAGGTGGGAAACCA-3′ R:5′-ACCCACGAGGCCAGGA-3′	AF201724.1
Porcine GAPDH (GAPDH)	F:5′-TCGGAGTGAACGGATTTGG-3′ R:5′-CCAGAGTTAAAAGCAGCCCT-3′	NM_001206359.1

3.2.9.6 Macrophage stimulation and TNF-α release

In vitro immunogenic response was assessed using mouse macrophages (RAW 264.7 cells, National Center for Cell Science, NCCS, Pune) according to previously described protocol [46, 425, 429]. Mouse macrophages were seeded at 5×10^4 cells per well in a 24-well plate (n=4) and cultured for 24 h and subjected to treatment with constructs leachate for 24 h and the conditioned media was collected thereafter. Additionally, we seeded macrophages on the microsphere laden constructs (n=4) and incubated them for 24 h and 48 h and collected conditioned culture medium at 24 h and 48 h. The conditioned media were collected for ELISA based quantification of the released TNF-α following manufacturer's protocol (Invitrogen, USA). Lipopolysaccharide (LPS, Sigma-Aldrich, USA) at 1000 ng/mL was used as positive control, and untreated cells (TCP) were taken as a negative control.

3.2.9.7 Immunohistological staining

Porcine stem cells were seeded onto zonal constructs and cultured for 21 days to evaluate the zone-specific ECM deposition. The cultured constructs were incubated in 10% neutral buffered formalin (NBF) for 24 h for fixation and thereafter washed with PBS. The fixed constructs were further permeabilized using 1% (v/v) triton-X 100 in PBS for 1 hr at room temperature followed by blocking using 10% (w/v) bovine serum albumin in PBS for 2 hr. Thereafter, the constructs were co-stained with mouse mono-clonal anti-collagen I and rabbit poly-clonal anti-collagen II primary antibodies (ABCAM, USA) respectively for 2 hr. The constructs were further stained with secondary anti-mouse or anti-rabbit antibodies for the respective primary antibodies for 2 hr and counterstained with DAPI (300nM, Thermofisher Scientific, USA) for 20 min before imaging. The fluorescent micrographs were obtained using an inverted fluorescence microscope (Axio Observer, Zeiss, Germany). The images obtained from different constructs (n=8) were used for calculating the field of view area stained with either collagen I and aggrecan or collagen I and collagen II by using Fiji (NIH ImageJ software) following previously defined protocol [449] to determine the expression ratio of ECM components.

3.2.10 Statistical Analysis

All experimental data have been reported in the form of mean ± standard deviation ($n \geq 3$). Statistical analysis was carried out by one-way analysis of variance (ANOVA) using Origin 9.1 (OriginLab, USA), and a Tukey test assessed the variance across groups. Groups were considered to possess statistically significant difference when $*p \leq 0.05$.

3.3 Results

3.3.1 Fabrication and characterization of growth factor loaded gelMA microspheres

The microspheres were fabricated using 7.5% w/v gelMA with the flow rates for aqueous and oil phases were kept at 20 µl/min and 2000 µl/min **(Figure 3.3A)** for an optimal size of below 200 µm **(Figure 3.3B I and ii)**. These spheres were washed thoroughly for removing traces of oil. The removal of oil is necessary for loading the microspheres and for the microspheres to reach swelling equilibrium. The sphere diameters post swelling were found to be 107.55 ± 16.68 µm and the distribution of the same is shown in **(Figure 3.3C)**. This step was performed before freeze-drying to get the equilibrium diameter of the spheres post loading. The water uptake ratio of the freeze-dried microspheres was found to reach equilibrium within 20 minutes at ~8 times **(Figure 3.3D)**. The loading efficacy of the spheres showed similar trends as to previously reported in the literature **(Figure 3.3E)** for gelMA microspheres [424, 445] [22,46]. The CTGF was loaded at 153.75 ± 7.55 ng/mg and TFGβ3 was loaded at 39.76 ± 3.38 ng/mg within the gelMA microspheres. These were further encapsulated within the biomaterial ink and the release profile was obtained from the crosslinked printed constructs. The profile revealed 39.54 ± 0.44 % release of CTGF and 45.93 ± 0.40% release of TFGβ3 after a period of 15 days **(Figure 3.3F)**. These would further lead to the differentiation of stem cells seeded onto the scaffolds in a variable manner according to the different zones of 3D printed constructs. The release profiles were fitted using Korsmeyer peppas model and the n values were found to be <0.5 indicating the release to be Fickian diffusion which is ideal for sustained release over longer duration and known to be characteristic of silk fibroin-based matrices **(Figure 3.3F-G)** [266, 425, 450].

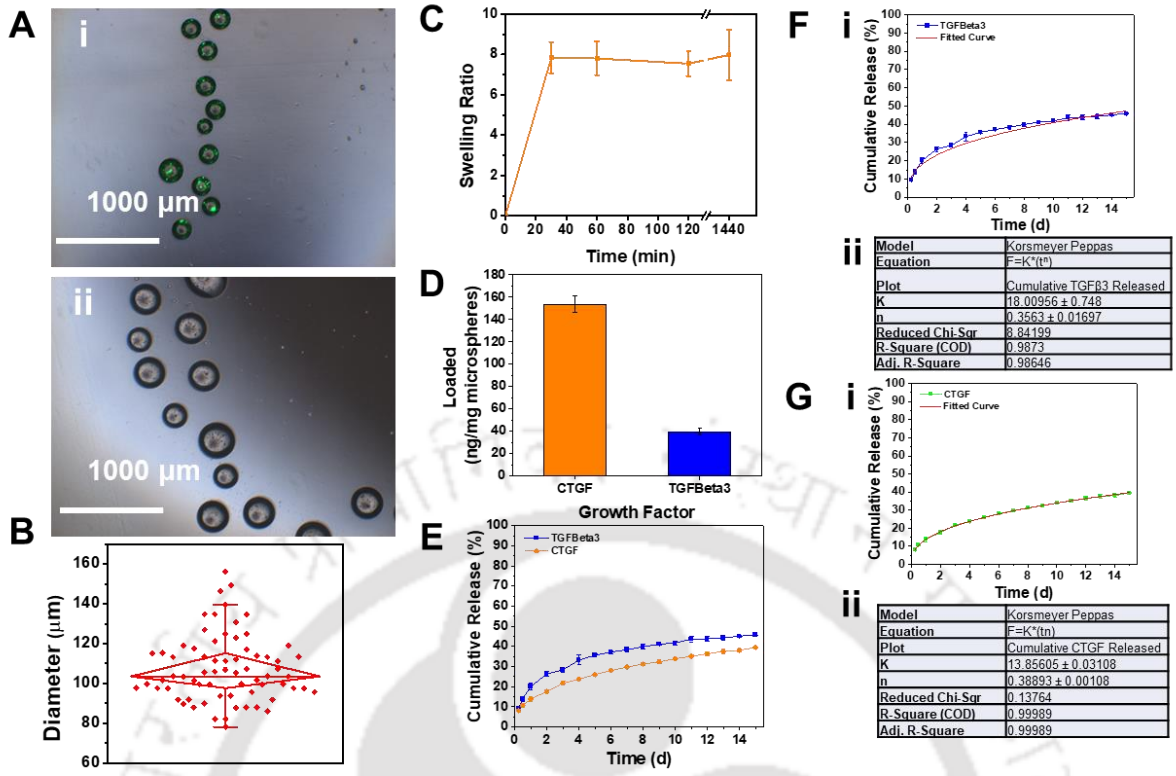

Figure 3.3: *(A) Representative micrographs of (i) Fluorescent dye loaded and (ii) Swollen crosslinked gelMA Microspheres. (B) Microsphere diameter calculated using ImageJ post swelling equilibrium. (C) Swelling ratio of gelMA microspheres. (D) Amount of CTGF and TGFβ3 loaded onto gelMA microspheres determined using ELISA. (E) Cumulative release of CTGF and TGFβ3 from microsphere encapsulated printed constructs for a period of 15 days determined using ELISA. Release profile of (F) TGFβ3 and (G) CTGF fitted using Korsmeyer peppas model with (i) curve fit and (ii) model equation and fit values.*

3.3.2 Formulation of photocrosslinking bioink and its printability characterization

The bioink composition was found to be printable when the percentage of gelMA and silkMA were raised over 1% (w/v) and 4% (w/v) respectively at 20°C **(Figure 3.4A)** while keeping the amount of *A. assama* SF constant at 1% (w/v). Hence, eliminating the boundary conditions, the final composition of the bioink for further experimentation was determined to be 7% (w/v) of gelMA, 2% (w/v) of silkMA (BMMA) and 1% (w/v) of *A. assama* SF. This bioink showed optimal printability at 20°C and hence was further used for the encapsulation of the microspheres. A concentration of 4 mg/ml of microspheres was chosen for the optimal loading and release profiles of the ink while maintaining printability. This 4 mg/ml loaded ink was used to test the influence of microsphere encapsulation on its rheological properties. The bioink was found to be shear thinning **(Figure 3.4C-F)** both with and without the microspheres. Though a ~10 fold reduction in the viscosity of the bioink was observed at higher shear strain

(Figure 3.4C), it does not effect the self-standing nature of the bioink post printing. Moreover, the bioink was stable under varying frequency within the linear viscoelastic range with and without the encapsulation of microspheres **(Figure 3.4F)**. The gel strength of bioink does not vary significantly in this scenario due to a similar strength within the LVER region. The bioink blend was stable and highly viscous under temperatures lower than 25°C **(Figure 3.4D)** both with and without the microspheres, hence temperatures 20-25°C can be used for printing. The bioink was found to retain its strength when subjected to multiple high stress-strain cycles **(Figure 3.4E)** with and without the microspheres. Though a slight decrease in the viscosity is observed post recovery but the bioink possesses amicable gel strength for printing self-standing structures. The characteristic amide I, II and III peaks were visible in the infrared spectra of silkMA, *A. assama* SF, gelatin and the crosslinked and uncrosslinked bioink compositions **(Figure 3.4B)**. Moreover, the glycidyl methacrylate peaks were visible in the gelMA, silkMA, and uncrosslinked and crosslinked bioink spectra. The shift in the cardinal regions of amide I (1710–1590 cm^{-1}), amide II (1570–1480 cm^{-1}) and amide III (1270–1200 cm^{-1}) regions were visible between the crosslinked and uncrosslinked bioinks as well as the bioink components [46].

The developed inks were further tested for their gelation, printing resolution and buckling effect to determine their suitability for fabrication of full thickness meniscal constructs. Both with and without microspheres the inks were found to be suited for apt resolution when checked with a 22-gauge nozzle **(Figure 3.4G and 3.4H)**. The buckling test showed little to no deviation in the microspheres loaded ink at the longest distance, while the ink without microspheres showed considerable buckling. This might be owed to the better packing density within the ink as the microspheres add to the solid volume of the ink. Further, the printing assessment showed excellent printing resolution of grid constructs of 2, 5 and 10 layers for both micro-sphere loaded as well as bare inks **(Figure 3.4I and 3.4J)**. These microsphere laden inks were further used for printing physiologically relevant meniscal constructs.

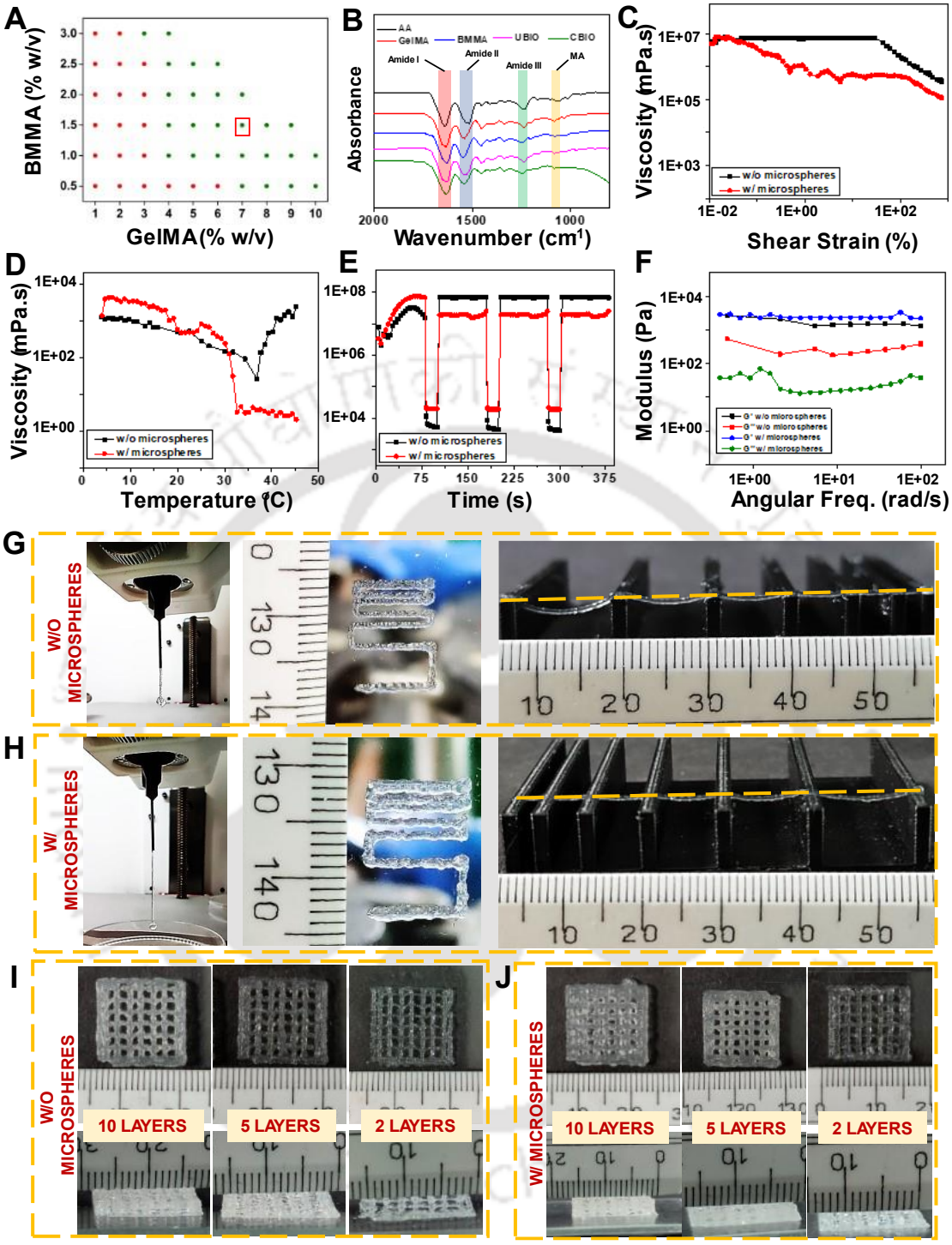

Figure 3.4: *(A) Printability matrix of the bioink for obtaining the optimized bioink composition. (B) Infrared spectra of silkMA(BMMA), gelMA, A. assama SF (AA), crosslinked biomaterial-ink (CBIO) and uncrosslinked biomaterial-ink (UBIO). The red region denotes amide I, blue region denotes amide II, green region denotes amide III and yellow region denotes the methacrylation (MA) peaks. Rheological properties of the optimized biomaterial-ink composition with 4mg/ml microspheres and without microspheres obtained through (C) amplitude sweep, (D) temperature sweep, (E) 3Interval Thixotropy Test (3ITT) and (F) temperature sweep. Gelation, printing resolution and buckling test for (F) biomaterial-ink and*

(G) microsphere loaded biomaterial-ink. 2, 5 and 10 layer grid constructs 3D printed using (I) biomaterial-ink and (J) microsphere loaded biomaterial-ink.

3.3.3 3D Printing of microsphere laden constructs and their characterization

Microsphere laden inks were used for the defect mitigation of a proof-of-concept 3D printed meniscus. A full thickness defect replica was printed and the defect site was subsequently modelled **(Figure 3.5A)**. The modelled meniscus defect was printed with the dual bioink strategy with an outer region (green), inner region (pink/red) and the middle orange region. The shape, geometry and conformity of the printed construct was found to be excellent and the construct was fitting in the defect site in a facile manner. This defect site modelling could be used for fabrication of patient specific 3D printed constructs using the one-step photopolymerizable bioinks and used by surgeons to suture into place or by the virtue of surgical glue. The hence fabricated construct could be made to conform to various irregular meniscectomies for healing of menisci. Furthermore, constructs were printed using the dual ink strategy and a gradient could be observed when fluorescently tagged spheres were encapsulated in the bioinks **(Figure 3.5B)**. The green labelled microspheres were exclusive to the outside section labelled ink 1 while the red labelled microspheres were exclusive to the inside section labelled ink 2. The intermediate section showed the presence of both green and red fluorescence prominently. This gradient dual ink printing would be ideal for printing 3D constructs with CTGF and TGFβ3 loaded microspheres encapsulated within the silkMA-gelMA-AASF blend bioink. The presence of methacrylated components aids in the quick one step fabrication of the printed constructs ensuring no settling of the microspheres within the bioink post printing [424, 435]. The microsphere laden constructs were analyzed using electron microscopy and the microspheres were found to be within the struts **(Figure 3.5C)**. 4 mg/ml microsphere encapsulation within the biomaterial-ink was used for 3D printing constructs that have been compared with the constructs without microspheres and evaluated for their favorable physicochemical properties.

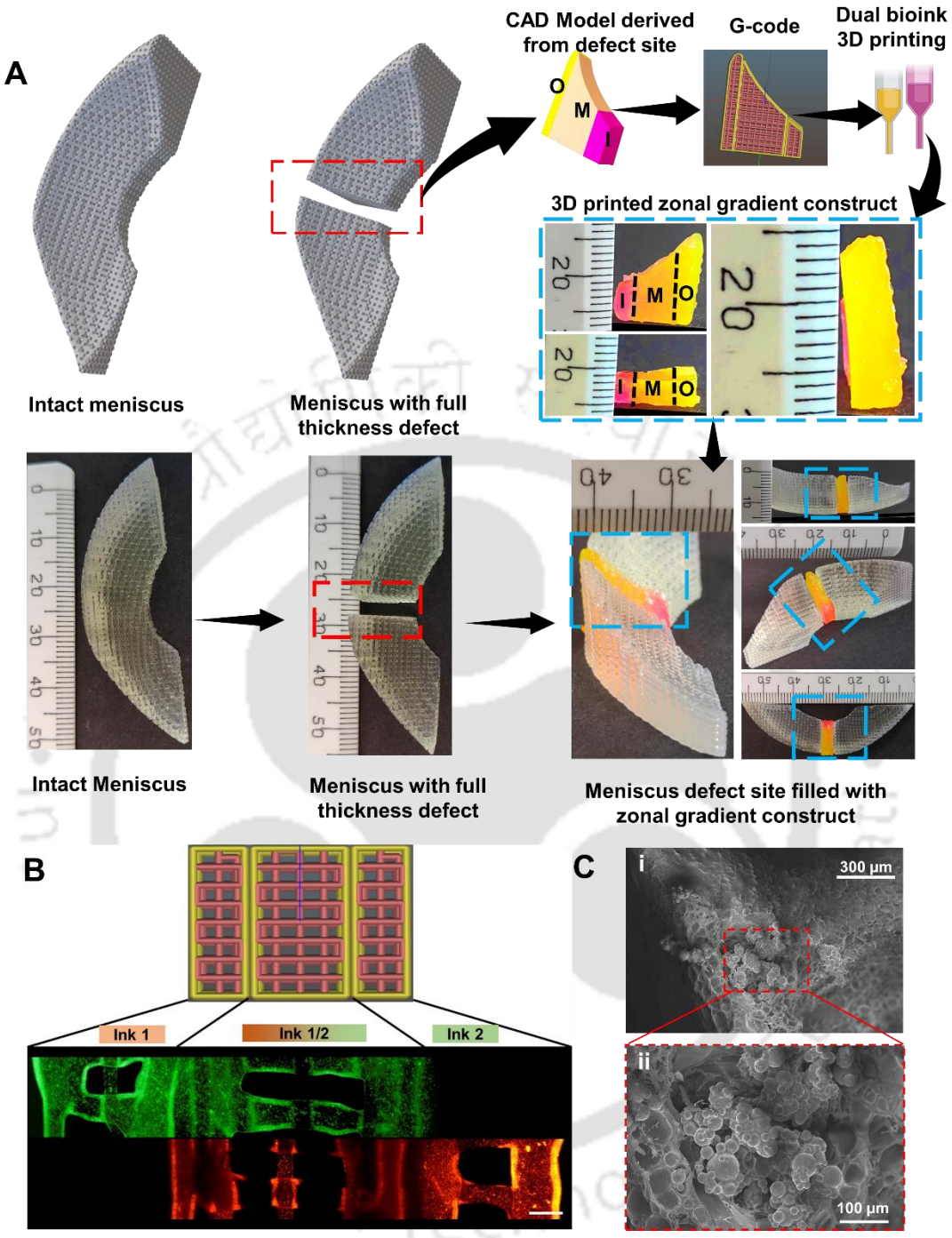

Figure 3.5: *(A) Representative figure demonstrating the meniscal repair using dual biomaterial-ink zonal printed constructs. The defect site has been modeled and fabricated using the dual biomaterial-ink 3D printing strategy and the resultant 3D construct has been incorporated into the defect site to elucidate the congruence of the printed construct. The symbols represent O: outer zone, M: middle zone and I: inner zone. The red dotted boxes represent defect site and the blue dotted box represent the 3D printed construct. (B) Representative fluorescent labelled colored dye laden grid constructs showing the dual bioink printing strategy for gradient formation. Scale Bar: 1000µm (C) Representative FESEM*

images of microspheres within the 3D printed constructs at (i) lower and (ii) higher magnification.

3.3.4 Swelling and degradability of 3D printed constructs with and without microspheres

The constructs with microspheres gained significantly higher 66.19 ± 3.31% weight as compared to the constructs without microspheres which only gained 47.62 ± 4.22% weight after 96 hours of incubation in PBS at 37ºC **(Figure 3.6A)**. The higher absorption could be attributed to the presence of microspheres within the printed constructs and hence is favourable for the diffusion to and from the constructs. This swelling potential is essential for the rapid exchange of growth factors, nutrients as well as the waste products to and from the 3D printed constructs ensuring optimal cellular response [46, 365, 451]. The inclusion of gelMA microspheres led to slight reduction of contact angle and increase in hydrophilicity. The contact angle was found to be 63.5±0.2 angle without the microspheres which reduced to 61.3±0.1 with the microspheres **(Figure 3.6D)**. The least reduction in weight of the printed constructs was observed in PBS after 35 days (5 weeks) of incubation **(Figure 3.6B)**. Constructs with microspheres (82.58 ± 5.92%) had a higher weight remaining as compared to constructs without microspheres (65.89 ± 2.98%) after 5 weeks in PBS. Similarly, under enzymatic conditions, constructs without microspheres degraded quicker and showed lower weight remaining (26.75 ± 1.20%) after 5 weeks than the constructs with microspheres (31.69 ± 5.97%). The presence of microspheres was found to decelerate the rate of degradation due to the higher packing density of the bulk volume of the constructs. This was also evident from the reduced apparent porosity of constructs with the microspheres (56.1±1.7%) as compared to constructs without the microspheres (63.4±1.5%) **(Figure 3.6C)**. The rate of degradation needs to be optimized for the resorption of the constructs while the regeneration process in underway and needs to be evaluated *in vivo* for further optimization [449].

3.3.5 Mechanical durability evaluation of 3D printed constructs with and without microspheres

The compressive mechanical strength of photocrosslinked constructs was found to be amicable **(Figure 3.6E-H)** w.r.t. the native tissue strength and complies with the strength reported earlier [46]. The compressive strength of the constructs with microspheres (129.47± 2.39 kPa) was found to increase significantly as compared to the constructs without the microspheres (94.09 ± 12.42 kPa) **(Figure 3.6E)**. The packing density increase due to the presence of microspheres could be attributed for this significant increase in the strength of the

photo-crosslinked constructs. The representative stress-strain curves **(Figure 3.6F)** of the printed constructs with and without microspheres shows that the compression profile was similar but the elasticity was higher without the microspheres.

Thereafter the cyclic compression of 100 cycles was performed on the grid infill constructs **(Figure 3.6G and 3.6H)** for evaluating the long-term compression stability of the constructs and their recovery post relaxation. Both the microsphere laden **(Figure 3.6G)** and bare constructs **(Figure 3.6H)** yielded similar stability under hyperphysiological compression of 20% [46, 416] for over 100 cycles and underwent slight strain hardening. This prolonged exposure to compressive stresses ensures the durability of the constructs due to the high cyclic load-bearing nature of the menisci.

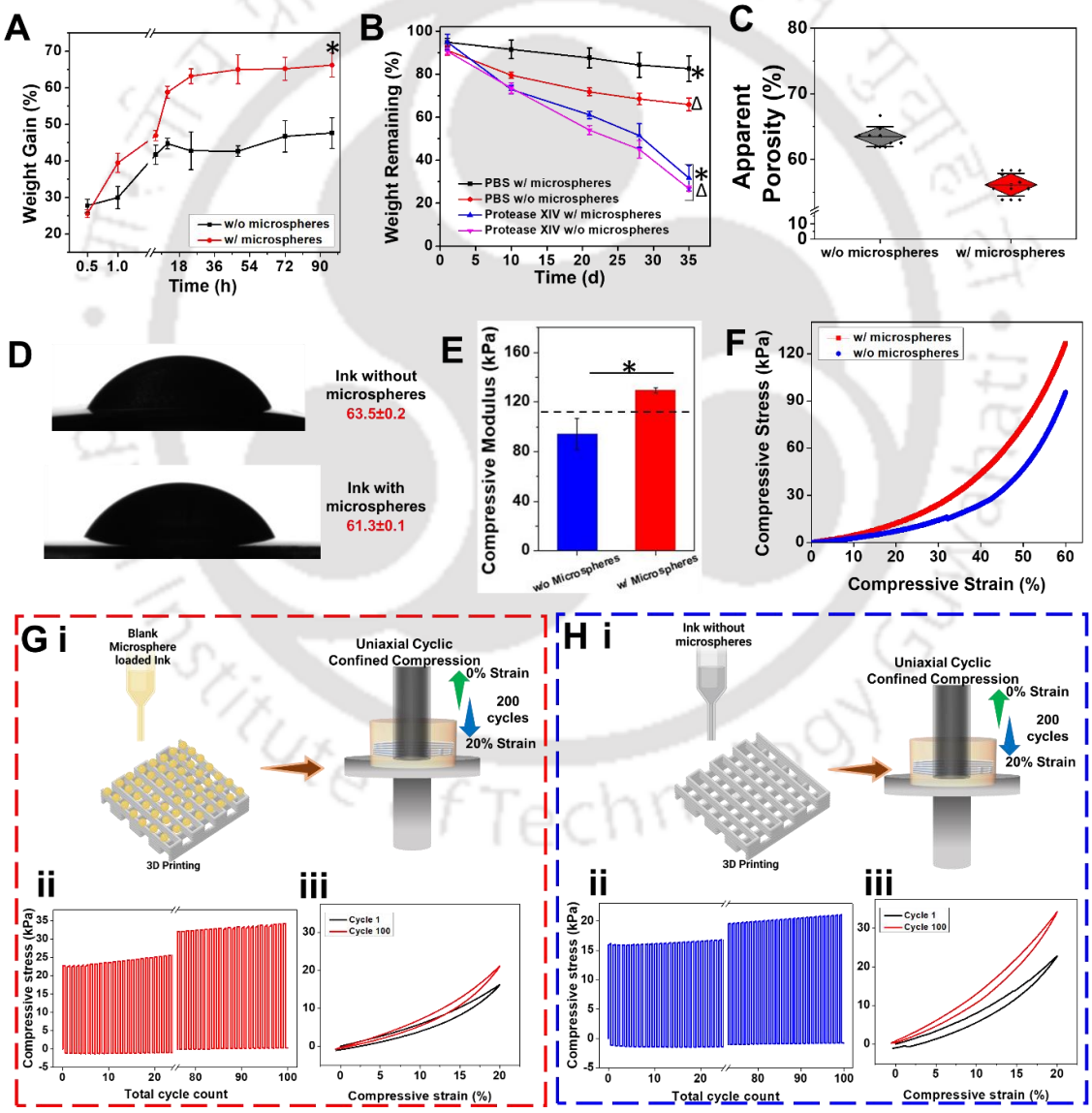

Figure 3.6: *(A) Swelling of 3D printed constructs measured at various intervals with and without microspheres. (B) Degradation profile of 3D printed constructs with and without*

*microspheres in the presence of protease XIV and in PBS. Microspheres were incorporated at 4mg/ml of biomaterial-ink. (C) Apparent porosity percentage for 3D constructs with and without microspheres measured using hexane displacement method. (n=8). (D) Representative contact angle measurement images and values carried out for the biomaterial-ink compositions without microspheres and with microspheres. (n=3). (E) Compressive moduli of 3D printed constructs with and without microspheres. (F) Representative stress-strain curve for 60% compression of 3D printed constructs with and without microspheres. (G) (i) Compressive cyclic testing of constructs with microspheres. (Made using www.biorender.com) (ii) Compressive moduli of 3D printed constructs for first and last 20 cycles of the 100 cycles at 20% compressive strain with 5mm/s cross head speed. (iii) The stress-strain curves of cycle 1 and cycle 100 for constructs. (H) (i) Compressive cyclic testing of constructs without microspheres. (Made using www.biorender.com) (ii) Compressive moduli of 3D printed constructs for first and last 20 cycles of the 100 cycles at 20% compressive strain with 5mm/s cross head speed. (iii) The stress-strain curves of cycle 1 and cycle 100 for constructs. * and Δ represents $p \leq 0.05$.*

3.3.6 Biological compatibility of blank microsphere laden constructs

ADSCs have been reported extensively for *in vivo* and clinical meniscus regeneration applications due to their multipotency, proliferation and ease of derivation from autologous sources [452-454]. Hence ADSCs derived from porcine sources were used for further biological evaluation of our constructs *in vitro*. Constructs with 4mg/ml of blank microspheres were printed and seeded with pADMSCs for evaluating their preliminary biocompatibility through cellular viability and proliferation studies. The seeded pADMSCs were found to be viable for 21 days as shown by the micrographs taken at day 1, 7, 14 and 21 **(Figure 3.7B)**. The green color signifies viable cellular population, and any bright red dots signify the dead cells. The cells could be seen to be evenly distributed on the constructs and increasing in number over the culture period. The proliferation of cells observed by alamar blue assay **(Figure 3.7C)** shows ~2 folds increase in the viable cell population over the period of 21 days. The DNA estimation yielded a similar trend as shown in the cellular proliferation assay. DNA content of the constructs increased from 17.78 ± 1.69 ng per unit wet weight of constructs on day 7 to 29.72 ± 6.12 ng per unit wet weight of constructs on day 21 **(Figure 3.7D)**. The rise in DNA content is significant on day 14 but steadily increases on day 21. The sulphated GAG deposited by the seeded pADMSCs was found to significantly increase from 2.68 ± 0.27 µg to 4.63 ± 0.20 µg and then steadily rises to 4.86 ± 0.81 µg when normalized to the wet weight of the constructs as observed on day 7, 14 and 21 respectively **(Figure 3.7Ei)**. Post normalization to the DNA content of the constructs the rise in sGAG content increased significantly from 68.14 ± 12.29 µg on day 7 to 113.18 ± 7.69 µg on day 21 **(Figure 3.7Eii)**. The sGAG deposition showed the bias brought about by the blank microsphere laden constructs on the pADMSCs for chondrogenic differentiation [4, 12, 23, 124, 147]. This might be due to the presence of

mulberry and non-mulberry silk fibroin blend and gelatin which has been well-known matrices for creating a chondrogenic differentiation bias and maintenance of stem cells towards chondrogenic lineage [365, 414, 427, 455-457]. Moreover, the presence of RGD sequences in the non-mulberry SF and gelMA aids in the proliferation and maintenance of seeded pADMSCs [46, 365]. The murine macrophages were subjected to different time points of exposure in the form of construct leachates as well as seeding on the constructs with blank microspheres and the secreted TNF-α was determined by the virtue of ELISA. The constructs show excellent immuno-compatibility **(Figure 3.8A)**. The constructs had an identical response to the tissue culture plate (negative control) which was significantly (~5 times) lower secretion of TNF-α than the LPS treated positive control. This would aid in the union of the constructs and reduce the chances of rejection caused by the acute inflammation. This response of the 3D printed constructs is in accordance with our previous silk-based matrices, composites and bioinks and biomaterial inks [46, 365] [429].

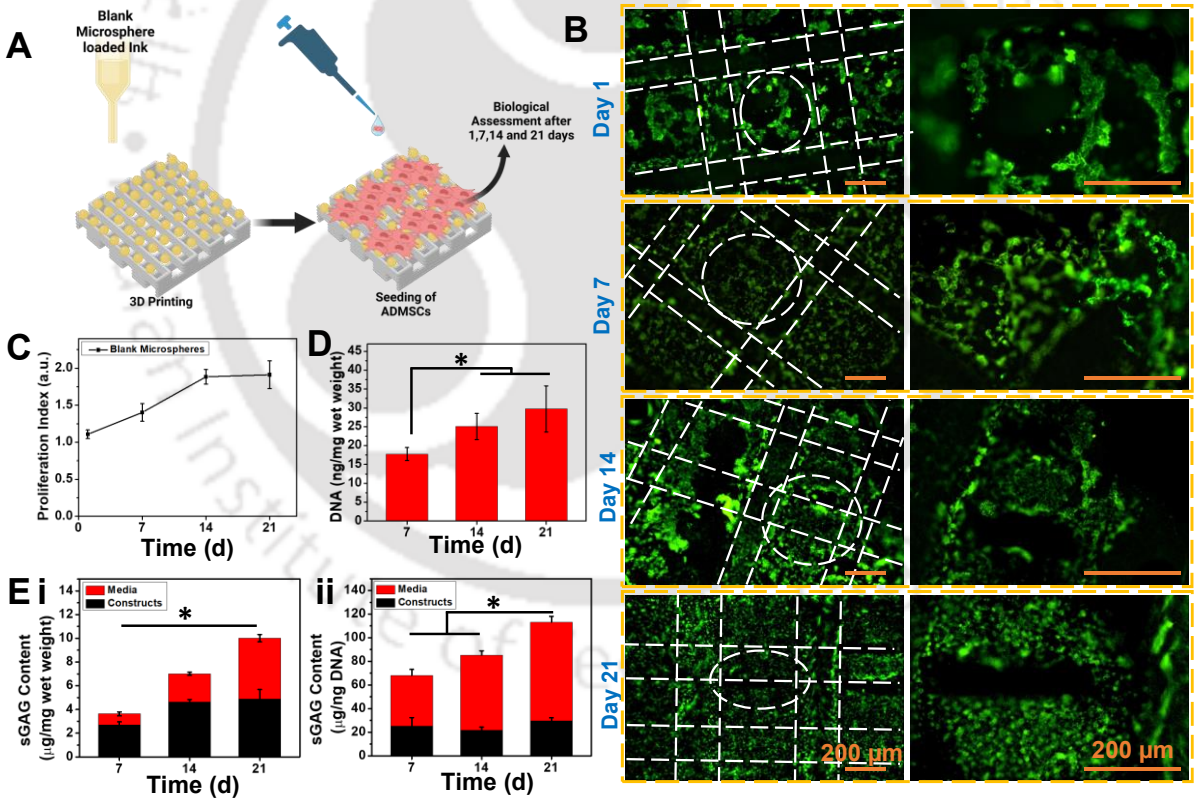

Figure 3.7: *(A) Biological assessment of blank microsphere laden constructs with porcine ADSCs. (Made using www.biorender.com) (B) Live-dead imaging of porcine ADSCs seeded onto microsphere laden 3D printed constructs with blank microspheres 1,7, 14 and 21 days of culture. The magnified areas have been marked with white circles. Scale bar: 200µm. (C) Cellular proliferation determined by Alamar Blue assay on the blank microsphere laden constructs. (D) DNA content normalized to wet weight of constructs (E) (i) sGAG content*

*normalized to wet weight of constructs and (ii) sGAG content normalized to DNA content of the constructs at 7, 14 and 21 days for constructs with blank microspheres. Microspheres were incorporated at 4mg/ml of biomaterial-ink. * represents p≤0.05.*

3.3.7 Growth factor-loaded microsphere-laden 3D constructs for zonal differentiation towards meniscal phenotypes

The DNA estimation of different zones of the growth factor microsphere laden constructs yielded varying patterns of proliferation of cells within the different regions **(Figure 3.8B ii)**. The rise in DNA content is significant on day 14 and day 21 in all the regions of the constructs and though the amount of DNA differs in the initial growth phase of 14 days, within the inner, middle and outer zones, the final content of DNA is similar in all zones after 21 days of incubation showing a significant rise at every analysis time point. The DNA content increases significantly from 44.42 ± 8.46 ng to 393.85 ± 46.53 ng in the outer zone, 50.72 ± 10.71 ng to 314.99 ± 35.57 ng in the middle zone and 31.20 ± 21.82 ng to 477.76 ± 68.30 ng in the inner zone from day 7 to day 21 respectively in all the cases. The sulphated GAG deposited by the seeded pADMSCs was found to significantly increase on day 14 and day 21 as compared to the estimated amounts on day 7. The highest rise was observed on day 21 within the middle and inner zones as the chondrogenic and fibrochondrogenic phenotypes were dominant in these regions. However, sGAG content rise was also observed in the outer region as well due to the presence of growth factors within the conditioned media **(Figure 3.8B iii)**. Post normalization to the DNA content of the constructs the rise in sGAG content was found to increase significantly from 2.65 ± 0.46 µg to 36.93 ± 10.31 µg in the outer zone, 5.07 ± 1.07 µg to 66.20 ± 9.75 µg in the middle zone and 4.44 ± 0.84 µg to 56.87 ± 15.64 µg in the inner zone from day 7 to day 21, respectively in all the cases.

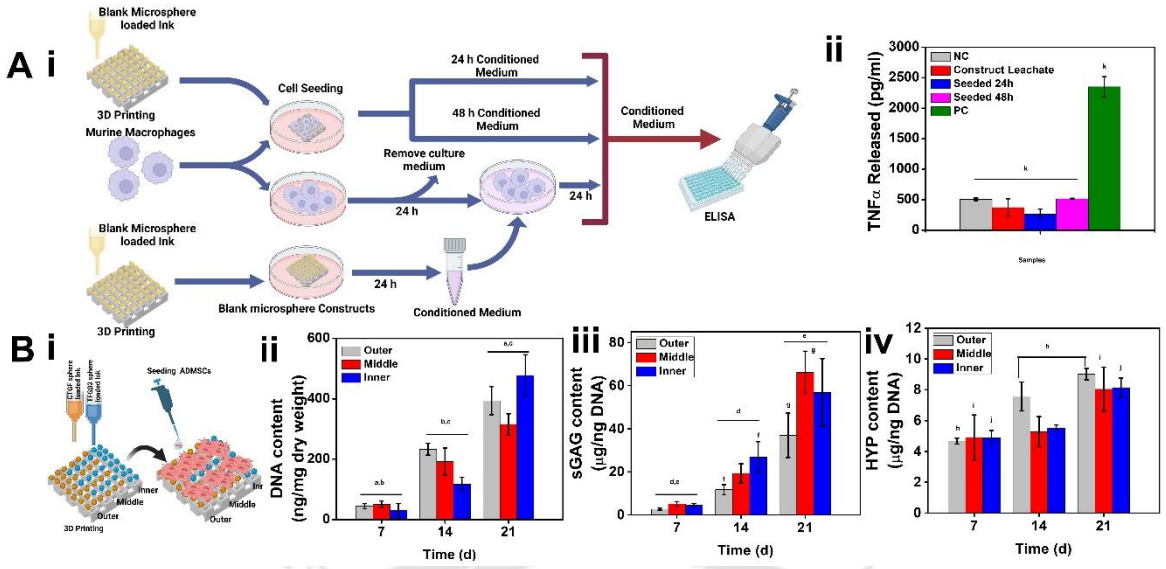

Figure 3.8: *(A) (i) In vitro immuno-compatibility assay. (Made using www.biorender.com) (ii) TNFα secretion by mouse macrophages treated with tissue culture dish (PC), LPS (NC) or construct leachate and seeded onto 3D printed constructs after 24h and 48h of seeding. (B) (i) Biochemical Estimation of growth factor loaded microsphere laden constructs. (Made using www.biorender.com) (ii) DNA Content, (iii) sGAG content and (iv) Hydroxyproline (HYP) content deposited by differentiating mesenchymal stem cells seeded in the Outer, Middle and Inner regions of growth factor microsphere laden gradient constructs post normalization with DNA content. a-k represents p≤0.05.*

The hydroxyproline (HYP) content which signifies the total collagen deposited by the seeded pADMSCs was found to significantly increase on day 21 as compared to the estimated amounts on day 7 in all the regions. The highest rise on day 14 was observed within the outer zone i.e., by the fibrogenic phenotype while the total collagen content rose to comparative levels by day 21 in all the zones **(Figure 3.8B iv)**. Post normalization to the DNA content of the constructs the rise in HYP content was found to increase significantly from 4.67 ± 0.18 µg to 9.02 ± 0.37 µg in the outer zone, 4.90 ± 1.45 µg to 8.03 ± 1.43 µg in the middle zone and 4.88 ± 0.46 µg to 8.14 ± 0.62 µg in the inner zone from day 7 to day 21, respectively in all the cases. TGFβ3 has been well known to drive chondrogenesis in MSCs under *in vitro* and *in vivo* conditions while significantly promoting cellular proliferation and collagen and sGAG synthesis [430, 458, 459]. The significant rise in total collagen and significantly higher sGAG deposition in the TGFβ3 loaded inner region was observed in the biochemical profile indicating chondrogenic differentiation of pADMSCs in the inner region of construct. Concurrently, the significant rise in total collagen deposition accompanied by lower sGAG deposition in the CTGF loaded outer region was observed in the biochemical profile indicating fibrogenic differentiation of pADMSCs in outer region of construct. CTGF has shown strong fibrogenic

differentiation bias on MSCs *in vitro* and *in vivo* while significantly promoting collagen I deposition and cellular proliferation with minimal chondrogenic bias [440, 441, 460]. Both TGFβ3 and CTGF induce cellular proliferation which was indicated by the high cellular proliferation in both the inner and outer regions. The pADMSCs seeded in the middle region received a simultaneous high concentration of CTGF and TGFβ3 leading to high sGAG deposition, total collagen deposition and cellular proliferation. This could be attributed to the well reported fibrochondrogenic bias on MSCs caused by a simultaneous exposure to CTGF and TGFβ3 [460, 461]. Further corroboration of the differentiation bias indicated by the ECM deposition profile was observed in the gene expression profile of the inner, middle and outer region cells **(Figure 3.9A)**. The cells within the inner zone showed upregulation of chondrogenic markers i.e. sox-9 from ~2 folds on day 7 to ~5.9 folds on day 21 **(Figure 3.9D)**, aggrecan from ~2.5 folds on day 7 to ~4.8 folds on day 21**(Figure 3.9E)** and collagen II from ~4 folds on day 7 to ~15 folds on day 21 **(Figure 3.9C)** while downregulation was seen with collagen I from ~0.5 folds on day 7 to no expression on day 21 **(Figure 3.9B)**. Consequently, the outer region showed upregulation of the fibroblastic marker collagen I from ~1.5 folds on day 7 to ~16 folds on day 21 **(Figure 3.9B)**. Chondrogenic markers for the outer i.e. collagen II, sox-9 and aggrecan either remained within the basal expression levels till day 14 or were found to be downregulated or unexpressed (collagen II) on day 21**(Figure 3.9C-E)**. The basal level expression of aggrecan could be correlated to the elevated sGAG deposition in the outer region during the culture period. The cells seeded in the middle region demonstrated upregulation of expression for both chondrogenic markers sox-9 from ~1.5 folds on day 7 to ~5 folds on day 21 **(Figure 3.9D)**, aggrecan from ~1.3 folds on day 7 to ~5.8 folds on day 21 **(Figure 3.9D)** and collagen II from ~2 folds on day 7 to ~3 folds on day 21 **(Figure 3.9C)** as well as fibroblastic marker collagen I from ~3 folds on day 7 to ~13 folds on day 21 **(Figure 3.9B)**. The sGAG secretion could also be correlated to the expression profile of aggrecan. These gene expression and matrix deposition profiles demonstrate the fibrochondrogenic differentiation of stem cells to match the cellularity and ECM deposition of the meniscal tissue [29, 153, 154, 224, 244].

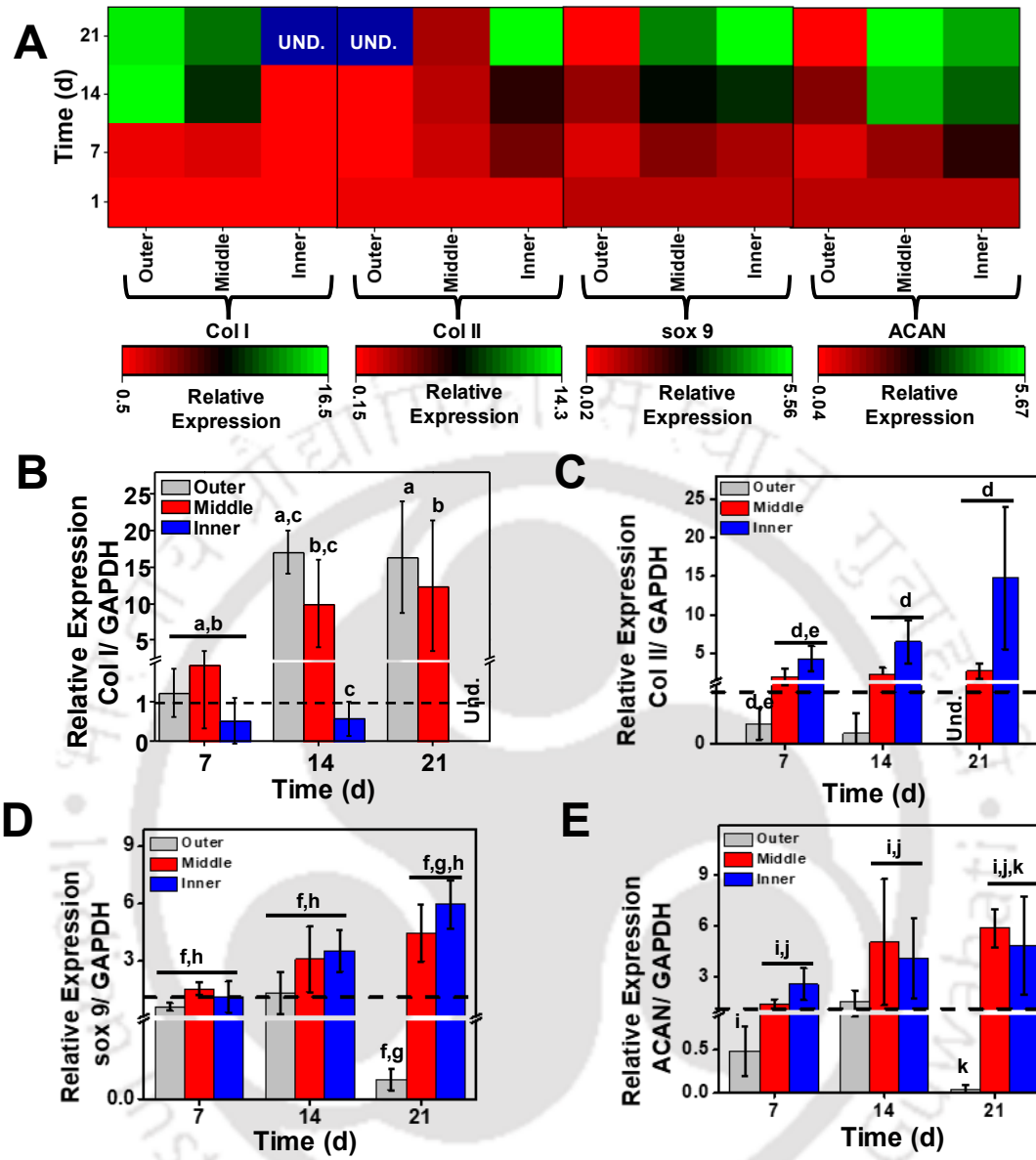

Figure 3.9: *(A) Heat-map of relative expression profile for the fibrochondrogenic genes within the various regions of the zonal constructs. Individual relative expression profiles of (B) Collagen I (Col I), (C) Collagen II (Col II), (D) sox9 and (E) Aggrecan (ACAN) genes of differentiating mesenchymal stem cells seeded in the Outer, Middle and Inner regions of growth factor microsphere laden gradient constructs. a-k represents p≤0.05.*

Furthermore, the zonal constructs were immunostained for determination of gradient deposition of collagen I and collagen II from outside to inside, produced as a result of the microspheres, which is characteristic of the meniscus tissue **(Figure 3.10A)**. The constructs were stained with collagen I and collagen II and the various regions showed the difference in expression of both the ECM proteins **(Figure 3.10B-D)**. The stained areas were evaluated using ImageJ and percentage of stained areas was found for collagen I and collagen II **(Figure 3.10D)**. Inner regions were found to express significantly higher collagen II, the outer regions

were found to possess significantly higher deposits of collagen I. The intermediate regions were found to possess collagen I and collagen II in the approximate ratio of 60:40 which indicates the presence of fibrochondrogenic phenotype [2]. Hence, the constructs were found to mimic the *in vivo* ECM deposition schema and could be used as an acellular treatment modality for full thickness meniscal tears and resections. Further, *in vivo* functional evaluation needs to be performed for determining the healing potential of the developed meniscal constructs.

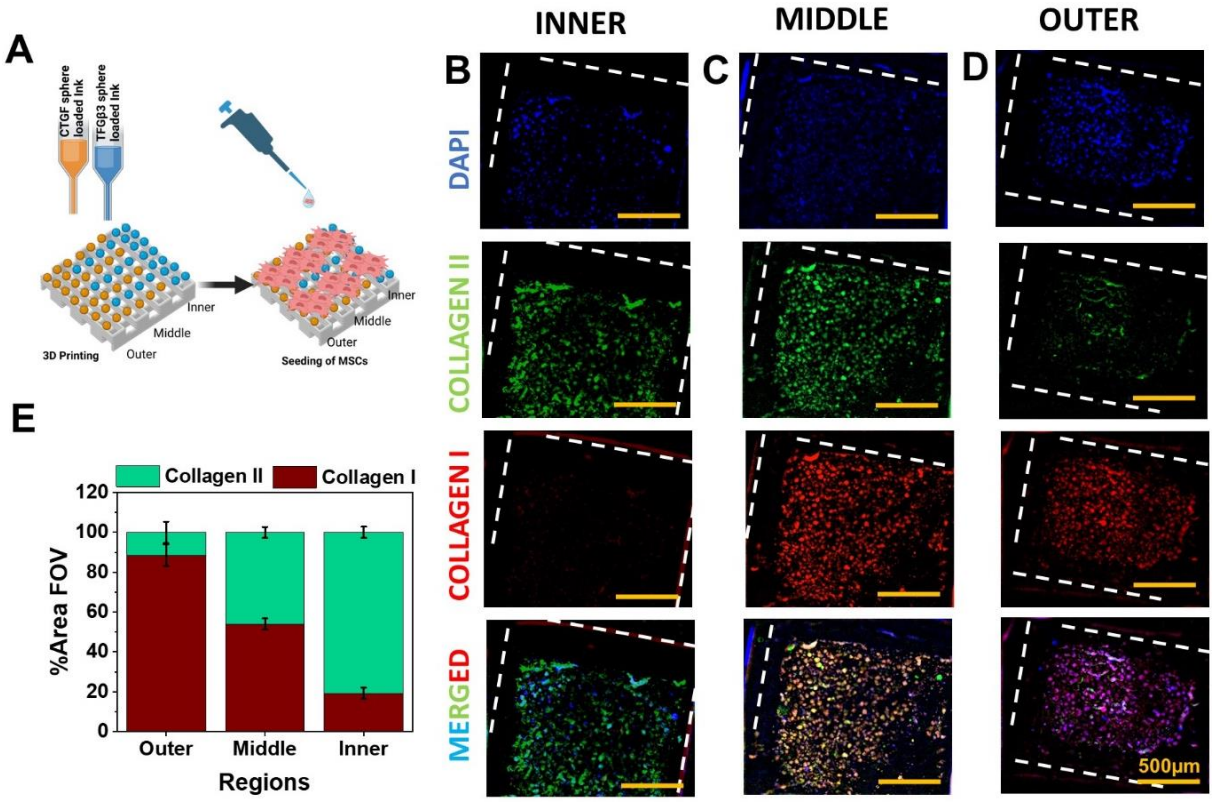

Figure 3.10: *(A) Schematic representation of the 3D printing and seeding of pADMSCs before culture. Collagen I (red) and collagen II (green) co-stained and nucleus (DAPI, blue) counter stained images from (B) inner, (C) middle and (D) outer regions of the zonal constructs. The white dotted lines indicate the edges of the 3D printed struts. Scale bar: 500µm. (E) Percentage Area FOV calculated using ImageJ for the different regions.*

3.4 Discussion

Meniscus is divided into chondrogenic inner, fibrochondrogenic middle and fibroblastic outer zones which are in tandem with the presence of vasculature in the menisci [30]. The inner and intermediate regions are largely avascular and the outer region receives scanty blood supply. This leads to inadequacies in the healing of full thickness meniscus tears and surgical resections. Implants that mimic the meniscus architecture as well as the zonal cellular and biochemical makeup are of prime importance in this regard. Here we aimed to develop growth factor loaded microsphere laden biomaterial inks suitable for 3D printed meniscal implants that show recapitulation of the zonal phenotypic and biochemical makeup of the native menisci. We fabricated gelMA microspheres using a customized microfluidic device and loaded with CTGF and TGFβ3 as fibroblastic and chondrogenic differentiation factors respectively using physical adsorption method. This was followed by the optimization of the photo-crosslinking mulberry and non-mulberry silk-based biomaterial ink blend. These loaded microspheres were further encapsulated within the ink and co-deposited to mimic the zonal morphology of the meniscus. The characterization of microspheres, microsphere laden bioinks and growth factor microsphere loaded 3D printed constructs was carried out in steps to determine their efficacy for meniscal tissue engineering applications.

The microfluidic fabrication yielded microspheres of uniform size and they were comparable to the previously observed sizes using the same technique [424]. The fabricated microspheres could uptake saline and reach equilibrium quickly. This behaviour further assisted in the loading of the microspheres with the growth factors (CTGF and TFGβ3) by the virtue of adsorption. The microspheres demonstrated a similar trend of adsorption as reported before [424, 445]. The further encapsulation of these growth-loaded microspheres could show a sustained release for 15 days following Fickian model which has been observed typically for silk matrices [266, 425, 450]. Further, the optimized bioink composition was used to encapsulate the microspheres. The Higher percentage of gelMA was deemed essential for the printabilty due to the optimal shear thinning property rendered by the thermo-reversible nature of gelatin [204, 365, 435, 462]. Gelatin is known to act as a bulking agent in silk based bioinks and its methacrylated form adds to the ease of construct fabrication [266] [54]. We found the ink to be thinning with increased temperature and shear while it also showed gel strength recovery of the bioink post high shear indulgence. All of these characteristics are essential for ensuring optimal printability using extrusion-based modality [204]. The bioink demonstrated a shift in the amide peaks before and after crosslinking mainly due to the interaction between

silkMA and *A. assama* [46, 365] rendering its stability while the methacrylate peak shift could be attributed to the photocrosslinking induced by the 405 nm light irradiation [435]. Furthermore, the signature peaks of methacrylate were visible in the methacrylated components, i.e., gelMA, silkMA and the bioinks. This was in accordance with the previously observed peaks of silkMA [435]. These bioink further showed optimal printability with and without the microspheres. The microspheres laden constructs using one-step dual bioink fabrication approach could recapitulate the 3 zones of the menisci. Further these constructs were taken for physio-chemical evaluation and the constructs with the microspheres showed better higher saline uptake, slower degradability, better wettability and lower porosity as compared to those without the microspheres. Furthermore, the microsphere loaded constructs showed higher compressive modulus and similar cyclic compression resistance. Biologically, the blank microsphere loaded constructs could show cellular proliferation and sGAG deposition over 21 days. Further, the growth factor loaded microsphere encapsulated constructs were found to significantly enhance cellular proliferation and induce fibrogenic differentiation in outer, fibrochondrogenic in the middle and chondrogenic differentiation in the inner region. This could be credited to the CTGF [440, 441, 460] released from the outer, CTGF and TFGβ3 [460, 461] co-released from the middle and TFGβ3 [430, 458, 459] released from the inner region. The collagen I/collagen II ratio was also found to mimic the regional variations of the native meniscus.

3.5 Salient Outcomes and Findings

1. We developed a growth factor loaded gelMA microsphere incorporated biomaterial ink blend that consists of silkMA, gelMA and AASF (muga) for 3D printing meniscal defect implants to potentially treat full thickness meniscal defects.
2. Our developed photo-curable ink showed optimal printability and sustained release of the growth factors from the encapsulated microspheres over long duration.
3. The fabricated constructs showed optimal swelling, long term degradability and robust mechanical properties essential for the fabrication of meniscal tissue engineering constructs.
4. The dual biomaterial-ink fabrication strategy was able to support zone-specific differentiation of pADMSCs as could be seen from the gene expression, biochemical ECM deposition and the immunostaining evaluation of the zonal constructs.
5. These 3D printed constructs could potentially be used as patient specific cell free approach for the healing of full thickness meniscal defects with the potential to aid in the chondrogenic, fibrochondrogenic and fibroblastic differentiation bias in the inner, middle and outer zones respectively.

CHAPTER 4

Development of photo-crosslinked silk-based autologous growth factor loaded 3D constructs for patient-specific treatment of partial and full thickness meniscal defects

This chapter reports photo-crosslinkable silkMA/gelMA/poly-ethylene glycol di-methacrylate (PEGDMA) based biomaterial-inks enriched with freeze-dried human growth factor rich plasma (GFRP) for 3D printing-based treatment of large and small meniscal tears. We screened the inks for their rheological properties, shape fidelity, printability, mechanical characteristics, porosity, swelling and GFRP release. Printed constructs were further evaluated for in vitro biological functionality using neo-natal human stem cells via proliferation, fibrochondrogenic differentiation and meniscus-specific ECM deposition.

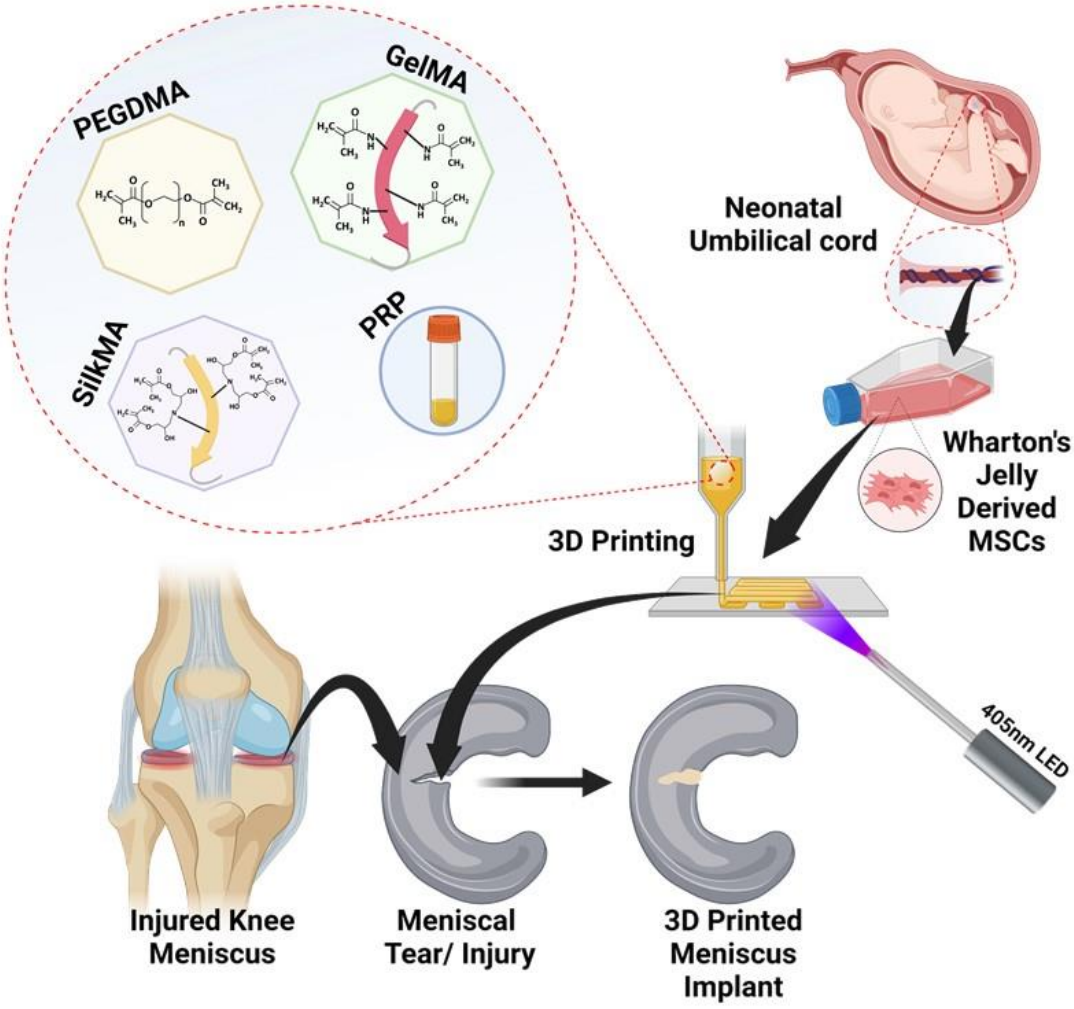

Outcomes of this chapter have been published as:

Ashutosh Bandyopadhyay, Baishali Ghibhela, Sayanti Shome, Samsamul Hoque, Samit K. Nandi, Biman B. Mandal. *Photo-polymerizable silk-based platelet rich plasma loaded bioink for potential patient specific partial and full thickness meniscal defects*. **Advanced Biology.** 2024. 8(5), e2300710. DOI: 10.1002/adbi.202300710

ABSTRACT

Non-healing tears in the avascular regions are followed with partial or full meniscectomy and are causatives of knee osteoarthritis and concurrent lifestyle hindrances in the young, adult and aged alike. Here we report ingenious photo-polymerizable autologous growth factor loaded 3D printed scaffolds for full/partial thickness meniscal defects. A shear thinning photo-crosslinkable silkMA-gelMA-PEGDMA biomaterial-ink was formulated and loaded with freeze-dried growth factor rich plasma (GFRP) derived from photoactivation of platelet enriched human plasma. The biomaterial-ink exhibits optimal rheological properties and shape fidelity for 3D printing. Initial evaluation revealed that the 3D printed scaffolds possess mechanical characteristics mimicking the native meniscus, favourable porosity and swelling characteristics and demonstrated sustained GFRP release. Further GFRP laden 3D scaffolds were screened with human neo-natal stem cells *in vitro*. Biomaterial-ink comprising of 25 mg/ml of GFRP (GFRP25) was found to be amicable for meniscus tissue engineering. Hence, GFRP25 ink was further evaluated for the rigorous rheological compliance, long term degradability (>6 weeks), GFRP release (>5 weeks) and mechanical durability (3 weeks). The sustained release of GFRP from the GFRP25 scaffolds aided in the proliferation of human neo-natal stem cells, while the gene expression and extracellular matrix deposition profile confirmed the meniscus-specific fibrochondrogenic differentiation of the seeded stem cells. Furthermore, GFRP25 constructs showed minimal inflammatory cytokine response *in vitro* and amenable *in vivo* immuno-compatibility. The GFRP25 biomaterial-ink composition and the printed 3D scaffolds could be a potential patient-specific treatment modality for meniscal defects.

4.1 Introduction

Knee menisci are a pair of fibrocartilaginous avascular viscoelastic tissues. They are macro-structurally semi-lunar wedges and act as a congruent cushion between the femoral condyle and tibial plateau. Meniscal tissue injuries and tears caused by sports injuries, old age and accidents [42] are a major cause of pain and discomfort among various groups of the populace. These tears lead to joint destabilization and further to osteoarthritic developments if left untreated in the long run. The conventional treatment modalities include surgical resection of partial or total meniscus [2, 378] which is sometimes followed up with the application of 3D meniscal implants fabricated using natural [463], synthetic [89] or hybrid materials [421] . Suturing of smaller tears is a common clinical practice as well. There is an urgent need of personalized 3D meniscal implants in the clinical scenario. This is a resultant of many factors such as the non-conformation of artificial meniscal implants due to manual shaping and sizing of fabricated (one-size-fits-all) implants, the infection risks from allografts, inconsistent mechanical compliance of the graft; being either too brittle or too stiff; as well as the poor biological integration of synthetic implants [79, 422, 464].

Meniscus is a complex mechanically active tissue, which bears the weight of the body and undergoes numerous cycles of confined compression. The meniscal tissue is majorly made up of collagen I and collagen II in varying ratios as well as glycosaminoglycans with respect to the region of the menisci [4, 23]. The major cellular phenotype within the menisci are fibrochondrocytes which confer the fibroblastic as well as chondrocytic extracellular matrix makeup [5] and they receive their nutrition via diffusion from the synovial capsule. The implants fabricated for menisci are hence sought to be mechanically resilient while being biologically active for efficient integration with the surrounding residual meniscal tissue at the suturing points post resection. This resilience could be improved with the shape and size congruence with the patient's own menisci, obtained via the MRI scanning and 3D modelling workflow for implant fabrication [5, 46].

3D printing/bioprinting has been a modality of choice for various tissue engineering scaffold and construct fabrication in the recent times [204]. Conventionally meniscal tissue engineering has attracted fabrication of composite scaffolds that consist of thermoplastic polymers and bioactive polymers such as chitosan, extracellular matrix, fibrin [138, 139, 372]. The presence of thermoplastics though aids in the mechanical stability, their meagre degradability, potentially harmful degradation products and potential for failure encourages the development of biomaterial-inks that can endure the loading of meniscal tissues while

providing the necessary bioactivity, degradability and tissue integration potential. Photocrosslinking polymers such as silkMA, gelMA, PEGDMA, PEGDA, carMA and HAMA have been envisaged for biomaterial-inks as they possess facile and rapid crosslinking under visible light, safe encapsulation of cells and growth factors and high mechanical and physico-chemical resilience [465]. Though photo-initiator concentration needs to be optimized for minimal loss of cellular viability for their optimal application [266].

The deficient healing of meniscus is due to the absence of vasculature in the mature human menisci [5]. This could be addressed by loading the implants with the growth factors derived from the patient's own plasma. Platelet rich plasma (PRP) is reported in literature as an autologous source of growth factors [466]. It has been typically applied as an injectable gel for musculoskeletal tissue regeneration applications [467, 468]. Growth factors can be obtained by infrared light based photoactivation of platelets as reported in the literature [469]. Further the platelets can be removed to ensure minimal immunogenicity [470, 471]. This would lead to growth factor rich plasma (GFRP) without the platelets can be used for tissue engineering applications. PRP has been reported to contain meniscus regenerating growth factors such as CTGF and TGFβ3 but lacks the mechanically stability for meniscal applications [472]. CTGF and TGFβ3 are known to induce meniscus regeneration by aiding in tissue resident meniscus cell recruitment, cellular proliferation and fibrochondrogenic differentiation bias [302]. GFRP could be encapsulated within suitable biomaterial-inks that lead to a sustained release pattern and aid in the regeneration of the meniscus without the potential for any immunogenic reaction from the platelets.

Human Wharton's jelly derived mesenchymal cells (hwJMSCs) are a nascent source of stem cells gaining recognition for their regenerative potential and applicability in clinical settings. There are several ongoing clinical trials involving hwJMSCs for the treatment and therapeutics [473]. Hence, these stem cells could be chosen for the evaluation of 3D printed constructs owing to their clinical relevance.

In this study we have formulated a photocrosslinkable biomaterial-ink blend that comprises of silkMA, gelMA, PEGDMA, lithium phenyl-2,4,6-trimethylbenzoylphosphinate (LAP) as the photo-initiator and varying amounts of freeze-dried GFRP (GFRP0, GFRP1, GFRP10, GFRP25 and GFRP50). This biomaterial-ink blend shows the necessary shear thinning rheology for the fabrication of highly intricate architecture. The photo-crosslinking could be achieved using a visible light source of 405 nm wavelength in 60 s, making the

fabrication a one-step process. The fabricated constructs were initially screened for their printability, porosity, water uptake, mechanical resilience, ability to support growth and proliferation of human Wharton's jelly derived mesenchymal stromal cells and ability to promote glycosaminoglycan deposition. This aided in the selection of GFRP25 (25 mg/ml GFRP) biomaterial-ink which was further evaluated for potential treatment of meniscal tears. The GFRP25 biomaterial-ink was rheologically characterized to ensure optimal printability for larger constructs. This was evaluated in a proof-of-concept anatomically relevant *in vitro* meniscus defect replica where the GFRP25 biomaterial-ink demonstrates the shape fidelity and printability required for printing patient-specific meniscus constructs. GFRP25 biomaterial-ink The GFRP25 constructs demonstrated prolonged slow degradability for >6 weeks under enzymatic and saline conditions and the sustained release of GFRP from the constructs was observed for >5 weeks. GFRP25 constructs were found to bear 2000 cycles of 0-20% confined compression/day for 3 weeks and their stress-strain hysteresis curve was monitored on days 1, 7, 14 and 21. Further, biological characterization of GFRP25 using hwJMSCs revealed the fibrochondrogenic differentiation competency of the constructs via the upregulation of fibrochondrogenic genes as well as deposition of meniscus specific extracellular matrix (ECM) components i.e., collagen I, collagen II and aggrecan after 21 days of culture. Additionally, the GFRP25 constructs were evaluated for their immuno-compatibility *in vitro* (murine and human monocyte derived macrophages response) via the release profile of inflammatory cytokine (TNFα and IL-1β). *In vivo* subcutaneous implantation in rabbit model for 1 and 3 weeks was carried out for assessing degradability and biocompatibility of the biomaterial-ink constructs. GFRP25 biomaterial-ink was evaluated for potential one-step facile fabrication of patient specific constructs to treat partial or full thickness meniscal defects.

4.2 Materials and Methods

4.2.1. Formulation of Biomaterial-ink Composition and 3D printing

4.2.1.1. Preparation of Bombyx mori silk fibroin methacrylate (silkMA)

Methacrylated *B. mori* silk fibroin (silkMA) was prepared using a pre-optimized protocol [435]. Briefly, *B. mori* cocoons were chopped, degummed in boiling 0.02M sodium carbonate solution (Na_2CO_3) for 30 min, washed thoroughly using distilled water, and air dried to obtain the degummed fibres. Obtained degummed fibres were dissolved in lithium bromide (LiBr, 9.3M) under stirring for 1h at 60°C. To this silk-LiBr solution, glycidyl methacrylate (GMA) was added at a feed ratio 0.06:1 while continuously stirring and further incubating at 60°C to react for 3h. This solution is further dialysed using a 12-14kDa cut-off dialysis membrane

against double distilled water for 96h to remove the unreacted GMA and residual LiBr and obtaining the regenerated *B.mori* silk fibroin methacrylate (silkMA). Gravimetric determination as sued to determine the concentration of silkMA and it was used as a stock for further use.

4.2.1.2. Preparation of gelatin methacrylate (gelMA)

Gelatin methacrylate (gelMA) was prepared according to the protocol mentioned previously with slight modification [447]. Briefly, gelatin type A from porcine skin was dissolved in 0.1M carbonate-bicarbonate buffer (CB buffer, pH 9.2-10.6) while stirring and maintaining at 60°C. The pH was adjusted to 9 using NaOH before reaction and methacrylic anhydride (MA, 94%) was added dropwise to the solution mixture at the feed ratio of 0.1:1 at intervals of 10-11 minute, while constantly adjusting the pH to 9 and thereafter allowed to react for 1.5h at 60°C. pH of the solution was adjusted to pH 7.4 using 1N HCl to stop the reaction. Obtained reaction mixture was dialyzed against double distilled water in a 12kDa cut-off dialysis membrane for 120h at 60^0C for removal of excess unreacted MA and any other byproducts. The dialyzed gelMA was frozen at -80°C and freeze-dried for storage and further reconstitution.

4.2.1.3 Preparation of freeze-dried growth factor rich plasma (GFRP)

Preparation for freeze-dried photoactivated platelet rich plasma lysate was carried out by introducing certain modifications in a protocol previously mentioned [469]. Platelet concentrate bags were secured from blood bank of GNRC hospital (Guwahati, Assam, India) before expiration and transported rapidly to laboratory under shaking conditions. The platelet bags were procured and used with appropriate collection, processing and handling protocols reviewed and approved by Institutional Ethics Committee, Institute of Neurological Sciences Trust, GNRC Hospitals (***Reference no. Inst/AS/2015/RR-2018/EC-104***). Initially platelet bags were collated from ≥5 patients to remove batch-to-batch variability of experimental results. The collated platelet-enriched-plasma (PEP) was taken further for platelet concentration by centrifuging at 300xg for 8 min at 12°C to separate platelet and buffy coat layer from the residual cells such as RBC. Obtained suspension was centrifuged at 1000xg for 10 min at 16°C to obtain the platelet pellet and plasma supernatant. The supernatant was reduced to 1/3rd of the volume and platelet pellet was gently resuspended to obtain platelet rich plasma suspension. This suspension was poured onto petri dishes kept in an ice bath for photoactivation using a polychromatic infrared light source (600-1300 nm, Philips R95) from a distance of 30 cm along

the central axis of the lamp for 15 min. The growth factor rich activated PEP was centrifuged at 1000xg for 15 min at 16°C to pellet down the platelets. The growth factor rich supernatant plasma was collected, freeze-dried and stored at -20°C under sterile conditions for further use. This freeze-dried form of the photoactivated growth factor rich plasma is referred to as GFRP in further mentions. Batches of freeze-dried GFRP isolated from multiple patients (n=3) was reconstituted at 1 mg/5 ml concentration in saline and used for the estimation of growth factors TGFβ3 and CTGF using ELISA kits (Krishgen biosystems, USA) following the manufacturers protocols for the respective kits.

4.2.1.4. Preparation of photo-crosslinking biomaterial-ink blend and 3D printing GFRP laden constructs

silkMA, gelMA and PEGDMA stocks were sterilized by autoclaving and stock solution of lithium phenyl-2,4,6-trimethylbenzoylphosphinate (LAP, Sigma Aldrich, U.S.A.) was filter sterilized (0.22μm). Concisely, the biomaterial-ink hydrogel blend was formulated by mixing silkMA, gelMA, PEGDMA (polyethylene glycol dimethacrylate, Mn 700, Sigma Aldrich, U.S.A.) and LAP to reach a final concentration of 5% (w/v), 10% (w/v), 5% (w/v) and 0.4% (w/v) respectively by mixing at 40°C under aseptic conditions until a uniform blend was obtained with no precipitating residues. Thereafter the blend was cooled to room temperature and GFRP was added at 0 - 0.5 % w/v to reach GFRP0, GFRP1, GFRP10, GFRP25 and GFRP50 blends (as shown in **Table 4.1**) in a sterile environment and pipetted until a uniform hydrogel is obtained. This biomaterial-ink blend was further used in uncrosslinked and crosslinked forms for 3D printing constructs for physico-chemical, mechanical and biological characterizations.

Table 4.1: *Biomaterial-ink compositions*

Nomenclature	Composition		
	GFRP (mg/ml ink)	Polymers	LAP
GFRP0	0	silkMA: 5% w/v gelMA: 10% w/v PEGDMA: 5% w/v	0.4% w/v
GFRP1	1		
GFRP10	10		
GFRP25	25		
GFRP50	50		

The constructs were printed using a BioX (Cellink, Sweden) bioprinter set with a temperature-controlled extruder at 18-20°C extruder temperature, print bed temperature at 10°C, a 22G blunt stainless-steel nozzle, print speed of 5-8 mm/s and 150-180 kPa pneumatic pressure. Grid designs with custom-made GCODES were printed for the various physicochemical, mechanical and biological experiments and the dimensions have been specified in the subsequent sections for each experiment. The constructs were crosslinked from a distance of 4 cm for 5 s along the central axis after printing each layer using the printer's 405 nm LED light source. The constructs were finally crosslinked for 20 s post printing full dimensions using a 405 nm, 40 W LED light source. A custom-made 3D model gcode **(Figure 4.1A)** with varying gap between strands was used to determine the printing resolution of GFRP0, GFRP1, GFRP10, GFRP25 and GFRP50 constructs. A custom-made 3D printed PLA mold **(Figure 4.1B)** was used to determine the buckling effect of GFRP0, GFRP1, GFRP10, GFRP25 and GFRP50 biomaterial-inks. Further another custom-made grid model **(Figure 4.1C)** was used to print the 2, 4 and 8 layered constructs of GFRP0, GFRP1, GFRP10, GFRP25 and GFRP50 biomaterial-inks.

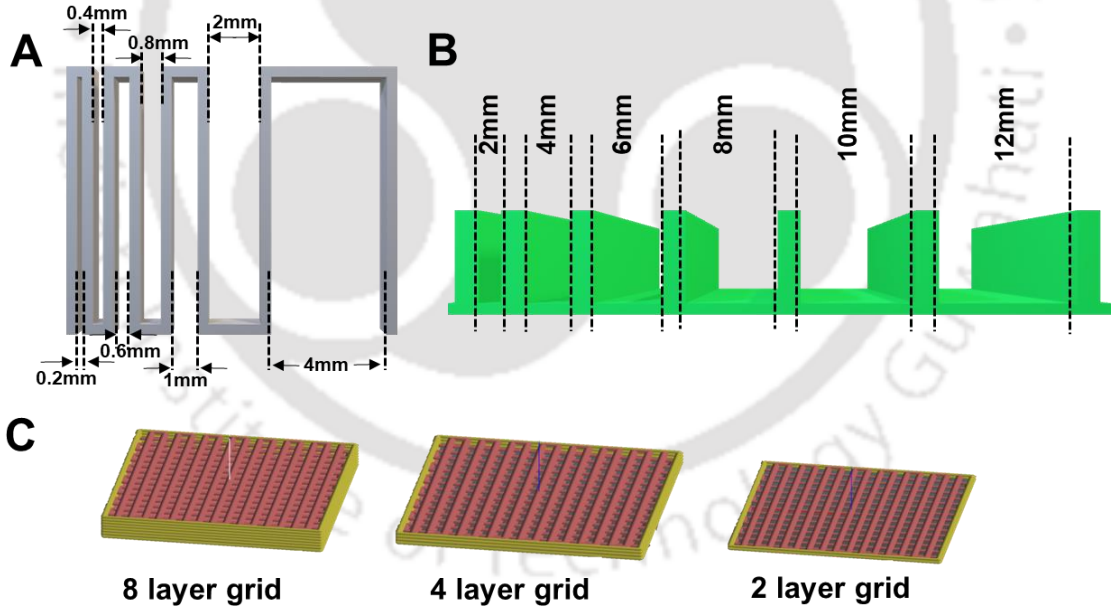

Figure 4.1: *(A) 3D CAD model for evaluation of printability of various inks. (B) 3D CAD model of custom designed PLA construct for evaluation of buckling in ink. (C) 3D CAD model of custom designed 15mm x 15mm grids with 8, 4 and 4 layers.*

4.2.2 Preliminary Rheological Characterization of Biomaterial-ink Blend

Biomaterial-ink compositions with varying amounts of GFRP were characterized rheologically in uncrosslinked forms through various tests to understand their flow characteristics using an MCR 302 rheometer (Anton Paar, Austria). Amplitude sweep, frequency sweep, temperature sweep as well as 3ITT (three-interval thixotropy) were performed on biomaterial-inks using stainless steel parallel plate (PP25, 25 mm diameter). For each test, the biomaterial-ink compositions were pipetted onto the temperature controlled lower plate of rheometer, and the gap in between the plates was set at 0.5mm. For amplitude sweep, the shear strain was varied from 0.001-1000% at constant angular frequency of 1 rad s^{-1}. The obtained linear viscoelastic region (LVER) of respective biomaterial-ink blend composition was further used to perform frequency sweeps. The angular frequency was varied from 0.01 to 100 rad s^{-1} at a constant shear strain amplitude of 1% to find out the stability of the biomaterial-ink blends at various frequencies of shear. Furthermore, temperature sweeps of the biomaterial-ink blends were performed over a wide range of 4°C to 45°C at constant angular frequency (1 rad s^{-1}) and shear strain amplitude (1%) to ascertain the temperature induced transition causative of the printable temperature range. This was followed by the 3ITT (three-interval thixotropy) test where biomaterial-inks were exposed to alternating cycles of long duration low shear strain amplitude (1%), low angular frequencies (1 rad s^{-1}) intercepted by short stretches of high shear strain (100%), high angular frequencies (100 rad s^{-1}) to evaluate the printability and self-standing nature of the biomaterial-ink.

4.2.3 Characterization of Printed 3D Constructs

4.2.3.1 Physiochemical characterization

4.2.3.1.1 Surface topography using Electron Microscopy

Microarchitecture, pore size and pore size distribution of the biomaterial-inks was observed using field emission scanning electron microscopy (FESEM, Sigma, ZEISS, U.S.A) with an accelerative voltage of 2 kV. Constructs were printed of dimensions 7x7x7 mm^3 and crosslinked. These constructs were freeze-dried and cut into sections for electron microscopy. The sectioned constructs were sputter-coated with gold before analysis. Further it was scanned under FESEM under high vacuum conditions.

4.2.3.1.2 Fourier Transform Infrared (FTIR) Spectroscopy

The infrared spectroscopy was done for ascertaining the structural conformational analysis of individual components as well as the blended biomaterial-inks via attenuated total reflection (ATR) mode of FTIR (Shimadzu, IR Affinity-1S WL). The components i.e., including silkMA, gelMA, PEGDMA, biomaterial-ink without GFRP (GFRP0) and biomaterial-ink with highest concentration of GFRP (GFRP50) were freeze dried and placed over the ATR crystal. Thereafter, spectra of all the samples were obtained in the range of 500 and 2500 cm^{-1}, a spectral resolution of 4 cm^{-1} and with 32 scan averages. Background readings were deducted from sample readings and all the spectra were noted at room temperature. Thereafter, the characteristic peak of individual components of biomaterial-ink, GFRP0 and GFRP50 were observed for changes caused by the photo-crosslinking and methacrylation.

4.2.3.1.3 Water uptake study

Water uptake behaviour of the constructs printed with different GFRP concentrations was studied based on previously mentioned protocol [435]. Concisely, the initial weight of 3D printed constructs (n = 5) was noted after freeze-drying (W_i) and they were subsequently incubated in phosphate buffered saline (PBS, pH 7.4, 37°C) until they attained equilibrium. Weight of swollen construct (W_s) were measured using a microbalance at various time intervals by slowly dabbing off the excess PBS using a wet tissue paper. Swelling ratio was expressed using the following equation: $Water\ Uptake\ (\%) = \frac{W_s}{W_i} \times 100$

Where, W_s denotes the weight of construct measured after different time intervals and W_i represents initial weight of construct.

15 x 15 x 1 mm^3 constructs were fabricated for all the compositions and photographic images were captured for the printed constructs in their freeze-dried state and after reaching swelling equilibrium.

4.2.3.1.4 Enzyme-assisted and saline based degradation profile

The *in vitro* enzyme assisted degradation study was performed on the 3D constructs with different GFRP concentrations based on previously mentioned protocol [46]. Degradation of silk based matrices have been found to accelerated under low doses of protease XIV (0.1 U/ml) as compared to very high doses of MMP-1 (8750 U/ml, 1.25 µg/ml) and MMP-2 (313 U/ml, 12.5 µg/ml) [474]. These MMP concentrations are significantly higher than the physiological

levels of MMPs *in vivo* after injury [475]. Protease XIV was hence chosen at a concentration of 0.5 U/ml for *in vitro* degradation evaluation. This study was conducted over the period of 45 days while incubating in PBS or a solution of protease XIV (from *Streptomyces griseus*, 3.5 units/mg, Sigma-Aldrich, U.S.A.). The 3D printed constructs (n = 5) were immersed in either non-proteolytic PBS solution (pH 7.4) or proteolytic PBS solution (pH 7.4) containing 0.5 U/ml protease XIV at 37°C. Constructs immersed in non-proteolytic PBS solution were considered as control for comparison of stability of hydrogels. Constructs were incubated by replacing enzyme solution every 2 days for a period of 45 days. Additionally, 0.05% (w/v) sodium azide was added to the enzyme solution for preventing microbial growth. The constructs were retrieved at different time points, weighed and the remaining mass was recorded for each time point. The consequent percentage of mass remaining was expressed as follows: $\%Weight\ remaining = \frac{W_r}{W_i} \times 100$

Where, W_r represent weight of construct measured after n days and W_i represent initial weight of construct.

4.2.3.1.5 Hexane displacement porosity estimation

Porosity of 3D printed constructs was analysed using predefined hexane displacement method [406]. In brief, the printed constructs of equal size (n = 4) were immersed in 13 mL of hexane (V_1) for 20 min each. Thereafter, the overall volume of hexane along with hexane-soaked constructs (V_2) was noted. Thereafter, the hexane-soaked constructs were removed and the residual volume of hexane solution in graduated cylinder (V_3) was noted. Discrepancy in volume of hexane due to evaporation was eliminated by keeping another graduated cylinder with hexane and without constructs as control. The percentage porosity of hydrogel constructs was calculated according to the equation: $Apparent\ Porosity\ (\%) = \frac{V_1 - V_3}{V_2 - V_3} \times 100$

Where (V_1 - V_3) denotes volume of hexane impregnated within printed constructs whereas (V_2 - V_3) denotes total volume of construct.

4.2.3.1.6 Cumulative release of GFRP

Cumulative release of platelet rich plasma lysate was evaluated by estimating the leachate derived from the printed constructs with varying amounts of GFRP in the biomaterial-ink composition. The initial amount of GFRP loaded into each construct (W_1) was noted according to the initial volume of the biomaterial-ink required for printing of each construct (n = 4). Further these constructs were incubated in PBS (pH 7.4) supplemented with 0.05% (w/v) sodium azide at 37°C over 40 days with complete removal and replacement of the incubation solution at various time intervals (0,1,3,5,7,14,21,28 and 40 days). Thereafter, 20 µL of leachate containing PBS was added with 200 µL of Bradford reagent (SIGMA-Aldrich, USA) for 20 min and the absorbance was read at 525 nm. The amount of GFRP proteins leached out (W_2) was determined from the standard curve and the cumulative GFRP release (%) was measured using the formula: $Cumulative\ Release\ of\ GFRP\ (\%) = \frac{W_2}{W_1} \times 100$

Where, W_1 represents initial amount of GFRP encapsulated into the printed constructs (mg) and W_2 denotes the amount of leached GFRP in the solution (mg).

4.2.3.2 Compressive strength evaluation of printed constructs

Acellular printed constructs (n = 5) were fabricated in 8x8x8 mm^3 dimension and incubated to reach swelling equilibrium in phosphate buffered saline (PBS, pH 7.4) at 37°C. Thereafter, uniaxial confined compressive stress test of the printed constructs was carried out using a universal tensile testing machine (Model 5944, Instron, USA) armed with a 100 N load cell. Printed constructs were exposed to a uniaxial confined compressive strain of 60% at rate of 5 mm min^{-1}. Further, the compressive stress vs strain curve was plotted and the mean compressive modulus as well as young's modulus was calculated using Bluehill 3 software. Additionally, printed constructs were also exposed to uniaxial compressive cyclic strain of 20% for 50 cycles of compression at a rate of 5 mm/min. While GFRP25 printed constructs were subjected to 2000 cycles of compression at the same rate every day and data was recorded after different intervals of incubation in PBS (1, 5, 7, 14 and 21days). The compressive stress-strain curve, compressive stress-cycle count curve of first 10 cycles and last 10 cycles as well as the hysteresis loop of compressive stress-strain for 1st cycle and last cycles were plotted to compare the aberration in terms of strength and stress profile of the constructs during the experimental duration for initial evaluation. GFRP25 constructs were analyzed via hysteresis stress-strain curves for cycle 1 and 2000 for all timepoints.

4.2.3.3. Printing a proof-of-concept 3D meniscal defect implant

An intact meniscus from our previous work [46] was printed and a defect was introduced in the same. Thereafter the CAD model of the defect was developed. It was printed using GFRP25 biomaterial-ink. These constructs were further used for evaluating the print fidelity of the biomaterial-ink, shape congruence of the printed constructs and the ability of the biomaterial-ink for printing full thickness meniscal defects.

4.2.4 Biological evaluation of printed constructs

4.2.4.1 Isolation of Wharton's Jelly Stem cells and cell seeding on printed constructs

Wharton's jelly stem cells were harvested from freshly collected Human umbilical cords through an explant-based method. The isolation protocol was in accordance with the previously established protocol [449]. Human umbilical cord was procured from GNRC Hospital (Guwahati, Assam, India) with appropriate collection, processing and handling protocols reviewed and approved by Institutional Ethics Committee (Institute of Neurological Sciences Trust, GNRC Hospitals; ***Reference no. Inst/AS/2015/RR-2018/EC-103***). For the transport of cords, ice cold sterile PBS (pH 7.4) was used, and they were processed within 2-3 hours of procurement. Sterile PBS was used to wash the cord tissue in order to remove remnant blood. Further, Wharton's jelly was dissected out from cord tissue used as explants. The explants were observed for the outcoming migrated cells which were trypsinized and reseeded to expand further. A preoptimized growth medium of DMEM (Gibco, USA); glucose 4500 mg/L supplemented with 10 % fetal bovine serum, FBS (Gibco, USA), 1X antibiotic-antimycotic mix (Gibco, USA) supplemented with 2ng/ml basic fibroblast growth factor (bFGF) was used. For the biological characterization of injectable hydrogel, cells within passage number of 3-8 were used.

Constructs of various groups GFRP0, GFRP1, GFRP10, GFRP25 and GFRP50 were printed in aseptic conditions and hwJMSCs were seeded on them. Cellular seeding density was maintained at 10^4 cells per mm^2 of constructs as per previous protocol [46]. Thereafter, the cell seeded 3D constructs were cultured in cell culture medium DMEM (high glucose, Gibco, USA); supplemented with 10 % fetal bovine serum, FBS (Gibco, USA), 1X antibiotic-antimycotic mix (Gibco, USA)) in an incubator at 37°C with 5% CO_2 and 85% humidity for their biological evaluation.

4.2.4.2 Biochemical analysis

Cell seeded printed constructs (n =4) of previously mentioned dimensions were utilized for estimation of DNA content and sGAG content following previously established protocol[46]. Concisely, cells seeded printed constructs of each group GFRP0, GFRP1, GFRP10, GFRP25 and GFRP50 were collected after different incubation time intervals of 1,7,14 and 21 days and digested using papain digestion cocktail (5 mM L-cysteine, 5 mM EDTA, 100 mM Na_2HPO_4 and 125 µg/mL papain, pH 6.2) for 16 h at 60°C in a hot air oven. Thereafter, picoGreen DNA assay kit (Invitrogen, USA) was used to estimate DNA content in accordance with the manufacturer's protocol. The digested samples were centrifuged and 25 µL of supernatant was diluted using 75 µL of 1X TE buffer. Thereafter, each sample was added with 100 µL of Quant-iT PicoGreen reagent (1:200 dilution in 1x TE buffer) and quantification was carried out using a microplate reader (Tecan infinite M200 PRO) with an excitation and emission maxima of 480 and 528 nm respectively. Standard curve for the DNA content estimation was generated using lambda phage DNA.

For quantification of deposited sGAG by the seeded hwJMSCs, 1,9-dimethylmethylene blue (DMMB) reagent was used according to previously optimized protocols [435]. In brief, 200 µL of DMMB reagent was added to 20 µL of papain digested samples and the absorbance was read at 525 nm. Chondroitin-6-sulfate (Sigma Aldrich, USA) was used to prepare the standard curve for sGAG quantification.

4.2.4.3. Cellular viability assay

Cell viability of the hwJMSCs seeded upon GFRP25 constructs was screened using live/dead assay kit. The assay dye solution was formulated by mixing calcein-AM (2 µM) and ethidium homodimer (4 µM) solutions (pH 7.4) following manufacturer's protocol (Sigma-Aldrich, USA). Cell viability was observed after 1,7,14 and 21 days of culture. Cell seeded printed constructs were washed mildly with PBS (pH 7.4) followed by incubation with calcein-AM and ethidium homodimer solution at 37°C and 5% CO_2 for 40 min. Thereafter, the live/dead reagent was aspirated, and the constructs were washed briefly in PBS before being visualized under an inverted fluorescence microscope (Nikon TiU2, Nikon, Japan). Green fluorescence by viable cells indicated integral plasma membrane and intracellular esterase activity that changes calcein AM to calcein while, dead cells were identified by the red fluorescence of ethidium homodimer entering inside through damaged plasma membranes.

4.2.4.4 Gene expression profile by Real-Time PCR analysis

Complete RNA was isolated from hwJMSCs seeded GFRP25 constructs (n = 4), after different incubation time points of 1,7,14, and 21 days, using TRIzol (Sigma Aldrich, USA) following our previously established protocol [476]. Briefly, cells seeded constructs were taken in tubes with TRI reagent and chopped with microscissors on ice container. The chopped constructs were then centrifuged at speed of 13000xg for 10 min and 4°C and the supernatant were relocated into fresh tubes to which chloroform was added and centrifuged. Then the upper aqueous layer was carefully removed into fresh tubes followed by addition of isopropanol to obtain mRNA. This mRNA was further pelleted using centrifugation and washed using pre-chilled DNA diluent (EtOH). The pellet was then air dried in laminar flow and reconstituted in nuclease free water. mRNA concentration was determined using microdrop spectrophotometric plate bundled with Multiskan Sky (Thermofisher Scientific, USA) and followed by cDNA synthesis using high capacity cDNA reverse transcription kit (Applied Biosystems, USA) and a PCR thermal cycler (Applied Biosystems, USA). Obtained cDNA was further used to perform real-Time PCR using the primer sequences for various human genes (listed in **Table 4.2**) and SYBR Green reagent (Invitrogen, USA) in a QuantStudio 5 (Applied Biosystems, USA) real-time PCR machine The run was carried under the set conditions of the holding stage (50°C for 2 min, 95°C for 10 min) and cycling stage (40 cycles of 95°C for 15 s and 60°C for 45 s). The results obtained were analysed by normalizing using β-actin, the endogenous housekeeping gene as well as the expression on day 1 via Ct method ($2^{-\Delta\Delta Ct}$).

Table 4.2: *Primer sequences used for gene expression analysis*

Gene	Sequence	Accession No.
Human sox-9 (sox-9)	F:5′-TTCCGCGACGTGGACAT-3′ R:5′GGCGGCAGGTACTGGTCAAACTC-3′	NM_213843.1
Human Aggrecan (acan)	F:5′-CCCAACCAGCCTGACAACTT-3′ R:5′-CCTTCTCGTGCCAGATCATCA-3′	NM_001164652.1
Human collagen Iα (col I)	F:5′-AGAAGAAGACATCCCACCAGTCA-3′ R:5′-AGATCACGTCATCGCACAACA-3′	XM_021067153.1
Human collagen IIα (col II)	F 5′-CAGGTGAAGGTGGGAAACCA-3′ R 5′-ACCCACGAGGCCAGGA-3′	AF201724.1
Human runx-2/cbfa-1 (runx-2)	F 5′-GACTGTGGTTACCGTCATGGC-3′ R 5′-ACTTGGTTTTTCATAACAGCGGA-3′	NM_001015051.4
Human osteocalcin (OCN)	F 5′-GTAGTGAAGAGACCCAGGCG-3′ F 5′-CGGATTGAGCTCACACACCT-3′	NM_199173.6
Human Beta Actin (β-actin)	F: 5′-CACCATTGGCAATGAGCGGTTC R:5′- AGGTCTTTGCGGATGTCCACGT-3′	NM_001101

4.2.4.5 Macrophage stimulation and inflammatory cytokine release profile

In vitro immunomodulatory response of printed GFRP25 composition was performed by using RAW 264.7 cells (mouse macrophages, acquired from National Center for Cell Science, NCCS, Pune) by estimating the amount of TNF-α (Tumor Necrosis Factor) and IL-1β (Interleukin 1β) released. RAW 264.7 cell lines were maintained in DMEM supplemented with 10% FBS, 1% anti-anti at 37°C and 5% CO_2 prior to seeding. The cells were seeded at the density of 5×10^4 cells per well in a 24-well plate and grown for 24 h. Four groups were taken into consideration for the *in vitro* study, a negative control group (Tissue culture plate without hydrogel), a positive control group (Lipopolysaccharide, 1000 ng ml^{-1}, LPS from *Escherichia coli*, Sigma Aldrich, USA) and two Experimental groups comprising of both printed GFRP25 constructs or their leachates in media. Thereafter, printed constructs were placed on seeded cells, or the cells were treated with the leachate medium derived from the constructs after 24 h. Post 24 h of stimulation the culture media with the released cytokines was collected for each group and used for the quantification of TNF-α and IL-1β release using their respective ELISA kits following the manufacturer's (Krishgen Biosystems, USA) protocol.

THP-1 (human monocyte cell line) procured from NCCS were cultured in suspension in RPMI 1640 media (Sigma Aldrich, USA) by observing standard protocols. THP-1 cells were seeded at a density of 5×10^4 cells per well in a 24-well plate or on the printed constructs at the same density for differentiation into adherent macrophages (M0) by treating with 100 ng mL^{-1} (162 nM) phorbol 12-myristate 13-acetate (PMA) (Sigma Aldrich, USA) for 24h. Consequently, the M0 macrophages in the well plate were treated with the leachate medium from the printed constructs, while the seeded cells were cultured on the printed constructs for 24 h while keeping 1000 ng ml^{-1} LPS stimulated cells as positive and unstimulated cells as negative controls in the well plate. The conditioned media were collected and used for the determination of human TNF-α and IL-1β released by the macrophages using respective ELISA kits in agreement to the manufacturer's (Krishgen Biosystems, USA) protocols.

4.2.4.6 *In vitro* immuno-fluorescence staining

3D printed GFRP25 constructs were seeded with hwJMSCs at previously mentioned density and cultured in basal medium for 21 days. Post incubation the constructs were preserved in 10% neutral buffered formalin (NBF) for 24 hr and thereafter washed with PBS. The fixed constructs were further permeabilized using 1% (v/v) triton-X 100 in PBS for 1 hr at room temperature followed by blocking using 10% (w/v) bovine serum albumin in PBS for 2 hr. Thereafter, the constructs were co-stained with mouse mono-clonal anti-collagen I, and rabbit poly-clonal anti-aggrecan or rabbit poly-clonal anti-collagen II primary antibodies (ABCAM, USA) respectively for 2 hr. The constructs were further stained with secondary anti-mouse or anti-rabbit antibodies for the respective primary antibodies for 2 h and counterstained with DAPI (300 nM, Thermofisher Scientific, USA) for 20 min before imaging. The fluorescent micrographs were obtained using an inverted fluorescence microscope (Axio Observer, Zeiss, Germany). The images obtained from different constructs (n = 8) were used for calculating the field of view area stained with either collagen I and aggrecan or collagen I and collagen II by using Fiji (NIH ImageJ software) following previously defined protocol [477] to determine the expression ratio of ECM components.

4.2.4.7 *In vivo* biocompatibility of acellular biomaterial-ink

In vivo biocompatibility of the scaffolds was assessed by implanting acellular GFRP25 biomaterial-ink into subcutaneous abdominal pockets of adult New Zealand white rabbits. The experimental and animal handling protocols were reviewed and sanctioned by the Institutional Animal Ethical Committee (IAEC), West Bengal University of Animal and Fishery Sciences

(WBUAFS), West Bengal, India (***Registration No. 763/GO/Re/SL/03/CPCSEA/02/2021-22 dated26.4.2022***). Three healthy adult rabbits of either sex, each weighing 1.5 - 1.8 kg were used. Subcutaneous pockets were surgically created by making two small incisions in the thoracolumbar regions on either side, then two sterile biomaterial-ink constructs (one per pocket, sterile, 5 mm × 5 mm × 1 mm) was inserted per animal (n = 6) put under anesthesia using Xylazine hydrochloride (5 mg/kg body weight; Injection xylaxin, Indian Immunologicals, Ahmedabad, India) and ketamine hydrochloride (33 mg/kg body weight; Ketalar, Parke-Davis, Hyderabad, India) intramuscularly. Thereafter the pockets were closed in place via surgical staples and the animals were closely monitored. The wound areas were cleaned superficially every day with 10% povidone–iodine draped dressing gauge and animals of each group received Meloxicam (0.3 mg/kg body weight; Injection Melonex, Intas Pharmaceuticals India, Ahmadabad, India) injection daily intramuscularly for 3 days. Three animals were sacrificed, after 1 week and the rest three animals after 3 weeks, by cervical dislocation. The implant site tissue surrounding the samples was retrieved along with the biomaterial-ink constructs and preserved for histological processing in 10% NBF for 24 h, followed by PBS wash and embedding in cryo-sectioning medium and freezing at -20°C for 6 hr. The tissue sectioning was done in a cryostat (CM1860 UV, Leica, Germany) with 18µm thick section and immunostained using DAPI for visualization of nuclei and anti-CD68 fluorescence-based antibody to observe the infiltration of cells and macrophages within the implanted biomaterial-ink constructs. Micrographs and z-stacked composites of stained sections were obtained using an inverted fluorescence microscope (Axio Observer, Zeiss, Germany).

4.2.5 Statistical analysis and image processing

Experiments that are quantitative by nature were performed in n≥3 and the results were represented as mean ± standard deviation. For statistical analysis of the data, one way ANOVA was carried out using Tukey's method. Statistical analysis and plotting were carried out with the help of OriginPro 2021 software (OriginLab corporation, USA) to analyse the significant difference between various sampling groups. Variations between groups of $^{*}p \leq 0.05$ were denoted to be statistically significant. All image processing and quantification were carried out using ImageJ and ZenBlue (Zeiss, Germany).

4.3 Results

4.3.1 Formulation and Characterization of Biomaterial-ink blend

Biomaterial-ink preparation was carried out in stages. Collated platelet rich plasma containing platelets was derived from ≥5 different patients to eliminate batch-to-batch variation. This collated platelet containing plasma was photo-activated followed by discarding of platelets to obtain the GFRP enriched with growth factors. This GFRP was freeze-dried (**Figure 4.2A**) and thereafter the obtained powder was used for further experiments. The GFRP lysate was reconstituted in saline and quantified for fibro-chondrogenic factors TGFβ3 and CTGF. TGFβ3 was found to be 798.5±172.2 pg and CTGF was found to be 1560.9±118 pg in every mg of reconstituted freeze-dried GFRP (Figure 1B). These growth factors stored within the 3D printed constructs along with plasma proteins are poised for potential regeneration of the largely avascular menisci. Secondly, the biomaterial-ink blend was formulated by blending silkMA, gelMA, PEGDMA, and LAP. This blend was labelled GFRP0. Further the various biomaterial-ink compositions were formulated as given in **Table 4.1**, but GFRP addition post 50 mg/ml was not carried out due to solubility and dispersion issues (data not presented here).

The infrared spectroscopic analysis of gelMA, silkMA(BMMA), PEGDMA, GFRP0 and GFRP50 biomaterial-inks was carried out (**Figure 4.2C**). All the protein polymers or the biomaterial-ink blends were found to show the cardinal peaks in the amide I (1710–1590 cm^{-1}), amide II (1570–1480 cm^{-1}) and amide III (1270–1200 cm^{-1}) regions. Peak shifts were observed from amide I (from ~1635 cm^{-1} to ~1650 cm^{-1}), amide II (from ~1546 cm^{-1} to ~1539 cm^{-1}) and amide III (~1247 cm^{-1} to ~1244 cm^{-1}) regions in the GFRP0 and GFRP50 biomaterial-inks when compared with gelMA and silkMA. Moreover, the signature peak was observed in the 940-950 cm^{-1} region among all the components due to the presence of methacrylate groups.

Shear thinning is a crucial feature that determines applicability of biomaterial-inks in micro-extrusion-based 3D printing. Preliminary rheological characterization of all the GFRP containing biomaterial-inks was carried out via amplitude sweep at 20°C to evaluate their shear thinning natures. All the compositions were found to be gradually shear thinning post ~100% shear strain. All biomaterial-ink compositions were found to be rapidly shear thinning at higher strain percentages (**Figure 4.2D**). Further the inks were assessed for their temperature induced gelation using temperature sweep and evaluation of loss factor (tan δ) (**Figure 4.2E-F**). tan δ was found to go below 1 for GFRP0 at 19.87°C, GFRP1 and GFRP10 at 20.87°C, GFRP25 and GFRP50 at 21.87°C, which indicate their temperature-induced gelation. Hence, printing temperatures for all biomaterial-inks could be set at 20°C.

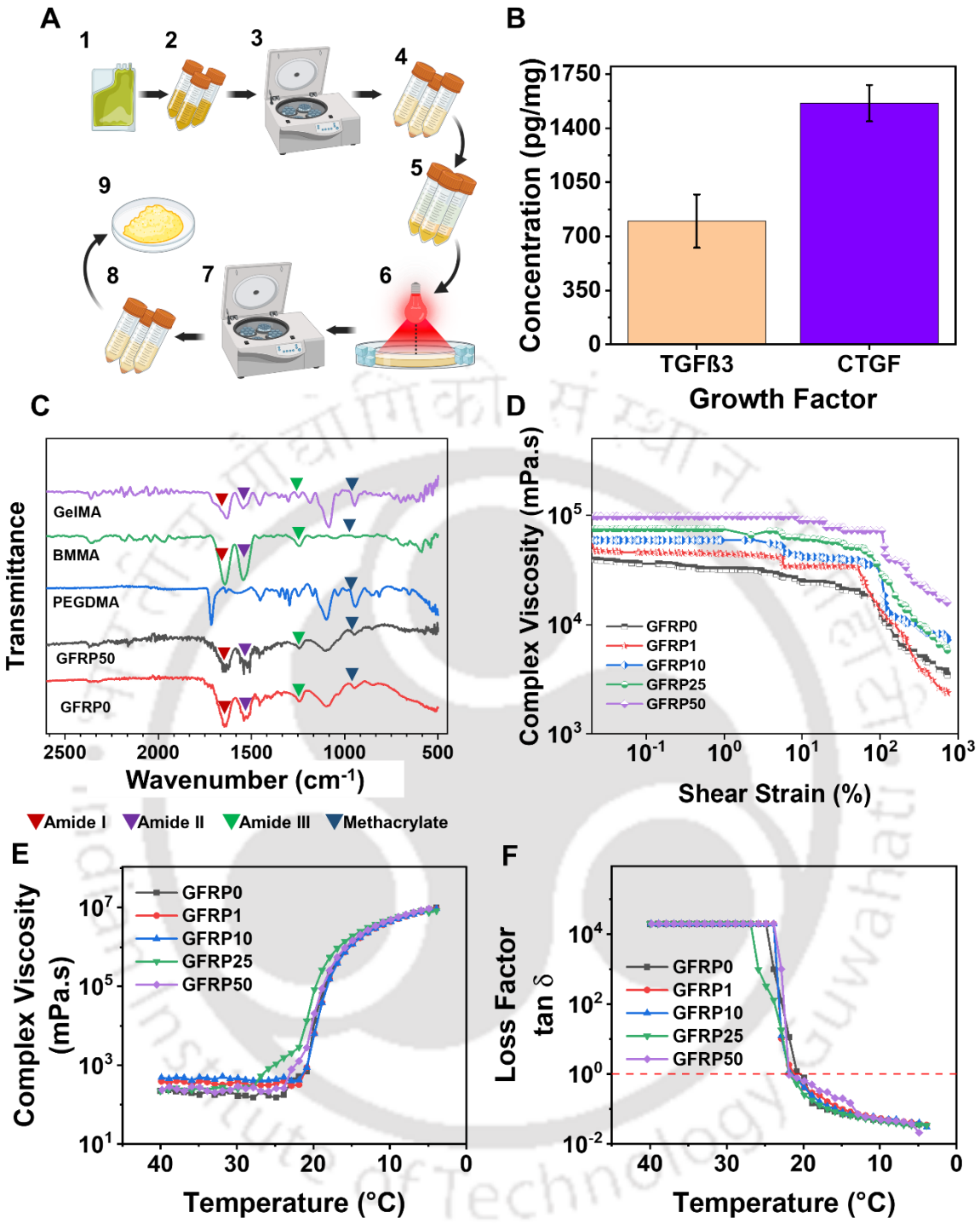

Figure 4.2: *(A) Schematic representation of the isolation procedure of GFRP: platelet enriched plasma (1) bags are procured from the blood bank and collected in centrifuge tubes (2). Thereafter, a preliminary centrifugation is performed (3) to further concentrate the plasma followed by its activation (4-6) and henceforth the platelets are separated using centrifugation (7) and the plasma with the growth factors is freeze-dried (8-9) for further use (Made with www.biorender.com). (B) ELISA based quantification of growth factors in reconstituted freeze-dried GFRP. (C) FTIR spectra of various biomaterial-ink components and the biomaterial-ink without GFRP (GFRP0) and with highest GFRP (GFRP50). (D) Amplitude sweep of the*

various biomaterial-ink compositions with increasing concentrations of GFRP. (E) Complex viscosity and (F) Loss factor of GFRP loaded biomaterial-inks observed under changing.

Inks demonstrated higher complex viscosity with the increase in the amount of GFRP lysate within the ink. High viscosity was demonstrated by GFRP0, GFRP1, GFRP10, GFRP25 and GFRP50 inks ensued with their shear thinning nature. Due to the shear thinning observed at 20°C, printability was assessed at extruder temperature of 20°C. The influence of GFRP on printability was assessed by comparing the gelation, filament extrusion, buckling and 3D fabrication of 2, 4 and 8 layer grid constructs using all the biomaterial-inks at 20°C **(Figure 4.3 and 4.4)**. The gelation **(Figure 4.4 A-E)** and printing resolution **(Figure 4.3)** were found to be improved with the addition of higher amounts of GFRP. The slight buckling that was observed in the GFRP0 ink **(Figure 4.3 A)** is found to reduce further with GFRP1, GFRP10, GFRP25 and GFRP50 **(Figure 4.3 B-E)**. This might be the resultant of a higher biomaterial-ink protein content, enhanced viscosity and better shear thinning of the ink. The 2-, 4- and 8-layer structures were found to be stable and showed apt resolution with all GFRP concentrations **(Figure 4.3 A-E iii)** in the biomaterial-inks. The grid structures were stable due to the quick photo-polymerization post fabrication of each layer demonstrating minimal shape distortion of lower layers.

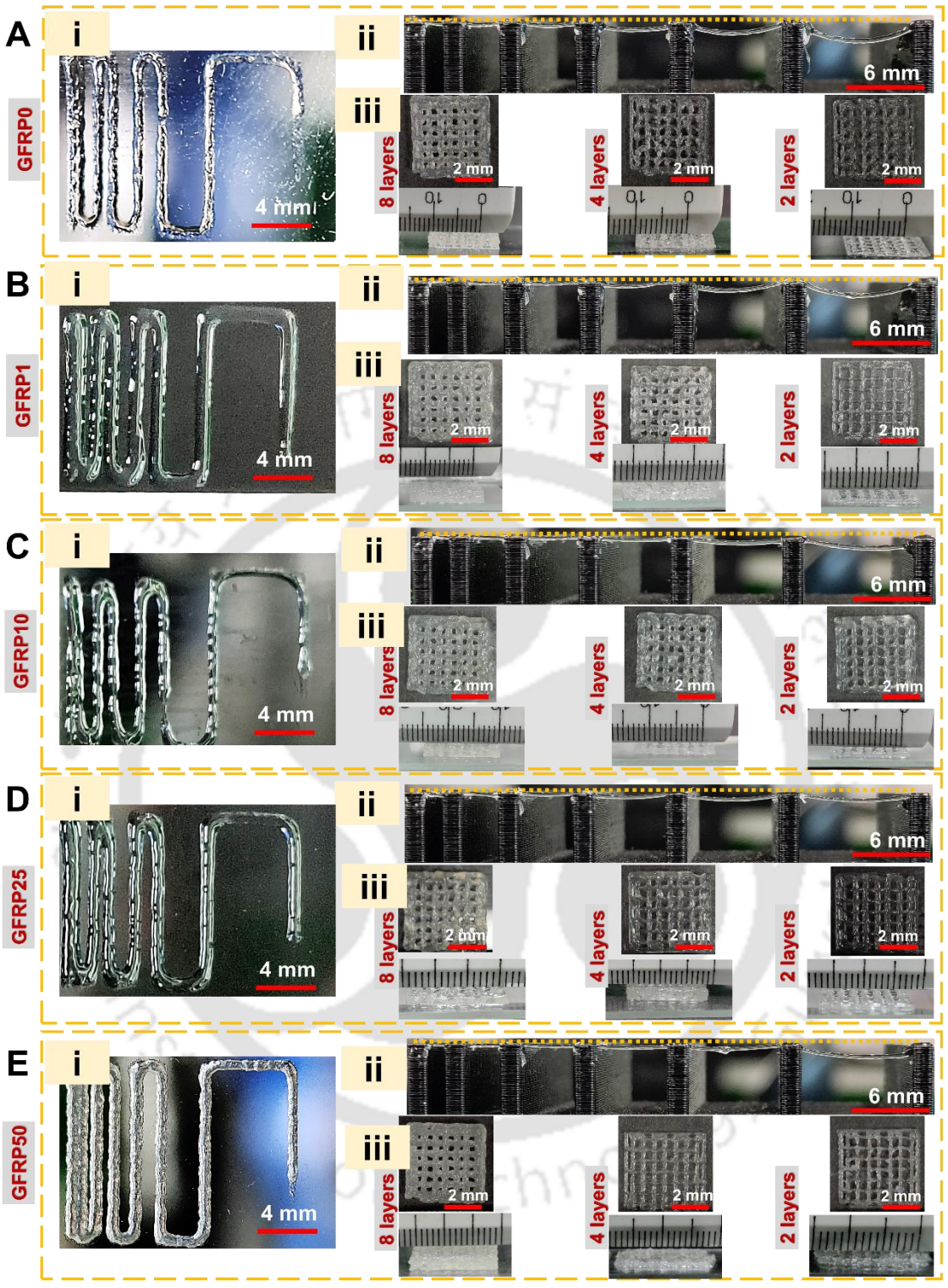

Figure 4.3: *Printability assessment of biomaterial-inks (A) GFRP0, (B) GFRP1, (C) GFRP10, (D) GFRP25 and (E) GFRP50. (i) Printing resolution assessment using successively reducing gaps between filaments. (ii) Buckling test using successively increasing gaps between pillars. (iii) Layered fabrication of 2, 4 and 8 layered constructs.*

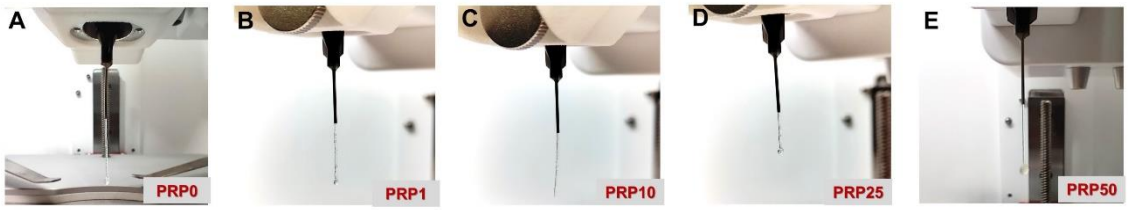

Figure 4.4: *Gelation of the ink generating uniform thread at 20°C for* ***(A)*** *GFRP0,* ***(B)*** *GFRP1,* ***(C)*** *GFRP10,* ***(D)*** *GFRP25 and* ***(E)*** *GFRP50 biomaterial-inks*

4.3.2 Physical, mechanical and GFRP release evaluation of 3D printed constructs

Water uptake, construct porosity and the micro-porous nature of the 3D printed constructs is a crucial factor for the efficient uptake of nutrients and potential homing of resident meniscal progenitors and synovial capsule stem cells. All the inks were used to print 3D constructs for various physical and mechanical characterization. All constructs were freeze-dried and immersed in PBS. All constructs showed rapid uptake (>3.5 times of respective dry weight) of PBS while reaching a swelling equilibrium in 1000 min (~16 h). This is essential for the nutrient uptake and survivability of cells seeded on the constructs. GFRP25 and GFRP50 construct groups showed highest water uptake ratios (~5 times of respective dry weight) **(Figure 4.5A)** as compared to the other groups. The images showing the minimal changes in construct shape and geometry (**Figure 4.6**), occurring due to the water uptake until equilibrium, show the stability of the constructs and the aptness of the biomaterial-inks for shape conformal meniscus tissue engineering constructs. 3D printed constructs of each group were subjected to hexane displacement analysis to quantify the percentage porosity of the printed struts apart from the macro-porous nature of the constructs. The constructs were found to possess increasing porosity values when the GFRP concentration reduced within the biomaterial-ink formulation **(Figure 4.5B)** suggesting compaction due to the rise in GFRP concentration for GFRP10, GFRP25 and GFRP50 inks. The percentage porosity values for the various groups have been listed in **Table 4.3**.

Table 4.3: *Percentage porosity of various 3D printed constructs*

GFRP concentration (mg/ml)	3D Printed Sample Group	Porosity (%)
0	GFRP0	71±4.2
1	GFRP1	70.7±3.5
10	GFRP10	56.7±11.9
25	GFRP25	53.5±7.9
50	GFRP50	50.6±8.2

The confined compressive and confined cyclic compression properties assessed for the grid constructs 3D constructs printed using the GFRP loaded biomaterial-inks showed their excellent compatibility for meniscus tissue engineering applications. The confined compressive properties of the different GFRP ink printed constructs was measured till 60% compressive strain and representative stress-strain curve for GFRP0, GFRP1, GFRP10, GFRP25 and GFRP50 **(Figure 4.5C-D)** showed >110 kPa compressive moduli. The compressive moduli calculated at the highest strain was found to be 180.4±16.7 kPa for GFRP0, 176.7±22.2 kPa for GFRP1, 143.6±5.7 kPa for GFRP10, 140.8±10.7 kPa for GFRP25 and 131.7±16 kPa for GFRP50 compositions **(Figure 4.5D)**. The compressive modulus reduced w.r.t. the increase in GFRP content of the biomaterial-ink. 3D printed constructs were subjected to 50 cycles of 20% compression and representative compressive stress-cycle count graphs for cycles 1-15 and 35-50 cycles were showed minimal deviation in the compressive stress values **(Figure 4.5E)**. In congruence, the cycle 1 and cycle 50 stress-strain hysteresis curves also depicted minimal deviation **(Figure 4.5F i-v)**. These demonstrate the stability of the crosslinked constructs under repeated cyclic compression.

The cumulative protein release profile for 3D printed constructs of varying GFRP concentrations while incubated in saline demonstrates the ability of the constructs to act as a reservoir for plasma proteins and growth factors **(Figure 4.7A)**. The GFRP0 and GFRP1 constructs released miniscule quantities of protein with a cumulative amount of 0.48±0.15 mg and 0.95±0.09 mg respectively after 10 days. This shows the stability of the photocrosslinked protein components of the biomaterial-inks (silkMA and gelMA) within the printed constructs and eliminates any influence they might have on the subsequent release profile assessment of the other constructs with higher amounts of GFRP encapsulation. Consequently, higher cumulative release of protein was found to occur in a sustained fashion from the GFRP10 (5.25±1.07 mg), GFRP25 (8.98±1.35 mg) and GFRP50 (12.64±1.23 mg) construct groups over 10 days of incubation in saline. This sustained release is essential for the preservation of growth factors within the constructs and their sustained release for maturation of cells seeded on the constructs.

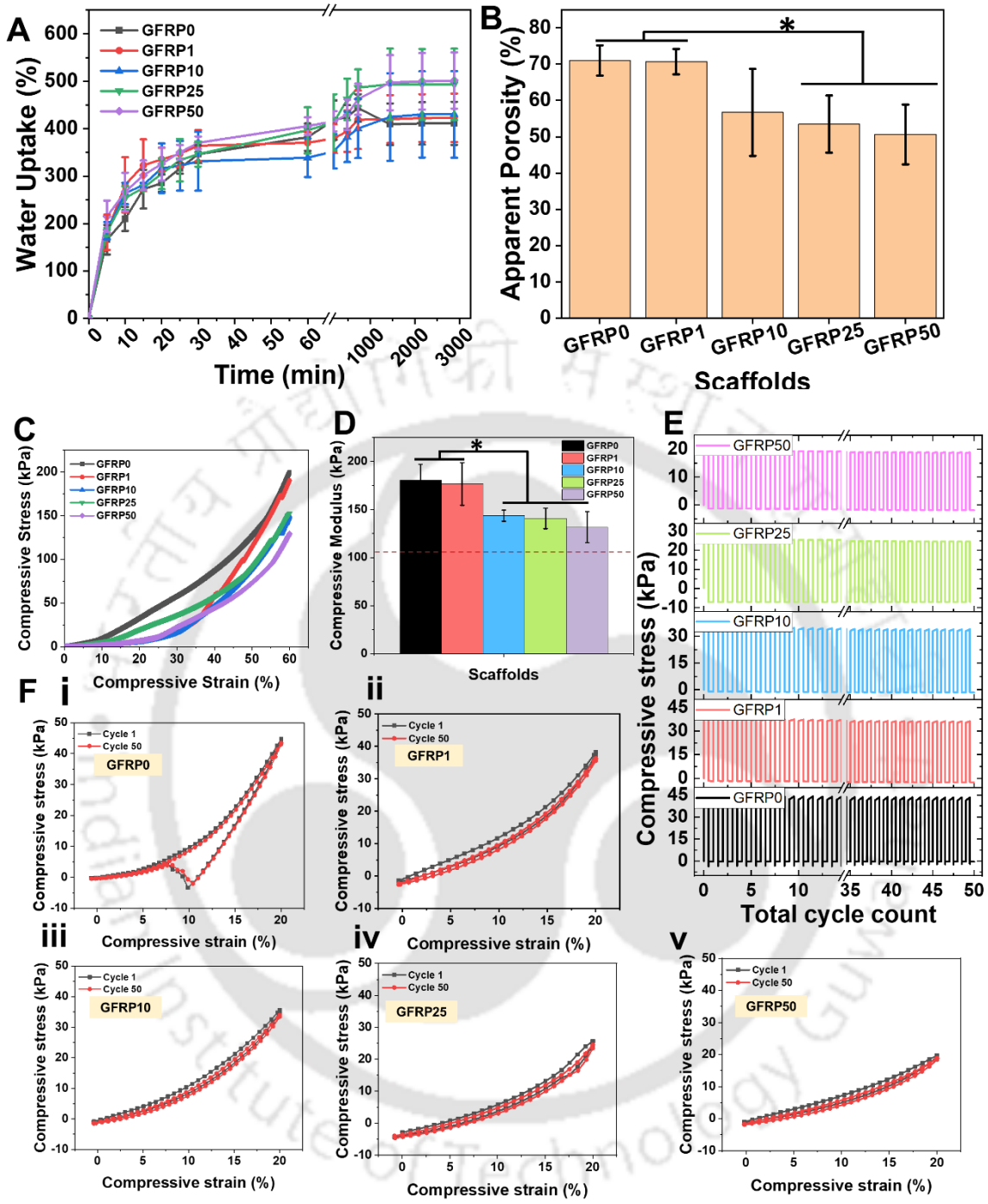

Figure 4.5: *(A) Water uptake ratio of freeze-dried constructs until equilibrium. (B) Porosity of 3D printed constructs with the various GFRP concentrations. (C) Representative stress-strain curve and (D) compressive moduli for the 3D printed constructs of various GFRP loaded biomaterial-inks upon confined uniaxial compression. (E) Representative compressive stress-cycle count graphs first 15 and last 15 cycles of confined uniaxial cyclic compression. (F i-v) Compressive stress-strain hysteresis curves for their first and last cycle for 3D printed constructs of various GFRP loaded biomaterial-inks. *p≤0.05*

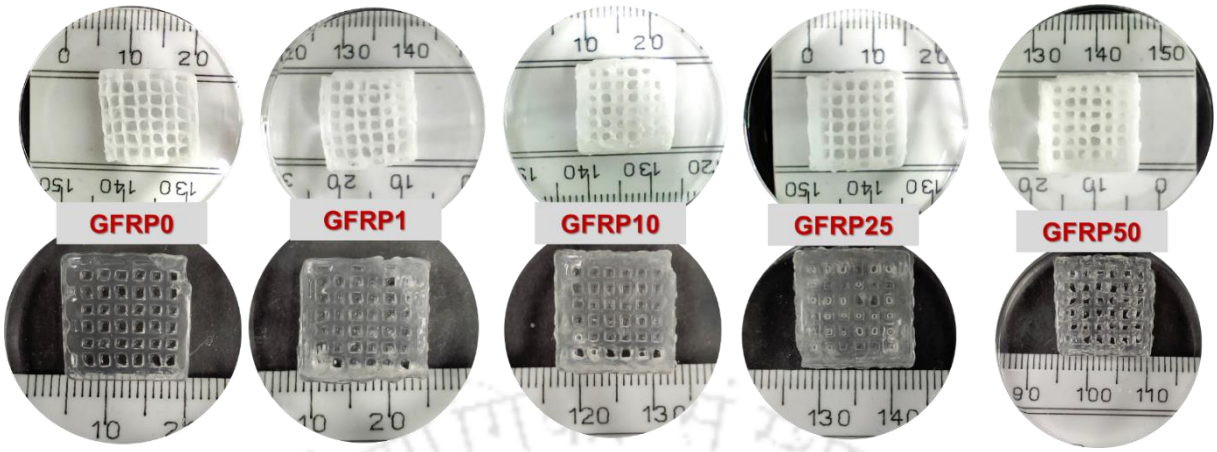

Figure 4.6: *Freeze-dried constructs (top row) and constructs after swelling equilibrium in saline (bottom row) for various GFRP biomaterial-inks.*

4.3.3 Human stromal cell biocompatibility for screening of biomaterial-inks for 3D printing

The GFRP based ink compositions showed amenable physico-chemical and mechanical behaviour and hence they were exposed to biocompatibility assessment to gain insights into the effect brought about by the varying GFRP concentrations. hwJMSCs were seeded on the 3D printed GFRP0, GFRP1, GFRP10, GFRP25 and GFRP50 construct groups and were subjected to MTT based cytotoxicity evaluation and all the constructs showed no reduction in cellular viability on day 1 and day 3 of evaluation **(Figure 4.7B)** and were found to support cellular proliferation. Further, the construct groups seeded with hwJMSCs were cultured for 21 days and the amount of DNA was quantified to evaluate the cellular proliferation **(Figure 4.7C)**. The DNA content increased for all the construct groups over the period of 21 days. A significant increase from 15.65±2.39 ng/mg, 15.28±1.95 ng/mg, 15.44±3.43 ng/mg, 15.52±2.51 ng/mg and 15.68±1.89 ng/mg to 62.36±3.89 ng/mg, 64.46±4.99 ng/mg, 72.65±4.39 ng/mg, 84.76±4.84 ng/mg and 85.66±3.98 ng/mg was observed in GFRP0, GFRP1, GFRP10, GFRP25 and GFRP50 groups. The increase in GFRP25 and GFRP50 groups after 14 and 21 days of culture was found to be significantly higher than the other groups. Furthermore, the estimation of sGAG from media and digested constructs was carried out as a preliminary evaluation for assessing the differentiation potential of hwJMSCs towards fibro-chondrogenic phenotype **(Figure 4.7D-E)**. The sGAG content was found to rise significantly from 2.34±0.89 µg/mg, 4.21±0.87 µg/mg, 4.91±0.68 µg/mg, 3.63±0.78 µg/mg and 5.23±0.89 µg/mg on day 1 to 26.78±3.48 µg/mg, 27.87±2.96 µg/mg, 39.78±2.79 µg/mg, 48.67±3.86 µg/mg and 50.29±3.79 µg/mg on day 21 for GFRP0, GFRP1, GFRP10, GFRP25 and GFRP50 constructs

respectively. The sGAG content normalized with the DNA content showed significant rise in all groups from day 1 to day 21. GFRP25 and GFRP50 constructs showed significant sGAG deposited per ng of DNA on day 7, 14 and day 21 and were significantly better than other groups with lower GFRP content. Concomitant to the DNA content, while being significantly higher than GFRP0, GFRP1 and GFRP10 groups, there was non-significant differences amongst the sGAG content on GFRP25 and GFRP50 constructs after day 14 and day 21 of incubation. Owing to the significantly better biological response, GFRP25 group was further subjected to physicochemical, mechanical and biological characterization.

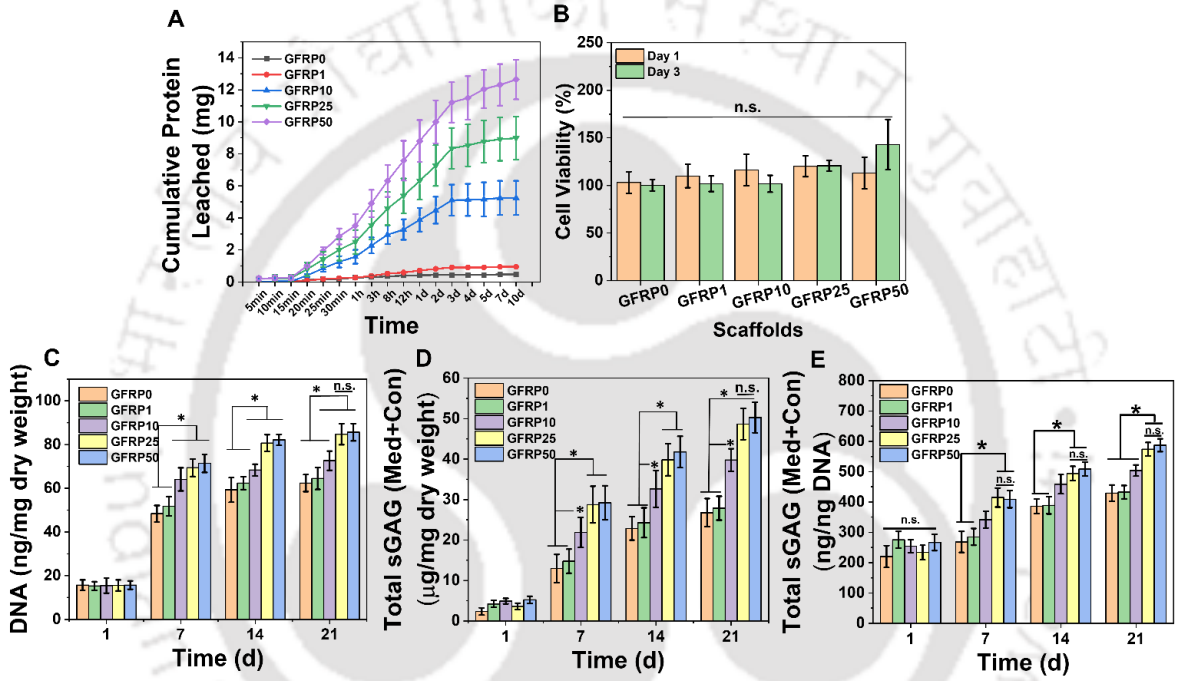

Figure 4.7: *(A) Cumulative release of protein from various 3D printed constructs without GFRP (GFRP0) and with GFRP (GFRP1, GFRP10, GFRP25, GFRP50). (B) MTT based cellular viability of hwJMSCs seeded on 3D printed constructs of various GFRP loaded biomaterial-inks. (C) DNA estimation, (D) total sGAG estimation and (E) DNA normalized sGAG content for hwJMSCs seeded 3D printed constructs with various GFRP loaded biomaterial-inks. *p≤0.05*

4.3.4 Suitability of GFRP25 ink for treatment of full thickness meniscal defects

4.3.4.1 Rheological characterization and printing a proof-of-concept meniscal defect construct

Post initial physicochemical, mechanical and biological screening, GFRP25 ink was further evaluated for its rheological nature to ensure high fidelity and self-standing printing. The GFRP25 biomaterial-ink was subjected to amplitude sweep at 18°C and the biomaterial-ink was found to undergo shear-thinning after experiencing ≥10^2% shear strain **(Figure 4.8A i)**. This increase in linear viscoelastic region (LVER) could be attributed to the lower temperature of evaluation. The LVER from this test was further used to conduct the frequency sweep and the GFRP25 blend showed a drop in viscosity as the frequency increased from 0.01-100 rad/s and stabilized beyond 1 rad/s **(Figure 4.8A ii).** The multiple interval thixotropy revealed that the GFRP25 blend could undergo multiple cycles of shear thinning from >10^5mPa.s in the low shear conditions to <10^2mPa.s in the higher shear conditions **(Figure 4.8A iii).** The temperature induced change in viscosity was observed in the GFRP25 blend from >10^5mPa.s to 10^3mPa.s at ~18°C **(Figure 4.8A iv)**. The replicative response of GFRP25 ink ensures reduced variability of the flow behaviour, essential for practical applications. The GFRP25 blend viscosity was found to be optimal at 18°C, hence 18°C was further utilized for printing. To evaluate the real-world applicability of GFRP25 ink for fabrication of full-thickness shape-conformal meniscus constructs a proof-of-concept meniscal construct was fabricated and a defect was introduced in the same (**Figure 4.8B,** highlighted red box). The defect was further modelled and was found to be 16 layer thick. GFRP25 ink was used along with a 22G blunt needle to fabricate a construct for filling the void **(Figure 4.8B)**. The ink showed amicable print fidelity and the fabricated construct demonstrated shape conformity. This, in essence, shows the potential for patient-specific fabrication of full thickness meniscal defects post resection of tears via the developed modality.

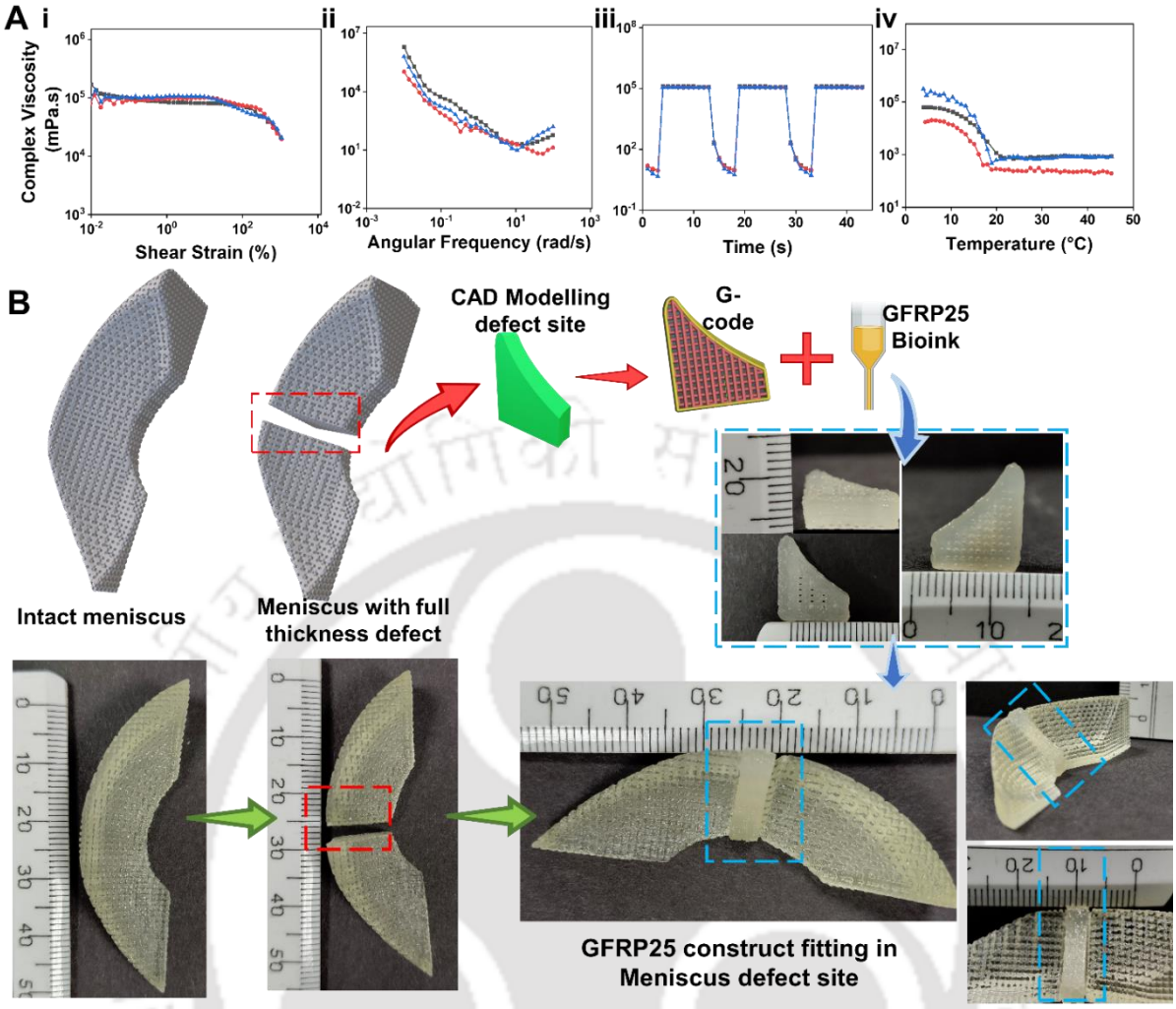

Figure 4.8: *(A) Rheological evaluation of GFRP25 biomaterial-ink through (i) amplitude sweep, (ii) frequency sweep, (iii) thixotropy test and (iv) temperature sweep. (B) Proof-of-concept fabrication of full thickness meniscal defect construct using GFRP25 biomaterial-ink with the respective workflow.*

4.3.4.2 Sustained GFRP release and long-term degradability of GFRP25 constructs

The GFRP25 constructs, encapsulating plasma proteins and the growth factors, are poised to act as a reservoir for the healing of avascular regions of the meniscus. Furthermore, the sustained release of encapsulated plasma proteins is indicative of the release of the growth factors as the construct components degrade minimally under saline (**Figure 4.10A**). The GFRP25 constructs were incubated in saline for longer duration and the cumulative GFRP release percentage was found to be 60.02±10.04% after 40 days of incubation **(Figure 4.10A)**. The curve fitting of this release profile using the Korsmeyer-Peppas model yielded close convergence to a gradient based Fickian diffusion model (K=22.3 ± 0.6 and n= 0.26 ± 0.01) **(Figure 4.9)**. This is indicative of the sustained release of GFRP from the 3D printed constructs

that would act as a precursor for the differentiation of stromal cells. The GFRP25 constructs showed struts of ~200µm in their freeze-dried state as could be seen from the representative electron micrograph of a construct **(Figure 4.10C)**.

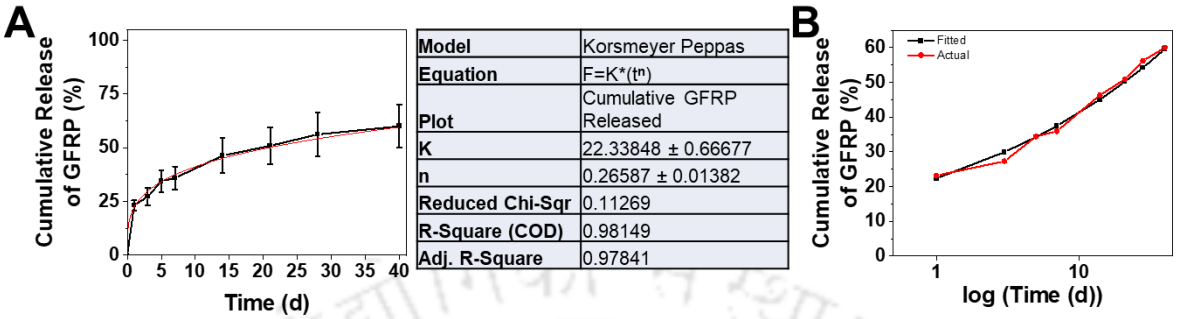

Model	Korsmeyer Peppas
Equation	F=K*(tⁿ)
Plot	Cumulative GFRP Released
K	22.33848 ± 0.66677
n	0.26587 ± 0.01382
Reduced Chi-Sqr	0.11269
R-Square (COD)	0.98149
Adj. R-Square	0.97841

Figure 4.9: *(A) Fitting of cumulative GFRP release profile using Korsmeyer-Peppas model where the red line represents the fitted curve and the table shows the parameters derived from the fitting. (B) Cumulative GFRP release and the fitted curve plotted against log(time).*

Degradation profile is crucial in dictating the stability of the constructs during meniscus regeneration and hence its potential applicability in the healing of the meniscus *in vivo*. While the degradation *in vivo* is dictated by various modulatory enzymes in the ECM such as matrix metalloproteinases, protease XIV was chosen for determination of degradability of GFRP25 constructs under non-specific proteolytic conditions. GFRP25 constructs were kept in saline as well as enzyme solution to evaluate the degradability of the same for 45 days (>6 weeks). The enzyme mediated degradation resulted in a residual construct weight of 76.8±3.5% and saline incubated constructs maintained a mean weight of 98.5±1.2% after 45 days of incubation **(Figure 4.10B).** This slow degradability could be attributed to the presence of PEGDMA and stability of photo-crosslinked polymers.

4.3.4.3 Long-term cyclic mechanical stability of GFRP 25 constructs

Meniscus tissue is subjected to numerous cyclic compressive stresses every day and these forces need to be accounted for while designing meniscus tissue scaffolds to ensure durability during the healing of avascular areas of meniscus [454]. The 3D printed GFRP25 scaffolds were subjected to a regimen of 2000 cycles of 20% uniaxial confined compressive strain each day for 21 days **(Figure 4.10D).** The corresponding hysteresis stress-strain curve of 2000th cycle for days 1, 5, 7, 14 and 21 **(Figure 4.10E)** shows highest strength on day 1 and thereafter subsequent reduction in strength from day 5 onwards but the reduction in strength is minimal thereafter and the constructs retain their strength till day 21. The stress-strain hysteresis curve of cycle 1 and cycle 2000 for day 1, 5, 7, 14 and 21 respectively **(Figure 4.10F-J)** show

minimal deviation between the first and last cycle of compression. Hence the stability of the GFRP25 3D printed constructs was established over 42000 cycles of interspersed compressive stress.

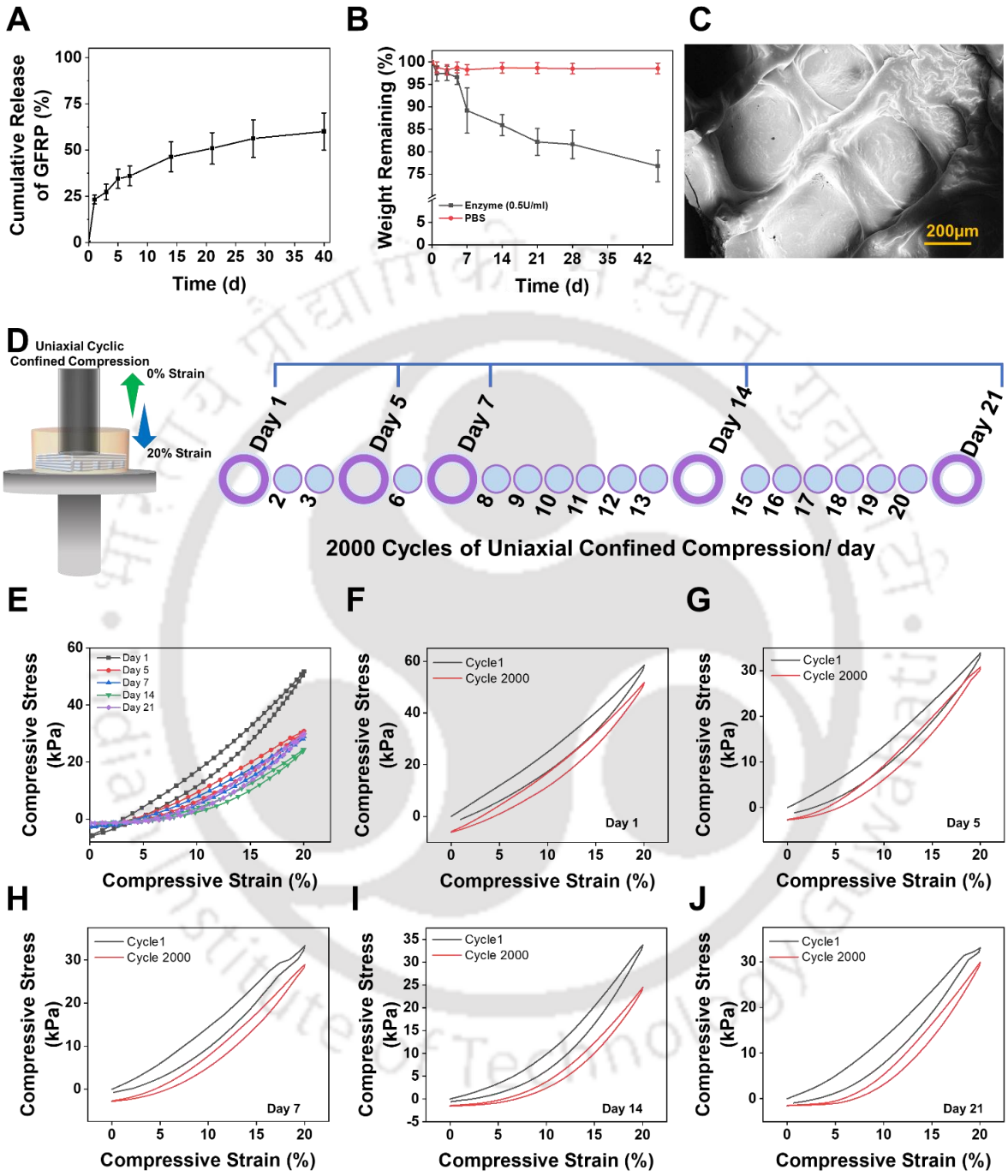

Figure 4.10: *(A) Cumulative release of GFRP from 3D printed GFRP25 constructs over 40 days. (B) Enzymatic and saline induced degradation profile for 3D printed GFRP25 constructs over 45 days. (C) Electron micrograph of GFRP25 constructs. (D) Schematic showing the cyclic uniaxial compressive evaluation regimen of the GFRP25 constructs. Representative hysteresis curve of GFRP 25 constructs at (E) cycle 2000 after 1, 5, 7, 14 and 21 days of incubation in saline and cycle 1 and cycle 2000 on (F) day 1, (G) day 5, (H) day 7, (I) day 14 and (J) day 21 post incubation in saline.*

4.3.4.4 Viability of hwJMSCs on GFRP25 constructs

GFRP25 constructs seeded with hwJMSCs demonstrate excellent viability and cellular proliferation, which is a remnant observation of the DNA estimation. Live dead staining of hwJMSCs seeded on GFRP25 constructs was conducted on day 1, 7, 14 and 21 and the representative micrographs show cells on the struts **(Figure 4.11A-D).** The cells were found to be viable and evenly distributed along the struts of the construct as well as visibly proliferate in 21 days **(Figure 4.11A-D iv).** These indicate the requisite suitability of the GFRP25 constructs to support stromal cells and sustain their proliferation over 3 weeks.

4.3.4.5 Human and murine macrophage-based *in vitro* immuno-genic reaction to GFRP25 constructs

In vitro immuno-compatibility of GFRP25 constructs was done by exposing them to murine and human monocytes derived macrophage cell lines and determining their macrophage-stimulation ability. Both GFRP25 constructs and GFRP25 construct-derived leachate media showed excellent immuno-compatibility and induced minimal secretion of inflammatory cytokines from murine macrophages as compared to the positive control (LPS stimulated). They demonstrated response more in tandem with the negative control of tissue culture dish.

The murine macrophages released 403.7 ± 60.1 pg/ml and 515.5 ± 8.7 pg/ml of TNF-α when incubated with constructs (CON) and construct leachate (LM) from GFRP 25 constructs, which was significantly lower to the 1657.9 ± 39.8 pg/ml secreted by the LPS treated macrophages and in tandem with 512.4 ± 19.8 pg/ml secreted by the unstimulated macrophages on TCP (**Figure 4.11E ii**). Similarly, the murine macrophages were found to secrete 338.4 ± 48.4 pg/ml and 490.2 ± 19.5 pg/ml of IL-1β when incubated with constructs (CON) and construct leachate (LM) from GFRP 25 constructs, which was significantly lower to the 2753.2 ± 33.7 pg/ml secreted by the LPS treated macrophages and in tandem with 426.8 ± 16.7 pg/ml secreted by the unstimulated macrophages on TCP (**Figure 4.11E iii**).

The human monocyte derived macrophages released 400 ± 23.8 pg/ml and 40 ± 11 pg/ml of TNF-α when incubated with constructs (CON) and construct leachate (LM) from GFRP 25 constructs, which was significantly lower to the 845.9 ± 45.8 pg/ml secreted by the LPS treated macrophages and in tandem with 219.9 ± 35.7 pg/ml secreted by the unstimulated macrophages on TCP (**Figure 4.11F ii**). Similarly, the human macrophages were found to secrete 64 ± 3 pg/ml and 62 ± 11.9 pg/ml of IL-1β when incubated with constructs (CON) and construct

leachate (LM) from GFRP 25 constructs, which was significantly lower to the 204 ± 22.8 pg/ml secreted by the LPS treated macrophages and in tandem with 34 ± 1.9 pg/ml secreted by the unstimulated macrophages on TCP (**Figure 4.11F iii**).

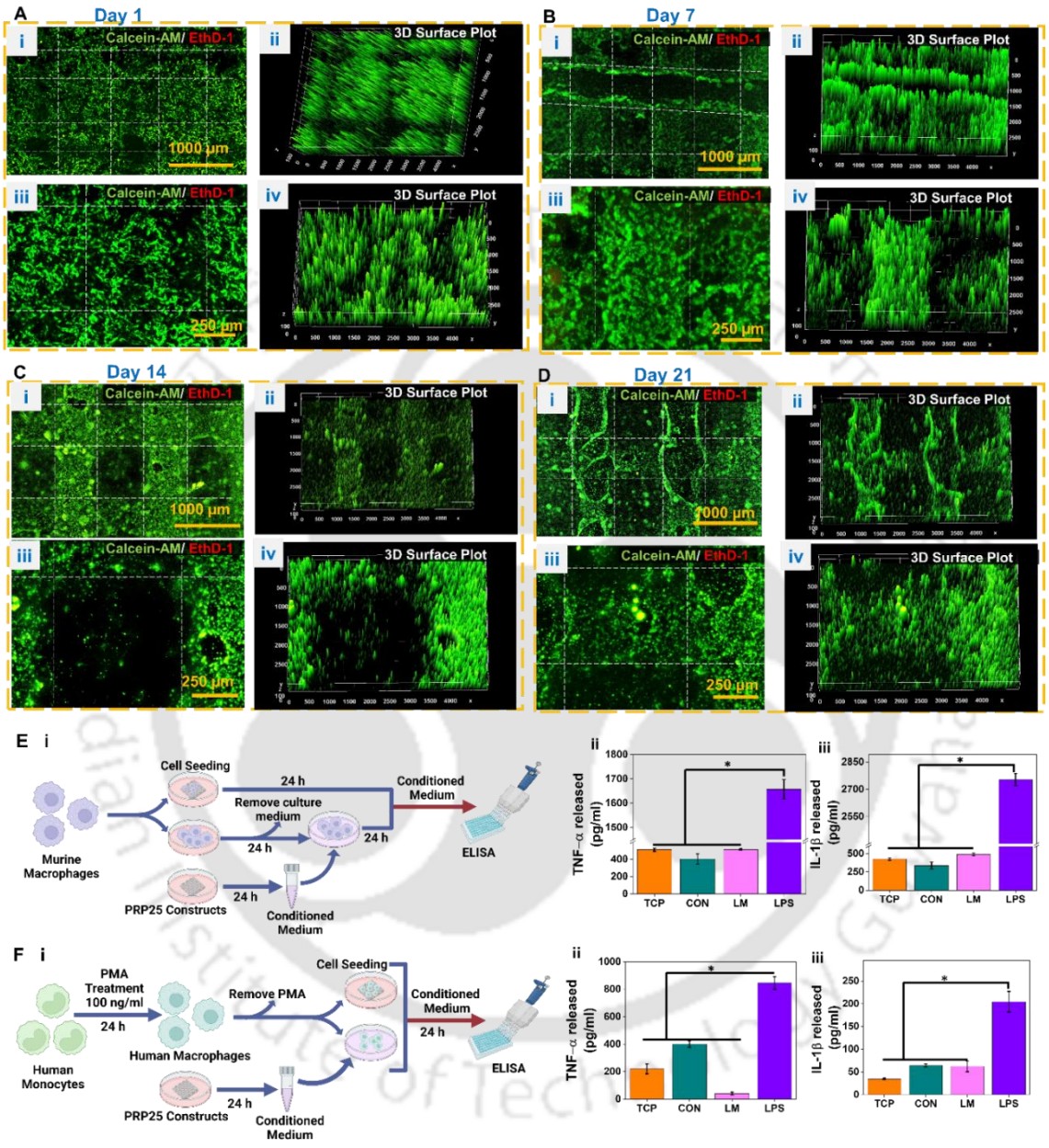

Figure 4.11: *(A-D) (i) Lower and (iii) higher magnification micrographs and their respective 3D surface plots (ii and iv) showing live (green) and dead (red) hwJMSCs cultured on GFRP25 constructs after 1, 7, 14 and 21 days of culture. (E) (i) Schematic showing the in vitro immuno-compatibility using murine RAW 264.7 macrophage cells (Made using www.biorender.com). ELISA based quantification of (ii) TNF-α and (iii) IL-1β released by murine macrophage cells. (F) (i) Schematic showing the in vitro immuno-compatibility using human monocyte (THP-1 cells) derived macrophage cells (Made using www.biorender.com). ELISA based quantification of (ii) TNF-α and (iii) IL-1β released by human macrophage cells. TCP (tissue culture plate) and LPS (lipopolysaccharide) were taken as positive and negative controls and CON*

*(constructs) seeded and LM (construct leachate medium) treated cells were taken as experimental groups. *p≤0.05*

4.3.4.6 Fibro-chondrogenic differentiation of hwJMSCs on GFRP25 constructs

Subsequently the expression of fibrochondrogenic genes specific to meniscal phenotypic differentiation, i.e. the chondrogenic (aggrecan , sox-9 and collagen II) and fibroblastic (collagen I) was evaluated and normalized using the housekeeping gene βactin as well as the day 1 expression and shown as a heatmap of the relative expression ($2^{-\Delta\Delta Ct}$) **(Figure 4.12A)**. Aggrecan (acan) was found to be upregulated >13 folds on day 7 and was significantly upregulated by ~28 folds on day 14 and >31 folds on day 21 **(Figure 4.12B)**. Sox-9 (sox9) was found to be upregulated by >14 folds on day 7 and significantly upregulated by ~22 folds on day 14 and >24 folds on day 21 **(Figure 4.12C)**. Collagen I (Col I) also showed an upregulation of >8 folds on day 7 and significantly higher upregulation of ~20 folds on day 14 and >22 folds on day 21 **(Figure 4.12D)**. Concomitantly, collagen II (col II) showed an upregulation of >9 folds on day 7 and it further increased significantly to ~17 folds on day 14 and >19 folds on day 21 **(Figure 4.12E)**. The upregulation of both chondrogenic and fibroblastic genes clearly demonstrate the fibrochondrogenic differentiation of the seeded stromal cells. Due to GFRP being a mixture of growth factors, osteogenic genes namely runx-2 (runx2) and osteocalcin (OCN) were also checked for their expression as their expression/up regulation might be indicative of ectopic mineralization. Runx-2 (runx2) expression was found to be ~0.8 folds on day 7 and ~0.6 folds on day 14 and the gene was unexpressed on day 21 **(Figure 4.12F)**. Concurrently, the expression of osteocalcin was also found to be ~0.7 folds on day 14 and it remained unexpressed on day 7 and day 21 **(Figure 4.12G)**. This downregulation indicates the minimal possibility of ectopic mineralization w.r.t. the GFRP released from the GFRP25 constructs.

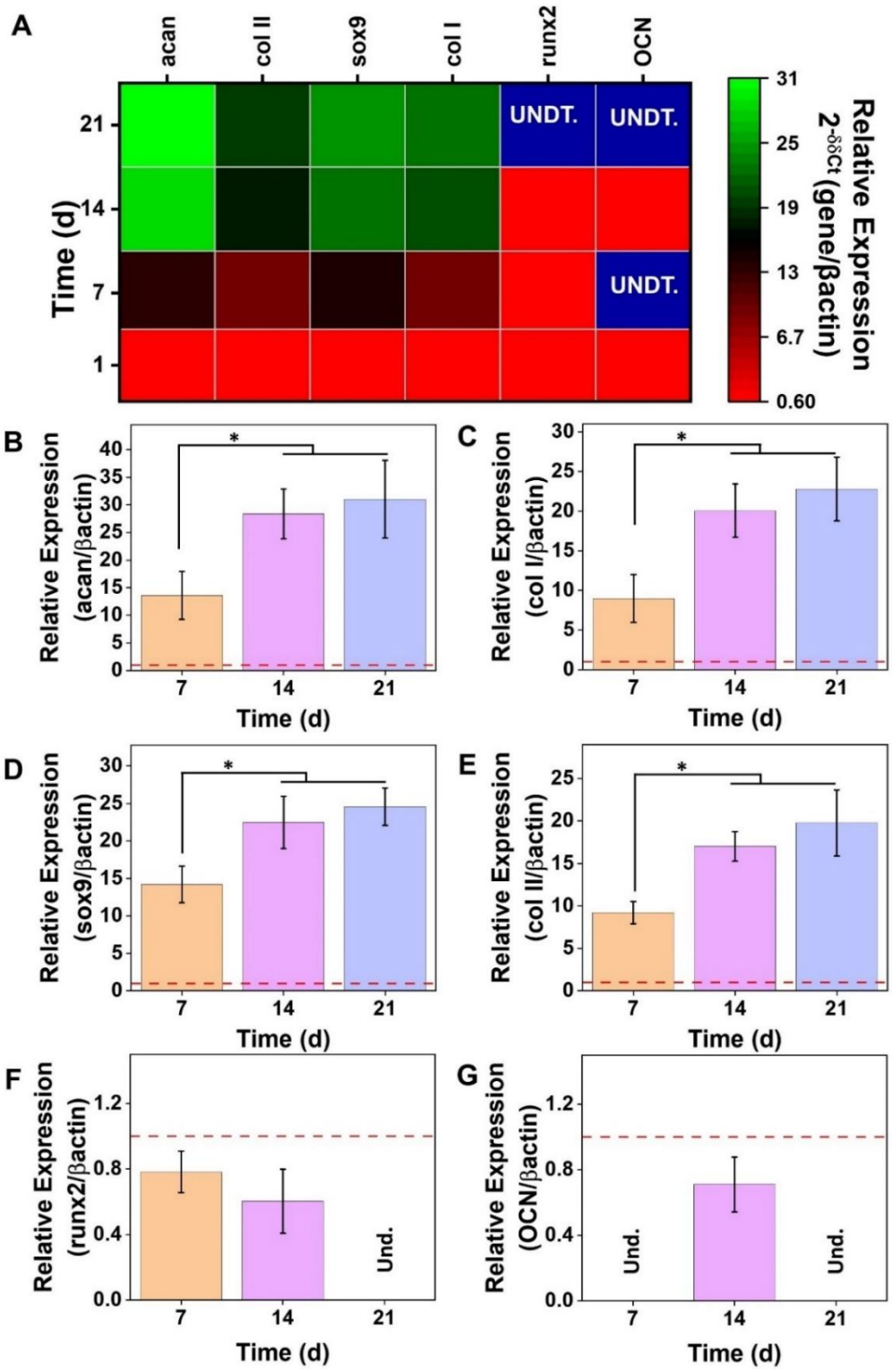

Figure 4.12: *(A) Heatmap of the gene expression profile ($2^{-\Delta\Delta Ct}$) of hwJMSCs seeded on GFRP25 constructs. Individual expression profiles ($2^{-\Delta\Delta Ct}$) of hwJMSCs seeded on GFRP25 constructs for (B) aggrecan (acan), (C) collagen I (colI), (D) sox-9 (sox9), (E) collagen II (col II), (F) cbfa-1 or runx-2 (runx2) and (G) osteocalcin (OCN) genes after 7, 14 and 21 days of incubation after normalization with housekeeping (βactin) and day 1 expression. *p≤0.05*

Consequently, enhanced protein level synthesis and deposition of fibrochondrogenic extracellular matrix could be seen in the immuno-stained constructs (**Figure 4.13B-C**) which is in tandem with the sGAG deposition observed in **Figure 4.7D-E.** This substantiates the differentiation bias produced by the GFRP growth factors being released from the GFRP25 constructs. This is critical for the efficient support and differentiation of resident MSCs from the meniscus, infrapatellar-fat-pad and synovial fluid. The hwJMSC seeded on GFRP25 constructs were matured for 21 days and the GFRP induced differentiation into fibrochondrogenic phenotype **(Figure 4.13A)** was evaluated by the virtue of antibody staining of the meniscus-specific chondrogenic ECM proteins (aggrecan, collagen II) and fibroblastic ECM protein (collagen I) deposited by the differentiated cells. The cells were found to differentiate into fibrochondrogenic phenotype and the deposition of aggrecan (ACAN) was colocalized with collagen I (col I) **(Figure 4.13C)** and the deposition of collagen II (col II) was also found to be colocalized with collagen I **(Figure 4.13B)**. The respective areas of aggrecan, collagen I and collagen II were calculated using ImageJ from various fields of view (FOV) **(Figure 4.13D)**. Collagen I and aggrecan co-stained sections were found to possess 53.2 ± 2.2% and 46.8 ± 2.2% covered by aggrecan and collagen I respectively. Concurrently, collagen I and collagen II co-stained sections were found to possess 56.8 ± 3.6% and 43.2 ± 3.6% covered by collagen I and collagen II respectively. This observed ~60:40 ratio of collagen I and collagen II is a potent indication of fibrochondrogenic differentiation [23].

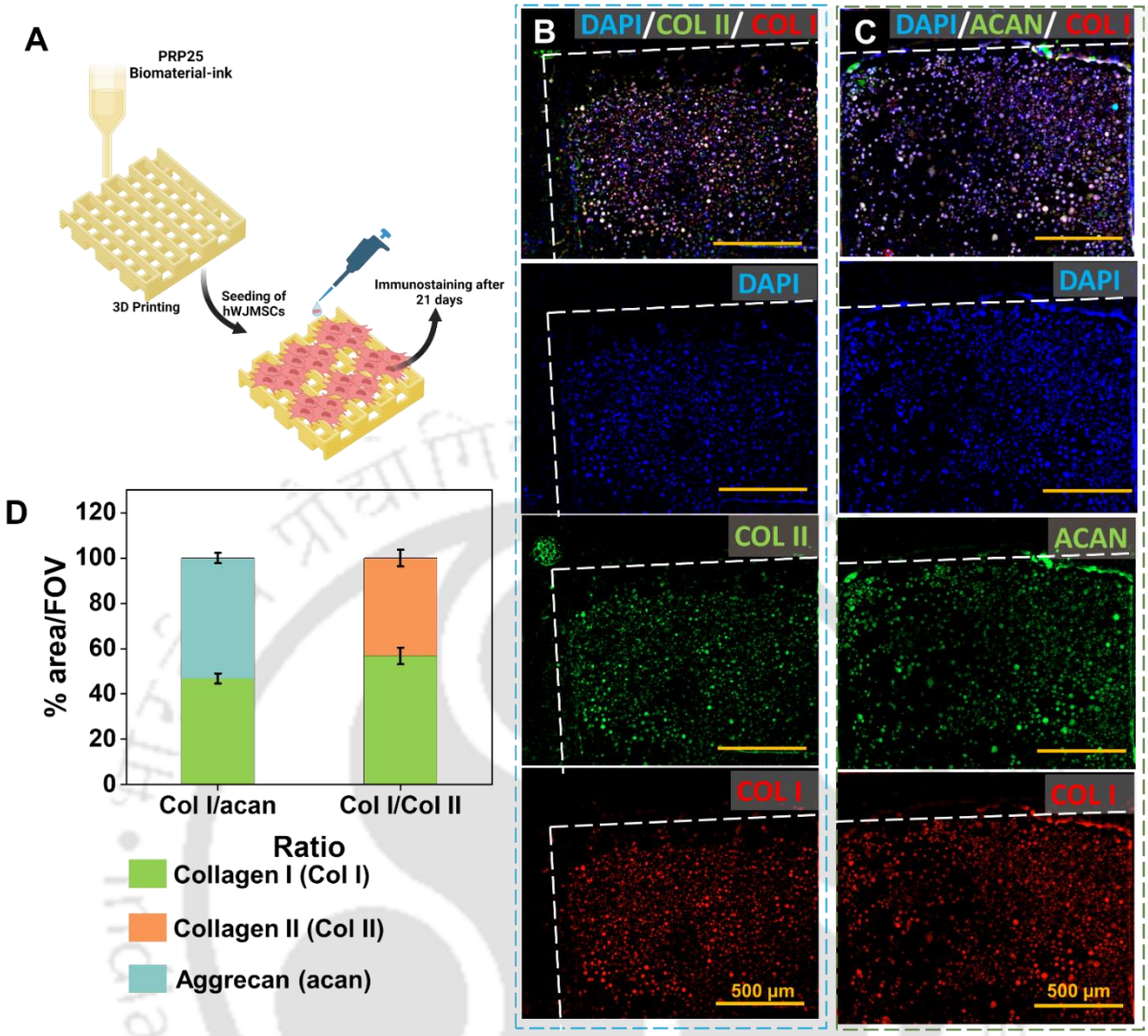

Figure 4.13: *(A) Schematic representation of hwJMSC seeding on GFRP25 constructs (Made with Www.biorender.com). Representative co-stained micrographs of hwJMSCs after 21 days of incubation on GFRP25 constructs with (B) nuclei (DAPI, blue), collagen II (COL II, green), collagen I (COL I, red) and merged images and (C) nuclei (DAPI, blue), aggrecan (ACAN, green), collagen I (COL I, red) and merged images. (D) Percentage area field of view (FOV) calculated from immuno-stained micrographs (n=8) depicting the expression of collagen I (Col I), aggrecan (acan) and collagen II (Col II).*

4.3.4.6 *In vivo* bio-compatibility and immuno-compatibility of GFRP25 ink

The slow degradation and the minimal infiltration of $CD68^{+}$ macrophages was observed in GFRP25 biomaterial-ink constructs that were retrieved after 1 week and 3 weeks of subcutaneous implantation in rabbits **(Figure 4.14B-E)** indicating excellent *in vivo* immuno-compatibility. The macrophage and cellular infiltration from the host tissue (marked as H) to the GFRP25 hydrogels (marked as BI) were found to be superficial as can be seen in the lower and higher magnification micrographs both at 1 week **(Figure 4.14B-C)** and at 3 weeks **(Figure**

4.14E). Furthermore, the macrophages were found to be reduced significantly after 3 weeks as compared to the 1 week, indicated by the reduced $CD68^+$ cells **(Figure 4.14F)**. This slower degradability is potentially advantageous for the potential treatment of slow healing avascular regions of the meniscus and retention of meniscus stability.

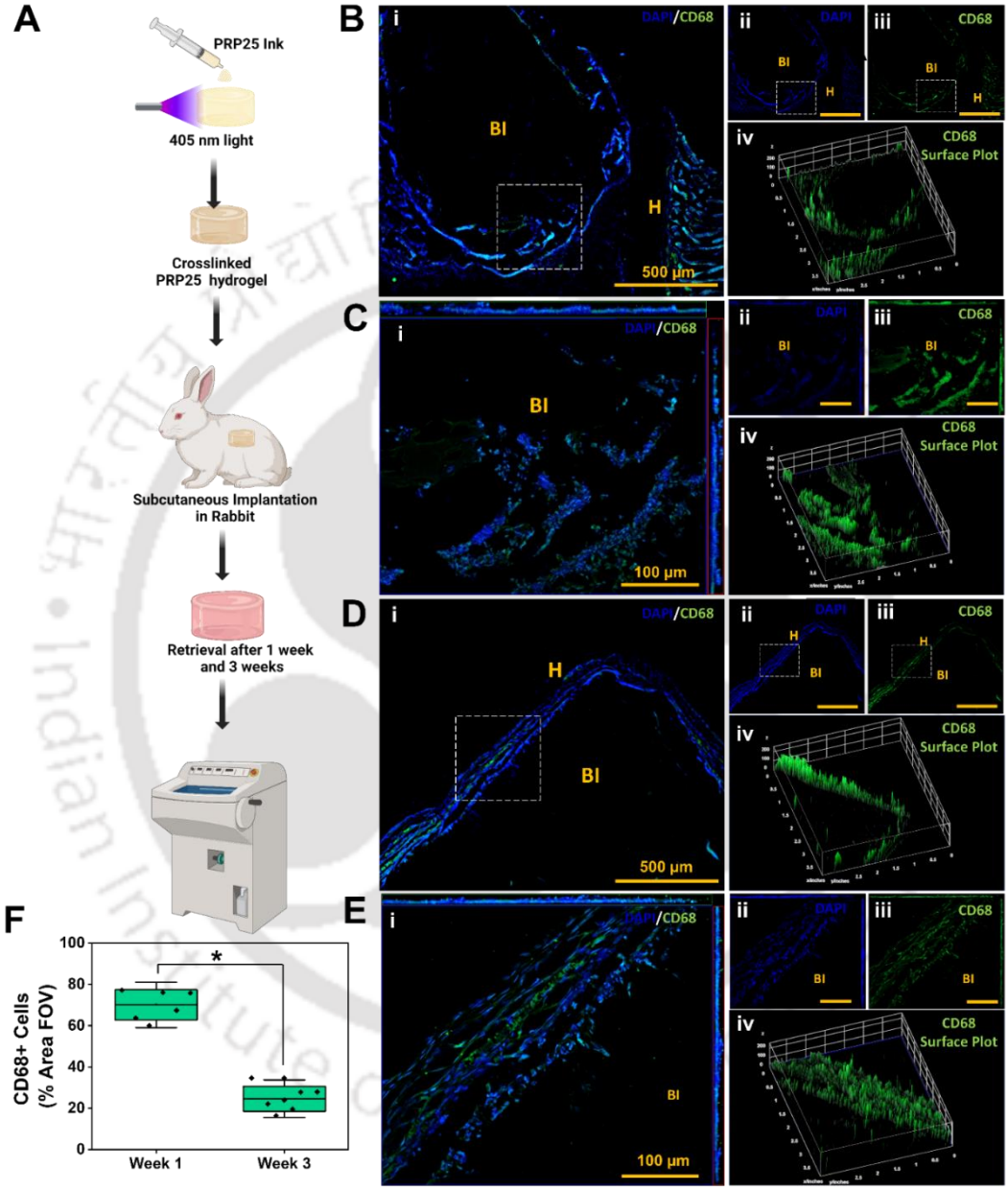

Figure 4.14: *(A) Schematic depicting the subcutaneous implantation of GFRP25 biomaterial-ink constructs in rabbit model (Made using www.biorender.com). CD68 (green) and DAPI (blue) stained micrographs of GFRP25 biomaterial-ink constructs retrieved after sub-cutaneous implantation of (B-C) 1 week and (D-E) 3 weeks. The BI marks biomaterial-ink region and H marks the host tissue regions. (B and D) Representative low magnification images and (C and E) high magnification 3D maximum intensity projection orthogonal images. (i) Merged images, (ii) DAPI stained images, (iii) CD68 stained images and (iv) 3D surface plot of CD68 staining. (F) $CD68^+$ positive cells calculated as a function of the % Area FOV using ImageJ. *$p \leq 0.05$*

4.4 Discussion

In this study, we 3D printed autologous growth factor loaded photo-crosslinking blend of silkMA, gelMA and PEGDMA into constructs for potential application in meniscus tissue engineering and treatment of partial and full-thickness meniscus resection. The blending of shear thinning viscoelastic gelMA and PEGDMA with silkMA enabled 3D printing of grid constructs at 20°C temperature (5-8 mm/s speed and at extrusion pressure of <180kPa) using a 22G nozzle. Further, these printed structures were crosslinked using visible LED light source (405 nm) within a span of 60s to yield mechanically resilient 3D constructs mimicking the native strength of both porcine [418] and human [31] meniscal tissue. Photo-polymerizable blend of silkMA/gelMA/PEGMDA as our base blend of polymers aided in achieving facile crosslinking using photopolymerization, endowing high biocompatibility, ensuring mechanical strength and resilience, and instant applicability which are essential for meniscal tear management [266].

The initial screening was conducted using increasing amounts of GFRP lysates (GFRP0, GFRP1, GFRP10, GFRP25 and GFRP50) in the base biomaterial-ink to evaluate the changes in functionality brought about by the encapsulated GFRP within the fabricated constructs in the domains of mechanical, physico-chemical and biological aptness for meniscal tissue engineering. Amide peak shifting within our biomaterial-ink blends were indicative of the crosslinking due to photopolymerization as observed previously for silkMA [435], gelMA and PEGDMA [478]. Initial amplitude sweep and temperature sweep assessment revealed the temperature induced gelation of all ink compositions and shear thinning of the ink at 20°C that is required for apt printability using micro-extrusion method [204]. We observed apt printing resolution and minimal layer distortion for all biomaterial-inks and the increased GFRP addition reduced buckling effect for GFRP25 and GFRP50 inks. This ensures better shape fidelity and printability of the biomaterial-inks. The constructs were found to uptake >3 times their dehydrated weight in saline within 30 minutes and reach equilibrium state of after 16h, indicating efficient media adsorption by the constructs, essential for exchange of nutrients and metabolites for the constructs [46, 365, 451]. The rehydrated morphology and size of the printed constructs was almost identical to their dehydrated state. Apart from the microporosity provided by the 3D grid, the porosity of the struts was found to be >50% for all inks, which is essential for two-fold benefit of nutrient exchange and sustained release of GFRP.

The printed grid constructs were subjected to physiologically relevant mechanical strength evaluation, pertinent for survival of meniscal tissue engineering scaffolds within the

knee joint. The constructs were exposed to confined compressive loading of 60% and hyper-physiological 20% cyclic confined compressive strain of 50 cycles for all the GFRP loaded compositions [46, 416]. All the constructs printed using various biomaterial-ink compositions showed a compressive modulus comparable to or greater than the equilibrium modulus of both native porcine [418] and human [31] meniscal tissue. Typically, menisci undergo 5-15% compressive strain in physiological loading conditions [46, 107]. But even hyper-physiological strains of 20% in a cyclic manner resulted in minimal deviation in the stress-strain cycle of our fabricated constructs, demonstrating the requisite initial stability for healing.

Protein leaching of printed GFRP0, GFRP1, GFRP10, GFRP25 and GFRP50 constructs in saline revealed that the leachate consisted of GFRP and was minimally affected by the ink components as observed in the release profile of GFRP0 and GFRP1 constructs for 10 days. Hence, GFRP caused no hindrance in the crosslinking of ink components and could be released in a sustained manner from the constructs. The constructs could act as growth factor reservoirs for regeneration of avascular meniscal defects [115, 442, 479].

Our ingenious procedure of photoactivating PRP and isolating GFRP by platelet elimination and freeze-drying from multiple collated platelet enriched plasma bags aids in the standardization of the presence of growth factors and plasma proteins within the biomaterial-inks. Interestingly, as opposed to previous applications [304-306], the sustained release of plasma proteins and growth factors from 3D printed constructs is a crucial advancement in the use of GFRP for meniscus tissue engineering applications. Seeded hwJMSCs were found to be viable after day 1 and day 3 with no reduction in viability. DNA quantification showed proliferation in the higher GFRP containing groups. GFRP25 and GFRP50 constructs performed significantly better in terms of cellular proliferation and sGAG deposition per unit DNA, while there was no significant difference between the GFRP25 and GFRP50 groups. sGAG is a crucial ECM component of meniscus [4], hence the 3 week assessment of sGAG deposition was used as parameter for selection of GFRP25 over other groups for further extensive evaluation *in vitro*.

Extensive rheological evaluation of the GFRP25 biomaterial-ink yielded similar results to initial evaluation. The thermo-reversible nature of gelMA and PEGDMA was evident in the amplitude sweep and temperature sweep [424]. Furthermore, thixotropy test showed the reversible thinning and regaining of gel strength for GFRP25 ink over multiple cycles [425]. The proof-of-concept GFRP25 printed construct mimicking the artificially resected portion of

our previously used meniscus model [46] demonstrated the congruence that could be achieved with minimal deviation ensuring patient-specificity.

GFRP25 constructs demonstrate sustained GFRP release over 40 days (>5 weeks) following a Fickian diffusion model and acted as a growth factor reservoir [477]. Furthermore, the excellent long term stability of GFRP25 constructs in enzymatic conditions over 45 days (>6 weeks) in vitro indicates the durability, desirable for slow healing of avascular meniscus [301, 454]. GFRP25 constructs could also sustain their mechanical stability over the period of 3 weeks for 42000 cumulative cycles of hyper-physiological (20%) compressive strain and demonstrated fatigue resistance comparable to previous reports for constructs and native meniscus during extended compressive cycling [416, 480].

Biologically, the GFRP25 constructs showed uniform distribution of live hwJMSCs seeded on them for 21 days and resulted in their fibrochondrogenic differentiation. The hallmarks of fibrochondrogenic differentiation aggrecan, sox-9, collagen I and collagen II [481, 482] were found to be upregulated while early osteogenic marker runx-2 [483] and late osteogenic marker osteocalcin [484] were found to be significantly downregulated for the stem cells seeded on GFRP25 constructs. This indicated minimal potency of GFRP25 constructs towards the ectopic bone formation. Marked expression of aggrecan, collagen I and collagen II was visualized in the immunofluorescence-based co-staining of cultured hwJMSCs seeded GFRP25 constructs after 3 weeks. This gene expression and ECM protein deposition profile implicates the fibrochondrogenic differentiation of the hwJMSCs seeded on GFRP25 constructs [108, 382, 485, 486]. Furthermore, the collagen I and collagen II expression could mimic the high collagen I/collagen II ratio of meniscus fibrocartilage [18, 487].

Immuno-compatibility of 3D printed constructs is a vital criterion for its application *in vivo* and subsequent prevention of graft rejection which may be accompanied by acute inflammation and non-integration with the host tissue [488, 489]. *In vitro* evaluation of our GFRP25 constructs demonstrated minimal release of inflammatory cytokine (TNFα and IL-1β) by murine and human macrophages as observed for the unstimulated control. Furthermore, *in vivo* assessment in rabbit subcutaneous pockets showed the significantly reduced $CD68^{+}$ cells (macrophages) in the vicinity of the implanted biomaterial-ink constructs which mimics our previously reported instances of minimal *in vivo* immunogenicity of silk and gelatin based matrices [46, 365, 424, 425]. This might also have been aided by the GFRP released from our constructs. GFRP is a major fraction of PRP, which has been traditionally reported to possess

anti-inflammatory and tissue remodelling effects in various tissues [466], especially in osteoarthritic knee [490]. This indicates the immuno-compatible nature of GFRP25 biomaterial-ink that would aid in the future *in vivo* functional assessments in animal knee meniscus defect models. Future *in vivo* evaluation has been planned in smaller animal models with major full-thickness meniscal defects for evaluation of healing potential of GFRP25 constructs, the cytokine profile of the knee joint upon application and the effect on the articular cartilages. Subsequent optimizations in the degradability and GFRP loading could be done for the larger animal trials w.r.t. to the duration of healing hence ascertaining the clinical significance of the developed biomaterial-ink. Additionally, 3D printed shape conformal GFRP25 constructs could be seeded with progenitor cells and pre-matured *in vitro* (under static environment as demonstrated in this work or dynamically in a bioreactor) to further accelerate the healing process. This would eliminate the drawbacks caused by the paucity of progenitors *in vivo*.

4.5 Salient outcomes and Findings

1. We developed an array of GFRP loaded photo-crosslinking biomaterial-ink (GFRP25) for potential meniscus tissue engineering applications.
2. GFRP25 biomaterial-ink showed facile and rapid fabrication potential, physiologically relevant mechanical properties, optimal porosity, amicable water uptake characteristics, long-term stability profile of >6 weeks under enzymatic conditions *in vitro* and *in vivo* stability for 3 weeks in rabbit model.
3. We demonstrated a proof-of-concept 3D printed defect filling regimen using the GFRP25 biomaterial-ink. GFRP was released from the printed constructs in a sustained manner over the period of >5 weeks *in vitro*.
4. hwJMSCs seeded on the printed GFRP25 scaffolds proliferated, differentiated into fibrochondrogenic phenotype and deposited fibrochondrogenic matrix over 3 weeks *in vitro*.
5. The GFRP25 printed 3D constructs elicited minimal inflammatory response *in vitro* and *in vivo*. We envisage that the developed photo-crosslinkable autologous growth factor loaded GFRP25 biomaterial-ink composition holds great potential for future applications in treatment of full thickness meniscal tears *in vivo* in animal models and could be optimized for further clinical applications in the future.

CHAPTER 5

Formulation of an injectable silk-based autologous growth factor incorporated photo-polymerizing hydrogel for patient-specific repair of meniscal defects and its functional analysis in rabbit meniscus defect model

This chapter describes the development of a patient-specific facile approach in the form of a silkMA/gelMA/PEGDA hydrogel loaded with the patient-derived autologous growth factor rich plasma that can be promptly photopolymerized (60s) for the treatment of small meniscal tears. The injectable hydrogel composition was assessed for swelling, degradability, compressive and tensile mechanical properties and sustained release of growth factor rich plasma. Human neonatal stem cells were encapsulated in the hydrogel for biological evaluation and assessed for proliferation, fibrochondrogenic differentiation, meniscus-specific matrix deposition and in vitro immunogenicity. Pilot-scale in vivo evaluation of hydrogel composition was conducted in rabbit meniscal tears and compared to untreated control.

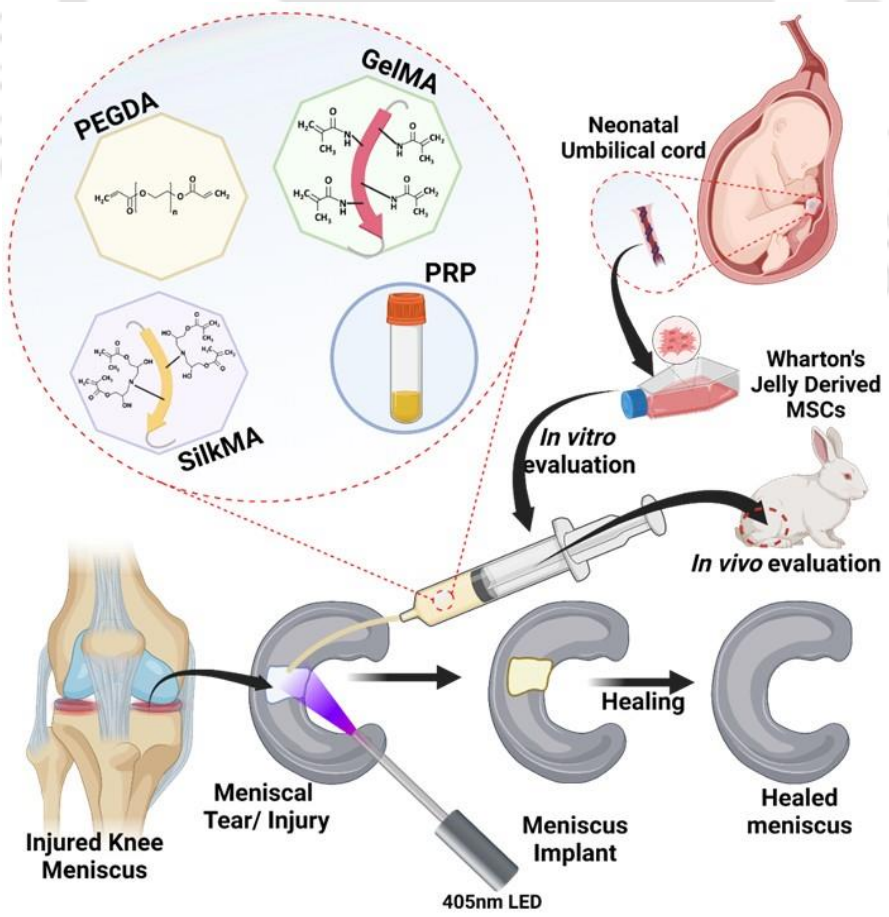

Outcomes of this chapter are published as:

Ashutosh Bandyopadhyay, Baishali Ghibhela, Sayanti Shome, Debajyoti Pal, Samit K. Nandi, Biman B. Mandal. *Silk-based injectable photocurable hydrogel loaded with autologous growth factors for patient-specific repair of meniscal defects in vivo*. **Applied Materials Today.** 2024, 37, 102111. DOI: 10.1016/j.apmt.2024.102111

ABSTRACT

Meniscus tears and injuries in the avascular region often lead to pain, swelling and locking of the knee joint due to the non-healing nature of fibrocartilaginous tissue. The current mandate of partial meniscectomy leads to osteoarthritis and loss of integrity of the knee joint. Stabilization of the torn meniscal tissue must be achieved at the earliest to prevent damage to articular cartilage. We have developed a patient-specific facile approach in the form of a silk-based injectable hydrogel blend comprising of silk fibroin methacrylate, gelatin methacrylate, polyethylene glycol diacrylate and patient-derived autologous growth factor rich plasma (GFRP) for ameliorating meniscal tears. Our hydrogel could be crosslinked promptly within 60 s and demonstrated robust physicochemical and mechanical resilience *in vitro*. The injectable hydrogel demonstrated amicable shear thinning, optimal water uptake behaviour (~1.2 times), sustained release of GFRP proteins (>70%) over 40 days and an intricate microporous architecture. We could observe sustained degradability (~40%) over 85 days under enzymatic conditions *in vitro*. Photocrosslinking imparts our hydrogel composition with physiologically relevant compressive strength and ample tensile strength to retain their position and aids in their stability over 3 weeks of confined cyclic compression cycles. Hydrogel-encapsulated human-derived neonatal mesenchymal stem cells showed >3 times proliferation, *in vitro* migration, fibrochondrogenic differentiation and meniscus-specific extracellular matrix deposition after 3 weeks. Our hydrogel demonstrated minimal *in vitro* immunogenicity when presented to murine and human macrophages. A pilot-scale *in vivo* evaluation demonstrated the healing capacity of the injectable hydrogel composition in full-thickness tears of rabbit menisci compared to untreated counterparts after 8 weeks of treatment. Our patient-specific photopolymerizable injectable hydrogel could be a potential translational treatment modality for various partial and full-thickness meniscal tears *in vivo*.

5.1 Introduction

Knee menisci are largely avascular fibrocartilage tissues that suffer significant injuries in the form of tears [68]. Restricted healing of meniscus tears renders the knee joint inflamed and painful. Meniscal tears lead to osteoarthritis if left intreated. The current treatment modalities include suturing of tears or resecting out the damaged portions [68] and sporadically using meniscal implants made of natural, synthetic or hybrid materials [421]. These approaches might lead to the protection of articular cartilage for varied durations, but often are accompanied by non-healing or compromised healing of the tears and hence are insufficient in preventing osteoarthritis at later stages [491]. The non-conformation of most implants, risk of allograft infections and the poor synthetic material integration necessitates the development of appropriate treatment modality for facile minimally invasive treatment of meniscal tears at an early stage to attain integration and healing of the tears [92].

Conventionally, repair and regeneration of large meniscal tears is carried out using patient-preferred meniscal graft of natural or synthetic polymers after partial or total meniscectomy. In many cases, smaller tears of the menisci are either resected out or sutured for potential healing [2, 378]. These treatment approaches meet with several difficulties related to compromised mechanical durability, improper shape conformity, absence of bioactivity, post-treatment osteoarthritis or post-surgical complications leading to the displacement of grafts and destabilization of menisci. The current FDA-approved implants for menisci are either made from natural materials (collagen) [492] or synthetic materials (polyurethane) [89]. Both categories of implants are not patient-specific and are fabricated according to a one-size-fits-all approach and require shaping by the surgeons on the operating table. Moreover, these implants are unsuitable for smaller meniscal tears which need partial or total debridement before implantation. Failure is typically associated with both kinds of implants due to non-integration or breakage (synthetic material) [98] and shrinking (natural material) [379]. Past studies have indicated promising results in the regeneration of whole meniscus by the virtue of 3D bioprinted constructs [113] and cell-laden conventional [493], electrospun [222] or decellularized matrix-derived scaffolds [494]. However, smaller irregular meniscal tears need to be addressed as their resection could destabilize the knee joint and their suture might fail upon constant compression and relaxation cycles due to small tissue suture margins. For translational needs, the application of non-patient or patient-derived stem cells and decellularized matrix could pose challenges such as discrepancy in the choice of stem cell sources, adverse reactions to allogenic or xenogenic extracellular matrix and difficult

regulatory approval process. Moreover, the repair of small irregular tears is difficult using scaffolds and 3D printed constructs due to the issues of shape and mechanical conformity. So there is a need for facile therapeutic approaches for smaller meniscal tear healing. Hence, an in-situ crosslinking hydrogel composition loaded with a patient-specific growth factor pool with the necessary degradability, mechanical strength, biocompatibility and regenerative capacity could be ideal for the irregular partial and full-thickness meniscal defects of smaller sizes.

Injectable hydrogels have been studied for the minimally invasive treatment of various diseases and tissue defects as they have the inherent property to conform to non-geometric spaces, act as suitable vehicle for the delivery of growth factors, drugs and molecules and act as viable scaffolding materials for the migration and proliferation of cells [380]. There are various methods reported for the preparation of crosslinked hydrogels including physical, chemical and pH-induced crosslinking [380]. Recently, photoactivation has emerged as a facile and rapid approach for crosslinking hydrogels/hydrogel blends with photoactivated precursor polymers (modified with photo-crosslinkable functional groups) such as *B. mori* silk fibroin methacrylate (silkMA), gelatin methacrylate (gelMA), hyaluronic acid methacrylate (HAMA), polyethylene glycol dimethacrylate (PEGDMA), polyethylene glycol diacrylate (PEGDA) and carrageenan methacrylate (carMA) [495, 496]. These polymers have been used for tissue engineering and as bioinks/biomaterial inks for 3D printing. They could hence be rheologically tuned to conform to injectable hydrogel applications. We have previously explored silkMA, gelMA, PEGDA and PEGDMA in various blends for bioprinting/3D printing applications, which suggest their suitability in potential injectable treatment approaches [266].

Platelet rich plasma (PRP) is a rich cocktail of autologous growth factors suspended in the plasma and has been used as an injectable treatment approach for musculoskeletal tissue regeneration [466]. Reports of infrared light photoactivated PRP lysate devoid of the cells have been a bane to this scenario as they minimize the chances of immune response while preserving all the growth factors [497]. PRP has shown effectivity in healing meniscal defects due to the presence of fibroblastic (CTGF, PDGF, FGF) and chondrogenic (TGFβ) growth factors [303]. Conventionally PRP lysate has been employed in its injectable liquid or semi-gelled state, but recently freeze-dried PRP has also been reported as a growth supplement [472]. Owing to its mechanically weak nature PRP gel is ineffective for direct applications in knee meniscus scaffolding, which require stable, supportive constructs that can be load bearing while aiding regeneration. Hence PRP could be incorporated into mechanically resilient treatment modalities

after removal of platelets and freeze-drying, and could be used as a rich source of sustained releasing growth factors in the treatment of meniscal injuries. Human Wharton's jelly derived mesenchymal cells (hwJMSCs) are gaining traction due to their inherent regenerative potential and applicability in clinical settings. Several ongoing clinical trials are using hwJMSCs for the treatment and therapeutic applications in diabetic foot ulcers, spinal cord injury, myocardial infarction and knee osteoarthritis [473]. Advancement of tissue engineering and organ regeneration-based strategies has caused a rise in the cryo-preservation of umbilical cords for eventual isolation and patient-specific treatment application of Wharton's jelly derived neonatal mesenchymal stem cells [498]. Hence, these stem cells are a lucrative option for the evaluation of treatment modalities with potential clinical relevance.

Here, we have reported an in situ photo-crosslinkable blend of silkMA, gelMA, PEGDA and GFRP along with lithium phenyl-2,4,6-trimethylbenzoylphosphinate (LAP) photoinitiator, that could be crosslinked using a visible light of 405nm wavelength in 60s. The formed hydrogels have been assessed extensively for their rheological properties, chemical conformation changes through infrared spectroscopy, mechanical properties, swelling behaviour, cross-sectional topography and porosity as well as long-term degradability properties. These hydrogels have been gauged for their potential of acting as a growth factor reservoir with sustained release of GFRP proteins encapsulated within the blend. Furthermore, the biological characterization of these hydrogels using human Wharton's jelly mesenchymal stromal cells (hwJMSCs) has been carried out, in tandem, for cellular proliferation and migration for 21 days. The cells encapsulated within the hydrogels have been evaluated for their gene expression profile to determine the potential fibro-chondrogenic differentiation commitment created by the presence of GFRP. The constructs have been digested to check for the biochemical deposition of sulphated glycosaminoglycans (sGAG) and cryo-sectioned and immuno-stained for the evaluation of the presence of the collagen I, collagen II and aggrecan secreted by the hydrogel encapsulated cells after 21 days of culture. Additionally, murine and human macrophages have been used for the *in vitro* evaluation of the release of inflammatory cytokines when cultured in the presence of hydrogel composition or its leachate thereof. These hydrogels have been further used for treatment of full-thickness meniscal defects in rabbit model. After 8 weeks, the hydrogel treated menisci demonstrated visible healing of the defects as compared to the un-treated control menisci. Hereby, we hypothesize that the developed hydrogel composition could be used for the potential patient-specific treatment of both minor and major meniscal tears.

5.2 Materials and methods

5.2.1 Preparation of Bombyx mori silk fibroin methacrylate (silkMA) and gelatin methacrylate (gelMA) and isolation of growth factor rich plasma (GFRP)

Methacrylated *B. mori* silk fibroin (silkMA) was prepared using a pre-optimized protocol [435] . Briefly, *B. mori* cocoons were chopped, degummed in boiling 0.02M sodium carbonate solution (Na_2CO_3) for 30 min, washed thoroughly using distilled water, and air dried to obtain the degummed fibres. Obtained degummed fibres were dissolved in lithium bromide (LiBr, 9.3M) under stirring for 1h at 60°C. To this silk-LiBr solution, glycidyl methacrylate (GMA) was added at a feed ratio 0.06:1 while continuously stirring and further incubating at 60°C to react for 3h. This solution is further dialysed using a 12-14kDa cut-off dialysis membrane against double distilled water for 96 h to remove the unreacted GMA and residual LiBr, obtaining the regenerated *B. mori* silk fibroin methacrylate (silkMA). Gravimetric determination was used to determine the concentration of silkMA and it was used as a stock for further use.

Gelatin methacrylate (gelMA) was prepared according to the protocol mentioned previously with slight modification[447]. Briefly, gelatin type A from porcine skin was dissolved in 0.1M carbonate-bicarbonate buffer (CB buffer, pH 9.2-10.6) while stirring and maintaining at 60°C. The pH was adjusted to 9 using NaOH before reaction and methacrylic anhydride (MA, 94%) was added dropwise to the solution mixture at the feed ratio of 0.1:1 at intervals of 10-11 min, while constantly adjusting the pH to 9 and thereafter allowed to react for 1.5h at 60°C. pH of the solution was adjusted to pH 7.4 using 1N HCl to stop the reaction. Obtained reaction mixture was dialyzed against double distilled water in a 12kDa cut-off dialysis membrane for 120h at 60^0C for removal of excess unreacted MA and any other byproducts. The dialyzed gelMA was frozen at -80°C and freeze-dried for storage and further reconstitution.

Preparation for freeze-dried growth factor rich plasma (GFRP) was carried out by introducing certain modifications in a protocol previously mentioned[469]. Platelet concentrate bags were secured from blood bank of GNRC hospital (Guwahati, Assam, India) with appropriate collection, processing and handling protocols reviewed and approved by Institutional Ethics Committee, Institute of Neurological Sciences Trust, GNRC Hospitals (***Reference no. Inst/AS/2015/RR-2018/EC-104***). Platelet bags were collected well before expiration and transported rapidly to laboratory under shaking conditions. Initially, the platelets

were concentrated by centrifuging at 300xg for 8 min at 12°C to separate platelet and buffy coat layer from the residual cells such as RBC. Obtained suspension was centrifuged at 1000xg for 10 min at 16°C to obtain the platelet pellet and plasma supernatant. The supernatant was reduced to 1/3rd of the volume and platelet pellet was gently resuspended to obtain platelet rich plasma suspension. This suspension was poured onto petri dishes kept in an ice bath for photoactivation using a polychromatic infrared light source (600-1300nm, Philips R95) from a distance of 30cm along the central axis of the lamp for 15min. The growth factor rich activated PRP was centrifuged at 1000xg for 15 min at 16°C to pellet down the platelets. The growth factor rich supernatant was collected, freeze-dried and stored at -20°C under sterile conditions for further use. This freeze-dried form of the growth factor rich plasma is referred to as GFRP in further mentions.

5.2.2 Preparation of photo-crosslinking hydrogel blend and its physico-chemical characterization

SilkMA, gelMA and PEGDA stocks were sterilized by autoclaving and stock solution of lithium phenyl-2,4,6-trimethylbenzoylphosphinate (LAP, Sigma Aldrich, U.S.A.) was filter sterilized (0.22µm). Concisely, the injectable hydrogel blend was formulated by mixing silkMA, gelMA, PEGDA (polyethylene glycol diacrylate, Mn 700, Sigma Aldrich, U.S.A.) and LAP to reach a final concentration of 5% (w/v), 10% (w/v), 5% (w/v) and 0.4% (w/v) respectively by mixing at 40°C under aseptic conditions until a uniform blend is obtained with no precipitating residues. Thereafter the blend was cooled to room temperature and GFRP was added at 0.25% (w/v) to the blend in a sterile environment and pipetted until a uniform hydrogel is obtained. This hydrogel blend was further used in uncrosslinked and crosslinked forms for fabrication of constructs for physico-chemical, mechanical and biological characterizations.

5.2.2.1 Rheological characterization of silk-based injectable hydrogel

Injectable hydrogel composition was characterized rheologically in both crosslinked and uncrosslinked forms through various tests to understand its flow behaviour and stability using an MCR 302 rheometer (Anton Paar, Austria). Amplitude sweep, frequency sweep, temperature sweep as well as 3ITT (three-interval thixotropy) were performed on hydrogel using stainless steel parallel plate (PP25, 25 mm diameter). For each test, the hydrogel composition was pipetted onto the temperature controlled lower plate of rheometer, and the gap in between the plates was set at 0.5mm. For the amplitude sweep, the shear strain was varied from 0.001-1000% at 25°C and constant angular frequency of 1 rad s^{-1}. The obtained linear viscoelastic

region (LVER) of gel in both crosslinked and uncrosslinked form was further used to perform a frequency sweep of hydrogel in both the states. The angular frequency was varied from 0.01 to 100 rad s^{-1} at 25°C and a constant shear strain amplitude of 1% to find out the stability of hydrogel at various frequencies of shear. Furthermore, a temperature sweep of the hydrogel (crosslinked and uncrosslinked form) was performed over a wide range of 4°C to 45°C at constant angular frequency (1 rad s^{-1}) and shear strain amplitude (1%) to ascertain the temperature induced transition in crosslinked and uncrosslinked states. This was followed by the 3ITT (three-interval thixotropy) test where hydrogel in both the forms was exposed to alternating cycles of low shear strain amplitude (1%), low angular frequencies (1 rad s^{-1}) interspersed by short stretches of high shear strain (100%), high angular frequencies (100 rad s^{-1}) at 25°C to evaluate the injectability and self-standing nature of the hydrogel.

5.2.2.2 Surface topography and pore size distribution of hydrogels

Microarchitecture, pore size and pore size distribution of the injectable hydrogel was observed using field emission scanning electron microscopy (FESEM, Sigma, ZEISS, U.S.A) with an accelerative voltage of 2 kV. The injectable hydrogel constructs were casted into molds made of PDMS (polydimethylsiloxane) of the dimensions 7x7x7 mm^3 and crosslinked for 60s. These constructs were freeze-dried and cut into sections for electron microscopy. The sectioned constructs were sputter-coated with gold before analysis. Further, it was scanned under FESEM under high vacuum conditions and the pore diameter of constructs were calculated using Fiji (ImageJ 1.53p, Wayne Rasband, NIH, U.S.A.) by randomly selecting 50 different pores from randomized regions on FESEM micrographs.

5.2.2.3 Fourier Transform Infrared (FTIR) spectroscopy

The infrared spectroscopy was done for the structural conformational analysis of individual components as well as the blended hydrogel via attenuated total reflection (ATR) mode of FTIR (Shimadzu, IR Affinity-1S WL). The components i.e., including silkMA, gelMA, PEGDA, uncrosslinked hydrogel and crosslinked hydrogel compositions were freeze-dried and placed over the ATR crystal. Thereafter, spectra of all the samples were obtained in the range of 800 and 2000 cm^{-1}, a spectral resolution of 4 cm^{-1} and with 32 scan averages. Background readings were deducted from sample readings and all the spectra were noted at room temperature. Thereafter, the characteristic peak of individual components of hydrogel, hydrogel composition and crosslinked hydrogel were observed for changes caused by the photo-crosslinking and methacrylation.

5.2.2.4 Water uptake study

Swelling behaviour of the injectable hydrogels was studied based on previously mentioned protocol [435]. Concisely, the initial weight of hydrogels constructs (n = 5) was noted (W_i) and they were subsequently incubated in phosphate buffered saline (PBS, pH 7.4, 37°C) until they attained equilibrium. Weight of swollen construct (W_s) were measured using a microbalance at various time intervals by slowly dabbing off the excess PBS using a wet tissue paper. Swelling ratio was expressed using the following equation: $Swelling\ Ratio = \frac{W_s}{W_i}$

where, W_s represents the weight of constructs measured after different time intervals and W_i represents the initial weight of constructs.

5.2.2.5 Enzyme-assisted degradation profile

The *in vitro* enzyme-assisted degradation study was performed on the injectable hydrogel composition based on previously optimized protocol [46]. This study was conducted over the period of 90 days while incubating in PBS or a solution of protease XIV (from *Streptomyces griseus*, 3.5 units/mg, Sigma-Aldrich, U.S.A.). The injectable hydrogel constructs (n = 5) were immersed in either non-proteolytic PBS solution (pH 7.4) or proteolytic PBS solution (pH 7.4) containing 0.5 U ml^{-1} protease XIV at 37°C. Constructs immersed in non-proteolytic PBS solution were considered as control for comparison of stability of hydrogels. Constructs were incubated by replacing enzyme solution every 2 days for a period of 90 days. Additionally, 0.05% (w/v) sodium azide was added to the enzyme solution for preventing microbial growth. The constructs were retrieved at different time points, weighed and the remaining mass was recorded for each time point. The consequent percentage of mass remaining was expressed as follows: $\%Weight\ Remaining = \frac{W_r}{W_i} \times 100$

where, W_r represents weight of constructs measured after n days and W_i represents initial weight of constructs.

5.2.2.6 Porosity estimation

Porosity of injectable hydrogel composition was analysed using predefined hexane displacement method [406]. In brief, the hydrogel constructs of equal size (n = 4) were immersed in 13 mL of hexane (V_1) for 20 min each. Thereafter, the overall volume of hexane along with hexane-soaked constructs (V_2) was noted. Thereafter, the hexane-soaked constructs were removed and the residual volume of hexane solution in graduated cylinder (V_3) was noted.

Discrepancy in volume of hexane due to evaporation was eliminated by keeping another graduated cylinder with hexane and without constructs as control. The percentage porosity of hydrogel constructs was calculated according to the equation: $Porosity(\%) = \frac{V_1 - V_3}{V_2 - V_3} \times 100$

Where (V_1 - V_3) denotes volume of hexane impregnated within injectable hydrogel constructs whereas (V_2 - V_3) denotes total volume of construct.

5.2.2.7 Cumulative release of GFRP

Cumulative release of growth factor rich plasma was evaluated by estimating the leachate derived from the injectable hydrogel composition. The initial amount of GFRP loaded into each construct (W_1) was noted according to the initial volume of the hydrogel required for preparation of each construct (n = 4). Further these constructs were incubated in PBS (pH 7.4) supplemented with 0.05% (w/v) sodium azide at 37˚C over 40 days with a complete removal and replacement of the incubation solution at various time intervals (0, 1, 3, 5, 7, 14, 21, 28 and 40 days). Thereafter, 20 µL of leachate containing PBS added with 200 µL of Bradford reagent (SIGMA-Aldrich, USA) for 20 min and the absorbance was read at 525 nm. The amount of GFRP proteins leached out (W_2) was determined from the standard curve and the cumulative GFRP release (%) was measured using the formula:

$$Cumulative\ release\ of\ GFRP\ (\%) = \frac{W_1}{W_2} \times 100$$

Where, W_1 represents initial amount of GFRP encapsulated into the hydrogel constructs (mg) and W_2 denotes the amount of leached GFRP in the solution (mg).

5.2.3 Mechanical characterization of injectable hydrogel

5.2.3.1 Compressive strength evaluation of injectable hydrogel

Acellular injectable hydrogel constructs (n = 5) were fabricated using photo-crosslinking in 7x7x7 mm^3 dimension PDMS molds and incubated to reach swelling equilibrium in phosphate buffered saline (PBS, pH 7.4) at 37˚C. Thereafter, uniaxial confined compressive stress test of the crosslinked hydrogel constructs was carried out using a universal tensile testing machine (Model 5944, Instron, USA) armed with a 100 N load cell. Injectable hydrogel constructs were exposed to a uniaxial confined compressive strain of 60% at rate of 5 mm/min. Further, the compressive stress vs strain curve was plotted and the mean compressive modulus as well as young's modulus was calculated using Bluehill 3 software. Additionally, hydrogel

constructs were also exposed to uniaxial compressive cyclic strain of 20% for 2000 cycles of compression at a crosshead speed of 5 mm/min every day for 21 days. A reading was done on 1, 3, 5, 7, 14 and 21 days and the compressive stress-strain curve hysteresis loop for 1st cycle and 2000th cycle were plotted to compare the aberration in terms of strength and stress profile of the constructs during the experimental duration.

5.2.3.2 Tensile strength evaluation of injectable hydrogel

Tensile strength and young's tensile modulus of injectable hydrogel constructs were estimated using universal tensile testing machine (Model 5944, Instron, USA) equipped with 100 N load cell. Experiment was executed by creating a major defect in porcine meniscus mimicking the radial tear of native meniscus injury **(Figure 5.1)**. Further, two holes were punched at the edges of the menisci antero-posteriorly for extension purpose. The defect was filled using injectable hydrogel composition and photo-crosslinked for 1 minute using a 405 nm wavelength 40W LED array. Thereafter, meniscus samples were exposed to 60% tensile strain at a crosshead speed of 5 mm/min. Further, the tensile stress-strain and young's tensile moduli were calculated using Bluehill 3 software and plotted using OriginPro 2021 (OriginLab corporation, U.S.A.).

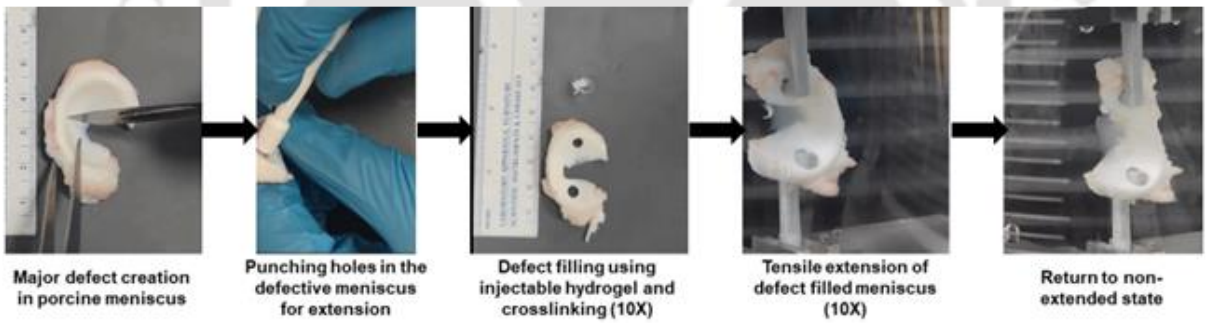

Figure 5.1: *Representative gross images of the tensile testing of hydrogel in porcine menisci.*

5.2.4 *In vitro* Biological evaluation of injectable hydrogel composition

5.2.4.1 Isolation of Wharton's Jelly stem cells and cell encapsulation within hydrogel constructs

Wharton's jelly stem cells were harvested from freshly collected Human umbilical cords through an explant-based method. The isolation protocol was in accordance with the previously established protocol [449]. Human umbilical cord was procured from GNRC Hospital (Guwahati, Assam, India) with appropriate collection, processing and handling protocols reviewed and approved by Institutional Ethics Committee (Institute of Neurological Sciences Trust, GNRC Hospitals; ***Reference no. Inst/AS/2015/RR-2018/EC-103***). For the transport of cords, ice cold sterile PBS (pH 7.4) was used and they were processed within 2-3 hours of procurement. Sterile PBS was used to wash the cord tissue to remove remnant blood. Further, Wharton's jelly was dissected out from cord tissue used as explants. Thereafter, explants were observed for the outcoming migrated cells which were trypsinized and reseeded to expand further. They were grown in a pre-optimized media (DMEM (Gibco, USA); glucose 4500 mg/L supplemented with 10 % fetal bovine serum, FBS (Gibco, USA), 1X antibiotic-antimycotic mix (Gibco, USA)) further supplemented with 2 ng/ml basic fibroblast growth factor (bFGF). For the biological characterization of injectable hydrogel, cells within passage numbers 3-8 were used.

Uncrosslinked injectable hydrogel composition along with PRP-lysate was prepared in aseptic conditions and hwJMSCs were blended within. These cell-laden hydrogels were poured into PDMS molds of 5x5x3 mm^3 volumes and photo-crosslinked using 40 W LED light source of 405 nm wavelength for 1 min. It was ensured that the cellular density was maintained at 10^6 cells per mL of hydrogel. Thereafter, the cell-laden hydrogel constructs were cultured in cell culture medium (DMEM (Gibco, USA); glucose 4500 mg/L supplemented with 10 % fetal bovine serum, FBS (Gibco, USA), 1X antibiotic-antimycotic mix (Gibco, USA)) in an incubator at 37°C with 5% CO_2 and 85 % humidity for assessing their viability, compatibility, proliferation, infiltration and gene expression.

5.2.4.2 Cellular viability assay

Cell viability of the hwJMSCs encapsulated within injectable hydrogel composition was screened using live/dead assay kit. The assay dye solution was formulated by mixing calcein-AM (2 μM) and ethidium homodimer (4 μM) solutions (pH 7.4) following manufacturer's

protocol (Sigma-Aldrich, USA). Cell viability was observed after 1, 7, 14 and 21 days of culture. Cell encapsulated injectable hydrogel constructs were washed mildly with PBS (pH 7.4), followed by incubation with calcein-AM and ethidium homodimer solution at 37°C and 5% CO_2 for 40 min. Thereafter, the live/dead reagent was aspirated, and the injectable hydrogel constructs were washed briefly in PBS to remove the extra stain. Further, the constructs were visualized under an inverted fluorescence microscope (Nikon Eclipse TiU2, Nikon, Japan). Green fluorescence indicates viable cells produced as a result of integral plasma membrane and intracellular esterase activity that changes calcein AM to calcein. In contrast, dead cells were identified by the entry of ethidium homodimer inside the dead cells through damaged plasma membranes and resulting in red fluorescence from the dead cells.

5.2.4.3 Cellular migration study

Cellular migration in injectable hydrogel composition was carried out using a previously established protocol [285] with slight modification. A layer of injectable hydrogel composition was laid upon a 1% (w/v) agarose-coated dish. Thereafter, a void was created in the injectable hydrogel composition using a PDMS pillar of 2 mm diameter to which 0.5% (w/v) agarose gel laden with hwJMSCs was filled. The migration of cells from agarose gel towards the injectable hydrogel composition was observed post-incubation for 1, 7, 14 and 21 days in culture medium at 37°C and 5% CO_2. In order to visualize the cellular migration, the agarose gel (with any residual cells) was carefully removed from the middle cavity space and Hoechst 33342 (Sigma Aldrich, USA) nuclei staining dye was used to stain for 30 minutes in dark. Post incubation, the images were taken using an inverted fluorescence microscope (Nikon TiU2, Nikon, Japan) and stitched using Microsoft Image Composite Editor. Thereafter, these stitched fluorescent images were processed using Fiji (ImageJ 1.53p, Wayne Rasband, NIH, U.S.A.) to plot the 3D surface profile showing the distribution of cells migrated into the injectable hydrogel composition from the agarose gel.

5.2.4.4 Estimation of DNA and sGAG content

Cell-laden injectable hydrogel constructs (n =4) of previously mentioned dimensions were utilized for estimation of DNA content and sGAG content following previously established protocol [46]. Concisely, cell-laden injectable hydrogel constructs were collected after different incubation time intervals of 1,7,14 and 21 days and digested using papain digestion cocktail (5 mM L-cysteine, 5 mM EDTA, 100 mM Na_2HPO_4 and 125 µg/mL papain, pH 6.2) for 16 h at 60°C in a hot air oven. Thereafter, picoGreen DNA assay kit (Invitrogen,

USA) was used to estimate DNA content according to the manufacturer's protocol. The digested samples were centrifuged and 25 µL of supernatant was diluted using 75 µL of 1X TE buffer. Thereafter, each sample was added with 100 µL of Quant-iT PicoGreen reagent (1:200 dilution in 1x TE buffer) and quantification was carried out using a microplate reader (Tecan infinite M200 PRO) with an excitation and emission maxima of 480 and 528 nm respectively. Standard curve for the DNA content estimation was generated using lambda phage DNA.

For quantification of total sulphated GAG (sGAG) the reagent used was 1,9-dimethylmethylene blue (DMMB). For the study, 200 µL of DMMB reagent was added to 20 µL of papain digested sample and the absorbance was read at 525 nm. Chondroitin-6-sulfate (Sigma Aldrich, USA) was used to prepare the standard curve.

5.2.4.5 Real-Time PCR analysis

Complete RNA was isolated from cell-laden injectable hydrogel constructs (n = 4) after different incubation time points of 1, 7, 14, and 21 days using TRIzol (Sigma Aldrich, USA) following the previously established protocol [476]. Briefly, cells encapsulated injectable hydrogel composition were taken in tubes into which TRI reagent was added. Thereafter, the constructs were chopped with microscissors on ice container and then centrifuged at speed of 13000g for 10 min and 4°C. The supernatant collected from the tubes were relocated into fresh tubes to which chloroform was added and centrifuged. Then the upper aqueous layer was carefully removed into fresh tubes followed by addition of isopropanol to obtain mRNA. This mRNA is further collected using centrifugation and the supernatant was carefully removed without dislodging the pellet. The pellet was washed using pre-chilled DNA diluent (EtOH) and further air-dried in laminar flow to obtain purified mRNA. mRNA concentration was determined using microdrop spectrophotometric analysis through Multiskan Sky (Thermofisher Scientific, USA) and followed with cDNA synthesis using high capacity cDNA reverse transcription kit (Applied Biosystems, USA) and a PCR thermal cycler (Applied Biosystems, USA). Obtained cDNA was further used to perform real-Time PCR using the primer sequences for human genes (listed in **Table 5.1**) and SYBR Green reagent (Invitrogen, USA) in a QuantStudio 5 (Applied Biosystems, USA) real-time PCR machine. The run was carried under the set conditions of the holding stage (50°C for 2 min, 95°C for 10 min) and cycling stage (40 cycles of 95°C for 15 s and 60°C for 45 s). The results obtained were analysed by normalizing using either only the endogenous housekeeping gene β-actin ($2^{-\Delta Ct}$) or with β-

actin as well as the expression on day 1 normalized to the corresponding β-actin via C_t method ($2^{-\Delta\Delta Ct}$). The primer sequences used and the respective accession numbers have been mentioned in **Table 5.1**.

Table 5.1: *Primer sequences for gene expression analysis*

Gene	Sequence	Accession No.
Human sox-9 (sox-9)	F:5′-TTCCGCGACGTGGACAT-3′ R:5′GGCGGCAGGTACTGGTCAAACTC-3′	NM_213843.1
Human Aggrecan (acan)	F:5′-CCCAACCAGCCTGACAACTT-3′ R:5′-CCTTCTCGTGCCAGATCATCA-3′	NM_001164652.1
Human Collagen Iα (col I)	F:5′-AGAAGAAGACATCCCACCAGTCA-3′ R:5′-AGATCACGTCATCGCACAACA-3′	XM_021067153.1
Human Collagen IIα (col II)	F 5′-CAGGTGAAGGTGGGAAACCA-3′ R 5′-ACCCACGAGGCCAGGA-3′	AF201724.1
Human RUNX-2 (runx-2)	F 5′-GACTGTGGTTACCGTCATGGC-3′ R 5′-ACTTGGTTTTTCATAACAGCGGA-3′	NM_001015051.4
Human Osteoclacin (OCN)	F 5′-GTAGTGAAGAGACCCAGGCG-3′ F 5′-CGGATTGAGCTCACACACCT-3′	NM_199173.6
Human β-actin (βactin)	F: 5′-CACCATTGGCAATGAGCGGTTC R:5′- AGGTCTTTGCGGATGTCCACGT-3′	NM_001101

5.2.4.6 Macrophage stimulation and inflammatory cytokine release profile

In vitro immunomodulatory response of silk-based injectable hydrogel composition was performed by using RAW 264.7 cells (mouse macrophages, acquired from National Center for Cell Science, NCCS, Pune) by estimating the amount of TNF-α (Tumor Necrosis Factor) and IL-1β (Interleukin 1β) released. RAW 264.7 cell lines were maintained in DMEM supplemented with 10% FBS, 1% anti-anti at 37°C and 5% CO_2 prior to seeding. The cells were seeded at the density of 5×10^4 cells per well in a 24-well plate and grown for 24 h. Four groups were taken into consideration for the *in vitro* study, a negative control group (Tissue culture plate without hydrogel), a positive control group (Lipopolysaccharide, 1000 ng ml^{-1}, LPS from *Escherichia coli*, Sigma Aldrich, USA) and two Experimental groups comprising of both hydrogel constructs or their leachates in media. Thereafter, hydrogel constructs were placed on seeded cells or they were treated with the leachate medium derived from the constructs after 24

h. Post 24 h of stimulation the culture media with the released cytokines was collected for each group and used for the quantification of TNF-α and IL-1β release using their respective ELISA kits following the manufacturer's (Krishgen Biosystems, USA) protocol.

THP-1 (human monocyte cell line) procured from NCCS were cultured in suspension in RPMI 1640 media (Sigma Aldrich, USA) by observing standard protocols. THP-1 cells were seeded at a density of 5×10^4 cells per well in a 24-well plate for differentiation into adherent macrophages (M0) by treating with 100 ng mL^{-1} (162 nm) phorbol 12-myristate 13-acetate (PMA) (Sigma Aldrich, USA) for 24h. Consequently, these M0 macrophages were treated with the leachate medium from the hydrogel constructs as well as the whole hydrogel constructs for 24 h while keeping 1000 ng ml^{-1} LPS and unstimulated cells as positive and negative controls. The conditioned media were collected and used for the determination of human TNF-α and IL-1β released by the macrophages using respective ELISA kits in agreement to the manufacturer's (Krishgen Biosystems, USA) protocols.

5.2.4.7 Cryo-sectioning and immunohistochemistry

The cell-laden hydrogel constructs were incubated in 10% neutral buffered formalin (NBF) for 24 h for fixation. This was followed by cryo-protective fixation in 15% (w/v) sucrose for 6 h followed by 30% (w/v) sucrose for 12 h. These constructs were further embedded in Polyfreeze (Tissue Freezing Medium, SIGMA, U.S.A.) and snap-frozen to -24°C prior to cryo-microtomy. The sample blocks were cryo-sectioned with slices of 12–15 µm thickness at -24°C using a cryomicrotome (Leica). Obtained cryo-sectioned slices were treated with 0.2% bovine serum albumin before immunostaining for removing the non-specific background staining. The treated sections were further immuno-stained using antibodies against ACAN (aggrecan) (Abcam, USA), COL I (Collagen I, Abcam, U.S.A.) and COL II (Collagen II, Abcam, USA). These sections were counted stained using DAPI by the virtue of aqueous mountant Fluormount with DAPI (SIGMA, U.S.A.) The co-stained sections were imaged using a fluorescence microscope for assessing the deposition of aggrecan, collagen I and collagen II by the hydrogel composition encapsulated hwJMSCs undergoing fibro-chondrogenic differentiation in the presence of GFRP (Eclipse Ti-2, Nikon, Japan). Co-stained micrographs were further assessed for the ratio of col I/col II and col I/acan using percentage area fraction calculated for various filed of views ($n \geq 8$) using ImageJ (Fiji) software.

5.2.5 *In vivo* functional evaluation in rabbit meniscus defect model

A pilot scale *in vivo* functional assessment of the hydrogel composition was assessed by implanting acellular hydrogel into meniscal defects of adult New Zealand white rabbits. The experimental and animal handling protocols were reviewed and sanctioned by the Institutional Animal Ethical Committee (IAEC), West Bengal University of Animal and Fishery Sciences (WBUAFS), West Bengal, India (***Registration No. 763/GO/Re/SL/03/CPCSEA/02/2021-22*** dated26.4.2022). Six healthy adult rabbits of either sex, each weighing 1.5 - 1.8 kg were put under anesthesia with Xylazine hydrochloride (5 mg/kg body weight; Injection xylaxin, Indian Immunologicals, Ahmedabad, India) and ketamine hydrochloride (33 mg/kg body weight; Ketalar, Parke-Davis, Hyderabad, India) intramuscularly. Knee joints were surgically opened to expose the menisci on each leg and full-thickness meniscal defects were created using a 0.5 mm surgical steel punch (**Figure 5.2**). The defects were either left blank or filled with the injectable hydrogel composition and crosslinked in situ for 60 s using a small hand-held 405 nm light array. Thereafter the knee joints of the animals were sutured and the animals were closely monitored. The sutured areas were cleaned superficially periodically with 10% povidone–iodine draped dressing gauge and animals of each group received Meloxicam (0.3 mg/kg body weight; Injection Melonex, Intas Pharmaceuticals India, Ahmadabad, India) injection daily intramuscularly as per prescription. Two animals were sacrificed, after 1 and 8 weeks respectively by cervical dislocation. The menisci were retrieved with utmost care and preserved for histological processing in 10% NBF for 24 h. The fixed samples were washed with PBS wash and embedded in cryo-sectioning medium and frozen at -20°C for 6 hr. The tissue sectioning was done in a cryomicrotome (CM1860 UV, Leica, Germany) with 18 µm thick section. The sections were stained with hematoxylin and eosin to gather an overall view and thereafter stained with Masson's trichrome (MT) and safranin-O/fast green (SO-FG) according to established protocols. Stitched brightfield micrographs of H&E and magnified micrographs of MT and SO-FG were obtained using an inverted microscope (Eclipse Ti2U, Nikon, Japan) for representation of the healing potential of the hydrogel.

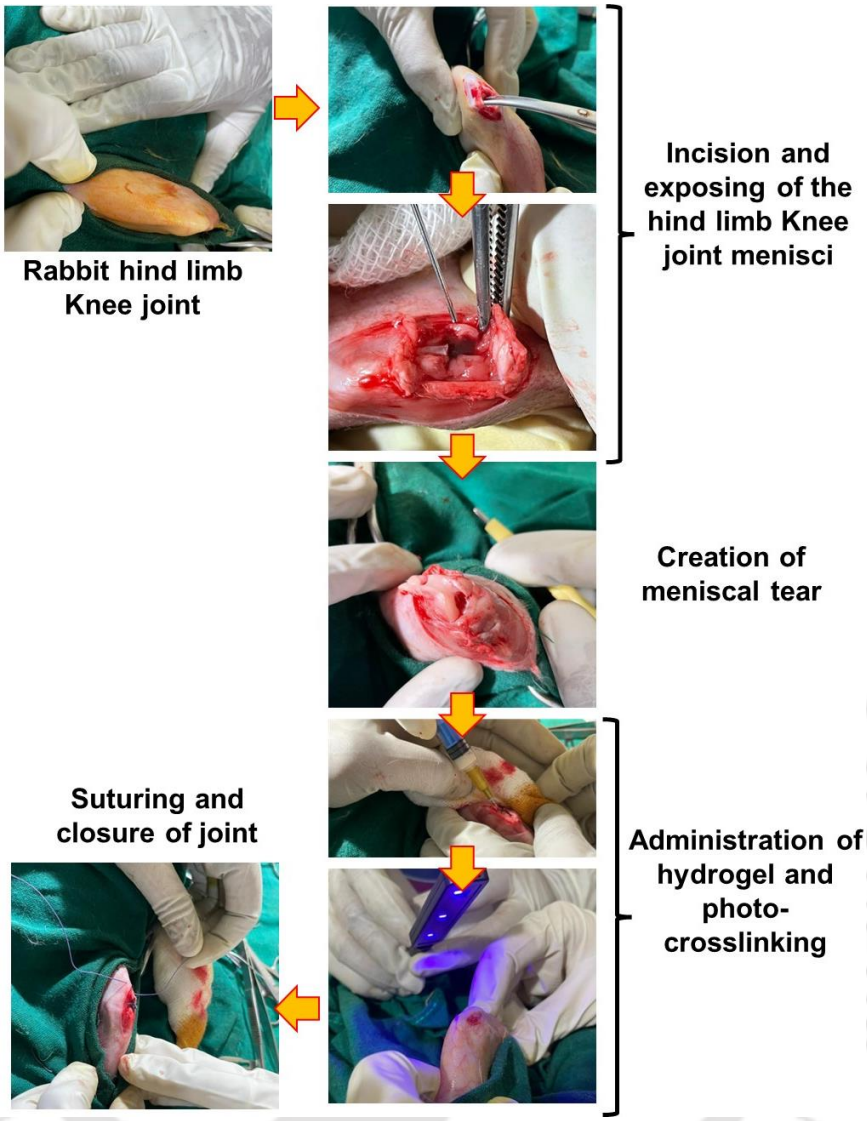

Figure 5.2: *The representative surgical procedure showing opening of the knee joint, creation of meniscal defect, application of hydrogel in the created meniscal defects and its crosslinking followed by the suturing and closure of knee joint.*

5.2.6 Statistical analysis

Experiments that are quantitative by nature were performed in quadruplets and the results were represented in terms of mean ± standard deviation. For statistical analysis of the data, Tukey's test ANOVA (one-way analysis of variance) was performed. It was carried out with the help of OriginPro 2021 software (OriginLab corporation, USA) to analyse the significant difference between various sampling groups. Statistically significant variations between groups were denoted for $^{*}p \leq 0.05$ and $^{\#}p \leq 0.01$.

5.3 Results

5.3.1 Physico-chemical characterization of hydrogel composition

5.3.1.1 Infrared spectroscopy

The crosslinking induced conformational changes in the functional groups was evaluated through Fourier transform infrared spectroscopy **(Figure 5.3A)**. The infrared spectroscopic spectra of silkMA, gelMA as well as the uncrosslinked hydrogel blend (UHYD) and crosslinked hydrogel blend (CHYD) were found to possess the signature amide I (1710–1590 cm^{-1}), amide II (1570–1480 cm^{-1}) and amide III (1270–1200 cm^{-1}) peaks characteristic of the proteins present in the hydrogel composition, i.e., silk, gelatin and GFRP. The uncrosslinked and crosslinked hydrogel blends showed shift in these peaks due to the crosslinking of the components. Additionally, methacrylate peaks at ~951 and ~1165 cm^{-1} represent the presence of methacrylate groups in all the components of the hydrogel as well as the uncrosslinked and crosslinked blends. These peaks were also found to shift and widen due to the crosslinking of the methacrylate groups.

5.3.1.2 Rheological characteristics

The rheological characterizations of the formulated hydrogel blend was carried out in both uncrosslinked and crosslinked states through amplitude, frequency, temperature and 3 interval thixotropy tests **(Figure 5.3B)**. The shear thinning nature of the injectable hydrogel blend was found through the amplitude sweep **(Figure 5.3B i)** where the gel progressively underwent shear-thinning from 10^{-3} to 10^{3} % shear strain within the linear viscoelastic region (LVR). The crosslinked hydrogel was found to possess 1000 folds higher viscosity as compared to the uncrosslinked hydrogel. Similarly, at constant amplitude and increasing frequency of shear strain from 0.01 to 100 rad/sec, the crosslinked and uncrosslinked hydrogels were found to undergo thinning and a higher viscosity was possessed by the crosslinked blend **(Figure 5.3B ii)**. Furthermore, the temperature sweep showed the stability of the crosslinked hydrogel **(Figure 5.3B iii)** under varying temperatures as it remained unaffected with higher viscosity from 4°C to as high as 45°C while the uncrosslinked hydrogel thinned rapidly past the temperature of 10°C. The injectability and gel strength recovery of the hydrogel was found through 3ITT **(Figure 5.3B iv)**. The low shear regions denote the gel strength of both crosslinked and uncrosslinked hydrogels but at higher shear strain and frequency the

uncrosslinked hydrogel showed major decline in viscosity while the crosslinked gel could hold a considerably higher (1000 folds) viscosity and gel strength.

5.3.1.3 Cross-sectional morphology, pore diameter and porosity

The hydrogel constructs should possess necessary porosity and pore diameter for cellular infiltration and migration and consequent integration of the same with the host menisci. The scanning electron micrographs from several sections of the hydrogel were assessed **(Figure 5.3C)**. The hydrogel constructs were found to possess an overall porous microarchitecture as shown in micrographs **(Figure 5.3C i-ii)**. Moreover, the presence of PRP proteins could be visualized from the threadlike structures on the struts of the porous microarchitecture **(Figure 5.4).** The average dimension of the pores was calculated from different fields of the electron micrographs using ImageJ (FIJI) in the vertical and horizontal section to be 67.6µm and 49.8µm respectively **(Figure 5.3D)**. The apparent porosity of hydrogel constructs was evaluated using hexane displacement method which denotes the volume of the microporous architecture **(Figure 5.3E)**. The average apparent porosity of the hydrogels was found to be ~47.5%.

5.3.1.4 Swelling ratio

Swelling ratio was evaluated to assess the property of the hydrogel blend to assist in the absorption of nutrients and exchange of metabolites from the surrounding medium. The water uptake occurring by the immersion of crosslinked hydrogel constructs in PBS **(Figure 5.3F)** was found to be ~1.2 times after the equilibration point of 24 h.

5.3.1.5 Cumulative release of PRP from hydrogel constructs

The hydrogel blends were incubated in PBS and their cumulative PRP release characteristics was evaluated for 40 days **(Figure 5.3G)** showing their ability to be used as a reservoir of autologous growth factor rich plasma post implantation. The cumulative release was found to be gradual and sustained as it reached ~75% over the period of 40 days when compared to the initially encapsulated amount. The release profile was found to follow Fickian diffusion **(Figure 5.5A-B)**, which is desirable for long-term release *in vitro* and *in vivo*. Moreover, the release profile of PRP from hydrogel was not affected by the hydrogel components as shown by the control hydrogel release profile where negligible cumulative protein release was observed as compared to the PRP loaded hydrogel **(Figure 5.5C)**.

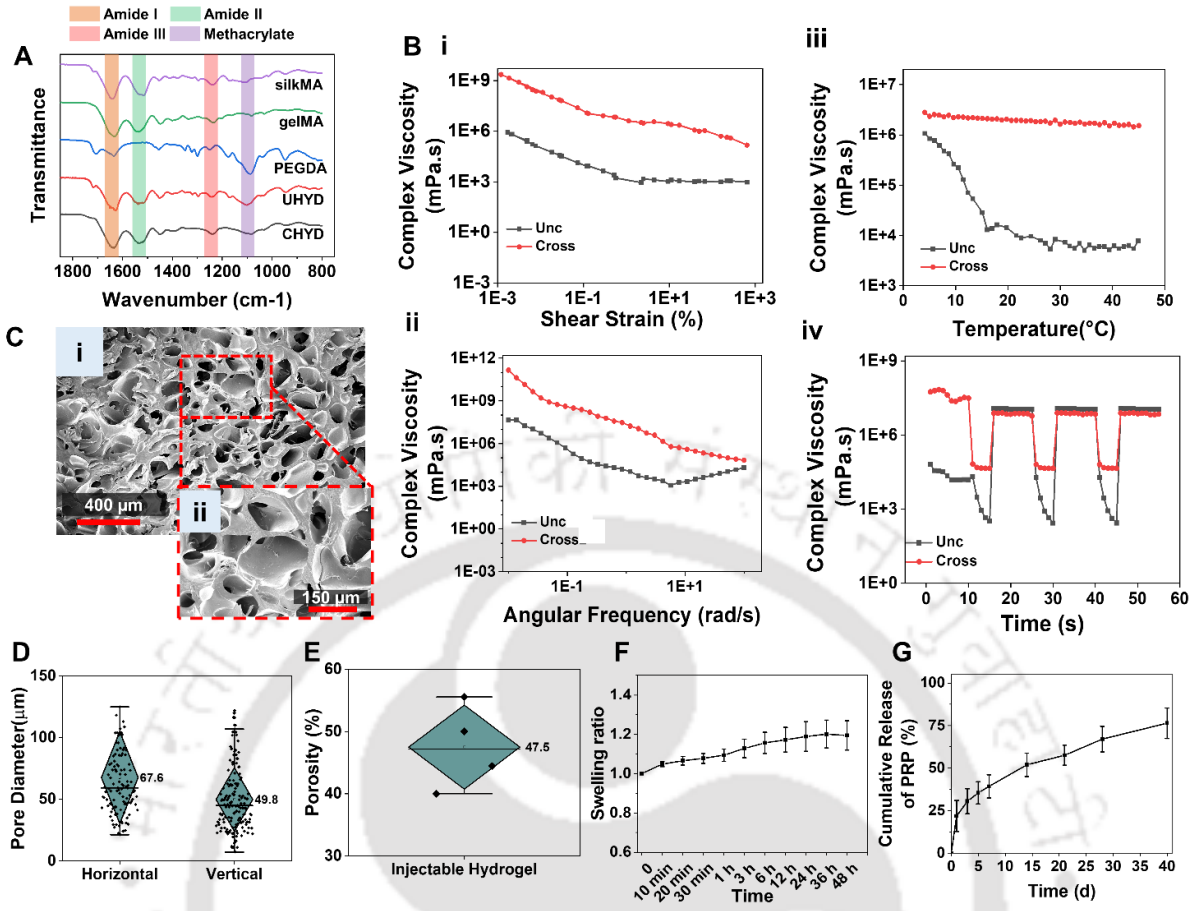

Figure 5.3: *(A) Infrared spectroscopy spectra of hydrogel composition in crosslinked (CHYD) and uncrosslinked (UHYD) forms as well as the various components silkMA (BMMA), gelMA (GMA) and PEGDA. (B) Rheological characterization of crosslinked (Cross) and uncrosslinked (Unc) hydrogel using (i) amplitude sweep, (ii) frequency sweep, (iii) temperature sweep and (iv) 3 interval thixotropy. (C) Electron micrographs of crosslinked hydrogels at various magnifications. (D) Pore diameter of the hydrogels measured from electron micrographs of horizontal and vertical sections of hydrogels. (E) Porosity of crosslinked hydrogels. (F) The swelling ratio of crosslinked hydrogel constructs. (G) Cumulative PRP release from crosslinked hydrogel constructs calculated for 40 days.*

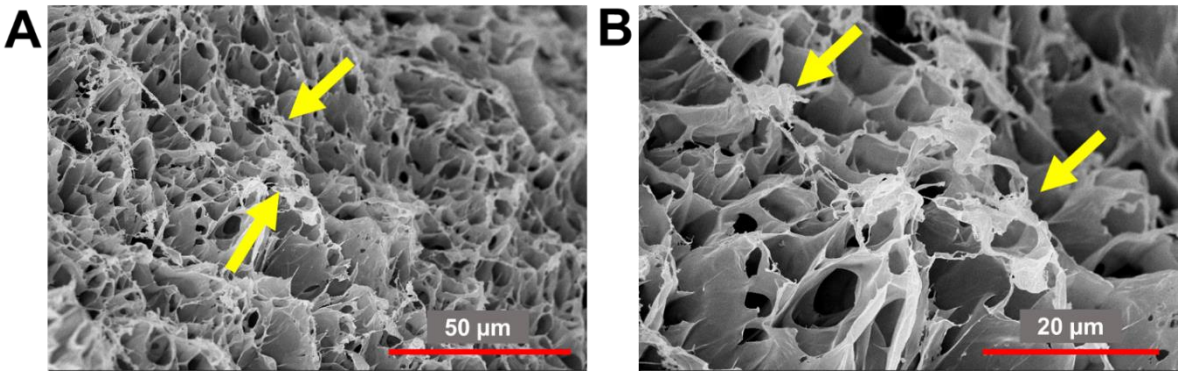

Figure 5.4: *Representative electron micrographs demonstrating the presence of GFRP within the injectable hydrogel at (A) lower and (B) higher magnifications.*

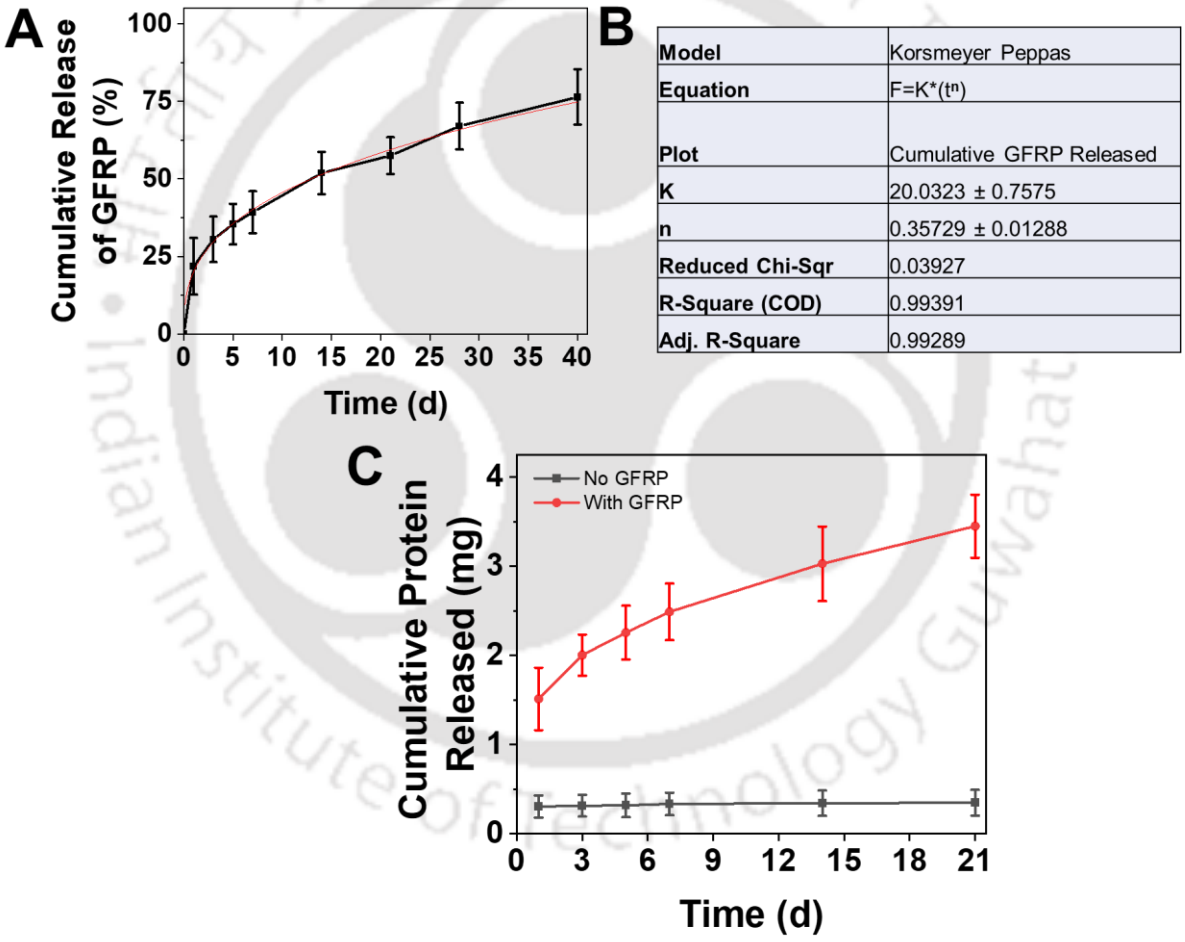

Model	Korsmeyer Peppas
Equation	$F=K*(t^n)$
Plot	Cumulative GFRP Released
K	20.0323 ± 0.7575
n	0.35729 ± 0.01288
Reduced Chi-Sqr	0.03927
R-Square (COD)	0.99391
Adj. R-Square	0.99289

Figure 5.5: *(A) Fitting of cumulative GFRP release profile using Korsmeyer- Peppas model where the red line represents the fitted curve and (B) the table shows the parameters derived from the fitting. (C) Cumulative protein release profile of hydrogel composition with GFRP and without GFRP for 21 days.*

5.3.1.6 Degradation profile

The hydrogel constructs were subjected to both saline (PBS) as well as proteolytic (0.5 U/ml Protease XIV in PBS) environments to assess their emulated degradation over the period of 85 days **(Figure 5.6A)**. The constructs in saline were initially found to swell and gain some weight while there was a constant gradual reduction in the weight of the constructs immersed in proteolytic environment. After the period of 85 days, the hydrogels in PBS were found to degrade minimally and hold >90% of the initial weight. In contrast, their enzymatically treated counterparts were found to degrade ~45% and retain >50% of their initial weight after 85 days of incubation with alternate day change of protease solution.

5.3.2 Mechanical properties of the injectable hydrogel

5.3.2.1 Confined uniaxial compressive properties

The confined compressive mechanical properties were evaluated by compressing 7x7x7 mm^3 constructs of hydrogel within Teflon molds and the stress-strain curve was obtained for the same. The stress-strain curve **(Figure 5.6B i)** showed almost linear compressive properties of the hydrogel up to 60% of compressive strain under confinement. The subsequently derived compressive modulus at the highest stress was found to be 676.7 kPa and young's modulus was derived from the initial linear region to be 217.3 kPa **(Figure 5.6B ii)**.

5.3.2.2 Confined uniaxial cyclic compressive properties

The constructs of previously mentioned dimensions were subjected to 20% compressive strain for 2000 cycles each day for 21 days and the stress-strain graphs were plotted for days 1, 3, 5, 7, 14 and 21. Cycle 2000 stress-strain curves were plotted **(Figure 5.6C i)** which show hardening of hydrogels until day 5 and thereafter normalization towards the day 1 values and eventually reaching below that. The stress-strain curve of the samples on day 1, 3, 5, 7, 14 and 21 days were plotted **(Figure 5.6C iii-viii)** for cycle 1 and cycle 2000 to show the changes comprehensively. The compressive stress values were found to rise from day 1 to day 3, stay above day 1 values till day 5 and then gradually reduce over the period of 21 days with the cumulative 42000 cycles of 20% compressive strain being applied on the same construct over these periods.

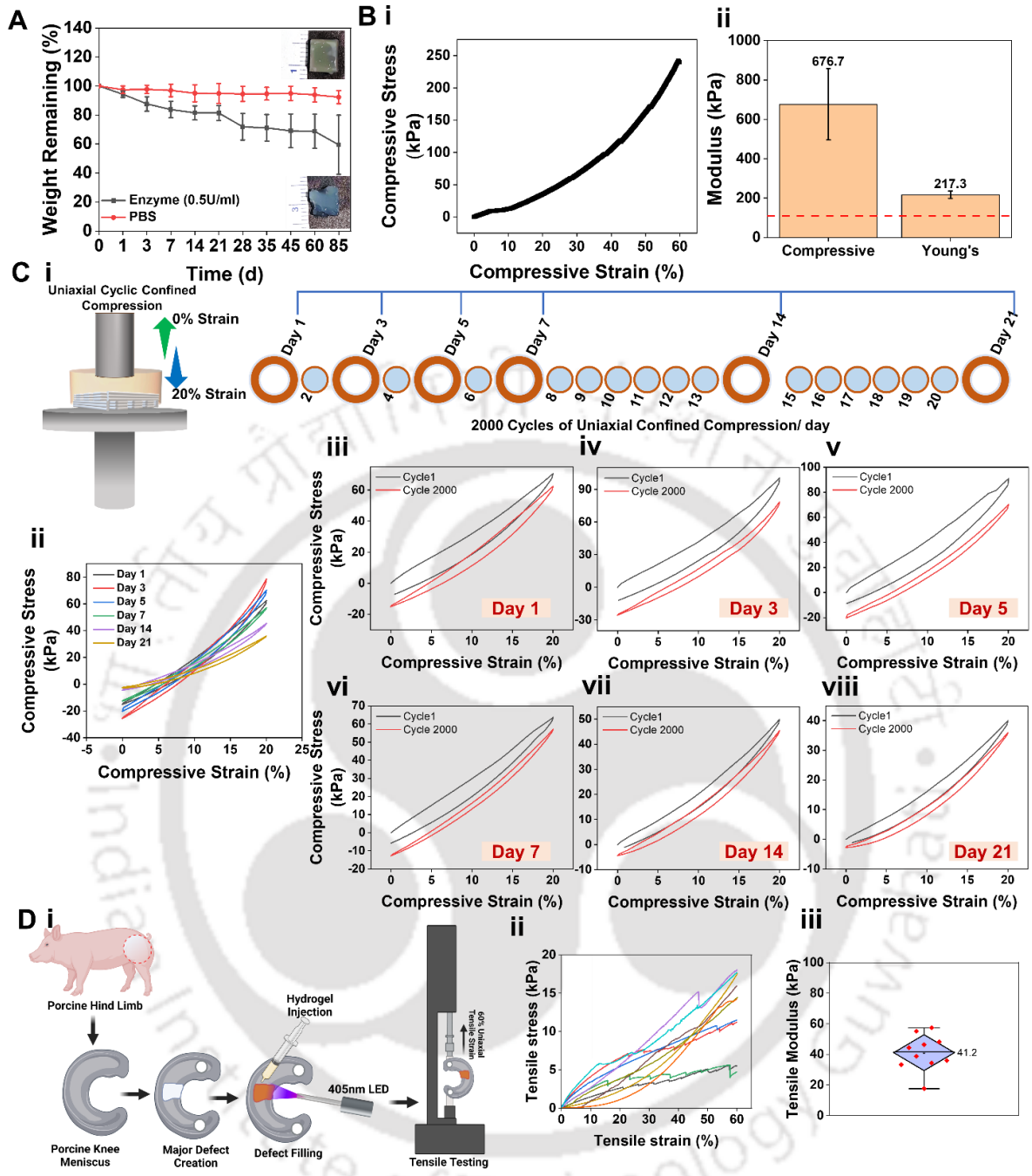

Figure 5.6: *(A) Degradation profile of crosslinked hydrogel constructs in enzyme and saline over 85 days (~12 weeks). (B) (i) Representative stress-strain curve and (ii) compressive and young's moduli derived from confined compressive test of crosslinked hydrogel. (C) (i) Schematic showing the uniaxial cyclic confined compression regimen of injectable hydrogel composition. (ii) Stress-strain hysteresis curves of cycle 2000 on days 1, 3, 5, 7, 14 and 21 of confined compression carried out on hydrogel constructs. Cycle 1 and cycle 2000 stress-strain hysteresis curves of crosslinked hydrogel upon confined compression on (iii) day 1, (iv) day 3, (v) day 5, (vi) day 7, (vii) day 14 and (viii) day 21. (D) (i) Schematic showing the regimen of tensile test performed for injectable hydrogel composition on porcine menisci ex-vivo (Made with www.biorender.com). (ii) Stress-strain curves and (iii) tensile young's modulus of unconfined uniaxial tensile test of injectable hydrogel done in porcine menisci.*

5.3.2.3 Unconfined uniaxial tensile extension properties

Major defects created in porcine menisci were treated with the injectable hydrogel composition and subjected to 60% extension **(Figure 5.6D i)**. The representative stress-strain curves were plotted **(Figure 5.6D ii)** showing different levels of compressive stress being borne by the menisci due to the randomness of the created defects of varying dimensions **(Figure 5.1)**. The corresponding tensile moduli obtained were found to be ~41.2 kPa **(Figure 5.6D iii)**.

5.3.3 Biological characterization of hydrogels *in vitro*

5.3.3.1 Cellular viability and migration of human neo-natal stem cells on hydrogels

The viability of hwJMSCs encapsulated within the hydrogels was visualized using live dead staining **(Figure 5.7A)** on days 1, 7, 14 and 21. The constructs showed apt biocompatibility and the viable cell population was found to rise from day 1 to day 21 as can be observed by the increase in the number of viable green-fluorescent cells within the constructs in the representative micrographs.

The migration of cells was visualized using Hoechst 33342 staining of nuclei of cells migrating from the central agarose gel (AG) region to the injectable hydrogel (IJ) composition over the period of 21 days as could be seen in the representative stitched micrographs **(Figure 5.7C)** as well as the corresponding surface plots showing the cells as peaks all over the injectable hydrogel (IJ) constructs **(Figure 5.7C)**.

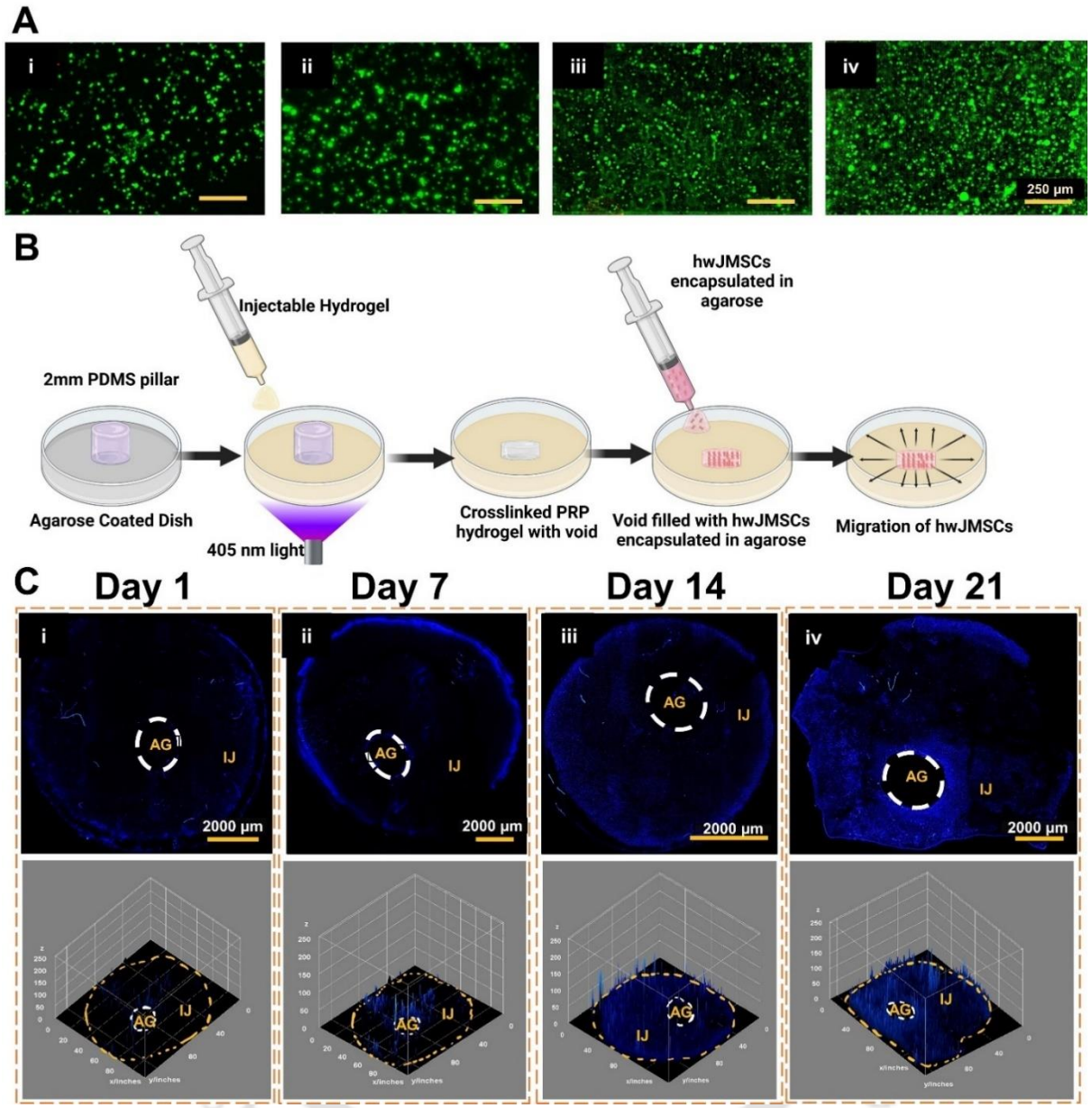

Figure 5.7: *(A) Viability of hwJMSCs within the crosslinked injectable hydrogels on (i) day 1, (ii) day 7, (iii) day 14 and (iv) day 21. Scale bar: 250µm. (B) Schematic showing the plan adapted for migration of hwJMSCs from the center to the periphery of the injectable hydrogel (Made with www.biorender.com) visualized using (C) nucleus staining (blue) and their respective intensity profile surface plot on (i) day 1, (ii) day 7, (iii) day 14 and (iv) day 21. Here, AG denotes the void where the agarose gel was deposited and the IJ denotes the injectable hydrogel. Scale bar: 2000µm*

5.3.3.2 Cellular proliferation and biochemical estimation for ECM deposition by human neo-natal stem cells

Cellular proliferation was evaluated using DNA quantification **(Figure 5.8B).** Cells were found to proliferate as evident from the significant rise in DNA content (>3 times) from 538.96 ± 47.98 ng/construct on day 1 to 1787.64 ± 473.75 ng/construct on day 21 (*$p \leq 0.05$). This rise corroborates the rise in live cell population in the live-dead micrographs. The sGAG content **(Figure 5.8C i)** was also found to rise in tandem with the DNA content and significantly increased (> 5 times) from 113 ± 58.64 µg/construct on day 1 to 552.27 ± 38.23 µg/construct on day 21 (*$p \leq 0.05$). When normalized with the DNA content on the respective days, the sGAG content was found to rise steadily from 262.11 ± 18.48 ng/ng DNA on day 1 to 321.74 ± 68.20 ng/ng DNA on day 21 **(Figure 5.8C ii)**.

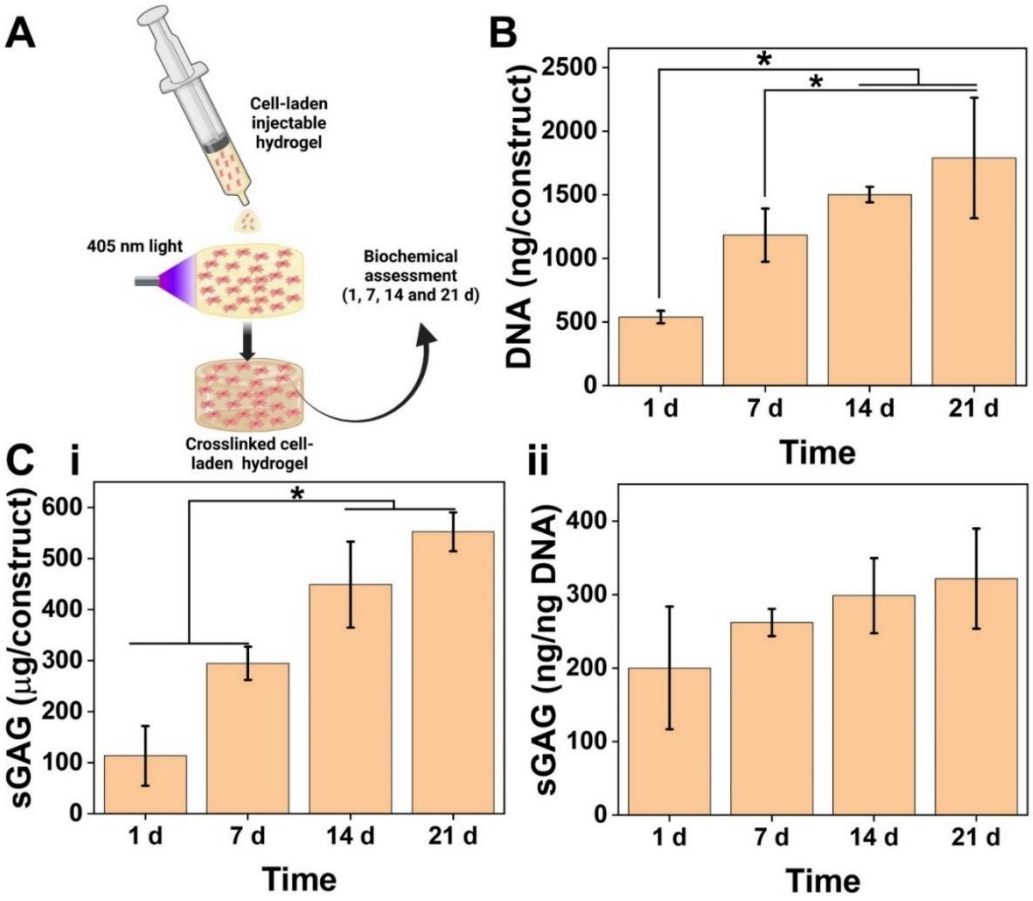

Figure 5.8: *(A) Encapsulation of hwJMSCs within the injectable hydrogel composition for further in vitro evaluation (Made with www.biorender.com). (B) DNA content, (C)(i) sGAG content and (ii) sGAG content normalized with DNA content quantified for hwJMSCs encapsulated within crosslinked hydrogels for day 1, 7, 14 and 21. *$p \leq 0.05$*

5.3.3.3 *In vitro* response of macrophages

Murine macrophages were stimulated minimally by the exposure to constructs and the leachates derived from them, when compared to the positive control of LPS and were found to possess similarity to TCP conditions for both TNF-α **(Figure 5.9A ii)** and IL-1β **(Figure 5.9A iii)** release. As compared to the 4144.9±99.5pg/ml of TNF-α released by the macrophages treated with LPS, the leachate medium (LM) treated macrophages (1307.2±3.9pg/ml) and macrophages treated directly (1215±48.7pg/ml) by the injectable hydrogel constructs (HYD) released significantly lower (>4 times) concentration of TNF-α and this behaviour was comparable to the TCP control (1280.9±49.4pg/ml). Similarly, the LPS treated macrophages released IL-1β (1097.8±350.7pg/ml) which was significantly higher (>40 times) than the macrophages treated with the leachate medium (LM, 8.9±2.2pg/ml) and the macrophages cultured directly in the presence of hydrogel constructs (HYD, 36±22.9pg/ml). This IL-1β secretion profile by the LM and HYD treated macrophages was comparable to the TCP grown macrophages (8.2±2.9pg/ml).

The human monocyte-derived macrophages were stimulated minimally by the hydrogels and the leachates derived from them, when compared with the TNF-α **(Figure 5.9B ii)** and IL-1β **(Figure 5.9A iii)** release of the positive control treatment of LPS. As compared to the 845.9±45.8pg/ml of TNF-α released by the macrophages treated with LPS, the leachate medium (LM) treated macrophages as well the macrophages treated by the direct presence of the injectable hydrogel constructs (HYD) released significantly lower (>3 times) concentration of 38.2±11pg/ml and 232.9±22.6pg/ml of TNF-α respectively which was comparable to the TCP control (242.7±6.8pg/ml). Similarly, the LPS-treated macrophages released significantly higher (>7 times) amount of IL-1β (204.4±22.8pg/ml) as compared to the macrophages treated with leachate medium (LM, 27.6±13.1pg/ml) and the macrophages cultured directly with hydrogels (HYD, 35.4±14.5pg/ml). This IL-1β release behaviour of LM and HYD was similar to TCP grown macrophages (34.2±1.5pg/ml).

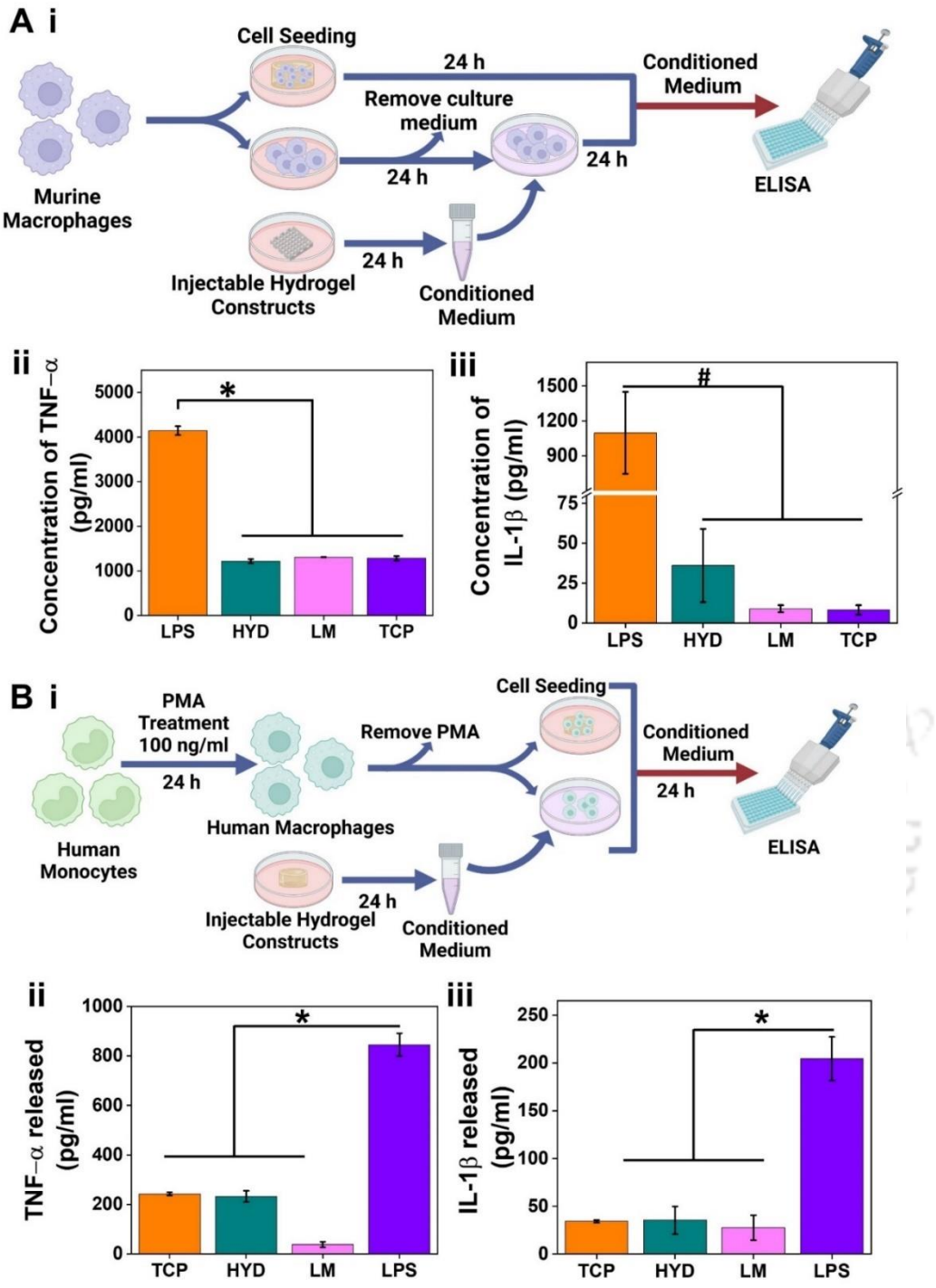

Figure 5.9: *(A) (i) Seeding on injectable hydrogel and injectable hydrogel derived leachate treatment of murine macrophages (RAW 264.7 cells) (Made with www.biorender.com). (ii) TNF-α and (iii) IL-1β secretion estimated using ELISA for murine macrophages. (B) (i) Seeding on injectable hydrogel and injectable hydrogel derived leachate treatment of human monocyte (THP-1) derived macrophages (Made with www.biorender.com). Human (ii) TNF-α and (iii) IL-1β secretion estimated using ELISA for human macrophages while both being cultured on tissue culture plate (TCP) and hydrogel surface (HYD) and treated with LPS (LPS) and hydrogel leachate (LM). *p≤0.05, #p≤0.01*

5.3.3.4 Gene expression profile of encapsulated neo-natal human stromal cells

The gene expression profile of the encapsulated hwJMSCs cultured in non-differentiating media within the hydrogel constructs demonstrated a fibro-chondrogenic bias. The differentiation was evaluated by the expression profiles of collagen Iα (col I), collagen IIα (col II), aggrecan (acan), SRY-box transcription factor 9 (sox-9), runt-related transcription factor 2 (runx-2) and osteocalcin (OCN) genes that were normalized to β-actin (β-actin) as a house-keeping gene **(Figure 5.10A)**. The expression of aggrecan **(Figure 5.10B)** was found to rise from > 2.5 folds on day 7 to ~8 folds on day 14 and be significantly high at >8 folds on day 21 when normalized to day 1. Sox-9 gene was upregulated >6 folds on day 7, >18 folds on day 14 and showed significantly high upregulation of >21 folds on day 21 **(Figure 5.10C)**. In tandem, collagen II was found to be upregulated by >6 folds on day 7, >13 folds on day 14 and showed a significantly high expression of >19 folds on day 21 when compared to day 1 **(Figure 5.10D)**. Concomitantly, an upregulation of >4.9 folds on day 7, >14.5 folds on day 14 and a significantly high >16.9 folds expression was observed for collagen I **(Figure 5.10E)**. Henceforth, osteogenic gene expression profile was also evaluated for the hwJMSCs encapsulated within the optimized hydrogel using runx-2 and osteocalcin expression. Minimal expression of ~0.5 folds on day 7 and day 21 was observed while no expression was observed on day 14 for osteogenic differentiation marker runx-2 **(Figure 5.10F)**. Supporting this, osteoblastic marker osteocalcin (OCN) was found to be expressed only on day 1 ($4.5x10^{-5}$) and unexpressed at later stages of culture **(Figure 5.10G)**.

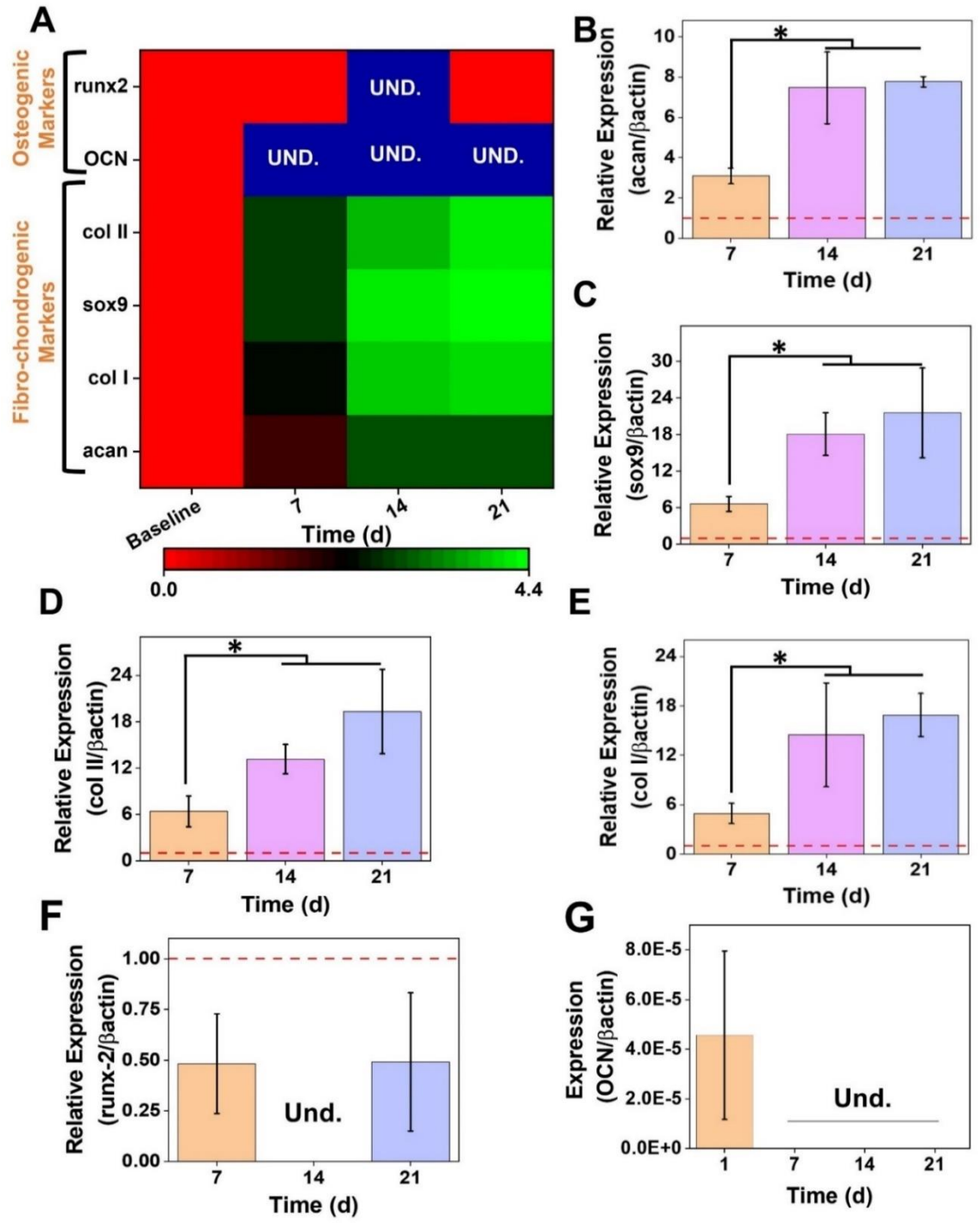

Figure 5.10: *(A) Gene expression profile heatmap showing the variation of fibrochondrocytic and osteogenic genes for hwJMSCs cultured within the injectable hydrogel composition (day 1 values have been used as baseline to normalize fold change values). (B) aggrecan (acan), (C) sox-9 (sox9), (D) collagen II (col II), (E) collagen I (col II), (F) runx-2 or cbfa-1 (runx-2) and (G) osteocalcin (OCN) genes for hwJMSCs encapsulated within crosslinked hydrogels and cultured for 1, 7, 14 and 21 days. runx-2 and OCN have been expressed as ΔCt while the others as ΔΔCt values. *p≤0.05*

5.3.3.5 Meniscus specific ECM deposition *in vitro* by human neo-natal stromal cells

Immuno-stained cryosections were stained and showed deposition of aggrecan and collagen I **(Figure 5.11B i-iv)** in the individual as well as merged images showing colocalized deposition by the cells around the counter-stained nuclei. Similarly, collagen I and collagen II co-stained sections were found to depict similar colocalized deposition of both the ECM proteins in the individual as well as merged micrographs **(Figure 5.11C i-iv)**. The percentage area per FOV **(Figure 5.11D)** was found to be 71.7±14.5% (col I) and 25.5±13.9% (acan) for col I/acan co-stained sections while it was 56.4±14.9% (col I) and 40.4±14.1% (col II) for col I/col II co-stained images.

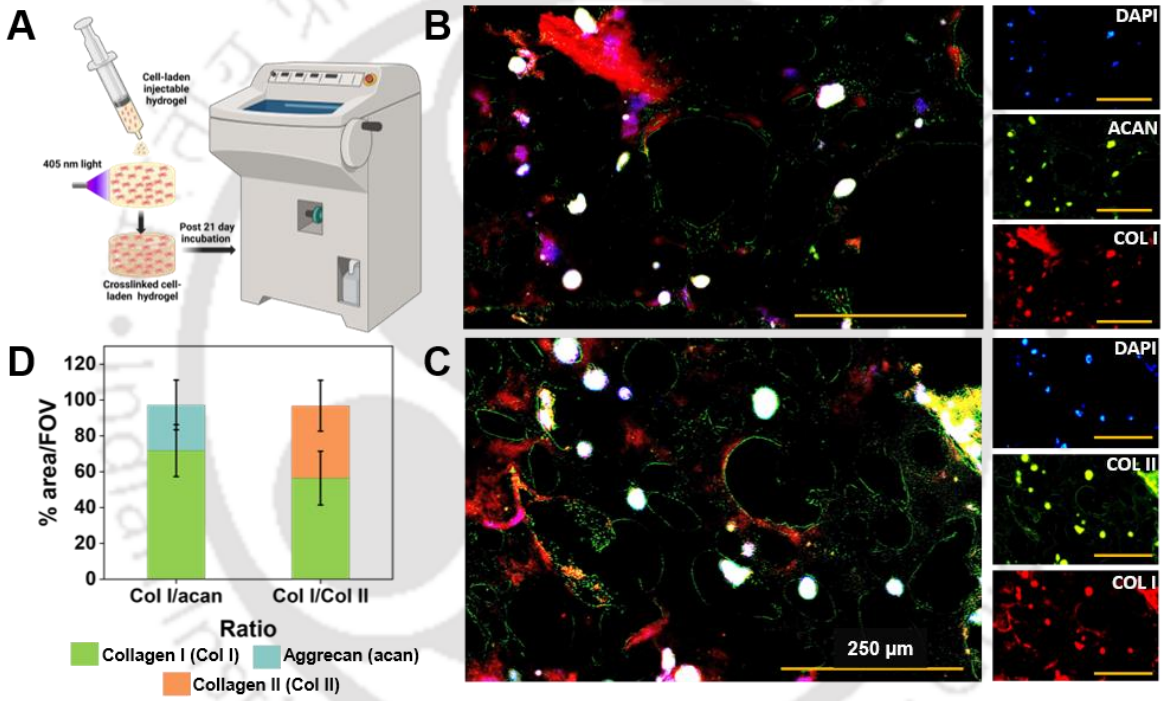

Figure 5.11: *(A) Immunohistochemistry of hydrogel encapsulated hwJMSCs cultured for 21 days (Made with www.biorender.com). Co-stained sections for (B) aggrecan (ACAN, green), collagen I (COL I, red) and nuclei (DAPI, blue) showing the concurrent deposition of aggrecan and collagen I. Co-stained sections for (C) collagen II (COL II, green), collagen I (COL I, red) and nuclei (DAPI, blue) showing the concurrent deposition for collagen II and collagen I. Scale bar: 250µm for all images. (D) Percentage area covered in field of view quantified using ImageJ expressed as ratio for collagen I/aggrecan and collagen I/ collagen II.*

5.3.4 *In vivo* functional evaluation for meniscus healing in rabbits

The pilot scale *in vivo* functional evaluation yielded positive results in the aspect of meniscal healing over 8 weeks. In the first week, animals treated with hydrogel **(Figure 5.12A)** demonstrated the gap being filled with the gel in the cross-sectioned micrographs. Additionally, the MT and SO-FG stains showed cellular migration towards the gap. Concurrently, after 1 week, the blank sample **(Figure 5.12B)** showed no sign of healing or matrix reorganization, and the gross morphology reflected the gap.

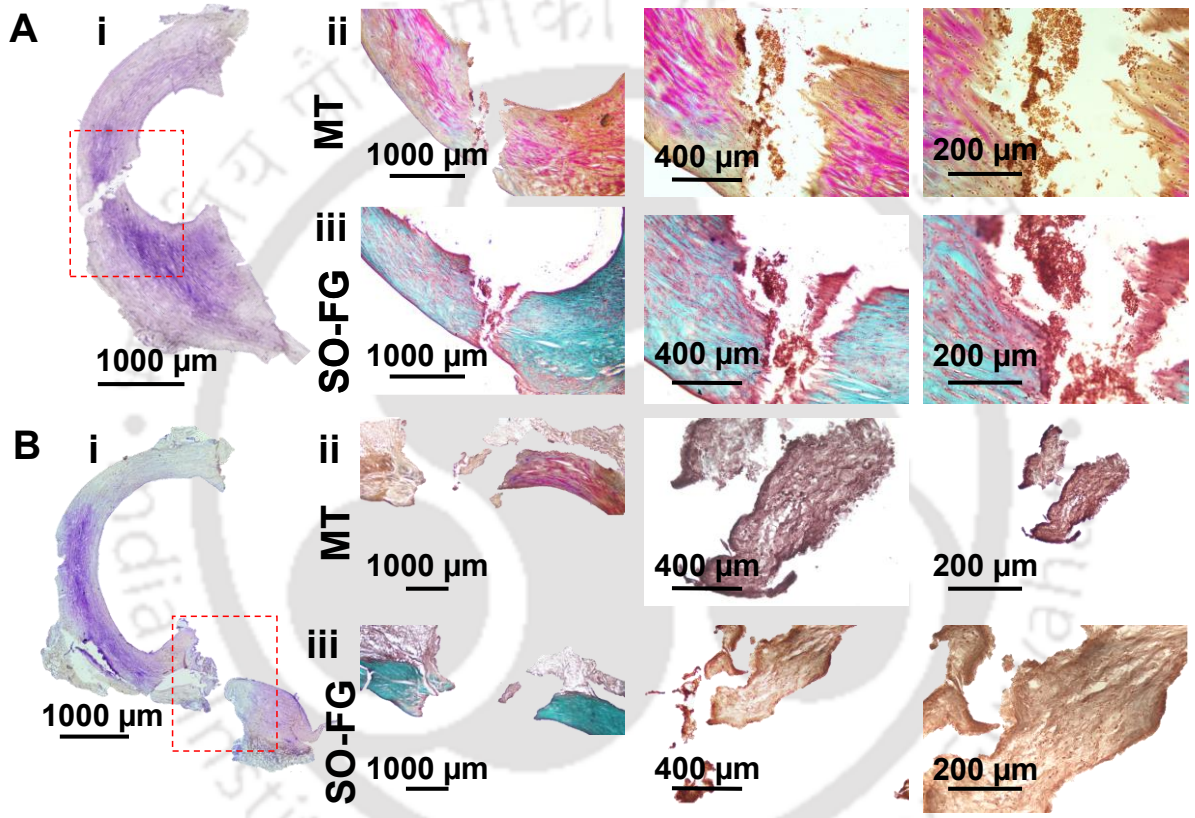

Figure 5.12: *Representative histological images of rabbit menisci with full thickness meniscal defects (A) treated with hydrogel and (B) untreated retrieved from the rabbits 1 week after surgery. (i) Micrographs stained with hematoxylin and eosin, (ii) Masson's trichrome (MT) and (iii) safranin-O and fast green (SO-FG).*

After 8 weeks, the injectable hydrogel-treated animals showed meniscus healing **(Figure 5.13A)** with visible indications of the new matrix formation depicted by the light blue regions within the red stained areas in MT stained **(Figure 5.13A ii)** and the orange region within the green stains in the SO-FG stained **(Figure 5.13A iii)** sections. These indicate the GAG deficient regions with new collagen deposition. Concurrently the untreated meniscus though showed

matrix reorganization in the MT **(Figure 5.13B ii)** and SO-FG **(Figure 5.13B iii)** stained regions but showed no signs of healing after 8 weeks.

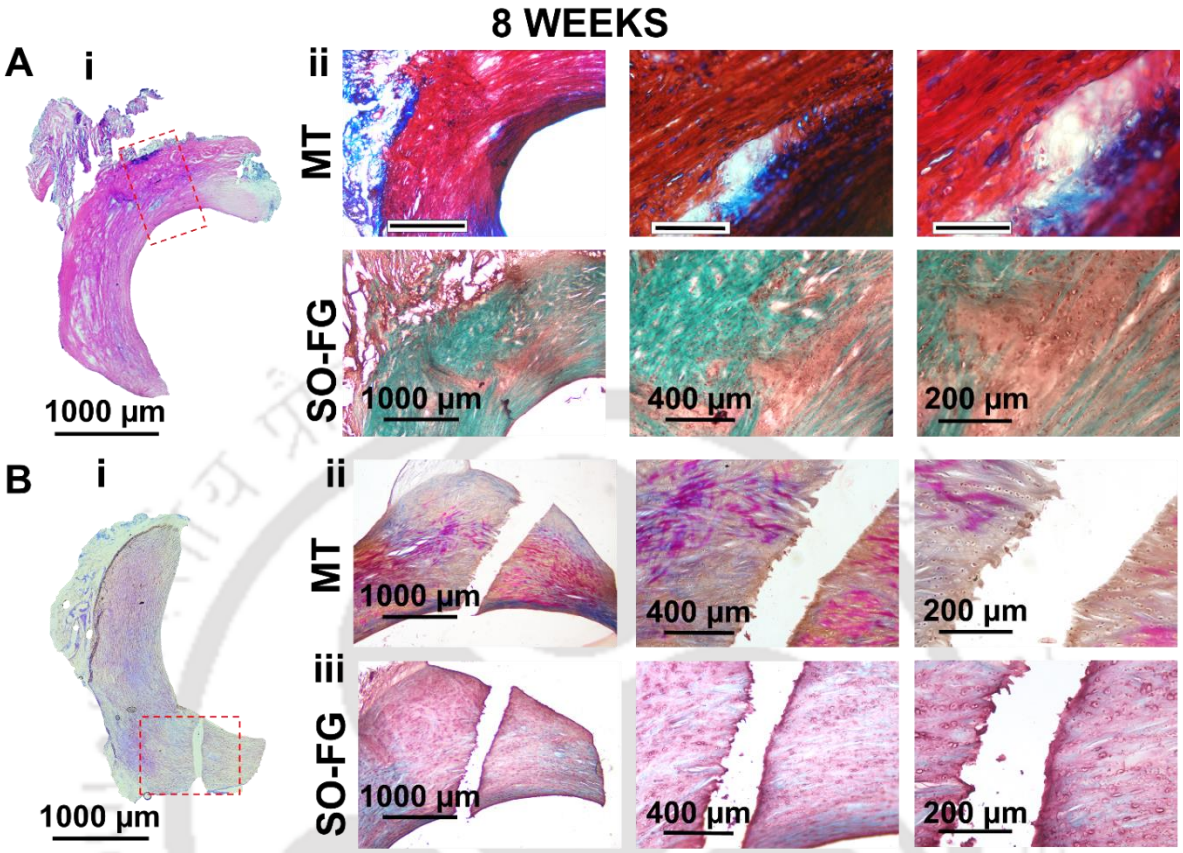

Figure 5.13: *Representative histological images of rabbit menisci with full thickness meniscal defects (A) treated with hydrogel and (B) untreated retrieved from the rabbits 8 week after surgery. (i) Micrographs stained with hematoxylin and eosin, (ii) Masson's trichrome (MT) and (iii) safranin-O and fast green (SO-FG).*

5.4 Discussion

Meniscus tears and injuries in the avascular regions are mosey in terms of healing. Moreover, the healed fibrous tissue formation leads to a mechanically compromised tissue. The resection of menisci in partial form or totality leads to poor long-term knee health and development of osteoarthritis [499]. The development of biocompatible autologous growth factor rich injectable hydrogels is imperative for the formulation of a versatile treatment modality for meniscus tears and injuries. Hereby we have developed a rapid polymerizing injectable hydrogel composition by blending silkMA, gelMA and PEGDA fortified with GFRP (a traditional patient-derived source of growth factors) that could be used for the facile treatment of meniscal tears. The developed in situ photo-crosslinking injectable hydrogel would conform to the irregular defects with the added vantage of being a patient-specific treatment owing to the patient-derived GFRP encapsulation.

We opted for the photocrosslinking approach owing to its facile nature as well as its ability to produce uniform and robust crosslinked structures in ≤60s [435]. This ability also ensures the in situ rapid polymerization ability of our composition under *in vivo* conditions, which ensures quick gelation without the need of mixing multiple components during injection as observed in multi-component hydrogels previously reported for meniscus healing [386]. The presence of silkMA and gelMA ensures biocompatibility as well as cell proliferation, as has been reported previously for applications in cartilage [293, 435] and fibrocartilage [144, 373]. The blend of gelMA and PEGDA has been previously noted for its suitability in the preservation of meniscus cell phenotype and aided in the prevention of dedifferentiation of encapsulated meniscus cells [258]. PEGDA also provides the requisite viscoelasticity, mechanical strength and durability to the hydrogel composition for its long-term stability in loading and unloading conditions [500, 501]. Additionally, the presence of PEGDA and gelMA assists in the shear thinning of the hydrogel composition. This is depicted by the rheological evaluation of the hydrogel composition. The hydrogel undergoes shear thinning in both crosslinked as well as uncrosslinked states showing its flow behaviour, while the viscosity was found to be 1000 folds higher for the crosslinked state. This behaviour ensures the optimal injectability of the hydrogel composition at ambient temperature of ~25°C. Our hydrogel composition undergoes temperature induced thinning at body temperatures (>25°C) similar to other synthetic polymers [387] and polymer composites [385], this would aid in the uniform spreading of the hydrogel and covering of the defect at body temperatures. While post crosslinking, the hydrogel retains it viscosity and undergoes no or minimal temperature induced thinning. The thermal and

variable shear frequency stability illustrated by our injectable hydrogel is further corroborated by the thixotropy test, where the hydrogel showed retention of gel strength under injection-mimicking high shear durations in a repeated fashion. Another perspective that needs to be stressed upon is the porosity and internal microarchitecture of the hydrogel. These influence the encapsulated autologous GFRP-derived growth factor release from the hydrogels, cellular infiltration into the hydrogel as well as nutrient transfusion through the hydrogel for the survivability of the cells. The formulated hydrogel composition showed optimal porosity (~47%) as could be seen from the hexane displacement method and was further corroborated by the electron micrographs which showed an interconnected network of macro and micro porous architecture decorated with the presence of GFRP proteins. The average pore size could be calculated from the electron micrographs and they were found to be apt for cellular proliferation, migration and infiltration within the hydrogels [417]. The pore sizes varied, and the average pore sizes were in the range of ~49-68 µm. These were corroborated with the swelling ratio of ~1.2 times by the hydrogel constructs within the first 24 h of incubation, showing its ability to reach equilibrium, necessary for the expedited exchange of nutrients and metabolites as well as growth factors [502]. Furthermore, the slow degradability of the hydrogels ensures their ability to retain their position within the body and perform their function, herein the regeneration of avascular regions of the menisci. The inhibited regenerative capacity of the target region would imply the incorporation of a growth factor rich hydrogel with a fairly slow degradation rate delivery vehicle to accommodate the regeneration in the region [301, 454]. Our hydrogel constructs showed clinically relevant degradation rates of <50% in enzymatic and <10% in saline over 12 weeks, which is required for the stabilization during initial healing of the avascular regions of the meniscus [503]. Furthermore, the constructs showed a sustained cumulative release of ~70% GFRP proteins over the period of 40 days**.** Our hydrogel was found to mimic the ability to act a reservoir of cocktail of autologous growth factors (GFRP) as reported in literature with other growth factors [385, 504].

Mechanical strength of meniscal repair modalities plays a very crucial role for its sustenance under the loading conditions borne by it within the knee joint [46, 107]. The knee joint physiology provides immense mechanical loading and unloading for several thousand cycles every day on the menisci. Hence, it is imperative that the treatment modalities should be able to bear the mechanical loading and unloading cycles for a longer duration of time. We observed the stability of our hydrogel constructs by providing 60% confined compressive load post swelling equilibrium as well as a hyper-physiological 20% confined compressive cyclic

load [46, 416] of 42000 cycles cumulatively at 1, 3, 5, 7, 14 and 21 days. The constructs were stable over the whole duration of 21 days and could resist the repetitive loading and unloading cycles and register no breakage at 60% loading as well. We observed our hydrogel to be highly stable and possessing at par or better compressive and tensile properties to the previously reported meniscus healing hydrogel compositions of dECM [382], gelatin/alginate [384], collagen/alginate [383] and fibrin gel [386]. This in turn suggests the stability of the meniscus while the patient undergoes initial de-loading and any limited mobility required during the meniscus repair and regeneration [503]. A shear-induced rise in mechanical strength could be observed on day 3 which sustained till day 5 and the strength dropped slowly over the next consecutive loading unloading cycles. This initial rise of mechanical strength maybe attributed to the rise in β-sheet content caused by incubation in saline in the presence of ions and the stress-induced hardening [373]. The compressive and young's moduli of our hydrogel constructs were well above the native moduli of porcine [418] and human menisci [31]. Further, the tensile retention properties of the hydrogel formulation were evaluated using a custom designed test on porcine meniscus samples. A major radial defect was created and treated by our hydrogel composition and the tensile extension was found to have no significant effect on the retention and stability of the filled defect region. The tensile young's modulus suggests the ability of our hydrogel composition to bear tensile loading during the healing process.

Further the biological evaluation of our hydrogel was carried out using hwJMSCs which were encapsulated within the hydrogel and cultured for various durations**.** The hydrogel constructs showed favourable environment as shown by the live dead micrographs. The cells were found to be evenly distributed within the hydrogels and an increase in their population was also observed over the period of 21 days. Concomitantly cellular migration towards our hydrogel composition from agarose gel was observed using agarose drop assay. Migrated cellular population rose significantly as could be seen on day 21 as compared to day 1. The stem cells were found to differentiate into fibrochondrogenic phenotype within the hydrogel and deposit ECM corresponding to their nature. The signs of stem cell differentiation could be found in the gene expression profile where fibrochondrogenic genes, i.e., aggrecan, sox-9, collagen I and collagen II [481, 482] were found to be upregulated significantly on later culture periods. Furthermore, osteogenic genes were checked for signs of ectopic mineralization. Early osteogenic marker runx-2 [483] as well as late osteogenic marker osteocalcin [484] were found to be down-regulated or remained unexpressed in later culture time points which negated our hypothesis of any ectopic mineralization and graft failure. The differentiation was supported by

the deposition of sGAG which was biochemically quantified to rise by ~4 times per hydrogel construct. Moreover, the immunofluorescence staining of the cryo-sectioned hydrogels depicted the hallmark ECM proteins, i.e., collagen I, collagen II and aggrecan deposition in the vicinity of the cells within the hydrogel constructs which is imperative of the fibrochondrogenic differentiation [485, 486]. Moreover, the image-based quantification of deposition of collagen I and collagen II from their fluorescence tagged micro-graphs showed a higher fraction of collagen I expression than collagen II which is a vital characteristic of the fibrochondrogenic tissue [18].

Immuno-compatibility is an important characteristic of any tissue engineering modality including hydrogels. To prevent graft rejection and further complication related to acute inflammation and the interference in tissue integration would prove to be detrimental for the hydrogels and hence need to be addressed beforehand [488, 489]. We evaluated the immuno-compatibility of our hydrogels *in vitro* and could observe minimal inflammatory cytokine (TNFα and IL-1β) release both by the murine as well as human macrophages. They were found to remain unstimulated in the presence of the bulk hydrogels as well as when treated with the leachates from the same. This is in tandem with the previous reports of our silk-based hydrogel blends [424, 425] both under *in vitro* as well as *in vivo*. The pilot scale functional evaluation of the hydrogel composition *in vivo* in full thickness meniscus tear rabbit model showed promising healing of the treated menisci after 8 weeks. As compared to the no-treatment control the gel treated menisci were found to be largely healed after 8 weeks and could be seen undergoing matrix reorganization, as observed in previous instances [385]. This accelerated healing indicates that the hydrogel could be further translated into a larger animal study in the future and further into pre-clinical trials.

The extensive physicochemical, mechanical and biological evaluation carried out for the photo-crosslinkable GFRP loaded injectable hydrogel composition suggests potential acellular implantation potential in treating small full-thickness defects and tears of the menisci. The quick crosslinking endowed by the photo-crosslinking modality, the presence of growth factor cocktail due to the encapsulation of GFRP, high mechanical strength, slow degradability, optimal swelling behaviour, cordial cellular proliferation and migration of encapsulated cells and the minimal immunogenicity elicited *in vitro,* highlight the suitability of our hydrogel composition for use in meniscal tissue regeneration and engineering applications. Further extensive *in vivo* functional evaluation in larger animal models could be carried out to determine pre-clinical potential of the hydrogel blend.

5.5 Salient outcomes and Findings

1. We developed a shear-thinning photocrosslinking injectable hydrogel loaded with autologous growth factors that possessed clinically relevant physicochemical, mechanical and biological properties for treating small meniscus defects.
2. The formulated silkMA/gelMA/PEGDA/GFRP hydrogel exhibits rapid photopolymerization under 405 nm light in 60 s.
3. The crosslinked hydrogels presented physiologically relevant long-term compressive mechanical characteristics and compressive strength mimicking the native human menisci and an amicable tensile strength.
4. Our hydrogel composition possesses optimal swelling, elaborate microporosity and sustained release of GFRP proteins for 40 days *in vitro*. Further, our hydrogels were stable under enzymatic conditions for >12 weeks *in vitro*.
5. The developed hydrogel composition was conducive to the migration and proliferation of encapsulated hwJMSCs, leading to the significant production of sulphated glycosaminoglycans (sGAG).
6. The presence of growth factor rich plasma could also aid in the differentiation of encapsulated stromal cells to fibro-chondrogenic lineage as implied from the gene expression profile and the immunohistochemical staining post 3 weeks of *in vitro* maturation showing significant collagen I, collagen II and aggrecan deposits.
7. Our hydrogel triggered a minimal inflammatory response in murine and human macrophages *in vitro*. The hydrogel was injected in full-thickness meniscus defects in rabbits for a pilot scale *in vivo* functional study, revealing the healing of created meniscus tears over 8 weeks.
8. We hypothesize that our developed hydrogel composition could be of pre-clinical and clinical relevance for potentially treating irregularly shaped partial and full-thickness meniscal tears.

CHAPTER 6

Evaluation of low intensity pulsed ultrasound actuation augmented maturation of human neonatal stromal cell-seeded autologous growth factor loaded silk-based 3D printed meniscus constructs

This chapter describes the effect of low intensity pulsed ultrasound (LIPUS) actuation on maturation of human neo-natal stem cell seeded GFRP loaded constructs. The constructs were 3D printed using the pre-optimized human GFRP loaded silkMA/gelMA/PEGDA hydrogel. Varying intensities of therapeutic LIPUS (100-300 mW/cm2 at 1MHz and 50% duty cycle) were applied for 20 minutes at a stipulated time every day and compared with the static stem cell seeded constructs. The study delves into the mechano-transductory roles of low intensity pulsed ultrasound (LIPUS) in regulating the inflammatory cytokines, fibro-chondrogenic differentiation markers and ECM synthesis of wJMSCs seeded onto 3D printed constructs in an effort to determine the accelerated regeneration of the avascular regions of the menisci. Physiologically relevant LIPUS intensities were identified for best anabolic effects and enhanced fibrochondrogenic differentiation.

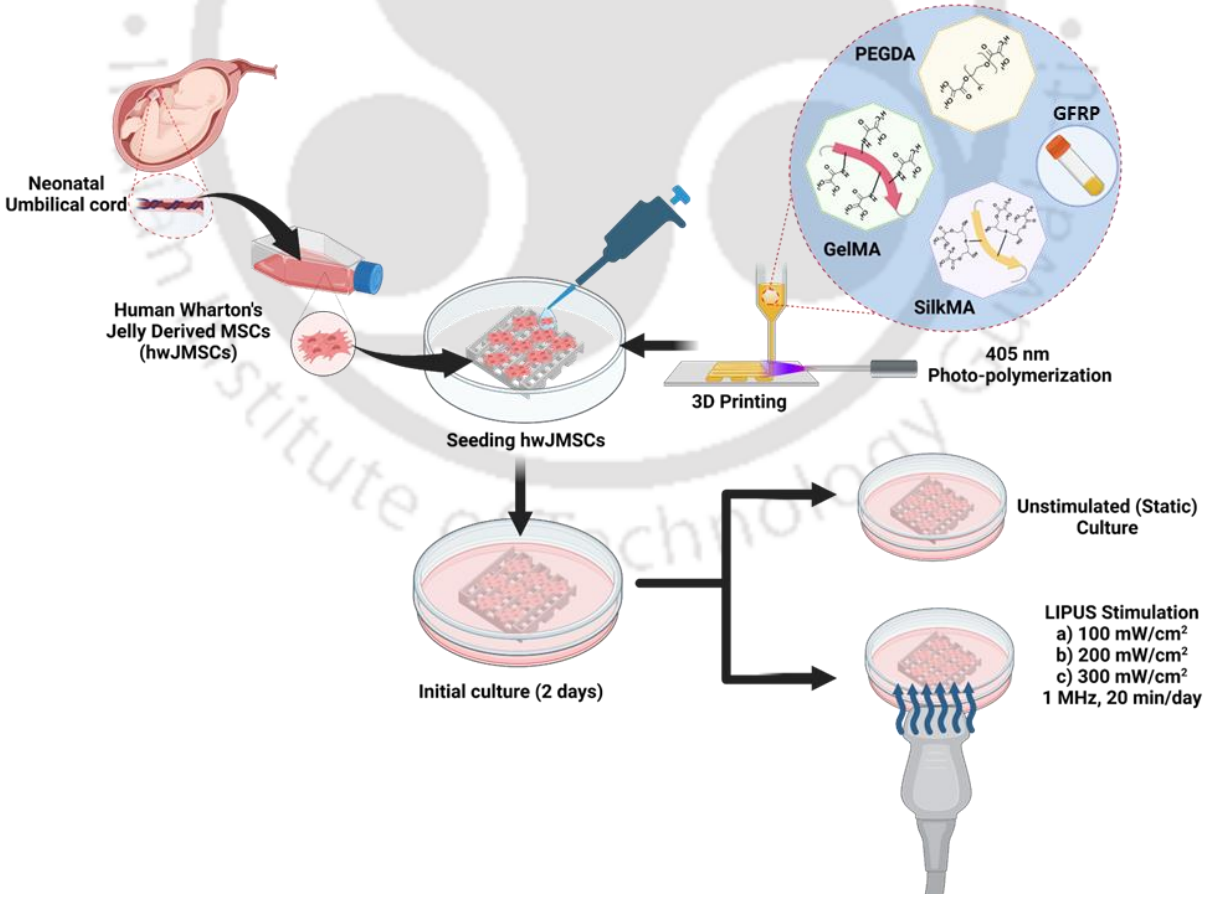

Outcomes of this chapter are under peer review in 'Advanced Healthcare Materials' as:

Ashutosh Bandyopadhyay, Ananya Dutta, Biman B. Mandal. *Ultrasound assisted maturation of 3D printed meniscus constructs loaded with stem cells and autologous growth factors in vitro*.

ABSTRACT

Knee meniscus fibrocartilage tissue is a largely avascular tissue that often suffers tears and injuries. Menisci are typically reported to undergo compromised healing and are often resected out partially or totally with a high risk of knee osteoarthritis. Mechanical stimulation has been reported to augment healing in menisci encompassing accelerated cellular proliferation and extracellular matrix (ECM) deposition. Here we have investigated the effect of low intensity pulsed ultrasound (LIPUS) based actuation on human stem cell seeded GFRP-loaded photo-polymerized silk-based 3D printed constructs. We provided varying energies of LIPUS (100-300mW/cm^2, 1MHz, 50% duty cycle) for 20 min/day and compared the effects to an unstimulated control (UC). DNA based cellular proliferation, biochemical quantification of sulphated glycosaminoglycans and hydroxyproline, gene expression profile of mechano-transduction, inflammatory, matrix degradation, and fibro-chondrogenic differentiation markers and immunostaining of collagen I/collagen II were carried out for LIPUS and UC conditions. In silico gene-gene and protein-protein interaction analysis revealed potential pathways involved in the LIPUS treatment. We found 200mW/cm^2 as a suitable high-physiological LIPUS intensity for accelerated fibrochondrogenic differentiation and ECM deposition as compared to UC. 100mW/cm^2 induced low-physiological stimulation and a chondrogenic bias while 300mW/cm^2 induced hyper-physiological inflammatory bias. 200mW/cm^2 could be further investigated *in vitro* and *in vivo* as a potential tissue maturation or treatment modality for meniscus tissue.

6.1 Introduction

Knee joints comprise of various skeletal tissues such as bone, ligaments, articular cartilage and fibrocartilage arranged in a fashion to bear the load of the body and ensuring smooth movements. The set of two meniscal fibrocartilages, lateral and medial, are majorly avascular tissues which endure the whole load of the upper body and act as cushions. They are prone to major hyper-physiological shear injuries called meniscal tears [42]. Their avascular nature presents the problem of non-healing which leads to knee joint inflammation, pain and osteoarthritis if left intreated. Currently suturing of tears, resection of the torn portions [2, 378] and few natural [463], synthetic [89] or hybrid materials [421] based meniscal implants are the clinically viable options. Though a short-term limited protection of articular cartilage can be observed, there is compromised or no healing of the tears with compromised mechanical strength scar tissue leading to delayed but certain osteoarthritis at later stages [377, 491]. Impaired implant conformation, infection risks from allografts and compromised tissue integration [79, 464, 505] act as precedents for the research and development of knee meniscus treatment modalities to achieve implant integration and healing of meniscal tears.

Platelet rich plasma lysate (PRP) has been used in traditional medicine as a remedy for tissue regeneration and repair [506, 507]. PRP is endowed with growth factors that have been known to possess fibrochondrogenic differentiation potential [508, 509] and possess anti-inflammatory characteristics [510]. In the past decade, 3D printing has emerged as the state-of-the-art technique for fabrication of patient specific scaffolds and constructs ideal for regeneration of tissues [204]. These treatment modalities could be combined in order to produce constructs that comply with the patient-derived shape and size of the meniscus as well as are loaded with patient-derived growth factors for unhindered healing potential of the avascular menisci. Furthermore, these constructs would assist in the homing and differentiation of mesenchymal stromal and progenitor cells in the vicinity and assist in the regeneration of menisci. Low intensity pulsed ultrasound (LIPUS) is the therapeutic form of mechanical ultrasound (with $<3W/cm^2$ energy and 0.75-1.5MHz frequency) that has demonstrated tissue regenerative potential for osteochondral tissues [511-514] and wound healing [515]. The hypothesis behind the anabolic effects demonstrated by LIPUS is based on the mechano-transduction caused in the pericellular matrix (PCM) and the consequent stimulation of extracellular matrix (ECM) synthetic pathways under physiological loading [516]. Hyper-physiological loading has been known to upregulate catabolic pathways and inflammatory response in various tissues and hence could be studied as a negative control [516].

Herein, we have used our pre-optimized human sourced GFRP loaded silk-based biomaterial-ink composition to 3D print meniscal tissue engineering scaffolds that are seeded with human Wharton's jelly derived mesenchymal stromal cells (wJMSCs). These constructs have been stimulated with varying intensities of LIPUS (100 mW/cm^2, 200 mW/cm^2 and 300 mW/cm^2) at 1MHz and 50% duty cycle for 20 minutes/day and compared with the static cultured wJMSC-seeded constructs. The present approach delves into the study of mechano-transductory roles of LIPUS in regulating the levels of inflammatory cytokines, fibro-chondrogenic differentiation markers and ECM synthesis of wJMSCs seeded onto autologous growth factor loaded constructs in an effort to determine the acceleration that could be achieved for regeneration of the avascular regions of the menisci. Our study focuses on the expression of genes pertaining to mechano-transduction (Rho-A, ROCK-1, YAP, Integrin α5, Integrin β1), inflammatory cytokines (IL-1α, cox-2, NF-κB), matrix degrading enzymes (MMP9, ADAMTS-4), and fibro-chondrogenic differentiation (aggrecan, collagen I, collagen II, sox-9). Also, we have conducted cellular proliferation evaluation, biochemical estimation of ECM components (sulphated glycosaminoglycans, sGAG) and immuno-histochemical staining of ECM components (collagen I and collagen II). We demonstrated the anabolic and catabolic effects of LIPUS intensities on the maturation of wJMSC seeded GFRP loaded constructs. This would aid in enhancing our understanding of the positive effects of LIPUS that could be imperative of a difference in healing of avascular meniscal tissues *in vivo*.

6.2 Materials and Methods

6.2.1 Formulation of Biomaterial-ink Composition and its characterization

6.2.1.1 Synthesis of biopolymers and isolation of freeze-dried GFRP

Methacrylated *B. mori* silk fibroin (silkMA) was prepared using a pre-optimized protocol [435]. Briefly, *B. mori* cocoons were chopped, degummed, washed thoroughly, and air dried to obtain the degummed fibres. Lithium bromide (LiBr, 9.3M) was used to dissolve degummed fibers and under stirring glycidyl methacrylate (GMA) was added to the silk-LiBr solution. After 3h of reaction under heat and stirring, the solution is dialysed using a 12-14kDa cut-off dialysis membrane for 96h to obtain silkMA. Gravimetric determination of silkMA concentration was done for the stock for further use.

Gelatin methacrylate (gelMA) was prepared according to the protocol mentioned previously with slight modification [447]. Briefly, gelatin type A was dissolved in 0.1M

carbonate-bicarbonate buffer (CB buffer, pH 9.2-10.6) and methacrylic anhydride (MA, 94%) was added dropwise to the solution mixture while constantly adjusting the pH to 9. Reaction was stopped by adjusting the solution pH to 7.4 using HCl followed by dialysis for 120h. Dialyzed gelMA was freeze-dried for storage and reconstitution.

Preparation for freeze-dried growth factor rich plasma was carried out by introducing certain modifications in a protocol previously mentioned [469]. Platelet concentrate bags were secured from blood bank of GNRC hospital (Guwahati, Assam, India) with appropriate collection, processing and handling protocols reviewed and approved by Institutional Ethics Committee, Institute of Neurological Sciences Trust, GNRC Hospitals (***Reference no. Inst/AS/2015/RR-2018/EC-104***). Pre-expiry platelet bags from n≥5 donors were transported rapidly to laboratory and centrifuged to separate residual cells such as RBC. Obtained suspension was centrifuged further to obtain the platelet pellet, plasma supernatant was reduced to 1/3rd of the volume and platelet pellet was gently resuspended. This suspension was photoactivated using polychromatic infrared light source (600-1300nm, Philips R95) in petri dishes kept on an ice bath. The growth factor rich activated PRP was centrifuged at 1000xg to remove platelets and obtained GFRP was freeze-dried and cryo-stored under sterile conditions for further use.

6.2.1.2 Formulation of biomaterial-ink blend and its Characterization

A blend of silkMA, gelMA and PEGDA was prepared from autoclaved sterile stocks to reach a final concentration of 5% (w/v), 10% (w/v), 5% (w/v) and filter-sterilized solution of lithium phenyl-2,4,6-trimethylbenzoylphosphinate (LAP, Sigma Aldrich, U.S.A.) was added to this blend to reach 0.4% (w/v) by mixing at 40°C under aseptic conditions. Thereafter the prepared blend was cooled to room temperature and sterile freeze-dried GFRP was added at 0.25 % w/v in a sterile environment and pipetted until a uniform hydrogel is obtained. This biomaterial-ink was further used in our experiments.

Uncrosslinked biomaterial-ink was characterized rheologically through various tests using an MCR 302 rheometer (Anton Paar, Austria) with a stainless steel parallel plate (PP25, 25 mm diameter) and a set gap between the plates of 0.5mm. Temperature sweep of the biomaterial-ink was carried out between 4°C-45°C at constant angular frequency of 1 rad s^{-1} and shear strain amplitude of 1%. Further tests were performed at the printing temperature. Amplitude sweep was performed between 0.001-1000% shear strain and at constant angular frequency of 1 rad s^{-1}. LVER (linear viscoelastic region) was obtained from the amplitude

sweep. Frequency sweep was performed between 0.01 to 100 rad s^{-1} strain frequencies and at constant strain amplitude of 1%. 3ITT (three-interval thixotropy test) was carried out by alternating shear strain amplitude and frequencies between cycles of 1%-1 rad s^{-1} and 100%-100 rad s^{-1} and measuring the complex viscosity of the biomaterial-ink.

Infrared spectroscopy was done for analysis silkMA, gelMA, PEGDA, GFRP, uncrosslinked ink (UBIO) and photocrosslinked ink (CBIO) in their freeze-dried state by placing over the ATR crystal of FTIR (Shimadzu, IR Affinity-1S WL). FTIR spectra was obtained between 500 and 2500 cm^{-1}, at spectral resolution of 4 cm^{-1} and averaged over 32 scans at room temperature and recorded after subtraction of background readings. Characteristic peak changes were identified for all the samples.

6.2.2 3D Printing biomaterial-ink and characterization of 3D printed scaffolds

Biomaterial-ink was 3D printed using a BioX (Cellink, Sweden) bioprinter with extruder set at 18-20°C, print bed set at 10°C, print speed of 5-8 mm/s, a 22G blunt stainless steel nozzle, pneumatic pressure of 150-180 kPa and a crosslinking time of 5s/layer from a distance of 4cm at 100% intensity of the 405nm LED of the printer. Printing resolution, buckling and multi-layer printability was assessed by printing grid designs and custom-made GCODES as described in previous chapters. 3D printed grid scaffolds were used for the various physicochemical and mechanical evaluations and aseptically printed grid constructs were used for biological experiments.

6.2.2.1 Porosity of printed scaffolds

Apparent porosity of 3D printed constructs was analysed using hexane displacement method where, acellular constructs of equal size ($10 \times 10 \times 10 mm^3$, n = 4) were immersed known volume of hexane (V_1) for 20 min each, followed by measuring the rise in hexane after soaking constructs (V_2) and finally measuring the residual volume after removal of hexane-soaked constructs (V_3). Apparent porosity of constructs was calculated according to the equation: $Porosity\ (\%) = \frac{V_1 - V_3}{V_2 - V_3} \times 100$

Here, (V_1 - V_3) denotes volume of hexane impregnated within 3D printed constructs whereas (V_2 - V_3) denotes total volume of construct. Discrepancy in volume of hexane due to evaporation was eliminated by keeping another graduated cylinder with hexane and without constructs as control.

6.2.2.2 Water uptake study

Uptake of saline was assessed for the 3D printed constructs ($10 \times 10 \times 1 mcm^3$, n = 5) by measuring their initial weight post-printing (W_i), immersing them in PBS (pH 7.4, 37°C) and weighing them at various points of time (W_s) until they reached equilibrium. Wet tissue paper was used to dab-off excess during measurements. Uptake ratio was calculated as follows: $Water\ Uptake\ ratio = \frac{W_s}{W_i}$

6.2.2.3 Mechanical strength and degradation under LIPUS stimulation

In vitro compressive modulus and cyclic compressive tests were performed on constructs with daily LIPUS stimulation. 3D printed constructs ($10 \times 10 \times 10 mm^3$) were stimulated with either 100, 200 or 300 mW/cm^2 LIPUS at 1MHz frequency and 50% duty cycle for 20 min/day or kept under static incubation. Compression test was conducted for 3D printed constructs upto 60% compression at 5mm/s crosshead speed using UTM (Instron 5944, USA) and young's moduli were evaluated for the same after 1, 7, 14 and 21 days of LIPUS stimulation. Moreover, a separate set of LIPUS stimulated constructs were subjected to 2000 cycles/day of 15% strain at a crosshead speed of 5mm/s using the UTM for 21 days consecutively and the hysteresis loop for 2000th cycle were plotted for day 1, 7, 14 and 21 for UC, 100, 200 or 300 mW/cm^2 LIPUS stimulation.

Non-enzymatic *in vitro* degradation in PBS^a (PBS pH 7.4 with 0.05 % (w/v) sodium azide) was assessed for the 3D printed constructs with or without LIPUS stimulation (200mW/cm^2,1MHz, 50% duty cycle, 20 min/day) over 21 days while incubating at 37°C. Unstimulated constructs were considered as control for comparison of stability of hydrogels and PBS^a solution was replaced every 2 days for a period of 21 days. Sodium azide served towards prevention of microbial growth. The constructs were weighed and the remaining mass was recorded at different time points. Percentage of mass remaining was calculated as: $\%Weight\ Remaining = \frac{W_r}{W_i} \times 100$

Where, W_r represents weight of construct measured after various timepoints during incubation and W_i represents initial weight of construct post-printing.

6.2.3 Biological Assessment of LIPUS stimulation on cell seeded constructs *in vitro*

6.2.3.1 Isolation of Wharton's Jelly Stem cells and cell seeding on 3D printed constructs

Human umbilical cords were procured from GNRC Hospital (Guwahati, Assam, India) following necessary protocols for collection, processing and handling, reviewed and approved by Institutional Ethics Committee (Institute of Neurological Sciences Trust, GNRC Hospitals; Reference no. **Inst/AS/2015/RR-2018/EC-103**). Cords were collected and transported in ice cold sterile PBS (pH 7.4). Cord tissue samples were washed with sterile PBS, dissected and the obtained Wharton's jelly was put as explants in a 6 well plate and incubated in basal culture medium of DMEM (high glucose, Gibco, USA) supplemented with 10% fetal bovine serum, FBS (Gibco, USA), 1X antibiotic-antimycotic mix (Gibco, USA) and 2ng/ml basic fibroblast growth factor (bFGF). Outcoming migrated cells were expanded further in basal medium till 3-8 passages for further seeding. Aseptically 3D printed constructs were seeded with wJMSCs at density of 10^4 cells mm^{-2} and cultured in basal medium without bFGF for biological evaluation.

6.2.3.2 Stimulation using LIPUS and subsequent culture

The constructs were divided into 4 groups: no stimulation control (**UC**), very low stimulation 100mW/cm^2 (**D100**), low stimulation 200mW/cm^2 (**D200**) and high stimulation 300mW/cm^2 (**D300**). All LIPUS stimulation were provided for 20 min/day using a commercially available ultrasound producing kit which is rated for an output of 100-2000 mW/cm^2 ultrasound waves at 1MHz and 50% duty cycle. Stimulation was carried out for a total duration of 21 days and the samples were collected on days 1, 7, 14 and 21 for different analyses (**Figure 6.1**).

6.2.3.3 Cellular proliferation and biochemical assays

DNA content based cellular proliferation was done for cell seeded constructs (n=4) of each group: UC, D100, D200 and D300 after different incubation of 1, 7, 14 and 21 days. Incubated constructs were collected and digested using papain digestion cocktail (5 mM L-cysteine, 5 mM EDTA, 100 mM Na_2HPO_4 and 125 µg/mL papain, pH 6.2) for 16 h at 60°C.

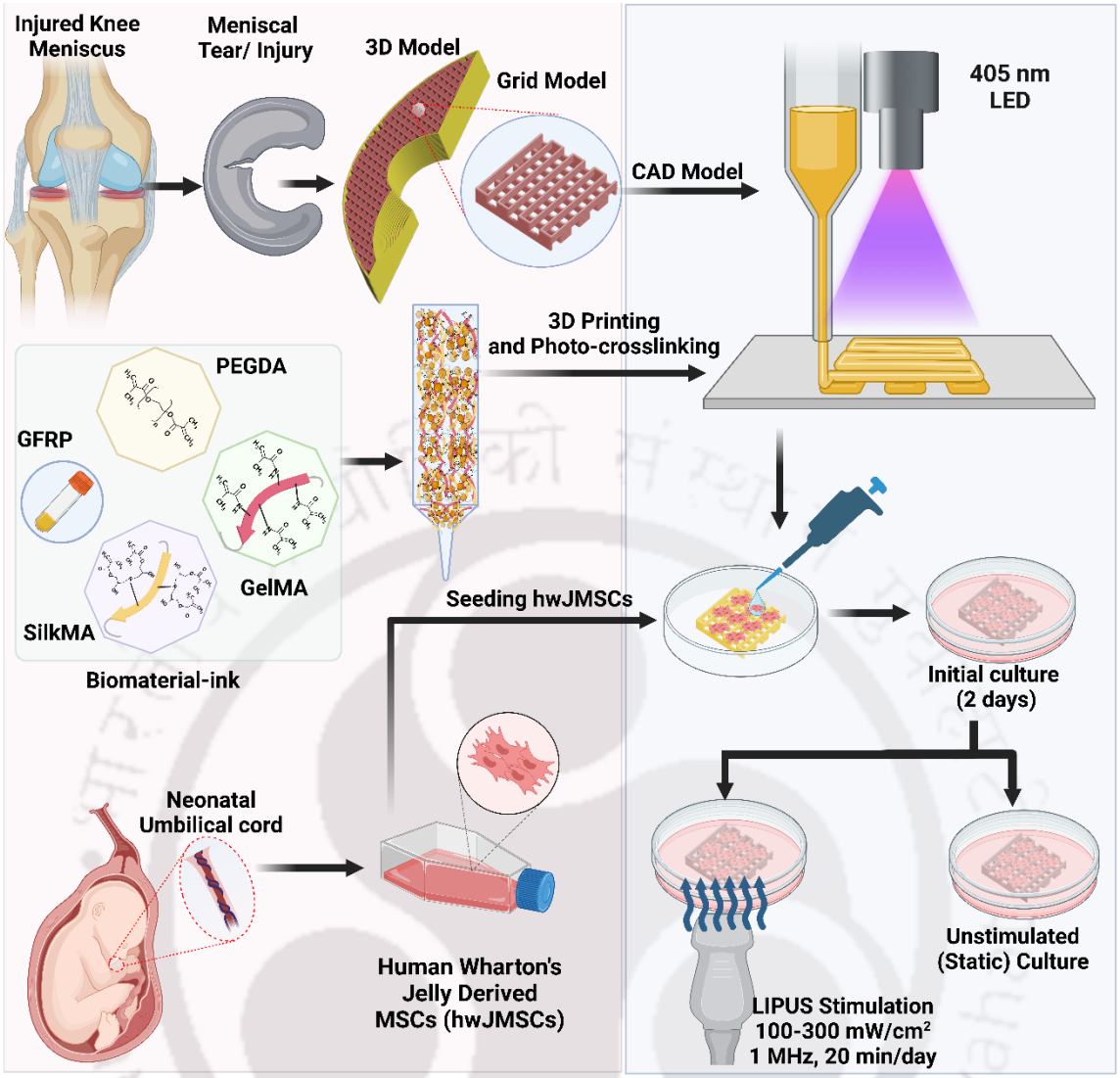

Figure 6.1: *Schematic showing the study where a grid construct fabricated using the GFRP loaded biomaterial-ink is 3D printed and seeded with hwJMSCs and cultured with LIPUS stimulation for the assessment of ultrasound induced effects in vitro. (**Made using www.biorender.com**)*

PicoGreen kit (Invitrogen, USA) was used to estimate DNA content in accordance to the manufacturer's protocol. Papain digested samples were centrifuged, diluted appropriately with TE buffer and added with Quant-iT PicoGreen reagent. The fluorescence readings were taken at an excitation and emission maxima of 480 and 528 nm and compared with a standard curve prepared using lambda phage DNA.

Centrifuged papain digested samples were added with 1,9-dimethylmethylene blue (DMMB) reagent and read for absorbance at 525 nm. A standard curve was prepared using Chondroitin-6-sulfate (Sigma Aldrich, USA) and readings were compared with the same for estimation of deposited sGAG.

Total collagen content was measured by hydroxyproline (HYP) quantification was done for cell seeded constructs (n=4) of each group: UC, D100, D200 and D300 after different incubation of 1, 7, 14 and 21 days. Incubated constructs were collected and acid hydrolysed in an oil bath. Hydrolysed samples were centrifuged and added with p-dimethylamino-benzaldehyde (PDAB, Sigma-Aldrich, USA) and chloramine-T (Sigma-Aldrich, USA) and read at 550nm. A standard curve was prepared using rat tail collagen and used for quantification of HYP content of the constructs.

6.2.3.4 Gene expression profile by Real-Time PCR and In silico gene and protein network prediction analyses

Constructs from UC, D100, D200 and D300 groups were collected and used for complete RNA isolation (n = 4) after different incubation time points of 1,7,14, and 21 days. RNA was isolated using TRIzol (Sigma Aldrich, USA) following pre-optimized protocol. Cell seeded constructs immersed in TRI reagent were chopped with microscissors on ice container. Post-incubation, the chopped constructs were centrifuged at 13000g for 10 min at 4°C. The supernatant obtained was mixed with chloroform, vortexed for uniform mixing and centrifuged to separate the aqueous layer. This upper aqueous layer was carefully removed into fresh tubes and pre-chilled isopropanol was added to precipitate the mRNA, which was then centrifuged to form a pellet. The pellet was washed repeatedly using pre-chilled DNA diluent (EtOH), air dried in laminar flow and reconstituted in nuclease free water. Concentration of obtained mRNA was determined using microdrop spectrophotometric plate on Multiskan Sky (Thermofisher Scientific, USA) followed with cDNA synthesis using high-capacity cDNA reverse transcription kit (Applied Biosystems, USA) and a PCR thermal cycler (Applied Biosystems, USA). Synthesized cDNA was furthered towards real-time PCR cycling using the primer for human genes (sequences as mentioned in **Table 6.1)** and SYBR Green reagent (Invitrogen, USA) in QuantStudio 5 (Applied Biosystems, USA) real-time PCR machine. The results obtained were normalized with respect to β-actin, the endogenous housekeeping gene via ΔC_t method ($2^{-\Delta C_t}$).

GeneMANIA (The GeneMANIA prediction server, https://genemania.org/) was used to analyze the interactions between fibrochondrogenic markers (sox9, col1α1, col2α1, acan), mechano-transduction and cell attachment markers (RhoA, ROCK-1, YAP1, Int-α5, Int-β1), matrix reconstruction and resorption markers (MMP-9, ADAMTS4) and cytokines (IL-1A, NFκβ, PTGS-2). The input genes are used to identify interactions from a large functional

association dataset and the parameters were set to output 15 related genes that are related by co-expression, pathways, co-localization, genetic and protein interactions and protein domain similarities. The network weightage was set to follow biological process based gene ontology.

Table 6.1: *Primer sequences for gene expression analysis*

Gene	Sequence	Accession No.
Human sox-9 (SOX9)	F:5′-TTCCGCGACGTGGACAT-3′ R:5′GGCGGCAGGTACTGGTCAAACTC-3′	NM_213843.1
Human Aggrecan (ACAN)	F:5′-CCCAACCAGCCTGACAACTT-3′ R:5′-CCTTCTCGTGCCAGATCATCA-3′	NM_001164652.1
Human collagen Iα (COL1A1)	F:5′-AGAAGAAGACATCCCACCAGTCA-3′ R:5′-AGATCACGTCATCGCACAACA-3′	XM_021067153.1
Human collagen IIα (COL2A1)	F:5′-CAGGTGAAGGTGGGAAACCA-3′ R:5′-ACCCACGAGGCCAGGA-3′	AF201724.1
Human RhoA (RHOA)	F:5′-TTCGTTGCCTGAGCAATGG-3′ R:5′-TCGGTATCTGGGTAGGAGAGG-3′	NM_001664.4
Human ROCK1 (ROCK1)	F:5′-GAATGTGACTGGTGGTCGGT-3′ R:5′-GCCCTAACCTCACTTCCCTG-3′	NM_005406.3
Human YAP (YAP1)	F:5′-TCCCAGATGAACGTCACAGC-3′ R:5′-GGTTCATGGCAAAACGAGGG-3′	NM_001130145.3
Human Integrin-α5 (INTA5)	F:5′-GGCTTCAACTTAGACGCGGA-3′ R:5′-GGCCGGTAAAACTCCACTGA-3′	NM_002205.4
Human Integrin-β1 (INTB1)	F:5′-GAAGGGTTGCCCTCCAGA-3′ R:5′-GCTTGAGCTTCTCTGCTGTT-3′	NM_002211.3
Human COX-2 (PTGS2)	F:5′-CCCTTGGGTGTCAAAGGTAA-3′ R:5′-GCCCTCGCTTATGATCTGTC-3′	NM_000963.4
Human IL-1α (IL1A)	F:5′-CCAGCCAGAGAGGGAGTCAT-3′ R:5′-CCTTCATGGAGTGGGCCATAG-3′	NM_000575.5
Human NFκβ (NFKB1)	F:5′-GCAGATGGCCCATACCTTCA-3′ R:5′-ACAGTGTTTTCCCACCAGGC-3′	NM_003998.4
Human MMP-9 (MMP9)	F:5′- TTTGAGTCCGGTGGACGATG-3′ R:5′- CTCCTCAAAGACCGAGTCCAG-3′	NM_004994.3
Human ADAMTS-4 (ADAMTS4)	F:5′-CTCAGGGTCCGTTCCTTTGG-3′ R:5′-CCAGACCCCTCAACTATCACC-3′	NM_005099.6
Human Beta Actin (β-actin)	F: 5′-CACCATTGGCAATGAGCGGTTC-3′ R:5′- AGGTCTTTGCGGATGTCCACGT-3′	NM_001101

Additionally, STRING (Search Tool for the Retrieval of Interacting Genes/Proteins, https://string-db.org/, version 12.0) analysis was conducted for the same set of input genes to understand the potential interactions between the proteins expressed by these genes using confidence score of 0.5. Networks showing relevant biological processes, functional interactions, tissue specific associations were obtained for the assessed genes.

6.2.3.5 Immunostaining assessment of matured 3D constructs

Cell seeded 3D printed constructs from all groups: UC, D100, D200 and D300 were collected after 14 and 21 days of culture and stimulation. The collected constructs were preserved in 10% neutral buffered formalin (NBF) for 24 hr, washed gently with PBS, permeabilized using 1% (v/v) triton-X 100 (1 hr, room temperature), blocked using 10% (w/v) bovine serum albumin (2 hr, room temperature) and immuno-stained with mouse mono-clonal anti-collagen I and rabbit poly-clonal anti-collagen II primary antibodies (ABCAM, USA) for 2 hr each at room temperature. Further, secondary Cy5 tagged anti-mouse and FITC tagged anti-rabbit antibodies (ABCAM, USA) were used separately for 2 hr each and counterstained with DAPI (Thermofisher Scientific, USA) for 20 min. The constructs were destained using PBS for 1 hr between each step. The fluorescent micrographs were obtained using an inverted fluorescence microscope (Axio Observer, Zeiss, Germany). Fluorescent micrographs obtained (n=8) were used for calculating the field of view area stained with collagen I and collagen II by using Fiji (NIH ImageJ software) to determine the expression ratio of ECM components.

6.2.4 Statistical Analysis and Image Processing

Experiments that are quantitative by nature were performed in $n \geq 3$ and the results were represented as mean ± standard deviation. For statistical analysis of the data, one way ANOVA was carried out using Tukey's method. Statistical analysis and plotting were carried out with the help of OriginPro 2021 software (OriginLab corporation, USA) to analyse the significant difference between various sampling groups. Variations between groups of $^{*}p \leq 0.05$ were denoted to be statistically significant. All image processing and quantification were carried out using ImageJ and ZenBlue (Zeiss, Germany).

6.3 Results

6.3.1 Characterization of Biomaterial-ink

6.3.1.1 Rheological Characterization of biomaterial-ink blend

The temperature induced change in viscosity was observed in the biomaterial-ink blend from >10^6mPa.s within the range of 4°C to 16°C to below 10^4mPa.s above 16°C and was found to stabilize after that to constant viscosity suggesting the liquification of the blend (**Figure 6.2A**). Hence, the biomaterial-ink blend was subjected to amplitude sweep at 16°C and the biomaterial-ink was found to undergo shear-thinning after experiencing ≥100% shear strain (**Figure 6.2B**). Further the frequency sweep of the biomaterial-ink blend showed a steady drop in viscosity as the frequency increased from 0.01-100 rad/s denoting the shear induced thinning pertaining to the increase in frequency (**Figure 6.2C**). The 3ITT revealed that the GFRP25 blend could undergo multiple cycles of shear thinning. The ink demonstrated complex viscosity change from ~10^8mPa.s in the low shear (mimicking the deposition) conditions to <10^5mPa.s in the higher shear (mimicking the extrusion) conditions (**Figure 6.2D**).

6.3.1.2 Fourier Transform Infrared Spectroscopy

The infrared spectroscopic analysis of gelMA, silkMA, PEGDA, GFRP, UBIO and CBIO was carried out (**Figure 6.2E**). All the protein polymers and the biomaterial-ink blends were found to show the cardinal peaks in the amide I (1710–1590 cm^{-1}), amide II (1570–1480 cm^{-1}) and amide III (1270–1200 cm^{-1}) regions. Peak shifts were observed from amide I (from ~1635 cm^{-1} to ~1650 cm^{-1}), amide II (from ~1546 cm^{-1} to ~1539 cm^{-1}) and amide III (~1247 cm^{-1} to ~1244 cm^{-1}) regions in the uncrosslinked and crosslinked biomaterial-inks when compared with gelMA and silkMA. Moreover, the signature peak was observed in the 1050 cm^{-1} region among the components containing methacrylate groups.

6.3.2 Characterization of 3D Printed constructs

6.3.2.1 Printability of Biomaterial ink

The biomaterial-ink was found to be shear thinning at 16°C, forming a thread like structure when extruded (**Figure 6.2F**). Further, the printing resolution was found to be amicable (**Figure 6.2G**) and printed filaments showed slight buckling for longer bridges (**Figure 6.2H**) which was not observed in printed constructs (**Figure 6.2I-K**) due to the stabilization resulting by layered crosslinking of the constructs.

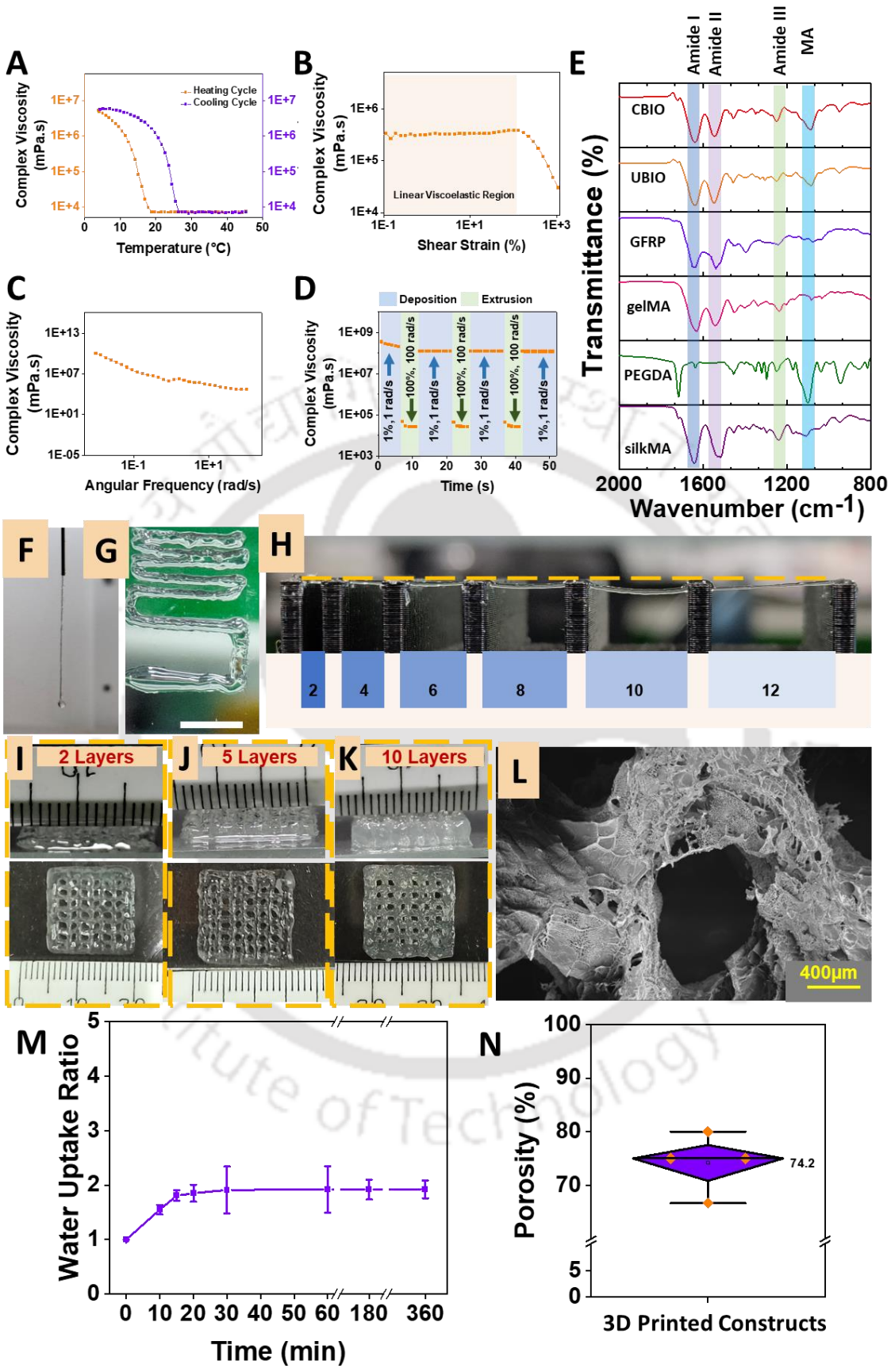

Figure 6.2: *Rheological characterization of GFRP laden biomaterial-ink showing (A) Temperature sweep, (B) Amplitude sweep, (C) Frequency sweep and (D) 3ITT test. (E) FTIR*

spectra of crosslinked (CBIO) and uncrosslinked (UBIO) biomaterial-ink and its various components GFRP, gelMA, PEGDA and silkMA. (F) Extrudability, (G) Printing resolution (Scale bar: 0.5 cm), (H) Buckling test (Scale in mm) and (I) 2-layered, (J) 5-layered and (K) 10-layered printability assessment for the biomaterial-ink. (L) Representative FESEM images of the cross-section of 3D printed construct. (M) Water uptake test for 3D printed grid constructs. (N) Porosity assessment for 3D printed grid constructs.

6.3.2.2 Water Uptake, Porosity and microstructure of 3D printed constructs

The biomaterial-ink blend was used to print constructs that were further subjected to evaluation of saline uptake properties and ensure the nutrient uptake ability. All constructs were found to rapidly uptake water ~2 times of their weight in saline and reached an equilibrium in ~20 min (**Figure 6.2M**). Furthermore, hexane displacement method showed the percentage porosity of the printed struts apart from the macroporous nature of the constructs. The constructs were found to possess ~74% porosity optimal for media holding and exchange (**Figure 6.2N**). The micro-architecture of cross-section of 3D printed struts shows interconnected pores and high porosity of the constructs (**Figure 6.2L**).

6.3.2.3 Effect of LIPUS on degradability and mechanical properties

3D printed constructs were kept in UC as well as LIPUS stimulated (100, 200 and 300mW/cm^2, 1MHz, 50% duty cycle, 20 min/day) conditions (**Figure 6.3A**) to evaluate the degradability of the same for 21 days (3 weeks). There was negligible degradation and the constructs retained >99% of their mass after 21 days (**Figure 6.3B**).

Further, the mechanical evaluation shows minimal deviation of compressive modulus after 1, 7, 14 and 21 days of LIPUS stimulation (**Figure 6.3C**). The compressive moduli increased from 296 ± 19 kPa to 346 ± 4 kPa for D100, 310 ± 14 kPa to 357 ± 18 kPa for D200, 312 ± 23 kPa to 336 ± 21 kPa for D300 and 306 ± 2 kPa to 345 ± 20 kPa for UC condition from day 1 to day 21 respectively.

Moreover, the change in hysteresis curve of the compressive modulus of cycle 2000 on day 21 for all conditions (**Figure 6.3Dii**) shows minimal deviations amongst the groups. The hysteresis curves for cycle 2000 on day 1, 7, 14 and 21 for UC (**Figure 6.3Diii**), D100 (**Figure 6.3Div**), D200 (**Figure 6.3Dv**) and D300 (**Figure 6.3Dvi**) show minimal deviation along the whole period of cyclic stimulation depicting the stability of the constructs under combined stimulation of LIPUS and cyclic compression.

6.3.3 Biological evaluation under LIPUS stimulation *in vitro*

6.3.3.1 Cellular Proliferation

DNA content was quantified and used to determine cellular proliferation over 21 days (**Figure 6.4A**). The DNA content increased for all the experimental groups over the period of 21 days showing cellular proliferation of wJMSCs on all the constructs. A significant increase from 18.5±0.9 ng/mg, 16.8±0.4 ng/mg, 17.8±0.6 ng/mg and 14.4±0.5 ng/mg on day 1 to 86.8±3.1 ng/mg, 90.4±1.3 ng/mg, 94.9±1.3 ng/mg and 58.2±0.2 ng/mg on day 21 was observed in UC, D100, D200 and D300 groups. The DNA content was found to be stunted in D300 group after 7, 14 and 21 days of culture at 46.3±2.4 ng/mg, 58.63±2.9 ng/mg and 61.3 ±1.2 ng/mg respectively which was significantly lesser than the UC, D100 and D200 groups at those respective timepoints. The cellular proliferation was hence found to be reduced significantly for D300 group as compared to the D100, D200 and UC groups.

6.3.3.2 sGAG Estimation

Estimation of sGAG from digested constructs was carried out in order to find the differentiation of wJMSCs towards fibro-chondrogenic phenotype (**Figure 6.4B and 6.4C**). The sGAG content was found to rise significantly from 6.59±1.91 µg/mg, 5.34±0.66 µg/mg, 5.53±1.92 µg/mg and 4.46±0.53 µg/mg on day 1 to 60.69±4.52 µg/mg, 88.44±0.58 µg/mg, 86.76±1.71 µg/mg and 39.4±0.71 µg/mg on day 21 for UC, D100, D200 and D300 groups respectively (**Figure 6.4B**). sGAG deposition in D100 and D200 groups was found to be significantly higher as compared to UC and D300 groups on day 7, 14 and day 21 of incubation. Similar trend was observed when the sGAG content was normalized with the DNA content. The sGAG content was found to rise significantly from 354.52±88.14 ng/ng, 316.98±30.89 ng/ng, 308.26±96.06 ng/ng and 311.46±47.95 ng/ng on day 1 to 699.42±43.52 ng/ng, 937.03±7.33 ng/ng, 914.52±11.56 ng/ng and 642.99±16.92 ng/ng on day 21 for UC, D100, D200 and D300 groups respectively (**Figure 6.4C**). Significantly higher amounts of sGAG was found to be deposited by cells of D100 and D200 groups as compared to D300 and UC. Interestingly the D100 group showed higher sGAG deposition as compared to D200 group suggesting a higher chondrogenic bias.

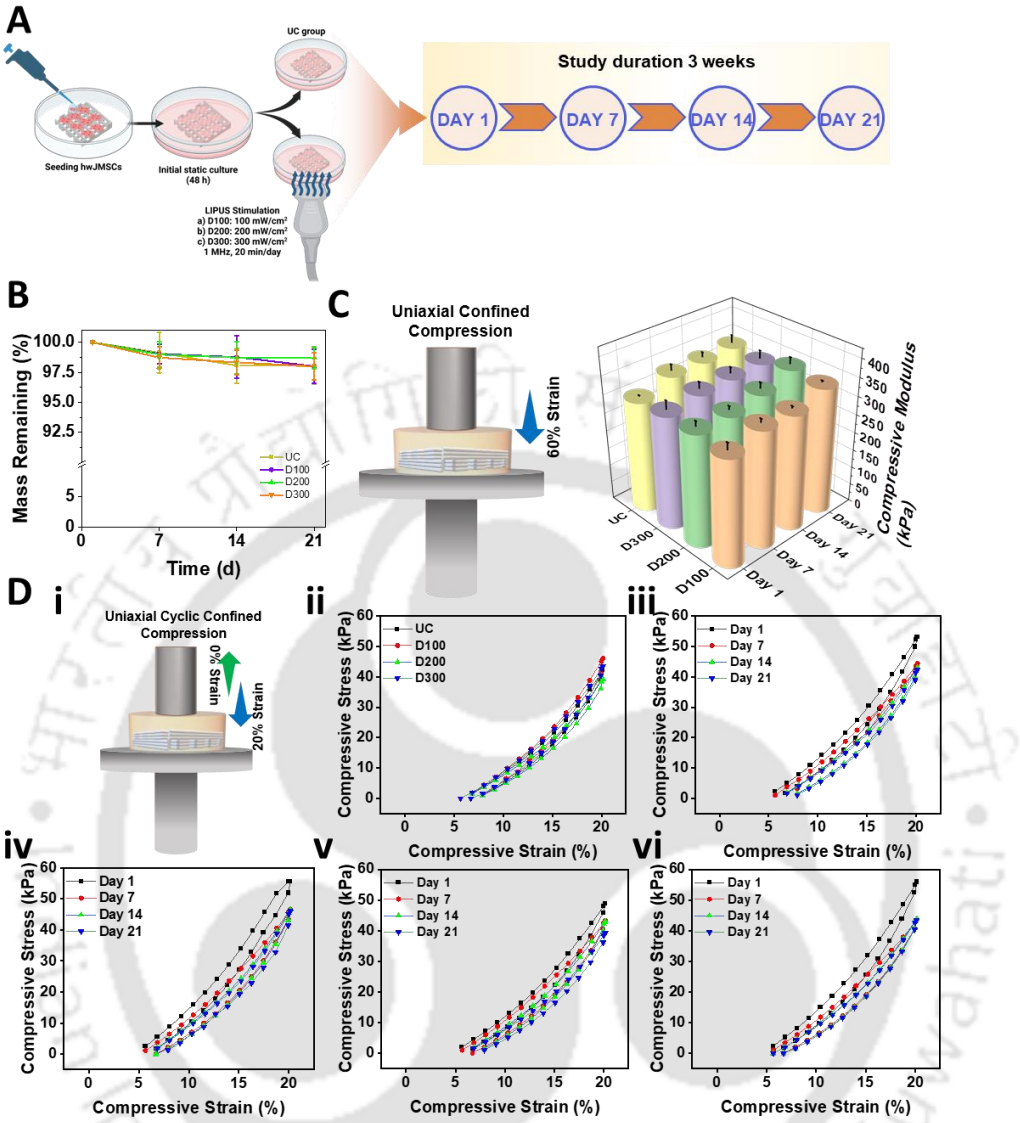

Figure 6.3: *(A) Representative LIPUS stimulation plan for 21 days. (B) Non-enzymatic degradability with and without LIPUS in PBS for 21 days. (Made using www.biorender.com) (C) Uniaxial confined compressive modulus derived from constructs from D100, D200, D300 and UC groups after day 1, 7, 14 and 21 days of incubation in PBS with or without LIPUS. (D) (i) Uniaxial cyclic confined compression conducted for 20% compressive strain on constructs stimulated or unstimulated with LIPUS. (ii) Representative stress-strain hysteresis curve for UC, D100, D200 and D300 groups after 2000 cycles of 20% compressive strain/day for 21 days. Representative stress-strain hysteresis curve for (iii) UC, (iv) D100, (v) D200 and (vi) D300 groups after 2000 cycles of 20% compressive strain/day for 1, 7, 14 and 21 days.*

6.3.3.3 Total Collagen content Estimation

Total collagen content was quantified by estimating the hydroxyproline (HYP) deposited over the constructs by the differentiating wJMSCs under LIPUS stimulation (**Figure 6.4D-E**). The total hydroxyproline content per unit wet weight of constructs was found to be increasing significantly over the period of 21 days from 56.8±1.1 ng/mg to 2715±26.3 ng/mg for D100, 69.4±5.8ng/mg to 2756±108 ng/mg for D200, 71.3±2.5 ng/mg to 1589±45.3 ng/mg for D300 and 77.7±0.9 ng/mg to 2310±73.6 ng/mg for UC groups (**Figure 6.4D**). When normalized with the DNA content of the constructs the HYP content rose from 3.4±0.4 ng/ng to 28.7±0.4 ng/ng for D100, 3.9±0.2 ng/ng to 29±0.9 ng/ng for D200, 4.9±0.3 ng/ng to 26.3±0.5 ng/ng for D300 and 4.2±0.2 ng/ng to 27.5±0.9 ng/ng for UC groups in 21 days (**Figure 6.4E**). The rise in HYP content is significantly higher for the D100 and D200 groups as compared to the D300 group under both normalizations on day 7, 14 and 21 (**Figure 6.4D**). D100 and D200 groups underwent significantly higher HYP deposition when normalized with construct weight as compared to the UC group on day 7, 14 and 21 (**Figure 6.4D**). When normalized with DNA content D100 and D200 show higher HYP deposition (not significant) as compared to the UC group (**Figure 6.4E**). Interestingly the HYP deposition of D300 is significantly lower than even the UC group on day 7, 14 and 21 (**Figure 6.4D**).

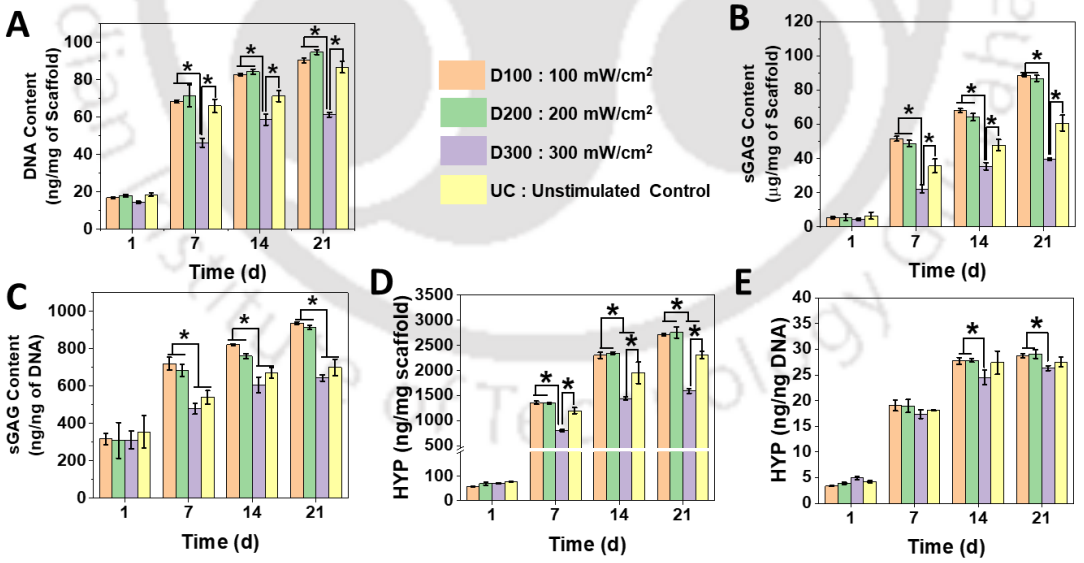

Figure 6.4: *(A) DNA content quantification using picrogreen assay for wJMSC seeded printed constructs after 1, 7, 14 and 21 days of culture. Sulphated glycosaminoglycans (sGAG) content deposited by the wJMSC seeded on printed constructs after 1, 7, 14 and 21 days of culture post normalized with (B) wet weight of constructs and (C) DNA content of the constructs. Hydroxyproline (HYP) content deposited by the wJMSC seeded on printed constructs after 1,*

*7, 14 and 21 days of culture normalized with (D) wet weight of the constructs and (E) DNA content of the constructs. (n≥3, *p≤ 0.05)*

6.3.3.4 Gene expression profile

The gene expression profile were plotted as a heatmap as shown in **Figure 6.5** and **Figure 6.6** and as individual bar-graphs in **Figure 6.6** and **Figure 6.7.**

Fibrochondrogenic Markers

The expression profile of chondrogenic markers was found to be upregulated for UC, D100 and D200 groups. SOX9 (sox-9) was found to be significantly upregulated for D100 (~20.4 times), D200 (~16.4 times) and UC (~12 times) groups on day 21 as compared to day 1 expression, while SOX9 was upregulated (~2.8 times) for D300 group which is significantly lower as compared to the other groups. Similarly, aggrecan (ACAN) expression was found to be upregulated significantly for D100 (~19.2 times), D200 (~18.5 times) and UC (~9.5 times) groups on day 21 as compared to day 1 expression, while D300 group demonstrated minimal upregulated from the basal level (~1.4 times) on day 21. Concurrently, collagen II (COL2A1) expression was also found to be significantly upregulated for D100 (~20.3 times), D200 (~18.03 times) and UC (~11.8 times) groups on day 21 when compared to day 1, while the D300 group showed downregulation on day 7 (~0.96 times), upregulation on day 14 (~1.03 times) and further downregulation on day 21 (~0.58 times). This is indicative of the elevated chondrogenic bias in the D100 group as compared to D200 and UC groups and the D300 group possessed minimal chondrogenic potential. Furthermore, collagen I (COL1A1) was significantly upregulated for D200 (~13.7 times) and UC (~11.94 times) on day 21 as compared to day 1. Concurrently, D300 group showed mild upregulation on day 7 (~1.9 times) and day 14 (~1.85 times) while a downregulation was observed on day 21 (~0.78 times) for collagen I. Similarly, D100 group demonstrated mild upregulation on day 14 (~1.1 times) and downregulation on day 21 (~0.9 times) for collagen I. This is indicative of the limited fibrogenic capacity of the D100 group and reduced ECM production capacity of the D300 group.

Mechano-stimulation Markers

Integrin α5 (INTA5) expression was found to be influenced by the differences in the mechanical stimulation. D100, D200 and UC groups demonstrated upregulated levels of Integrin α5 on day 7 (~5.43 times, ~4.7 times and ~5.46 times respectively) and day 14 (~1.58 times, ~6.22 times and ~7.88 times respectively) as compared to day 1. While Integrin α5

expression drops on day 21 to below basal level for D100 (~0.11 times) and near basal level for D200 (~1.001 times) and UC (~1.04 times) as compared to day 1. On the contrary, the Integrin α5 expression in D300 groups rises slightly above basal level and stays constant on day 7 (~1.34 times), day 14 (~1.44 times) and day 21 (~1.82 times).

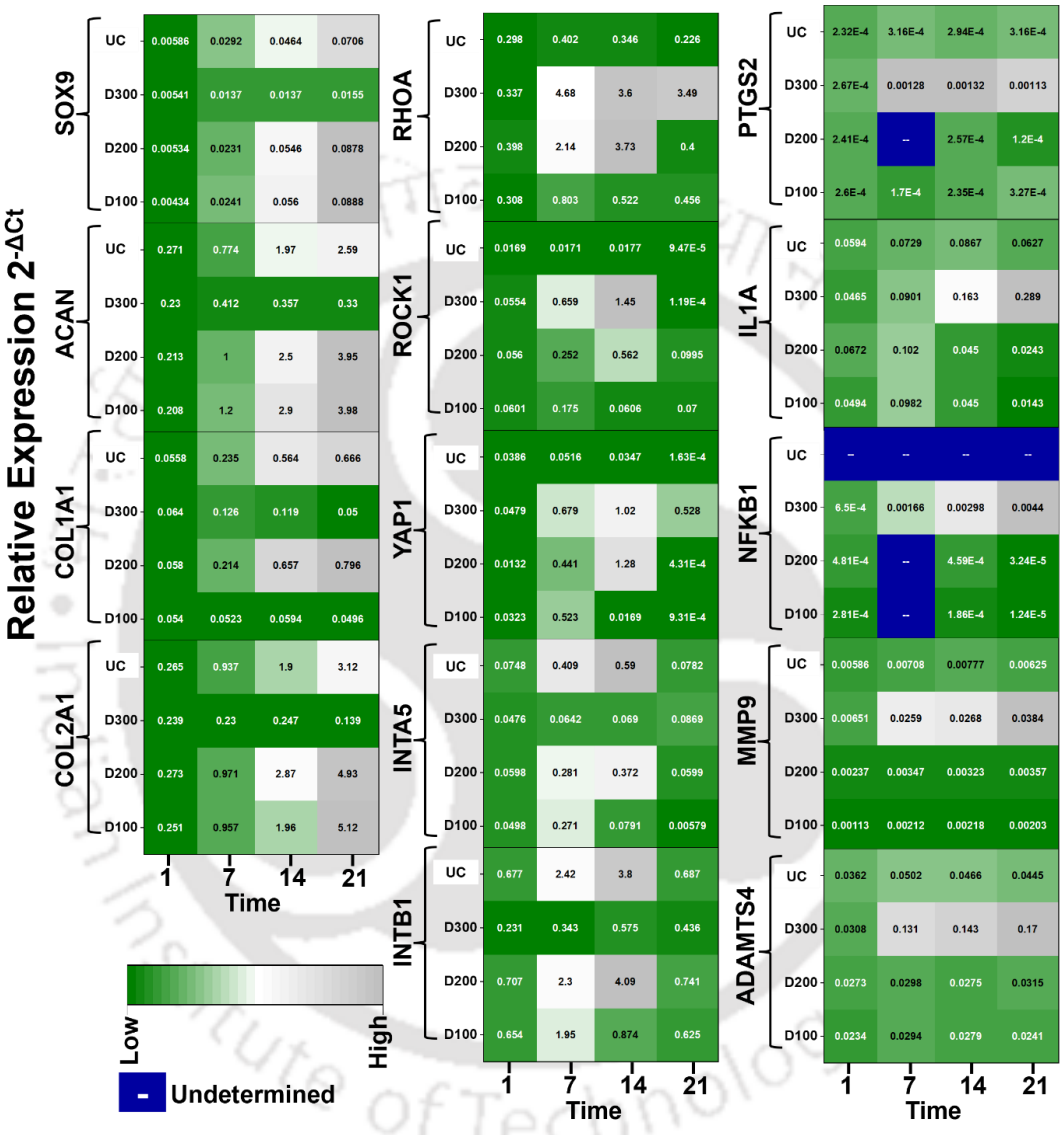

Figure 6.5: *Heatmap representation of gene expression profile with $2^{-\Delta Ct}$ for fibrochondrogenic markers: SOX9, aggrecan (ACAN), collagen I (COL1A1) and collagen II (COL2A1); mechano-transduction markers: RhoA (RHOA), ROCK1, YAP1, Integrin α5 (INTA5) and Integrin β1 (INTB1); inflammatory markers: Cox-2/PTGS2, IL1α (IL1A) and NF-κβ1 (NFKB1) and ECM resorption markers: MMP9 and ADAMTS4 for day 1, 7, 14 and 21 of culture after normalization with β-actin.*

Concurrently, Integrin β1 (INTB1) expression showed a similar trend in response to the mechanical stimulus. D100 group showed significant upregulation of Integrin β1 on day 7

(~2.98 times), while it is downregulated to near-basal level on day 14 (~1.34 times) and below basal level on day 21 (~0.96 times) as compared to day 1. D200 and UC groups demonstrate upregulation of Integrin β1 expression on day 7 (~3.24 times and ~3.56 times respectively) and day 14 (~5.78 times and ~5.61 times respectively) as compared to day 1. While on day 21, Integrin β1 is downregulated to near-basal level for D200 (~1.04 times) and UC (~1.01 times) as compared to day 1. D300 induces upregulation of Integrin β1 above basal level on day 7 (~1.48 times), a rise on day 14 (~2.48 times) and a further decrease on day 21 (~1.89 times) as compared to day 1.

RhoA (Ras homolog family member A) is a marker responsive to mechanical stimulation and hence is found to regulate differently for different stimulation conditions. D100 group demonstrated significant upregulation of RhoA on day 7 (~2.61 times), while it was upregulated slightly above basal level on day 14 (~1.69 times) and day 21 (~1.48 times) as compared to day 1. D200 group demonstrated a significantly higher upregulation of RhoA on day 7 (~5.39 times) and day 14 (~9.37 times) with a steep reduction in expression to basal level observed on day 21 (~1.003 times) as compared to day 1. UC group demonstrated the near basal level expression of RhoA on day 7 (~1.35 times) and day 14 (~1.16 times) with a reduction in expression below basal level on day 21 (~0.76 times) as compared to day 1. In contrast, D300 group showed significantly high upregulation of RhoA on day 7 (~13.91 times), day 14 (~10.68 times) and day 21 (~10.35 times) as compared to day 1 demonstrating the effect of high stimulation.

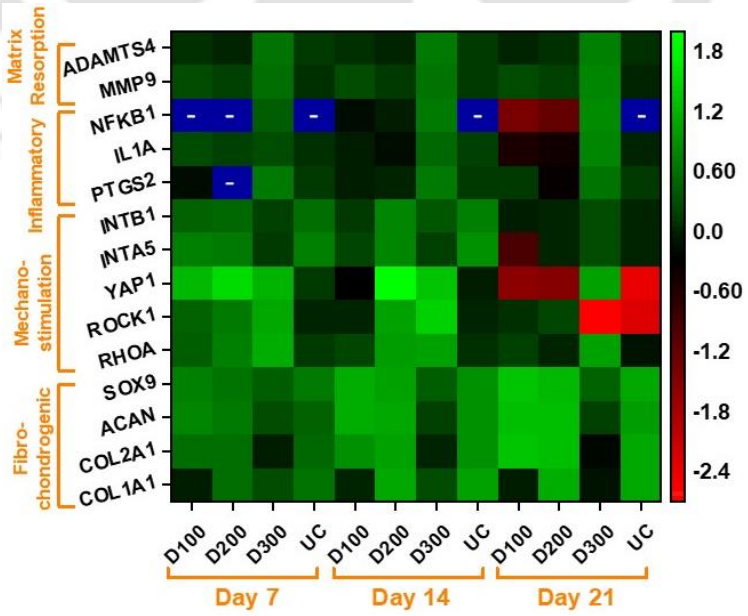

Figure 6.6: *Heatmap representation of gene expression profile with upregulation or downregulation of various markers for day 7, 14 and 21 of culture.*

ROCK1 (Rho-associated, coiled-coil containing protein kinase 1) is a down-stream marker regulated by mechanical stimulation and is found to be expressed differently for different stimulation conditions. ROCK1 for D100 group was found to be significantly upregulated on day 7 (~2.91 times) and upregulated above basal level with a relatively reduced expression on day 14 (~1.69 times) and day 21 (~1.48 times). D200 group demonstrates significantly upregulated ROCK1 on day 7 (~4.49 times), which elevated on day 14 (~10.03 times) and reduced closer to basal level on day 21 (~1.78 times). UC group demonstrated near basal level expression of ROCK1 on day 7 (~1.02 times) and day 14 (~1.05 times) followed by a downregulation below basal level on day 21 (~0.006 times). In contrast to all the groups, D300 group demonstrated a significantly upregulated ROCK1 expression on day 7 (~11.9 times) and day 14 (~26.2 times) indicative of the higher stimulation but was followed by a downregulation below basal level on day 21 (~0.002 times).

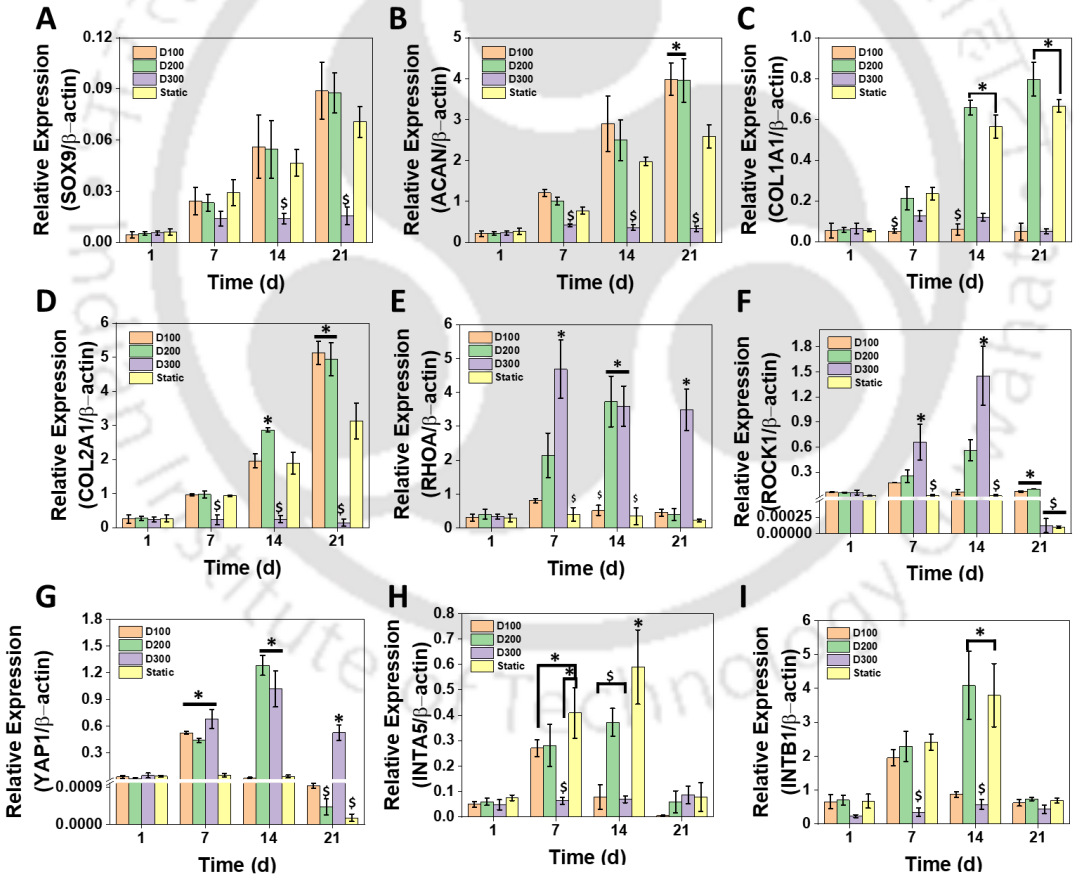

Figure 6.7: *Gene expression profile with $2^{-\Delta Ct}$ for fibrochondrogenic markers: (A) SOX9, (B) aggrecan (ACAN), (C) collagen I (COL1A1), (D) collagen II (COL2A1) and for mechano-transduction markers: (E) RhoA (RHOA), (F) ROCK1, (G) YAP1, (H) Integrin α5 (INTA5) and (I) Integrin β1 (INTB1) for day 1, 7, 14 and 21 of culture after normalization with β-actin.*

**p≤0.05 for significantly higher expression than other groups and $p≤0.05 for significantly lower expression than other groups.*

YAP1 (yes-associated protein 1) is a part of the Hippo pathway affected by the RhoA and ROCK1. D100 group demonstrated significant upregulation of YAP1 on day 7 (~16.18 times) followed by a significant downregulation below basal level on day 14 (~0.52 times) and day 21 (~0.028 times). D200 group showed significant upregulation of YAP1 on day 7 (~33.29 times) and day 14 (~96.88 times) with a steep downregulation below basal level on day 21 (~0.032 times). The UC group showed minimal upregulation of YAP1 above basal level on day 7 (~1.33 times) and a subsequent downregulation below basal level on day 14 (~0.89 times) and day 21 (~0.004 times). Further, D300 group maintained a significant YAP1 upregulation on day 7 (~14.18 times), day 14 (~21.28 times) and day 21 (~11.04 times). These variations occurring in YAP1 levels due to mechanical stimulation lead to different downstream effector pathways leading to various cell fates.

Inflammatory Markers

The expression of inflammatory marker NF-κβ1 (NFKB1) was found to be below basal level for D100 group on day 14 (~0.66 times) and day 21 (~0.04 times) and was not determinable on day 7 as compared to day 1. D200 group demonstrated a similar trend where no expression of NF-κβ1 was observed on day 7 and it was downregulated below basal level on day 14 (~0.95 times) and day 21 (~0.06 times) as compared to day 1. Interestingly, the UC condition showed no expression of NF-κβ1 on any time point. Concurrently, D300 group demonstrated a pro-inflammatory response and NF-κβ1 was found to be significantly upregulated on day 7 (~2.55 times), day 14 (~4.58 times) and day 21 (~6.77 times) as compared to day 1.

The expression of IL1A was found to vary based on the amount of stimulation. For D100, IL1A expression was slightly upregulated from basal level on day 7 (~1.98 times), while further being downregulated below basal level on day 14 (~0.91 times) and day 21 (~0.29 times) as compared to day 1. For D200, IL1A was upregulated above basal level on day 7 (~1.51 times) and was found to be downregulated below basal level on day 14 (~0.67 times) and day 21 (~0.36 times) as compared to day 1. UC group showed IL1A upregulation close to basal level on day 7 (~1.22 times), day 14 (~1.46 times) and day 21 (~1.05 times) as compared to day 1. Interestingly, D300 group demonstrated a significantly high upregulation on day 7 (~1.94 times), day 14 (~3.51 times) and day 21 (~6.22 times) as compared to day 1.

COX-2/PTGS-2 (PTGS2) expression was found to differ based on the mechanical stimulation intensity. D100 stimulation demonstrates below basal level expression on day 7 (~0.65 times) and day 14 (~0.9 times) and slight upregulation to basal level on day 21 (~1.26 times) as compared to day 1. D200 group shows no expression on day 7, near basal level expression on day 14 (~1.06 times) and downregulation on day 21 (~0.49 times) as compared to day 1. Interestingly, UC group demonstrates a steady expression of COX-2 above basal level on day 7 (~1.36 times), day 14 (~1.26 times) and day 21 (~1.36 times) as compared to day 1. In contrast to all these, D300 group showed significant and maintained upregulation of COX-2 on day 7 (~4.78 times), day 14 (~4.93 times) and day 21 (~4.23 times) as compared to day 1, denoting the mechanical stimulation triggered inflammatory pathways.

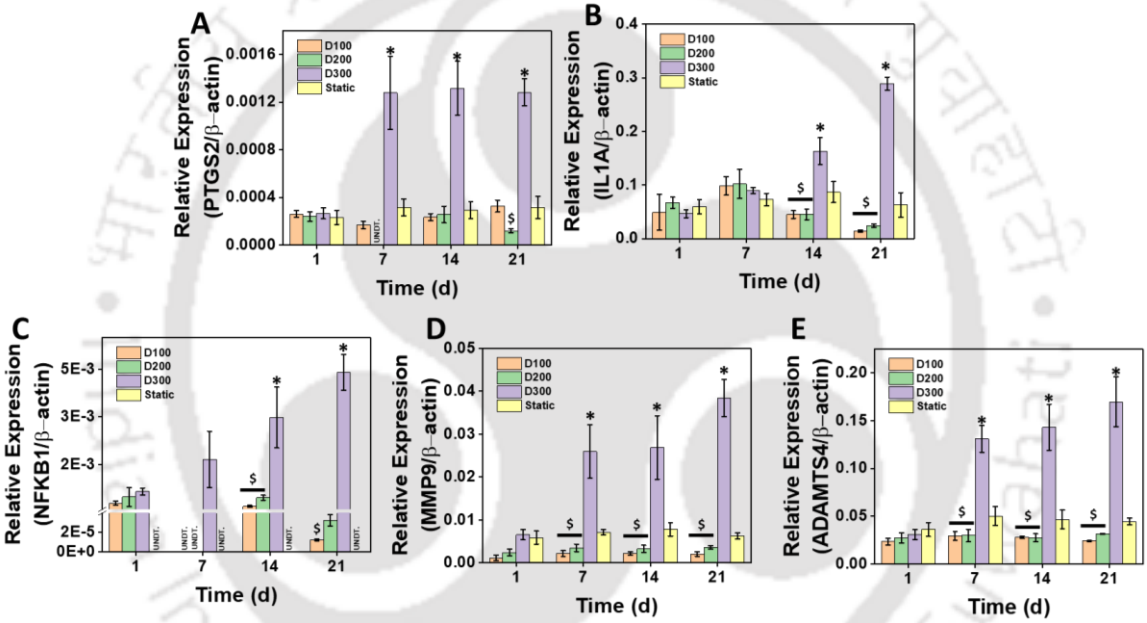

Figure 6.8: *Gene expression profile with $2^{-\Delta Ct}$ for inflammatory markers: (A) Cox-2/PTGS2, (B) IL1α (IL1A) and (C) NF-κβ1 (NFKB1) and ECM resorption markers: (D) MMP9 and (E) ADAMTS4 for day 1, 7, 14 and 21 of culture after normalization with β-actin. *p≤0.05 for significantly higher expression than other groups and $p≤0.05 for significantly lower expression than other groups.*

Matrix Resorption Markers

MMP-9 (MMP9) expression was found to be above basal level for D100 group on day 7 (~1.25 times), day 14 (~1.19 times) and day 21 (~1.02 times) as compared to day 1. Similarly, D200 group demonstrates above basal level MMP-9 expression on day 7 (~1.46 times), day 14 (~1.36 times) and day 21 (~1.5 times) as compared to day 1. UC group shows a similar trend and a slightly upregulated MMP-9 expression on day 7 (~1.2 times), day 14 (~1.32 times) and day 21 (~1.06 times) as compared to day 1. In contrast, D300 group shows significant

upregulation of MMP-9 on day 7 (~3.98 times), day 14 (~4.11 times) and day 21 (~5.9 times) as compared to day 1, depicting the higher bias for activation of matrix resorption markers.

ADAMTS-4 (ADAMTS4) expression was found to be upregulated close to basal level for D100 group on day 7 (~1.25 times), day 14 (~1.19 times) and day 21 (~1.02 times) as compared to day 1. D200 and UC groups show upregulation above basal level on day 7 (~1.08 times and ~1.38 times respectively), day 14 (~1.005 times and ~1.28 times respectively) and day 21 (~1.15 times and ~1.23 times respectively). In contrast, D300 group shows significant upregulation above basal level on day 7 (~4.25 times), day 14 (~4.64 times) and day 21 (~5.5 times) as compared to day 1, depicting a similar trend as observed for MMP-9.

6.3.3.5 In silico gene and protein network prediction analysis

In silico-analysis gene prediction analysis through GeneMania using our expressed genes as Input genes revealed the various genes that are typically known to be co-expressed and are involved in the regulation of mechano-transduction response, cell adhesion to the substrate, regulation of cellular proliferation, tissue and ECM remodelling, inflammatory, collagen synthesis and chondrogenesis pathways (**Figure 6.9A, Table 6.2**). The output genes include TEAD1-3 which form complex with YAP acting as an effector of mechanical stimulus on cells, TIMP1 and ADAMTS5 correspond to tissue and ECM remodelling, COL1A2 is associated with ECM deposition, HAPLN1, COMP and SPP1 are associated with chondrogenesis, ITGA11, ITGA10, DAAM1 are associated with cellular adhesion and IL1R2 is corresponding to inflammatory response.

Table 6.2: *Output genes derived from GeneMania analysis*

Output Gene	Details
IL1R2	interleukin 1 receptor type 2
TEAD1	TEA domain transcription factor 1
TIMP1	tissue inhibitor of metalloproteinases (TIMP) metallopeptidase inhibitor 1
COL1A2	collagen type i alpha 2 chain
DAAM1	dishevelled associated activator of morphogenesis 1
COMP	cartilage oligomeric matrix protein
HAPLN1	hyaluronan and proteoglycan link protein 1
SPP1	secreted phosphoprotein 1
CEACAM1	CEA cell adhesion molecule 1
ITGA11	integrin subunit alpha 11

TEAD2	TEA domain transcription factor 2
ITGA10	integrin subunit alpha 10
TEAD3	TEA domain transcription factor 3
ADAMTS5	ADAM metallopeptidase with thrombospondin type 1 motif 5
CEACAM8	CEA cell adhesion molecule 8

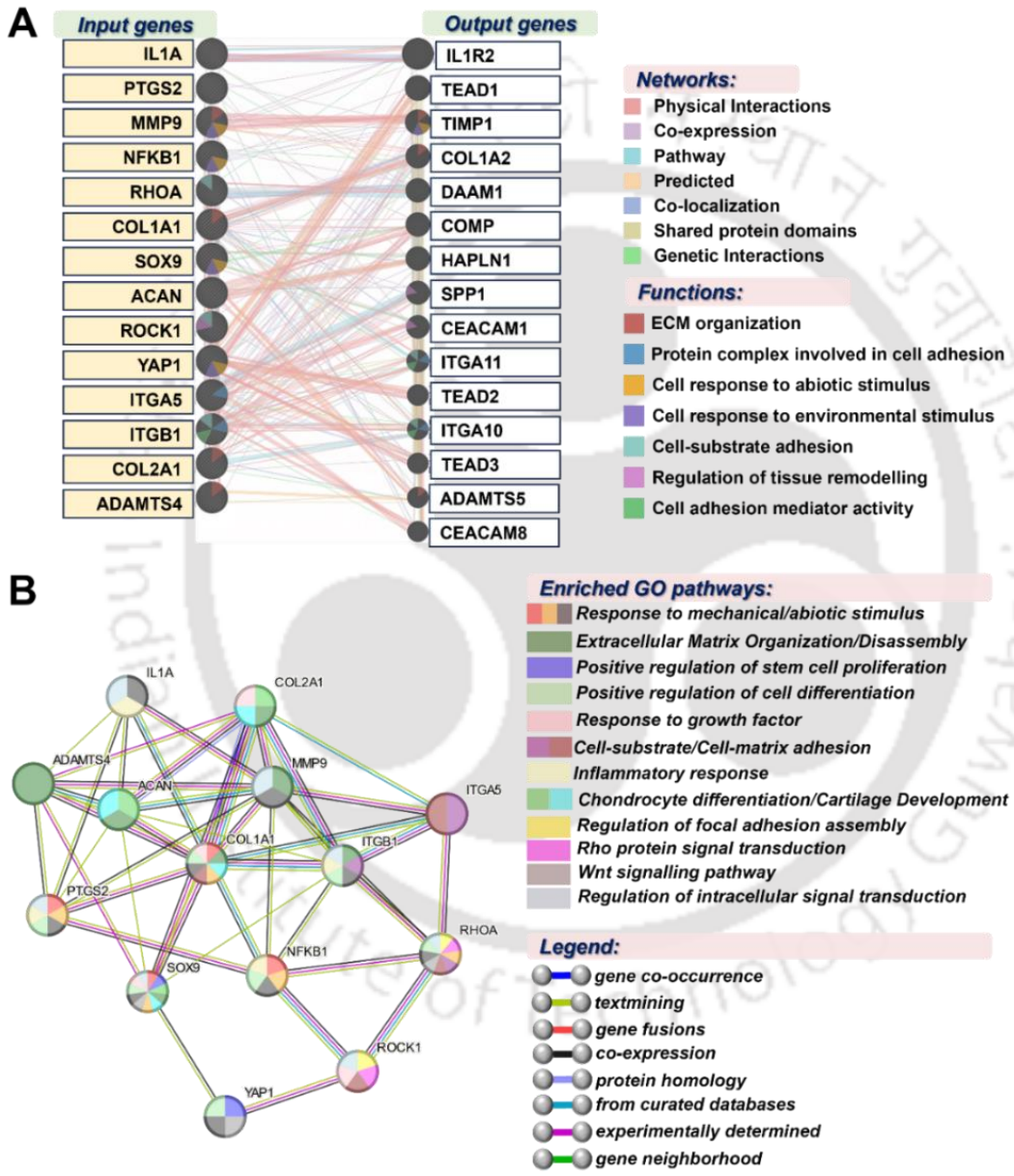

Figure 6.9: *(A) Gene Network representing the GeneMania analysis of predicted gene-gene interactions between the input genes (used for RT-PCR expression) and output genes (predicted genes). (B) PPI network generated using StringDB analysis representing the predictive interaction of proteins encoded by the input genes to output various enriched gene-ontology (GO) pathways.*

Furthermore, we used the same input genes to study the associated protein-protein interaction (PPI) pathways, that could be potentially enriched, using String-DB. We observed that the input genes are reported to be involved in the gene ontology (GO) pathways (**Figure 6.9B**) corresponding to response to mechanical/abiotic stimulus (RHOA, YAP1, SOX9, NFKB1, PTGS2, IL1A, ITGB1, COL1A1, MMP9), extracellular matrix organization/disassembly (ADAMTS4, MMP9, ITGB1, COL1A1, COL2A1, ACAN, SOX9), positive regulation of stem cell proliferation (SOX9, YAP1), positive regulation of cell differentiation (PTGS2, COL1A1, SOX9, ITGB1, NFKN1, RHOA, YAP1), chondrocyte differentiation and cartilage development (ACAN, SOX9, COL2A1, COL1A1), cell-substrate/cell-matrix adhesion/regulation of focal adhesion assembly (COL1A1, ITGA5, ITGB1, RHOA, ROCK1), inflammatory response (IL1A, ITGB1, NFKB1, PTGS2), Rho protein signal transduction (RHOA, ROCK1), Wnt signalling pathway (SOX9, COL1A1, NFKB1, YAP1, RHOA) and regulation of intracellular signal transduction (RHOA, ROCK1, SOX9, MMP9, PTGS2, ITGB1, IL1A).

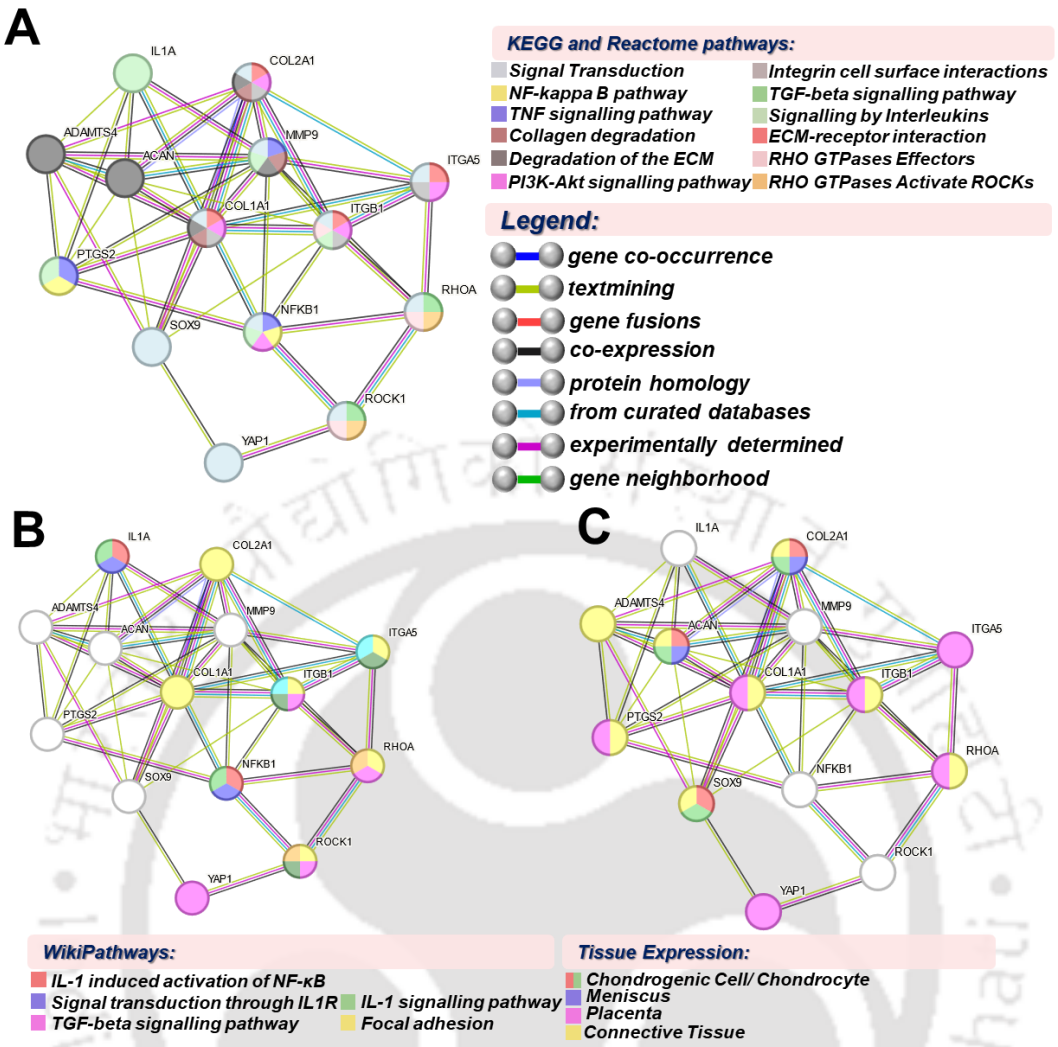

Figure 6.10: *PPI network generated using StringDB analysis representing the predictive interaction of proteins encoded by the input genes to output various enriched (A) KEGG and reactome pathways, (B) WikiPathways and (C) Tissue Expression.*

Additionally, the input genes were found to enrich various KEGG and reactome pathways (ECM receptor interaction, TNF signalling, TGF-beta signalling, NF-kappa B, PI3K-Akt signalling, RHO GTPases activate ROCKS, Integrin cell surface interactions, Collagen degradation, degradation of the ECM, signalling by Interleukins, RHO GTPases effectors and signal transduction) (**Figure 6.10A**) and Wiki Pathways (IL-1 activation of NF-κβ, signal transduction through IL1, IL-1 signalling, focal adhesion and TGF-beta signalling) (**Figure 6.10B**). Concurrently, the input genes could be enriched for tissue-specific/cell-specific expression in chondrogenic cell/chondrocyte(ACAN, COL2A1, SOX9), meniscus (ACAN, COL2A1), placenta (ITGA5, ITGB1, RHOA, COL1A1, PTGS2, YAP1) and connective tissue (RHOA, ITGB1, COL1A1, ACAN, ADAMTS4, COL2A1, SOX9, PTGS2) (**Figure 6.10C**).

6.3.3.6 Immunostaining of cell-seeded constructs post maturation

The constructs from various groups were co-stained for collagen I (red fluorescence) and collagen II (green fluorescence) to determine the fibrochondrogenic differentiation potential and the ECM deposition on the constructs of different stimulation groups. D100 demonstrated progressively higher collagen II deposition as compared to collagen I deposition after 14 days (**Figure 6.11A**) and 21 days (**Figure 6.11E**) of culture under stimulation. D200 group was found to possess high depositions of both collagen I and collagen II on day 14 (**Figure 6.11B**) and day 21 (**Figure 6.11F**). D300 group showed small deposits of collagen II and meagre deposition of collagen I after 14 days of stimulation and culture (**Figure 6.11C**) and a slightly higher amount of collagen I and collagen II were found to be deposited after 21 days of stimulation and culture (**Figure 6.11G**). UC culture conditions promoted similar trend for collagen I and collagen II to the D200 group showing high collagen I and collagen II after 14 days (**Figure 6.11D**) and 21 days (**Figure 6.11H**).

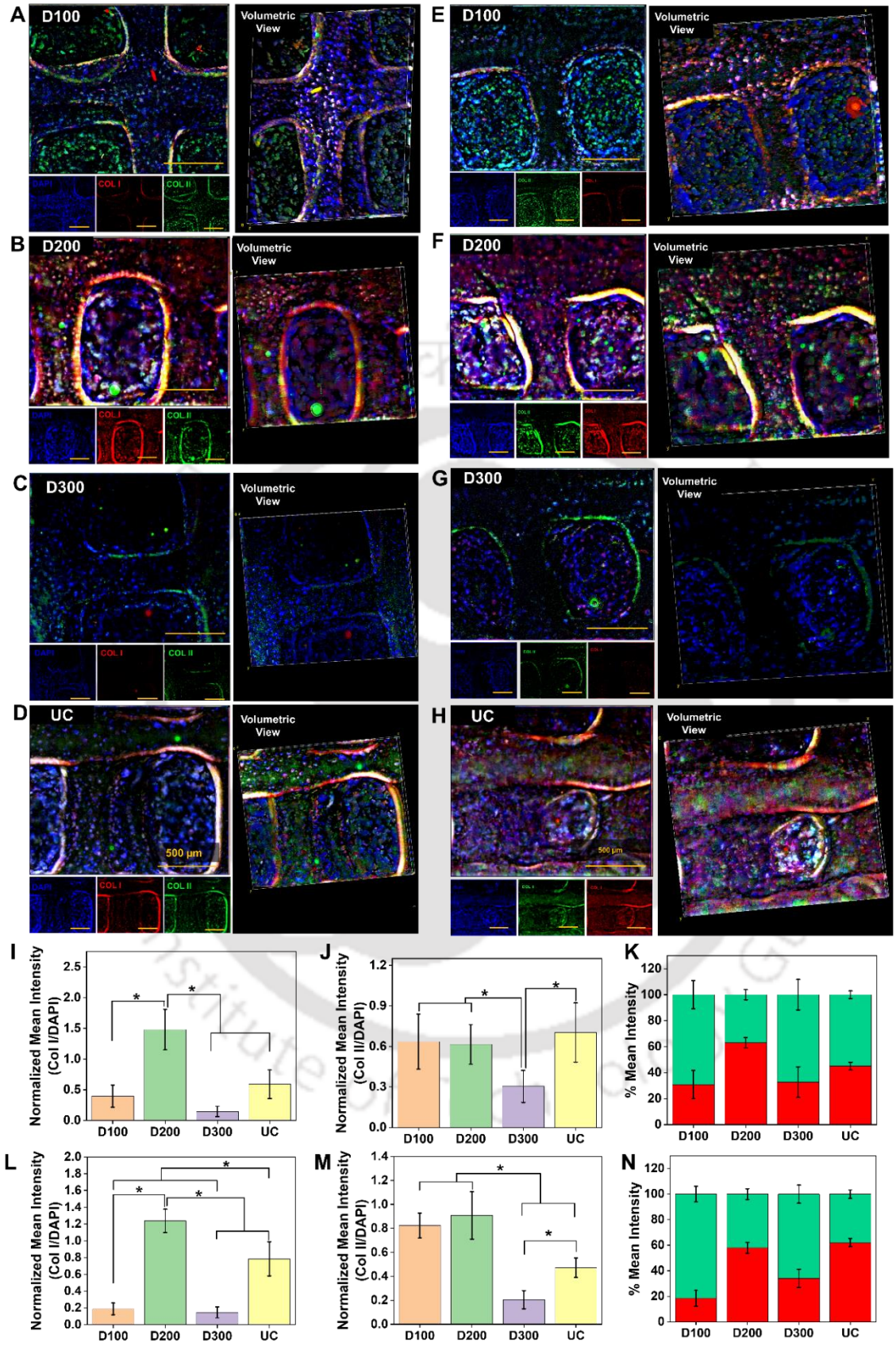

Figure 6.11: *Representative fluorescence-stained micrographs with collagen I (red), collagen II (green) and nuclei (blue) of constructs after 14 days for* ***(A)*** *D100 group,* ***(B)*** *D200 group,*

*(**C**) D300 group and (**D**) UC group. Representative fluorescence-stained micrographs with collagen I (red), collagen II (green) and nuclei (blue) of constructs after 21 days for (**E**) D100 group, (**F**) D200 group, (**G**) D300 group and (**H**) UC group. ImageJ based quantification of fluorescence intensity for (**I**) Collagen I/DAPI and (**J**) Collagen II/DAPI. (**K**) Relative fraction of % mean fluorescence intensities of Collagen I (red) and Collagen II (green) after 14 days for all groups. ImageJ based quantification of fluorescence intensity for (**E**) Collagen I/DAPI and (**F**) Collagen II/DAPI. (**G**) Relative fraction of % mean fluorescence intensities of Collagen I (red) and Collagen II (green) after 21 days for all groups. *p≤0.05*

Collagen I was found to be significantly higher in D200 as compared to other groups on day 14 (**Figure 6.11I**)**.** Collagen I expression was significantly high for D200 as compared to other groups and UC group was found to possess higher expression of collagen I as compared to D100 and D300 on day 21 (**Figure 6.11L**). Collagen II was expressed significantly higher in D100 and D200 groups as compared to D300, and the UC group also showed significantly higher collagen II expression than D300 after 14 days (**Figure 6.11J**). Collagen II was expressed significantly higher in D100 and D200 as compared to D300 and UC groups and significantly higher in UC group as compared to D300 group on day 21 (**Figure 6.11M**). Collagen I/Collagen II ratio was found to be closing towards 30:70 for D100, 60:40 for D200, 30:70 for D300 and 50:50 for UC group on day 14 (**Figure 6.11K**). Further, Collagen I/Collagen II ratio was found to be at 20:80 for D100, 60:40 for D200, 35:65 for D300 and 60:40 for UC groups on day 21 (**Figure 6.11N**).

6.4 Discussion

Meniscal cells are known to respond to mechanical stimulation such as hydrostatic [348], compression [224] and tensile [359]. All of these attempts have resulted in the meniscus cell proliferation and accelerated secretion of ECM under physiological strains. Ultrasound (LIPUS) on the other hand has been utilized for the regeneration of various tissues such as osteochondral [511-513] and skin [515], and fracture healing [511, 514] by the virtue of anabolic effects reported to increase deposition of collagen and sGAG and accelerated cellular proliferation and migration. Here, we aimed to evaluate the potential of varying intensities of LIPUS for accelerating and/or assisting in the fibrochondrogenic differentiation of wJMSCs seeded on silk based GFRP loaded 3D printed constructs as compared to their UC (unstimulated control) counterparts. We studied physiologically relevant forces (100 mW/cm^2 and 200 mW/cm^2 at 1MHz and 50% duty cycle for 20 min/day) that we hypothesized to produce anabolic effects and enhance fibrochondrogenic differentiation and hyper-physiological stimulus (300 mW/cm^2 at 1MHz and 50% duty cycle for 20 min/day) that we hypothesized would play a role in catabolism, hindered differentiation and maturation into fibrochondrogenic phenotype when compared with the static unstimulated control (UC).

The silk based GFRP loaded hydrogel biomaterial-ink composition was found to be thinning under high shear and higher temperatures. These properties are endowed by the presence of gelMA and PEGDA [424, 517]. silkMA aids in crosslinking of the biomaterial ink, while also establishing high mechanical strength over long periods[435]. Additionally, the biomaterial-ink components, i.e., silkMA, PEGDA, gelMA and GFRP have been utilized for various musculoskeletal, cartilage and cardiac tissue engineering applications with high degree of biocompatibility and immuno-compatibility [266, 435, 469]. GFRP is known to possess factors responsible for regeneration of meniscus tissue *in vitro* and *in vivo* [389]. Further, infrared spectroscopy showed the cardinal amide I, II and III peaks of the silkMA and gelMA and methacrylation peak of the PEGDA, silkMA and gelMA to be present in the biomaterial-ink composition before and after crosslinking. This is in accordance with our previous observations of photo-curable biomaterial-inks [435]. The biomaterial-ink was found to be shear-thinning and stable post crosslinking during printing of multi-layered constructs. Though the biomaterial-ink was found to be buckling at longer distances, it does not affect multi-layered printing due to the crosslinking carried out after each layer. Printed constructs contained highly porous microarchitecture, as visualized in the electron micrographs, with ~74% apparent porosity and a rapid water uptake capacity of ~2 times within 20 min. This is

essential for the diffusion of culture medium, waste products [1] and the release of encapsulated GFRP. The strength and robustness of constructs is an important aspect for meniscus tissue engineering applications [4]. The GFRP loaded constructs showed no signs of degradation under LIPUS and were stable under pursued mechanical compression for 21 days bearing a total of 42000 cycles of 20% compression and LIPUS of various intensities. This is further corroborated by the constant compressive modulus under various LIPUS stimulation after 21 days. This resilience is desired of constructs conducive for applications in meniscus tissue engineering [503]. The compressive modulus of the constructs exceeded the equilibrium compressive modulus of both porcine and human menisci [1] at all time points. Further, wJMSCs were chosen as a model neonatal source of stem cells that are being dubbed as a potent source of engineering patient-specific tissue constructs and various regenerative applications [473]. These stem cells were seeded upon the 3D constructs and incubated without stimulation for 2 days to usher cell adherence and thereafter were evaluated for their response to varying degrees of LIPUS stimulation. UC group with no stimulation of LIPUS was used as a control to evaluate the effect of GFRP encapsulated within the constructs on the stem cells. According to our observations, LIPUS stimulation was perceived differently by the seeded stem cells pertaining to the rise in intensity of the LIPUS. We had divided the stimulation into 3 groups: D100 (100mW/cm^2) as low-physiological stimulation, D200 (200mW/cm^2) as high-physiological stimulation and D300 (300mW/cm^2) as hyper-physiological stimulation. D100, D200 and UC group demonstrated significantly higher cellular proliferation as compared to D300 group on all later time-points. D300 was found to halt the cellular proliferation after day 7. Similar trend was observed in sGAG and HYP deposition which indicate that D100, D200 and UC groups primarily aid in the cellular proliferation and ECM deposition at the proteomic level and D300 actively hinders the same. Further, evaluation of gene expression profile reveals the underlying implications of the mechanical stimulation at the mRNA expression level.

The D100 group provides a prominent chondrogenic bias with a significant upregulation of sox9, aggrecan and collagen II after 7, 14 and 21 days. In D100, the low-physiological mechanical stimulation triggers the signal transduction pathway via upregulation of Integrin α5/Integrin β1 as observed in literature [518, 519]. This upregulation is found diminished on day 14 and downregulated on day 21. The Integrin α5/Integrin β1 is known to regulate expression of RhoA and its downstream effectors ROCK1 and finally YAP1 [520] which is known to bind with TEAD to upregulate CCN2 expression [521]. This pathway is found to be upregulated for D100 group at day 7, followed by a consequent fall of mRNA levels of RhoA

and ROCK1 to basal levels and YAP1 below basal levels on and after day 14. This is an indicator of the ECM production towards chondrogenic phenotype following CCN2 downregulation after 7 days aided by the downregulation of YAP1 [522]. This is corresponding to the stress-fibre stabilization induced by the downregulation of YAP1 gene which is known to prominently aid in chondrogenic differentiation [521]. Also, the D100 stimulation showed significantly downregulated inflammatory cytokines and basal level expression of matrix resorption markers on day 14 and day 21 as observed in other dynamic mechanical stimulation forms that are known to be physiologically conducive for reduction of inflammatory markers [523, 524]. The immunostaining of D100 group and the subsequent fluorescence quantification of collagen I, collagen II and collagen I/collagen II ratio further mirrored our biochemical and gene expression profile observations in reflecting the chondrogenic differentiation with rise in the collagen II deposition and sGAG deposition from day 14 to day 21.

D300 group was deemed to undergo sustained hyper-physiological stimulation that produced detrimental effect on cellular proliferation and differentiation. This is reflected in the basal level expression of Integrin α5/Integrin β1, which is an indicator of mechanical over-stimulation [525, 526]. This was accompanied by sustained high expression of RhoA, ROCK1 and YAP1 on days 7, 14 and 21. These in-turn might have mediated significant upregulation of inflammatory cytokine markers (NFκβ, IL1α and cox-2) and matrix resorption markers (MMP9 and ADAMTS4) [512] accompanied by downregulation of matrix synthesis markers (collagen I and collagen II), which progressively resembled cells that possess unstable stress fibres and degenerative gene expression profile [527]. This is mirrored by the reduced biochemical deposition of sGAG and hydroxyproline and the fluorescence-stained constructs showing significantly low deposition of both collagen I and collagen II as compared to the other groups.

UC group on the other hand demonstrated characteristic fibrochondrogenic gene expression profile where the GFRP growth factors and the 3D printed matrix assisted upregulation of Integrin α5/Integrin β1 on day 7 and day 14. The mechanical stimulation markers were close to basal levels with a slight upregulation of RhoA and basal level expression of ROCK1 and YAP1. Also, the anti-inflammatory effects of GFRP can be seen in the non-expression (NFκβ) or basal level expression of inflammatory markers (IL1α and cox-2) [510]. Moreover, matrix remodelling, and resorption marker expression were also close to basal level (MMP9 and ADAMTS4). This is further iterated by the biochemical deposition of high levels of sGAG and HYP and the collagen I and collagen II depositions. Interestingly the collagen

I/collagen II was 50:50 on day 14, however the ratio reached 60:40 on day 21 mimicking the native composition of the meniscus ECM [4].

D200 group demonstrated a higher fibrochondrogenic bias generation as compared to the UC group apart from the chondrogenic bias of D100 and inflammatory bias of D300. The D200 stimulation upregulated the fibrochondrogenic genes (sox9, aggrecan, collagen I, collagen II) on all time points. This could be attributed to the Integrin α5/Integrin β1 mediated activation of RhoA, ROCK1 and YAP1 mediated pathway uptil day 14 and the consequent reduction of the expression of RhoA, ROCK1 and YAP1 to basal levels on day 21. The initial YAP1 mediated activation of CCN2 and TGF-β pathways [528] and ROCK1 mediated activation of sox9 [520] could have contributed to the fibrochondrogenic differentiation and ECM deposition. This additionally aided in the downregulation of NFκβ, IL1A and cox2 which has been observed in the literature[523, 524]. While aiding in deposition of matrix, the moderate stimulation of D200 group still promoted basal level expression of matrix remodelling and resorption markers, i.e., MMP9 and ADAMTS4. D200 group was found to be most suitable for early deposition of abundant fibrochondrogenic ECM, i.e., collagen I, collagen II and sGAG, while maintaining the 60:40 ratio from day 14 timepoint as compared to the UC group (where the ratio reached 60:40 on day 21).

The gene interaction and PPI network analysis corroborated our findings where downstream effectors of mechanical stimulation were found to influence the differentiation of D100 group towards the chondrogenic phenotype, D300 group towards an inflammatory phenotype with hindered cellular proliferation and differentiation and D200 and UC groups towards fibrochondrogenic phenotype. Our in-silico analysis highlights the importance of the analysed genes in the downstream pathways pertaining to cell proliferation, stem cell differentiation, chondrogenic differentiation, cell adhesion, matrix remodelling, inflammatory response and intracellular signal transduction curated from GO, KEGG, Reactome and Wiki Pathways. This substantiates the effect of various intensities of LIPUS stimulation on potentially triggered pathways leading to the differential effects in observed groups. In clinical setting this may be translated as shown in **Figure 6.11**. Here, we envisage that upon assessment of injury, 3D CAD modelling would be carried out based on the MRI scan and further followed up with formulation of GFRP loaded biomaterial-ink and printing the constructs according to patient's requirement. Further, the fabricated constructs could be seeded with patient-derived stem cells and implanted and followed up with LIPUS stimulation regimen until integration and healing of the meniscus.

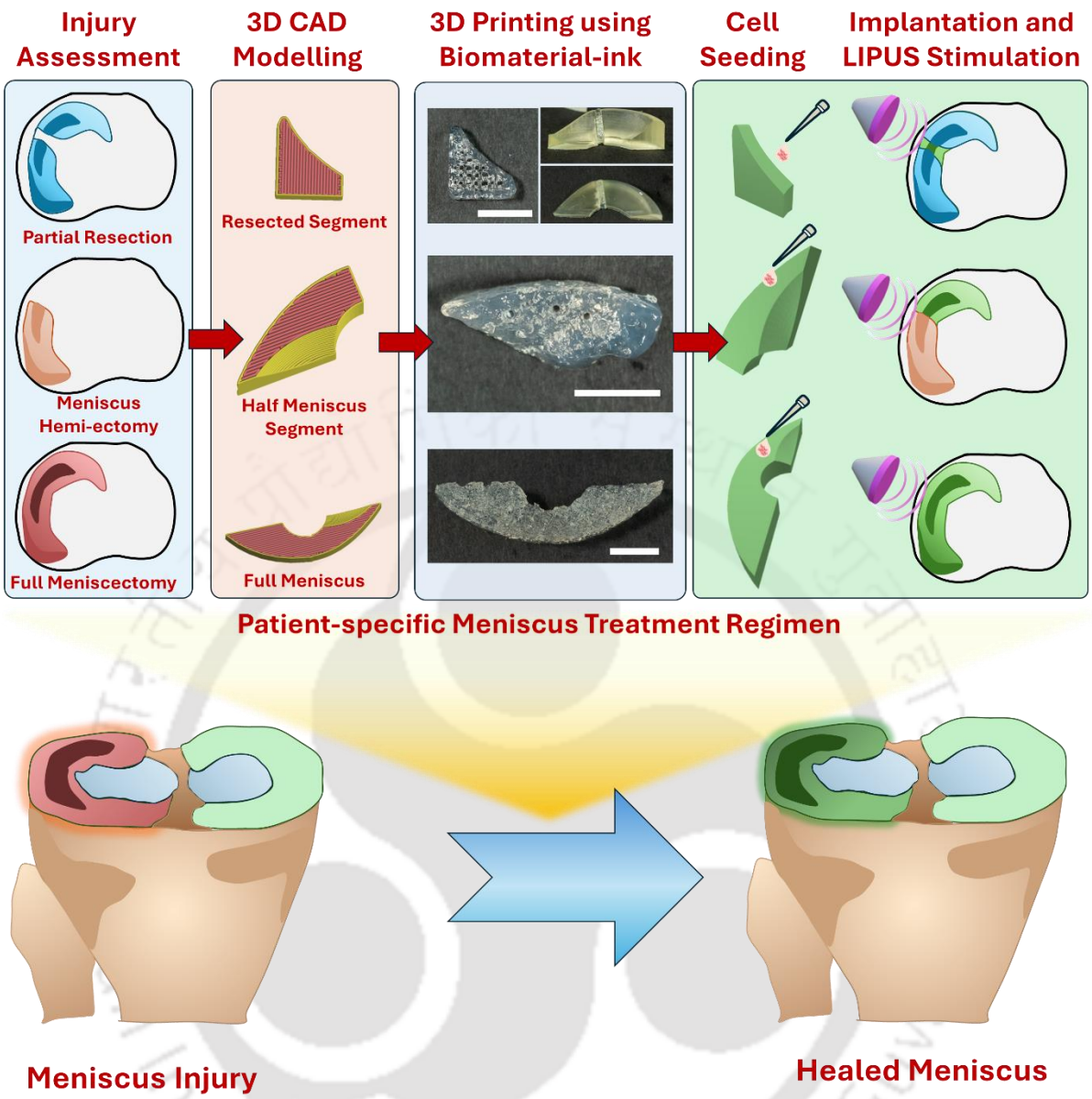

Figure 6.12: *Conceptualization of the potential treatment approach for partial resection, hemi-ectomy or full meniscectomy through CAD modelling, 3D printing using formulated biomaterial-ink, seeding of patient-derived stem cells, implantation followed by LIPUS stimulation. Scale bar: 1cm.*

6.5 Salient outcomes and Findings

1. We fabricated GFRP loaded 3D printed silk based photocrosslinked constructs seeded with wJMSCs and used LIPUS stimulation for assessing their differentiation towards fibrochondrogenic phenotype.
2. Physiochemical and mechanical properties were found to be unchanged for LIPUS treated constructs as compared to unstimulated control.
3. Cellular proliferation, biochemical analysis, gene expression profiling and immunostaining for collagen I and collagen II revealed the effects of LIPUS treatment.
4. Low-physiological stimulation (D100 group: 100mW/cm^2) was found to induce chondrogenic bias, high-physiological stimulation (D200 group: 200mW/cm^2) and no stimulation (UC group) was found to induce fibrochondrogenic phenotype and hyper-physiological stimulation (D300 group: 300mW/cm^2) resulted in hindered cell proliferation, ECM deposition and triggering of inflammatory and matrix resorption pathways.
5. PPI and gene-gene interaction analysis showed the potential genes and pathways involved in the varying behaviour with and without LIPUS treatment.
6. High-physiological LIPUS stimulation (200mW/cm^2) for fibrochondrogenic differentiation and it needs to be further evaluated for meniscus regeneration capacity *in vivo*.

SUMMARY AND FUTURE PERSPECTIVES

SUMMARY AND FUTURE PERSPECTIVES

Current clinically approved approaches for meniscus tear treatment including meniscectomy, allograft transplantation and implants have their respective drawbacks. Meniscus replacement using current FDA approved implants and the subsequent regeneration are riddled with issues of non-compliant size, shape, biocompatibility, non-degradability and mechanical strength. Meniscus tears of varying sizes need to be addressed differently, while taking into account the compliance of physico-chemical, mechanical and biological parameters. In this regard, the Objectives 1-5 (Chapter 2-6) of this thesis (**Figure S1**) provide potential translational solutions that can be employed to address the issues associated with the current clinical scenario. This dissertation tries to orchestrate clinically relevant meniscus implants, keeping into account the essential design considerations described in Chapter 1, i.e., biocompatibility, patient-specific shape and size, recapitulation of native mechanical properties, biodegradability and incorporation of patient-derived biological cues.

In Objective-1, a biomaterial ink was formulated using *B. mori* silk fibroin, *A. assama* silk fibroin and gelatin. This ink possessed the requisite shear thinning and temperature-induced gelation and was used for 3D printing implants that were enzymatically crosslinked. 3D printing rendered patient-specific shape and size, while the presence of silk-fibroin/gelatin blend rendered physico-chemical and biological compatibility for the sustenance of native meniscus cells and their extracellular matrix deposition. The 3D scaffolds proved to be mechanically mimicking the native meniscus and was found to be immunocompatible. In Objective-2, the 3D printing procedure was optimized further by the virtue of photocrosslinking polymers. *B. mori* silk fibroin and gelatin were methacrylated and blended with *A. assama* silk fibroin to enable one-step photopolymerized fabrication. Additionally, in this objective, the zonal complexity of the meniscus was recapitulated using a dual-ink printing approach with the photocrosslinking ink encapsulating growth factor loaded microspheres. These constructs could lead to zonal differentiation of seeded stem cells providing a mode for the regeneration of zonal cellular phenotype and extracellular matrix profile of the meniscus. The use of patient-derived growth factors is an incumbent approach of the future as it leads to better regeneration potential in the clinical setting. Hence, objective 3 focussed on further improvement of the photocrosslinking ink by incorporation of autologous growth factor rich plasma and polyethylene glycol dimethacrylate. This improved ink aided by acting as a reservoir of autologous growth factors

and thereby improving the potential acceptance in clinical scenarios. The 3D printed implants in objective 3 could release growth factor rich plasma for weeks, degraded in a slow and sustained manner and provided much more enhanced mechanical compliance.

Smaller meniscus tears are often either ignored or debrided upon detection leading to development of osteoarthritis in the long run. Moreover, the limitation of fabrication size for 3D printers limits the use of 3D printing for these kinds of defects. Realising the potential of the optimized biomaterial-ink composition from objective 3, it was carried forward in objective 4 with the switch to polyethylene glycol diacrylate for better strength and injectability. This tweaked formulation of *B mori* silk fibroin methacrylate, gelatin methacrylate, polyethylene glycol diacrylate and growth factor rich plasma was used as an injectable hydrogel for small meniscus tears that can be perilous to treat using 3D printing. The injectable hydrogel composition was found to be mechanically compliant to meniscus upon crosslinking and promoted proliferation, migration and fibrochondrogenic differentiation of neo-natal human stem cells. This hydrogel was tested *in vivo* as well and was found to heal full thickness defects in rabbit meniscus.

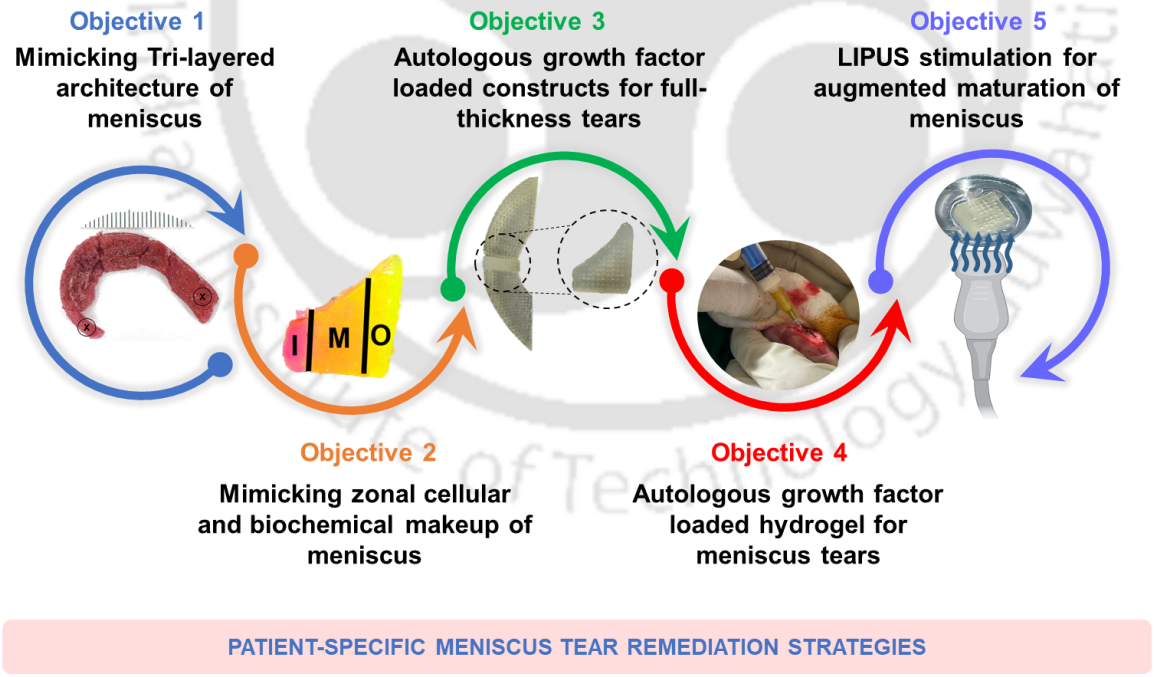

Figure S1: *Schematics illustrating the developed treatment modalities for meniscus tears.*

Meniscus is a mechanically loaded tissue with cyclic load-bearing properties. Additionally, the mechanical stimulation of implants have been known to provide better regeneration of meniscus *in vitro* and *in vivo*. This perspective was evaluated in objective 5. Here, non-invasive mechanical stimulation was provided using low intensity pulsed ultrasound on neo-natal stem cells that were seeded over 3D scaffolds printed using the injectable hydrogel as an ink. The mechanical stimulation led to augmentation of cellular proliferation and differentiation as compared to the static controls. Modern treatment approaches could be a combinatorial therapy as described in this chapter. Further, *in vivo* evaluations of these approaches in larger animal models would prove to be incremental in the optimization of these patient-specific treatment approaches for future clinical applications.

Future perspectives of this thesis work (**Figure S2**) would include the application of the developed treatment approaches in larger animal models such as goat, sheep and pig for further optimization of the formulations of inks towards the load-bearing characteristics of the knee. The photo-crosslinking inks developed in this thesis can be used as induced pluripotent stem cell-loaded bioinks to further development of cellularized treatment approaches with higher patient-compliance. Furthermore, the photo-polymerising inks could also be optimized for use in volumetric bioprinting of meniscal implants that can be used for treatment of meniscus tears. The developed inks are facile for use in the laboratory settings and hence can be commercialized as off-the-shelf inks for research purposes. The developed 3D printed constructs seeded with neo-natal stem cells and matured *in vitro* can be used as alternative pharmaceutical drug-testing platforms for anti-inflammatory drugs. Concerted efforts directed towards the further optimization of the treatment approaches discussed in this thesis could lead to clinical translation in humans.

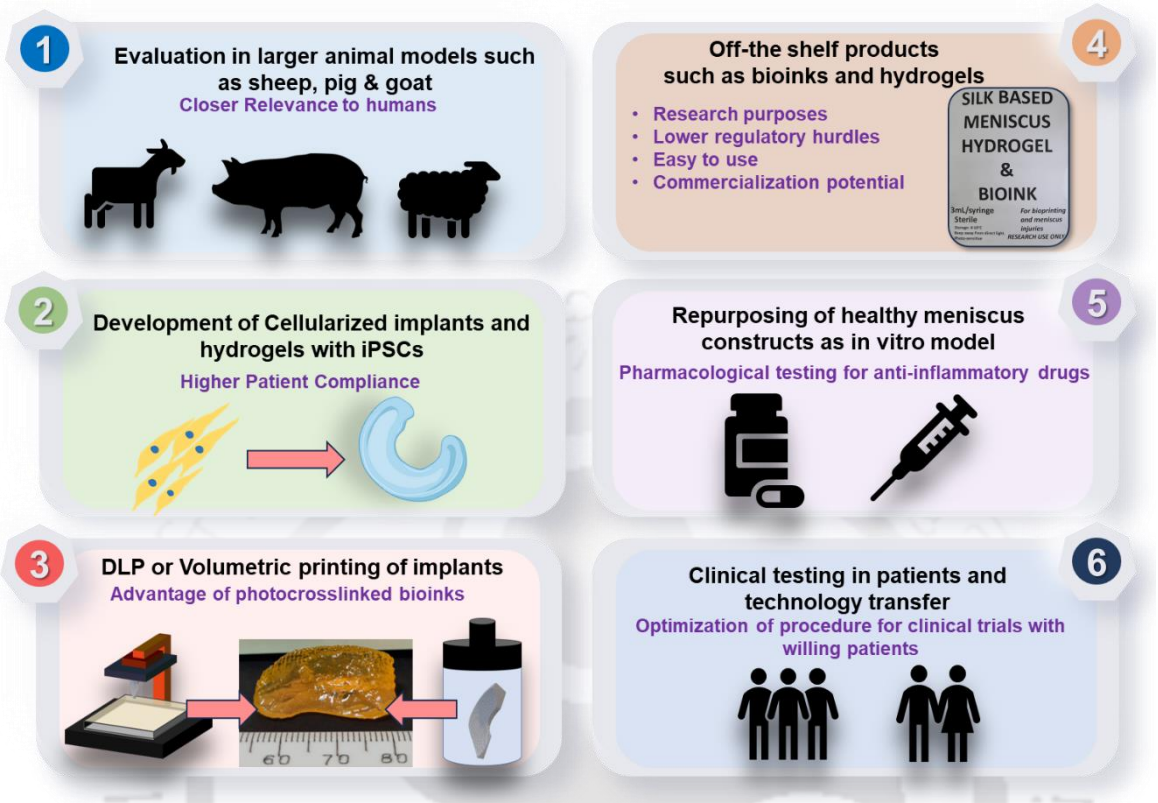

Figure S2: *Schematics illustrating the future perspectives of the present thesis.*

BIBLIOGRAPHY

[1] Bandyopadhyay, A., et al. Silk: A Promising Biomaterial Opening New Vistas Towards Affordable Healthcare Solutions, Journal of the Indian Institute of Science, Springer India, 2019, pp. 445-487 **DOI**.10.1007/s41745-019-00114-y

[2] Makris, E.A., et al. The knee meniscus: Structure-function, pathophysiology, current repair techniques, and prospects for regeneration, Biomaterials, 2011, pp. 7411-7431 **DOI**.10.1016/j.biomaterials.2011.06.037

[3] Masouros, S.D., et al. Biomechanics of the meniscus-meniscal ligament construct of the knee, Knee Surg Sports Traumatol Arthrosc 16(12) (2008) 1121-32 **DOI**.10.1007/s00167-008-0616-9

[4] Athanasiou, K.A., Sanchez-Adams, J. Engineering the Knee Meniscus, Synthesis Lectures on Tissue Engineering 1(1) (2009) 1-97 **DOI**.10.1007/978-3-031-02576-1

[5] Fox, A.J.S., et al. The basic science of human knee menisci: structure, composition, and function., Sports health 4(4) (2012) 340-51 **DOI**.10.1177/1941738111429419

[6] Ghadially, F.N., et al. Ultrastructure of rabbit semilunar cartilages., Journal of anatomy 125(Pt 3) (1978) 499-517

[7] Hellio Le Graverand, M.P., et al. The cells of the rabbit meniscus: their arrangement, interrelationship, morphological variations and cytoarchitecture., Journal of anatomy 198(Pt 5) (2001) 525-35 **DOI**.10.1046/j.1469-7580.2000.19850525.x

[8] Nakata, K., et al. Human meniscus cell: characterization of the primary culture and use for tissue engineering., Clinical Orthopaedics and Related Research (391 Suppl) (2001) S208-18

[9] Webber, R.J., et al. Cell culture of rabbit meniscal fibrochondrocytes: Proliferative and synthetic response to growth factors and ascorbate, Journal of Orthopaedic Research 3(1) (1985) 36-42 **DOI**.10.1002/jor.1100030104

[10] Moon, M.S., et al. The normal and regenerated meniscus in rabbits. Morphologic and histologic studies., Clinical Orthopaedics and Related Research (182) (1984) 264-9

[11] Mueller, S.M., et al. Meniscus cells seeded in type I and type II collagen-GAG matrices *in vitro*., Biomaterials 20(8) (1999) 701-9 **DOI**.10.1016/s0142-9612(98)00189-6

[12] Pangborn, C.A., Athanasiou, K.A. Effects of Growth Factors on Meniscal Fibrochondrocytes, Tissue Engineering 11(7-8) (2005) 1141-1148 **DOI**.10.1089/ten.2005.11.1141

[13] Miller, R.R., Rydell, P.A. Primary culture of microvascular endothelial cells from canine meniscus, Journal of Orthopaedic Research 11(6) (1993) 907-911 **DOI**.10.1002/jor.1100110618

[14] Ahluwalia, S., et al. Distribution of smooth muscle actin-containing cells in the human meniscus, Journal of Orthopaedic Research 19(4) (2001) 659-664 **DOI**.10.1016/S0736-0266(00)00041-3

[15] Mueller, S.M., et al. alpha-smooth muscle actin and contractile behavior of bovine meniscus cells seeded in type I and type II collagen-GAG matrices., Journal of biomedical materials research 45(3) (1999) 157-66 **DOI**.10.1002/(sici)1097-4636(19990605)45:3<157::aid-jbm1>3.0.co;2-b

[16] Arnoczky, S.P., Warren, R.F. The microvasculature of the meniscus and its response to injury, The American Journal of Sports Medicine 11(3) (1983) 131-141 **DOI**.10.1177/036354658301100305

[17] Melrose, J., et al. Comparative spatial and temporal localisation of perlecan, aggrecan and type I, II and IV collagen in the ovine meniscus: an ageing study, Histochem Cell Biol 124(3-4) (2005) 225-35 **DOI**.10.1007/s00418-005-0005-0

[18] Kambic, H.E., McDevitt, C.A. Spatial organization of types I and II collagen in the canine meniscus, J Orthop Res 23(1) (2005) 142-9 **DOI**.10.1016/j.orthres.2004.06.016

[19] Verdonk, P.C., et al. Characterisation of human knee meniscus cell phenotype, Osteoarthritis and Cartilage 13(7) (2005) 548-560 **DOI**.10.1016/j.joca.2005.01.010

[20] Valiyaveettil, M., et al. The concentration, gene expression, and spatial distribution of aggrecan in canine articular cartilage, meniscus, and anterior and posterior cruciate ligaments: a new molecular distinction between hyaline cartilage and fibrocartilage in the knee joint, Connect Tissue Res 46(2) (2005) 83-91 **DOI**.10.1080/03008200590954113

[21] Upton, M.L., et al. Region-specific constitutive gene expression in the adult porcine meniscus, J Orthop Res 24(7) (2006) 1562-70 **DOI**.10.1002/jor.20146

[22] Cao, M., et al. Generation of nitric oxide by lapine meniscal cells and its effect on matrix metabolism: Stimulation of collagen production by arginine, Journal of Orthopaedic Research 16(1) (1998) 104-111 **DOI**.10.1002/jor.1100160118

[23] Sweigart, M.A., Athanasiou, K.A. Toward Tissue Engineering of the Knee Meniscus, Tissue Engineering 7(2) (2001) 111-129 **DOI**.10.1089/107632701300062697

[24] Ghadially, F.N., et al. Ultrastructure of normal and torn menisci of the human knee joint, Journal of anatomy 136(Pt 4) (1983) 773-91

[25] Aspden, R.M., et al. Collagen orientations in the meniscus of the knee joint, Journal of Anatomy 140 (Pt 3)(Pt 3) (1985) 371-80

[26] McDevitt, C.A., Webber, R.J. The ultrastructure and biochemistry of meniscal cartilage, Clinical Orthopaedics and Related Research (252) (1990) 8-18

[27] Skaggs, D.L., et al. Radial tie fibers influence the tensile properties of the bovine medial meniscus., Journal of orthopaedic research : official publication of the Orthopaedic Research Society 12(2) (1994) 176-85 **DOI**.10.1002/jor.1100120205

[28] Hopker, W.W., et al. Changes of the elastin compartment in the human meniscus, Virchows Arch A Pathol Anat Histopathol 408(6) (1986) 575-92 **DOI**.10.1007/BF00705337

[29] Scott, P.G., et al. Isolation and characterization of small proteoglycans from different zones of the porcine knee meniscus, Biochim Biophys Acta 1336(2) (1997) 254-62 **DOI**.10.1016/s0304-4165(97)00040-8

[30] Tanaka, T., et al. Comparison of biochemical characteristics of cultured fibrochondrocytes isolated from the inner and outer regions of human meniscus, Knee Surg Sports Traumatol Arthrosc 7(2) (1999) 75-80 **DOI**.10.1007/s001670050125

[31] Morejon, A., et al. Compressive properties and hydraulic permeability of human meniscus: relationships with tissue structure and composition, Frontiers in bioengineering and biotechnology 8 (2021) 622552 **DOI**.10.3389/fbioe.2020.622552

[32] Rodeo, S.A., et al. Biological and Mechanical Predictors of Meniscus Function: Basic Science to Clinical Translation, Journal of Orthopaedic Research 38(5) (2020) 937-945 **DOI**.10.1002/jor.24552

[33] Walker, P.S., Hajek, J.V. The load-bearing area in the knee joint, J Biomech 5(6) (1972) 581-9 **DOI**.10.1016/0021-9290(72)90030-9

[34] Gabrion, A., et al. Relationship between ultrastructure and biomechanical properties of the knee meniscus, Surg Radiol Anat 27(6) (2005) 507-10 **DOI**.10.1007/s00276-005-0031-6

[35] Shaffer, B., et al. Preoperative sizing of meniscal allografts in meniscus transplantation, Am J Sports Med 28(4) (2000) 524-33 **DOI**.10.1177/03635465000280041301

[36] Shrive, N.G., et al. Load-bearing in the knee joint, Clinical Orthopaedics and Related Research (131) (1978) 279-87

[37] Zhu, W., et al. Anisotropic viscoelastic shear properties of bovine meniscus., Clinical Orthopaedics and Related Research (306) (1994) 34-45

[38] Kurosawa, H., et al. Load-Bearing Mode of the Knee-Joint - Physical Behavior of the Knee-Joint with or without Menisci, Clinical Orthopaedics and Related Research (149) (1980) 283-290

[39] Paul, J.P. Force actions transmitted by joints in the human body, Proc R Soc Lond B Biol Sci 192(1107) (1976) 163-72 **DOI**.10.1098/rspb.1976.0004

[40] Fetzer, G.B., et al. Potential Market for New Meniscus Repair Strategies–Evaluation of the MOON Cohort, The journal of knee surgery 22(03) (2009) 180-186 **DOI**.10.1055/s-0030-1247746

[41] Baker, B.E., et al. Review of meniscal injury and associated sports, The American journal of sports medicine 13(1) (1985) 1-4 **DOI**.10.1177/036354658501300101

[42] Clayton, R.A., Court-Brown, C.M. The epidemiology of musculoskeletal tendinous and ligamentous injuries, Injury 39(12) (2008) 1338-1344 **DOI**.10.1016/j.injury.2008.06.021

[43] Englund, M., et al. Patient-relevant outcomes fourteen years after meniscectomy: influence of type of meniscal tear and size of resection, Rheumatology 40(6) (2001) 631-639 **DOI**.10.1093/rheumatology/40.6.631

[44] Lohmander, L.S., et al. The long-term consequence of anterior cruciate ligament and meniscus injuries: osteoarthritis, The American journal of sports medicine 35(10) (2007) 1756-1769 **DOI**.10.1177/0363546507307396

[45] Valdez, G., et al. Meniscus Injuries of the Knee, American Academy of Physical Medicine and Rehabilitation, 2021,

[46] Ashutosh, B., Biman, B.M. A three-dimensional printed silk-based biomimetic tri-layered meniscus for potential patient-specific implantation, Biofabrication 12(1) (2019) 015003 **DOI**.10.1088/1758-5090/ab40fa

[47] Arnoczky, S.P., Warren, R.F. Microvasculature of the human meniscus, The American journal of sports medicine 10(2) (1982) 90-95 **DOI**.10.1177/036354658201000205

[48] Greis, P.E., et al. Meniscal injury: I. Basic science and evaluation, JAAOS-Journal of the American Academy of Orthopaedic Surgeons 10(3) (2002) 168-176 **DOI**.10.5435/00124635-200205000-00003

[49] Buma, P., et al. Tissue engineering of the meniscus, Biomaterials 25(9) (2004) 1523-1532 **DOI**.10.1016/S0142-9612(03)00499-X

[50] Fairbank, T.J. Knee joint changes after meniscectomy, The Journal of bone and joint surgery. British volume 30B(4) (1948) 664-670

[51] Berjon, J.J., et al. Degenerative lesions in the articular cartilage after meniscectomy: preliminary experimental study in dogs., The Journal of trauma 31(3) (1991) 342-50 **DOI**.10.1097/00005373-199103000-00006

[52] Allen, P.R., et al. Late degenerative changes after meniscectomy. Factors affecting the knee after operation., The Journal of bone and joint surgery. British volume 66(5) (1984) 666-71 **DOI**.10.1302/0301-620X.66B5.6548755

[53] Zielinska, B., et al. Meniscal tissue explants response depends on level of dynamic compressive strain, Osteoarthritis and cartilage 17(6) (2009) 754-760 **DOI**.10.1016/j.joca.2008.11.018

[54] HOUGH JR, A.J., WEBBER, R.J. Pathology of the Meniscus, Clinical Orthopaedics and Related Research 252(252) (1990) 32-40

[55] Berthiaume, M.-J., et al. Meniscal tear and extrusion are strongly associated with progression of knee osteoarthritis as assessed by quantitative magnetic resonance imaging, Annals of the rheumatic diseases 64(4) (2004) 556-63 **DOI**.10.1136/ard.2004.023796

[56] Fahmy, N., et al. Meniscal pathology and osteoarthritis of the knee, The Journal of Bone & Joint Surgery British Volume 65(1) (1983) 24-28 **DOI**.10.1302/0301-620X.65B1.6687393

[57] Lange, A., et al. Degenerative meniscus tears and mobility impairment in women with knee osteoarthritis, Osteoarthritis and cartilage 15(6) (2007) 701-708 **DOI**.10.1016/j.joca.2006.11.004

[58] Bamac, B., et al. Evaluation of medial and lateral meniscus thicknesses in early osteoarthritis of the knee with magnetic resonance imaging, Saudi medical journal 27(6) (2006) 854

[59] Adams, M.E., et al. The glycosaminoglycans in menisci in experimental and natural osteoarthritis, Arthritis & Rheumatism: Official Journal of the American College of Rheumatology 26(1) (1983) 69-76 **DOI**.10.1002/art.1780260111

[60] Sugita, T., et al. Radial displacement of the medial meniscus in varus osteoarthritis of the knee, Clinical Orthopaedics and Related Research (1976-2007) 387(387) (2001) 171-177 **DOI**.10.1097/00003086-200106000-00023

[61] Beaufils, P., Pujol, N. Does anyone still need meniscectomy?, Joint Bone Spine 84(4) (2016) 389-392

[62] Moon, M.S., Chung, I.S. Degenerative changes after meniscectomy and meniscal regeneration., International orthopaedics 12(1) (1988) 17-9 **DOI**.10.1007/BF00265736

[63] McGinity, J.B., et al. Partial or total meniscectomy: a comparative analysis, The Journal of bone and joint surgery. American volume 59(6) (1977) 763-6

[64] Jackson, J.P. Degenerative changes in the knee after meniscectomy., British medical journal 2(5604) (1968) 525-7 **DOI**.10.1136/bmj.2.5604.525

[65] Wang, D., et al. Clinical Replacement Strategies for Meniscus Tissue Deficiency, Cartilage 13(1_suppl) (2021) 262S-270S **DOI**.10.1177/19476035211060512

[66] Gee, S.M., et al. The burden of meniscus injury in young and physically active populations, Clinics in sports medicine 39(1) (2020) 13-27 **DOI**.10.1016/j.csm.2019.08.008

[67] Chaudhary, D.H.F., et al. Results of meniscus repair over menisectomy in bucket handle tear of medial meniscus: Study of 30 cases, International Journal of Orthopaedics Sciences 7(1) (2021) 553-556 **DOI**.10.22271/ortho.2021.v7.i1i.2541

[68] Luvsannyam, E., et al. Meniscus tear: pathology, incidence, and management, Cureus 14(5) (2022) e25121 **DOI**.10.7759/cureus.25121

[69] de Albornoz, P.M., Forriol, F. The meniscal healing process, Muscles, ligaments and tendons journal 2(1) (2012) 10

[70] Dandy, D. The arthroscopic anatomy of symptomatic meniscal lesions, The Journal of Bone & Joint Surgery British Volume 72(4) (1990) 628-633 **DOI**.10.1302/0301-620X.72B4.2380218

[71] Jackson, T., et al. Epidemiology, injury patterns, and treatment of meniscal tears in pediatric patients: a 16-year experience of a single center, Orthopaedic journal of sports medicine 7(12) (2019) 2325967119890325 **DOI**.10.1177/2325967119890325

[72] Li, Z., et al. Biomechanically, structurally and functionally meticulously tailored polycaprolactone/silk fibroin scaffold for meniscus regeneration, Theranostics 10(11) (2020) 5090-5106 **DOI**.10.7150/thno.44270

[73] Englund, M., et al. Patient-relevant outcomes fourteen years after meniscectomy: influence of type of meniscal tear and size of resection., Rheumatology (Oxford, England) 40(6) (2001) 631-9 **DOI**.10.1093/rheumatology/40.6.631

[74] Southworth, T.M., et al. Meniscal allograft transplants, Clinics in Sports Medicine 39(1) (2020) 93-123 **DOI**.10.1016/j.csm.2019.08.013

[75] Bonanzinga, T., et al. Long sports career and satisfactory clinical outcomes after Meniscal Allograft Transplantation (MAT) in young professional athletes involved in strenuous sports,

Knee Surgery, Sports Traumatology, Arthroscopy 30(7) (2022) 2314-2319 **DOI**.10.1007/s00167-021-06779-2

[76] Stevenson, C., et al. Meniscal allograft transplantation: undersizing grafts can lead to increased rates of clinical and mechanical failure, Knee Surgery, Sports Traumatology, Arthroscopy 27(6) (2019) 1900-1907 **DOI**.10.1007/s00167-019-05398-2

[77] Trentacosta, N., et al. Meniscal allograft transplantation: state of the art, Sports Med Arthrosc 24(2) (2016) e23-e33 **DOI**.10.1097/Jsa.0000000000000107

[78] Seiter, M.N., et al. Segmental meniscus allograft transplantation, Arthroscopy Techniques 10(3) (2021) e697-e703 **DOI**.10.1016/j.eats.2020.10.059

[79] Pereira, H., et al. Meniscal allograft transplants and new scaffolding techniques, EFORT open reviews 4(6) (2019) 279-295 **DOI**.10.1302/2058-5241.4.180103

[80] Rosso, F., et al. Meniscal allograft transplantation: A systematic review, American Journal of Sports Medicine, SAGE Publications Inc., 2015, pp. 998-1007 **DOI**.10.1177/0363546514536021

[81] Paletta Jr, G.A., et al. The effect of allograft meniscal replacement on intraarticular contact area and pressures in the human knee: a biomechanical study, The American journal of sports medicine 25(5) (1997) 692-698 **DOI**.10.1177/036354659702500519

[82] Winkler, P.W., et al. Association between meniscal allograft tears and early surgical meniscal allograft failure, The American Journal of Sports Medicine 49(12) (2021) 3302-3311 **DOI**.10.1177/03635465211032970

[83] Condron, N.B., et al. Concomitant Meniscotibial Ligament Reconstruction Decreases Meniscal Extrusion Following Medial Meniscus Allograft Transplantation: A Cadaveric Analysis, Arthroscopy: The Journal of Arthroscopic & Related Surgery 38(11) (2022) 3080-3089 **DOI**.10.1016/j.arthro.2022.06.015

[84] Houck, D.A., et al. Similar clinical outcomes following collagen or polyurethane meniscal scaffold implantation: a systematic review, Knee Surgery, Sports Traumatology, Arthroscopy 26(8) (2018) 2259-2269 **DOI**.10.1007/s00167-018-4838-1

[85] Gian Andrea, L., et al. Satisfactory clinical results and low failure rate of medial collagen meniscus implant (CMI) at a minimum 20 years of follow-up, Knee Surgery, Sports Traumatology, Arthroscopy 29(12) (2021) 4270-4277 **DOI**.10.1007/s00167-021-06556-1

[86] Butt, U., et al. Meniscal scaffold for the treatment of partial meniscal defect—clinical and radiological outcomes in a two-year follow-up, International Orthopaedics 45(4) (2021) 977-983 **DOI**.10.1007/s00264-020-04811-7

[87] Kovacs, B.K., et al. MR variability of collagen meniscal implant remodelling in patients with good clinical outcome, Knee Surgery, Sports Traumatology, Arthroscopy 29(1) (2021) 90-99 **DOI**.10.1007/s00167-019-05715-9

[88] Grassi, A., et al. Minimum 10-Year clinical outcome of lateral collagen meniscal implants for the replacement of partial lateral meniscal defects: further results from a prospective

multicenter study, Orthopaedic Journal of Sports Medicine 9(5) (2021) 2325967121994919 **DOI**.10.1177/2325967121994919

[89] Accadbled, F., et al. Implantation of an actifit® polyurethane meniscal scaffold 18 Months after subtotal lateral meniscectomy in a 13-year-old male adolescent, The American Journal of Case Reports 21 (2020) e920688-1 **DOI**.10.12659/AJCR.920688

[90] Leroy, A., et al. Actifit® polyurethane meniscal scaffold: MRI and functional outcomes after a minimum follow-up of 5 years, Orthopaedics & Traumatology: Surgery & Research 103(4) (2017) 609-614 **DOI**.10.1016/J.OTSR.2017.02.012

[91] Baynat, C., et al. Actifit® synthetic meniscal substitute: Experience with 18 patients in Brest, France, Orthopaedics & Traumatology: Surgery & Research 100(8 Suppl) (2014) S385-S389 **DOI**.10.1016/J.OTSR.2014.09.007

[92] Reale, D., et al. A Comparison Between Polyurethane and Collagen Meniscal Scaffold for Partial Meniscal Defects: Similar Positive Clinical Results at a Mean of 10 Years of Follow-Up, Arthroscopy: The Journal of Arthroscopic & Related Surgery 38(4) (2022) 1279-1287 **DOI**.10.1016/j.arthro.2021.09.011

[93] Verdonk, R., et al. Tissue ingrowth after implantation of a novel, biodegradable polyurethane scaffold for treatment of partial meniscal lesions, The American journal of sports medicine 39(4) (2011) 774-782 **DOI**.10.1177/0363546511398040

[94] Van Minnen, B., et al. In vivo resorption of a biodegradable polyurethane foam, based on 1, 4-butanediisocyanate: A three-year subcutaneous implantation study, Journal of Biomedical Materials Research Part A: An Official Journal of The Society for Biomaterials, The Japanese Society for Biomaterials, and The Australian Society for Biomaterials and the Korean Society for Biomaterials 85(4) (2008) 972-982 **DOI**.10.1002/jbm.a.31574

[95] Sandmann, G.H., et al. Biomechanical comparison of menisci from different species and artificial constructs, BMC musculoskeletal disorders 14(1) (2013) 1-8 **DOI**.10.1186/1471-2474-14-324

[96] Shemesh, M., et al. Effects of a novel medial meniscus implant on the knee compartments: imaging and biomechanical aspects, Biomechanics and Modeling in Mechanobiology 19(6) (2020) 2049-2059 **DOI**.10.1007/s10237-020-01323-6

[97] Farr, J., et al. Early Clinical Results of the NUsurface® Meniscus Implant vs. Non-Surgical Controls at 12 Months, Arthroscopy: The Journal of Arthroscopic & Related Surgery 37(1) (2021) e20-e21 **DOI**.10.1016/j.arthro.2020.12.043

[98] Kohli, S., et al. Failure rates and clinical outcomes of synthetic meniscal implants following partial meniscectomy: a systematic review, Knee Surgery & Related Research 34(1) (2022) 1-9 **DOI**.10.1186/s43019-022-00155-1

[99] Hélder, P., et al. Integration of polyurethane meniscus scaffold during ACL revision is not reliable at 5years despite favourable clinical outcome, Knee Surgery, Sports Traumatology, Arthroscopy 30(10) (2022) 3422-3427 **DOI**.10.1007/s00167-022-06946-z

[100] Hershman, E., et al. Superior Improvements in Knee Pain and Function with a Novel Synthetic Medial Meniscus Replacement Implant Compared to Non-surgical Care in Subjects

with Knee Pain Following Partial Meniscectomy: Two-year Results from Two Prospective US Clinical Trials, Orthopaedic Journal of Sports Medicine 9(7_suppl4) (2021) 2325967121S00206 **DOI**.10.1177/2325967121S00206

[101] Kwon, H., et al. Surgical and tissue engineering strategies for articular cartilage and meniscus repair, Nature Reviews Rheumatology 15(9) (2019) 550-570 **DOI**.10.1038/s41584-019-0255-1

[102] Azhim, A., et al. Bio-Engineered Meniscus for Tissue Engineering, Meniscus of the Knee - Function, Pathology and Management, IntechOpen, 2019, **DOI**.10.5772/intechopen.80553

[103] Bilgen, B., et al. Current Concepts in Meniscus Tissue Engineering and Repair, Advanced Healthcare Materials 7(11) (2018) 1701407 **DOI**.10.1002/adhm.201701407

[104] Guo, W., et al. Advances and Prospects in Tissue-Engineered Meniscal Scaffolds for Meniscus Regeneration, Stem Cells International 2015 (2015) 517520 **DOI**.10.1155/2015/517520

[105] Kawamura, S., et al. BIOMECHANICS AND HEALING RESPONSE OF THE MENISCUS, Oper Techn Sport Med 11(2) (2003) 68-76 **DOI**.10.1053/otsm.2003.35899

[106] Yan, R., et al. A collagen-coated sponge silk scaffold for functional meniscus regeneration, Journal of tissue engineering and regenerative medicine 13(2) (2019) 156-173 **DOI**.10.1002/term.2777

[107] Mandal, B.B., et al. Multilayered silk scaffolds for meniscus tissue engineering, Biomaterials 32(2) (2011) 639-651 **DOI**.10.1016/j.biomaterials.2010.08.115

[108] Zhong, G., et al. Injectable ECM hydrogel for delivery of BMSCs enabled full-thickness meniscus repair in an orthotopic rat model, Bioactive materials 5(4) (2020) 871-879 **DOI**.10.1016/j.bioactmat.2020.06.008

[109] Baek, J., et al. Meniscus tissue engineering using a novel combination of electrospun scaffolds and human meniscus cells embedded within an extracellular matrix hydrogel, Journal of Orthopaedic Research 33(4) (2015) 572-583 **DOI**.10.1002/jor.22802

[110] Shimomura, K., et al. Enhanced repair of meniscal hoop structure injuries using an aligned electrospun nanofibrous scaffold combined with a mesenchymal stem cell-derived tissue engineered construct, Biomaterials 192 (2019) 346-354 **DOI**.10.1016/j.biomaterials.2018.11.009

[111] Choi, J.R., et al. Current status and perspectives of human mesenchymal stem cell therapy, Hindawi, 2019,

[112] Yuan, X., et al. Stem cell delivery in tissue-specific hydrogel enabled meniscal repair in an orthotopic rat model, Biomaterials 132 (2017) 59-71 **DOI**.10.1016/J.BIOMATERIALS.2017.04.004

[113] Chae, S., et al. 3D cell-printing of biocompatible and functional meniscus constructs using meniscus-derived bioink, Biomaterials 267 (2021) 120466 **DOI**.10.1016/j.biomaterials.2020.120466

[114] Zhang, Z., et al. 3D Printing Super Strong Hydrogel for Artificial Meniscus, ACS Applied Polymer Materials 1(8) (2019) 2023-2032 **DOI**.10.1021/acsapm.9b00304

[115] Lee, C.H., et al. Protein-releasing polymeric scaffolds induce fibrochondrocytic differentiation of endogenous cells for knee meniscus regeneration in sheep., Science translational medicine 6(266) (2014) 266ra171 **DOI**.10.1126/scitranslmed.3009696

[116] Kang, H.-W., et al. A 3D bioprinting system to produce human-scale tissue constructs with structural integrity, Nature biotechnology 34(3) (2016) 312-319 **DOI**.10.1038/nbt.3413

[117] Burgess, C.J., De Cicco, F.L. Meniscectomy, Treasure Island (FL): StatPearls Publishing2023

[118] Lee, B.-S., et al. Partial meniscectomy for degenerative medial meniscal root tears shows favorable outcomes in well-aligned, nonarthritic knees, The American journal of sports medicine 47(3) (2019) 606-611 **DOI**.10.1177/0363546518819225

[119] Faucett, S.C., et al. Meniscus root repair vs meniscectomy or nonoperative management to prevent knee osteoarthritis after medial meniscus root tears: clinical and economic effectiveness, The American Journal of Sports Medicine 47(3) (2019) 762-769 **DOI**.10.1177/0363546518755754

[120] Yoon, K.H., Park, K.H. Meniscal repair, Knee surgery & related research 26(2) (2014) 68 **DOI**.10.5792/ksrr.2014.26.2.68

[121] Brindle, T., et al. The meniscus: review of basic principles with application to surgery and rehabilitation., Journal of athletic training 36(2) (2001) 160-9

[122] Messner, K., Gao, J. The menisci of the knee joint. Anatomical and functional characteristics, and a rationale for clinical treatment., Journal of anatomy 193 (Pt 2)(Pt 2) (1998) 161-78 **DOI**.10.1046/J.1469-7580.1998.19320161.X

[123] Adams, S.B., et al. Tissue engineering for meniscus repair., The journal of knee surgery 18(1) (2005) 25-30 **DOI**.10.1055/s-0030-1248154

[124] Hoben, G.M., Athanasiou, K.A. Meniscal repair with fibrocartilage engineering., Sports Med Arthrosc 14(3) (2006) 129-37 **DOI**.10.1097/00132585-200609000-00004

[125] Omoumi, P., et al. Meniscal calcifications: morphologic and quantitative evaluation by using 2D inversion-recovery ultrashort echo time and 3D ultrashort echo time 3.0-T MR imaging techniques—feasibility study, Radiology 264(1) (2012) 260 **DOI**.10.1148/radiol.12111439

[126] Bjerre-Bastos, J.J., et al. Joint biomarker response to mechanical stimuli in osteoarthritis–a scoping review, Osteoarthritis and Cartilage Open 5(4) (2023) 100390 **DOI**.10.1016/j.ocarto.2023.100390

[127] Zhai, G. Clinical relevance of biochemical and metabolic changes in osteoarthritis, Advances in Clinical Chemistry, Elsevier2021, pp. 95-120 **DOI**.10.1016/bs.acc.2020.06.001

[128] Rongen, J.J., et al. Biomaterials in search of a meniscus substitute, Biomaterials 35(11) (2014) 3527-3540 **DOI**.10.1016/j.biomaterials.2014.01.017

[129] Szojka, A., et al. Biomimetic 3D printed scaffolds for meniscus tissue engineering, Bioprinting 8 (2017) 1-7 **DOI**.10.1016/j.bprint.2017.08.001

[130] McCorry, M.C., et al. A model system for developing a tissue engineered meniscal enthesis, Acta biomaterialia 56 (2017) 110-117 **DOI**.10.1016/j.actbio.2016.10.040

[131] Pan, Z., et al. Delivery of epidermal growth factor receptor inhibitor via a customized collagen scaffold promotes meniscal defect regeneration in a rabbit model, Acta Biomaterialia 62 (2017) 210-221 **DOI**.10.1016/j.actbio.2017.07.008

[132] Cengiz, I.F., et al. Suturable regenerated silk fibroin scaffold reinforced with 3D-printed polycaprolactone mesh: biomechanical performance and subcutaneous implantation, Journal of Materials Science: Materials in Medicine 30(6) (2019) 1-17 **DOI**.10.1007/s10856-019-6265-3

[133] Klarmann, G.J., et al. 3D printing a universal knee meniscus using a custom collagen ink, Bioprinting 31 (2023) e00272 **DOI**.10.1016/j.bprint.2023.e00272

[134] Chen, M., et al. PCL-MECM-based hydrogel hybrid scaffolds and meniscal fibrochondrocytes promote whole meniscus regeneration in a rabbit meniscectomy model, ACS applied materials & interfaces 11(44) (2019) 41626-41639 **DOI**.10.1021/acsami.9b13611

[135] Guo, W., et al. 3D-printed cell-free PCL–MECM scaffold with biomimetic micro-structure and micro-environment to enhance in situ meniscus regeneration, Bioactive materials 6(10) (2021) 3620-3633 **DOI**.10.1016/j.bioactmat.2021.02.019

[136] Woodfield, T., et al. Rapid prototyping of anatomically shaped, tissue-engineered implants for restoring congruent articulating surfaces in small joints, Cell proliferation 42(4) (2009) 485-497 **DOI**.10.1111/j.1365-2184.2009.00608.x

[137] Sun, Y., et al. 3D-bioprinting ready-to-implant anisotropic menisci recapitulate healthy meniscus phenotype and prevent secondary joint degeneration, Theranostics 11(11) (2021) 5160-5173 **DOI**.10.7150/thno.54864

[138] Asgarpour, R., et al. Development of meniscus-inspired 3D-printed PCL scaffolds engineered with chitosan/extracellular matrix hydrogel, Polymers for Advanced Technologies 32(12) (2021) 4721-4732 **DOI**.10.1002/PAT.5465

[139] Sun, Y., et al. Generating ready-to-implant anisotropic menisci by 3D-bioprinting protein-releasing cell-laden hydrogel-polymer composite scaffold, Applied Materials Today 18 (2020) **DOI**.10.1016/j.apmt.2019.100469

[140] Luis, E., et al. 3D Direct Printing of Silicone Meniscus Implant Using a Novel Heat-Cured Extrusion-Based Printer, Polymers 12(5) (2020) 1031 **DOI**.10.3390/polym12051031

[141] Hurmuz, M., et al. Hydrogel Based Biomeniscus 3D Printed Seeded with Human Adipose Derived Mesenchymal Stem cells, Journal of Medical Biomedical and Applied Sciences 8 (2020) 382-387 **DOI**.10.15520/JMBAS.V8I4.225

[142] Zhang, Z., et al. Modeling-Based Assessment of 3D Printing-Enabled Meniscus Transplantation, Healthcare 7(2) (2019) 69 **DOI**.10.3390/healthcare7020069

[143] Sooriyaarachchi, D., et al. Hybrid fabrication of biomimetic meniscus scaffold by 3D printing and parallel electrospinning, Elsevier B.V., 2019, pp. 528-534 **DOI**.10.1016/j.promfg.2019.06.216

[144] Jian, Z., et al. 3D bioprinting of a biomimetic meniscal scaffold for application in tissue engineering, Bioactive Materials 6(6) (2021) 1711-1726 **DOI**.10.1016/j.bioactmat.2020.11.027

[145] Gruber, H.E., et al. Three-dimensional culture of human meniscal cells: Extracellular matrix and proteoglycan production, BMC Biotechnology 8 (2008) 54 **DOI**.10.1186/1472-6750-8-54

[146] Bhargava, M.M., et al. The Effect of Cytokines on the Proliferation and Migration of Bovine Meniscal Cells, The American Journal of Sports Medicine 27(5) (1999) 636-643 **DOI**.10.1177/03635465990270051601

[147] Pangborn, C.A., Athanasiou, K.A. Growth factors and fibrochondrocytes in scaffolds., Journal of orthopaedic research : official publication of the Orthopaedic Research Society 23(5) (2005) 1184-90 **DOI**.10.1016/j.orthres.2005.01.019

[148] Bahcecioglu, G., et al. Construction and in vitro testing of a multilayered, tissue-engineered meniscus, Journal of bioactive and compatible polymers 29(3) (2014) 235-253 **DOI**.10.1177/0883911514529688

[149] Hoben, G.M., et al. Self-Assembly of Fibrochondrocytes and Chondrocytes for Tissue Engineering of the Knee Meniscus, Tissue Engineering 13(5) (2007) 939-946 **DOI**.10.1089/ten.2006.0116

[150] Kawamura, K., et al. Adenoviral-mediated transfer of TGF-beta1 but not IGF-1 induces chondrogenic differentiation of human mesenchymal stem cells in pellet cultures., Experimental hematology 33(8) (2005) 865-72 **DOI**.10.1016/j.exphem.2005.05.010

[151] Sekiya, I., et al. In vitro cartilage formation by human adult stem cells from bone marrow stroma defines the sequence of cellular and molecular events during chondrogenesis., Proceedings of the National Academy of Sciences of the United States of America 99(7) (2002) 4397-402 **DOI**.10.1073/pnas.052716199

[152] Worster, A.A., et al. Chondrocytic differentiation of mesenchymal stem cells sequentially exposed to transforming growth factor-β1 in monolayer and insulin-like growth factor-I in a three-dimensional matrix, Journal of Orthopaedic Research 19(4) (2001) 738-749 **DOI**.10.1016/S0736-0266(00)00054-1

[153] Hoben, G.M., et al. Fibrochondrogenesis in Two Embryonic Stem Cell Lines: Effects of Differentiation Timelines, Stem Cells 26(2) (2008) 422-430 **DOI**.10.1634/stemcells.2007-0641

[154] Hoben, G.M., et al. Fibrochondrogenesis of hESCs: growth factor combinations and cocultures., Stem cells and development 18(2) (2009) 283-92 **DOI**.10.1089/scd.2008.0024

[155] Van Osch, G.J.V.M., et al. Considerations on the use of ear chondrocytes as donor chondrocytes for cartilage tissue engineering., Biorheology 41(3-4) (2004) 411-21

[156] Deng, Y., et al. Isolation and chondroinduction of a dermis-isolated, aggrecan-sensitive subpopulation with high chondrogenic potential, Arthritis & Rheumatism 56(1) (2007) 168-176 **DOI**.10.1002/art.22300

[157] Ikeda, T., et al. The combination of SOX5, SOX6, and SOX9 (the SOX trio) provides signals sufficient for induction of permanent cartilage, Arthritis & Rheumatism 50(11) (2004) 3561-3573 **DOI**.10.1002/art.20611

[158] Mizuno, S., Glowacki, J. Chondroinduction of Human Dermal Fibroblasts by Demineralized Bone in Three-Dimensional Culture, Experimental Cell Research 227(1) (1996) 89-97 **DOI**.10.1006/excr.1996.0253

[159] Betre, H., et al. Chondrocytic differentiation of human adipose-derived adult stem cells in elastin-like polypeptide, Biomaterials 27(1) (2006) 91-99 **DOI**.10.1016/j.biomaterials.2005.05.071

[160] Estes, B.T., et al. Potent induction of chondrocytic differentiation of human adipose-derived adult stem cells by bone morphogenetic protein 6, Arthritis & Rheumatism 54(4) (2006) 1222-1232 **DOI**.10.1002/art.21779

[161] Gimble, J.M., Guilak, F. Adipose-derived adult stem cells: isolation, characterization, and differentiation potential, Cytotherapy 5(5) (2003) 362-369 **DOI**.10.1080/14653240310003026

[162] Park, Y., et al. BMP-2 induces the expression of chondrocyte-specific genes in bovine synovium-derived progenitor cells cultured in three-dimensional alginate hydrogel, Osteoarthritis and Cartilage 13(6) (2005) 527-536 **DOI**.10.1016/j.joca.2005.02.006

[163] Xiaoyi, L., et al. TEMPO-Oxidized Cellulose Nanofiber-Alginate Hydrogel as a Bioink for Human Meniscus Tissue Engineering, Frontiers in Bioengineering and Biotechnology 9 (2021) 766399 **DOI**.10.3389/fbioe.2021.766399

[164] Alexander, R.A.S., et al. Time course of 3D fibrocartilage formation by expanded human meniscus fibrochondrocytes in hypoxia, Journal of Orthopaedic Research 40(2) (2021) 495-503 **DOI**.10.1002/jor.25046

[165] Matthew, A.-B., et al. Effect of cell seeding density on matrix-forming capacity of meniscus fibrochondrocytes and nasal chondrocytes in meniscus tissue engineering, The FASEB Journal 34(4) (2020) 5538-5551 **DOI**.10.1096/fj.201902559r

[166] Alexander, R.A.S., et al. Hypoxia and TGF-β3 Synergistically Mediate Inner Meniscus-Like Matrix Formation by Fibrochondrocytes, Tissue Engineering Part A 25(5-6) (2019) 446-456 **DOI**.10.1089/ten.tea.2018.0211

[167] Yan, L., et al. Plasticity of Human Meniscus Fibrochondrocytes: A Study on Effects of Mitotic Divisions and Oxygen Tension, Scientific Reports 7(1) (2017) 12148 **DOI**.10.1038/s41598-017-12096-x

[168] Rachel, H.K., et al. Effect of conditioned media from fibrochondrocytes, combined with TGFβ3 treatment and type I collagen-based hydrogel, for meniscus tissue engineering, 2016 Korean Society of Biotechnology Spring Conference and International Symposium, The Korean Society of Biotechnology, 2016, p. 255

[169] Andrea Rodrigues, E., et al. PLDLA/PCL-T Scaffold for Meniscus Tissue Engineering, BioResearch Open Access 2(2) (2013) 138-47 **DOI**.10.1089/biores.2012.0293

[170] Brendon, M.B., et al. Autologous Human Fibrochondrocytes From Meniscectomy Debris are a Potent Cell Source for Meniscus Tissue Engineering, (2007) **DOI**.10.1115/sbc2007-176525

[171] Sweigart, M.A., et al. Fibrochondrocytes and their Use in Tissue Engineering of the Meniscus, in: Ashammakhi, N., Ferretti, P. (Eds.), Topics in Tissue Engineering, University of Oulu2003, pp. 1-19

[172] Hong Suk, K., et al. Meniscal repair *in vivo* using human chondrocyte-seeded PLGA mesh scaffold pretreated with platelet-rich plasma, Journal of Tissue Engineering and Regenerative Medicine 11(2) (2017) 471-480 **DOI**.10.1002/term.1938

[173] Daniel, J.H., Kyriacos, A.A. Alteration of the Fibrocartilaginous Nature of Scaffoldless Constructs Formed from Leporine Meniscus Cells and Chondrocytes through Manipulation of Culture and Processing Conditions, Cells Tissues Organs 197(5) (2013) 360-71 **DOI**.10.1159/000346252

[174] Yoo, J.J., et al. Scaffold Seeding Conditions and Meniscal Repair in an Experimental Model, 56th Annual Meeting of the Orthopaedic Research Society, Orthopaedic Research Society, 2010,

[175] Christian, W., et al. Healing potential of transplanted allogeneic chondrocytes of three different sources in lesions of the avascular zone of the meniscus: a pilot study, Archives of Orthopaedic and Trauma Surgery 126(9) (2006) 599-605 **DOI**.10.1007/s00402-005-0100-7

[176] Giuseppe, M.P., et al. Cell-based therapy for meniscal repair: a large animal study, American Journal of Sports Medicine 32(1) (2004) 146-58 **DOI**.10.1177/0095399703258790

[177] Caminal, M., et al. Use of a chronic model of articular cartilage and meniscal injury for the assessment of long-term effects after autologous mesenchymal stromal cell treatment in sheep, New Biotechnology 31(5) (2014) 492-498 **DOI**.10.1016/j.nbt.2014.07.004

[178] Jung, J.W., et al. A new method of fabricating a blend scaffold using an indirect three-dimensional printing technique, Biofabrication 7(4) (2015) 045003 **DOI**.10.1088/1758-5090/7/4/045003

[179] Sofia Hidalgo, P., et al. Evaluation of culture conditions for in vitro meniscus repair model systems using bone marrow-derived mesenchymal stem cells, Connective Tissue Research 61(3-4) (2019) 322-337 **DOI**.10.1080/03008207.2019.1680656

[180] Matthias, K., et al. Bone Marrow Aspirate Concentrate for the Treatment of Avascular Meniscus Tears in a One-Step Procedure—Evaluation of an In Vivo Model, International Journal of Molecular Sciences 20(5) (2019) **DOI**.10.3390/ijms20051120

[181] Sung Hwan, B., et al. Magnetic Resonance Imaging (MRI) of a Hypertrophy of Cartilage and Simultaneous Regeneration of a Damaged Meniscus after Autologous Bone Marrow Aspirates Concentrate (BMAC) Transplantation: a Case Report and Literature Review, Investigative Magnetic Resonance Imaging 21(3) (2017) **DOI**.10.13104/imri.2017.21.3.187

[182] Desando, G., et al. Autologous Bone Marrow Concentrate in a Sheep Model of Osteoarthritis: New Perspectives for Cartilage and Meniscus Repair, Tissue Engineering Part C-methods 22(6) (2016) 608-19 **DOI**.10.1089/ten.tec.2016.0033

[183] Matsukura, Y., et al. Mesenchymal stem cells in synovial fluid increase after meniscus injury, Clinical Orthopaedics and Related Research 472(5) (2014) 1357-1364 **DOI**.10.1007/s11999-013-3418-4

[184] Qiaoyin, T., et al. Stem Cells as a Novel Biomedicine for the Repair of Articular Meniscus: Pharmacology and Applications, Frontiers in Pharmacology 13 (2022) 897635 **DOI**.10.3389/fphar.2022.897635

[185] Nobutake, O., et al. Synovial mesenchymal stem cells promote the meniscus repair in a novel pig meniscus injury model, Journal of Orthopaedic Research 39(1) (2020) 177-183 **DOI**.10.1002/jor.24846

[186] Yusuke, N., et al. Synovial mesenchymal stem cells promote healing after meniscal repair in microminipigs, Osteoarthritis and Cartilage 23(6) (2015) 1007-17 **DOI**.10.1016/j.joca.2015.02.008

[187] Hisako, K., et al. Transplantation of synovial stem cells to promote healing after meniscal suture repair, Nihon rinsho. Japanese journal of clinical medicine (2015)

[188] Yoshiya, Muneta Syngeneic, minor mismatched, and major mismatched transplantation of synovial mesenchymal stem cells in a rat massive meniscal defect model, Osteoarthritis and Cartilage 20 (2011) **DOI**.10.1016/j.joca.2012.02.458

[189] Yiying, Q., et al. Targeted transplantation of iron oxide-labeled, adipose-derived mesenchymal stem cells in promoting meniscus regeneration following a rabbit massive meniscal defect, Experimental and Therapeutic Medicine 11(2) (2016) 458-466 **DOI**.10.3892/etm.2015.2944

[190] Maria Luisa, G.-F., et al. Assessment of regeneration in meniscal lesions by use of mesenchymal stem cells derived from equine bone marrow and adipose tissue, American Journal of Veterinary Research 77(7) (2016) 779-88 **DOI**.10.2460/ajvr.77.7.779

[191] Jaewoo, P., et al. Regenerative Repair of Damaged Meniscus with Autologous Adipose Tissue-Derived Stem Cells, BioMed Research International 2014 (2014) 436029 **DOI**.10.1155/2014/436029

[192] Hatsushika, D., et al. Repetitive allogeneic intraarticular injections of synovial mesenchymal stem cells promote meniscus regeneration in a porcine massive meniscus defect model., Osteoarthritis and cartilage 22(7) (2014) 941-50 **DOI**.10.1016/j.joca.2014.04.028

[193] Shaoqi, H., et al. Characterization and Comparison of Postnatal Rat Meniscus Stem Cells at Different Developmental Stages, Stem Cells Translational Medicine 8(12) (2019) 1318-1329 **DOI**.10.1002/sctm.19-0125

[194] Weiliang, S., et al. Intra-Articular Injection of Human Meniscus Stem/Progenitor Cells Promotes Meniscus Regeneration and Ameliorates Osteoarthritis Through Stromal Cell-Derived Factor-1/CXCR4-Mediated Homing, Stem Cells Translational Medicine 3(3) (2014) 387-94 **DOI**.10.5966/sctm.2012-0170

[195] Weiliang, S., et al. Osteoarthritis Prevention Through Meniscal Regeneration Induced by Intra-Articular Injection of Meniscus Stem Cells, Stem Cells and Development 22(14) (2013) 2071-82 **DOI**.10.1089/scd.2012.0563

[196] Alvarez-Viejo, M., et al. Quantifying mesenchymal stem cells in the mononuclear cell fraction of bone marrow samples obtained for cell therapy, Transplantation proceedings, Elsevier, 2013, pp. 434-439 **DOI**.10.1016/j.transproceed.2012.05.091

[197] Chowdhury, A., et al. Effect of interleukin-1beta treatment on co-cultures of human meniscus cells and bone marrow mesenchymal stromal cells, BMC Musculoskelet Disord 14 (2013) 216 **DOI**.10.1186/1471-2474-14-216

[198] Frese, L., et al. Adipose tissue-derived stem cells in regenerative medicine, Transfusion Medicine and Hemotherapy 43(4) (2016) 268-274 **DOI**.10.1159/000448180

[199] Diekman, B.O., et al. Chondrogenesis of adult stem cells from adipose tissue and bone marrow: induction by growth factors and cartilage-derived matrix, Tissue Engineering Part A 16(2) (2010) 523-533 **DOI**.10.1089/ten.TEA.2009.0398

[200] Morito, T., et al. Synovial fluid-derived mesenchymal stem cells increase after intra-articular ligament injury in humans, Rheumatology 47(8) (2008) 1137-1143 **DOI**.10.1093/rheumatology/ken114

[201] Sakaguchi, Y., et al. Comparison of human stem cells derived from various mesenchymal tissues: superiority of synovium as a cell source, Arthritis & Rheumatism: Official Journal of the American College of Rheumatology 52(8) (2005) 2521-2529 **DOI**.10.1002/art.21212

[202] Hatakeyama, A., et al. Isolation and characterization of synovial mesenchymal stem cell derived from hip joints: a comparative analysis with a matched control knee group, Stem Cells International 2017 (2017) 9312329 **DOI**.10.1155/2017/9312329

[203] Mauck, R.L., et al. Regional multilineage differentiation potential of meniscal fibrochondrocytes: implications for meniscus repair, The Anatomical Record: Advances in Integrative Anatomy and Evolutionary Biology: Advances in Integrative Anatomy and Evolutionary Biology 290(1) (2007) 48-58 **DOI**.10.1002/ar.20419

[204] Mehrotra, S., et al. 3D Printing/Bioprinting Based Tailoring of in Vitro Tissue Models: Recent Advances and Challenges, ACS Applied Bio Materials 2(4) (2019) 1385-1405 **DOI**.10.1021/acsabm.9b00073

[205] Jay, M.P., et al. Negative Outcomes of Poly(l-Lactic Acid) Fiber-Reinforced Scaffolds in an Ovine Total Meniscus Replacement Model, Tissue Engineering Part A 22(17-18) (2016) 1116-25 **DOI**.10.1089/ten.tea.2016.0143

[206] Najmuddin, J.G., Kyriacos, A.A. Additive and synergistic effects of bFGF and hypoxia on leporine meniscus cell-seeded PLLA scaffolds, Journal of Tissue Engineering and Regenerative Medicine 4(2) (2010) 115-22 **DOI**.10.1002/term.221

[207] Najmuddin, J.G., Kyriacos, A.A. Effects of hydrostatic pressure on leporine meniscus cell-seeded PLLA scaffolds, Journal of Biomedical Materials Research Part A 92(3) (2009) 896-905 **DOI**.10.1002/jbm.a.32451

[208] Promnil, S., et al. Electrospun Poly(lactic acid) and Silk Fibroin Based Nanofibrous Scaffold for Meniscus Tissue Engineering, Polymers (Basel) 14(12) (2022) **DOI**.10.3390/polym14122435

[209] Shunsuke, S., et al. Biomechanical assessment of a novel meniscal scaffold compared to partial meniscectomy: A study on porcine meniscal injury, Journal of Biomedical Materials Research Part B 111(4) (2022) 895-902 **DOI**.10.1002/jbm.b.35199

[210] Dan Grigore, C., et al. Meniscus-shaped cell-free polyglycolic acid scaffold for meniscal repair in a sheep model, Journal of Biomedical Materials Research Part B 108(3) (2020) 809-818 **DOI**.10.1002/jbm.b.34435

[211] Tomohiko, M., et al. Establishment of novel meniscal scaffold structures using polyglycolic and poly-l-lactic acids, Journal of Biomaterials Applications 32(2) (2017) 150-161 **DOI**.10.1177/0885328217713631

[212] Dan, L., et al. Construction of Tissue Engineered Meniscus with Bone Marrow Mesenchymal Stem Cells in Vitro, Journal of Tissue Engineering and Reconstructive Surgery (2013) 251-255 **DOI**.10.3969/j.issn.1673-0364.2013.05.003

[213] Cao, Y. Tissue Engineered Meniscus Constructed by DFs in the Repair of Meniscus Defects, Journal of Tissue Engineering and Reconstructive Surgery (2013) **DOI**.10.3969/j.issn.1673-0364.2013.02.002

[214] Lingfeng, H., et al. Improving the Mechanical Properties and Tribological Behavior of Sulfobetaine Polyurethane Based on Hydrophobic Chains to Be Applied as Artificial Meniscus, ACS Applied Materials and Interfaces 15(25) (2023) 29801-29812 **DOI**.10.1021/acsami.3c02940

[215] Aad, D., et al. Polyurethane Scaffold for the Treatment of Partial Meniscus Deficiency: European Multi-center Study, Arthroscopy 37(1) (2021) **DOI**.10.1016/j.arthro.2020.12.015

[216] Vincenzo, C., et al. Polyurethane scaffold implants for partial meniscus lesions: delayed intervention leads to an inferior outcome, Knee Surgery, Sports Traumatology, Arthroscopy 29(1) (2019) 109-116 **DOI**.10.1007/s00167-019-05760-4

[217] Eun-Ho, S., et al. Multilayered Polyurethane–Hydroxyapatite Composite for Meniscus Replacements, Macromolecular Materials and Engineering 304(1) (2019) **DOI**.10.1002/mame.201800352

[218] Matthias, K., et al. Tissue Engineering of Large Full-Size Meniscus Defects by a Polyurethane Scaffold: Accelerated Regeneration by Mesenchymal Stromal Cells, Stem Cells International 2018 (2018) 8207071 **DOI**.10.1155/2018/8207071

[219] Vrancken, A.C.T., et al. Short term evaluation of an anatomically shaped polycarbonate urethane total meniscus replacement in a goat model, PLOS ONE 10(7) (2015) e0133138 **DOI**.10.1371/journal.pone.0133138

[220] Zahra, A., et al. Characterization of Macroporous Polycaprolactone/Silk Fibroin/Gelatin/Ascorbic Acid Composite Scaffolds and In Vivo Results in a Rabbit Model for Meniscus Cartilage Repair, Cartilage 13(2_suppl) (2021) 1583S-1601S **DOI**.10.1177/19476035211035418

[221] Hao, L., et al. 3D Printed Poly(ε-Caprolactone)/Meniscus Extracellular Matrix Composite Scaffold Functionalized With Kartogenin-Releasing PLGA Microspheres for Meniscus Tissue Engineering, Frontiers in Bioengineering and Biotechnology 9 (2021) 662381 **DOI**.10.3389/fbioe.2021.662381

[222] Yangyang, L., et al. Cell-free 3D wet-electrospun PCL/silk fibroin/Sr2+ scaffold promotes successful total meniscus regeneration in a rabbit model, Acta Biomaterialia 113 (2020) 196-209 **DOI**.10.1016/j.actbio.2020.06.017

[223] Ibrahim Fatih, C., et al. Entrapped in cage (EiC) scaffolds of 3D-printed polycaprolactone and porous silk fibroin for meniscus tissue engineering, Biofabrication 12(2) (2020) 025028 **DOI**.10.1088/1758-5090/ab779f

[224] Bahcecioglu, G., et al. A 3D printed PCL/hydrogel construct with zone-specific biochemical composition mimicking that of the meniscus, Biofabrication 11(2) (2019) 025002 **DOI**.10.1088/1758-5090/aaf707

[225] van Bochove, B., et al. Preparation of designed poly (trimethylene carbonate) meniscus implants by stereolithography: challenges in stereolithography, Macromolecular bioscience 16(12) (2016) 1853-1863 **DOI**.10.1002/mabi.201600290

[226] Ding, G., et al. Meniscal transplantation and regeneration using functionalized polyurethane bionic scaffold and digital light processing 3D printing, Chemical Engineering Journal 431 (2022) 133861 **DOI**.10.1016/j.cej.2021.133861

[227] Ge, Q., et al. 3D printing of highly stretchable hydrogel with diverse UV curable polymers, Science advances 7(2) (2021) eaba4261 **DOI**.10.1126/sciadv.aba4261

[228] Thiago Domingues, S., et al. Towards Bioinspired Meniscus-Regenerative Scaffolds: Engineering a Novel 3D Bioprinted Patient-Specific Construct Reinforced by Biomimetically Aligned Nanofibers, International Journal of Nanomedicine 17 (2022) 1111-1124 **DOI**.10.2147/ijn.s353937

[229] Oylum Colpankan, G., et al. Fabrication of 3D Printed poly(lactic acid) strut and wet-electrospun cellulose nano fiber reinforced chitosan-collagen hydrogel composite scaffolds for meniscus tissue engineering, Journal of Biomaterials Applications 37(4) (2022) 683-697 **DOI**.10.1177/08853282221109339

[230] Jihye, B., et al. Collagen fibrous scaffolds for sustained delivery of growth factors for meniscal tissue engineering, Nanomedicine 17(2) (2022) 77-93 **DOI**.10.2217/nnm-2021-0313

[231] Erik, W.D., et al. Pneumatospinning Biomimetic Scaffolds for Meniscus Tissue Engineering, Frontiers in Bioengineering and Biotechnology 10 (2022) 810705 **DOI**.10.3389/fbioe.2022.810705

[232] Grassi, A., et al. Lateral collagen meniscus implant (CMI): techniques and outcomes—a narrative review, Annals of Joint 7 (2021) 18-18 **DOI**.10.21037/aoj-21-2

[233] Salim, A.G., et al. Biomechanical characterization of a novel collagen-hyaluronan infused 3D-printed polymeric device for partial meniscus replacement, Journal of Biomedical Materials Research Part B 107(8) (2019) 2457-2465 **DOI**.10.1002/jbm.b.34336

[234] Vasif, H. Collagen Based Multilayer Scaffolds for Meniscus Tissue Engineering: In Vivo Test Results, Biomaterials and Medical Applications 02(01) (2018) **DOI**.10.4172/2577-0268.1000112

[235] Jihye, B., et al. Repair of Avascular Meniscus Tears with Electrospun Collagen Scaffolds Seeded with Human Cells, Tissue Engineering Part A 22(5-6) (2016) 436-48 **DOI**.10.1089/ten.tea.2015.0284

[236] Shuhei, O., et al. A new method for meniscus repair using type I collagen scaffold and infrapatellar fat pad, Journal of Biomaterials Applications 29(10) (2015) 1439-48 **DOI**.10.1177/0885328215568984

[237] Zahra, A., et al. Development of meniscus cartilage using polycaprolactone and decellularized meniscus surface modified by gelatin, hyaluronic acid biomacromolecules: A rabbit model, International Journal of Biological Macromolecules 213 (2022) 498-515 **DOI**.10.1016/j.ijbiomac.2022.05.140

[238] Betül, B., et al. Comparison of physical therapy and arthroscopic partial meniscectomy treatments in degenerative meniscus tears and the effect of combined hyaluronic acid injection with these treatments: A randomized clinical trial, Journal of Back and Musculoskeletal Rehabilitation 34(5) (2021) 767-774 **DOI**.10.3233/bmr-200284

[239] Alessandra, B., et al. Quantitative Evaluation of Meniscal Healing Process of Degenerative Meniscus Lesions Treated with Hyaluronic Acid: A Clinical and MRI Study, Journal of Clinical Medicine 9(7) (2020) **DOI**.10.3390/jcm9072280

[240] Tomohiko, M., et al. Hyaluronic acid promotes proliferation and migration of human meniscus cells via a CD44-dependent mechanism, Connective Tissue Research 60(2) (2019) 117-127 **DOI**.10.1080/03008207.2018.1465053

[241] Gokhan, B., et al. Hydrogels of agarose, and methacrylated gelatin and hyaluronic acid are more supportive for in vitro meniscus regeneration than three dimensional printed polycaprolactone scaffolds, International Journal of Biological Macromolecules 122 (2019) 1152-1162 **DOI**.10.1016/j.ijbiomac.2018.09.065

[242] Rachel, H.K., et al. Chondrogenically primed tonsil-derived mesenchymal stem cells encapsulated in riboflavin-induced photocrosslinking collagen-hyaluronic acid hydrogel for meniscus tissue repairs, Acta Biomaterialia 53 (2017) 318-328 **DOI**.10.1016/j.actbio.2017.01.081

[243] Francisco, F., et al. VEGF, BMP-7, Matrigel TM , Hyaluronic Acid, In Vitro Cultured Chondrocytes and Trephination for Healing of the Avascular Portion of the Meniscus. An Experimental Study in Sheep, Current Stem Cell Research & Therapy 10(1) (2014) 69-76 **DOI**.10.2174/1574888x09666140710115356

[244] Gokhan, B., et al. Anatomical meniscus construct with zone specific biochemical composition and structural organization, bioRxiv (2019) **DOI**.10.1101/665067

[245] Najmuddin, J.G., et al. Effects of agarose mould compliance and surface roughness on self-assembled meniscus-shaped constructs, Journal of Tissue Engineering and Regenerative Medicine 3(7) (2009) 521-30 **DOI**.10.1002/term.191

[246] Yangfan, D., et al. Cyclic freeze-thaw grinding to decellularize meniscus for fabricating porous, elastic scaffolds, Journal of Biomedical Materials Research Part A 110(11) (2022) 1824-1839 **DOI**.10.1002/jbm.a.37435

[247] William, L.C., et al. Decellularized small intestine submucosa device for temporomandibular joint meniscus repair: Acute timepoint safety study, PLOS ONE 17(8) (2022) e0273336 **DOI**.10.1371/journal.pone.0273336

[248] Jordana, M.S., et al. Decellularized Three-Dimensional Biomimetic Scaffolds as In Vitro Model For Tendon And Meniscus Regeneration, The FASEB Journal 36(S1) (2022) **DOI**.10.1096/fasebj.2022.36.s1.r3116

[249] Jingwei, L., et al. The Design and Characterization of a Strong Bio-Ink for Meniscus Regeneration, International Journal of bioprinting 8(4) (2022) 600 **DOI**.10.18063/ijb.v8i4.600

[250] Haiyan, L., et al. Nanofiber configuration affects biological performance of decellularized meniscus extracellular matrix incorporated electrospun scaffolds, Biomedical Materials 16(6) (2021) **DOI**.10.1088/1748-605x/ac28a5

[251] Yong, H., et al. Preparation and Characterization of an Optimized Meniscal Extracellular Matrix Scaffold for Meniscus Transplantation, Frontiers in Bioengineering and Biotechnology 8 (2020) 779 **DOI**.10.3389/fbioe.2020.00779

[252] Lucas, P.L., et al. Meniscus-Derived Matrix Bioscaffolds: Effects of Concentration and Cross-Linking on Meniscus Cellular Responses and Tissue Repair, International Journal of Molecular Sciences 21(1) (2019) **DOI**.10.3390/ijms21010044

[253] Fatihah, Y., et al. Engineered Meniscus Scaffolds using Sonication Decellularization Treatment System, International Journal of Integrated Engineering 11(3) (2019) **DOI**.10.30880/ijie.2019.11.03.009

[254] Farrah, M., et al. Tissue-Derived Extracellular Matrix Bioscaffolds: Emerging Applications in Cartilage and Meniscus Repair, Tissue Engineering Part B-reviews 23(4) (2017) 386-398 **DOI**.10.1089/ten.teb.2016.0431

[255] Zheng-Zheng, Z., et al. Scaffolds drive meniscus tissue engineering, RSC Advances 5(95) (2015) 77851-77859 **DOI**.10.1039/c5ra13859k

[256] Yuan, Z., et al. AMECM/DCB scaffold prompts successful total meniscus reconstruction in a rabbit total meniscectomy model, Biomaterials 111 (2016) 13-26 **DOI**.10.1016/j.biomaterials.2016.09.017

[257] Wenbin, L., et al. Printability Optimization of Gelatin-Alginate Bioinks by Cellulose Nanofiber Modification for Potential Meniscus Bioprinting, Journal of Nanomaterials 2020 (2020) 1-13 **DOI**.10.1155/2020/3863428

[258] Benjamin, A., et al. Meniscus cell regional phenotypes: Dedifferentiation and reversal by biomaterial embedding, Journal of Orthopaedic Research 39(10) (2020) 2177-2186 **DOI**.10.1002/jor.24954

[259] Zhang, Y., et al. Development of decellularized meniscus extracellular matrix and gelatin/chitosan scaffolds for meniscus tissue engineering, Bio-medical Materials and Engineering 30(2) (2019) 125-132 **DOI**.10.3233/bme-191038

[260] Marrella, A., et al. 3D Porous Gelatin/PVA Hydrogel as Meniscus Substitute Using Alginate Micro-Particles as Porogens, Polymers 10(4) (2018) **DOI**.10.3390/polym10040380

[261] Melika, S., et al. Optimization strategies on the structural modeling of gelatin/chitosan scaffolds to mimic human meniscus tissue, Materials Science and Engineering: C 33(8) (2013) 4777-85 **DOI**.10.1016/j.msec.2013.07.036

[262] Atsushi, N., et al. Biodegradable Gelatin Hydrogels Incorporating Fibroblast Growth Factor 2 Promote Healing of Horizontal Tears in Rabbit Meniscus, Arthroscopy 28(2) (2012) 255-63 **DOI**.10.1016/j.arthro.2011.08.294

[263] Numpaisal, P., et al. STUDY OF SILK STRAIN AND ITS PREPARATION FOR MENISCUS TISSUE ENGINEERING SCAFFOLD, Orthopaedic Proceedings 105-B(SUPP_7) (2023) 75-75 **DOI**.10.1302/1358-992x.2023.7.075

[264] Siripanyo, P., et al. Effect of Silk Fibroin Content on Physical and Mechanical Properties of Electrospun Poly(lactic acid)/Silk Fibroin Nanofibers for Meniscus Tissue Engineering Scaffold, Journal of physics 2175(1) (2022) **DOI**.10.1088/1742-6596/2175/1/012016

[265] Biman, B.M., et al. Stem cell-based meniscus tissue engineering, Tissue Engineering Part A 17(21-22) (2011) 2749-61 **DOI**.10.1089/ten.tea.2011.0031

[266] Dey, S., et al. Photocrosslinkable Silk-Based Biomaterials for Regenerative Medicine and Healthcare Applications, Regenerative Engineering and Translational Medicine 9(2) (2022) 181-201 **DOI**.10.1007/s40883-022-00277-8

[267] Jeencham, R., et al. Reinforcement of Injectable Hydrogel for Meniscus Tissue Engineering by Using Cellulose Nanofiber from Cassava Pulp, Polymers 15(9) (2023) **DOI**.10.3390/polym15092092

[268] Zhong, C., et al. Repairing Avascular Meniscal Lesions by Recruiting Endogenous Targeted Cells Through Bispecific Synovial-Meniscal Aptamers, American Journal of Sports Medicine 51(5) (2023) 1177-1193 **DOI**.10.1177/03635465231159668

[269] Margaret, E.P., et al. A biofabrication method to align cells within bioprinted photocrosslinkable and cell-degradable hydrogel constructs via embedded fibers, Biofabrication 13(4) (2021) **DOI**.10.1088/1758-5090/ac25cc

[270] Gizem, Z., et al. Preparation of hybrid meniscal constructs using hydrogels and acellular matrices, Journal of Biomaterials Science-polymer Edition 34(5) (2022) 587-611 **DOI**.10.1080/09205063.2022.2135078

[271] Bernal, P.N., et al. Volumetric Bioprinting of Complex Living-Tissue Constructs within Seconds, Advanced Materials 31(42) (2019) 1904209 **DOI**.10.1002/adma.201904209

[272] Rockwood, D.N., et al. Materials fabrication from Bombyx mori silk fibroin, Nature protocols 6(10) (2011) 1612 **DOI**.10.1038/nprot.2011.379

[273] Goel, A. Surgical Sutures-A Review, Delhi Journal of Ophthalmology 26(3) (2016) 159-162 **DOI**. 10.7869/djo.161

[274] Omenetto, F.G., Kaplan, D.L. New opportunities for an ancient material, Science 329(5991) (2010) 528-531 **DOI**.10.1126/science.1188936

[275] Konwarh, R., et al. Opportunities and challenges in exploring Indian nonmulberry silk for biomedical applications, Proceedings of the Indian National Science Academy 83(1) (2017) 41288 **DOI**.10.16943/ptinsa/2017/41288

[276] Kundu, S., et al. Nonmulberry silk biopolymers, Biopolymers 97(6) (2012) 455-467 **DOI**.10.1002/bip.22024

[277] Rahmathulla, V. Management of climatic factors for successful silkworm (Bombyx mori L.) crop and higher silk production: A Review, Psyche: A Journal of Entomology 2012 (2012) 1-12 **DOI**.10.1155/2012/121234

[278] Gupta, P., et al. Mimicking form and function of native small diameter vascular conduits using mulberry and non-mulberry patterned silk films, ACS applied materials & interfaces 8(25) (2016) 15874-15888 **DOI**.10.1021/acsami.6b00783

[279] Moses, J.C., et al. Multifunctional Cell Instructive Silk-Bioactive Glass Composite Reinforced Scaffolds Toward Osteoinductive, Proangiogenic, and Resorbable Bone Grafts, Advanced healthcare materials 7(10) (2018) 1701418 **DOI**.10.1002/adhm.201701418

[280] Gupta, A., et al. Molecular architecture of silk fibroin of Indian golden silkmoth, Antheraea assama, Scientific reports 5 (2015) 12706 **DOI**.10.1038/srep12706

[281] Mandal, B.B., Kundu, S. A novel method for dissolution and stabilization of non-mulberry silk gland protein fibroin using anionic surfactant sodium dodecyl sulfate, Biotechnology and bioengineering 99(6) (2008) 1482-1489 **DOI**.10.1002/bit.21699

[282] Mandal, B.B., Kundu, S.C. Osteogenic and adipogenic differentiation of rat bone marrow cells on non-mulberry and mulberry silk gland fibroin 3D scaffolds, Biomaterials 30(28) (2009) 5019-5030 **DOI**.10.1016/j.biomaterials.2009.05.064

[283] Mandal, B.B., Kundu, S.C. Cell proliferation and migration in silk fibroin 3D scaffolds, Biomaterials 30(15) (2009) 2956-2965 **DOI**.10.1016/j.biomaterials.2009.02.006

[284] Gangrade, A., Mandal, B.B. An Injectable Carbon Nanotube Impregnated Silk Based Multifunctional Hydrogel for Localized Targeted and On Demand Anticancer Drug Delivery, ACS Biomaterials Science & Engineering 5(5) (2019) 2365-2381 **DOI**.10.1021/acsbiomaterials.9b00416

[285] Chouhan, D., et al. In Situ Forming Injectable Silk Fibroin Hydrogel Promotes Skin Regeneration in Full Thickness Burn Wounds, Advanced healthcare materials 7(24) (2018) 1801092 **DOI**.10.1002/adhm.201801092

[286] Kumar, M., et al. Immunomodulatory injectable silk hydrogels maintaining functional islets and promoting anti-inflammatory M2 macrophage polarization, Biomaterials 187 (2018) 1-17 **DOI**.10.1016/j.biomaterials.2018.09.037

[287] Bhunia, B.K., Mandal, B.B. Modulation of extracellular matrix by annulus fibrosus cells on tailored silk based angle-ply intervertebral disc construct, Materials & Design 158 (2018) 74-87 **DOI**.10.1016/j.matdes.2018.08.015

[288] Chouhan, D., et al. Role of non-mulberry silk fibroin in deposition and regulation of extracellular matrix towards accelerated wound healing, Acta biomaterialia 48 (2017) 157-174 **DOI**.10.1016/j.actbio.2016.10.019

[289] Chouhan, D., et al. Functionalized PVA–silk blended nanofibrous mats promote diabetic wound healing via regulation of extracellular matrix and tissue remodelling, Journal of tissue engineering and regenerative medicine 12(3) (2018) e1559-e1570 **DOI**.10.1002/term.2581

[290] Murphy, A.R., Kaplan, D.L. Biomedical applications of chemically-modified silk fibroin, Journal of materials chemistry 19(36) (2009) 6443-6450 **DOI**.10.1039/b905802h

[291] Acharya, C., et al. The effect of lactose-conjugated silk biomaterials on the development of fibrogenic fibroblasts, Biomaterials 29(35) (2008) 4665-4675 **DOI**.10.1016/j.biomaterials.2008.08.033

[292] Meinel, L., et al. Silk based biomaterials to heal critical sized femur defects, Bone 39(4) (2006) 922-931 **DOI**.10.1016/j.bone.2006.04.019

[293] Kim, S.H., et al. Precisely printable and biocompatible silk fibroin bioink for digital light processing 3D printing, Nature Communications 9(1) (2018) 1620 **DOI**.10.1038/s41467-018-03759-y

[294] Rnjak-Kovacina, J., et al. The effect of sterilization on silk fibroin biomaterial properties, Macromolecular bioscience 15(6) (2015) 861-874 **DOI**.10.1002/mabi.201500013

[295] Hofmann, S., et al. Effect of sterilization on structural and material properties of 3-D silk fibroin scaffolds, Acta biomaterialia 10(1) (2014) 308-317 **DOI**.10.1016/j.actbio.2013.08.035

[296] Kundu, B., et al. Silk fibroin biomaterials for tissue regenerations, Advanced drug delivery reviews 65(4) (2013) 457-470 **DOI**.10.1016/j.addr.2012.09.043

[297] Yucel, T., et al. Silk-based biomaterials for sustained drug delivery, Journal of Controlled Release 190 (2014) 381-397 **DOI**.10.1016/j.jconrel.2014.05.059

[298] Numata, K., et al. Mechanism of enzymatic degradation of beta-sheet crystals, Biomaterials 31(10) (2010) 2926-2933 **DOI**.10.1016/j.biomaterials.2009.12.026

[299] Hu, Y., et al. The relationship between secondary structure and biodegradation behavior of silk fibroin scaffolds, Advances in Materials Science and Engineering 2012 (2012) **DOI**.10.1155/2012/185905

[300] Jorge, D.-H., et al. MENISCAL TISSUE EXPRESION OF FIVE DIFFERENT GROWTH FACTORS (IGF, IL-1β; TGF-β, PDGF-β AND VEGF) IN THE FIRST THREE WEEKS AFTER A MENISCAL LESION IN THE AVASCULAR ZONE: AN EXPERIMENTAL STUDY IN RABBITS, Orthopaedic Proceedings 93-B (2011) 160 **DOI**.10.1302/0301-620X.93BSUPP_II.0930160

[301] Longo, U.G., et al. Biological strategies to enhance healing of the avascular area of the meniscus, Stem cells international 2012 (2012) 528359 **DOI**.10.1155/2012/528359

[302] Solaiman, T., et al. Effect of dose and release rate of CTGF and TGFβ3 on avascular meniscus healing, Journal of Orthopaedic Research 37(7) (2019) 1555-1562 **DOI**.10.1002/jor.24287

[303] Mona Helal, O., et al. Ultrasound Guided Platelet Rich Plasma Injection in Post Traumatic Knee Meniscus Lesion, Journal of Advances in Medicine and Medical Research 35(5) (2023) 48-56 **DOI**.10.9734/jammr/2023/v35i54971

[304] Bondariev, G., et al. Comparative analysis of the use of L-PRP/L-PCP injections, arthroscopic partial resection and nonsteroidal anti-inflammatory drugs in the treatment of the meniscus tears, Клітинна та органна трансплантологія 10(1) (2022) **DOI**.10.22494/cot.v10i1.133

[305] Yiying, Q., et al. Wnt5a/PRP synergistically inhibits IL-1β induced inflammatory activity through NF-κB signaling pathway and prevents cartilage damage and promotes meniscus regeneration, Journal of Tissue Engineering and Regenerative Medicine 15(7) (2021) 612-624 **DOI**.10.1002/term.3198

[306] Michella, H.H., et al. The regenerative effect of different growth factors and platelet lysate on meniscus cells and mesenchymal stromal cells and proof of concept with a functionalized meniscus implant, Journal of Tissue Engineering and Regenerative Medicine 15(7) (2021) 648-659 **DOI**.10.1002/term.3218

[307] Esparza, R., et al. Cell study of the three areas of the meniscus: effect of growth factors in an experimental model in sheep, Journal of Orthopaedic Research 30(10) (2012) 1647-1651 **DOI**.10.1002/jor.22110

[308] Ionescu, L., et al. Delivery of FGF from nanofiber-microsphere composites for meniscus tissue engineering, 2011 IEEE 37th Annual Northeast Bioengineering Conference (NEBEC), IEEE, 2011, pp. 1-2 **DOI**.10.1109/NEBC.2011.5778704

[309] MacBarb, R.F., et al. A chondroitinase-ABC and TGF-β1 treatment regimen for enhancing the mechanical properties of tissue-engineered fibrocartilage, Acta biomaterialia 9(1) (2013) 4626-4634 **DOI**.10.1016/j.actbio.2012.09.037

[310] Kim, Y.I., et al. Overexpression of TGF-β1 enhances chondrogenic differentiation and proliferation of human synovium-derived stem cells, Biochemical and biophysical research communications 450(4) (2014) 1593-1599 **DOI**.10.1016/j.bbrc.2014.07.045

[311] Bochyńska, A.I., et al. The effect of tissue surface modification with collagenase and addition of TGF-β3 on the healing potential of meniscal tears repaired with tissue glues in vitro, Journal of Materials Science: Materials in Medicine 28(1) (2017) 1-7 **DOI**.10.1007/s10856-016-5832-0

[312] Forriol, F., et al. Meniscal repair possibilities using bone morphogenetic protein-7, Injury 45 (2014) S15-S21 **DOI**.10.1016/S0020-1383(14)70005-1

[313] Ozeki, N., et al. Transplantation of Achilles tendon treated with bone morphogenetic protein 7 promotes meniscus regeneration in a rat model of massive meniscal defect, Arthritis & Rheumatism 65(11) (2013) 2876-2886 **DOI**.10.1002/art.38099

[314] Ionescu, L.C., et al. Growth factor supplementation improves native and engineered meniscus repair in vitro, Acta biomaterialia 8(10) (2012) 3687-3694 **DOI**.10.1016/j.actbio.2012.06.005

[315] Puetzer, J.L., et al. The effect of IGF-I on anatomically shaped tissue-engineered menisci, Tissue Engineering Part A 19(11-12) (2013) 1443-1450 **DOI**.10.1089/ten.TEA.2012.0645

[316] He, W., et al. Enhancement of meniscal repair in the avascular zone using connective tissue growth factor in a rabbit model, Chinese Medical Journal 124(23) (2011) 3968-3975 **DOI**.10.3760/cma.j.issn.0366-6999.2011.23.023

[317] Gilat, R., Cole, B.J. Meniscal allograft transplantation: indications, techniques, outcomes, Arthroscopy 36(4) (2020) 938-939 **DOI**.10.1016/j.arthro.2020.01.025

[318] Zhang, Z.-Z., et al. Role of scaffold mean pore size in meniscus regeneration, Acta biomaterialia 43 (2016) 314-326 **DOI**.10.1016/j.actbio.2016.07.050

[319] Ghodbane, S.A., et al. Partial meniscus replacement with a collagen-hyaluronan infused three-dimensional printed polymeric scaffold, Tissue Engineering Part A 25(5-6) (2019) 379-389 **DOI**.10.1089/ten.TEA.2018.0160

[320] Majd, S.E., et al. An in vitro study of cartilage–meniscus tribology to understand the changes caused by a meniscus implant, Colloids and Surfaces B: Biointerfaces 155 (2017) 294-303 **DOI**.10.1016/j.colsurfb.2017.04.034

[321] Schmidt, T.A., et al. Boundary lubrication of articular cartilage: role of synovial fluid constituents, Arthritis & Rheumatism 56(3) (2007) 882-891 **DOI**.10.1002/art.22446

[322] Majd, S.E., et al. Role of hydrophobicity on the adsorption of synovial fluid proteins and biolubrication of polycarbonate urethanes: Materials for permanent meniscus implants, Materials & Design 83 (2015) 514-521 **DOI**.10.1016/j.matdes.2015.06.075

[323] Majd, S.E., et al. Both hyaluronan and collagen type II keep proteoglycan 4 (lubricin) at the cartilage surface in a condition that provides low friction during boundary lubrication, Langmuir 30(48) (2014) 14566-14572 **DOI**.10.1021/la504345c

[324] Kobayashi, M., Takahara, A. Tribological properties of hydrophilic polymer brushes under wet conditions, The Chemical Record 10(4) (2010) 208-216 **DOI**.10.1002/tcr.201000001

[325] Hu, L., et al. Synergistic hydration lubrication of polyurethane meniscus based on zwitterionic structures and hyaluronic acid, Tribology International 179 (2023) 108167 **DOI**.10.1016/j.triboint.2022.108167

[326] Morgese, G., et al. Nanoassemblies of tissue-reactive, polyoxazoline graft-copolymers restore the lubrication properties of degraded cartilage, Acs Nano 11(3) (2017) 2794-2804 **DOI**.10.1021/acsnano.6b07847

[327] Tan, X., et al. Mechanised lubricating silica nanoparticles for on-command cargo release on simulated surfaces of joint cavities, Chemical Communications 55(18) (2019) 2593-2596 **DOI**.10.1039/c8cc10069a

[328] Liu, L., et al. Meniscus-Inspired Self-Lubricating and Friction-Responsive Hydrogels for Protecting Articular Cartilage and Improving Exercise, ACS nano 17(23) (2023) 24308-24319 **DOI**.10.1021/acsnano.3c10139

[329] Fan, Z., et al. Anti-inflammation and joint lubrication dual effects of a novel hyaluronic acid/curcumin nanomicelle improve the efficacy of rheumatoid arthritis therapy, ACS applied materials & interfaces 10(28) (2018) 23595-23604 **DOI**.10.1021/acsami.8b06236

[330] Moro, T., et al. Surface grafting of artificial joints with a biocompatible polymer for preventing periprosthetic osteolysis, Nature materials 3(11) (2004) 829-836 **DOI**.10.1038/nmat1233

[331] Klein, J. Molecular mechanisms of synovial joint lubrication, Proceedings of the Institution of Mechanical Engineers, Part J: Journal of Engineering Tribology 220(8) (2006) 691-710 **DOI**.10.1243/13506501jet143

[332] Chen, M., et al. Lubrication at physiological pressures by polyzwitterionic brushes, science 323(5922) (2009) 1698-1701 **DOI**.10.1126/science.1169399

[333] Wang, Y., et al. Articular cartilage-inspired surface functionalization for enhanced lubrication, Advanced Materials Interfaces 6(12) (2019) 1900180 **DOI**.10.1002/admi.201900180

[334] Kyomoto, M., et al. Poly (ether-ether-ketone) orthopedic bearing surface modified by self-initiated surface grafting of poly (2-methacryloyloxyethyl phosphorylcholine), Biomaterials 34(32) (2013) 7829-7839 **DOI**.10.1016/j.biomaterials.2013.07.023

[335] Zheng, Y., et al. Bioinspired hyaluronic acid/phosphorylcholine polymer with enhanced lubrication and anti-inflammation, Biomacromolecules 20(11) (2019) 4135-4142 **DOI**.10.1021/acs.biomac.9b00964

[336] Das, S., et al. Synergistic interactions between grafted hyaluronic acid and lubricin provide enhanced wear protection and lubrication, Biomacromolecules 14(5) (2013) 1669-1677 **DOI**.10.1021/bm400327a

[337] Tsinman, T.K., et al. Intrinsic and growth-mediated cell and matrix specialization during murine meniscus tissue assembly, The FASEB Journal 35(8) (2021) e21779 **DOI**.10.1096/fj.202100499R

[338] Grogan, S.P., et al. Gene expression profiles of the meniscus avascular phenotype: a guide for meniscus tissue engineering, Journal of Orthopaedic Research® 36(7) (2018) 1947-1958 **DOI**.10.1002/jor.23864

[339] Szojka, A.R., et al. Engineered human meniscus' matrix-forming phenotype is unaffected by low strain dynamic compression under hypoxic conditions, PloS one 16(3) (2021) e0248292 **DOI**.10.1371/journal.pone.0248292

[340] Zhang, Z.-Z., et al. Orchestrated biomechanical, structural, and biochemical stimuli for engineering anisotropic meniscus, Science translational medicine 11(487) (2019) eaao0750 **DOI**.10.1126/scitranslmed.aao0750

[341] Gupta, T., et al. IL-1 and iNOS gene expression and NO synthesis in the superior region of meniscal explants are dependent on the magnitude of compressive strains, Osteoarthritis and cartilage 16(10) (2008) 1213-1219 **DOI**.10.1016/j.joca.2008.02.019

[342] Fink, C., et al. The effect of dynamic mechanical compression on nitric oxide production in the meniscus, Osteoarthritis and Cartilage 9(5) (2001) 481-487 **DOI**.10.1053/joca.2001.0415

[343] Shin, S.-j., et al. Regulation of matrix turnover in meniscal explants: role of mechanical stress, interleukin-1, and nitric oxide, Journal of Applied Physiology 95(1) (2003) 308-313 **DOI**.10.1152/japplphysiol.00131.2003

[344] Upton, M.L., et al. Differential effects of static and dynamic compression on meniscal cell gene expression, Journal of orthopaedic research 21(6) (2003) 963-969 **DOI**.10.1016/S0736-0266(03)00063-9

[345] Imler, S.M., et al. Combined effects of growth factors and static mechanical compression on meniscus explant biosynthesis, Osteoarthritis and Cartilage 12(9) (2004) 736-744 **DOI**.10.1016/j.joca.2004.05.007

[346] Suzuki, T., et al. Hydrostatic pressure modulates mRNA expressions for matrix proteins in human meniscal cells, Biorheology 43(5) (2006) 611-622

[347] Zellner, J., et al. Dynamic hydrostatic pressure enhances differentially the chondrogenesis of meniscal cells from the inner and outer zone, Journal of Biomechanics 48(8) (2015) 1479-1484 **DOI**.10.1016/j.jbiomech.2015.02.003

[348] Zhang, Y., et al. Cyclic Hydrostatic Compress Force Regulates Apoptosis of Meniscus Fibrochondrocytes via Integrin α5β1, Physiological Research 68(4) (2019) 639-649 **DOI**.10.33549/physiolres.934088

[349] Marsano, A., et al. Use of hydrodynamic forces to engineer cartilaginous tissues resembling the non-uniform structure and function of meniscus, Biomaterials 27(35) (2006) 5927-5934 **DOI**.10.1016/j.biomaterials.2006.08.020

[350] Aufderheide, A.C., Athanasiou, K.A. A direct compression stimulator for articular cartilage and meniscal explants, Annals of biomedical engineering 34(9) (2006) 1463-1474 **DOI**.10.1007/s10439-006-9157-x

[351] Ballyns, J.J., Bonassar, L.J. Dynamic compressive loading of image-guided tissue engineered meniscal constructs, Journal of biomechanics 44(3) (2011) 509-516 **DOI**.10.1016/j.jbiomech.2010.09.017

[352] Huey, D.J., et al. Tension-compression loading with chemical stimulation results in additive increases to functional properties of anatomic meniscal constructs, PloS one 6(11) (2011) e27857 **DOI**.10.1371/journal.pone.0027857

[353] Puetzer, J.L., et al. The effect of the duration of mechanical stimulation and post-stimulation culture on the structure and properties of dynamically compressed tissue-engineered

menisci, Tissue Engineering Part A 18(13-14) (2012) 1365-1375 **DOI**.10.1089/ten.TEA.2011.0589

[354] Bilgen, B., et al. Design of a biaxial mechanical loading bioreactor for tissue engineering, JoVE (Journal of Visualized Experiments) (74) (2013) e50387 **DOI**.10.3791/50387

[355] Szojka, A.R., et al. Human engineered meniscus transcriptome after short-term combined hypoxia and dynamic compression, Journal of tissue engineering 12 (2021) 2041731421990842 **DOI**.10.1177/2041731421990842

[356] Shadi, M., et al. Optimizing artificial meniscus by mechanical stimulation of the chondrocyte-laden acellular meniscus using ad hoc bioreactor, Stem Cell Research & Therapy 13(1) (2022) 1-15 **DOI**.10.1186/s13287-022-03058-w

[357] Upton, M.L., et al. Biaxial strain effects on cells from the inner and outer regions of the meniscus, Connective tissue research 47(4) (2006) 207-214 **DOI**.10.1080/03008200600846663

[358] Okazaki, Y., et al. Differences between the root and horn cells of the human medial meniscus from the osteoarthritic knee in cellular characteristics and responses to mechanical stress, J Orthop Sci 26(2) (2021) 230-236 **DOI**.10.1016/j.jos.2020.02.015

[359] Irwin, R.M., et al. Differential response of inner and outer zone meniscal cells to tensile load under non-inflammatory and inflammatory conditions, Osteoarthritis and Cartilage 29 (2021) S3-S4 **DOI**.10.1016/j.joca.2021.05.011

[360] Puetzer, J.L., et al. Driving hierarchical collagen fiber formation for functional tendon, ligament, and meniscus replacement, Biomaterials 269 (2021) 120527 **DOI**.10.1016/j.biomaterials.2020.120527

[361] Babaei, M., et al. Effects of low-intensity pulsed ultrasound stimulation on cell seeded 3D hybrid scaffold as a novel strategy for meniscus regeneration: An in vitro study, Journal of Tissue Engineering and Regenerative Medicine 16(9) (2022) 812-824 **DOI**.10.1002/term.3331

[362] Kamatsuki, Y., et al. Possible reparative effect of low-intensity pulsed ultrasound (LIPUS) on injured meniscus, Journal of Cell Communication and Signaling 13(2) (2019) 193-207 **DOI**.10.1007/s12079-018-0496-9

[363] Cui, X., et al. Thermal inkjet printing in tissue engineering and regenerative medicine, Recent patents on drug delivery & formulation 6(2) (2012) 149-155 **DOI**.10.2174/187221112800672949

[364] Filardo, G., et al. Patient-specific meniscus prototype based on 3D bioprinting of human cell-laden scaffold, Bone & joint research 8(2) (2019) 101-106 **DOI**.10.1302/2046-3758.82.BJR-2018-0134.R1

[365] Singh, Y.P., et al. 3D bioprinting using cross-linker-free silk–gelatin bioink for cartilage tissue engineering, ACS applied materials & interfaces 11(37) (2019) 33684-33696 **DOI**.10.1021/acsami.9b11644

[366] Luis, E., et al. 3D printed silicone meniscus implants: Influence of the 3D printing process on properties of silicone implants, Polymers 12(9) (2020) 2136 **DOI**.10.3390/polym12092136

[367] Araujo Borges, R., et al. 3D printed PCU/UHMWPE polymeric blend for artificial knee meniscus, Tribology International 122 (2018) 1-7 **DOI**.10.1016/j.triboint.2018.01.065

[368] Deng, X., et al. Precision 3D printed meniscus scaffolds to facilitate hMSCs proliferation and chondrogenic differentiation for tissue regeneration, Journal of Nanobiotechnology 19(1) (2021) 400 **DOI**.10.1186/s12951-021-01141-7

[369] Gupta, S., et al. Meniscal tissue engineering via 3D printed PLA monolith with carbohydrate based self-healing interpenetrating network hydrogel, International Journal of Biological Macromolecules 162 (2020) 1358-1371 **DOI**.10.1016/j.ijbiomac.2020.07.238

[370] Abar, B., et al. 3D printing of high-strength, porous, elastomeric structures to promote tissue integration of implants, Journal of Biomedical Materials Research Part A 109(1) (2021) 54-63 **DOI**.10.1002/jbm.a.37006

[371] Zhu, L.-y., et al. Influence of deformed primitive architecture on mechanical behavior of artificial porous meniscus, Materials & Design 186 (2020) 108303 **DOI**.10.1016/j.matdes.2019.108303

[372] Zhou, Z.-X., et al. Facile strategy on hydrophilic modification of poly (ε-caprolactone) scaffolds for assisting tissue-engineered meniscus constructs in vitro, Frontiers in Pharmacology 11 (2020) 471 **DOI**.10.3389/fphar.2020.00471

[373] Costa, J.B., et al. 3D bioprinted highly elastic hybrid constructs for advanced fibrocartilaginous tissue regeneration, Chemistry of Materials 32(19) (2020) 8733-8746 **DOI**.10.1021/acs.chemmater.0c03556

[374] Rhee, S., et al. 3D bioprinting of spatially heterogeneous collagen constructs for cartilage tissue engineering, ACS Biomaterials Science & Engineering 2(10) (2016) 1800-1805 **DOI**.10.1021/acsbiomaterials.6b00288

[375] Narayanan, L.K., et al. 3D-bioprinting of polylactic acid (PLA) nanofiber–alginate hydrogel bioink containing human adipose-derived stem cells, ACS biomaterials science & engineering 2(10) (2016) 1732-1742 **DOI**.10.1021/acsbiomaterials.6b00196

[376] Grogan, S.P., et al. Digital micromirror device projection printing system for meniscus tissue engineering, Acta Biomaterialia 9(7) (2013) 7218-7226 **DOI**.10.1016/j.actbio.2013.03.020

[377] Yang, Y., et al. Biomimetic anisotropic reinforcement architectures by electrically assisted nanocomposite 3D printing, Advanced materials (Deerfield Beach, Fla.) 29(11) (2017) **DOI**.10.1002/adma.201605750

[378] Johnson, B., et al. Anterior meniscopexy: a meniscal sparing technique for the treatment of locking but intact discoid lateral meniscus, Knee Surgery, Sports Traumatology, Arthroscopy 26(4) (2018) 1158-1163 **DOI**.10.1007/s00167-017-4546-2

[379] Bulgheroni, E., et al. Comparative Study of Collagen versus Synthetic-Based Meniscal Scaffolds in Treating Meniscal Deficiency in Young Active Population, CARTILAGE 7(1) (2016) 29-38 **DOI**.10.1177/1947603515600219

[380] Singh, Y.P., et al. Injectable hydrogels: a new paradigm for osteochondral tissue engineering, Journal of Materials Chemistry B 6(35) (2018) 5499-5529 **DOI**.10.1039/c8tb01430b

[381] Singh, Y.P., et al. Silk hydrogel-based delivery of cell and bioactive molecules for osteochondral tissue engineering applications, Hydrogels for Tissue Engineering and Regenerative Medicine, Elsevier2024, pp. 483-507 **DOI**.10.1016/B978-0-12-823948-3.00037-3

[382] Wua, J., et al. An injectable extracellular matrix derived hydrogel for meniscus repair and regeneration, Acta Biomaterialia 16 (2015) 49-59 **DOI**.10.1016/J.ACTBIO.2015.01.027

[383] Puetzer, J.L., Bonassar, L.J. High density type I collagen gels for tissue engineering of whole menisci, Acta Biomaterialia 9(8) (2013) 7787-7795 **DOI**.10.1016/J.ACTBIO.2013.05.002

[384] Resmi, R., et al. Injectable self-crosslinking hydrogels for meniscal repair: A study with oxidized alginate and gelatin, Carbohydrate Polymers 234 (2020) 115902 **DOI**.10.1016/J.CARBPOL.2020.115902

[385] Chen, C., et al. Repair of a Meniscal Defect in a Rabbit Model Through Use of a Thermosensitive, Injectable, In Situ Crosslinked Hydrogel With Encapsulated Bone Mesenchymal Stromal Cells and Transforming Growth Factor β1:, https://doi.org/10.1177/0363546519898519 48(4) (2020) 884-894 **DOI**.10.1177/0363546519898519

[386] Kim, J.-A., et al. Injectable fibrin/polyethylene oxide semi-IPN hydrogel for a segmental meniscal defect regeneration, The American Journal of Sports Medicine 49(6) (2021) 1538-1550 **DOI**.10.1177/0363546521998021

[387] Chen, J.-P., Cheng, T.-H. Thermo-Responsive Chitosan-graft-poly(N-isopropylacrylamide) Injectable Hydrogel for Cultivation of Chondrocytes and Meniscus Cells, Macromolecular Bioscience 6(12) (2006) 1026-1039 **DOI**.10.1002/MABI.200600142

[388] Zhang, H., et al. Enhanced Meniscal Repair by Overexpression of hIGF-1 in a Full-thickness Model, Clinical Orthopaedics and Related Research® 467(12) (2009) 3165-3174 **DOI**.10.1007/s11999-009-0921-8

[389] Ishida, K., et al. The Regenerative Effects of Platelet-Rich Plasma on Meniscal Cells In Vitro and Its In Vivo Application with Biodegradable Gelatin Hydrogel, https://home.liebertpub.com/ten 13(5) (2007) 1103-1112 **DOI**.10.1089/TEN.2006.0193

[390] Proctor, C., et al. Material properties of the normal medial bovine meniscus, Journal of orthopaedic research 7(6) (1989) 771-782 **DOI**.10.1002/jor.1100070602

[391] Herwig, J., et al. Chemical changes of human knee joint menisci in various stages of degeneration, Annals of the rheumatic diseases 43(4) (1984) 635 **DOI**.10.1136/ard.43.4.635

[392] Petersen, W., Tillmann, B. Collagenous fibril texture of the human knee joint menisci, Anatomy and embryology 197(4) (1998) 317-324 **DOI**.10.1007/s004290050141

[393] McAndrews, P.T., Arnoczky, S.P. Meniscal repair enhancement techniques, Clinics in sports medicine 15(3) (1996) 499-510 **DOI**.10.1016/S0278-5919(20)30108-3

[394] Izuta, Y., et al. Meniscal repair using bone marrow-derived mesenchymal stem cells: experimental study using green fluorescent protein transgenic rats, The Knee 12(3) (2005) 217-223 **DOI**.10.1016/j.knee.2001.06.001

[395] Port, J., et al. Meniscal repair supplemented with exogenous fibrin clot and autogenous cultured marrow cells in the goat model, The American journal of sports medicine 24(4) (1996) 547-555 **DOI**.10.1177/036354659602400422

[396] Welsing, R.T., et al. Effect on tissue differentiation and articular cartilage degradation of a polymer meniscus implant: a 2-year follow-up study in dogs, The American journal of sports medicine 36(10) (2008) 1978-1989 **DOI**.10.1177/0363546508319900

[397] Vrancken, A.C.T., et al. Synthetic meniscus replacement: a review, International orthopaedics 37(2) (2013) 291-299 **DOI**.10.1007/s00264-012-1682-7

[398] Bradley, M.P., et al. Porcine small intestine submucosa for repair of goat meniscal defects, Orthopedics 30(8) (2007) 650 **DOI**.10.3928/01477447-20070801-15

[399] Dong, L., et al. 3D-printed poly (ε-caprolactone) scaffold integrated with cell-laden chitosan hydrogels for bone tissue engineering, Scientific reports 7(1) (2017) 13412 **DOI**.10.1038/s41598-017-13838-7

[400] Du, X., et al. 3D printing of mesoporous bioactive glass/silk fibroin composite scaffolds for bone tissue engineering, Materials Science and Engineering: C 103 (2019) 109731 **DOI**.10.1016/j.msec.2019.05.016

[401] Huang, L., et al. Bacterial cellulose nanofibers promote stress and fidelity of 3D-printed silk based hydrogel scaffold with hierarchical pores, Carbohydrate polymers 221 (2019) 146-156 **DOI**.10.1016/j.carbpol.2019.05.080

[402] Gu, Y., et al. Reversible physical crosslinking strategy with optimal temperature for 3D bioprinting of human chondrocyte-laden gelatin methacryloyl bioink, Journal of biomaterials applications 33(5) (2018) 609-618 **DOI**.10.1177/0885328218805864

[403] Romanazzo, S., et al. Meniscus ECM-functionalised hydrogels containing infrapatellar fat pad-derived stem cells for bioprinting of regionally defined meniscal tissue, Journal of tissue engineering and regenerative medicine 12(3) (2018) e1826-e1835 **DOI**.10.1002/term.2602

[404] Vepari, C., Kaplan, D.L. Silk as a biomaterial, Progress in polymer science 32(8-9) (2007) 991-1007 **DOI**.10.1016/j.progpolymsci.2007.05.013

[405] Gupta, P., et al. Biomimetic, osteoconductive non-mulberry silk fiber reinforced tricomposite scaffolds for bone tissue engineering, ACS applied materials & interfaces 8(45) (2016) 30797-30810 **DOI**.10.1021/acsami.6b11366

[406] Singh, Y.P., et al. Hierarchically structured seamless silk scaffolds for osteochondral interface tissue engineering, Journal of Materials Chemistry B 6(36) (2018) 5671-5688 **DOI**.10.1039/c8tb01344f

[407] Patient Contributed Image Repository 2001,

[408] Fedorov, A., et al. 3D Slicer as an image computing platform for the Quantitative Imaging Network, Magnetic resonance imaging 30(9) (2012) 1323-1341 **DOI**.10.1016/j.mri.2012.05.001

[409] Petousis, M., et al. Study of a 3D knee model, 7th International Conference on New Horizons in Industry, Business and Education, Chios Island, Greece, 2011, pp. 25-26

[410] Vairis, A., et al. Evaluating the efficacy of a numerical model of a human anatomy joint, 2013 24th EAEEIE Annual Conference (EAEEIE 2013), IEEE, 2013, pp. 170-173

[411] Kumar, J.P., et al. Cross-linked silk sericin–gelatin 2D and 3D matrices for prospective tissue engineering applications, RSC advances 6(107) (2016) 105125-105136 **DOI**.10.1039/c6ra18654h

[412] Janani, G., et al. Functional hepatocyte clusters on bioactive blend silk matrices towards generating bioartificial liver constructs, Acta biomaterialia 67 (2018) 167-182 **DOI**.10.1016/j.actbio.2017.11.053

[413] M, J.C., et al. Mimicking Hierarchical Complexity of the Osteochondral Interface Using Electrospun Silk–Bioactive Glass Composites, ACS Applied Materials & Interfaces 9(9) (2017) 8000-8013 **DOI**.10.1021/acsami.6b16590

[414] Singh, Y.P., et al. Potential of agarose/silk fibroin blended hydrogel for in vitro cartilage tissue engineering, ACS applied materials & interfaces 8(33) (2016) 21236-21249 **DOI**.10.1021/acsami.6b08285

[415] Bhardwaj, N., et al. Potential of 3-D tissue constructs engineered from bovine chondrocytes/silk fibroin-chitosan for in vitro cartilage tissue engineering, Biomaterials 32(25) (2011) 5773-5781 **DOI**.10.1016/j.biomaterials.2011.04.061

[416] Lutolf, M., Hubbell, J. Synthetic biomaterials as instructive extracellular microenvironments for morphogenesis in tissue engineering, Nature biotechnology 23(1) (2005) 47-55 **DOI**.10.1038/nbt1055

[417] Bhunia, B.K., Mandal, B.B. Exploring gelation and physicochemical behavior of in situ bioresponsive silk hydrogels for disc degeneration therapy, ACS Biomaterials Science & Engineering 5(2) (2018) 870-886 **DOI**.10.1021/acsbiomaterials.8b01099

[418] Abdelgaied, A., et al. Comparison of the biomechanical tensile and compressive properties of decellularised and natural porcine meniscus, Journal of biomechanics 48(8) (2015) 1389-1396 **DOI**.10.1016/j.jbiomech.2015.02.044

[419] Vishwakarma, A., et al. Engineering immunomodulatory biomaterials to tune the inflammatory response, Trends in biotechnology 34(6) (2016) 470-482 **DOI**.10.1016/j.tibtech.2016.03.009

[420] James, S.L., et al. Global, regional, and national incidence, prevalence, and years lived with disability for 354 diseases and injuries for 195 countries and territories, 1990–2017: a systematic analysis for the Global Burden of Disease Study 2017, The Lancet 392(10159) (2018) 1789-1858 **DOI**.10.1016/S0140-6736(18)32279-7

[421] Ghisa, C., Zaslav, K.R. Current state of off the shelf scaffolds and implants for meniscal replacement, Journal of Cartilage & Joint Preservation 2(1) (2022) 100040 **DOI**.10.1016/j.jcjp.2022.100040

[422] Chen, Y., et al. Current advances in the development of natural meniscus scaffolds: innovative approaches to decellularization and recellularization, Cell and tissue research 370(1) (2017) 41-52 **DOI**.10.1007/s00441-017-2605-0

[423] Baek, J., et al. Bioactive proteins delivery through core-shell nanofibers for meniscal tissue regeneration, Nanomedicine: Nanotechnology, Biology and Medicine 23 (2020) 102090 **DOI**.10.1016/j.nano.2019.102090

[424] Mehrotra, S., et al. Engineering microsphere-loaded non-mulberry silk-based 3D bioprinted vascularized cardiac patches with oxygen-releasing and immunomodulatory potential, ACS Applied Materials & Interfaces 13(43) (2021) 50744-50759 **DOI**.10.1021/acsami.1c14118

[425] Moses, J.C., et al. Chondroprotective and osteogenic effects of silk-based bioinks in developing 3D bioprinted osteochondral interface, Bioprinting 17 (2020) e00067 **DOI**.10.1016/j.bprint.2019.e00067

[426] Shi, W., et al. Structurally and functionally optimized silk-fibroin–gelatin scaffold using 3D printing to repair cartilage injury in vitro and in vivo, Advanced materials 29(29) (2017) 1701089 **DOI**.10.1002/adma.201701089

[427] Chawla, S., et al. Elucidating role of silk-gelatin bioink to recapitulate articular cartilage differentiation in 3D bioprinted constructs, Bioprinting 7 (2017) 1-13 **DOI**.10.1016/j.bprint.2017.05.001

[428] Antich, C., et al. Bio-inspired hydrogel composed of hyaluronic acid and alginate as a potential bioink for 3D bioprinting of articular cartilage engineering constructs, Acta biomaterialia 106 (2020) 114-123 **DOI**.10.1016/j.actbio.2020.01.046

[429] Bhunia, B.K., et al. 3D printing of annulus fibrosus anatomical equivalents recapitulating angle-ply architecture for intervertebral disc replacement, Applied Materials Today 23 (2021) 101031 **DOI**.10.1016/j.apmt.2021.101031

[430] Bian, L., et al. Enhanced MSC chondrogenesis following delivery of TGF-β3 from alginate microspheres within hyaluronic acid hydrogels in vitro and in vivo, Biomaterials 32(27) (2011) 6425-6434 **DOI**.10.1016/j.biomaterials.2011.05.033

[431] Lam, T., et al. Photopolymerizable gelatin and hyaluronic acid for stereolithographic 3D bioprinting of tissue-engineered cartilage, Journal of Biomedical Materials Research Part B: Applied Biomaterials 107(8) (2019) 2649-2657 **DOI**.10.1002/jbm.b.34354

[432] Gaudet, I.D., Shreiber, D.I. Characterization of methacrylated type-I collagen as a dynamic, photoactive hydrogel, Biointerphases 7(1) (2012) 25 **DOI**.10.1007/s13758-012-0025-y

[433] Zhuang, H., et al. Gelatin-methacrylamide gel loaded with microspheres to deliver GDNF in bilayer collagen conduit promoting sciatic nerve growth, International journal of nanomedicine 11 (2016) 1383-1394 **DOI**.10.2147/IJN.S96324

[434] Mihaila, S.M., et al. Photocrosslinkable kappa-carrageenan hydrogels for tissue engineering applications, Advanced healthcare materials 2(6) (2013) 895-907 **DOI**.10.1002/adhm.201200317

[435] Bandyopadhyay, A., et al. 3D bioprinting of photo-crosslinkable silk methacrylate (SilMA)-polyethylene glycol diacrylate (PEGDA) bioink for cartilage tissue engineering, Journal of Biomedical Materials Research Part A 110(4) (2022) 884-898 **DOI**.10.1002/jbm.a.37336

[436] Mello, M.A., Tuan, R.S. Effects of TGF-β1 and triiodothyronine on cartilage maturation: In vitro analysis using long-term high-density micromass cultures of chick embryonic limb mesenchymal cells, Journal of orthopaedic research 24(11) (2006) 2095-2105 **DOI**.10.1002/jor.20233

[437] Shi, Y., Massagué, J. Mechanisms of TGF-β signaling from cell membrane to the nucleus, cell 113(6) (2003) 685-700 **DOI**.10.1016/s0092-8674(03)00432-x

[438] Johnstone, B., et al. In vitrochondrogenesis of bone marrow-derived mesenchymal progenitor cells, Experimental cell research 238(1) (1998) 265-272 **DOI**.10.1006/excr.1997.3858

[439] Tuli, R., et al. Transforming growth factor-β-mediated chondrogenesis of human mesenchymal progenitor cells involves N-cadherin and mitogen-activated protein kinase and Wnt signaling cross-talk, Journal of Biological Chemistry 278(42) (2003) 41227-41236 **DOI**.10.1074/jbc.M305312200

[440] Lee, C.H., et al. CTGF directs fibroblast differentiation from human mesenchymal stem/stromal cells and defines connective tissue healing in a rodent injury model, The Journal of clinical investigation 120(9) (2010) 3340-3349 **DOI**.10.1172/JCI43230

[441] Lee, C.H., et al. Fibroblastic differentiation of human mesenchymal stem cells using connective tissue growth factor, 2006 international conference of the IEEE engineering in medicine and biology Society, IEEE, 2006, pp. 775-778 **DOI**.10.1109/IEMBS.2006.259866

[442] Tarafder, S., et al. Engineered Healing of Avascular Meniscus Tears by Stem Cell Recruitment, Scientific Reports 8(1) (2018) 1-9 **DOI**.10.1038/s41598-018-26545-8

[443] Zhao, X., et al. Injectable stem cell-laden photocrosslinkable microspheres fabricated using microfluidics for rapid generation of osteogenic tissue constructs, Advanced Functional Materials 26(17) (2016) 2809-2819 **DOI**.10.1002/adfm.201504943

[444] Sheikhi, A., et al. Microfluidic-enabled bottom-up hydrogels from annealable naturally-derived protein microbeads, Biomaterials 192 (2019) 560-568 **DOI**.10.1016/j.biomaterials.2018.10.040

[445] Nguyen, A.H., et al. Gelatin methacrylate microspheres for controlled growth factor release, Acta biomaterialia 13 (2015) 101-110 **DOI**.10.1016/j.actbio.2014.11.028

[446] Rothrauff, B.B., et al. Point-of-Care Procedure for Enhancement of Meniscal Healing in a Goat Model Utilizing Infrapatellar Fat Pad-Derived Stromal Vascular Fraction Cells Seeded in Photocrosslinkable Hydrogel, Am J Sports Med 47(14) (2019) 3396-3405 **DOI**.10.1177/0363546519880468

[447] Lee, B.H., et al. Synthesis and characterization of types A and B gelatin methacryloyl for bioink applications, Materials 9(10) (2016) 797 **DOI**.10.3390/ma9100797

[448] Gao, Y., Ma, Q. Bacterial infection microenvironment-responsive porous microspheres by microfluidics for promoting anti-infective therapy, Smart Medicine 1(1) (2022) e20220012 **DOI**.10.1002/SMMD.20220012

[449] Moses, J.C., et al. Silk-Based Bioengineered Diaphyseal Cortical Bone Unit Enclosing an Implantable Bone Marrow toward Atrophic Nonunion Grafting, Advanced Healthcare Materials 11(6) (2022) 2102031 **DOI**.10.1002/adhm.202102031

[450] Lin, X., et al. Stimuli-responsive silk fibroin for on-demand drug delivery, Smart Medicine 2(2) (2023) e20220019 **DOI**.10.1002/SMMD.20220019

[451] Singh, Y.P., et al. 3D Bioprinted Silk-Based In Vitro Osteochondral Model for Osteoarthritis Therapeutics, Advanced Healthcare Materials 11(24) (2022) 2200209 **DOI**.10.1002/adhm.202200209

[452] Dai, T.y., et al. In vivo studies of mesenchymal stem cells in the treatment of meniscus injury, Orthopaedic Surgery 13(8) (2021) 2185-2195 **DOI**.10.1111/os.13002

[453] Itose, M., et al. Knee meniscus regeneration using autogenous injection of uncultured adipose tissue-derived regenerative cells, Regenerative Therapy 21 (2022) 398-405 **DOI**.10.1016/j.reth.2022.09.003

[454] Twomey-Kozak, J., Jayasuriya, C.T. Meniscus repair and regeneration: A systematic review from a basic and translational science perspective, Clinics in sports medicine 39(1) (2020) 125-163 **DOI**.10.1016/j.csm.2019.08.003

[455] Chameettachal, S., et al. Regulation of chondrogenesis and hypertrophy in silk fibroin-gelatin-based 3D bioprinted constructs, ACS Biomaterials Science & Engineering 2(9) (2016) 1450-1463 **DOI**.10.1021/acsbiomaterials.6b00152

[456] Chakraborty, J., et al. Development of a biomimetic arch-like 3D bioprinted construct for cartilage regeneration using gelatin methacryloyl and silk fibroin-gelatin bioinks, Biofabrication 15(3) (2023) 035009 **DOI**.10.1088/1758-5090/acc68f

[457] Bhardwaj, N., et al. Potential of silk fibroin/chondrocyte constructs of muga silkworm Antheraea assamensis for cartilage tissue engineering, Journal of Materials Chemistry B 4(21) (2016) 3670-3684 **DOI**.10.1039/c6tb00717a

[458] Fan, H., et al. TGF-β3 immobilized PLGA-gelatin/chondroitin sulfate/hyaluronic acid hybrid scaffold for cartilage regeneration, Journal of biomedical materials research Part A 95(4) (2010) 982-992 **DOI**.10.1002/jbm.a.32899

[459] Park, J.S., et al. Chondrogenic potential of stem cells derived from amniotic fluid, adipose tissue, or bone marrow encapsulated in fibrin gels containing TGF-β3, Biomaterials 32(32) (2011) 8139-8149 **DOI**.10.1016/j.biomaterials.2011.07.043

[460] Tong, Z., et al. Controlling the fibroblastic differentiation of mesenchymal stem cells via the combination of fibrous scaffolds and connective tissue growth factor, Tissue Engineering Part A 17(21-22) (2011) 2773-2785 **DOI**.10.1089/ten.TEA.2011.0219

[461] Lee, C., et al. Fibrochondrocytes Generated From Human Mesenchymal Stem Cells By The Dynamic Duo of CTGF and TGFβ3: Implications in Regeneration of Knee Meniscus, Intervertebral Discs and Tendon/Ligaments, Orthopaedic Research Society 2011 Annual Meeting, 2011,

[462] Bandyopadhyay, A., et al. Easy and affordable method for rapid prototyping of tissue models in vitro using three-dimensional bioprinting, Biocybernetics and Biomedical Engineering 38(1) (2018) 158-169 **DOI**.10.1016/j.bbe.2017.12.001

[463] Grassi, A., et al. Clinical outcomes and complications of a collagen meniscus implant: a systematic review, International orthopaedics 38(9) (2014) 1945-1953 **DOI**.10.1007/s00264-014-2408-9

[464] Temenoff, J.S., Mikos, A.G. Tissue engineering for regeneration of articular cartilage, Biomaterials 21(5) (2000) 431-440 **DOI**.10.1016/s0142-9612(99)00213-6

[465] Zhang, Q., et al. Shedding light on 3D printing: Printing photo-crosslinkable constructs for tissue engineering, Biomaterials 286 (2022) 121566 **DOI**.10.1016/j.biomaterials.2022.121566

[466] Shome, S., et al. Recent advances in platelet-rich plasma and its derivatives: therapeutic agents for tissue engineering and regenerative medicine, Progress in Biomedical Engineering (2023) **DOI**.10.1088/2516-1091/ad1338

[467] Pan, W., et al. PRP-chitosan thermoresponsive hydrogel combined with black phosphorus nanosheets as injectable biomaterial for biotherapy and phototherapy treatment of rheumatoid arthritis, Biomaterials 239 (2020) 119851 **DOI**.10.1016/j.biomaterials.2020.119851

[468] Gao, X., et al. Fabrication and properties of an injectable sodium alginate/PRP composite hydrogel as a potential cell carrier for cartilage repair, Journal of Biomedical Materials Research Part A 107(9) (2019) 2076-2087 **DOI**.10.1002/jbm.a.36720

[469] Irmak, G., et al. Sustained release of growth factors from photoactivated platelet rich plasma (PRP), Eur J Pharm Biopharm 148 (2020) 67-76 **DOI**.10.1016/j.ejpb.2019.11.011

[470] Paterson, K.L., et al. Intra-articular injection of photo-activated platelet-rich plasma in patients with knee osteoarthritis: a double-blind, randomized controlled pilot study, BMC Musculoskeletal Disorders 17(1) (2016) 1-9 **DOI**.10.1186/s12891-016-0920-3

[471] Freitag, J., et al. Photoactivated platelet-rich plasma therapy for a traumatic knee chondral lesion, Case Reports 2012 (2012) bcr2012006858 **DOI**.10.1136/bcr-2012-006858

[472] Horimizu, M., et al. An improved freeze-dried PRP-coated biodegradable material suitable for connective tissue regenerative therapy, Cryobiology 66(3) (2013) 223-232 **DOI**.10.1016/j.cryobiol.2013.01.006

[473] Marino, L., et al. Mesenchymal stem cells from the Wharton's jelly of the human umbilical cord: biological properties and therapeutic potential, Int J stem cells 12(2) (2019) 218-226 **DOI**.10.15283/ijsc18034

[474] Brown, J., et al. Impact of silk biomaterial structure on proteolysis, Acta biomaterialia 11 (2015) 212-221 **DOI**.10.1016/j.actbio.2014.09.013

[475] Naito, K., et al. Measurement of matrix metalloproteinases (MMPs) and tissue inhibitor of metalloproteinases-1 (TIMP-1) in patients with knee osteoarthritis: comparison with generalized osteoarthritis, Rheumatology (Oxford, England) 38(6) (1999) 510-515 **DOI**.10.1093/rheumatology/38.6.510

[476] Bhardwaj, N., Kundu, S.C. Chondrogenic differentiation of rat MSCs on porous scaffolds of silk fibroin/chitosan blends, Biomaterials 33(10) (2012) 2848-2857 **DOI**.10.1016/j.biomaterials.2011.12.028

[477] Moses, J.C., Mandal, B.B. Mesoporous silk-bioactive glass nanocomposites as drug eluting multifunctional conformal coatings for improving osseointegration and bactericidal properties of metal implants, ACS Applied Materials & Interfaces 14(13) (2022) 14961-14980 **DOI**.10.1021/acsami.2c00093

[478] Mamaghani, K.R., et al. Synthesis and microstructural characterization of GelMa/PEGDA hybrid hydrogel containing graphene oxide for biomedical purposes, Materials Today: Proceedings 5(7) (2018) 15635-15644 **DOI**.10.1016/j.matpr.2018.04.173

[479] Shimomura, K., et al. Region-Specific Effect of the Decellularized Meniscus Extracellular Matrix on Mesenchymal Stem Cell–Based Meniscus Tissue Engineering, The American Journal of Sports Medicine 45(3) (2017) 604-611 **DOI**.10.1177/0363546516674184

[480] Miller, A.T., et al. Compressive cyclic ratcheting and fatigue of synthetic, soft biomedical polymers in solution, Journal of the mechanical behavior of biomedical materials 54 (2016) 268-282 **DOI**.10.1016/j.jmbbm.2015.09.034

[481] Bousnaki, M., et al. Fibro/chondrogenic differentiation of dental stem cells into chitosan/alginate scaffolds towards temporomandibular joint disc regeneration, Journal of Materials Science: Materials in Medicine 29(7) (2018) 1-17 **DOI**.10.1007/s10856-018-6109-6

[482] Qin, S., et al. Fibrochondrogenic differentiation potential of tendon-derived stem/progenitor cells from human patellar tendon, Journal of Orthopaedic Translation 22 (2020) 101-108 **DOI**.10.1016/j.jot.2019.08.006

[483] Zou, L., et al. Use of RUNX2 expression to identify osteogenic progenitor cells derived from human embryonic stem cells, Stem cell reports 4(2) (2015) 190-198 **DOI**.10.1016/j.stemcr.2015.01.008

[484] Kusuma, G.D., et al. Ectopic bone formation by mesenchymal stem cells derived from human term placenta and the decidua, PLoS One 10(10) (2015) e0141246 **DOI**.10.1371/journal.pone.0141246

[485] An, Y.-H., et al. Meniscus regeneration with injectable Pluronic/PMMA-reinforced fibrin hydrogels in a rabbit segmental meniscectomy model, Journal of Tissue Engineering 12 (2021) 20417314211050141 **DOI**.10.1177/20417314211050141

[486] Wu, J., et al. Regional-specific meniscal extracellular matrix hydrogels and their effects on cell–matrix interactions of fibrochondrocytes, Biomedical Materials 17(1) (2021) 014105 **DOI**.10.1088/1748-605X/ac4178

[487] Roberts, S., et al. Immunohistochemical study of collagen types I and II and procollagen IIA in human cartilage repair tissue following autologous chondrocyte implantation, The Knee 16(5) (2009) 398-404 **DOI**.10.1016/j.knee.2009.02.004

[488] Almawash, S., et al. Current and Future Prospective of Injectable Hydrogels—Design Challenges and Limitations, Pharmaceuticals 15(3) (2022) 371 **DOI**.10.3390/ph15030371

[489] Říhová, B. Immunocompatibility and biocompatibility of cell delivery systems, Advanced drug delivery reviews 42(1-2) (2000) 65-80 **DOI**.10.1016/s0169-409x(00)00054-5

[490] Moussa, M., et al. Platelet rich plasma (PRP) induces chondroprotection via increasing autophagy, anti-inflammatory markers, and decreasing apoptosis in human osteoarthritic cartilage, Experimental cell research 352(1) (2017) 146-156 **DOI**.10.1016/j.yexcr.2017.02.012

[491] Pujol, N., et al. Long-term outcomes of all-inside meniscal repair, Knee Surgery, Sports Traumatology, Arthroscopy 23(1) (2015) 219-224 **DOI**.10.1007/s00167-013-2553-5

[492] Zaffagnini, S., et al. Prospective Long-Term Outcomes of the Medial Collagen Meniscus Implant Versus Partial Medial Meniscectomy, The American Journal of Sports Medicine 39(5) (2011) 977-985 **DOI**.10.1177/0363546510391179

[493] Moradi, L., et al. Regeneration of meniscus tissue using adipose mesenchymal stem cells-chondrocytes co-culture on a hybrid scaffold: In vivo study, Biomaterials 126 (2017) 18-30 **DOI**.10.1016/j.biomaterials.2017.02.022

[494] Xia, B., et al. Development of a decellularized meniscus matrix-based nanofibrous scaffold for meniscus tissue engineering, Acta biomaterialia 128 (2021) 175-185 **DOI**.10.1016/j.actbio.2021.03.074

[495] Yang, X., et al. Photocrosslinked methacrylated natural macromolecular hydrogels for tissue engineering: A review, International Journal of Biological Macromolecules 246 (2023) 125570 **DOI**.10.1016/j.ijbiomac.2023.125570

[496] Hakim Khalili, M., et al. Additive Manufacturing and Physicomechanical Characteristics of PEGDA Hydrogels: Recent Advances and Perspective for Tissue Engineering, Polymers 15(10) (2023) 2341 **DOI**.10.3390/polym15102341

[497] Irmak, G., Gümüşderelioğlu, M. Photo-activated platelet-rich plasma (PRP)-based patient-specific bio-ink for cartilage tissue engineering, Biomedical Materials 15(6) (2020) 065010 **DOI**.10.1088/1748-605X/ab9e46

[498] Arutyunyan, I., et al. Umbilical cord tissue cryopreservation: a short review, Stem cell research & therapy 9(1) (2018) 1-7 **DOI**.10.1186/s13287-018-0992-0

[499] Whitehouse, M.R., et al. Repair of torn avascular meniscal cartilage using undifferentiated autologous mesenchymal stem cells: From in vitro optimization to a first-in-human study, Stem Cells Translational Medicine 6(4) (2017) 1237-1248 **DOI**.10.1002/sctm.16-0199

[500] Fathi-Achachelouei, M., et al. Dual growth factor delivery using PLGA nanoparticles in silk fibroin/PEGDMA hydrogels for articular cartilage tissue engineering, Journal of Biomedical Materials Research Part B: Applied Biomaterials 108(5) (2020) 2041-2062 **DOI**.10.1002/jbm.b.34544

[501] Killion, J.A., et al. Mechanical properties and thermal behaviour of PEGDMA hydrogels for potential bone regeneration application, Journal of the mechanical behavior of biomedical materials 4(7) (2011) 1219-1227 **DOI**.10.1016/j.jmbbm.2011.04.004

[502] Lu, D., et al. Macroporous methacrylated hyaluronic acid hydrogel with different pore sizes for in vitro and in vivo evaluation of vascularization, Biomedical Materials 17(2) (2022) 025006 **DOI**.10.1088/1748-605X/ac494b

[503] Chirichella, P.S., et al. Treatment of knee meniscus pathology: rehabilitation, surgery, and orthobiologics, PM&R 11(3) (2019) 292-308 **DOI**.10.1016/j.pmrj.2018.08.384

[504] Shan, B.H., Wu, F.G. Hydrogel-Based Growth Factor Delivery Platforms: Strategies and Recent Advances, Advanced Materials (2023) 2210707 **DOI**.10.1002/adma.202210707

[505] Alsousou, J., et al. The role of platelet-rich plasma in tissue regeneration, Platelets 24(3) (2013) 173-182 **DOI**.10.3109/09537104.2012.684730

[506] Griffin, J.W., et al. Platelet-rich plasma in meniscal repair: does augmentation improve surgical outcomes?, Clinical Orthopaedics and Related Research 473 (2015) 1665-1672

[507] Martínez-Zapata, M.J., et al. Efficacy and safety of the use of autologous plasma rich in platelets for tissue regeneration: a systematic review, Transfusion 49(1) (2009) 44-56 **DOI**.10.1111/j.1537-2995.2008.01945.x

[508] Koch, M., et al. Bone marrow aspirate concentrate for the treatment of avascular meniscus tears in a one-step procedure—evaluation of an in vivo model, International journal of molecular sciences 20(5) (2019) 1120 **DOI**.10.3390/ijms20051120

[509] Everhart, J.S., et al. Platelet-rich plasma reduces failure risk for isolated meniscal repairs but provides no benefit for meniscal repairs with anterior cruciate ligament reconstruction, The American journal of sports medicine 47(8) (2019) 1789-1796 **DOI**.10.1177/0363546519852616

[510] El-Sharkawy, H., et al. Platelet-rich plasma: growth factors and pro-and anti-inflammatory properties, Journal of periodontology 78(4) (2007) 661-669 **DOI**.10.1902/jop.2007.060302

[511] Naito, K., et al. Low-intensity pulsed ultrasound (LIPUS) increases the articular cartilage type II collagen in a rat osteoarthritis model, Journal of Orthopaedic Research 28(3) (2010) 361-369 **DOI**.10.1002/jor.20995

[512] Zhao, Z., et al. Mechanotransduction pathways in the regulation of cartilage chondrocyte homoeostasis, Journal of cellular and molecular medicine 24(10) (2020) 5408-5419 **DOI**.10.1111/jcmm.15204

[513] Aliabouzar, M., et al. Effects of scaffold microstructure and low intensity pulsed ultrasound on chondrogenic differentiation of human mesenchymal stem cells, Biotechnology and bioengineering 115(2) (2018) 495-506 **DOI**.10.1002/bit.26480

[514] Ren, L., et al. Involvement of p38 MAPK pathway in low intensity pulsed ultrasound induced osteogenic differentiation of human periodontal ligament cells, Ultrasonics 53(3) (2013) 686-690 **DOI**.10.1016/j.ultras.2012.10.008

[515] Zhou, S., et al. Molecular mechanisms of low intensity pulsed ultrasound in human skin fibroblasts, Journal of Biological Chemistry 279(52) (2004) 54463-54469 **DOI**.10.1074/jbc.M404786200

[516] Kusuyama, J., et al. Low intensity pulsed ultrasound (LIPUS) influences the multilineage differentiation of mesenchymal stem and progenitor cell lines through ROCK-Cot/Tpl2-MEK-ERK signaling pathway, Journal of Biological Chemistry 289(15) (2014) 10330-10344 **DOI**.10.1074/jbc.M113.546382

[517] Melo, B.A.G., et al. 3D Printed Cartilage-Like Tissue Constructs with Spatially Controlled Mechanical Properties, Advanced Functional Materials 29(51) (2019) 1906330 **DOI**.10.1002/adfm.201906330

[518] Friedland, J.C., et al. Mechanically activated integrin switch controls α5β1 function, Science 323(5914) (2009) 642-644 **DOI**.10.1126/science.1168441

[519] Lucchinetti, E., et al. The effect of mechanical load on integrin subunits α5 and β1 in chondrocytes from mature and immature cartilage explants, Cell and tissue research 315(3) (2004) 385-391 **DOI**.10.1007/s00441-003-0836-8

[520] McKee, C., et al. Compression induced chondrogenic differentiation of embryonic stem cells in three-dimensional polydimethylsiloxane scaffolds, Tissue Engineering Part A 23(9-10) (2017) 426-435 **DOI**.10.1089/ten.TEA.2016.0376

[521] Heng, B.C., et al. Role of YAP/TAZ in cell lineage fate determination and related signaling pathways, Frontiers in cell and developmental biology 8 (2020) 735 **DOI**.10.3389/fcell.2020.00735

[522] Hallström, G.F., et al. Microenvironmental mechanoactivation through Yap/Taz suppresses chondrogenic gene expression, Molecular Biology of the Cell 34(7) (2023) ar73 **DOI**.10.1091/mbc.E22-12-0543

[523] Chowdhury, T.T., et al. Dynamic compression inhibits the synthesis of nitric oxide and PGE2 by IL-1β-stimulated chondrocytes cultured in agarose constructs, Biochemical and Biophysical Research Communications 285(5) (2001) 1168-1174 **DOI**.10.1006/bbrc.2001.5311

[524] Fu, S., et al. Mechanical loading inhibits cartilage inflammatory signalling via an HDAC6 and IFT-dependent mechanism regulating primary cilia elongation, Osteoarthritis and Cartilage 27(7) (2019) 1064-1074 **DOI**.10.1016/j.joca.2019.03.003

[525] Dieterle, M.P., et al. Integrins, cadherins and channels in cartilage mechanotransduction: Perspectives for future regeneration strategies, Expert Reviews in Molecular Medicine 23 (2021) e14 **DOI**.10.1017/erm.2021.16

[526] Zhang, K., et al. Beta1 integrin inhibits apoptosis induced by cyclic stretch in annulus fibrosus cells via ERK1/2 MAPK pathway, Apoptosis 21(1) (2016) 13-24 **DOI**.10.1007/s10495-015-1180-7

[527] Fang, T., et al. Molecular mechanisms of mechanical load-induced osteoarthritis, International Orthopaedics 45(5) (2021) 1125-1136 **DOI**.10.1007/s00264-021-04938-1

[528] Li, Y., et al. Regulation and mechanism of YAP/TAZ in the mechanical microenvironment of stem cells (Review), Molecular medicine reports 24(1) (2021) 1-11 **DOI**.10.3892/mmr.2021.12145

LIST OF PUBLICATIONS

Publications from Ph.D. Thesis

(A) Journal Publications

1. **Ashutosh Bandyopadhyay**, Suvro Kanti Chowdhury, Souradeep Dey, Joseph Christakiran Moses, and Biman B. Mandal. "*Silk: A promising biomaterial opening new vistas towards affordable healthcare solutions*". **Journal of the Indian Institute of Science**. 2019, 99(3), 445-487, **DOI:** 10.1007/s41745-019-00114-y.

2. **Ashutosh Bandyopadhyay**, Baishali Ghibhela, Biman B. Mandal. *Current advances in engineering meniscal tissues: "Insights into 3D printing, injectable hydrogels and physical stimulation based strategies"*. **Biofabrication**. 2024, 16(2), 022006, **DOI:**10.1088/1758-5090/ad22f0.

3. **Ashutosh Bandyopadhyay** and Biman B. Mandal. "*A three-dimensional printed silk-based biomimetic tri-layered meniscus for potential patient-specific implantation*". **Biofabrication**. 2019, 12(1), 015003, **DOI:** 10.1088/1758-5090/ab40fa. (*Top cited paper award 2022, IOP*)

4. **Ashutosh Bandyopadhyay**, Biman B. Mandal. "*Photocrosslinkable silk-based bioinks embedded with growth factor loaded microspheres towards cell-free 3D printing approach for biomimetic regeneration of meniscal tissue*". **Applied Materials Today**. 2024. 36. 102049, **DOI:** 10.1016/j.apmt.2023.102049.

5. **Ashutosh Bandyopadhyay**, Baishali Ghibhela, Sayanti Shome, Samsamul Hoque, Samit K. Nandi, Biman B. Mandal. "*Photo-polymerizable autologous growth-factor loaded silk-based biomaterial-inks towards 3D printing-based regeneration of meniscus tears*". **Advanced Biology**. 2024; 8(5), e2300710, **DOI:** 10.1002/adbi.202300710.

6. **Ashutosh Bandyopadhyay**, Baishali Ghibhela, Sayanti Shome, Debajyoti Pal, Samit K. Nandi, Biman B. Mandal. *"Silk-based injectable photocurable hydrogel loaded with autologous platelet rich plasma lysate for repair of partial and full thickness meniscal defects"*. **Applied Materials Today**. 2024. 37.1020111, **DOI:** 10.1016/j.apmt.2024.102111.

7. **Ashutosh Bandyopadhyay**, Ananya Datta, Biman B. Mandal. *"Ultrasound assisted maturation of 3D printed meniscus constructs loaded with stem cells and autologous growth factors in vitro"*. (***Manuscript under peer review in Advanced Healthcare Materials***)

(B) Patents

Biman B. Mandal, Yogendra Pratap Singh, **Ashutosh Bandyopadhyay**, Shreya Mehrotra, Joseph Christakiran Moses, Bibhas K. Bhunia, G. Janani, Dimple Chauhan. *"Development of Silk Based Bioinks for 3D Printing and Uses Thereof"*. Indian Patent Number: 415089; Granted on: 21st Dec. 2022.

(C) Conference Publications

Ashutosh Bandyopadhyay, Baishali Ghibhela, Sayanti Shome, Biman B. Mandal. "*Silk Based Photocrosslinkable Growth Factor Laden Injectable Hydrogel for Meniscus Defects"*, **Tissue Engineering Part A**. 2023, 29(13-14), 667.

(D) Conference, Seminar, Workshop Participation/Presentations

1. **Ashutosh Bandyopadhyay**, Baishali Ghibhela, Sayanti Shome, Biman B. Mandal. "*Silk Based Photocrosslinkable Growth Factor Laden Injectable Hydrogel for Meniscus Defects"*. Tissue Engineering and Regenerative Medicine International Society European Chapter 2023 (TERMIS-EU 2023), Manchester, United Kingdom, 28-31 March 2023. (Poster)

2. **Ashutosh Bandyopadhyay**, Baishali Ghibhela, Sayanti Shome, Biman B. Mandal. *"Silk Based Autologous Growth Factor Enriched 3D Printed Constructs for Patient Specific Partial and Full Thickness Meniscus Defects"*. International Conference on Biomaterials, Regenerative Medicine and Devices 2022 (BioRemedi 2022), Guwahati, India, 14-18 December 2022. (SBAOI Bajpai Saha Student Award Winner)

3. **Ashutosh Bandyopadhyay**, Bibrita Bhar, Chitra Jaiswal, Souradeep Dey, Sayanti Shome, Biman B. Mandal. "*Silk Based 3D Printing of Human Tissue" Models*. North East Research Conclave (NERC-2022), Guwahati, India, 20-22 May 2022 (Student Stall)

4. **Ashutosh Bandyopadhyay**, Biman B. Mandal. *"Functional Biomimetic 3D Printed Human Meniscus Tissue Constructs using Human Mesenchymal Stem Cells and Human-Derived Platelet Rich Plasma Lysate"*. 3rd National Biomedical Research Competition (NBRCOM 2021), Online, 6-10 December 2021. (Virtual Poster)

5. **Ashutosh Bandyopadhyay**, Biman B. Mandal. "*Growth factor laden silk-based biomimetic 3D printed meniscus for inducing fibrochondrogenic differentiation of stem cells"*. International Conference On Advanced Material For Better Tommorow (AMBT-2021), Online, 13-17 July 2021. (Best Poster Award)

6. **Ashutosh Bandyopadhyay**, Biman B. Mandal. *"Biomimetic, Growth Factor Laden Silk-based 3D Printed Meniscus Induce Fibrochondrocytic Differentiation of Stem Cells"*.

International e-symposium on Smart Polymers: Applications in Current Scenario (SPACS-2021), Online, 15-16 January 2021. (Flash Talk).

7. **Ashutosh Bandyopadhyay**, Biman B. Mandal. "*Growth Factor Laden Silk-based Biomimetic 3D Printed Meniscus For Inducing Fibrochondrogenic Differentiation Of Stem Cells*". India-Japan Cooperative Programme YNU Symposium 2021, Sakura Science Exchange Program, Online, 27 December 2021. (Poster)

8. **Ashutosh Bandyopadhyay**, Biman B. Mandal. *"Rapid Prototyping of Biomimetic Silk based Functional 3D Constructs for Meniscus Tissue Engineering"*. International Conference on Functional Nanomaterials (ICFNM 2019), IIT BHU, India, 22-25 February 2019. (Poster)

9. **Ashutosh Bandyopadhyay**, Biman B. Mandal. "*3D Printed Biomimetic Silk-based Functional Constructs for Meniscus Tissue Engineering"*. Research Conclave 2019 (RC-2019), IIT Guwahati. (Poster)

(E) <u>Selected Awards and Achievements</u>

1. **DST Travel Grant 2023 (SERB**) by Department of Science and Technology, Govt. of India for attending the TERMIS-EU 2023 held at Manchester, United Kingdom (28th -31st March 2023).

2. **Bajpai-Saha Student Award 2022** by Society for Biomaterials and Artificial Organs (India), received at BIO-Remedi 2022, IIT Guwahati, December 2022.

3. **New Generation Innovation and Entrepreneurship Development Centre (Newgen-IEDC) Student project grant** awarded for project titled: "3D Printed Silk-based Affordable Patient-specific Platelet Rich Plasma Functionalized Knee Meniscus Implants for Treatment of Knee Injuries", (Grant of Rs. 2,50,000), 2021-2022.

4. **Best Poster Presentation Award** by Society for Interdisciplinary Research in Materials and Biology, received at AMBT 2021, IIT BHU, Jul 2021.

5. Presented the work on 3D printing of Meniscus, awarded with **Guwahati Biotech Park Talent Search Contest** 4th Position prize (Cash Prize Rs. 15,000), organized by Guwahati Biotech Park, Guwahati, Assam, 2019.

6. "**Third Prize for model presentation**" to Team (Silk based 3D bioprinted human tissues, members included Dey S, Bandyopadhyay A, Mehrotra S, Bhunia BK and Mandal BB), presented our work on "3D Bioprinting" and was awarded in Research Conclave'19 at IIT Guwahati during 14th to 17th March, 2019.

7. **"Best project from IIT Guwahati" to** Team (Silk-Bots), presented our work on "3D Bioprinting" and was awarded in TechExpo 2018 organized by Techniche 2018 at IIT Guwahati from 30th August to 2nd September 2018.

Publications from Other Collaborative Research Projects

(A) Journal Publications

1. **Bandyopadhyay A**, Mandal BB, Bhardwaj N. 3D bioprinting of photo-crosslinkable silk methacrylate (SilMA)-polyethylene glycol diacrylate (PEGDA) bioink for cartilage tissue engineering. ***Journal of Biomedical Materials Research-A***. 2022;110(4):884-98. **DOI:** 10.1002/jbm.a.37336
2. Mehrotra S, Moses JC, **Bandyopadhyay A**, Mandal BB. 3D Printing/Bioprinting Based Tailoring of in Vitro Tissue Models: Recent Advances and Challenges. ***ACS Applied Bio Materials***. 2019;2(4):1385-405. **DOI:** 10.1021/acsabm.9b00073
3. Singh YP, **Bandyopadhyay A**, Mandal BB. 3D Bioprinting Using Cross-Linker-Free Silk-Gelatin Bioink for Cartilage Tissue Engineering. ***ACS Applied Materials Interfaces***. 2019;11(37):33684-96. **DOI:** 10.1021/acsami.9b11644
4. Bhunia BK, Dey S, **Bandyopadhyay A**, Mandal BB. 3D printing of annulus fibrosus anatomical equivalents recapitulating angle-ply architecture for intervertebral disc replacement. ***Applied Materials Today***. 2021;23:101031. **DOI:** 10.1016/j.apmt.2021.101031
5. Mehrotra S, Singh RD, **Bandyopadhyay A**, Janani G, Dey S, Mandal BB. Engineering Microsphere-Loaded Non-mulberry Silk-Based 3D Bioprinted Vascularized Cardiac Patches with Oxygen-Releasing and Immunomodulatory Potential. ***ACS Applied Materials and Interfaces***. 2021;13(43):50744-59. **DOI:** 10.1021/acsami.1c14118
6. Bhattacharya A, Mahata S, **Bandyopadhyay A**, Mandal BB, Manivannan V. Application of 2,4,5-tris(2-pyridyl)imidazole as 'turn-off' fluorescence sensor for Cu(II) and Hg(II) ions and cell imaging. ***Luminescence***. 2022;37(6):883-91. **DOI:** 10.1002/bio.4232
7. Moses JC, Dey S, **Bandyopadhyay A**, Agarwala M, Mandal BB. Silk-Based Bioengineered Diaphyseal Cortical Bone Unit Enclosing an Implantable Bone Marrow toward Atrophic Nonunion Grafting. ***Advanced Healthcare Materials***. 2022;11(6):e2102031. **DOI:** 10.1002/adhm.202102031Singh YP, Moses JC, **Bandyopadhyay A**, Mandal BB. 3D Bioprinted Silk-Based In Vitro Osteochondral Model for Osteoarthritis Therapeutics. ***Advanced Healthcare Materials***. 2022;11(24):e2200209. **DOI:** 10.1002/adhm.202200209

8. Dey S, Jaiswal C, Shome S, Bhar B, **Bandyopadhyay A**, Manikumar K, et al. Photocrosslinkable Silk-Based Biomaterials for Regenerative Medicine and Healthcare Applications. ***Regenerative Engineering and Translational Medicine***. 2022;9(2):181-201. **DOI:** 10.1007/s40883-022-00277-8

9. Morang S, **Bandyopadhyay A**, Mandal BB, Karak N. Asymmetric Hard Domain-Induced Robust Resilient Biocompatible Self-Healable Waterborne Polyurethane for Biomedical Applications. ***ACS Applied Bio Materials***. 2023;6(7):2771-84. **DOI:** 10.1021/acsabm.3c00243

10. Morang S, **Bandyopadhyay A**, Rajput JH, Mandal BB, Poundarik A, Karak N. Robust Self-Healable and Three-Dimensional Printable Thermoplastic Elastomeric Waterborne Polyurethane for Artificial Muscle and Biomedical Scaffold Applications. ***ACS Applied Polymer Materials***. 2023;5(10):8518-32. **DOI:** 10.1021/acsapm.3c01627

11. Shome S, Kodieswaran M, Dadheech R, Chevella M, Sensharma S, Awasthi S, et al. Recent advances in platelet-rich plasma and its derivatives: therapeutic agents for tissue engineering and regenerative medicine. ***Progress in Biomedical Engineering***. 2024;6(1). **DOI:** 10.1088/2516-1091/ad1338

12. Bhunia BK, **Bandyopadhyay A**, Dey S, Mandal BB. Silk-hydrogel functionalized with human decellularized Wharton's jelly extracellular matrix as a minimally invasive injectable hydrogel system for potential nucleus pulposus tissue replacement therapy. ***International Journal of Biological Macromolecules***. 2024;254:127686. **DOI:** 10.1016/j.ijbiomac.2023.127686

13. Morang S, **Bandyopadhyay A**, Borah N, Kar A, Mandal BB, Karak N. Photoluminescent Self-Healable Waterborne Polyurethane/Mo and S Co-doped Graphitic Carbon Nitride Nanocomposite with Bioimaging and Encryption Capability. ***ACS Applied Bio Materials***. 2024;7(3):1910-24. **DOI:** 10.1021/acsabm.3c01259

14. Singh YP, **Bandyopadhyay A**, Dey S, Bhardwaj N, Mandal BB. Trends and advances in silk based 3D printing/bioprinting towards cartilage tissue engineering and regeneration. ***Progress in Biomedical Engineering***. 2024;6(2). **DOI:** 10.1088/2516-1091/ad2d59

(B) Book Chapters

1.Yogendra Pratap Singh, **Ashutosh Bandyopadhyay**, Nandana Bhardwaj and Biman B. Mandal. *"Silk hydrogel-based delivery of cell and bioactive molecules for osteochondral tissue engineering applications",* Hydrogels for Tissue Engineering and Regenerative Medicine, pp. 483-507. Elsevier Inc., 2023. **DOI:** 10.1016/B978-0-12-823948-3.00037-3

2.Yogendra Pratap Singh, Joseph Christakiran Moses, **Ashutosh Bandyopadhyay**, Bibrita Bhar, Bhaskar Birru, Nandana Bhardwaj, and Biman B. Mandal. *"State-of-the-art strategies and future interventions in bone and cartilage repair for personalized regenerative therapy",* Regenerated Organs, pp. 203-248. Academic Press, 2021.

(C) <u>Conference Publications</u>

1.Souradeep Dey, Amritha Bhat, Janani G., **Ashutosh Bandyopadhyay**, Vartik Shandilya, Raghvendra Gupta, Biman B. Mandal. *"Perfusion bioreactor based 3D printed in vitro liver model for drug screening applications"*. Tissue Engineering Part A 2023, 29(13-14), PP-129.

2.Chitra Jaiswal, **Ashutosh Bandyopadhyay**, Biman B. Mandal. *"Development of silk fibroin-based tri-culture 3D in vitro model of breast cancer for high throughput anticancer drug screening"*. Tissue Engineering Part A 2023, 29(13-14), PP-128.

3.Bibrita Bhar, Eshani Das, Kodieswaran Manikumar, **Ashutosh Bandyopadhyay**, Biman B. Mandal. *"Silk based 3D printed human skin model for high-throughput screening of topical formulations"*. Tissue Engineering Part A 2023, 29(13-14), PP-297.

PERMISSIONS

CCC Marketplace

Order Confirmation

Thank you, your order has been placed. An email confirmation has been sent to you. Your order license details and printable licenses will be available within 24 hours. Please access Manage Account for final order details.

This is not an invoice. Please go to manage account to access your order history and invoices.

CUSTOMER INFORMATION

Payment by invoice: You can cancel your order until the invoice is generated by contacting customer service.

Billing Address

Mr. Ashutosh Bandyopadhyay
Indian Institute of Technology Guwahati
NL102, Biosciences and Bioengineering
Indian Institute of Technology Guwahati
North Guwahati
Guwahati, Assam 781039
India

+91 8777529851
ashutoshasb@gmail.com

Customer Location

Mr. Ashutosh Bandyopadhyay
Indian Institute of Technology Guwahati
NL102, Biosciences and Bioengineering
Indian Institute of Technology Guwahati
North Guwahati
Guwahati, Assam 781039
India

PO Number (optional)

N/A

Payment options

Invoice

PENDING ORDER CONFIRMATION

Confirmation Number: Pending

Order Date: 30-Jan-2024

1. Biofabrication

0.00 USD

Order License ID	Pending	**Publisher**	IOP Publishing	Special Terms Apply
ISSN	1758-5090	**Portion**	Chapter/article	
Type of Use	Republish in a thesis/dissertation			

LICENSED CONTENT

Publication Title	Biofabrication	**Country**	United Kingdom of Great Britain and Northern Ireland
Author/Editor	Institute of Physics (Great Britain)	**Rightsholder**	IOP Publishing, Ltd
Date	01/01/2009	**Publication Type**	e-Journal
Language	English	**URL**	http://iopscience.iop.org/1758-5090

REQUEST DETAILS

Portion Type	Chapter/article	**Rights Requested**	Main product
Page Range(s)	1-69	**Distribution**	Worldwide
Total Number of Pages	70	**Translation**	Original language of publication
Format (select all that apply)	Print, Electronic	**Copies for the Disabled?**	No
Who Will Republish the Content?	Author of requested content	**Minor Editing Privileges?**	Yes

Duration of Use	Life of current edition	**Incidental Promotional Use?**	No
Lifetime Unit Quantity	Up to 999	**Currency**	USD

NEW WORK DETAILS

Title	Silk Based Three Dimensional Bioprinting for Meniscus Tissue Engineering	**Institution Name**	Indian Institute of Technology Guwahati
		Expected Presentation Date	2024-04-30
Instructor Name	Prof. Biman B. Mandal		

ADDITIONAL DETAILS

Order Reference Number	N/A	**The Requesting Person / Organization to Appear on the License**	Ashutosh Bandyopadhyay

REQUESTED CONTENT DETAILS

Title, Description or Numeric Reference of the Portion(s)	Whole article	**Title of the Article / Chapter the Portion Is From**	Current advances in engineering meniscal tissues: insights into 3D printing, injectable hydrogels and physical stimulation based strategies
Editor of Portion(s)	N/A	**Author of Portion(s)**	Institute of Physics (Great Britain)
Volume / Edition	N/A	**Issue, if Republishing an Article From a Serial**	N/A
Page or Page Range of Portion	1-69	**Publication Date of Portion**	2024-01-26

RIGHTSHOLDER TERMS AND CONDITIONS

These special terms and conditions are in addition to the standard terms and conditions for CCC's Republication Service and, together with those standard terms and conditions, govern the use of the Works. As the User you will make all reasonable efforts to contact the author(s) of the article which the Work is to be reused from, to seek consent for your intended use. Contacting one author who is acting expressly as authorised agent for their co-author(s) is acceptable. User will reproduce the following wording prominently alongside the Work: the source of the Work, including author, article title, title of journal, volume number, issue number (if relevant), page range (or first page if this is the only information available) and date of first publication; and a link back to the article (via DOI); and if practicable, and IN ALL CASES for new works published under any of the Creative Commons licences, the words "© IOP Publishing. Reproduced with permission. All rights reserved" Without the express permission of the author(s) and the Rightsholder of the article from which the Work is to be reused, User shall not use it in any way which, in the opinion of the Rightsholder, could: (i) distort or alter the author(s)' original intention(s) and meaning; (ii) be prejudicial to the honour or reputation of the author(s); and/or (iii) imply endorsement by the author(s) and/or the Rightsholder. This licence does not apply to any article which is credited to another source and which does not have the copyright line '© IOP Publishing Ltd'. User must check the copyright line of the article from which the Work is to be reused to check that IOP Publishing Ltd has all the necessary rights to be able to grant permission. User is solely responsible for identifying and obtaining separate licences and permissions from the copyright owner for reuse of any such third party material/figures which the Rightsholder is not the copyright owner of. The Rightsholder shall not reimburse any fees which User pays for a republication license for such third party content. This licence does not apply to any material/figure which is credited to another source in the Rightsholder's publication or has been obtained from a third party. User must check the Version of Record of the article from which the Work is to be reused, to check whether any of the material in the Work is third party material. Third party citations and/or copyright notices and/or permissions statements may not be included in any other version of the article from which the Work is to be reused and so cannot be relied upon by the User. User is solely responsible for identifying and obtaining separate licences and permissions from the copyright owner for reuse of any such third party material/figures where the Rightsholder is not the copyright owner. The Rightsholder shall not reimburse any fees which User pays for a republication license for such third party content. User and CCC acknowledge that the Rightsholder may, from time to time, make changes or additions to these special terms and conditions without express notification, provided that these shall not apply to permissions already secured and paid for by User prior to such change or addition. User acknowledges that the Rightsholder (which includes companies within its group and third parties for whom it publishes its titles) may make use of personal data collected through the service in the course of their business. If User is the author of the Work, User may automatically have the right to reuse it under the rights granted back when User transferred the copyright in the article to the Rightsholder. User should check the copyright form and the relevant author rights policy to check whether permission is required. If User is the author of the Work and does require permission for proposed reuse of the Work, User should select 'Author of requested content' as the Requestor Type. The Rightsholder shall not reimburse any fees which User pays for a republication license. If User is the author of the article which User wishes to reuse in User's thesis or dissertation, the republication licence covers the right to include the Version of Record of the article, provided it is not then shared or deposited online. User must include citation details. Where User wishes to share their thesis or dissertation online, they should remove the Version of Record before uploading it. User may include a Preprint or the Accepted Manuscript (after the embargo period) in the online version of the thesis or dissertation, provided they do so in accordance with the Rightsholder's policies on sharing Preprints or Accepted Manuscripts. User may need to obtain separate permission for any third party content included within the article. User must check this with the copyright owner of such third party content. Any online or commercial use of User's thesis or dissertation containing the article, including publication via ProQuest, would need to be expressly notified in writing to the Rightsholder at the time of request and would require separate written permission from the Rightsholder. As well as CCC, the Rightsholder shall have the right to bring any legal action that it deems necessary to enforce its rights should it consider that the Work infringes those rights in any way. For

content reuse requests that qualify for permission under the STM Permissions Guidelines, which may be updated from time to time, the STM Permissions Guidelines supplement the terms and conditions contained in this license.

SPECIAL RIGHTSHOLDER TERMS AND CONDITIONS

When you transferred the copyright in your article to IOP, we granted back to you certain rights, including the right to include all or part of the Final Published Version of the article within any thesis or dissertation provided it is not then shared or deposited online. Full details can be found in our Author Rights Policy. If you are required by your institution to share your thesis/dissertation publicly (such as in an institutional repository), the Final Published Version would need to be removed prior to publication online or in print. Your institution should be able to withhold the IOP article section of your thesis from this version. However, you should still reference the article, include the abstract and provide a DOI link to it on IOPscience so that people know that it has been published. Please include citation details, "© IOP Publishing. Reproduced with permission. All rights reserved" and for online use, a link to the Version of Record. Please note you may need to obtain separate permission for any third party content you included within your article. If you do not wish to remove the IOP article section of your thesis, you also have the following alternative options: 1) Our Author Rights Policy allows authors to post the Accepted Manuscript in certain places after the embargo period has elapsed. This includes your institutional repository, subject to certain restrictions (please see the full terms and conditions in our Author Rights Policy linked in the signature of this email.). Therefore, an option may be to include your Accepted Manuscript article version in your thesis or dissertation, as it would allow you to place the unaltered dissertation onto your repository after the embargo period. Please note that your article is still within its embargo period. An Embargo Period is 'a period of 12 months from the Date of Publication'. 2) A further option would be to include the Author's Original or Preprint version of the article, provided that you do so in line with our Preprint pre-publication policy.

Total Items: 1

Total Due: 0.00 USD

Accepted: Marketplace Permissions General Terms and Conditions and any applicable Publisher Terms and Conditions

SPRINGER NATURE LICENSE
TERMS AND CONDITIONS

Jan 22, 2024

This Agreement between Indian Institute of Technology Guwahati -- Ashutosh Bandyopadhyay ("You") and Springer Nature ("Springer Nature") consists of your license details and the terms and conditions provided by Springer Nature and Copyright Clearance Center.

License Number	5714040027534
License date	Jan 22, 2024
Licensed Content Publisher	Springer Nature
Licensed Content Publication	Journal of the Indian Institute of Science
Licensed Content Title	Silk: A Promising Biomaterial Opening New Vistas Towards Affordable Healthcare Solutions
Licensed Content Author	Ashutosh Bandyopadhyay et al
Licensed Content Date	Aug 24, 2019
Type of Use	Thesis/Dissertation
Requestor type	academic/university or research institute
Format	print and electronic
Portion	full article/chapter
Will you be translating?	no
Circulation/distribution	200 - 499

Author of this Springer Nature content	yes
Title of new work	Silk Based Three Dimensional Bioprinting for Meniscus Tissue Engineering
Institution name	Indian Institute of Technology Guwahati
Expected presentation date	Apr 2024
Requestor Location	Indian Institute of Technology Guwahati NL102, Biosciences and Bioengineering Indian Institute of Technology Guwahati North Guwahati Guwahati, Assam 781039 India Attn: Indian Institute of Technology Guwahati
Total	0.00 USD

Terms and Conditions

Springer Nature Customer Service Centre GmbH Terms and Conditions

The following terms and conditions ("Terms and Conditions") together with the terms specified in your [RightsLink] constitute the License ("License") between you as Licensee and Springer Nature Customer Service Centre GmbH as Licensor. By clicking 'accept' and completing the transaction for your use of the material ("Licensed Material"), you confirm your acceptance of and obligation to be bound by these Terms and Conditions.

1. Grant and Scope of License

1. 1. The Licensor grants you a personal, non-exclusive, non-transferable, non-sublicensable, revocable, world-wide License to reproduce, distribute, communicate to the public, make available, broadcast, electronically transmit or create derivative works using the Licensed Material for the purpose(s) specified in your RightsLink Licence Details only. Licenses are granted for the specific use requested in the order and for no other use, subject to these Terms and Conditions. You acknowledge and agree that the rights granted to you under this License do not include the right to modify, edit, translate, include in collective works, or create derivative works of the Licensed Material in whole or in part unless expressly stated in your RightsLink Licence Details. You may use the Licensed Material only as permitted under this Agreement and will not reproduce, distribute, display, perform, or otherwise use or exploit any Licensed Material in any way, in whole or in part, except as expressly permitted by this License.

1. 2. You may only use the Licensed Content in the manner and to the extent permitted by these Terms and Conditions, by your RightsLink Licence Details and

by any applicable laws.

1. 3. A separate license may be required for any additional use of the Licensed Material, e.g. where a license has been purchased for print use only, separate permission must be obtained for electronic re-use. Similarly, a License is only valid in the language selected and does not apply for editions in other languages unless additional translation rights have been granted separately in the License.

1. 4. Any content within the Licensed Material that is owned by third parties is expressly excluded from the License.

1. 5. Rights for additional reuses such as custom editions, computer/mobile applications, film or TV reuses and/or any other derivative rights requests require additional permission and may be subject to an additional fee. Please apply to journalpermissions@springernature.com or bookpermissions@springernature.com for these rights.

2. Reservation of Rights

Licensor reserves all rights not expressly granted to you under this License. You acknowledge and agree that nothing in this License limits or restricts Licensor's rights in or use of the Licensed Material in any way. Neither this License, nor any act, omission, or statement by Licensor or you, conveys any ownership right to you in any Licensed Material, or to any element or portion thereof. As between Licensor and you, Licensor owns and retains all right, title, and interest in and to the Licensed Material subject to the license granted in Section 1.1. Your permission to use the Licensed Material is expressly conditioned on you not impairing Licensor's or the applicable copyright owner's rights in the Licensed Material in any way.

3. Restrictions on use

3. 1. Minor editing privileges are allowed for adaptations for stylistic purposes or formatting purposes provided such alterations do not alter the original meaning or intention of the Licensed Material and the new figure(s) are still accurate and representative of the Licensed Material. Any other changes including but not limited to, cropping, adapting, and/or omitting material that affect the meaning, intention or moral rights of the author(s) are strictly prohibited.

3. 2. You must not use any Licensed Material as part of any design or trademark.

3. 3. Licensed Material may be used in Open Access Publications (OAP), but any such reuse must include a clear acknowledgment of this permission visible at the same time as the figures/tables/illustration or abstract and which must indicate that the Licensed Material is not part of the governing OA license but has been reproduced with permission. This may be indicated according to any standard referencing system but must include at a minimum 'Book/Journal title, Author, Journal Name (if applicable), Volume (if applicable), Publisher, Year, reproduced with permission from SNCSC'.

4. STM Permission Guidelines

4. 1. An alternative scope of license may apply to signatories of the STM Permissions Guidelines ("STM PG") as amended from time to time and made available at https://www.stm-assoc.org/intellectual-property/permissions/permissions-guidelines/.

4. 2. For content reuse requests that qualify for permission under the STM PG, and which may be updated from time to time, the STM PG supersede the terms and

conditions contained in this License.

4. 3. If a License has been granted under the STM PG, but the STM PG no longer apply at the time of publication, further permission must be sought from the Rightsholder. Contact journalpermissions@springernature.com or bookpermissions@springernature.com for these rights.

5. Duration of License

5. 1. Unless otherwise indicated on your License, a License is valid from the date of purchase ("License Date") until the end of the relevant period in the below table:

Reuse in a medical communications project	Reuse up to distribution or time period indicated in License
Reuse in a dissertation/thesis	Lifetime of thesis
Reuse in a journal/magazine	Lifetime of journal/magazine
Reuse in a book/textbook	Lifetime of edition
Reuse on a website	1 year unless otherwise specified in the License
Reuse in a presentation/slide kit/poster	Lifetime of presentation/slide kit/poster. Note: publication whether electronic or in print of presentation/slide kit/poster may require further permission.
Reuse in conference proceedings	Lifetime of conference proceedings
Reuse in an annual report	Lifetime of annual report
Reuse in training/CME materials	Reuse up to distribution or time period indicated in License
Reuse in newsmedia	Lifetime of newsmedia
Reuse in coursepack/classroom materials	Reuse up to distribution and/or time period indicated in license

6. Acknowledgement

6. 1. The Licensor's permission must be acknowledged next to the Licensed Material in print. In electronic form, this acknowledgement must be visible at the same time as the figures/tables/illustrations or abstract and must be hyperlinked to the journal/book's homepage.

6. 2. Acknowledgement may be provided according to any standard referencing system and at a minimum should include "Author, Article/Book Title, Journal name/Book imprint, volume, page number, year, Springer Nature".

7. Reuse in a dissertation or thesis

7. 1. Where 'reuse in a dissertation/thesis' has been selected, the following terms apply: Print rights of the Version of Record are provided for; electronic rights for use only on institutional repository as defined by the Sherpa guideline (www.sherpa.ac.uk/romeo/) and only up to what is required by the awarding institution.

7. 2. For theses published under an ISBN or ISSN, separate permission is required. Please contact journalpermissions@springernature.com or bookpermissions@springernature.com for these rights.

7. 3. Authors must properly cite the published manuscript in their thesis according to current citation standards and include the following acknowledgement: '*Reproduced with permission from Springer Nature*'.

8. License Fee

You must pay the fee set forth in the License Agreement (the "License Fees"). All amounts payable by you under this License are exclusive of any sales, use, withholding, value added or similar taxes, government fees or levies or other assessments. Collection and/or remittance of such taxes to the relevant tax authority shall be the responsibility of the party who has the legal obligation to do so.

9. Warranty

9. 1. The Licensor warrants that it has, to the best of its knowledge, the rights to license reuse of the Licensed Material. **You are solely responsible for ensuring that the material you wish to license is original to the Licensor and does not carry the copyright of another entity or third party (as credited in the published version).** If the credit line on any part of the Licensed Material indicates that it was reprinted or adapted with permission from another source, then you should seek additional permission from that source to reuse the material.

9. 2. EXCEPT FOR THE EXPRESS WARRANTY STATED HEREIN AND TO THE EXTENT PERMITTED BY APPLICABLE LAW, LICENSOR PROVIDES THE LICENSED MATERIAL "AS IS" AND MAKES NO OTHER REPRESENTATION OR WARRANTY. LICENSOR EXPRESSLY DISCLAIMS ANY LIABILITY FOR ANY CLAIM ARISING FROM OR OUT OF THE CONTENT, INCLUDING BUT NOT LIMITED TO ANY ERRORS, INACCURACIES, OMISSIONS, OR DEFECTS CONTAINED THEREIN, AND ANY IMPLIED OR EXPRESS WARRANTY AS TO MERCHANTABILITY OR FITNESS FOR A PARTICULAR PURPOSE. IN NO EVENT SHALL LICENSOR BE LIABLE TO YOU OR ANY OTHER PARTY OR ANY OTHER PERSON OR FOR ANY SPECIAL, CONSEQUENTIAL, INCIDENTAL, INDIRECT, PUNITIVE, OR EXEMPLARY DAMAGES, HOWEVER CAUSED, ARISING OUT OF OR IN CONNECTION WITH THE DOWNLOADING, VIEWING OR USE OF THE LICENSED MATERIAL REGARDLESS OF THE FORM OF ACTION, WHETHER FOR BREACH OF CONTRACT, BREACH OF WARRANTY, TORT, NEGLIGENCE, INFRINGEMENT OR OTHERWISE (INCLUDING, WITHOUT LIMITATION, DAMAGES BASED ON LOSS OF PROFITS, DATA, FILES, USE, BUSINESS OPPORTUNITY OR CLAIMS OF THIRD PARTIES), AND WHETHER OR NOT THE PARTY HAS BEEN ADVISED OF THE POSSIBILITY OF SUCH DAMAGES. THIS LIMITATION APPLIES NOTWITHSTANDING ANY FAILURE OF ESSENTIAL PURPOSE OF ANY LIMITED REMEDY PROVIDED HEREIN.

10. Termination and Cancellation

10. 1. The License and all rights granted hereunder will continue until the end of the applicable period shown in Clause 5.1 above. Thereafter, this license will be terminated and all rights granted hereunder will cease.

10. 2. Licensor reserves the right to terminate the License in the event that payment is not received in full or if you breach the terms of this License.

11. General

11. 1. The License and the rights and obligations of the parties hereto shall be construed, interpreted and determined in accordance with the laws of the Federal Republic of Germany without reference to the stipulations of the CISG (United Nations Convention on Contracts for the International Sale of Goods) or to Germany´s choice-of-law principle.

11. 2. The parties acknowledge and agree that any controversies and disputes arising out of this License shall be decided exclusively by the courts of or having jurisdiction for Heidelberg, Germany, as far as legally permissible.

11. 3. This License is solely for Licensor's and Licensee's benefit. It is not for the benefit of any other person or entity.

Questions? For questions on Copyright Clearance Center accounts or website issues please contact springernaturesupport@copyright.com or +1-855-239-3415 (toll free in the US) or +1-978-646-2777. For questions on Springer Nature licensing please visit https://www.springernature.com/gp/partners/rights-permissions-third-party-distribution

Other Conditions:

Version 1.4 - Dec 2022

Questions? customercare@copyright.com.

Order Number: 1441516
Order Date: 24 Jan 2024

Payment Information

Ashutosh Bandyopadhyay
ashutoshasb@gmail.com
Payment method: Invoice

Billing Address:
Mr. Ashutosh Bandyopadhyay
Indian Institute of Technology G uwahati
NL102, Biosciences and Bioengi neering
Indian Institute of Technology G uwahati
North Guwahati
Guwahati, Assam 781039
India

+91 8777529851
ashutoshasb@gmail.com

Customer Location:
Mr. Ashutosh Bandyopadhyay
Indian Institute of Technology G uwahati
NL102, Biosciences and Bioengi neering
Indian Institute of Technology G uwahati
North Guwahati
Guwahati, Assam 781039
India

Order Details

1. Biofabrication

Billing Status: Open

Order License ID	1441516-1	**Type of Use**	Republish in a thesis/dissertation
Order detail status	Completed		
ISSN	1758-5090	**Publisher**	IOP Publishing
		Portion	Chapter/article

0.00 USD
Republication Permission

LICENSED CONTENT

Publication Title	Biofabrication	**Country**	United Kingdom of Great Britain and Northern Ireland
Author/Editor	Institute of Physics (Great Britain)	**Rightsholder**	IOP Publishing, Ltd
Date	01/01/2009	**Publication Type**	e-Journal
Language	English	**URL**	http://iopscience.iop.org/1758-5090

REQUEST DETAILS

Portion Type	Chapter/article	**Rights Requested**	Main product
Page Range(s)	1-17	**Distribution**	Worldwide
Total Number of Pages	17	**Translation**	Original language of publication
Format (select all that apply)	Print, Electronic	**Copies for the Disabled?**	No
Who Will Republish the Content?	Author of requested content	**Minor Editing Privileges?**	Yes
		Incidental Promotional Use?	No
Duration of Use	Life of current and all future editions	**Currency**	USD
Lifetime Unit Quantity	Up to 499		

NEW WORK DETAILS

Title	Silk Based Three Dimensional Bioprinting for Meniscus Tissue Engineering	**Institution Name**	Indian Institute of Technology Guwahati
		Expected Presentation Date	2024-04-30
Instructor Name	Prof. Biman B. Mandal		

ADDITIONAL DETAILS

The Requesting Person / Organization to Appear on the License	Ashutosh Bandyopadhyay

REQUESTED CONTENT DETAILS

Title, Description or Numeric Reference of the Portion(s)	Whole article	**Title of the Article / Chapter the Portion Is From**	A three-dimensional printed silk-based biomimetic tri-layered meniscus for potential patient-specific implantation
Editor of Portion(s)	N/A	**Author of Portion(s)**	Institute of Physics (Great Britain)
Volume / Edition	12	**Publication Date of Portion**	2019-10-21
Page or Page Range of Portion	1-17		

IOP Publishing, Ltd Terms and Conditions

These special terms and conditions are in addition to the standard terms and conditions for CCC's Republication Service and, together with those standard terms and conditions, govern the use of the Works. As the User you will make all reasonable efforts to contact the author(s) of the article which the Work is to be reused from, to seek consent for your intended use. Contacting one author who is acting expressly as authorised agent for their co-author(s) is acceptable. User will reproduce the following wording prominently alongside the Work: the source of the Work, including author, article title, title of journal, volume number, issue number (if relevant), page range (or first page if this is the only information available) and date of first publication; and a link back to the article (via DOI); and if practicable, and IN ALL CASES for new works published under any of the Creative Commons licences, the words "© IOP Publishing. Reproduced with permission. All rights reserved" Without the express permission of the author(s) and the Rightsholder of the article from which the Work is to be reused, User shall not use it in any way which, in the opinion of the Rightsholder, could: (i) distort or alter the author(s)' original intention(s) and meaning; (ii) be prejudicial to the honour or reputation of the author(s); and/or (iii) imply endorsement by the author(s) and/or the Rightsholder. This licence does not apply to any article which is credited to another source and which does not have the copyright line '© IOP Publishing Ltd'. User must check the copyright line of the article from which the Work is to be reused to check that IOP Publishing Ltd has all the necessary rights to be able to grant permission. User is solely responsible for identifying and obtaining separate licences and permissions from the copyright owner for reuse of any such third party material/figures which the Rightsholder is not the copyright owner of. The Rightsholder shall not reimburse any fees which User pays for a republication license for such third party content. This licence does not apply to any material/figure which is credited to another source in the Rightsholder's publication or has been obtained from a third party. User must check the Version of Record of the article from which the Work is to be reused, to check whether any of the material in the Work is third party material. Third party citations and/or copyright notices and/or permissions statements may not be included in any other version of the article from which the Work is to be reused and so cannot be relied upon by the User. User is solely responsible for identifying and obtaining separate licences and permissions from the copyright owner for reuse of any such third party material/figures where the Rightsholder is not the copyright owner. The Rightsholder shall not reimburse any fees which User pays for a republication license for such third party content. User and CCC acknowledge that the Rightsholder may, from time to time, make changes or additions to these special terms and conditions without express notification, provided that these shall not apply to permissions already secured and paid for by User prior to such change or addition. User acknowledges that the Rightsholder (which includes companies within its group and third parties for whom it publishes its titles) may make use of personal data collected through the service in the course of their business. If User is the author of the Work, User may automatically have the right to reuse it under the rights granted back when User transferred the copyright in the article to the Rightsholder. User should check the copyright form and the relevant author rights policy to check whether permission is required. If User is the author of the Work and does require permission for proposed reuse of the Work, User should select 'Author of requested content' as the Requestor Type. The Rightsholder shall not reimburse any fees which User pays for a republication license. If User is the author of the article which User wishes to reuse in User's thesis or dissertation, the republication licence covers the right to include the Version of Record of the article, provided it is not then shared or deposited online. User must include citation details. Where User wishes to share their thesis or dissertation online, they should remove the Version of Record before uploading it. User may include a Preprint or the Accepted Manuscript (after the embargo period) in the online version of the thesis or dissertation, provided they do so in accordance with the Rightsholder's policies on sharing Preprints or Accepted Manuscripts. User may need to obtain separate permission for any third party content included within the article. User must check this with the copyright owner of such third party content. Any online or commercial use of User's thesis or dissertation containing the article, including publication via ProQuest, would need to be expressly notified in writing to the Rightsholder at the time of request and would require separate written permission from the Rightsholder. As well as CCC, the Rightsholder shall have the right to bring any legal action that it deems necessary to enforce its rights should it consider that the Work infringes those rights in any way. For content reuse requests that qualify for permission under the STM Permissions Guidelines, which may be updated from time to time, the STM Permissions Guidelines supplement the terms and conditions contained in this license.

IOP Publishing, Ltd Special Terms and Conditions

When you transferred the copyright in your article to IOP, we granted back to you certain rights, including the right to include all or part of the Final Published Version of the article within any thesis or dissertation provided it is not then shared or deposited online. Full details can be found in our Author Rights Policy. If you are required by your institution to share your thesis/dissertation publicly (such as in an institutional repository), the Final Published Version would need to be removed prior to publication online or in print. Your institution should be able to withhold the IOP article section of your thesis from this version. However, you should still reference the article, include the abstract and provide a DOI link to it on IOPscience so that people know that it has been published. Please include citation details, "© IOP Publishing. Reproduced with permission. All rights reserved" and for online use, a link to the Version of Record. Please note you may need to obtain separate permission for any third party content you included within your article. If you do not wish to remove the IOP article section of your thesis, you also have the following alternative options: 1) Our Author Rights Policy allows authors to post the Accepted Manuscript in certain places after the embargo period has elapsed. This includes your institutional repository, subject to certain restrictions (please see the full terms and conditions in our Author Rights Policy linked in the signature of this email.). Therefore, an option may be to include your Accepted Manuscript article version in your thesis or dissertation, as it would allow you to place the unaltered dissertation onto your repository after the embargo period. Please note that your article is outside of its embargo period. An Embargo Period is 'a period of 12 months from the Date of Publication'. 2) A further option would be to include the Author's Original or Preprint version of the article, provided that you do so in line with our Preprint pre-publication policy.

Total Items: 1

Subtotal: 0.00 USD

Order Total: 0.00 USD

Marketplace Permissions General Terms and Conditions

The following terms and conditions ("General Terms"), together with any applicable Publisher Terms and Conditions, govern User's use of Works pursuant to the Licenses granted by Copyright Clearance Center, Inc. ("CCC") on behalf of the applicable Rightsholders of such Works through CCC's applicable Marketplace transactional licensing services (each, a "Service").

1) **Definitions.** For purposes of these General Terms, the following definitions apply:

"License" is the licensed use the User obtains via the Marketplace platform in a particular licensing transaction, as set forth in the Order Confirmation.

"Order Confirmation" is the confirmation CCC provides to the User at the conclusion of each Marketplace transaction. "Order Confirmation Terms" are additional terms set forth on specific Order Confirmations not set forth in the General Terms that can include terms applicable to a particular CCC transactional licensing service and/or any Rightsholder-specific terms.

"Rightsholder(s)" are the holders of copyright rights in the Works for which a User obtains licenses via the Marketplace platform, which are displayed on specific Order Confirmations.

"Terms" means the terms and conditions set forth in these General Terms and any additional Order Confirmation Terms collectively.

"User" or "you" is the person or entity making the use granted under the relevant License. Where the person accepting the Terms on behalf of a User is a freelancer or other third party who the User authorized to accept the General Terms on the User's behalf, such person shall be deemed jointly a User for purposes of such Terms.

"Work(s)" are the copyright protected works described in relevant Order Confirmations.

2) **Description of Service.** CCC's Marketplace enables Users to obtain Licenses to use one or more Works in accordance with all relevant Terms. CCC grants Licenses as an agent on behalf of the copyright rightsholder identified in the relevant Order Confirmation.

3) **Applicability of Terms.** The Terms govern User's use of Works in connection with the relevant License. In the event of any conflict between General Terms and Order Confirmation Terms, the latter shall govern. User acknowledges that Rightsholders have complete discretion whether to grant any permission, and whether to place any limitations on any grant, and that CCC has no right to supersede or to modify any such discretionary act by a Rightsholder.

4) **Representations; Acceptance.** By using the Service, User represents and warrants that User has been duly authorized by the User to accept, and hereby does accept, all Terms.

5) **Scope of License; Limitations and Obligations.** All Works and all rights therein, including copyright rights, remain the sole and exclusive property of the Rightsholder. The License provides only those rights expressly set forth in the terms and conveys no other rights in any Works

6) **General Payment Terms.** User may pay at time of checkout by credit card or choose to be invoiced. If the User chooses to be invoiced, the User shall: (i) remit payments in the manner identified on specific invoices, (ii) unless otherwise specifically stated in an Order Confirmation or separate written agreement, Users shall remit payments upon receipt of the relevant invoice from CCC, either by delivery or notification of availability of the invoice via the Marketplace platform, and (iii) if the User does not pay the invoice within 30 days of receipt, the User may incur a service charge of 1.5% per month or the maximum rate allowed by applicable law, whichever is less. While User may exercise the rights in the License immediately upon receiving the Order Confirmation, the License is automatically revoked and is null and void, as if it had never been issued, if CCC does not receive complete payment on a timely basis.

7) **General Limits on Use.** Unless otherwise provided in the Order Confirmation, any grant of rights to User (i) involves only the rights set forth in the Terms and does not include subsequent or additional uses, (ii) is non-exclusive and non-transferable, and (iii) is subject to any and all limitations and restrictions (such as, but not limited to, limitations on duration of use or circulation) included in the Terms. Upon completion of the licensed use as set forth in the Order Confirmation, User shall either secure a new permission for further use of the Work(s) or immediately cease any new use of the Work(s) and shall render inaccessible (such as by deleting or by removing or severing links or other locators) any further copies of the Work. User may only make alterations to the Work if and as expressly set forth in the Order Confirmation. No Work may be used in any way that is unlawful, including without limitation if such use would violate applicable sanctions laws or regulations, would be defamatory, violate the rights of third parties (including such third parties' rights of copyright, privacy, publicity, or other tangible or intangible property), or is otherwise illegal, sexually explicit, or obscene. In addition, User may not conjoin a Work with any other material that may result in damage to the reputation of the Rightsholder. Any unlawful use will render any licenses hereunder null and void. User agrees to inform CCC if it becomes aware of any infringement of any rights in a Work and to cooperate with any reasonable request of CCC or the Rightsholder in connection therewith.

8) **Third Party Materials.** In the event that the material for which a License is sought includes third party materials (such as photographs, illustrations, graphs, inserts and similar materials) that are identified in such material as having been used by permission (or a similar indicator), User is responsible for identifying, and seeking separate licenses (under this Service, if available, or otherwise) for any of such third party materials; without a separate license, User may not use such third party materials via the License.

9) **Copyright Notice.** Use of proper copyright notice for a Work is required as a condition of any License granted under the Service. Unless otherwise provided in the Order Confirmation, a proper copyright notice will read substantially as follows: "Used with permission of [Rightsholder's name], from [Work's title, author, volume, edition number and year of copyright]; permission conveyed through Copyright Clearance Center, Inc." Such notice must be provided in a reasonably legible font size and must be placed either on a cover page or in another location that any person, upon gaining access to the material which is the subject of a permission, shall see, or in the case of republication Licenses, immediately adjacent to the Work as used (for example, as part of a by-line or footnote) or in the place where substantially all other credits or notices for the new work containing the republished Work are located. Failure to include the required notice results in loss to the Rightsholder and CCC, and the User shall be liable to pay liquidated damages for each such failure equal to twice the use fee specified in the Order Confirmation, in addition to the use fee itself and any other fees and charges specified.

10) **Indemnity.** User hereby indemnifies and agrees to defend the Rightsholder and CCC, and their respective employees and directors, against all claims, liability, damages, costs, and expenses, including legal fees and expenses, arising out of any use of a Work beyond the scope of the rights granted herein and in the Order Confirmation, or any use of a Work which has been altered in any unauthorized way by User, including claims of defamation or infringement of rights of copyright, publicity, privacy, or other tangible or intangible property.

11) **Limitation of Liability.** UNDER NO CIRCUMSTANCES WILL CCC OR THE RIGHTSHOLDER BE LIABLE FOR ANY DIRECT, INDIRECT, CONSEQUENTIAL, OR INCIDENTAL DAMAGES (INCLUDING WITHOUT LIMITATION DAMAGES FOR LOSS OF BUSINESS PROFITS OR INFORMATION, OR FOR BUSINESS INTERRUPTION) ARISING OUT OF THE USE OR INABILITY TO USE A WORK, EVEN IF ONE OR BOTH OF THEM HAS BEEN ADVISED OF THE POSSIBILITY OF SUCH DAMAGES. In any event, the total liability of the Rightsholder and CCC (including their respective employees and directors) shall not exceed the total amount actually paid by User for the relevant License. User assumes full liability for the actions and omissions of its principals, employees, agents, affiliates, successors, and assigns.

12) **Limited Warranties.** THE WORK(S) AND RIGHT(S) ARE PROVIDED "AS IS." CCC HAS THE RIGHT TO GRANT TO USER THE RIGHTS GRANTED IN THE ORDER CONFIRMATION DOCUMENT. CCC AND THE RIGHTSHOLDER DISCLAIM ALL OTHER WARRANTIES RELATING TO THE WORK(S) AND RIGHT(S), EITHER EXPRESS OR IMPLIED, INCLUDING WITHOUT LIMITATION IMPLIED WARRANTIES OF MERCHANTABILITY OR FITNESS FOR A PARTICULAR PURPOSE. ADDITIONAL RIGHTS MAY BE REQUIRED TO USE ILLUSTRATIONS, GRAPHS, PHOTOGRAPHS, ABSTRACTS, INSERTS, OR OTHER PORTIONS OF THE WORK (AS OPPOSED TO THE ENTIRE WORK) IN A MANNER CONTEMPLATED BY USER; USER UNDERSTANDS AND AGREES THAT NEITHER CCC NOR THE RIGHTSHOLDER MAY HAVE SUCH ADDITIONAL RIGHTS TO GRANT.

13) **Effect of Breach.** Any failure by User to pay any amount when due, or any use by User of a Work beyond the scope of the License set forth in the Order Confirmation and/or the Terms, shall be a material breach of such License. Any breach not cured within 10 days of written notice thereof shall result in immediate termination of such License without further notice. Any unauthorized (but licensable) use of a Work that is terminated immediately upon notice thereof may be liquidated by payment of the Rightsholder's ordinary license price therefor; any unauthorized (and unlicensable) use that is not terminated immediately for any reason (including, for example, because materials containing the Work cannot reasonably be recalled) will be subject to all remedies available at law or in equity, but in no event to a payment of less than three times the Rightsholder's ordinary license price for the most closely analogous licensable use plus Rightsholder's and/or CCC's costs and expenses incurred in collecting such payment.

14) **Additional Terms for Specific Products and Services.** If a User is making one of the uses described in this Section 14, the additional terms and conditions apply:

a) ***Print Uses of Academic Course Content and Materials (photocopies for academic coursepacks or classroom handouts).*** For photocopies for academic coursepacks or classroom handouts the following additional terms apply:

i) The copies and anthologies created under this License may be made and assembled by faculty members individually or at their request by on-campus bookstores or copy centers, or by off-campus copy shops and other similar entities.

ii) No License granted shall in any way: (i) include any right by User to create a substantively non-identical copy of the Work or to edit or in any other way modify the Work (except by means of deleting material immediately preceding or following the entire portion of the Work copied) (ii) permit "publishing ventures" where any particular anthology would be systematically marketed at multiple institutions.

iii) Subject to any Publisher Terms (and notwithstanding any apparent contradiction in the Order Confirmation arising from data provided by User), any use authorized under the academic pay-per-use service is limited as follows:

A) any License granted shall apply to only one class (bearing a unique identifier as assigned by the institution, and thereby including all sections or other subparts of the class) at one institution;

B) use is limited to not more than 25% of the text of a book or of the items in a published collection of essays, poems or articles;

C) use is limited to no more than the greater of (a) 25% of the text of an issue of a journal or other periodical or (b) two articles from such an issue;

D) no User may sell or distribute any particular anthology, whether photocopied or electronic, at more than one institution of learning;

E) in the case of a photocopy permission, no materials may be entered into electronic memory by User except in order to produce an identical copy of a Work before or during the academic term (or analogous period) as to which any particular permission is granted. In the event that User shall choose to retain materials that are the subject of a photocopy permission in electronic memory for purposes of producing identical copies more than one day after such retention (but still within the scope of any permission granted), User must notify CCC of such fact in the applicable permission request and such retention shall constitute one copy actually sold for purposes of calculating permission fees due; and

F) any permission granted shall expire at the end of the class. No permission granted shall in any way include any right by User to create a substantively non-identical copy of the Work or to edit or in any other way modify the Work (except by means of deleting material immediately preceding or following the entire portion of the Work copied).

iv) Books and Records; Right to Audit. As to each permission granted under the academic pay-per-use Service, User shall maintain for at least four full calendar years books and records sufficient for CCC to determine the numbers of copies made by User under such permission. CCC and any representatives it may designate shall have the right to audit such books and records at any time during User's ordinary business hours, upon two days' prior notice. If any such audit shall determine that User shall have underpaid for, or underreported, any photocopies sold or by three percent (3%) or more, then User shall bear all the costs of any such audit; otherwise, CCC shall bear the costs of any such audit. Any amount determined by such audit to have been underpaid by User shall immediately be paid to CCC by User, together with interest thereon at the rate of 10% per annum from the date such amount was originally due. The provisions of this paragraph shall survive the termination of this License for any reason.

b) ***Digital Pay-Per-Uses of Academic Course Content and Materials (e-coursepacks, electronic reserves, learning management systems, academic institution intranets).*** For uses in e-coursepacks, posts in electronic reserves, posts in learning management systems, or posts on academic institution intranets, the following additional terms apply:

i) The pay-per-uses subject to this Section 14(b) include:

A) **Posting e-reserves, course management systems, e-coursepacks for text-based content,** which grants authorizations to import requested material in electronic format, and allows electronic access to this material to members of a designated college or university class, under the direction of an instructor designated by the college or university, accessible only under appropriate electronic controls (e.g., password);

B) **Posting e-reserves, course management systems, e-coursepacks for material consisting of photographs or other still images not embedded in text,** which grants not only the authorizations described in Section 14(b)(i)(A) above, but also the following authorization: to include the requested material in course materials for use consistent with Section 14(b)(i)(A) above, including any necessary resizing, reformatting or modification of the resolution of such requested material (provided that such modification does not alter the underlying editorial content or meaning of the requested material, and provided that the resulting modified content is used solely within the scope of, and in a manner consistent with, the particular authorization described in the Order Confirmation and the Terms), but not including any other form of manipulation, alteration or editing of the requested material;

C) **Posting e-reserves, course management systems, e-coursepacks or other academic distribution for audiovisual content,** which grants not only the authorizations described in Section 14(b)(i)(A) above, but also the following authorizations: (i) to include the requested material in course materials for use consistent with Section 14(b)(i)(A) above; (ii) to display and perform the requested material to such members of such class in the physical classroom or remotely by means of streaming media or other video formats; and (iii) to "clip" or reformat the requested material for purposes of time or content management or ease of delivery, provided that such "clipping" or reformatting does not alter the underlying editorial content or meaning of the requested material and that the resulting material is used solely within the scope of, and in a manner consistent with, the particular authorization described in the Order Confirmation and the Terms. Unless expressly set forth in the relevant Order Conformation, the License does not authorize any other form of manipulation, alteration or editing of the requested material.

ii) Unless expressly set forth in the relevant Order Confirmation, no License granted shall in any way: (i) include any right by User to create a substantively non-identical copy of the Work or to edit or in any other way modify the Work (except by means of deleting material immediately preceding or following the entire portion of the Work copied or, in the case of Works subject to Sections 14(b)(1)(B) or (C) above, as described in such Sections) (ii) permit "publishing ventures" where any particular course materials would be systematically marketed at multiple institutions.

iii) Subject to any further limitations determined in the Rightsholder Terms (and notwithstanding any apparent contradiction in the Order Confirmation arising from data provided by User), any use authorized under the electronic course content pay-per-use service is limited as follows:

A) any License granted shall apply to only one class (bearing a unique identifier as assigned by the institution, and thereby including all sections or other subparts of the class) at one institution;

B) use is limited to not more than 25% of the text of a book or of the items in a published collection of essays, poems or articles;

C) use is limited to not more than the greater of (a) 25% of the text of an issue of a journal or other periodical or (b) two articles from such an issue;

D) no User may sell or distribute any particular materials, whether photocopied or electronic, at more than one institution of learning;

E) electronic access to material which is the subject of an electronic-use permission must be limited by means of electronic password, student identification or other control permitting access solely to students and instructors in the class;

F) User must ensure (through use of an electronic cover page or other appropriate means) that any person, upon gaining electronic access to the material, which is the subject of a permission, shall see:

- a proper copyright notice, identifying the Rightsholder in whose name CCC has granted permission,
- a statement to the effect that such copy was made pursuant to permission,
- a statement identifying the class to which the material applies and notifying the reader that the material has been made available electronically solely for use in the class, and
- a statement to the effect that the material may not be further distributed to any person outside the class, whether by copying or by transmission and whether electronically or in paper form, and User must also ensure that such cover page or other means will print out in the event that the person accessing the material chooses to print out the material or any part thereof.

G) any permission granted shall expire at the end of the class and, absent some other form of authorization, User is thereupon required to delete the applicable material from any electronic storage or to block electronic access to the applicable material.

iv) Uses of separate portions of a Work, even if they are to be included in the same course material or the same university or college class, require separate permissions under the electronic course content pay-per-use Service. Unless otherwise provided in the Order Confirmation, any grant of rights to User is limited to use completed no later than the end of the academic term (or analogous period) as to which any particular permission is granted.

v) Books and Records; Right to Audit. As to each permission granted under the electronic course content Service, User shall maintain for at least four full calendar years books and records sufficient for CCC to determine the numbers of copies made by User under such permission. CCC and any representatives it may designate shall have the right to audit such books and records at any time during User's ordinary business hours, upon two days' prior notice. If any such audit shall determine that User shall have underpaid for, or underreported, any electronic copies used by three percent (3%) or more, then User shall bear all the costs of any such audit; otherwise, CCC shall bear the costs of any such audit. Any amount determined by such audit to have been underpaid by User shall immediately be paid to CCC by User, together with interest thereon at the rate of 10% per annum from the date such amount was originally due. The provisions of this paragraph shall survive the termination of this license for any reason.

c) ***Pay-Per-Use Permissions for Certain Reproductions (Academic photocopies for library reserves and interlibrary loan reporting) (Non-academic internal/external business uses and commercial document delivery).*** The License expressly excludes the uses listed in Section (c)(i)-(v) below (which must be subject to separate license from the applicable Rightsholder) for: academic photocopies for library reserves and interlibrary loan reporting; and non-academic internal/external business uses and commercial document delivery.

i) electronic storage of any reproduction (whether in plain-text, PDF, or any other format) other than on a transitory basis;

ii) the input of Works or reproductions thereof into any computerized database;

iii) reproduction of an entire Work (cover-to-cover copying) except where the Work is a single article;

iv) reproduction for resale to anyone other than a specific customer of User;

v) republication in any different form. Please obtain authorizations for these uses through other CCC services or directly from the rightsholder.

Any license granted is further limited as set forth in any restrictions included in the Order Confirmation and/or in these Terms.

d) ***Electronic Reproductions in Online Environments (Non-Academic-email, intranet, internet and extranet).*** For "electronic reproductions", which generally includes e-mail use (including instant messaging or other electronic transmission to a defined

group of recipients) or posting on an intranet, extranet or Intranet site (including any display or performance incidental thereto), the following additional terms apply:

i) Unless otherwise set forth in the Order Confirmation, the License is limited to use completed within 30 days for any use on the Internet, 60 days for any use on an intranet or extranet and one year for any other use, all as measured from the "republication date" as identified in the Order Confirmation, if any, and otherwise from the date of the Order Confirmation.

ii) User may not make or permit any alterations to the Work, unless expressly set forth in the Order Confirmation (after request by User and approval by Rightsholder); provided, however, that a Work consisting of photographs or other still images not embedded in text may, if necessary, be resized, reformatted or have its resolution modified without additional express permission, and a Work consisting of audiovisual content may, if necessary, be "clipped" or reformatted for purposes of time or content management or ease of delivery (provided that any such resizing, reformatting, resolution modification or "clipping" does not alter the underlying editorial content or meaning of the Work used, and that the resulting material is used solely within the scope of, and in a manner consistent with, the particular License described in the Order Confirmation and the Terms.

15) **Miscellaneous.**

a) User acknowledges that CCC may, from time to time, make changes or additions to the Service or to the Terms, and that Rightsholder may make changes or additions to the Rightsholder Terms. Such updated Terms will replace the prior terms and conditions in the order workflow and shall be effective as to any subsequent Licenses but shall not apply to Licenses already granted and paid for under a prior set of terms.

b) Use of User-related information collected through the Service is governed by CCC's privacy policy, available online at www.copyright.com/about/privacy-policy/.

c) The License is personal to User. Therefore, User may not assign or transfer to any other person (whether a natural person or an organization of any kind) the License or any rights granted thereunder; provided, however, that, where applicable, User may assign such License in its entirety on written notice to CCC in the event of a transfer of all or substantially all of User's rights in any new material which includes the Work(s) licensed under this Service.

d) No amendment or waiver of any Terms is binding unless set forth in writing and signed by the appropriate parties, including, where applicable, the Rightsholder. The Rightsholder and CCC hereby object to any terms contained in any writing prepared by or on behalf of the User or its principals, employees, agents or affiliates and purporting to govern or otherwise relate to the License described in the Order Confirmation, which terms are in any way inconsistent with any Terms set forth in the Order Confirmation, and/or in CCC's standard operating procedures, whether such writing is prepared prior to, simultaneously with or subsequent to the Order Confirmation, and whether such writing appears on a copy of the Order Confirmation or in a separate instrument.

e) The License described in the Order Confirmation shall be governed by and construed under the law of the State of New York, USA, without regard to the principles thereof of conflicts of law. Any case, controversy, suit, action, or proceeding arising out of, in connection with, or related to such License shall be brought, at CCC's sole discretion, in any federal or state court located in the County of New York, State of New York, USA, or in any federal or state court whose geographical jurisdiction covers the location of the Rightsholder set forth in the Order Confirmation. The parties expressly submit to the personal jurisdiction and venue of each such federal or state court.

Last updated October 2022

ELSEVIER

Photocrosslinkable silk-based bioinks embedded with growth factor loaded microspheres towards cell-free 3D printing approach for biomimetic regeneration of meniscal tissue

Author: Ashutosh Bandyopadhyay,Biman B. Mandal

Publication: Applied Materials Today

Publisher: Elsevier

Date: February 2024

JOHN WILEY AND SONS LICENSE
TERMS AND CONDITIONS

Jun 13, 2024

This Agreement between Ashutosh Bandyopadhyay, Indian Institute of Technology Guwahati ("You") and John Wiley and Sons ("John Wiley and Sons") consists of your license details and the terms and conditions provided by John Wiley and Sons and Copyright Clearance Center.

License Number	5806881126927
License date	Jun 13, 2024
Licensed Content Publisher	John Wiley and Sons
Licensed Content Publication	Advanced Biology
Licensed Content Title	Photo-Polymerizable Autologous Growth-Factor Loaded Silk-Based Biomaterial-Inks toward 3D Printing-Based Regeneration of Meniscus Tears
Licensed Content Author	Ashutosh Bandyopadhyay, Baishali Ghibhela, Sayanti Shome, et al
Licensed Content Date	Feb 25, 2024
Licensed Content Volume	8
Licensed Content Issue	5
Licensed Content Pages	22
Type of use	Dissertation/Thesis

Requestor type	Author of this Wiley article
Format	Print and electronic
Portion	Full article
Will you be translating?	No
Title of new work	Silk Based Three Dimensional Bioprinting for Meniscus Tissue Engineering
Institution name	Indian Institute of Technology Guwahati
Expected presentation date	Jun 2024
The Requesting Person / Organization to Appear on the License	Ashutosh Bandyopadhyay, Indian Institute of Technology Guwahati
Requestor Location	Indian Institute of Technology Guwahati NL102, Biosciences and Bioengineering Indian Institute of Technology Guwahati North Guwahati Guwahati, Assam 781039 India Attn: Indian Institute of Technology Guwahati
Publisher Tax ID	EU826007151
Total	0.00 USD
Terms and Conditions	

TERMS AND CONDITIONS

This copyrighted material is owned by or exclusively licensed to John Wiley & Sons, Inc. or one of its group companies (each a"Wiley Company") or handled on behalf of a society with which a Wiley Company has exclusive publishing rights in relation to a particular work (collectively "WILEY"). By clicking "accept" in connection with completing this licensing transaction, you agree that the following terms and conditions apply to this transaction (along with the billing and payment terms and conditions established by the

Copyright Clearance Center Inc., ("CCC's Billing and Payment terms and conditions"), at the time that you opened your RightsLink account (these are available at any time at http://myaccount.copyright.com).

Terms and Conditions

- The materials you have requested permission to reproduce or reuse (the "Wiley Materials") are protected by copyright.

- You are hereby granted a personal, non-exclusive, non-sub licensable (on a stand-alone basis), non-transferable, worldwide, limited license to reproduce the Wiley Materials for the purpose specified in the licensing process. This license, **and any CONTENT (PDF or image file) purchased as part of your order,** is for a one-time use only and limited to any maximum distribution number specified in the license. The first instance of republication or reuse granted by this license must be completed within two years of the date of the grant of this license (although copies prepared before the end date may be distributed thereafter). The Wiley Materials shall not be used in any other manner or for any other purpose, beyond what is granted in the license. Permission is granted subject to an appropriate acknowledgement given to the author, title of the material/book/journal and the publisher. You shall also duplicate the copyright notice that appears in the Wiley publication in your use of the Wiley Material. Permission is also granted on the understanding that nowhere in the text is a previously published source acknowledged for all or part of this Wiley Material. Any third party content is expressly excluded from this permission.

- With respect to the Wiley Materials, all rights are reserved. Except as expressly granted by the terms of the license, no part of the Wiley Materials may be copied, modified, adapted (except for minor reformatting required by the new Publication), translated, reproduced, transferred or distributed, in any form or by any means, and no derivative works may be made based on the Wiley Materials without the prior permission of the respective copyright owner.**For STM Signatory Publishers clearing permission under the terms of the STM Permissions Guidelines only, the terms of the license are extended to include subsequent editions and for editions in other languages, provided such editions are for the work as a whole in situ and does not involve the separate exploitation of the permitted figures or extracts,** You may not alter, remove or suppress in any manner any copyright, trademark or other notices displayed by the Wiley Materials. You may not license, rent, sell, loan, lease, pledge, offer as security, transfer or assign the Wiley Materials on a stand-alone basis, or any of the rights granted to you hereunder to any other person.

- The Wiley Materials and all of the intellectual property rights therein shall at all times remain the exclusive property of John Wiley & Sons Inc, the Wiley Companies, or their respective licensors, and your interest therein is only that of having possession of and the right to reproduce the Wiley Materials pursuant to Section 2 herein during the continuance of this Agreement. You agree that you own no right, title or interest in or to the Wiley Materials or any of the intellectual property rights therein. You shall have no rights hereunder other than the license as provided for above in Section 2. No right, license or interest to any trademark, trade name, service mark or other branding ("Marks") of WILEY or its licensors is granted hereunder, and you agree that you shall not assert any such right, license or

interest with respect thereto

- NEITHER WILEY NOR ITS LICENSORS MAKES ANY WARRANTY OR REPRESENTATION OF ANY KIND TO YOU OR ANY THIRD PARTY, EXPRESS, IMPLIED OR STATUTORY, WITH RESPECT TO THE MATERIALS OR THE ACCURACY OF ANY INFORMATION CONTAINED IN THE MATERIALS, INCLUDING, WITHOUT LIMITATION, ANY IMPLIED WARRANTY OF MERCHANTABILITY, ACCURACY, SATISFACTORY QUALITY, FITNESS FOR A PARTICULAR PURPOSE, USABILITY, INTEGRATION OR NON-INFRINGEMENT AND ALL SUCH WARRANTIES ARE HEREBY EXCLUDED BY WILEY AND ITS LICENSORS AND WAIVED BY YOU.

- WILEY shall have the right to terminate this Agreement immediately upon breach of this Agreement by you.

- You shall indemnify, defend and hold harmless WILEY, its Licensors and their respective directors, officers, agents and employees, from and against any actual or threatened claims, demands, causes of action or proceedings arising from any breach of this Agreement by you.

- IN NO EVENT SHALL WILEY OR ITS LICENSORS BE LIABLE TO YOU OR ANY OTHER PARTY OR ANY OTHER PERSON OR ENTITY FOR ANY SPECIAL, CONSEQUENTIAL, INCIDENTAL, INDIRECT, EXEMPLARY OR PUNITIVE DAMAGES, HOWEVER CAUSED, ARISING OUT OF OR IN CONNECTION WITH THE DOWNLOADING, PROVISIONING, VIEWING OR USE OF THE MATERIALS REGARDLESS OF THE FORM OF ACTION, WHETHER FOR BREACH OF CONTRACT, BREACH OF WARRANTY, TORT, NEGLIGENCE, INFRINGEMENT OR OTHERWISE (INCLUDING, WITHOUT LIMITATION, DAMAGES BASED ON LOSS OF PROFITS, DATA, FILES, USE, BUSINESS OPPORTUNITY OR CLAIMS OF THIRD PARTIES), AND WHETHER OR NOT THE PARTY HAS BEEN ADVISED OF THE POSSIBILITY OF SUCH DAMAGES. THIS LIMITATION SHALL APPLY NOTWITHSTANDING ANY FAILURE OF ESSENTIAL PURPOSE OF ANY LIMITED REMEDY PROVIDED HEREIN.

- Should any provision of this Agreement be held by a court of competent jurisdiction to be illegal, invalid, or unenforceable, that provision shall be deemed amended to achieve as nearly as possible the same economic effect as the original provision, and the legality, validity and enforceability of the remaining provisions of this Agreement shall not be affected or impaired thereby.

- The failure of either party to enforce any term or condition of this Agreement shall not constitute a waiver of either party's right to enforce each and every term and condition of this Agreement. No breach under this agreement shall be deemed waived or excused by either party unless such waiver or consent is in writing signed by the party granting such waiver or consent. The waiver by or consent of a party to a breach of any provision of this Agreement shall not operate or be construed as a waiver of or consent to any other or subsequent breach by such other party.

- This Agreement may not be assigned (including by operation of law or otherwise) by you without WILEY's prior written consent.

- Any fee required for this permission shall be non-refundable after thirty (30) days from receipt by the CCC.

- These terms and conditions together with CCC's Billing and Payment terms and conditions (which are incorporated herein) form the entire agreement between you and WILEY concerning this licensing transaction and (in the absence of fraud) supersedes all prior agreements and representations of the parties, oral or written. This Agreement may not be amended except in writing signed by both parties. This Agreement shall be binding upon and inure to the benefit of the parties' successors, legal representatives, and authorized assigns.

- In the event of any conflict between your obligations established by these terms and conditions and those established by CCC's Billing and Payment terms and conditions, these terms and conditions shall prevail.

- WILEY expressly reserves all rights not specifically granted in the combination of (i) the license details provided by you and accepted in the course of this licensing transaction, (ii) these terms and conditions and (iii) CCC's Billing and Payment terms and conditions.

- This Agreement will be void if the Type of Use, Format, Circulation, or Requestor Type was misrepresented during the licensing process.

- This Agreement shall be governed by and construed in accordance with the laws of the State of New York, USA, without regards to such state's conflict of law rules. Any legal action, suit or proceeding arising out of or relating to these Terms and Conditions or the breach thereof shall be instituted in a court of competent jurisdiction in New York County in the State of New York in the United States of America and each party hereby consents and submits to the personal jurisdiction of such court, waives any objection to venue in such court and consents to service of process by registered or certified mail, return receipt requested, at the last known address of such party.

WILEY OPEN ACCESS TERMS AND CONDITIONS

Wiley Publishes Open Access Articles in fully Open Access Journals and in Subscription journals offering Online Open. Although most of the fully Open Access journals publish open access articles under the terms of the Creative Commons Attribution (CC BY) License only, the subscription journals and a few of the Open Access Journals offer a choice of Creative Commons Licenses. The license type is clearly identified on the article.

The Creative Commons Attribution License

The Creative Commons Attribution License (CC-BY) allows users to copy, distribute and transmit an article, adapt the article and make commercial use of the article. The CC-BY license permits commercial and non-

Creative Commons Attribution Non-Commercial License

The Creative Commons Attribution Non-Commercial (CC-BY-NC)License permits use, distribution and reproduction in any medium, provided the original work is properly cited and is not used for commercial purposes.(see below)

Creative Commons Attribution-Non-Commercial-NoDerivs License

The Creative Commons Attribution Non-Commercial-NoDerivs License (CC-BY-NC-ND) permits use, distribution and reproduction in any medium, provided the original work is properly cited, is not used for commercial purposes and no modifications or adaptations are made. (see below)

Use by commercial "for-profit" organizations

Use of Wiley Open Access articles for commercial, promotional, or marketing purposes requires further explicit permission from Wiley and will be subject to a fee.

Further details can be found on Wiley Online Library
http://olabout.wiley.com/WileyCDA/Section/id-410895.html

Other Terms and Conditions:

v1.10 Last updated September 2015

Questions? customercare@copyright.com.

Silk-based injectable photocurable hydrogel loaded with autologous growth factors for patient-specific repair of meniscal defects in vivo

Author: Ashutosh Bandyopadhyay,Baishali Ghibhela,Sayanti Shome,Debajyoti Pal,Samit K. Nandi,Biman B. Mandal

Publication: Applied Materials Today

Publisher: Elsevier

Date: April 2024